

**Curtin University**

School of Electrical Engineering, Computing and Mathematical Sciences

---

**Synthesis of Metal Boranes as Solid-State Electrolytes for Next  
Generation Battery Applications**

**Diego Holanda Pereira de Souza**

**0000-0001-7587-8326**

**This thesis is presented for the Degree of  
Doctor of Philosophy  
of  
Curtin University**

**October 2022**

# DECLARATION

---

To the best of my knowledge and belief this thesis contains no material previously published by any other person except where due acknowledgement has been made.

This thesis contains no material which has been accepted for the award of any other degree or diploma in any university.

Name: Diego Holanda Pereira de Souza

Signature:

Date: 13 October 2022

# COPYRIGHT STATEMENT

---

I have obtained permission from the copyright owners to use any third-party copyright material reproduced in the thesis, or to use any of my own published work in which the copyright is held by another party.

*Dedicated to my parents, José and Rosângela, my fiancée, Adriana, and my sister, Tatiana.*

*“Be brave. Take risks. Nothing can substitute experience.”*

(Paulo Coelho)

*“One day, you will leave this world behind. So live a life you will remember.”*

(Avicii)

# ACKNOWLEDGMENTS

---

I would like to initially thank my parents for the whole support and incentive they have given me towards my education. They are my safe harbour, and I am thankful for everything they have done for me in my life.

A special thanks to my fiancée, Dr Adriana Pires Vieira, who has been present in my life since my master's degree by giving me extra support and motivation to achieve my goals. I am also thankful for the encouragement and help she gave me to achieve some awards during my Ph.D. She is also my best friend, and I will always be thankful for her patience and companionship during all these years.

I would like to sincerely thank my Ph.D. supervisor, Assoc Prof Mark Paskevicius, for giving me the opportunity to work in such high-impact research project, for always being available to discuss the project, for encouraging me towards my Ph.D., for his patience and for helping me on what I needed. It was great to work with him, and I will always be very thankful for all his help. I also would like to acknowledge my co-supervisors, Dr Terry Humphries and Prof Craig Buckley, for their great effort to provide an outstanding research environment and their contributions towards my Ph.D. research project and its outcomes.

I also want to express my deepest gratitude to everyone from the Hydrogen Storage Research Group, researchers: Dr Adriana, Dr Kasper, Dr Jacob, Dr Mauricio, Dr Yurong, Dr Yu, and Ph.D. students: Enrico, Lucas, and Sruthy (now doctors), my borane friends, Amanda and Tom (who shared with me the "happiest" moments working with boron-chemistry), Ainee (and Daniel), Lucie (also my coffee, beach and surfing friend), Aneeka, El, Bithiah, Praveen, and Simon. I also would like to thank Jason and the other Ph.D. students from the building 120 ("the dungeon"). I also thank all my friends outside university, in Australia and in Brazil, who shared great moments with me during my Ph.D.

I acknowledge the facilities, scientific and technical assistance from Curtin University and John de Laeter Centre, the support from Curtin-Australian Technology Network (ATN) South American Scholarship and Tuition Fee-Offset Scholarship through Curtin University. I also thank Dr Thomas Becker from Curtin University for his help in Raman data collection, and Dr

Jacob Martin for his work on the elaboration of the front cover of my published paper at Sustainable Energy and Fuels journal.

I acknowledge the University of Western Australia, especially Dr Stephen Moggach for his help in single-crystal XRD data collection and analysis, and Dr Gareth Nealon for his help in solid-state NMR data collection. I also acknowledge the Australian Synchrotron, especially Dr Anita D'Angelo for XRD experiment conduction and data collection. I also thank Dr Anton Gradišek from the Jožef Stefan Institute in Slovenia, for solid-state NMR experiment conduction and data collection and analysis.

Muito obrigado a todos!

# STATEMENT OF CONTRIBUTIONS

---

**CHAPTER 1:** Presents an introduction and literature review of the Ph.D. project, which was originally written by myself with suggestions and corrections made by Assoc Prof Mark Paskevicius, Dr Terry Humphries and Prof Craig Buckley.

**CHAPTER 2:** Presents the experimental section of the thesis, including materials and methodology and a brief overview of the characterisation techniques that were used to conduct the project. It was originally written by myself with suggestions and corrections made by Assoc Prof Mark Paskevicius, Dr Terry Humphries and Prof Craig Buckley.

**CHAPTER 3:** Presents the paper entitled “Hydrated Alkali-B<sub>11</sub>H<sub>14</sub> Salts as Potential Solid-State Electrolytes”, which was originally written by myself with a revision made by all co-authors. This paper has been published at the Journal of Materials Chemistry A (<https://doi.org/10.1039/d1ta01551f>). An additional statement that details the co-authors’ contributions can be found at the end of this thesis (Appendix B).

**CHAPTER 4:** Presents the paper entitled “Hydrated Lithium *nido*-Boranes for Solid-Liquid Hybrid Batteries”, which was originally written by myself with a revision made by all co-authors. This paper has been published at the Sustainable Energy and Fuels Journal (<https://doi.org/10.1039/d2se00843b>). An additional statement that details the co-authors’ contributions can be found at the end of this thesis (Appendix B).

**CHAPTER 5:** Presents the paper entitled “Na<sub>2</sub>B<sub>11</sub>H<sub>13</sub> and Na<sub>11</sub>(B<sub>11</sub>H<sub>14</sub>)<sub>3</sub>(B<sub>11</sub>H<sub>13</sub>)<sub>4</sub> as Potential Solid-State Electrolytes for Na-Ion Batteries”, which was originally written by myself with a revision made by all co-authors. This paper has been published at the Dalton Transactions Journal (<https://doi.org/10.1039/d2dt01943d>). An additional statement that details the co-authors’ contributions can be found at the end of this thesis (Appendix B).



**CHAPTER 6:** Presents the conclusion of the Ph.D. thesis and suggestions for future work based on the outcomes of the project, which was originally written by myself with suggestions and corrections made by Assoc Prof Mark Paskevicius, Dr Terry Humphries and Prof Craig Buckley.

---

Diego Holanda Pereira de Souza  
(Ph.D. Candidate's Signature)

---

Mark Paskevicius  
(Supervisor's Signature)

# ABSTRACT

---

The replacement of the liquid electrolyte of conventional batteries with solid ionic conductors has been presented as a promising strategy for the development of energy storage devices (solid-state batteries) with increased safety, energy density, durability and reduced costs. Metal-boranes have shown promising features as solid-state electrolytes, due to their high ionic conductivity properties and good compatibility with alkali-metal anodes. However, more research needs to be conducted in order to establish cost-effective synthetic processes and to improve their properties as solid-state electrolytes, such as enhanced ionic conductivity at room temperature and stability against electrode materials. Therefore, the main objectives of this thesis are to optimise the syntheses of different metal-boranes, to work on strategies to improve their ionic conductivity, such as mechanical modification, coordination with water and anion mixing, to characterise and to investigate their potential to be used as solid-state electrolytes.

$MB_{11}H_{14} \cdot (H_2O)_n$ , ( $M = Li$  and  $Na$ ) and anhydrous  $KB_{11}H_{14}$  had their synthetic process optimised via reaction of  $(CH_3)_3NHB_{11}H_{14}$  with a strong alkaline aqueous solution of  $MOH$  ( $M = Li, Na$  or  $K$ ). All three samples decompose at temperatures higher than  $200\text{ }^\circ\text{C}$  with consequent release of  $H_2$ .  $KB_{11}H_{14}$  undergoes a polymorphic structural transition upon heating at  $\approx 130\text{ }^\circ\text{C}$  from triclinic ( $P\bar{1}$ ) to cubic ( $Fm\bar{3}m$ ).  $LiB_{11}H_{14} \cdot (H_2O)_n$  and  $NaB_{11}H_{14} \cdot (H_2O)_n$  were indexed in a cubic polymorph ( $Fm\bar{3}m$ ). They exhibit high ionic conductivities at room temperature (RT),  $1.8 \times 10^{-4}\text{ S cm}^{-1}$  and  $1.1 \times 10^{-3}\text{ S cm}^{-1}$ , respectively, and conductivity at sub-zero temperatures, such as  $-30\text{ }^\circ\text{C}$ . They also present an oxidative stability limit of  $2.1\text{ V vs. Li}^+/\text{Li}$  and  $2.6\text{ V vs. Na}^+/\text{Na}$ , respectively.  $KB_{11}H_{14}$  exhibits lower ionic conductivity results than  $LiB_{11}H_{14} \cdot (H_2O)_n$  and  $NaB_{11}H_{14} \cdot (H_2O)_n$ , due to its larger cation size. This salt has its ionic conductivity enhanced after assuming the high temperature (HT) disordered structure, and reaches  $1.2 \times 10^{-4}\text{ S cm}^{-1}$  at  $150\text{ }^\circ\text{C}$ . All three samples,  $LiB_{11}H_{14} \cdot (H_2O)_n$ ,  $NaB_{11}H_{14} \cdot (H_2O)_n$  and  $KB_{11}H_{14}$ , were individually ball-milled for 12 hours in an attempt to increase ionic conductivity properties by inducing defects in the structure. However, only  $KB_{11}H_{14}$  showed a more significant improvement of the ionic conductivity by  $\approx 1$  order of magnitude after mechanical modification.

Samples of  $\text{LiB}_{11}\text{H}_{14}$  with different water content in the crystal structure,  $\text{LiB}_{11}\text{H}_{14}\cdot 2\text{H}_2\text{O}$ ,  $\alpha\text{-LiB}_{11}\text{H}_{14}\cdot(\text{H}_2\text{O})_n$  ( $n < 2$ ) and anhydrous  $\text{LiB}_{11}\text{H}_{14}$ , were synthesised in order to investigate the influence of water on the properties of the material. They were prepared via reaction of recrystallised  $(\text{CH}_3)_3\text{NHB}_{11}\text{H}_{14}$  with an aqueous solution of  $\text{LiOH}$ . Thermal analysis of the solid samples show that  $\text{LiB}_{11}\text{H}_{14}\cdot 2\text{H}_2\text{O}$  melts at  $\approx 70^\circ\text{C}$ , which classifies it as an ionic liquid, whereas  $\alpha\text{-LiB}_{11}\text{H}_{14}\cdot(\text{H}_2\text{O})_n$  undergoes a polymorphic phase transition near the same temperature. Rietveld refinement of  $\alpha\text{-LiB}_{11}\text{H}_{14}\cdot(\text{H}_2\text{O})_n$  at RT reveals that the sample is formed by a mixture of at least three  $\text{LiB}_{11}\text{H}_{14}$  polymorphic structures, and at HT, it assumes a cubic (space group  $I\bar{a}\bar{3}d$ ) polymorphic phase. Anhydrous  $\text{LiB}_{11}\text{H}_{14}$  undergoes a polymorphic phase change at  $112^\circ\text{C}$ , and all three samples decompose at temperatures higher than  $200^\circ\text{C}$ . The ionic conductivity observed for all three samples at  $30^\circ\text{C}$  is in the order of  $10^{-6}\text{ S cm}^{-1}$ , and only  $\alpha\text{-LiB}_{11}\text{H}_{14}\cdot(\text{H}_2\text{O})_n$  reaches a liquid-like ionic conductivity at  $60^\circ\text{C}$  ( $1.2 \times 10^{-2}\text{ S cm}^{-1}$ ) owing to its polymorphic phase transition. The oxidative stability limit observed for  $\alpha\text{-LiB}_{11}\text{H}_{14}\cdot(\text{H}_2\text{O})_n$  is  $2.8\text{ V vs. Li}^+/\text{Li}$ . The stability of this sample against Li metal was also assessed through galvanostatic cycling at  $60^\circ\text{C}$  with the addition of traces of either the ionic liquid (IL)  $\text{LiB}_{11}\text{H}_{14}\cdot 2\text{H}_2\text{O}$  or a liquid electrolyte (LE) at their interfaces. Battery tests were also performed using  $\alpha\text{-LiB}_{11}\text{H}_{14}\cdot(\text{H}_2\text{O})_n$  as the solid-state electrolyte (SSE) and  $\text{TiS}_2$  as the cathode with addition of a liquid electrolyte at the interface ( $\text{Li}/\text{LE}/\text{SSE}/\text{SSE}+\text{TiS}_2$ ), which retained 83% of its capacity from its first cycle at  $0.4\text{ C}$  after 50 cycles.

The synthesis of  $\text{Na}_2\text{B}_{11}\text{H}_{13}$  was optimised through reaction of recrystallised  $(\text{CH}_3)_3\text{NHB}_{11}\text{H}_{14}$  with  $\text{NaH}$  in THF.  $\text{Na}_{11}(\text{B}_{11}\text{H}_{14})_3(\text{B}_{11}\text{H}_{13})_4$  was also prepared in order to investigate the influence of anion mixing on the properties of the material as SSE. The mixed-anion solid-solution was synthesised via reaction of recrystallised  $(\text{CH}_3)_3\text{NHB}_{11}\text{H}_{14}$  with  $\text{NaOH}$  in aqueous solution.  $\text{Na}_2\text{B}_{11}\text{H}_{13}$  undergoes a polymorphic phase transition at  $\approx 170^\circ\text{C}$ , and assumes a body-centred cubic structure, indexed in the space group  $Pm\bar{3}n$ . The sample  $\text{Na}_{11}(\text{B}_{11}\text{H}_{14})_3(\text{B}_{11}\text{H}_{13})_4$  partially stabilises the HT  $\text{Na}_2\text{B}_{11}\text{H}_{13}$  polymorph at RT, which enhances its ionic conductivity.  $\text{Na}_2\text{B}_{11}\text{H}_{13}$  exhibits an ionic conductivity of  $2.5 \times 10^{-7}\text{ S cm}^{-1}$  at  $30^\circ\text{C}$ , whereas the mixed-anion solid-solution  $\text{Na}_{11}(\text{B}_{11}\text{H}_{14})_3(\text{B}_{11}\text{H}_{13})_4$  shows an increase of  $\approx 2$  orders of magnitude at the same temperature ( $4.7 \times 10^{-5}\text{ S cm}^{-1}$  at  $30^\circ\text{C}$ ). This result is also higher than the ionic conductivity observed for anhydrous  $\text{NaB}_{11}\text{H}_{14}$  at the same temperature ( $2 \times 10^{-6}\text{ S cm}^{-1}$ ). After assuming

the HT polymorph,  $\text{Na}_2\text{B}_{11}\text{H}_{13}$  reaches an ionic conductivity of  $7.7 \times 10^{-3} \text{ S cm}^{-1}$  at  $200 \text{ }^\circ\text{C}$ . Both samples exhibit an oxidative stability limit of  $2.1 \text{ V vs. Na}^+/\text{Na}$ .

All metal-boranes here synthesised demonstrate promising features for further research and application as solid-state electrolytes in batteries.

# Ph.D. ACHIEVEMENTS

---

## PUBLICATIONS

1. D. H. P. Souza, K.T. Møller, S.A. Moggach, T.D. Humphries, A.M. D'Angelo, C.E. Buckley, M. Paskevicius, Hydrated Alkali-B<sub>11</sub>H<sub>14</sub> Salts as Potential Solid-State Electrolytes, *J. Mater. Chem. A*. 9 (2021) 15027–15037. <https://doi.org/10.1039/d1ta01551f>.
2. D. H. P. Souza, T.D. Humphries, Y. Liu, A. Gradišek, A.M. D'Angelo, C.E. Buckley, M. Paskevicius, Hydrated Lithium *nido*-Boranes for Solid-Liquid Hybrid Batteries, *Sustain. Energy Fuels*. 6 (2022) 4614–4625. <https://doi.org/10.1039/D2SE00843B>.
3. Front cover, *Sustain. Energy Fuels*. 6 (2022) 4541–4542. <https://doi.org/10.1039/D2SE90067J>.
4. D. H. P. Souza, A.M. D'Angelo, T.D. Humphries, C.E. Buckley, M. Paskevicius, Na<sub>2</sub>B<sub>11</sub>H<sub>13</sub> and Na<sub>11</sub>(B<sub>11</sub>H<sub>14</sub>)<sub>3</sub>(B<sub>11</sub>H<sub>13</sub>)<sub>4</sub> as Potential Solid-State Electrolytes for Na-Ion Batteries, *Dalton Trans.* 51 (2022) 13848–13857. <https://doi.org/10.1039/D2DT01943D>.

## MEDIA PUBLICATIONS

1. D. H. P. Souza, How new batteries can help address the global warming crisis, Fairfax, 2021. <https://www.canberratimes.com.au/story/7363579/how-new-batteries-can-help-address-the-global-warming-crisis/>
2. Radio interview for RTR FM 92.1. <https://rtrfm.com.au/story/2021-pitch-it-competition-award-diego-holanda-pereira-de-souza/>

## CONFERENCES

1. D. H. P. Souza, K.T. Møller, S.A. Moggach, T.D. Humphries, C.E. Buckley, M. Paskevicius. *nido*-Borate Salts as Solid-State Electrolytes in Batteries. *Australian Institute of Physics Congress* (Nov 2020). Perth – Australia.
2. Attendance at the Universities Australia Conference 2021 to receive the Universities Australia Award for the Pitch it Clever Competition. *Universities Australia Conference* (Jul 2021). Canberra – Australia.

3. D. H. P. Souza, C.E. Buckley, M. Paskevicius. Lithium Boron-Hydrogen Salts as Battery Electrolytes. *Lithium Battery and Energy Metals Conference* (Sep 2021). Perth – Australia.
4. D. H. P. Souza, T.D. Humphries, C.E. Buckley, M. Paskevicius. New Solid-State Materials for Lithium Ion Battery Technology. *Australian Institute of Physics Congress* (Nov 2021). Perth – Australia.
5. D. H. P. Souza, C.E. Buckley, M. Paskevicius. Hydrated Metal Boranes for Solid-State Batteries. *Euroboron Conference* (Jul 2022). Barcelona – Spain.

## **AWARDS**

1. Merit-based Curtin – Australian Technology Network Ph.D. Scholarship.
2. University Australia Award 2021 – Pitch it Clever.  
<https://www.youtube.com/watch?v=Gq7UT75VVNY>
3. Curtin Visualise your Thesis 2021. <https://doi.org/10.6084/m9.figshare.16585628.v1>
4. Runner-up Best Small Talk 2021 Australian Institute of Physics conference.
5. Persolkelly Future Scientist Award 2022.

# LIST OF FIGURES

---

<b>Figure 1.1.</b> Renewable power capacity increase worldwide from 2016 to 2021. Data was obtained from IRENA’s renewable energy statistics [4].	2
<b>Figure 1.2.</b> Types of energy storage technologies based on the kind of stored energy and examples. PCM and CSP stand for Phase Change Materials and Concentrated Solar Power, respectively. Reproduced with permission [5]. Copyright 2018, Elsevier.	3
<b>Figure 1.3.</b> Schematic representation of a conventional battery with a liquid electrolyte. Upon discharge the ions and electrons flow from the anode to the cathode.	4
<b>Figure 1.4.</b> Type of rechargeable batteries and their respective year of creation, type of electrode materials and electrochemical reactions. Reproduced and adapted with permission [9]. Copyright 2008, Springer Nature.	4
<b>Figure 1.5.</b> Schematic representation of a sodium-sulphur battery with its main components. Reproduced with permission [5]. Copyright 2018, Elsevier.	5
<b>Figure 1.6.</b> Schematic representation of a Li-ion battery. Li intercalated in the layers of graphene is used as the anode, and a layered structure of LiCoO <sub>2</sub> is used as the cathode. An organic liquid electrolyte is used to move Li <sup>+</sup> between the electrodes. Reproduced with permission [5]. Copyright 2018, Elsevier.	7
<b>Figure 1.7.</b> Schematic representation of a battery with a solid electrolyte constituting a SSB. During discharge the ions and electrons flow from the anode to the cathode.	7
<b>Figure 1.8.</b> Schematic representation of a solid-state battery with the main requirements for a material to be used as solid-state electrolyte in practical applications. Reproduced with permission [22]. Copyright 2018, Elsevier.	8
<b>Figure 1.9.</b> A) Schematic representation of cation migration in solid inorganic electrolytes through Schottky (vacancies) and Frenkel (interstitial) defects and grain boundary. Reproduced and adapted with permission [23]. Copyright 2020, Springer Nature. B) Paddle-wheel mechanism represented by the anion reorientation dynamics of a B <sub>12</sub> H <sub>12</sub> <sup>2-</sup> structure. Reproduced and adapted with permission [26]. Copyright 2017, American Chemical Society.	9

**Figure 1.10.** Schematic representation of lithium dendrite formation and penetration in liquid-electrolyte-batteries (A, B) and solid-state electrolyte batteries (C, D). The reduction of  $\text{Li}^+$  ions at the grain boundaries, which can become a pathway for electrons (yellow) owing to their small band-gap, of a solid-state polycrystalline electrolyte forms Li filaments (blue), which propagates and lead to a short circuit. Reproduced with permission [30]. Copyright 2021, Springer Nature.....10

**Figure 1.11.** Schematic representation of Li stripping at a constant current in a Li/SSE system.  $\text{Li}^+$  ions are injected into the SSE, which can form Li vacancies in the electrode. Vacancy accumulation near the interface leads to the formation of large voids and reduced Li/SSE contact points, which concentrates current and accelerates contact loss. Reproduced with permission [32]. Copyright 2020, Elsevier. ....10

**Figure 1.12.** Summary of the properties observed for the main classes of materials investigated for application as solid-state electrolytes. ESW, PEO and ASSB stand for Electrochemical Stability Window, Polyethylene Oxide, and All-Solid-State-Batteries, respectively. Reproduced with permission [18]. Copyright 2020, Elsevier. ....11

**Figure 1.13.** The three most common classes of borane structures: *closo*-boranes, as in  $\text{B}_{12}\text{H}_{12}^{2-}$ , *nido*-boranes, as in  $\text{B}_{11}\text{H}_{13}^{2-}$ , and *arachno*-boranes, as in  $\text{B}_{10}\text{H}_{15}^-$ . Reproduced and adapted with permission. [48]. Copyright 2009, Springer Nature. ....13

**Figure 1.14.** Solid-state  $\text{Li}^+$  (left) [53,58–61] and  $\text{Na}^+$  (right) [59,61–64] conductivity of some common boron-hydrogen materials as a function of temperature. The liquid electrolyte  $\text{LiBF}_4/\text{EMIBF}_4$  [57] and the solid-electrolyte  $\text{Na-}\beta\text{-Al}_2\text{O}_3$  [46] (dashed lines) were added for comparison. ....14

**Figure 1.15.** Solid-state  $\text{Li}^+$  (left) [60,83–85] and  $\text{Na}^+$  (right) [61,62,79,86–88] conductivity of some mixed-anion boron-hydrogen materials. The ionic liquid electrolyte  $\text{LiBF}_4/\text{EMIBF}_4$  [57] and the solid-electrolyte  $\text{Na-}\beta\text{-Al}_2\text{O}_3$  [46] (dashed lines) were added for comparison. ....19

**Figure 2.1** A) Reaction set-up used to synthesise  $\text{NaB}_{11}\text{H}_{14}\cdot(\text{C}_6\text{H}_{14}\text{O}_3)_n$  in a three-neck round-bottom flask equipped with a thermometer, a mechanical stirrer and a dropping funnel under a constant stream of argon from a Schlenk line. B) Resulting suspension of yellow liquid ( $\text{NaB}_{11}\text{H}_{14}\cdot(\text{C}_6\text{H}_{14}\text{O}_3)_n$ ) and white powder ( $\text{NaBr}$ ) after completion of reaction. ....37

**Figure 2.2** A) Solid powder of  $\text{NaB}_{11}\text{H}_{14}\cdot(\text{C}_6\text{H}_{14}\text{O}_3)_n$ . B) Solid powder of  $(\text{CH}_3)_3\text{NHB}_{11}\text{H}_{14}$ . ....38



<b>Figure 2.3</b> Custom-made Schlenk flask to allow filtration of mixtures in an inert atmosphere. The solid is represented in orange and the liquid in yellow. Reproduced with permission [8]. Copyright 2018, American Chemical Society. ....	41
<b>Figure 2.4</b> ‘L-shaped’ quartz NMR tube containing $\approx 40$ mg of sample used to investigate the $^{11}\text{B}$ spin-lattice NMR relaxation rates. ....	43
<b>Figure 2.5</b> Two different methods of production of X-rays. A) X-ray tube [18]. B) Synchrotron. The electrons are initially accelerated in the linear accelerator (LinAc), which are then transferred to the booster ring to increase energy before moving to the storage ring. Reproduced and adapted with permission [19]. Copyright 2021, Springer Nature.....	45
<b>Figure 2.6</b> Bragg’s law illustration. Reproduced and adapted with permission [20]. Copyright 2010, Elsevier.....	45
<b>Figure 2.7</b> Illustration of the method used to select and transfer a single-crystal to a capillary inside an argon glovebox for further single-crystal XRD analysis.....	48
<b>Figure 2.8</b> Schematic representation of a DSC/TGA.....	49
<b>Figure 2.9</b> Relationship between voltage and current as a function of time of an ideal resistor in AC circuit. It is said that voltage and current are in phase as both reach their maximum and minimum at the same time [37]. ....	52
<b>Figure 2.10</b> Current response to applied AC potential as a function of time demonstrating the resulting phase shift. Reproduced with permission [38]. Copyright 2019, Springer Nature. .	53
<b>Figure 2.11</b> Nyquist plots and their schematic equivalent circuit model for (a) a resistor, (b) a capacitor, (c) a capacitor and a resistor in series, (d) a resistor and a capacitor in parallel. Reproduced and adapted with permission [34]. Copyright 2018, Elsevier.....	54
<b>Figure 2.12</b> Representation of a typical Nyquist plot observed for solid electrolytes in a symmetric cell with ion-blocking electrodes [40], and its correspondent Randles circuit model. Reproduced and adapted with permission from [41]. Copyright 2013, Royal Society of Chemistry.....	55
<b>Figure 2.13</b> BOLA™ PTFE (polytetrafluoroethylene) ‘Swagelok-type’ Teflon cell assembly and cross-sectional view. The electrochemical cell is formed with a pellet of the solid-state electrolyte (SSE) sandwiched between two gold foils and pressed between stainless steel (SS) electrodes. A spring is placed between SS rods to allow for a uniform pressure and possible expansion of the cell during heating [45]. PTFE is used for its high temperature resistance ( $\approx 260$ °C) and its electrical resistance. ....	56

**Figure 2.14** a) Voltage profile and the corresponding interfacial (Int), bulk and grain boundary (GB) resistances during stripping/plating experiment on a Li/LLZO/Li symmetric cell at low stack pressure. b) Schematic representation of dissolution (stripping) process with resulting pore formation and reduction of contact area between Li and SSE, and c) schematic representation of deposition (plating) process. Reproduced with permission from [50]. Copyright 2019, American Chemical Society. ....61

**Figure 2.15** Schematic representation of the three different cells prepared with  $\alpha$ -LiB<sub>11</sub>H<sub>14</sub>·(H<sub>2</sub>O)<sub>n</sub> as SSE to conduct galvanostatic stripping/plating cycling experiment. A) Li/ $\alpha$ -LiB<sub>11</sub>H<sub>14</sub>·(H<sub>2</sub>O)<sub>n</sub>/Li in a coin cell, B) Li/LE/ $\alpha$ -LiB<sub>11</sub>H<sub>14</sub>·(H<sub>2</sub>O)<sub>n</sub>/LE/Li in a Swagelok-type cell (LE = liquid electrolyte, 1.0 M LiPF<sub>6</sub> EC/DMC (v/v = 50/50)), C) Li/IL/ $\alpha$ -LiB<sub>11</sub>H<sub>14</sub>·(H<sub>2</sub>O)<sub>n</sub>/IL/Li in a Swagelok-type cell (IL = ionic liquid, LiB<sub>11</sub>H<sub>14</sub>·2H<sub>2</sub>O). ....61

**Figure 2.16** Coin cell assembly and cross-sectional view. The electrochemical cell is formed with a nickel foam (a soft separator), a spacer, and a pellet of the solid-state electrolyte (SSE) sandwiched between two lithium foils that are all pressed between coin cases. ....62

**Figure 2.17** Schematic representation of the solid-liquid hybrid batteries prepared for the conduction of the battery tests at 60 °C. A) Li/LE/ $\alpha$ -LiB<sub>11</sub>H<sub>14</sub>·(H<sub>2</sub>O)<sub>n</sub>/ $\alpha$ -LiB<sub>11</sub>H<sub>14</sub>·(H<sub>2</sub>O)<sub>n</sub>+TiS<sub>2</sub> cell prepared with addition of one drop of 1.0 M LiPF<sub>6</sub> EC/DMC (v/v = 50/50) on the interface Li/SSE. B) Li/IL/ $\alpha$ -LiB<sub>11</sub>H<sub>14</sub>·(H<sub>2</sub>O)<sub>n</sub>/IL/ $\alpha$ -LiB<sub>11</sub>H<sub>14</sub>·(H<sub>2</sub>O)<sub>n</sub>+TiS<sub>2</sub> cell prepared with addition of 1 mg of LiB<sub>11</sub>H<sub>14</sub>·2H<sub>2</sub>O on each interface. ....64

**Figure 3.1** Spectroscopic characterisation of (CH<sub>3</sub>)<sub>3</sub>NHB<sub>11</sub>H<sub>14</sub>. (A) <sup>11</sup>B{<sup>1</sup>H} NMR spectrum (128 MHz) in CD<sub>3</sub>CN.  $\delta$  (B<sub>11</sub>H<sub>14</sub><sup>-</sup>) = -14.2, -16.0 and -16.8 ppm (B) FTIR spectrum with stretching modes at 3165 (<sup>+</sup>N-H), 2495 (B-H), and 970 cm<sup>-1</sup> (C-N<sup>+</sup>), and bending modes at 1466 (CH<sub>3</sub>), 1448 (CH<sub>3</sub>), 1385 (CH<sub>3</sub>), 1413 (<sup>+</sup>N-H) and 1032 cm<sup>-1</sup> (B-H) [45]. ....83

**Figure 3.2** XRPD pattern ( $\lambda_{\text{CuK}\alpha} = 1.54056 \text{ \AA}$ ) for (CH<sub>3</sub>)<sub>3</sub>NHB<sub>11</sub>H<sub>14</sub> at room temperature. ....84

**Figure 3.3** (A) <sup>11</sup>B{<sup>1</sup>H} and (B) <sup>11</sup>B NMR spectra (D<sub>2</sub>O, 128 MHz) of aqueous solution resulting from the reaction of (CH<sub>3</sub>)<sub>3</sub>NHB<sub>11</sub>H<sub>14</sub> with LiOH after heating. B<sub>11</sub>H<sub>13</sub><sup>2-</sup> is represented by the signals at -20.6 and -31.7 ppm [46]. Additional resonances are also observed from B(OH)<sub>4</sub><sup>-</sup> at 1.62 ppm [47] and BH<sub>4</sub><sup>-</sup> at -41.9 ppm [48], which are expected to be formed in boron based aqueous solutions with high pH. ....84

**Figure 3.4** <sup>11</sup>B {<sup>1</sup>H} NMR spectrum (128 MHz) in D<sub>2</sub>O of aqueous solution of Li<sub>2</sub>B<sub>11</sub>H<sub>13</sub> after reducing its pH with addition of 1 mol L<sup>-1</sup> HCl solution to 10 (blue spectrum), 7.5 (green spectrum), 5.5 (red spectrum) and 4.5 (black spectrum). ....85

**Figure 3.5**  $^{11}\text{B}\{^1\text{H}\}$  NMR spectrum (128 MHz) of diethyl ether layer (top) in  $\text{DMSO-}d_6$  after conducting a liquid-liquid extraction of the aqueous solution at pH 4.5, and  $^{11}\text{B}\{^1\text{H}\}$  NMR spectrum (128 MHz) of the aqueous layer in  $\text{D}_2\text{O}$  after performing the extraction (bottom). The resonances at  $\delta = -14.2, -16.0$  and  $-16.8$  ppm in the top  $^{11}\text{B}\{^1\text{H}\}$  NMR spectrum represent  $\text{B}_{11}\text{H}_{14}^-$ . Boric acid is observed at  $\delta = 19.4$  ppm in the aqueous layer (bottom spectrum), and the small triplet represent remaining  $\text{B}_{11}\text{H}_{14}^-$  that was not extracted by diethyl ether. ....86

**Figure 3.6**  $^{11}\text{B}\{^1\text{H}\}$  NMR spectra (128 MHz) of  $\text{LiB}_{11}\text{H}_{14}$ ,  $\text{NaB}_{11}\text{H}_{14}$ , and  $\text{KB}_{11}\text{H}_{14}$  in  $\text{DMSO-}d_6$  (top to bottom), which show the presence of  $\text{B}_{11}\text{H}_{14}^-$  anion in all spectra, observed at  $\delta = -14.2, -16.0$  and  $-16.8$  ppm. The resonances at  $\delta = 18.8, -9.6, -10.7, -23.3, -29.1,$  and  $-40.0$  ppm observed in the spectra of  $\text{LiB}_{11}\text{H}_{14}$  and  $\text{NaB}_{11}\text{H}_{14}$  represent  $\text{B}_{11}\text{H}_{13}\text{OH}^-$ , which is formed as a by-product in the reaction.....87

**Figure 3.7**  $^{11}\text{B}\{^1\text{H}\}$  NMR spectra (128 MHz) in  $\text{DMSO-}d_6$  of  $\text{LiB}_{11}\text{H}_{14}$  obtained after drying the organic layer that was extracted from aqueous solution at (A) pH 4.5 and (B) pH 7.5 at  $80^\circ\text{C}$ . The amount of  $\text{B}_{11}\text{H}_{13}\text{OH}^-$  is approximately 12 mol% in (A) and 4 mol% in (B) based on integration of the NMR peaks.....88

**Figure 3.8** FTIR transmittance spectra of solid-state (A)  $\text{LiB}_{11}\text{H}_{14}\cdot(\text{H}_2\text{O})_n$ , (B)  $\text{NaB}_{11}\text{H}_{14}\cdot(\text{H}_2\text{O})_n$ , and (C)  $\text{KB}_{11}\text{H}_{14}$ . The wide band observed at  $3200 - 3800\text{ cm}^{-1}$  (O–H stretching) and the sharp band at  $1610\text{ cm}^{-1}$  (H–O–H bending) in (A) and (B) confirm the presence of water in the compounds [54]. The B–H stretching frequency is identified as a sharp peak at  $\approx 2500\text{ cm}^{-1}$  and the B–H bending mode is observed at  $\approx 1020\text{ cm}^{-1}$  for all the samples [53].....89

**Figure 3.9** FTIR spectra of (a)  $\text{B}_{11}\text{H}_{14}^-$  and (b)  $\text{B}_{11}\text{H}_{13}\text{OH}^-$  calculated at the B31LYP/aug-cc-pvdz level of theory. ....90

**Figure 3.10** TDA-MS data at  $m/z$  18 (water) of solid-state  $\text{LiB}_{11}\text{H}_{14}\cdot(\text{H}_2\text{O})_n$ ,  $\text{NaB}_{11}\text{H}_{14}\cdot(\text{H}_2\text{O})_n$ , and  $\text{KB}_{11}\text{H}_{14}$  samples. Approximately 5 mg of each compound was used for analysis and heated from  $25$  to  $300^\circ\text{C}$  ( $\Delta T/\Delta t = 2^\circ\text{C min}^{-1}$ ) under high vacuum ( $< 8 \times 10^{-4}$  mbar).....91

**Figure 3.11** TDA-MS data at  $m/z$  2 (hydrogen) of solid-state  $\text{LiB}_{11}\text{H}_{14}\cdot(\text{H}_2\text{O})_n$ ,  $\text{NaB}_{11}\text{H}_{14}\cdot(\text{H}_2\text{O})_n$ , and  $\text{KB}_{11}\text{H}_{14}$  samples. Approximately 5 mg of each compound was used for analysis and heated from  $25$  to  $300^\circ\text{C}$  ( $\Delta T/\Delta t = 2^\circ\text{C min}^{-1}$ ) under high vacuum ( $< 8 \times 10^{-4}$  mbar).....91

**Figure 3.12** TGA-DSC measurement of  $\text{LiB}_{11}\text{H}_{14}\cdot(\text{H}_2\text{O})_n$  in the temperature range  $100 - 250^\circ\text{C}$  ( $\Delta T/\Delta t = 10^\circ\text{C min}^{-1}$ , Ar flow =  $40\text{ mL min}^{-1}$ ). Approximately 7 mg of compound was used for analysis. A mass loss of 1.5% is observed between  $150$  and  $205^\circ\text{C}$ , which may be attributed

to water and hydrogen release, and 2.4% between 205 and 225 °C from hydrogen release, as a result of decomposition of the material. ....	92
<b>Figure 3.13</b> TGA-DSC measurement of $\text{NaB}_{11}\text{H}_{14}\cdot(\text{H}_2\text{O})_n$ in the temperature range 100 – 250 °C ( $\Delta T/\Delta t = 10 \text{ }^\circ\text{C min}^{-1}$ , Ar flow = 40 mL $\text{min}^{-1}$ ). Approximately 7 mg of compound was used for analysis. A mass loss of 1.4% is observed between 100 and 205 °C, which may be attributed to water release, and 2.9% between 205 and 225 °C from hydrogen and water release, as a result of decomposition of the material. ....	92
<b>Figure 3.14</b> TGA-DSC measurement of $\text{KB}_{11}\text{H}_{14}$ in the temperature range 100 – 250 °C ( $\Delta T/\Delta t = 10 \text{ }^\circ\text{C min}^{-1}$ , Ar flow = 40 mL $\text{min}^{-1}$ ). Approximately 7 mg of compound was used for analysis. The sample undergoes a phase transition at 140 °C represented by the endothermic peak on DSC plot and loses 2.9% of mass between 200 and 220 °C from hydrogen release, as a result of decomposition of the material. ....	93
<b>Figure 3.15</b> DSC plots for pristine and ball-milled (B.M.) $\text{KB}_{11}\text{H}_{14}$ upon heating and cooling between 40 and 170 °C ( $\Delta T/\Delta t = 10 \text{ }^\circ\text{C min}^{-1}$ ) under 40 mL $\text{min}^{-1}$ of argon flow. ....	94
<b>Figure 3.16</b> XRPD pattern for $\text{LiB}_{11}\text{H}_{14}\cdot(\text{H}_2\text{O})_n$ , $\text{NaB}_{11}\text{H}_{14}\cdot(\text{H}_2\text{O})_n$ , and $\text{KB}_{11}\text{H}_{14}$ at room temperature. $\lambda = 1.54056 \text{ \AA}$ . Asterisks at $2\theta = 31.8^\circ$ and $45.5^\circ$ in the $\text{NaB}_{11}\text{H}_{14}\cdot(\text{H}_2\text{O})_n$ pattern represent inadvertent NaCl contamination. ....	94
<b>Figure 3.17</b> XRPD data and Rietveld refinement plot for $\text{KB}_{11}\text{H}_{14}$ . Experimental data as red circles, calculated diffraction pattern as black line and the difference plot in blue. Tick marks show positions (listed top to bottom) for (a) $\alpha\text{-KB}_{11}\text{H}_{14}$ ( $P1$ , 86.9(2) wt%); (b) $\text{K}_2\text{SO}_4$ ( $Pnam$ , 13.1(2) wt%). $R_{\text{wp}} = 4.85$ . $\lambda = 0.563476(5) \text{ \AA}$ . ....	97
<b>Figure 3.18</b> Crystal structure of $\alpha\text{-KB}_{11}\text{H}_{14}$ ( $P1$ ). K (blue), B (green), H (white). Structure viewed (a) along the $a$ -axis and (b) along the $b$ -axis. ....	98
<b>Figure 3.19</b> <i>In-situ</i> synchrotron XRPD data of $\text{KB}_{11}\text{H}_{14}$ during heating and cooling, $\lambda = 0.563516(6) \text{ \AA}$ . A reversible polymorphic phase transition is seen near 135 °C on heating and 85 °C on subsequent cooling. A minor impurity of $\text{K}_2\text{SO}_4$ is present with persistent peaks across all temperatures (red line). ....	99
<b>Figure 3.20</b> XRPD pattern for $\text{NaB}_{11}\text{H}_{14}\cdot(\text{H}_2\text{O})_n$ at room temperature (top), at $-100 \text{ }^\circ\text{C}$ (centre) and at room temperature after natural heating (bottom). The sample was mounted in a capillary under argon atmosphere and measured with a Mo $\text{K}\alpha$ source ( $\lambda = 0.7093 \text{ \AA}$ ). Asterisks at $14.5^\circ$ , $20.5^\circ$ and $24.2^\circ$ represent inadvertent NaCl contamination. ....	100

**Figure 3.21** Crystal structure of  $\text{LiB}_{11}\text{H}_{14}\cdot 2\text{H}_2\text{O}$  ( $C2/c$ ). Li (blue), B (green), O (red) and H (white). The structure is viewed along the  $b$ -axis (top) and  $a$ -axis (bottom) demonstrating the lithium coordination that alternate along the  $b$ -axis.....101

**Figure 3.22** Solid-state ionic conductivity of  $\text{NaB}_{11}\text{H}_{14}\cdot(\text{C}_6\text{H}_{14}\text{O}_3)_n$ ,  $\text{LiB}_{11}\text{H}_{14}\cdot(\text{H}_2\text{O})_n$  (before and after B.M.),  $\text{NaB}_{11}\text{H}_{14}\cdot(\text{H}_2\text{O})_n$  (before and after B.M.),  $\text{KB}_{11}\text{H}_{14}$  (before and after B.M.), and  $\text{LiBF}_4/\text{EMIBF}_4$  [59]. .....105

**Figure 3.23** Magnified Nyquist plot of pristine  $\text{LiB}_{11}\text{H}_{14}\cdot(\text{H}_2\text{O})_n$  (left) and  $\text{NaB}_{11}\text{H}_{14}\cdot(\text{H}_2\text{O})_n$  (right) in the high-frequency region at 0, 25, and 50 °C. ....106

**Figure 3.24** Nyquist plot of pristine and ball-milled (B.M.)  $\text{KB}_{11}\text{H}_{14}$  at 100 °C (left) and 160 °C (right) from 100 Hz to 1 MHz. ....107

**Figure 3.25** TPPA of  $\text{KB}_{11}\text{H}_{14}$  heated from room temperature to 170 °C ( $\Delta T/\Delta t = 10 \text{ }^\circ\text{C min}^{-1}$ ). A volume increase of the pellet can be observed at  $\approx 120\text{-}140 \text{ }^\circ\text{C}$ . ....108

**Figure 3.26** Ionic conductivity of pristine and ball-milled (two measurements)  $\text{KB}_{11}\text{H}_{14}$  with data points between 110 and 130 °C. All measurements show a drop in ionic conductivity in this range of temperature, which is associated to the order-disorder phase transition.....109

**Figure 3.27** Arrhenius plots of ionic conductivities of  $\text{LiB}_{11}\text{H}_{14}\cdot(\text{H}_2\text{O})_n$ ,  $\text{NaB}_{11}\text{H}_{14}\cdot(\text{H}_2\text{O})_n$ , and  $\text{NaB}_{11}\text{H}_{14}\cdot(\text{C}_6\text{H}_{14}\text{O}_3)_n$  compared with other Li (left) and Na (right) single anion boron-hydrogen materials:  $\text{LiCB}_{11}\text{H}_{12}$  [70],  $\text{LiCB}_9\text{H}_{10}$  [9],  $\text{LiBH}_4$  [22],  $\text{Li}_2\text{B}_{12}\text{H}_{12}$  [71],  $\text{LiNaB}_{12}\text{H}_{12}$  [72], Li-7-CB<sub>10</sub>H<sub>13</sub> [21],  $\text{NaCB}_{11}\text{H}_{12}$  [70],  $\text{Na}_2\text{B}_{12}\text{H}_{12}$  [22],  $\text{Na}_2\text{B}_{10}\text{H}_{10}$  [69],  $\text{NaBH}_4$  [69], Na-7-CB<sub>10</sub>H<sub>13</sub> [21], Na-7,8-C<sub>2</sub>B<sub>9</sub>H<sub>12</sub> [21],  $\text{NaCB}_9\text{H}_{10}$  [20].  $\text{NaB}_{11}\text{H}_{14}$  (A) and (C) are the commercial version of  $\text{NaB}_{11}\text{H}_{14}$  that were obtained from two different batches [21], and (B) is a sample of  $\text{NaB}_{11}\text{H}_{14}$  that was synthesised using decaborane [25]. The solid lines represent the ionic conductivity of the materials synthesised in this work.....111

**Figure 3.28** Arrhenius plots of ionic conductivities of  $\text{LiB}_{11}\text{H}_{14}\cdot(\text{H}_2\text{O})_n$ ,  $\text{NaB}_{11}\text{H}_{14}\cdot(\text{H}_2\text{O})_n$ , and  $\text{NaB}_{11}\text{H}_{14}\cdot(\text{C}_6\text{H}_{14}\text{O}_3)_n$  compared with other Li (left) [9,73,74] and Na (right) [1,25,75–78] mixed anion boron-hydrogen solid-state electrolytes. The solid lines represent the ionic conductivity of the materials synthesised in this work. ....112

**Figure 3.29** Linear Sweep Voltammograms of (A)  $\text{Li}/\text{LiB}_{11}\text{H}_{14}\cdot(\text{H}_2\text{O})_n/\text{LiB}_{11}\text{H}_{14}\cdot(\text{H}_2\text{O})_n+\text{C}/\text{Pt}/\text{Al}$  and (B)  $\text{Na}/\text{NaB}_{11}\text{H}_{14}\cdot(\text{H}_2\text{O})_n/\text{NaB}_{11}\text{H}_{14}\cdot(\text{H}_2\text{O})_n+\text{C}/\text{Pt}/\text{Al}$  cells at a scan rate of  $50 \mu\text{V s}^{-1}$  at 60 °C between 1.5 and 8.0 V (1<sup>st</sup> run) and 1.5 and 4.5 V (2<sup>nd</sup> run). The black dashed lines represent the linear regression lines fitted to the background and to the anodic current to obtain the oxidation potential.....113

**Figure 3.30** Linear Sweep Voltammogram of Li/LiBH<sub>4</sub>/LiBH<sub>4</sub>+C/Pt/Al cell at a scan rate of 50 μV s<sup>-1</sup> at 60 °C between 1.5 and 4.5 V. The black dashed lines represent the linear regression lines fitted to the background and to the anodic current to obtain the oxidation potential. ....114

**Figure 3.31** XRPD profiles of LiB<sub>11</sub>H<sub>14</sub>·(H<sub>2</sub>O)<sub>n</sub> (left) and NaB<sub>11</sub>H<sub>14</sub>·(H<sub>2</sub>O)<sub>n</sub> (right) at room temperature before (black) and after (red) second run of LSV experiment. Asterisks at 2θ = 30.2° in the LiB<sub>11</sub>H<sub>14</sub>·(H<sub>2</sub>O)<sub>n</sub> and at 31.8° in the NaB<sub>11</sub>H<sub>14</sub>·(H<sub>2</sub>O)<sub>n</sub> patterns represent inadvertent LiCl and NaCl contamination, respectively. ....115

**Figure 4.1** Raman spectra of solid-state LiB<sub>11</sub>H<sub>14</sub>·2H<sub>2</sub>O (black), α-LiB<sub>11</sub>H<sub>14</sub>·(H<sub>2</sub>O)<sub>n</sub> (red), and LiB<sub>11</sub>H<sub>14</sub> (green). ....136

**Figure 4.2** <sup>11</sup>B{<sup>1</sup>H} NMR spectra (128 MHz) of LiB<sub>11</sub>H<sub>14</sub>·2H<sub>2</sub>O (black), α-LiB<sub>11</sub>H<sub>14</sub>·(H<sub>2</sub>O)<sub>n</sub> (red), and LiB<sub>11</sub>H<sub>14</sub> (green) in CD<sub>3</sub>CN. The resonances at δ = -14.2, -16.0 and -16.8 ppm that are observed in all spectra are due to B<sub>11</sub>H<sub>14</sub><sup>-</sup>. B<sub>11</sub>H<sub>13</sub>OH<sup>-</sup> (δ = 18.8, -9.6, -10.7, -23.3, -29.1, and -40.0 ppm) can be identified in the spectra of LiB<sub>11</sub>H<sub>14</sub> by small intensity peaks. ....137

**Figure 4.3** <sup>11</sup>B{<sup>1</sup>H} NMR spectra (128 MHz) of filtrate in CD<sub>3</sub>CN (top) and precipitate in D<sub>2</sub>O (bottom) after mixing α-LiB<sub>11</sub>H<sub>14</sub>·(H<sub>2</sub>O)<sub>n</sub> in acetonitrile. The <sup>11</sup>B{<sup>1</sup>H} NMR spectrum of the filtrate shows the presence of B<sub>11</sub>H<sub>14</sub><sup>-</sup> anion (δ = -14.2, -16.0 and -16.8 ppm), whereas the precipitate shows the presence of a borate species at 11.8 ppm. ....138

**Figure 4.4** Solid-state <sup>11</sup>B MAS NMR spectra of α-LiB<sub>11</sub>H<sub>14</sub>·(H<sub>2</sub>O)<sub>n</sub> (red) and b-LiB<sub>11</sub>H<sub>14</sub>·(H<sub>2</sub>O)<sub>n</sub> (black), which was added for comparison to show the position of B<sub>11</sub>H<sub>14</sub><sup>-</sup> (δ = -15.4 and -17.7 ppm), at RT [42,54]. The presence of a borate species can be seen in the spectrum of α-LiB<sub>11</sub>H<sub>14</sub>·(H<sub>2</sub>O)<sub>n</sub> at ≈ 1 ppm. ....139

**Figure 4.5** XRPD pattern for LiB<sub>11</sub>H<sub>14</sub>·2H<sub>2</sub>O, α-LiB<sub>11</sub>H<sub>14</sub>·(H<sub>2</sub>O)<sub>n</sub>, and LiB<sub>11</sub>H<sub>14</sub> at room temperature with magnified insets in the range of 2θ = 12 – 22°. λ = 1.54056 Å. ....140

**Figure 4.6** XRPD (λ = 1.54056 Å) pattern (left) and <sup>11</sup>B{<sup>1</sup>H} NMR spectrum (128 MHz) in D<sub>2</sub>O (right) for the product of the reaction of LiOH and H<sub>3</sub>BO<sub>3</sub> at RT. Red stars in the XRPD pattern at 2θ = 20.5° and 32.6° represent unreacted LiOH and the broad diffraction halos at ≈ 10° and ≈ 20° 2θ are due to the sample holder, but may mask other amorphous halos. ....141

**Figure 4.7** XRPD (λ = 1.54056 Å) and Rietveld refinement of LiB<sub>11</sub>H<sub>14</sub>·2H<sub>2</sub>O. R<sub>wp</sub> = 3.71 %. Green and blue lines represent Bragg position from space group C2/c (LiB<sub>11</sub>H<sub>14</sub>·2H<sub>2</sub>O) [42], 97.0(3) wt%, and the indexed space group Pbcn (LiB<sub>11</sub>H<sub>14</sub>·(H<sub>2</sub>O)<sub>n</sub>), 3.0(3) wt%, respectively. ....142

**Figure 4.8** DSC/TGA measurement of  $\text{LiB}_{11}\text{H}_{14}\cdot 2\text{H}_2\text{O}$  in the temperature range 30 – 300 °C ( $\Delta T/\Delta t = 10 \text{ }^\circ\text{C min}^{-1}$ , Ar flow = 40 mL  $\text{min}^{-1}$ ). Approximately 7 mg of sample was used for analysis. The melting event is characterised by the endothermic feature at 73 °C, and the exothermic peak at 233 °C represents its decomposition accompanied by a mass loss of 12.5(2)%. .....142

**Figure 4.9** TPPA of  $\text{LiB}_{11}\text{H}_{14}\cdot 2\text{H}_2\text{O}$  heated from RT to 230 °C ( $\Delta T/\Delta t = 10 \text{ }^\circ\text{C min}^{-1}$ ). The sample starts melting at  $\approx 60 \text{ }^\circ\text{C}$ , solidifies again upon heating, and starts decomposing at  $\approx 220 \text{ }^\circ\text{C}$ , when it becomes a yellow solid. ....143

**Figure 4.10** Left: SR-XRPD ( $\lambda = 0.590827(4) \text{ \AA}$ ) and Rietveld refinement of sample  $\alpha$ - $\text{LiB}_{11}\text{H}_{14}\cdot(\text{H}_2\text{O})_n$  at RT,  $R_{\text{wp}} = 5.37\%$ . Brown, green and blue lines indicate Bragg positions from space groups  $Pbca$  ( $\text{LiB}_{11}\text{H}_{14}$ ) [32], 70.0(1) wt%,  $C2/c$  ( $\text{LiB}_{11}\text{H}_{14}\cdot 2\text{H}_2\text{O}$ ) [42], 4.10(11) wt%, and the indexed space group  $Pbcn$  ( $\text{LiB}_{11}\text{H}_{14}\cdot(\text{H}_2\text{O})_n$ ), 25.9(1) wt%, respectively. Right: SR-XRPD ( $\lambda = 0.590827(4) \text{ \AA}$ ) and Rietveld refinement of  $\alpha$ - $\text{LiB}_{11}\text{H}_{14}\cdot(\text{H}_2\text{O})_n$  at 100 °C,  $R_{\text{wp}} = 3.08\%$ . Blue lines indicate Bragg position from space group  $la3d$ . .....144

**Figure 4.11** (A) *In-situ* SR-XRPD data of  $\alpha$ - $\text{LiB}_{11}\text{H}_{14}\cdot(\text{H}_2\text{O})_n$  during heating (5 °C  $\text{min}^{-1}$ ) and cooling (6 °C  $\text{min}^{-1}$ ). A reversible polymorphic phase transition occurs at  $\approx 70 \text{ }^\circ\text{C}$  on heating and at  $\approx 55 \text{ }^\circ\text{C}$  on subsequent cooling. Red line represents temperature. (B) SR-XRPD patterns of HT (high temperature)  $\alpha$ - $\text{LiB}_{11}\text{H}_{14}\cdot(\text{H}_2\text{O})_n$  at 100 °C (red) and RT (room temperature)  $\alpha$ - $\text{LiB}_{11}\text{H}_{14}\cdot(\text{H}_2\text{O})_n$  (black).  $\lambda = 0.590827(4) \text{ \AA}$ . .....145

**Figure 4.12** DSC/TGA measurement of  $\alpha$ - $\text{LiB}_{11}\text{H}_{14}\cdot(\text{H}_2\text{O})_n$  in the temperature range 30 – 300 °C ( $\Delta T/\Delta t = 10 \text{ }^\circ\text{C min}^{-1}$ , Ar flow = 40 mL  $\text{min}^{-1}$ ). Approximately 7 mg of sample was used for analysis. The phase change event is characterised by the endothermic feature at 70 °C, and the exothermic peak at 225 °C represents its decomposition accompanied by a mass loss of 8.4(4)%. .....146

**Figure 4.13** TPPA of  $\alpha$ - $\text{LiB}_{11}\text{H}_{14}\cdot(\text{H}_2\text{O})_n$  heated from RT to 220 °C ( $\Delta T/\Delta t = 10 \text{ }^\circ\text{C min}^{-1}$ ). The sample changes phase near 70 °C, and it does not melt. The pellet expands and keeps its solid shape upon heating. It starts decomposing at  $\approx 215 \text{ }^\circ\text{C}$ , when it becomes a yellow solid. ..147

**Figure 4.14** XRPD ( $\lambda = 1.54056 \text{ \AA}$ ) and Rietveld refinement of  $\text{LiB}_{11}\text{H}_{14}$ .  $R_{\text{wp}} = 4.05\%$ . Blue lines represent Bragg position from space group  $Pbca$  [32]. .....148

**Figure 4.15** DSC/TGA measurement of  $\text{LiB}_{11}\text{H}_{14}$  in the temperature range 30 – 300 °C ( $\Delta T/\Delta t = 10 \text{ }^\circ\text{C min}^{-1}$ , Ar flow = 40 mL  $\text{min}^{-1}$ ). Approximately 7 mg of sample was used for analysis. The

phase change event is characterised by the endothermic feature at 112 °C, and the exothermic peak at 211 °C represents its decomposition accompanied by a mass loss of 1.8(2)%.....148

**Figure 4.16** A) Solid-state ionic conductivity of  $\text{LiB}_{11}\text{H}_{14}\cdot 2\text{H}_2\text{O}$  (green),  $\alpha\text{-LiB}_{11}\text{H}_{14}\cdot(\text{H}_2\text{O})_n$  (red), and  $\text{LiB}_{11}\text{H}_{14}$  (blue), as a function of temperature. Dehydrated  $\text{LiB}_{11}\text{H}_{14}$  (brown) [32],  $b\text{-LiB}_{11}\text{H}_{14}\cdot(\text{H}_2\text{O})_n$  (orange) [42], and ionic liquid electrolyte  $\text{LiBF}_4/\text{EMIBF}_4$  (grey) [24] are plotted for comparison. The solid lines denote the ionic conductivity of the materials synthesised in this work. Closed and open symbols represent heating and cooling regimes, respectively. B) Solid-state ionic conductivity of  $\alpha\text{-LiB}_{11}\text{H}_{14}\cdot(\text{H}_2\text{O})_n$  over four cycles of heating and cooling measurements.....151

**Figure 4.17** A) Equivalent circuit model used to fit impedance data ( $R_1+Q_1/R_2+Wo$ ), where  $R_1$  is the internal resistance,  $R_2$  is the surface-layer resistance, CPE1 ( $Q_1$ ) is the constant phase element and  $Wo_1$  is the open Warburg element [75,76]. B) Nyquist plots of the Au-symmetric cell for  $\alpha\text{-LiB}_{11}\text{H}_{14}\cdot(\text{H}_2\text{O})_n$  at 30 and 90 °C.....151

**Figure 4.18** Solid-state ionic conductivity of  $\alpha\text{-LiB}_{11}\text{H}_{14}\cdot(\text{H}_2\text{O})_n$  compared with other lithium boron-hydrogen salts [28–32,35,42,78].....154

**Figure 4.19** Left: *In-situ* SR-XRPD ( $\lambda = 0.563516(6)$  Å) data of  $b\text{-LiB}_{11}\text{H}_{14}\cdot(\text{H}_2\text{O})_n$  during cooling at  $1\text{ °C min}^{-1}$ . No significant change can be observed in the temperature range used to conduct the experiment (RT to  $-175\text{ °C}$ ). Red line represents temperature. Right:  $^{11}\text{B}$  spin-lattice relaxation rates of  $b\text{-LiB}_{11}\text{H}_{14}\cdot(\text{H}_2\text{O})_n$  as a function of inverse temperature. The solid line represents the best model fit to a relaxation model considering two types of dynamic processes with different activation energies and a temperature-independent contribution to relaxation due to interactions with paramagnetic impurities in the sample.....155

**Figure 4.20** Linear Sweep Voltammogram of  $\text{Li}/\alpha\text{-LiB}_{11}\text{H}_{14}\cdot(\text{H}_2\text{O})_n/\alpha\text{-LiB}_{11}\text{H}_{14}\cdot(\text{H}_2\text{O})_n+\text{C}/\text{Pt}/\text{Al}$  cells at a scan rate of  $50\text{ }\mu\text{V s}^{-1}$  at  $30\text{ °C}$  between 1.6 and 5.2 V (1<sup>st</sup> cycle) and 1.6 and 5.1 V (2<sup>nd</sup> cycle). The oxidative limit was estimated by the interception of the red dashed lines, which represent the linear regression lines of the background and the anodic current.....156

**Figure 4.21** Galvanostatic cycling profiles at  $60\text{ °C}$  with a current density of 25 and  $50\text{ }\mu\text{A cm}^{-2}$  for 1 h in each direction of a  $\text{Li}/\alpha\text{-LiB}_{11}\text{H}_{14}\cdot(\text{H}_2\text{O})_n/\text{Li}$  coin cell (grey),  $\text{Li}/\text{LE}/\alpha\text{-LiB}_{11}\text{H}_{14}\cdot(\text{H}_2\text{O})_n/\text{LE}/\text{Li}$  Swagelok-type cell (black), and  $\text{Li}/\text{IL}/\alpha\text{-LiB}_{11}\text{H}_{14}\cdot(\text{H}_2\text{O})_n/\text{IL}/\text{Li}$  Swagelok-type cell (red), where LE stands for liquid electrolyte (1.0 M  $\text{LiPF}_6$  EC/DMC) and IL is ionic liquid ( $\text{LiB}_{11}\text{H}_{14}\cdot 2\text{H}_2\text{O}$ ).....158



**Figure 4.22** Endurable time control measurement used to identify the critical current density of the Li/ $\alpha$ -LiB<sub>11</sub>H<sub>14</sub>·(H<sub>2</sub>O)<sub>n</sub>/Li symmetric cell at 60 °C from 25 to 775  $\mu\text{A cm}^{-2}$ . Short circuit failure happens at 775  $\mu\text{A cm}^{-2}$ , therefore the CCD is determined to be 750  $\mu\text{A cm}^{-2}$ . .....159

**Figure 4.23** Nyquist plots of the Li-symmetric cell (Swagelok-type) for  $\alpha$ -LiB<sub>11</sub>H<sub>14</sub>·(H<sub>2</sub>O)<sub>n</sub> after 1 hour stabilisation at 60 °C with (right) and without (left) addition of the ionic liquid (LiB<sub>11</sub>H<sub>14</sub>·2H<sub>2</sub>O) at the interface Li/SSE. Data was fitted using the equivalent circuit model (R1+Q1/R2+Wo) presented in Fig. 4.17A.....160

**Figure 4.24** A) Schematic representation of the solid-state battery Li/LE/ $\alpha$ -LiB<sub>11</sub>H<sub>14</sub>·(H<sub>2</sub>O)<sub>n</sub>/ $\alpha$ -LiB<sub>11</sub>H<sub>14</sub>·(H<sub>2</sub>O)<sub>n</sub>+TiS<sub>2</sub> in a Swagelok-type cell. B) Discharge/charge profiles at 0.05, 0.1, 0.2, 0.3 and 0.4 C (1.7 – 2.5 V) at 60 °C. C) Capacity retention at different C-rates. D) Discharge/charge profiles at 0.4 C for 50 cycles at 60 °C after being initially cycled at 0.05, 0.1, 0.2 and 0.3 C. E) Coulombic efficiency and discharge specific capacity at 0.1 C for the first 6 cycles and at 0.2 C from the 7<sup>th</sup> to the 65<sup>th</sup> cycle. ....163

**Figure 4.25** A) Schematic representation of the solid-state battery Li/IL/ $\alpha$ -LiB<sub>11</sub>H<sub>14</sub>·(H<sub>2</sub>O)<sub>n</sub>/IL/ $\alpha$ -LiB<sub>11</sub>H<sub>14</sub>·(H<sub>2</sub>O)<sub>n</sub>+TiS<sub>2</sub> in a Swagelok-type cell. B) Discharge/charge profiles at 0.05, 0.1, 0.2, 0.3 and 0.4 C (1.7 – 2.5 V) at 60 °C. C) Capacity retention at different C-rates compared to the cell of Li/LE/ $\alpha$ -LiB<sub>11</sub>H<sub>14</sub>·(H<sub>2</sub>O)<sub>n</sub>/ $\alpha$ -LiB<sub>11</sub>H<sub>14</sub>·(H<sub>2</sub>O)<sub>n</sub>+TiS<sub>2</sub>. D) Discharge/charge profiles at 0.4 C for 50 cycles at 60 °C. ....165

**Figure 5.1** Solid-state <sup>11</sup>B MAS NMR spectra of NaB<sub>11</sub>H<sub>14</sub>·(H<sub>2</sub>O)<sub>n</sub>, Na<sub>11</sub>(B<sub>11</sub>H<sub>14</sub>)<sub>3</sub>(B<sub>11</sub>H<sub>13</sub>)<sub>4</sub> and Na<sub>2</sub>B<sub>11</sub>H<sub>13</sub> at room temperature.  $\delta$  (B<sub>11</sub>H<sub>14</sub><sup>-</sup>) = -15.2 and -17.9 ppm, and  $\delta$  (B<sub>11</sub>H<sub>13</sub><sup>2-</sup>) = -21.5 and -32.2 ppm. ....184

**Figure 5.2** <sup>11</sup>B NMR (left) and <sup>11</sup>B{<sup>1</sup>H} NMR (right) spectra (128 MHz) of Na<sub>11</sub>(B<sub>11</sub>H<sub>14</sub>)<sub>3</sub>(B<sub>11</sub>H<sub>13</sub>)<sub>4</sub> and Na<sub>2</sub>B<sub>11</sub>H<sub>13</sub> in D<sub>2</sub>O at room temperature.  $\delta$  (B<sub>11</sub>H<sub>14</sub><sup>-</sup>) = -15.1, -16.2 and -17.3 ppm, and  $\delta$  (B<sub>11</sub>H<sub>13</sub><sup>2-</sup>) = -20.6 and -31.8 ppm. The peak observed at the resonance 14.6 ppm for Na<sub>11</sub>(B<sub>11</sub>H<sub>14</sub>)<sub>3</sub>(B<sub>11</sub>H<sub>13</sub>)<sub>4</sub> is assigned to a boron oxide species formed as a by-product.....185

**Figure 5.3** XRPD pattern ( $\lambda$  = 1.54056 Å) for Na<sub>11</sub>(B<sub>11</sub>H<sub>14</sub>)<sub>3</sub>(B<sub>11</sub>H<sub>13</sub>)<sub>4</sub>, Na<sub>2</sub>B<sub>11</sub>H<sub>13</sub> and NaB<sub>11</sub>H<sub>14</sub>·(H<sub>2</sub>O)<sub>n</sub> [11] (added for comparison) at room temperature. Asterisk at  $2\theta$  = 31.8° in the NaB<sub>11</sub>H<sub>14</sub>·(H<sub>2</sub>O)<sub>n</sub> pattern represent inadvertent NaCl contamination from synthesis [11]. .....186

**Figure 5.4** XRPD pattern ( $\lambda$  = 1.54056 Å) for Na<sub>11</sub>(B<sub>11</sub>H<sub>14</sub>)<sub>3</sub>(B<sub>11</sub>H<sub>13</sub>)<sub>4</sub> and Na<sub>2</sub>B<sub>11</sub>H<sub>13</sub> at room temperature and simulated diffraction lines for NaOH [49] and NaH [50] that were obtained from the Crystallography Open Database (COD) [51–56]. Data show that there is no evidence

for remanent crystalline NaOH in the sample of  $\text{Na}_{11}(\text{B}_{11}\text{H}_{14})_3(\text{B}_{11}\text{H}_{13})_4$ , neither remanent crystalline NaH in the  $\text{Na}_2\text{B}_{11}\text{H}_{13}$  powder.....187

**Figure 5.5** Solid-state  $^{11}\text{B}$  MAS NMR spectra of  $\text{Na}_{11}(\text{B}_{11}\text{H}_{14})_3(\text{B}_{11}\text{H}_{13})_4$  at room temperature with magnified region from 30 to -5 ppm.  $\delta(\text{B}_{11}\text{H}_{14}^-) = -15.2$  and  $-17.9$  ppm,  $\delta(\text{B}_{11}\text{H}_{13}^{2-}) = -21.5$  and  $-32.2$  ppm. The peaks observed between 10 and 22 ppm, and the peak at  $\approx 1$  ppm are assigned to a boron oxide species (by-product) formed with  $\text{BO}_3$  and  $\text{BO}_4$  units, respectively [57–59].....188

**Figure 5.6**  $^1\text{H}$  NMR spectrum (400 MHz) of  $\text{Na}_2\text{B}_{11}\text{H}_{13}$  in  $\text{D}_2\text{O}$ .  $\delta(\text{D}_2\text{O}) = 4.6$  ppm [66],  $\delta(\text{THF}) = 1.7$  and  $3.6$  ppm [65,66], and  $\delta(\text{B}_{11}\text{H}_{13}^{2-}) = -0.6 - 1.5$  ppm. ....189

**Figure 5.7** Left: *In-situ* SR-XRPD data ( $\lambda = 0.590827(4)$  Å) of  $\text{Na}_2\text{B}_{11}\text{H}_{13}$  during heating ( $5$  °C  $\text{min}^{-1}$ ) and cooling ( $6$  °C  $\text{min}^{-1}$ ). A reversible polymorphic phase transition is seen at  $\approx 170$  °C on heating and  $90$  °C on subsequent cooling. Red line represents temperature. Right: DSC plot ( $\Delta T/\Delta t = 10$  °C  $\text{min}^{-1}$ , Ar flow =  $40$  mL  $\text{min}^{-1}$ ) for  $\text{Na}_2\text{B}_{11}\text{H}_{13}$  upon heating and cooling between  $40$  and  $220$  °C. ....190

**Figure 5.8** DSC/TGA measurement for  $\text{Na}_2\text{B}_{11}\text{H}_{13}$  in the temperature range  $50 - 350$  °C. Approximately  $5$  mg of sample was used for the analysis ( $\Delta T/\Delta t = 10$  °C  $\text{min}^{-1}$ , Ar flow =  $40$  mL  $\text{min}^{-1}$ ). A mass loss of  $5.5(2)$  wt% is observed between  $80$  and  $220$  °C and  $3.1(2)$  wt% between  $220$  and  $340$  °C. ....191

**Figure 5.9** Left:  $^1\text{H}$  NMR spectrum (400 MHz) of  $\text{Na}_2\text{B}_{11}\text{H}_{13}$  in  $\text{D}_2\text{O}$  after a DSC/TGA experiment heated to  $220$  °C.  $\delta(\text{D}_2\text{O}) = 4.6$  ppm [66], and  $\delta(\text{B}_{11}\text{H}_{13}^{2-}) = -0.6 - 1.5$  ppm. Right:  $^{11}\text{B}$   $\{^1\text{H}\}$  NMR spectrum (128 MHz) of the same sample in  $\text{D}_2\text{O}$ .  $\delta(\text{B}_{11}\text{H}_{14}^-) = -15.3, -16.2$  and  $-17.3$  ppm, and  $\delta(\text{B}_{11}\text{H}_{13}^{2-}) = -20.6$  and  $-31.7$  ppm [11]. ....191

**Figure 5.10** SR-XRPD patterns ( $\lambda = 0.590827(4)$  Å) for  $\text{Na}_2\text{B}_{11}\text{H}_{13}$  at  $30$  °C *BH* (before heating),  $30$  °C *AH* (after heating),  $140$  °C and  $200$  °C (during *in-situ* heating experiment).....192

**Figure 5.11** SR-XRPD ( $\lambda = 0.590827(4)$  Å) and Rietveld refinement of  $\text{Na}_2\text{B}_{11}\text{H}_{13}$  at  $200$  °C (heating). Experimental data as black line, calculated diffraction pattern as red line, and difference plot in grey. Blue tick marks represent Bragg position from space group *Pm3n*.  $R_{\text{wp}} = 2.93\%$ .....193

**Figure 5.12** XRPD pattern ( $\lambda = 1.54056$  Å) for  $\text{Na}_{11}(\text{B}_{11}\text{H}_{14})_3(\text{B}_{11}\text{H}_{13})_4$  at room temperature (blue), and SR-PXD data ( $\lambda = 0.590827(4)$  Å) for  $\text{Na}_2\text{B}_{11}\text{H}_{13}$  at  $200$  °C (black) and at room temperature after being heated to  $220$  °C (red). Dashed lines at  $1.05, 1.17$  Å $^{-1}$  (RT polymorph) and at  $1.13$  Å $^{-1}$  (HT polymorph) were added to show the similarities between the

diffractograms. The diffractograms were plotted with the x-axis in scattering vector to compare XRPD results obtained using different wavelengths. ....194

**Figure 5.13** Top: SR-XRPD ( $\lambda = 0.590827(4) \text{ \AA}$ ) and Rietveld refinement of  $\text{Na}_2\text{B}_{11}\text{H}_{13}$  at 200 °C (heating).  $R_{\text{wp}} = 2.93\%$ . Bottom: XRPD pattern ( $\lambda = 1.54056 \text{ \AA}$ ) and partial Rietveld refinement for  $\text{Na}_{11}(\text{B}_{11}\text{H}_{14})_3(\text{B}_{11}\text{H}_{13})_4$  at room temperature. Peaks at  $Q = 1.05$  and  $1.17 \text{ \AA}^{-1}$  were fitted using simple peak functions and are not indexed or based on a crystal structure.  $R_{\text{wp}} = 3.44\%$ . Experimental data, calculated diffraction pattern and difference plot are shown in black, red and grey, respectively. Blue tick marks represent Bragg position from space group  $Pm\bar{3}n$  for both samples. The diffractograms were plotted with the x-axis in scattering vector to compare XRPD results that were obtained using different wavelengths. ....195

**Figure 5.14** DSC/TGA measurement for  $\text{Na}_{11}(\text{B}_{11}\text{H}_{14})_3(\text{B}_{11}\text{H}_{13})_4$  in the temperature range 50 – 350 °C. Approximately 5 mg of the sample was used ( $\Delta T/\Delta t = 10 \text{ }^\circ\text{C min}^{-1}$ , Ar flow = 40 mL  $\text{min}^{-1}$ ). ....196

**Figure 5.15** DSC plots for  $\text{NaB}_{11}\text{H}_{14} \cdot (\text{H}_2\text{O})_n$ , [11]  $\text{Na}_{11}(\text{B}_{11}\text{H}_{14})_3(\text{B}_{11}\text{H}_{13})_4$  and  $\text{Na}_2\text{B}_{11}\text{H}_{13}$  from 50 – 350 °C. Approximately 5 mg of each sample was used ( $\Delta T/\Delta t = 10 \text{ }^\circ\text{C min}^{-1}$ , Ar flow = 40 mL  $\text{min}^{-1}$ ). The exothermic event occurs at a higher temperature as the  $\text{B}_{11}\text{H}_{14}^-$  content in the sample decreases. ....197

**Figure 5.16** Solid-state ionic conductivity of  $\text{Na}_2\text{B}_{11}\text{H}_{13}$  and  $\text{Na}_{11}(\text{B}_{11}\text{H}_{14})_3(\text{B}_{11}\text{H}_{13})_4$  as a function of temperature compared to other sodium single anion (left) [11,12,14,15,27,43,70,71] and mixed anion (right) [22,23,29,31,70,72] hydridoborate materials. bcc- $\text{NaCB}_{11}\text{H}_{12}$  represents the ionic conductivity of the mechanically-milled  $\text{NaCB}_{11}\text{H}_{12}$ , which presents a body-centered cubic (bcc) polymorph at RT [19]. The solid-state electrolyte  $\text{Na-}\beta\text{-Al}_2\text{O}_3$  was also added for comparison in both plots [1]. The solid green lines denote the ionic conductivity of the samples synthesised in the present work. ....198

**Figure 5.17** Solid-state ionic conductivity of  $\text{Na}_2\text{B}_{11}\text{H}_{13}$  and  $\text{Na}_{11}(\text{B}_{11}\text{H}_{14})_3(\text{B}_{11}\text{H}_{13})_4$  as a function of temperature compared to  $\text{NaB}_{11}\text{H}_{14}$  [27] and  $\text{NaB}_{11}\text{H}_{14} \cdot (\text{H}_2\text{O})_n$  [11]. ....198

**Figure 5.18** A) Impedance circuit model used to fit Nyquist plots, where  $R_1$  is the internal resistance,  $R_2$  is the surface-layer resistance,  $CPE_1$  or  $Q_1$  is the constant phase element and  $W_{o1}$  is the open Warburg element [73,74]. B) Nyquist plots of the Au-symmetric cell for  $\text{Na}_2\text{B}_{11}\text{H}_{13}$  at room temperature, 100 and 200 °C. C) Nyquist plots of the Au-symmetric cell for  $\text{Na}_{11}(\text{B}_{11}\text{H}_{14})_3(\text{B}_{11}\text{H}_{13})_4$  at 30 and 170 °C. At low temperatures, the data is presented as a semi-circle (charge transfer resistance of the sample) with a spike line (Warburg element) at the

low frequency region, which is related to the Na<sup>+</sup> diffusion [43,73,74]. Upon increase of temperature, the semi-circle decreases, and only the linear component can be observed.199

**Figure 5.19** Linear Sweep Voltammogram of Na/SSE/SSE+C/Pt/Al cell, with SSE = Na<sub>2</sub>B<sub>11</sub>H<sub>13</sub> (grey) and Na<sub>11</sub>(B<sub>11</sub>H<sub>14</sub>)<sub>3</sub>(B<sub>11</sub>H<sub>13</sub>)<sub>4</sub> (yellow) cell at a scan rate of 50 μV s<sup>-1</sup> at 30 °C between 1.7 and 4.0 V. The red dashed lines represent the background and the anodic current fitted to obtain the oxidation potential. ....202

**Figure A.1** Calculated structure of (a) B<sub>11</sub>H<sub>14</sub><sup>-</sup> and (b) B<sub>11</sub>H<sub>13</sub>OH<sup>-</sup>. Boron atoms are violet spheres; H atoms are white spheres; O atom is red sphere. ....219

# LIST OF TABLES

---

<b>Table 1.1.</b> Approximate phase-transition temperatures with the technique used to determine each of them, structural symmetries and space groups of the low temperature (LT) and high temperature (HT) phases for several lithium and sodium-boranes. ....	15
<b>Table 1.2.</b> Different strategies used to enhance the ionic conductivity of some lithium and sodium boranes. ....	17
<b>Table 1.3.</b> Oxidative stability limit of some lithium and sodium boranes against Li and Na metal, respectively. The sulphide $\text{Li}_{10}\text{GeP}_2\text{S}_{12}$ and the oxide $\text{Li}_7\text{La}_3\text{Zr}_2\text{O}_{12}$ solid electrolytes were also added for comparison. ....	20
<b>Table 1.4.</b> Battery tests performed with different lithium and sodium boranes as solid-state electrolytes. ....	21
<b>Table 2.1</b> List of chemicals used and their specifications.....	34
<b>Table 2.2</b> Parameters used to conduct <i>in-situ</i> SR-XRPD experiments. Wavelength was refined using a NIST $\text{LaB}_6$ 660b line position standard. Temperature was controlled using an Oxford Cryosystems Cryostream Plus.....	47
<b>Table 2.3</b> Parameters used to conduct DSC/TGA experiments. All samples were analysed at $\Delta T/\Delta t = 10 \text{ }^\circ\text{C min}^{-1}$ with a constant Ar flow ( $40 \text{ mL min}^{-1}$ ).....	50
<b>Table 2.4</b> Parameters used for EIS measurements of each sample upon heating. Temperature was monitored by a K-type thermocouple $\approx 5 \text{ mm}$ from the pellet and controlled with a tube furnace. B.M. stands for ball-milled samples. ....	57
<b>Table 2.5</b> Temperature range used for determination of the activation energy of ionic conductivity for each compound. ....	58
<b>Table 2.6</b> Parameters used to conduct LSV measurements for each sample. ....	60
<b>Table 2.7</b> Details of the charge/discharge cycling experiments performed for each cell, with the number of cycles (discharge and charge from 1.7 – 2.5 V vs. $\text{Li}^+/\text{Li}$ ) performed at each C-rate ( $1 \text{ C} = 239 \text{ mA g}^{-1}$ ). All batteries were assembled in a Swagelok-type cell, and all measurements were performed at $60 \text{ }^\circ\text{C}$ . ....	65
<b>Table 3.1</b> The refined $\text{KB}_{11}\text{H}_{14}$ structural parameters at $25 \text{ }^\circ\text{C}$ in space group $P1$ derived from XRPD data.....	95

<b>Table 3.2</b> Structural Data Extracted from Refinements of the XRPD Data for $\text{KB}_{11}\text{H}_{14}$ and $\text{LiB}_{11}\text{H}_{14}\cdot 2\text{H}_2\text{O}$ .	102
<b>Table 3.3</b> The refined $\text{LiB}_{11}\text{H}_{14}\cdot 2\text{H}_2\text{O}$ structural parameters at 21.9 °C in space group ( $C2/c$ ) derived from single crystal data.	102
<b>Table 4.1</b> Structural parameters determined from Rietveld refinement of the XRPD data from this work and other related compounds.	149
<b>Table 4.2</b> Pellet thickness at RT and ionic conductivity results at 30 and 90 °C for sample $\alpha\text{-LiB}_{11}\text{H}_{14}\cdot (\text{H}_2\text{O})_n$ at different cycles.	152
<b>Table 4.3</b> Activation energy of some lithium boron-hydrogen salts.	153
<b>Table 4.4</b> Interfacial resistance for the systems $\text{Li}/\text{IL}/\alpha\text{-LiB}_{11}\text{H}_{14}\cdot (\text{H}_2\text{O})_n/\text{IL}/\text{Li}$ ( $\text{IL} = \text{LiB}_{11}\text{H}_{14}\cdot 2\text{H}_2\text{O}$ ) and $\text{Li}/\alpha\text{-LiB}_{11}\text{H}_{14}\cdot (\text{H}_2\text{O})_n/\text{Li}$ and circuit component values $R1$ and $R2$ from Nyquist plots shown in Fig. 4.23.	161
<b>Table 5.1</b> Activation energy of $\text{Na}_{11}(\text{B}_{11}\text{H}_{14})_3(\text{B}_{11}\text{H}_{13})_4$ and $\text{Na}_2\text{B}_{11}\text{H}_{13}$ compared to other sodium hydridoborate salts.	200
<b>Table A.1</b> Calculated bond distances and angles for $\text{B}_{11}\text{H}_{14}^-$ at B31LYP/aug-cc-pvdz level of theory.	219
<b>Table A.2</b> Calculated bond distances and angles for $\text{B}_{11}\text{H}_{13}\text{OH}^-$ at B31LYP/aug-cc-pvdz level of theory.	222
<b>Table A.3</b> Optimised atomic coordinates for $\text{B}_{11}\text{H}_{14}^-$ at B31LYP/aug-cc-pvdz level of theory.	225
<b>Table A.4</b> Optimised atomic coordinates for $\text{B}_{11}\text{H}_{13}\text{OH}^-$ at B31LYP/aug-cc-pvdz level of theory.	226
<b>Table A.5</b> NPA charge and $^{11}\text{B}$ NMR spectroscopy chemical shift (ppm) analysis for $\text{B}_{11}\text{H}_{14}^-$ and $\text{B}_{11}\text{H}_{13}\text{OH}^-$ calculated at the B31LYP/aug-cc-pvdz level of theory.	227
<b>Table A.6</b> Observed and calculated $^{11}\text{B}$ NMR chemical shifts (ppm) for $\text{B}_{11}\text{H}_{14}^-$ calculated at the B31LYP/aug-cc-pvdz level of theory. Solvent is $\text{CD}_3\text{CN}$ .	228
<b>Table A.7</b> Observed and calculated $^{11}\text{B}$ NMR chemical shifts (ppm) for $\text{B}_{11}\text{H}_{13}\text{OH}^-$ calculated at the B31LYP/aug-cc-pvdz level of theory. Solvent is $\text{CD}_3\text{CN}$ .	229

# TABLE OF CONTENTS

---

<b>CHAPTER 1 Introduction and Literature Review .....</b>	<b>1</b>
1.1 RENEWABLE ENERGY AND ENERGY STORAGE.....	2
1.2 SOLID-STATE BATTERIES .....	6
1.3 BORANES – AN OVERVIEW .....	12
1.4 BORANES AS SOLID-STATE ELECTROLYTES .....	14
1.5 REFERENCES.....	23
<b>CHAPTER 2 Experimental .....</b>	<b>33</b>
2.1 INTRODUCTION.....	34
2.2 CHEMICALS.....	34
2.3 SYNTHESIS.....	35
2.3.1 Synthesis of trimethylammonium <i>nido</i> -tetradecahydroundecaborane, (CH <sub>3</sub> ) <sub>3</sub> NHB <sub>11</sub> H <sub>14</sub> .....	36
2.3.2 Synthesis of alkali metal <i>nido</i> -tetradecahydroundecaborane, LiB <sub>11</sub> H <sub>14</sub> ·(H <sub>2</sub> O) <sub>n</sub> , NaB <sub>11</sub> H <sub>14</sub> ·(H <sub>2</sub> O) <sub>n</sub> and KB <sub>11</sub> H <sub>14</sub> .....	38
2.3.3 Synthesis of lithium <i>nido</i> -tetradecahydroundecaborane, LiB <sub>11</sub> H <sub>14</sub> ·2H <sub>2</sub> O, a- LiB <sub>11</sub> H <sub>14</sub> ·(H <sub>2</sub> O) <sub>n</sub> (n < 2), and LiB <sub>11</sub> H <sub>14</sub> .....	39
2.3.4 Synthesis of mixed anion <i>nido</i> -borane, Na <sub>11</sub> (B <sub>11</sub> H <sub>14</sub> ) <sub>3</sub> (B <sub>11</sub> H <sub>13</sub> ) <sub>4</sub> .....	40
2.3.5 Synthesis of disodium <i>nido</i> -tridecahydroundecaborane, Na <sub>2</sub> B <sub>11</sub> H <sub>13</sub> .....	40
2.4 CHARACTERISATION.....	41
2.4.1 Nuclear Magnetic Resonance (NMR) spectroscopy.....	41
2.4.2 Raman spectroscopy .....	43
2.4.3 Fourier Transformed Infrared (FTIR) Spectroscopy .....	44
2.4.4 X-Ray Diffraction (XRD) .....	44
2.4.5 Simultaneous Differential Scanning Calorimetry and Thermogravimetry Analysis (DSC/TGA).....	49
2.4.6 Thermal Decomposition Analysis by Mass Spectrometry (TDA-MS).....	50
2.4.7 Temperature Programmed Photographic Analysis (TPPA) .....	51
2.4.8 Theoretical Calculations.....	51

2.4.9 Electrochemical Impedance Spectroscopy (EIS) .....	52
2.4.10 Linear Sweep Voltammetry (LSV).....	59
2.4.11 Galvanostatic Cycling (GC) .....	60
2.4.12 Battery Assembly and Electrochemical Measurements .....	63
2.4.13 Critical Current Density (CCD) Test .....	65
2.5 REFERENCES .....	66
<b>CHAPTER 3 Hydrated Alkali-B<sub>11</sub>H<sub>14</sub> Salts as Potential Solid-State Electrolytes.....</b>	<b>72</b>
ABSTRACT.....	73
3.1 INTRODUCTION.....	73
3.2 EXPERIMENTAL .....	75
3.2.1 Chemicals .....	75
3.2.2 Synthesis of trimethylammonium <i>nido</i> -tetradecahydrundecaborane, (CH <sub>3</sub> ) <sub>3</sub> NHB <sub>11</sub> H <sub>14</sub> .....	75
3.2.3 Synthesis of alkali metal <i>nido</i> -tetradecahydrundecaborane, MB <sub>11</sub> H <sub>14</sub> (M = Li, Na, K) .....	76
3.2.4 Characterisation .....	77
3.2.4.1 Nuclear Magnetic Resonance .....	77
3.2.4.2 Fourier Transformed Infrared Spectroscopy.....	77
3.2.4.3 Thermogravimetry and Differential Scanning Calorimetry .....	77
3.2.4.4 Thermal Decomposition Analysis by Mass Spectrometry (TDA-MS) .....	78
3.2.4.5 X-Ray Powder Diffraction .....	78
3.2.4.6 Synchrotron X-Ray Powder Diffraction.....	78
3.2.4.7 Single-Crystal X-Ray Crystallography .....	79
3.2.4.8 Electrochemical Evaluation .....	80
3.2.4.9 Temperature Programmed Photographic Analysis (TPPA) .....	81
3.2.4.10 Theoretical Calculations .....	82
3.3 RESULTS AND DISCUSSION .....	82
3.3.1 Sample preparation and characterisation .....	82
3.3.2 Structural characterisation.....	94
3.3.3 Solid-state ionic conductivity .....	105
3.4 CONCLUSIONS.....	116
3.6 REFERENCES.....	117



<b>CHAPTER 4 Hydrated Lithium <i>nido</i>-Boranes for Solid-Liquid Hybrid Batteries .....</b>	<b>126</b>
ABSTRACT.....	127
4.1 INTRODUCTION.....	127
4.2 EXPERIMENTAL SECTION .....	129
4.2.1 Chemicals .....	129
4.2.2 Synthesis of lithium <i>nido</i> -tetradecahydroundecaborane, $\text{LiB}_{11}\text{H}_{14}\cdot 2\text{H}_2\text{O}$ , $\alpha$ - $\text{LiB}_{11}\text{H}_{14}\cdot (\text{H}_2\text{O})_n$ ( $n < 2$ ), and $\text{LiB}_{11}\text{H}_{14}$ .....	129
4.2.3 Synthesis of hydrated lithium <i>nido</i> -tetradecahydroundecaborane ( $Fm\bar{3}m$ polymorph), $b\text{-LiB}_{11}\text{H}_{14}\cdot (\text{H}_2\text{O})_n$ .....	130
4.2.4 Characterisation .....	131
4.2.4.1 Raman Spectroscopy .....	131
4.2.4.2 Nuclear Magnetic Resonance (NMR) Spectroscopy .....	131
4.2.4.3 Structural Characterisation .....	132
4.2.4.4 Simultaneous Differential Scanning Calorimetry (DSC) and Thermogravimetry Analysis (TGA).....	132
4.2.4.5 Temperature Programmed Photographic Analysis (TPPA) .....	133
4.2.4.6 Electrochemical Impedance Spectroscopy (EIS) .....	133
4.2.4.7 Linear Sweep Voltammetry (LSV) .....	134
4.2.4.8 Galvanostatic Cycling (GC) .....	134
4.2.4.9 Critical Current Density (CCD) Test .....	135
4.2.4.10 Battery Assembly and Electrochemical Measurements .....	135
4.3 RESULTS AND DISCUSSION .....	136
4.3.1 Sample characterisation.....	136
4.3.2. Solid-State Ionic Conductivity .....	150
4.3.3 Electrochemical stability .....	156
4.3.4 Battery Test .....	161
4.4 CONCLUSION.....	165
4.5 REFERENCES.....	166
<b>CHAPTER 5 <math>\text{Na}_2\text{B}_{11}\text{H}_{13}</math> and <math>\text{Na}_{11}(\text{B}_{11}\text{H}_{14})_3(\text{B}_{11}\text{H}_{13})_4</math> as Potential Solid-State Electrolytes for Na-Ion Batteries.....</b>	<b>177</b>
ABSTRACT.....	178
5.1 INTRODUCTION.....	178

5.2 EXPERIMENTAL SECTION .....	179
5.2.1 Chemicals .....	179
5.2.2 Synthesis of mixed anion <i>nido</i> -borane, $\text{Na}_{11}(\text{B}_{11}\text{H}_{14})_3(\text{B}_{11}\text{H}_{13})_4$ .....	180
5.2.3 Synthesis of disodium <i>nido</i> -tridecahydroundecaborane, $\text{Na}_2\text{B}_{11}\text{H}_{13}$ .....	180
5.2.4 Characterisation .....	181
5.2.4.1 Nuclear Magnetic Resonance (NMR) Spectroscopy .....	181
5.2.4.2 X-Ray Powder Diffraction (XRPD) .....	181
5.2.4.3 Synchrotron X-Ray Powder Diffraction (SR-XRPD) .....	181
5.2.4.4 Differential Scanning Calorimetry and Thermogravimetric analysis (DSC/TGA) .....	182
5.2.4.5 Electrochemical Impedance Spectroscopy (EIS) .....	182
5.2.4.6 Linear Sweep Voltammetry (LSV) .....	183
5.3 RESULTS AND DISCUSSION .....	183
5.3.1 Sample characterisation.....	183
5.3.2 Electrochemical Analysis.....	197
5.4 CONCLUSION.....	203
5.5 REFERENCES.....	204
<b>CHAPTER 6 Conclusions and Directions for Future Work.....</b>	<b>213</b>
<b>APPENDIX A DFT Calculations for <math>\text{B}_{11}\text{H}_{14}^-</math> and <math>\text{B}_{11}\text{H}_{13}\text{OH}^-</math> .....</b>	<b>218</b>
<b>APPENDIX B Co-author Attribution Statement .....</b>	<b>230</b>
<b>APPENDIX C Permission from the Copyright Owners .....</b>	<b>236</b>

# CHAPTER 1

## Introduction and Literature Review

---

## 1.1 RENEWABLE ENERGY AND ENERGY STORAGE

The increasing impact of global warming and the limited supply of fossil fuels have led governments around the world to work on a transition towards a low-carbon economy with consequent development of the renewable energy sector [1]. As such, an international climate agreement applicable to all nations, called the Paris Agreement, was set in 2015, which seeks to limit global warming at 1.5 – 2.0 °C, compared to pre-industrial levels [2]. Moreover, the European Union has proposed to achieve a reduction of the greenhouse gas emissions by 80 - 95%, relative to 1990 levels, by mid-century [3]. As a result, there has been an increase in renewable energy generation capacity worldwide over the years, with an addition of 257 GW in 2021, which brings to a total of 3,064 GW of renewable power capacity around the world (Fig. 1.1) [4].

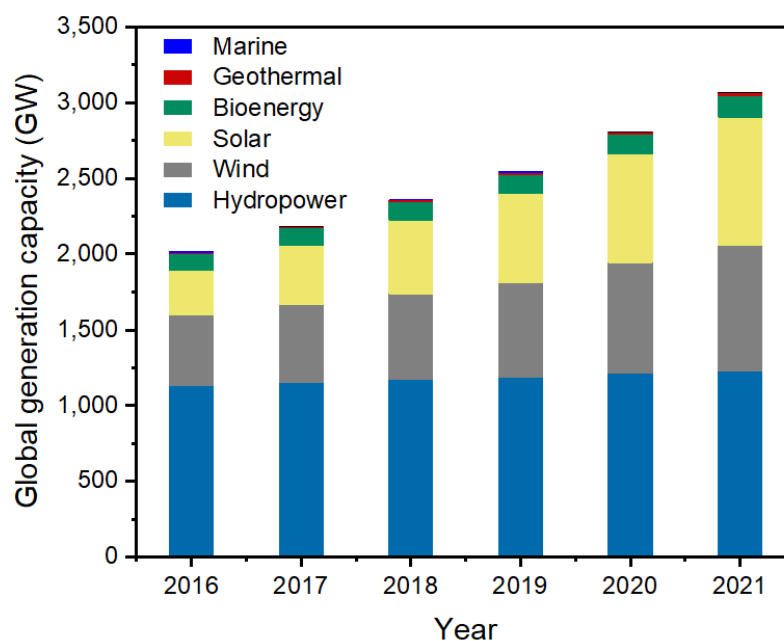


**Figure 1.1.** Renewable power capacity increase worldwide from 2016 to 2021. Data was obtained from IRENA's renewable energy statistics [4].

Although the use of renewable energy sources is growing, their intermittent nature remains a problem, which hinders their potential to become the main supplier of electricity and to replace fossil fuel baseload power generation [1]. This problem can be solved by storing excess renewable electrical energy in energy storage technologies, which are usually split into five categories: mechanical, electrochemical, electrical, chemical, and thermal energy storage (Fig. 1.2).

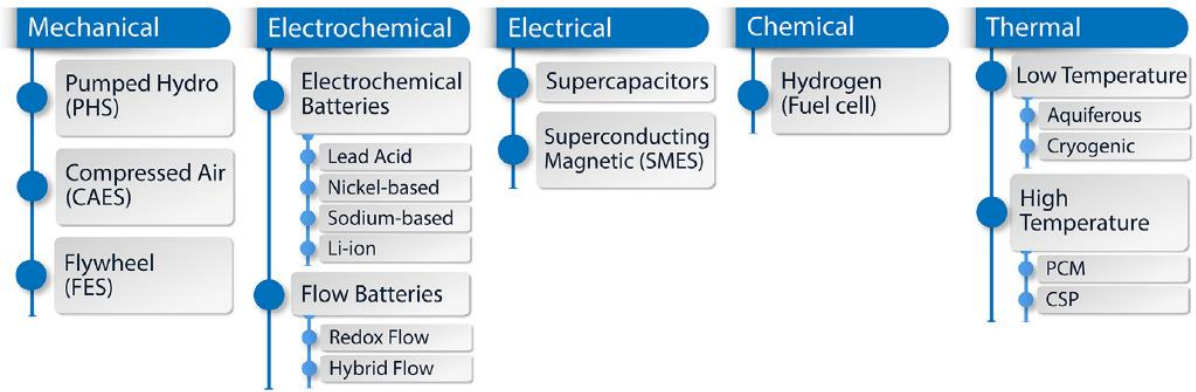


**Figure 1.2.** Types of energy storage technologies based on the kind of stored energy and examples. PCM and CSP stand for Phase Change Materials and Concentrated Solar Power, respectively. Reproduced with permission [5]. Copyright 2018, Elsevier.

Each of the electrical energy storage devices present particularities that can be advantageous or not depending on the situation to be used and operational parameters, such as small or large-scale storage capacity, short or long-term storage requirement, portability, cost and others [5]. Among the types of energy storage, electrochemical batteries are considered mature technologies that provide portability and flexibility, as they can be easily installed in different areas in small quantities for small-scale purpose or as several battery units for grid-scale [6]. Compared to other types of energy storage and generation, batteries also have the ability to quickly respond to fluctuations from renewable energy by providing a stable grid almost instantly [6–8]. Besides that, batteries have been on the market for several years, they are easy to manufacture, and they present relatively high energy density and long cycle life [7,8].

All electrochemical batteries are simple in concept and their working principles are similar to each other. They are formed by two electrodes (an anode and a cathode), which are connected with an electrolyte (an ionic conductor material) and with an external circuit (an electrical conductor material) [9]. Upon discharge, the anode oxidises, releasing ions that migrate through the electrolyte to the cathode. This process simultaneously forms a current that flows through an external electrical circuit (also from the anode to the cathode), generating power by charge balancing the ion flow [9] (Fig. 1.3). In rechargeable, or secondary, batteries this process can be reversed. During charging, the ions migrate in the opposite way through the electrolyte, from the cathode to the anode, driven by an external potential difference and electrical current [9,10].

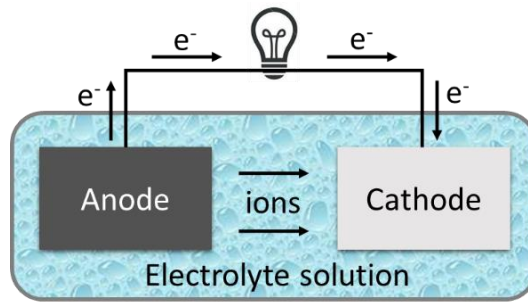


**Figure 1.3.** Schematic representation of a conventional battery with a liquid electrolyte. Upon discharge the ions and electrons flow from the anode to the cathode.

The most common secondary batteries are shown in Fig. 1.4, with their respective chemistry and invention year.

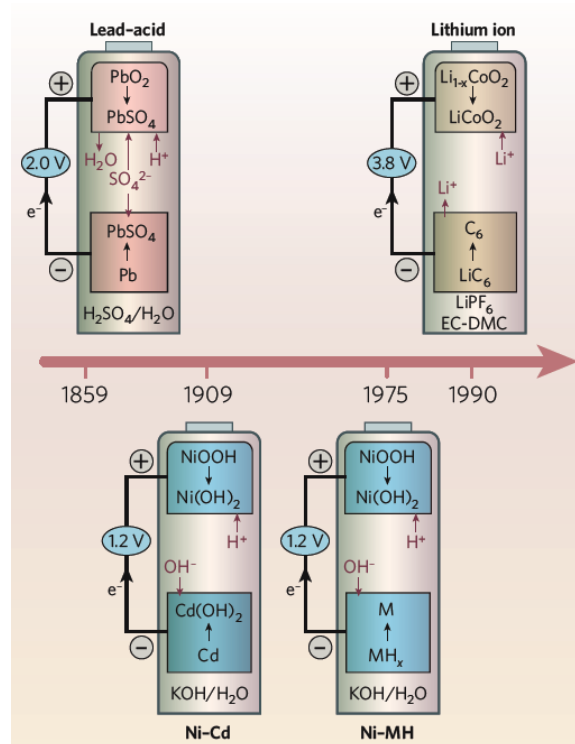


**Figure 1.4.** Type of rechargeable batteries and their respective year of creation, type of electrode materials and electrochemical reactions. Reproduced and adapted with permission [9]. Copyright 2008, Springer Nature.

The most mature rechargeable battery is the lead-acid battery. Created in 1859, this type of electrochemical device is still widely employed in vehicles. They present low cost, and high efficiency, but low energy density, slow charge-rate, limited temperature operability and

environmental issues [5]. Nickel-based batteries have also been on the market for a long time, however their high cost and the environmental impact that the heavy metals (cadmium and nickel) can cause inhibit their use for grid energy storage applications [5].

Among the different types of secondary batteries, lithium-ion batteries, which have been on the market for  $\approx 30$  years and have been powering several electronic devices, such as laptops, cellphones and electric vehicles, are seen as one of the most promising solutions for energy storage applications [5]. They present high energy efficiency, and low maintenance requirements, however these kind of batteries exhibit elevated cost ( $\approx \$132/\text{kWh}$  in 2021) [1,5,11,12]. The price of an electric vehicle (EV) battery should be below  $\$100/\text{kWh}$ , ideally  $\$80/\text{kWh}$ , for EVs to be produced and sold at a similar price as internal combustion vehicles [11,13]. The cost of Li-ion batteries is also related to the price of lithium metal, which has increased  $\approx 500\%$  between January 2021 and January 2022, owing to the growing demand from electric vehicles [14]. Besides that, Li-ion batteries employ an organic solvent as liquid electrolyte, which brings safety concerns, limits the operational temperature range and reduces energy density [12,15]. Therefore, research has been conducted on the development of batteries that use more abundant and cheaper metals than lithium, such as sodium (Na). The sodium-sulphur (Na-S) battery is a type of electronic device that uses molten Na as the anode, molten sulphur as the cathode and sodium  $\beta$ -alumina ( $\text{NaAl}_{11}\text{O}_{17}$ ) as a solid electrolyte (Fig. 1.5) [5,8].

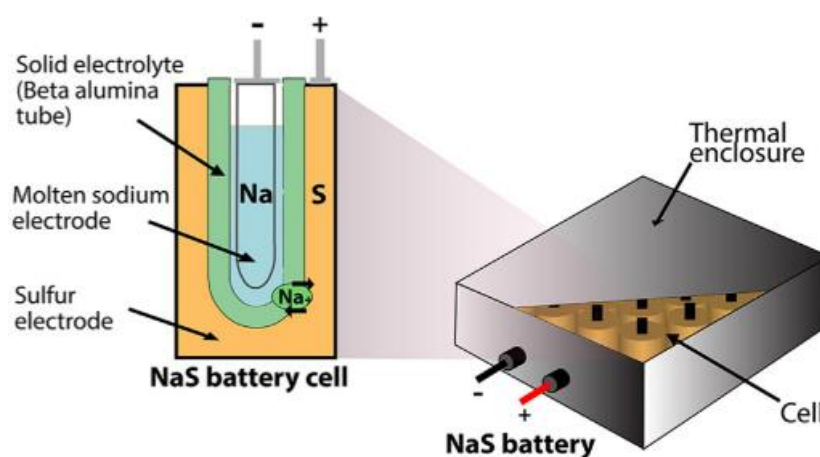


**Figure 1.5.** Schematic representation of a sodium-sulphur battery with its main components. Reproduced with permission [5]. Copyright 2018, Elsevier.

Na-S batteries operate at high temperatures (300 – 350 °C) to ensure the electrodes are in the liquid state and good ionic conductivity of the electrolyte. These batteries present high energy and power density, high durability and low manufacturing cost. However, they exhibit severe safety issues, as they possess high risks of fire and explosion if the electrodes come into contact with one another. Moreover, Na-S batteries also present high operation and maintenance costs [5,8].

All current generation of batteries present disadvantages that hinder their application as electrical energy storage devices. Research on the development of batteries that possess higher energy storage capacity, durability, safety and lower costs is necessary not only for the growth of the renewable energy sector, but also for the development of electronic devices with more processing power and for the production of electric vehicles with reduced costs, for example [9]. A type of device that promises to fulfil several of the requirements necessary for large-scale energy storage applications is the solid-state batteries, which have been seen as a promising alternative to become the next generation of batteries.

## **1.2 SOLID-STATE BATTERIES**

The replacement of the liquid electrolyte with a solid material is a potential alternative for the development of batteries with increased energy storage capacity, as the solid electrolyte promises compatibility with anode materials that possess high theoretical capacity, such as pure Li (3860 mAh g<sup>-1</sup>) [16] and Na (1165 mAh g<sup>-1</sup>) metals [17,18].

The conventional lithium-ion batteries use Li intercalated in graphite as the anode (Fig. 1.6) that reaches a maximum of 372 mAh g<sup>-1</sup>, by formation of the LiC<sub>6</sub> intercalation compound, which is about 10 times lower than the theoretical gravimetric capacity of pure Li metal, significantly reducing the energy density of the cell [19].



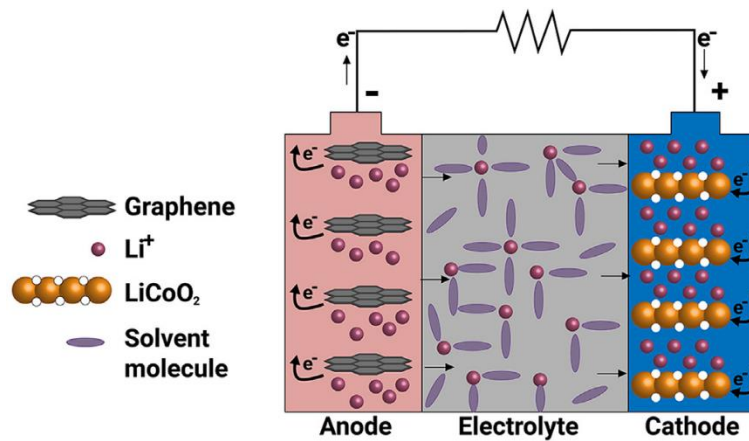


**Figure 1.6.** Schematic representation of a Li-ion battery. Li intercalated in the layers of graphene is used as the anode, and a layered structure of  $\text{LiCoO}_2$  is used as the cathode. An organic liquid electrolyte is used to move  $\text{Li}^+$  between the electrodes. Reproduced with permission [5]. Copyright 2018, Elsevier.

The replacement of the flammable liquid electrolyte with an electrochemically stable solid component would enhance safety, facilitate the production of batteries in smaller sizes, eliminate the risks of leaking, and enhance thermal stability, allowing the use of the device in places with extreme weather [15,20,21]. Fig. 1.7 shows a schematic representation of a solid-state battery (SSB), which is formed by the replacement of the liquid electrolyte from conventional batteries with a solid ionic conductor material.

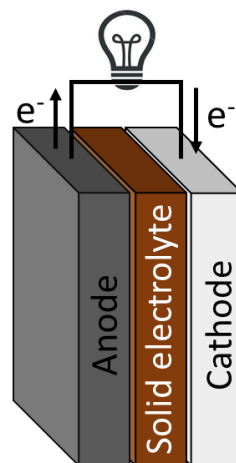


**Figure 1.7.** Schematic representation of a battery with a solid electrolyte constituting a SSB. During discharge the ions and electrons flow from the anode to the cathode.

The development of solid-state batteries relies on the research of solid materials that can meet the requirements to be used as electrolytes, such as liquid-like ionic conductivity ( $\approx 1$

mS cm<sup>-1</sup> at room temperature), high electrochemical stability, good mechanical properties, low electronic conductivity, environmental friendliness, low cost, and others (Fig. 1.8) [18,22].

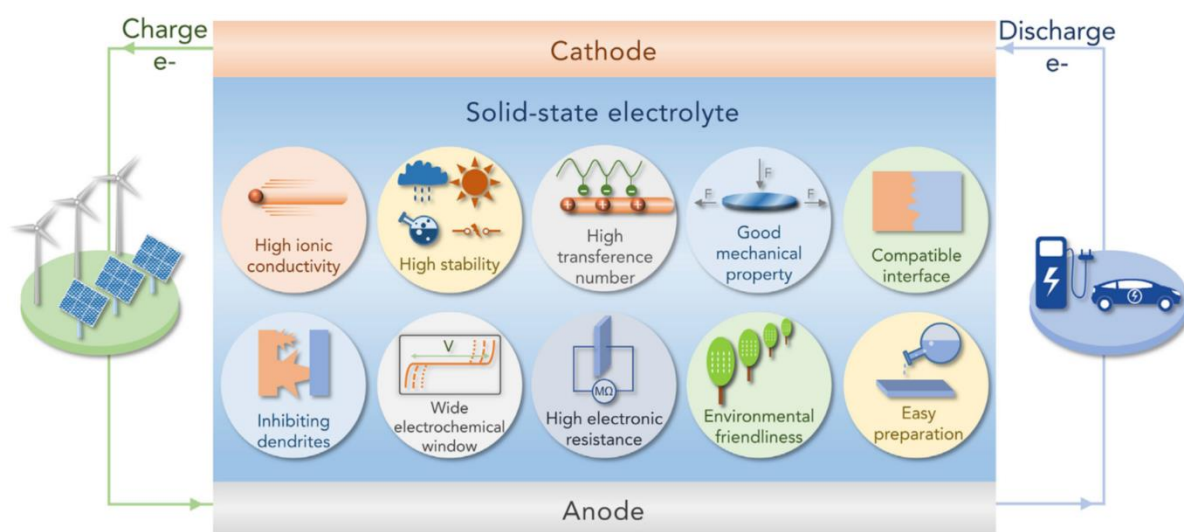


**Figure 1.8.** Schematic representation of a solid-state battery with the main requirements for a material to be used as solid-state electrolyte in practical applications. Reproduced with permission [22]. Copyright 2018, Elsevier.

The migration of cations through liquid electrolytes is facilitated by the solvent medium and the solvation shell that forms around the ion, as well as dissolved salts that can work as ionic carriers. In contrast, the diffusion of cations in solid-state electrolytes is usually dependent on the amount of defects in the structure, however the ion-transport mechanisms depend on the type of material that forms the solid [20]. The cation movement in solid inorganic compounds can occur through vacancies (Schottky-type) and interstitial (Frenkel-type) defects of the crystal structure and through free space at grain boundaries as shown in Fig. 1.9A [22–24]. Another common mechanism of cation transport is known as paddle-wheel, in which the high anion reorientation dynamics can lower the activation energy for cation hopping and facilitate the migration of the cation through the structure, as usually seen in boron-hydrogen materials (Fig. 1.9B) [25].

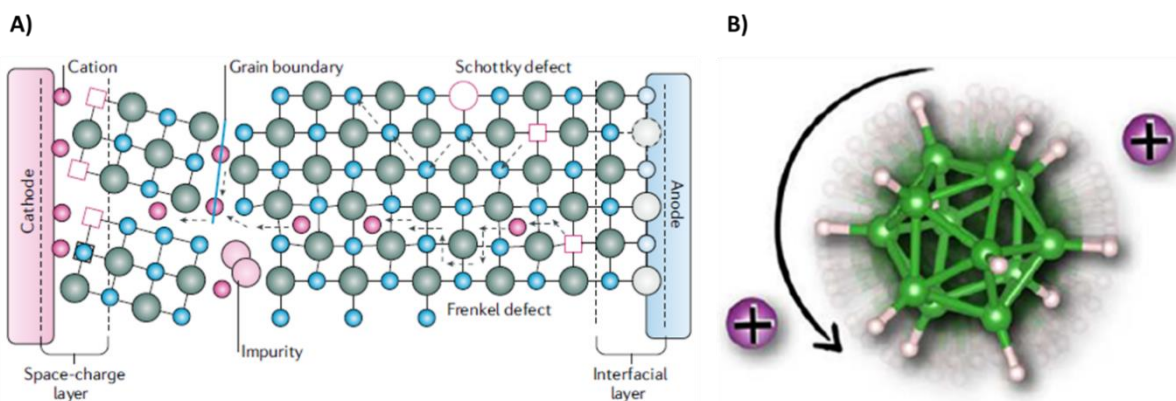


**Figure 1.9.** A) Schematic representation of cation migration in solid inorganic electrolytes through Schottky (vacancies) and Frenkel (interstitial) defects and grain boundary. Reproduced and adapted with permission [23]. Copyright 2020, Springer Nature. B) Paddle-wheel mechanism represented by the anion reorientation dynamics of a  $B_{12}H_{12}^{2-}$  structure. Reproduced and adapted with permission [26]. Copyright 2017, American Chemical Society.

Besides the challenges associated with the development of suitable solid-state electrolytes (SSE), the solid-solid interface between SSE-electrodes is also another important field of research that needs to be considered for practical application of solid-state batteries [27,28]. As well as liquid-electrolytes, solid-state materials can also be susceptible to dendrite formation against Li and Na metal, which can lead to a short circuit of the battery [17,29]. Liu *et al.* [30] recently reported that the phenomenon of dendrite formation and growth in Li-batteries with polycrystalline solid-state ceramic electrolytes, as in  $Li_7La_3Zr_2O_{12}$ , is based on the formation and propagation of Li filaments at the grain boundaries, which differs from what is observed in liquid electrolytes, where dendrite formation always starts at the interface between Li/electrolyte (Fig. 1.10). It was found that due to the small bandgap presented by grain boundaries (1 – 3 eV), they can become a source of electrons from current leakage.  $Li^+$  ions can then be reduced prematurely by the electrons from the grain boundaries of the solid-state electrolyte before reaching the cathode with consequent formation of Li filaments. The interconnection of the filaments propagates into the structure, which leads to battery failure [30]. The same mechanism of dendrite formation and growth has also been reported for  $LiBH_4$  as solid-state electrolyte [31].

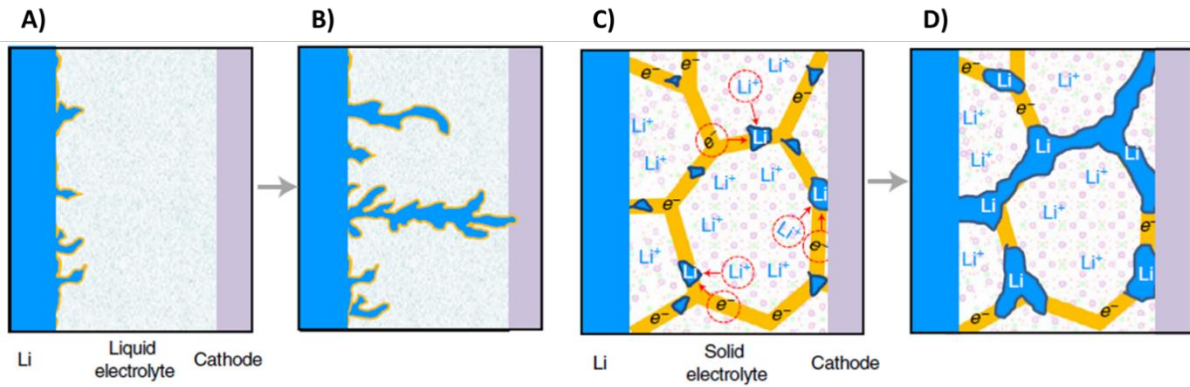


**Figure 1.10.** Schematic representation of lithium dendrite formation and penetration in liquid-electrolyte-batteries (A, B) and solid-state electrolyte batteries (C, D). The reduction of  $\text{Li}^+$  ions at the grain boundaries, which can become a pathway for electrons (yellow) owing to their small band-gap, of a solid-state polycrystalline electrolyte forms Li filaments (blue), which propagates and lead to a short circuit. Reproduced with permission [30]. Copyright 2021, Springer Nature.

Another challenge associated with the development of solid-state batteries is electrode-electrolyte contact loss, which can increase upon cycling, especially at high current densities [28,32,33]. Stripping of pure lithium metal generates vacancy sites in the Li electrode, which accumulates with time by forming voids at the Li-SSE interface. These voids reduce interfacial contact between electrode-electrolyte. At a constant current, there is an increase in the local current density leading to concentrated Li-ion flux at the remaining contact points, which further increases the contact loss (Fig. 1.11) [28,32].

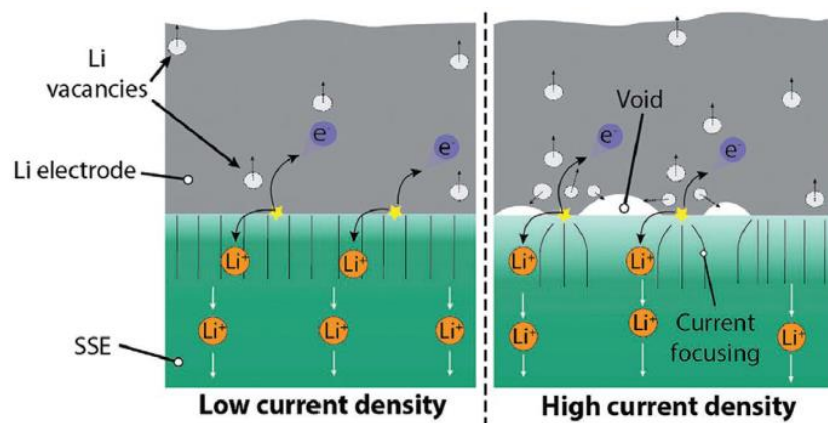


**Figure 1.11.** Schematic representation of Li stripping at a constant current in a Li/SSE system.  $\text{Li}^+$  ions are injected into the SSE, which can form Li vacancies in the electrode. Vacancy accumulation near the interface leads to the formation of large voids and reduced Li/SSE contact points, which concentrates current and accelerates contact loss. Reproduced with permission [32]. Copyright 2020, Elsevier.

The search for materials that can effectively work as solid-state electrolytes by fulfilling all the requirements presented in Fig. 1.8, by presenting good electrode compatibility and by reducing the production, operability and maintenance costs is a challenge and further research is required. Sulphides [34], oxides [35], polymers [36] and more recently, metal-boranes [37] are types of materials that have been investigated for applications as solid-state electrolytes. Fig. 1.12 summarises the main advantages and disadvantages observed for each class of material.

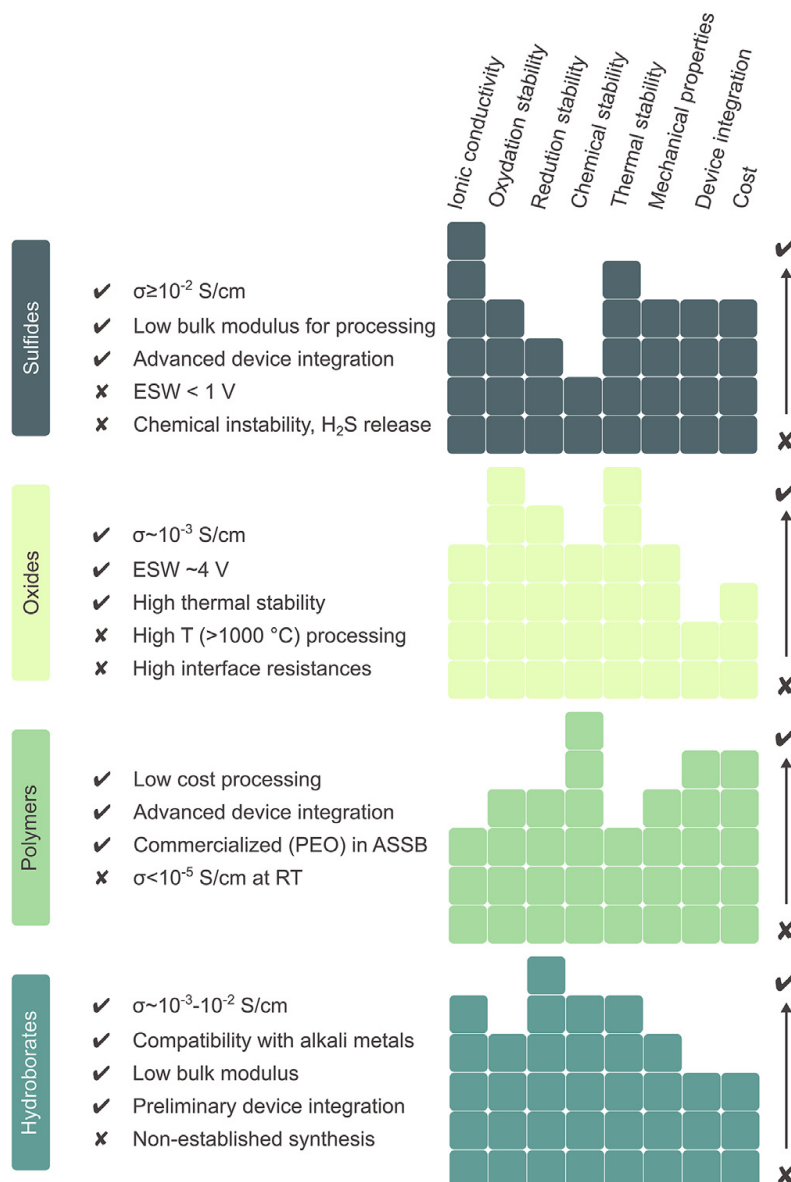


**Figure 1.12.** Summary of the properties observed for the main classes of materials investigated for application as solid-state electrolytes. ESW, PEO and ASSB stand for Electrochemical Stability Window, Polyethylene Oxide, and All-Solid-State-Batteries, respectively. Reproduced with permission [18]. Copyright 2020, Elsevier.

Sulphide-based compounds have attracted great interest from researchers due to their superionic conductivity properties at room temperature ( $> 10 \text{ mS cm}^{-1}$ ) [38,39], sometimes even higher than the liquid electrolytes, however their low chemical stability in air and their low electrochemical stability against Li and Na metals hinder their practical application as solid-state electrolytes [18,40,41]. Certain oxide-based ceramics also present high ionic conductivity properties at room temperature, however electrode-electrolyte interfacial issues and high processing costs are their downsides [21,42]. Polymers have also been investigated as potential solid-state electrolytes, but they usually present low ionic conductivity and poor electrode compatibility [43–45]. Boron-hydrogen salts, also known as hydroborates, are now emerging as a potential class of solid-state electrolytes [18,37,46] owing to the promising combination of properties they exhibit (Fig. 1.12), as further discussed.

### 1.3 BORANES – AN OVERVIEW

Boron (B) is an element from group 13 of the periodic table and is the only non-metal within this family. The chemical properties of boron mostly differ from the elements from its group and share more similarities with neighbours carbon (C) and silicon (Si), elements from the adjacent group 14, owing to the boron's tendency to form covalent bonds, as in boranes (e.g.  $\text{B}_5\text{H}_9$ ), and oxide structures, as in borates (e.g.  $[\text{B}_3\text{O}_6]^{3-}$ ) [24,47].

Boron covalently bonds with hydrogen to form bridging (B–H–B) or terminal bonding (B–H or B–H<sub>2</sub> or B–H<sub>3</sub>) [46]. The hydrogen-bridging bond is an important characteristic from boron chemistry, which is usually unseen in carbon chemistry, and allows the formation of a great variety of boron-clusters with different properties [47]. Boron can also form compounds with carbon, which yields a large family of B–C clusters called carboranes, with nitrogen, such as ammonia borane ( $\text{NH}_3\text{BH}_3$ ), and with metals, also known as metallaboranes [24].

Boron clusters can be neutrally charged or ionic, and they are usually classified in three different families according to their structure, *closo*, *nido* and *arachno*-boranes. The *closo*-boranes are the most stable group of boron cluster with a closed polyhedral cage-like structure and formula  $\text{B}_n\text{H}_n^{2-}$  ( $n = 5 - 12$ ). The *nido*-boranes are formed with 1 empty corner, present a 'nest-like' structure and general formula  $\text{B}_n\text{H}_n^{4-}$ , and the less stable structure is called *arachno*-boranes due to their cage's similarity with spiders' webs. They have a formula  $\text{B}_n\text{H}_n^{6-}$  and 2 empty corners (Fig. 1.13) [24,46,47].



**Figure 1.13.** The three most common classes of borane structures: *closo*-boranes, as in  $B_{12}H_{12}^{2-}$ , *nido*-boranes, as in  $B_{11}H_{13}^{2-}$ , and *arachno*-boranes, as in  $B_{10}H_{15}^{-}$ . Reproduced and adapted with permission. [48]. Copyright 2009, Springer Nature.

It is believed that the study of boranes started about 120 years ago, but a boom in the research of these compounds happened only in the 1950s with support from the U.S. and Soviet Union governments to develop high-energy fuels for military purposes [46]. By this time, it was found that more energy is released from the combustion of boranes than hydrocarbon fuels, and boron-hydrogen materials were considered promising powerful propellants for rockets and aircrafts [46]. However, increasing research has revealed that the applications of boranes go beyond military purposes, and these compounds are also used in chemical reactions as reducing agents, in the medicine for cancer treatment and in the energy sector [46]. As such, sodium borohydride ( $NaBH_4$ ) is widely used in organic reactions for the reduction of aldehydes and ketones in their corresponding alcohols [49].  $^{10}B$ , one of the boron isotopes, has high neutron absorption properties, and boranes have been used on boron neutron capture therapy (BNCT) for the treatment of cancer [50].  $NaBH_4$  and ammonia borane ( $NH_3BH_3$ ) have been studied as materials for hydrogen storage and fuels for fuel cells [51]. Several metal boranes and carboranes have shown high ionic conductivity properties, especially after assuming a disordered polymorphic structure at high temperatures, and now, increasing research has been conducted for the development of batteries with boron clusters as solid-state electrolytes [52].

## 1.4 BORANES AS SOLID-STATE ELECTROLYTES

In 2007, Matsuo *et al.* [53] reported an unusual phenomenon observed for the ionic conductivity of  $\text{LiBH}_4$  upon heating. They demonstrated that the  $\text{Li}^+$  conductivity of  $\text{LiBH}_4$  increased 5 orders of magnitude from  $10^{-8} \text{ S cm}^{-1}$  at  $\approx 30^\circ\text{C}$  to  $10^{-3} \text{ S cm}^{-1}$  at  $\approx 120^\circ\text{C}$  due to a structural transition from orthorhombic (low temperature phase) to hexagonal polymorph (high temperature phase). This increase in ionic conductivity due to an order-disorder polymorphic transition is not limited to boranes and has also been reported for phosphate [54,55] and sulphate [56] compounds. Since then, the investigation of the ionic conductivity properties of other metal-boranes, especially Li and Na-boranes, has been conducted in an attempt to find a suitable solid-state electrolyte for the next generation of batteries. Fig. 1.14 shows the thermal behaviour of the  $\text{Li}^+$  and  $\text{Na}^+$  conductivity of some boron-hydrogen salts. The liquid electrolyte 1 mol  $\text{L}^{-1}$  solution of 1-ethyl-3-methylimidazolium tetrafluoroborate (EMIBF<sub>4</sub>) with lithium tetrafluoroborate ( $\text{LiBF}_4$ ) [57], and the solid-electrolyte Na- $\beta$ - $\text{Al}_2\text{O}_3$  [46], which is currently used in Na-S batteries, were added to the plots for comparison.

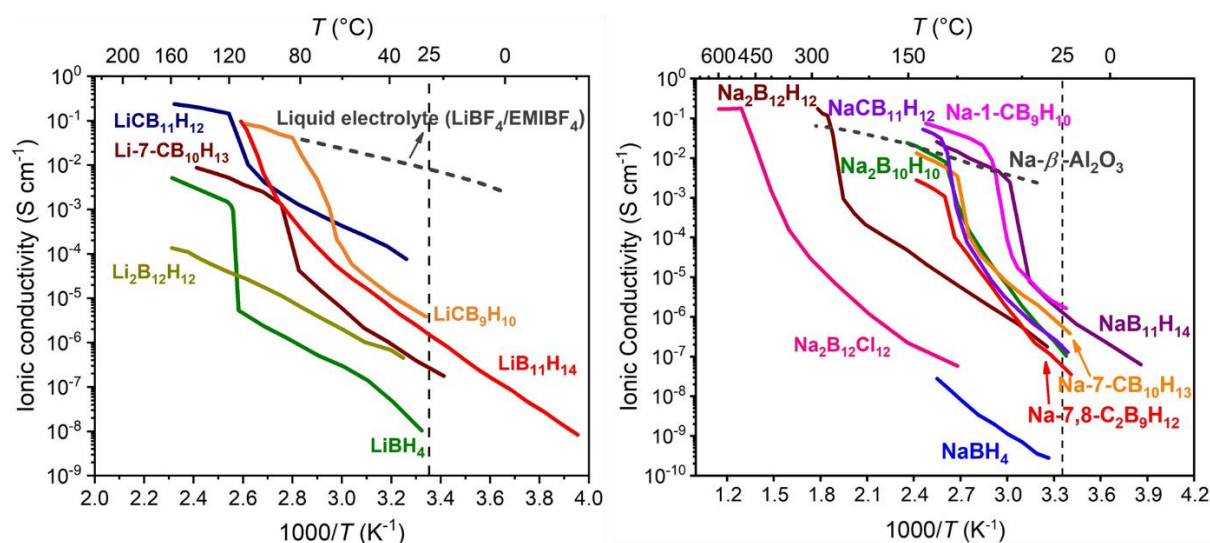


**Figure 1.14.** Solid-state  $\text{Li}^+$  (left) [53,58–61] and  $\text{Na}^+$  (right) [59,61–64] conductivity of some common boron-hydrogen materials as a function of temperature. The liquid electrolyte  $\text{LiBF}_4/\text{EMIBF}_4$  [57] and the solid-electrolyte Na- $\beta$ - $\text{Al}_2\text{O}_3$  [46] (dashed lines) were added for comparison.

As it can be seen in Fig. 1.14, the majority of the boranes exhibit a sudden step-function increase in ionic conductivity after undergoing an order-disorder polymorphic transition. Some compounds, such as  $\text{LiCB}_{11}\text{H}_{12}$  and  $\text{LiCB}_9\text{H}_{10}$  present even higher  $\text{Li}^+$  conductivity than



the liquid electrolyte  $\text{LiBF}_4/\text{EMIBF}_4$  after their polymorphic phase transition, as well as what is observed for the samples  $\text{Na}_2\text{B}_{12}\text{H}_{12}$ ,  $\text{NaCB}_{11}\text{H}_{12}$  and  $\text{Na-1-CB}_9\text{H}_{10}$ , when compared to the solid-state  $\text{Na-}\beta\text{-Al}_2\text{O}_3$ . It has been demonstrated that the order-disorder polymorphic transition observed in the majority of the metal boranes leads to rapid rotation of the anion, which facilitates the migration of the cation through the structure, a process known as paddle-wheel mechanism (Fig. 1.9B) [25,46,65]. The dynamics of the anion coupled with the partially filled cationic sites in the lattice result in increased cationic conductivity and decreased activation energy for ionic conductivity. Table 1.1 shows the polymorphic transition temperature reported for some lithium and sodium boranes, and the crystallographic symmetry they present before and after the order-disorder phase transition, which always results in a more symmetric crystal structure.

**Table 1.1.** Approximate phase-transition temperatures with the technique used to determine each of them, structural symmetries and space groups of the low temperature (LT) and high temperature (HT) phases for several lithium and sodium-boranes.

Compound	Symmetry of LT structure	$T_{\text{trans}}$ (heating)	Symmetry of HT structure	Ref
$\text{LiBH}_4$	Orthorhombic ( $Pnma$ )	117 °C (NMR) <sup>a</sup>	Hexagonal ( $P6_3mc$ )	[53,66]
$\text{NaBH}_4$	Tetragonal ( $P4_2/nmc$ )	-83 °C (NMR)	Cubic ( $Fm\bar{3}m$ )	[67,68]
$\text{Li}_2\text{B}_{12}\text{H}_{12}$	Cubic ( $Pa\bar{3}$ )	355 °C (XRD) <sup>b</sup>	Cubic ( $Pa\bar{3}$ )	[69]
$\text{Na}_2\text{B}_{12}\text{H}_{12}$	Monoclinic ( $P2_1/n$ )	1.) 257 °C (NPD) <sup>c</sup> 2.) 272 °C (NPD)	1.) Partially disordered Cubic ( $Pm\bar{3}n$ ) 2.) Fully disordered Cubic ( $Im\bar{3}m$ )	[70]
$\text{Na}_2\text{B}_{12}\text{Cl}_{12}$	Cubic ( $Pa\bar{3}$ )	475 °C (DSC) <sup>d</sup>	Cubic ( $Fm\bar{3}m$ )	[63]
$\text{LiCB}_{11}\text{H}_{12}$	Orthorhombic ( $Pca2_1$ )	120 °C (DSC)	Cubic ( $Fm\bar{3}m$ )	[71,72]

<b>NaCB<sub>11</sub>H<sub>12</sub></b>	Orthorhombic ( <i>Pca2<sub>1</sub></i> )	105 °C (DSC)	Cubic ( <i>Fm<math>\bar{3}m</math></i> )	[71,72]
<b>Li<sub>2</sub>B<sub>10</sub>H<sub>10</sub></b>	Hexagonal ( <i>P6<sub>4</sub>22</i> )	367 °C (DSC)	-	[73]
<b>Na<sub>2</sub>B<sub>10</sub>H<sub>10</sub></b>	Monoclinic ( <i>P2<sub>1</sub>/c</i> )	100 °C (DSC)	Cubic ( <i>Fm<math>\bar{3}m</math></i> )	[64,66]
<b>LiCB<sub>9</sub>H<sub>10</sub></b>	Partially disordered Orthorhombic ( <i>Cmc2<sub>1</sub></i> ) at 60 °C	65 °C (DSC)	Hexagonal ( <i>P3<sub>1</sub>c</i> )	[74]
<b>NaCB<sub>9</sub>H<sub>10</sub></b>	Monoclinic ( <i>P2<sub>1</sub>/c</i> )	1.) -30 °C (XRD) 2.) 27 °C (DSC)	1.) Partially disordered Orthorhombic ( <i>Pna2<sub>1</sub></i> ) 2.) Fully disordered Hexagonal ( <i>P3<sub>1</sub>c</i> )	[74,75]
<b>LiB<sub>11</sub>H<sub>14</sub></b>	Orthorhombic ( <i>Pbca</i> )	112 °C (DSC)	Cubic ( <i>Fm<math>\bar{3}</math></i> )	[60]
<b>NaB<sub>11</sub>H<sub>14</sub></b>	Orthorhombic ( <i>Pnma</i> )	84 °C (DSC)	Cubic ( <i>I-43d</i> )	[59]
<b>Li-7-CB<sub>10</sub>H<sub>13</sub></b>	Monoclinic ( <i>P2<sub>1</sub>/n</i> )	67 °C (DSC)	Orthorhombic ( <i>Aea2</i> )	[59]
<b>Na-7-CB<sub>10</sub>H<sub>13</sub></b>	Orthorhombic ( <i>Pna2<sub>1</sub></i> )	60 °C (DSC)	Cubic ( <i>Fm<math>\bar{3}m</math></i> )	[59]

<sup>a</sup>NMR: Nuclear Magnetic Resonance. <sup>b</sup>XRD: X-Ray Diffraction. <sup>c</sup>NPD: Neutron Powder Diffraction. <sup>d</sup>DSC: Differential Scanning Calorimetry.

It is observed that lithium boranes tend to have higher polymorphic phase transition temperatures than their corresponding sodium boranes. The same trend has also been reported for borohydrides, with an increase in the transition temperature with cation size decrease: CsBH<sub>4</sub> < RbBH<sub>4</sub> < KBH<sub>4</sub> < NaBH<sub>4</sub> < LiBH<sub>4</sub> [46,76]. The size of the anion can also play an important role, with sodium boranes with larger anions tending to present higher transition temperatures. A fine example of this is seen when the hydrogen atoms from Na<sub>2</sub>B<sub>12</sub>H<sub>12</sub> are replaced by chlorine as in Na<sub>2</sub>B<sub>12</sub>Cl<sub>12</sub> (Table 1.1) [63]. The transition temperature is also significantly reduced with the chemical modification of the anions through

replacement of a boron atom with a carbon.  $\text{LiCB}_{11}\text{H}_{12}$  and  $\text{NaCB}_{11}\text{H}_{12}$  exhibit much lower transition temperatures than their corresponding boranes  $\text{Li}_2\text{B}_{12}\text{H}_{12}$  and  $\text{Na}_2\text{B}_{12}\text{H}_{12}$ . The same trend is observed for  $\text{LiCB}_9\text{H}_{10}$  and  $\text{NaCB}_9\text{H}_{10}$  when compared to  $\text{Li}_2\text{B}_{10}\text{H}_{10}$  and  $\text{Na}_2\text{B}_{10}\text{H}_{10}$ , respectively (Table 1.1). Therefore, carboranes assume a disordered polymorphic structure with superionic conductivity at temperatures closer to room temperature than their corresponding boranes. The replacement of a boron with a carbon results in the anion becoming monovalent, which reduces the number of cations in the structure to keep charge neutrality. According to Tang *et al.* [59,74], this results in reduced cation-site blockage and decreased strength of cation-anion Coulombic interactions, which are all likely to be responsible for the reduced polymorphic transition temperature and increased ionic conductivity observed in carboranes (Table 1.1 and Fig. 1.14) [59,74].

The *nido*-boranes, as in  $\text{LiB}_{11}\text{H}_{14}$ ,  $\text{NaB}_{11}\text{H}_{14}$ ,  $\text{Li-7-CB}_{10}\text{H}_{13}$ ,  $\text{Na-7-CB}_{10}\text{H}_{13}$ , also present much lower transition temperatures than the *closo*-borane dianions  $\text{B}_{10}\text{H}_{10}^{2-}$  and  $\text{B}_{12}\text{H}_{12}^{2-}$  (Table 1.1), and higher ionic conductivity properties over a wider range of temperature (Fig. 1.14). The chemical modification of the anions is only one of the several approaches that has been used to increase the cationic conductivity of the metal boranes. Table 1.2 demonstrates other successful strategies that have been employed to tune the ionic conductivity properties of some lithium and sodium boron-hydrogen salts.

**Table 1.2.** Different strategies used to enhance the ionic conductivity of some lithium and sodium boranes.

Modification	Material	Approximate ionic conductivity near 30 – 40 °C ( $\text{S cm}^{-1}$ )	Justification	Ref
-	$\text{Li}_2\text{B}_{12}\text{H}_{12}$	$10^{-8}$	-	[77]
Mechanical modification	Mechanically ball-milled $\text{Li}_2\text{B}_{12}\text{H}_{12}$	$10^{-5}$	Formation of cation vacancies	[77]
-	$\text{NaCB}_{11}\text{H}_{12}$	$10^{-6}$	-	[78]
Mechanical modification	Mechanically ball-milled $\text{NaCB}_{11}\text{H}_{12}$	$10^{-3}$	Stabilisation of the $\text{HT}^a$ polymorph at $\text{RT}^b$	[78]

-	$\text{LiCB}_9\text{H}_{10}$	$10^{-6}$	-	[61]
-	$\text{LiCB}_{11}\text{H}_{12}$	$10^{-5}$	-	[61]
Mixing of different boron-hydrogen anions	$\text{Li}_2(\text{CB}_9\text{H}_{10})(\text{CB}_{11}\text{H}_{12})$	$10^{-3}$	Stabilisation of the HT disordered polymorph	[61]
-	$\text{NaBH}_4$	$10^{-10}$	-	[62]
-	$\text{Na}_2\text{B}_{12}\text{H}_{12}$	$10^{-7}$	-	[79]
Mixing of different boron-hydrogen anions	$\text{Na}_3(\text{BH}_4)(\text{B}_{12}\text{H}_{12})$	$10^{-3}$	Formation of channels and voids in the lattice, which facilitate $\text{Na}^+$ migration	[79]
-	$\text{LiBH}_4$	$10^{-8}$	-	[53]
Oxide composite formation	$\text{LiBH}_4\text{-Al}_2\text{O}_3$	$10^{-4}$	Formation of B-O bonds at the interface	[80]
Hydration	$\text{LiBH}_4\cdot\text{H}_2\text{O}$	$10^{-4}$	$\text{Li}^+$ migration is facilitated by water motion in the lattice	[81]
Ammoniation	$\text{LiBH}_4\cdot 1/2\text{NH}_3$	$10^{-4}$	$\text{NH}_3$ coordinates with interstitial $\text{Li}^+$ , facilitating its migration through framework	[82]

<sup>a</sup>HT: High Temperature. <sup>b</sup>RT: Room Temperature.

Among these strategies presented in Table 1.2, the formation of mixed-borane solid solutions has gained attention from several researchers, and different materials with high ionic conductivity properties have been prepared (Fig. 1.15).

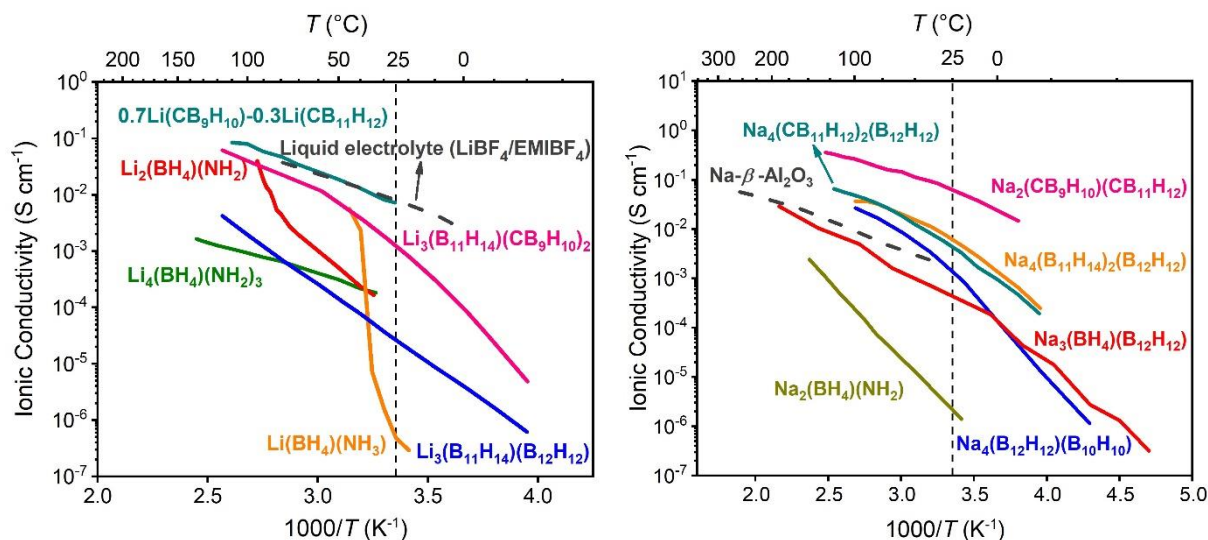


**Figure 1.15.** Solid-state  $\text{Li}^+$  (left) [60,83–85] and  $\text{Na}^+$  (right) [61,62,79,86–88] conductivity of some mixed-anion boron-hydrogen materials. The ionic liquid electrolyte  $\text{LiBF}_4/\text{EMIBF}_4$  [57] and the solid-electrolyte  $\text{Na-}\beta\text{-Al}_2\text{O}_3$  [46] (dashed lines) were added for comparison.

As such,  $\text{Na}_2(\text{CB}_9\text{H}_{10})(\text{CB}_{11}\text{H}_{12})$ ,  $\text{Na}_4(\text{CB}_{11}\text{H}_{12})_2(\text{B}_{12}\text{H}_{12})$  and  $\text{Na}_4(\text{B}_{11}\text{H}_{14})_2(\text{B}_{12}\text{H}_{12})$  exhibit  $\text{Na}^+$  conductivity at room temperature even higher than the solid electrolyte  $\text{Na-}\beta\text{-Al}_2\text{O}_3$  [61,87,88], whereas  $0.7\text{Li}(\text{CB}_9\text{H}_{10})\text{-}0.3\text{Li}(\text{CB}_{11}\text{H}_{12})$  [83] shows  $\text{Li}^+$  conductivity properties identical to the ionic liquid electrolyte  $\text{LiBF}_4/\text{EMIBF}_4$  (Fig. 1.15). As shown in Table 1.2, the formation of mixed-borane solid solution may increase defects, facilitating migration of the cation through the structure, and/or may stabilise the high temperature polymorph at lower temperatures [61,79].

The coordination of boranes with neutral ligands, such as water, e.g.  $\text{LiBH}_4\cdot\text{H}_2\text{O}$  [81], and ammonia, e.g.  $\text{LiBH}_4\cdot 1/2\text{NH}_3$  [82], also seems to be a good strategy to enhance ionic conductivity properties (Table 1.2), as the coordinated neutral ligand may help the migration of the cation through the structure. However this field of research is yet to be explored in detail, therefore hydrated *nido*-boranes were investigated as potential solid-state electrolytes in this thesis. Other modification strategies, such as ball-milling and anion-mixtures, were also

studied as an attempt to improve the ionic conductivity properties of the materials synthesised in this thesis.

Researchers have also analysed the electrochemical stability of some lithium and sodium boron-hydrogen materials against pure Li and Na metal, respectively, as an assessment of their application as solid-state electrolytes (Table 1.3). The materials listed in Table 1.3 were all assessed experimentally through a similar mechanism, by preparing a pellet of the sample with addition of graphite on one face to improve oxidation kinetics and enhance electronic conductivity. The voltammetry was also performed at very slow scan rates ( $< 100 \mu\text{V s}^{-1}$ ) to avoid overestimation of the oxidation result [89,90].

**Table 1.3.** Oxidative stability limit of some lithium and sodium boranes against Li and Na metal, respectively. The sulphide  $\text{Li}_{10}\text{GeP}_2\text{S}_{12}$  and the oxide  $\text{Li}_7\text{La}_3\text{Zr}_2\text{O}_{12}$  solid electrolytes were also added for comparison.

<b>Material</b>	<b>Approximate oxidative stability limit vs. <math>M^+/M</math> (<math>M = \text{Li or Na}</math>)</b>	<b>Ref</b>
$\text{LiBH}_4$	2.0 V vs. $\text{Li}^+/\text{Li}$	[90,91]
$\text{Li}_2\text{B}_{12}\text{H}_{12}$	3.3 V vs. $\text{Li}^+/\text{Li}$	[91]
$\text{LiB}_{11}\text{H}_{14}$	2.6 V vs. $\text{Li}^+/\text{Li}$	[60]
$\text{NaBH}_4$	1.9 V vs. $\text{Na}^+/\text{Na}$	[90–92]
$\text{Na}_2\text{B}_{12}\text{H}_{12}$	3.5 V vs. $\text{Na}^+/\text{Na}$	[91,92]
$\text{Na}_2\text{B}_{10}\text{H}_{10}$	3.0 V vs. $\text{Na}^+/\text{Na}$	[90]
$\text{NaB}_{11}\text{H}_{14}$	2.6 V vs. $\text{Na}^+/\text{Na}$	[87]
$\text{Na}_4(\text{CB}_{11}\text{H}_{12})_2(\text{B}_{12}\text{H}_{12})$	4.1 V vs. $\text{Na}^+/\text{Na}$	[90,93]
$\text{Li}_{10}\text{GeP}_2\text{S}_{12}$ (LGPS)	2.1 V vs. $\text{Li}^+/\text{Li}$	[89]
$\text{Li}_7\text{La}_3\text{Zr}_2\text{O}_{12}$ (LLZO)	2.9 V vs. $\text{Li}^+/\text{Li}$ (theoretical) 4.0 V vs. $\text{Li}^+/\text{Li}$ (experimental)	[89]

The sulphide  $\text{Li}_{10}\text{GeP}_2\text{S}_{12}$  (LGPS) and the ceramic  $\text{Li}_7\text{La}_3\text{Zr}_2\text{O}_{12}$  (LLZO) are considered some of the most promising solid electrolytes [89], and they show electrochemical stability against lithium metal comparable to other metal boron-hydrogen materials.

The high ionic conductivity properties and the relatively high oxidative stability limit of boranes against pure alkali metal (e.g. Li and Na) have led researchers to investigate their application as solid-state electrolytes in proof-of-concept batteries with different cathode materials, as shown in Table 1.4.

**Table 1.4.** Battery tests performed with different lithium and sodium boranes as solid-state electrolytes.

Cathode and theoretical capacity	Electrolyte	Anode	Operating Voltage	Highlight	Ref
S+C composite 1672 mAh g <sup>-1</sup>	0.7Li(CB <sub>9</sub> H <sub>10</sub> )- 0.3Li(CB <sub>11</sub> H <sub>12</sub> )	Li	1.0 – 2.5 V	≈ 63% (1053 mAh g <sup>-1</sup> ) of the theoretical capacity was retained after 20 cycles at 1C <sup>a</sup> (1672 mA g <sup>-1</sup> ) at RT.	[83]
TiS <sub>2</sub> 239 mAh g <sup>-1</sup>	Li <sub>2</sub> (B <sub>11</sub> H <sub>14</sub> )(CB <sub>11</sub> H <sub>12</sub> )	Li	1.6 – 2.5 V	≈ 64% (153 mAh g <sup>-1</sup> ) of the theoretical capacity was retained after 150 cycles at 0.1C (23.9 mA g <sup>-1</sup> ) for the first 5 cycles and at 0.5C (119.5 mA g <sup>-1</sup> ) from the 6 <sup>th</sup> cycle at 60 °C and under 3.2 MPa.	[60]
NaCrO <sub>2</sub> 120 mAh g <sup>-1</sup>	Na <sub>4</sub> (B <sub>12</sub> H <sub>12</sub> )(B <sub>10</sub> H <sub>10</sub> )	Na	2.25 – 3.25 V	≈ 54% (65 mAh g <sup>-1</sup> ) of the theoretical capacity was retained after 250 cycles at 0.05C (6 mA	[94]

				g <sup>-1</sup> ) for the first 3 cycles and at 0.2C (24 mA g <sup>-1</sup> ) from the 4 <sup>th</sup> cycle at 60 °C.
Na <sub>3</sub> (VOPO <sub>4</sub> ) <sub>2</sub> F 130 mAh g <sup>-1</sup>	Na <sub>4</sub> (CB <sub>11</sub> H <sub>12</sub> ) <sub>2</sub> (B <sub>12</sub> H <sub>12</sub> )	Na	2.50 – 4.15 V	≈ 60% (78 mAh g <sup>-1</sup> ) of the theoretical capacity was retained after 800 cycles at 0.1C (13 mA g <sup>-1</sup> ) for the first 2 cycles and at 0.2C (26 mA g <sup>-1</sup> ) from the 3 <sup>rd</sup> cycle at RT. [88]

<sup>n</sup>C stands for the C-rate, in which the current fully charges or discharges the battery in 1/n hours.

The high capacity retention after several cycles observed in the batteries prepared with boranes as electrolytes demonstrate the great potential of these materials to be used in solid-state batteries. However, more research needs to be conducted in order to address the current challenges associated with the use of boranes as solid-state electrolytes, such as, high cost of synthesis and SSE-electrode interfacial issues [88,94–96]. *Closo*-boranes and carboranes usually present elevated preparation costs [95], and alternative synthetic routes with more affordable reactants or synthesis optimisation of other type of boranes, such as *nido*-boranes, need to be found in order to make their use more economically viable. Boron-hydrogen materials may also be susceptible to dendrite formation against Li and Na anodes [31], as well as to SSE-electrode contact loss upon cycling [97], and addressing those issues is detrimental for commercial application of SSBs. Therefore, synthesis optimisation of metal-boranes, assessment and enhancement of their properties as solid-state electrolytes are necessary studies for the development of SSBs, and they are the main focus of this thesis.



## 1.5 REFERENCES

- [1] M.A. Hannan, A.Q. Al-Shetwi, R.A. Begum, S.E. Young, M.M. Hoque, P.J. Ker, M. Mansur, K. Alzaareer, The value of thermal management control strategies for battery energy storage in grid decarbonization: Issues and recommendations, *J. Clean. Prod.* 276 (2020) 124223. <https://doi.org/10.1016/j.jclepro.2020.124223>.
- [2] F.B. Martins, R.B. Benassi, R.R. Torres, F.A. de Brito Neto, Impacts of 1.5 °C and 2 °C global warming on Eucalyptus plantations in South America, *Sci. Total Environ.* 825 (2022) 153820. <https://doi.org/10.1016/j.scitotenv.2022.153820>.
- [3] C. Jägemann, M. Fürsch, S. Hagspiel, S. Nagl, Decarbonizing Europe's power sector by 2050 - Analyzing the economic implications of alternative decarbonization pathways, *Energy Econ.* 40 (2013) 622–636. <https://doi.org/10.1016/j.eneco.2013.08.019>.
- [4] IRENA, Renewable Energy Statistics 2022, Abu Dhabi, 2022. [www.irena.org/Publications](http://www.irena.org/Publications).
- [5] M.C. Argyrou, P. Christodoulides, S.A. Kalogirou, Energy storage for electricity generation and related processes: Technologies appraisal and grid scale applications, *Renew. Sustain. Energy Rev.* 94 (2018) 804–821. <https://doi.org/10.1016/j.rser.2018.06.044>.
- [6] Battery storage, ARENA, (2022). <https://arena.gov.au/renewable-energy/battery-storage/> (accessed June 21, 2022).
- [7] X. Cao, N. Zhao, A cooperative management strategy for battery energy storage system providing Enhanced Frequency Response, *Energy Reports.* 8 (2022) 120–128. <https://doi.org/10.1016/j.egyr.2021.11.092>.
- [8] G.J. May, A. Davidson, B. Monahov, Lead batteries for utility energy storage: A review, *J. Energy Storage.* 15 (2018) 145–157. <https://doi.org/10.1016/j.est.2017.11.008>.
- [9] M. Armand, J. Tarascon, Building better batteries, *Nature.* 451 (2008) 652–657. <https://doi.org/10.1038/451652a>
- [10] A.M. Abakumov, S.S. Fedotov, E. V. Antipov, J.M. Tarascon, Solid state chemistry for developing better metal-ion batteries, *Nat. Commun.* 11 (2020) 1–14. <https://doi.org/10.1038/s41467-020-18736-7>.
- [11] V. Henze, Battery Pack Prices Fall to an Average of \$132/kWh, But Rising Commodity Prices Start to Bite, BloombergNEF. (2021). <https://about.bnef.com/blog/battery-pack-prices-fall-to-an-average-of-132-kwh-but-rising-commodity-prices-start-to-bite/>

- (accessed September 12, 2022).
- [12] F. Zheng, M. Kotobuki, S. Song, M.O. Lai, L. Lu, Review on solid electrolytes for all-solid-state lithium-ion batteries, *J. Power Sources*. 389 (2018) 198–213. <https://doi.org/10.1016/j.jpowsour.2018.04.022>.
- [13] A. Saiyid, UPDATE: Bringing down battery costs will enable automakers to meet Biden’s 50% EV sales goal: GM officia, *S&P Glob.* (2021). <https://cleanenergynews.ihsmarkit.com/research-analysis/bringing-down-battery-costs-will-enable-automakers-to-meet-bid.html> (accessed September 12, 2022).
- [14] R. Kurmelovs, ‘Gone ballistic’: lithium price rockets nearly 500% in a year amid electric vehicle rush, *Guard.* (2022). <https://www.theguardian.com/australia-news/2022/feb/09/gone-ballistic-lithium-price-rockets-nearly-500-in-a-year-amid-electric-vehicle-rush> (accessed May 5, 2022).
- [15] A. Mauger, C.M. Julien, A. Paoella, M. Armand, K. Zaghib, Building Better Batteries in the Solid State: A Review, *Materials*. 12 (2019) 3892. <https://doi.org/10.3390/ma12233892>.
- [16] M. Ue, K. Uosaki, Recent progress in liquid electrolytes for lithium metal batteries, *Curr. Opin. Electrochem.* 17 (2019) 106–113. <https://doi.org/10.1016/j.coelec.2019.05.001>.
- [17] W. Luo, C.F. Lin, O. Zhao, M. Noked, Y. Zhang, G.W. Rubloff, L. Hu, Ultrathin Surface Coating Enables the Stable Sodium Metal Anode, *Adv. Energy Mater.* 7 (2017) 1–6. <https://doi.org/10.1002/aenm.201601526>.
- [18] L. Duchêne, A. Remhof, H. Hagemann, C. Battaglia, Status and prospects of hydroborate electrolytes for all-solid-state batteries, *Energy Storage Mater.* 25 (2020) 782–794. <https://doi.org/10.1016/j.ensm.2019.08.032>.
- [19] W. Zhang, F. Zhang, F. Ming, H.N. Alshareef, Sodium-ion battery anodes: Status and future trends, *EnergyChem.* 1 (2019) 100012. <https://doi.org/10.1016/j.enchem.2019.100012>.
- [20] J.C. Bachman, S. Muy, A. Grimaud, H. Chang, N. Pour, S.F. Lux, O. Paschos, F. Maglia, S. Lupart, P. Lamp, L. Giordano, Y. Shao-Horn, Inorganic Solid-State Electrolytes for Lithium Batteries: Mechanisms and Properties Governing Ion Conduction, *Chem. Rev.* 116 (2016) 140–162. <https://doi.org/10.1021/acs.chemrev.5b00563>.
- [21] L. Wang, J. Li, G. Lu, W. Li, Q. Tao, C. Shi, H. Jin, G. Chen, S. Wang, Fundamentals of Electrolytes for Solid-State Batteries: Challenges and Perspectives, *Front. Mater.* 7

- (2020) 1–5. <https://doi.org/10.3389/fmats.2020.00111>.
- [22] Y. Lu, L. Li, Q. Zhang, Z. Niu, J. Chen, Electrolyte and Interface Engineering for Solid-State Sodium Batteries, *Joule*. 2 (2018) 1747–1770. <https://doi.org/10.1016/j.joule.2018.07.028>.
- [23] Q. Zhao, S. Stalin, C.Z. Zhao, L.A. Archer, Designing solid-state electrolytes for safe, energy-dense batteries, *Nat. Rev. Mater.* 5 (2020) 229–252. <https://doi.org/10.1038/s41578-019-0165-5>.
- [24] P.W. Atkins, T.L. Overton, J.P. Rourke, M.T. Weller, F.A. Armstrong, Shriver and Atkins' Inorganic Chemistry, 5th ed., Oxford University Press, Oxford, 2010.
- [25] M. Paskevicius, B.R.S. Hansen, M. Jørgensen, B. Richter, T.R. Jensen, Multifunctionality of silver *closo*-boranes, *Nat. Commun.* 8 (2017) 10–15. <https://doi.org/10.1038/ncomms15136>.
- [26] K.E. Kweon, J.B. Varley, P. Shea, N. Adelman, P. Mehta, T.W. Heo, T.J. Udovic, V. Stavila, B.C. Wood, Structural, Chemical, and Dynamical Frustration: Origins of Superionic Conductivity in *closo*-Borate Solid Electrolytes, (2017) 9142–9153. <https://doi.org/10.1021/acs.chemmater.7b02902>.
- [27] Z. Yu, X. Zhang, C. Fu, H. Wang, M. Chen, G. Yin, H. Huo, J. Wang, Dendrites in Solid-State Batteries: Ion Transport Behavior, Advanced Characterization, and Interface Regulation, *Adv. Energy Mater.* 11 (2021) 1–25. <https://doi.org/10.1002/aenm.202003250>.
- [28] Y. Lu, C.-Z. Zhao, H. Yuan, X.-B. Cheng, J.-Q. Huang, Q. Zhang, Critical current density in solid-state lithium metal batteries: mechanism, influences, and strategies, *Adv. Funct. Mater.* 31 (2021) 2009925. <https://doi.org/10.1002/adfm.202009925>.
- [29] F. Mo, J. Ruan, S. Sun, Z. Lian, S. Yang, X. Yue, Y. Song, Y.N. Zhou, F. Fang, G. Sun, S. Peng, D. Sun, Inside or Outside: Origin of Lithium Dendrite Formation of All Solid-State Electrolytes, *Adv. Energy Mater.* 9 (2019) 1–10. <https://doi.org/10.1002/aenm.201902123>.
- [30] X. Liu, R. Garcia-Mendez, A.R. Lupini, Y. Cheng, Z.D. Hood, F. Han, A. Sharafi, J.C. Idrobo, N.J. Dudney, C. Wang, C. Ma, J. Sakamoto, M. Chi, Local electronic structure variation resulting in Li 'filament' formation within solid electrolytes, *Nat. Mater.* 20 (2021) 1485–1490. <https://doi.org/10.1038/s41563-021-01019-x>.
- [31] F. Mo, J. Ruan, S. Sun, Z. Lian, S. Yang, X. Yue, Y. Song, Inside or Outside : Origin of

- Lithium Dendrite Formation of All Solid-State Electrolytes, 1902123 (2019) 1–10. <https://doi.org/10.1002/aenm.201902123>.
- [32] E. Kazyak, R. Garcia-Mendez, W.S. LePage, A. Sharafi, A.L. Davis, A.J. Sanchez, K.H. Chen, C. Haslam, J. Sakamoto, N.P. Dasgupta, Li Penetration in Ceramic Solid Electrolytes: Operando Microscopy Analysis of Morphology, Propagation, and Reversibility, *Matter*. 2 (2020) 1025–1048. <https://doi.org/10.1016/j.matt.2020.02.008>.
- [33] C. Yang, H. Xie, W. Ping, K. Fu, B. Liu, J. Rao, J. Dai, C. Wang, G. Pastel, L. Hu, An Electron/Ion Dual-Conductive Alloy Framework for High-Rate and High-Capacity Solid-State Lithium-Metal Batteries, *Adv. Mater.* 31 (2019) 1–7. <https://doi.org/10.1002/adma.201804815>.
- [34] J. Lau, R.H. DeBlock, D.M. Butts, D.S. Ashby, C.S. Choi, B.S. Dunn, Sulfide solid electrolytes for lithium battery applications, *Adv. Energy Mater.* 8 (2018) 1800933. <https://doi.org/10.1002/aenm.201800933>.
- [35] R. Wei, S. Chen, T. Gao, W. Liu, Challenges, fabrications and horizons of oxide solid electrolytes for solid-state lithium batteries, *Nano Sel.* 2 (2021) 2256–2274. <https://doi.org/10.1002/nano.202100110>.
- [36] S. Choudhury, S. Stalin, D. Vu, A. Warren, Y. Deng, P. Biswal, L.A. Archer, Solid-state polymer electrolytes for high-performance lithium metal batteries, *Nat. Commun.* 10 (2019) 1–8. <https://doi.org/10.1038/s41467-019-12423-y>.
- [37] F. Cuevas, M.B. Amdisen, M. Baricco, C.E. Buckley, Y.W. Cho, P.E. de Jongh, L.M. de Kort, J.B. Grinderslev, V. Gulino, B.C. Hauback, M. Heere, T. Humphries, T.R. Jensen, S. Kim, K. Kisu, Y.-S. Lee, H.-W. Li, R. Mohtadi, K.T. Møller, P. Ngene, D. Noréus, S. Orimo, M. Paskevicius, M. Polanski, S. Sartori, L.N. Skov, M.H. Sørby, B.C. Wood, V.A. Yartys, M. Zhu, M. Latroche, Metallic and complex hydride-based electrochemical storage of energy, *Prog. Energy*. 4 (2022) 032001. <https://iopscience.iop.org/article/10.1088/2516-1083/ac665b>.
- [38] N. Kamaya, K. Homma, Y. Yamakawa, M. Hirayama, R. Kanno, M. Yonemura, T. Kamiyama, Y. Kato, S. Hama, K. Kawamoto, A. Mitsui, A lithium superionic conductor, *Nat. Mater.* 10 (2011) 682–686. <https://doi.org/10.1038/nmat3066>.
- [39] Y. Kato, S. Hori, T. Saito, K. Suzuki, M. Hirayama, A. Mitsui, M. Yonemura, H. Iba, R. Kanno, High-power all-solid-state batteries using sulfide superionic conductors, *Nat.*

- Energy. 1 (2016) 1–7. <https://doi.org/10.1038/nenergy.2016.30>.
- [40] W.D. Richards, L.J. Miara, Y. Wang, J.C. Kim, G. Ceder, Interface Stability in Solid-State Batteries, *Chem. Mater.* 28 (2016) 266–273. <https://doi.org/10.1021/acs.chemmater.5b04082>.
- [41] J. Lee, T. Lee, K. Char, K.J. Kim, J.W. Choi, Issues and Advances in Scaling up Sulfide-Based All-Solid-State Batteries, *Acc. Chem. Res.* 54 (2021) 3390–3402. <https://doi.org/10.1021/acs.accounts.1c00333>.
- [42] Z. Ding, J. Li, J. Li, C. An, Review—Interfaces: key issue to be solved for all solid-state lithium battery technologies, *J. Electrochem. Soc.* 167 (2020) 070541. <https://doi.org/10.1149/1945-7111/ab7f84>.
- [43] D. Karabelli, K.P. Birke, M. Weeber, A performance and cost overview of selected solid-state electrolytes: Race between polymer electrolytes and inorganic sulfide electrolytes, *Batteries*. 7 (2021) 18. <https://doi.org/10.3390/batteries7010018>.
- [44] J. Feng, L. Wang, Y. Chen, P. Wang, H. Zhang, X. He, PEO based polymer-ceramic hybrid solid electrolytes: a review, *Nano Converg.* 8 (2021). <https://doi.org/10.1186/s40580-020-00252-5>.
- [45] K.S. Ngai, S. Ramesh, K. Ramesh, J.C. Juan, A review of polymer electrolytes: fundamental, approaches and applications, *Ionics*. 22 (2016) 1259–1279. <https://doi.org/10.1007/s11581-016-1756-4>.
- [46] B.R.S. Hansen, M. Paskevicius, H. Li, E. Akiba, T.R. Jensen, Metal boranes: Progress and applications, *Coord. Chem. Rev.* 323 (2016) 60–70. <https://doi.org/10.1016/j.ccr.2015.12.003>.
- [47] G.L. Miessler, D.A. Tarr, *Inorganic Chemistry*, 3rd ed., Pearson Prentice Hall, Upper Saddle River, N.J., 2004.
- [48] K. Wade, Bonding with boron, *Nat. Chem.* 1 (2009) 92. <https://doi.org/10.1038/nchem.158>.
- [49] D.E. Ward, C.K. Rhee, Chemoselective reductions with sodium borohydride. Aldehydes vs. ketones, *Synth. Commun.* 18 (1988) 1927–1933. <https://doi.org/10.1080/00397918808068259>.
- [50] M.F. Hawthorne, The Role of Chemistry in the Development of Boron Neutron Capture Therapy of Cancer, *Angew. Chemie Int. Ed. English*. 32 (1993) 950–984. <https://doi.org/10.1002/anie.199309501>.

- [51] U.B. Demirci, P. Miele, Sodium borohydride versus ammonia borane, in hydrogen storage and direct fuel cell applications, *Energy Environ. Sci.* 2 (2009) 627–637. <https://doi.org/10.1039/b900595a>.
- [52] Y. Pang, Y. Liu, J. Yang, S. Zheng, C. Wang, Hydrides for solid-state batteries: A review, *Mater. Today Nano.* 18 (2022) 100194. <https://doi.org/10.1016/j.mtnano.2022.100194>.
- [53] M. Matsuo, Y. Nakamori, S. Orimo, H. Maekawa, H. Takamura, Lithium superionic conduction in lithium borohydride accompanied by structural transition, *Appl. Phys. Lett.* 91 (2007) 224103. <https://doi.org/10.1063/1.2817934>.
- [54] T. Scholz, C. Schneider, M.W. Terban, Z. Deng, R. Eger, M. Etter, R.E. Dinnebier, P. Canepa, B. V. Lotsch, Order-Disorder Transition driven Superionic Conduction in the New Plastic Polymorph of  $\text{Na}_4\text{P}_2\text{S}_6$ , *ChemRxiv.* (2021) (in revision). <https://doi.org/10.26434/chemrxiv-2021-7r31q>.
- [55] S. Saha, G. Rouse, M. Courty, Y. Shakhova, M. Kirsanova, F. Fauth, V. Pomjakushin, A.M. Abakumov, J.M. Tarascon, Structural Polymorphism in  $\text{Na}_4\text{Zn}(\text{PO}_4)_2$  Driven by Rotational Order-Disorder Transitions and the Impact of Heterovalent Substitutions on Na-Ion Conductivity, *Inorg. Chem.* 59 (2020) 6528–6540. <https://doi.org/10.1021/acs.inorgchem.0c00612>.
- [56] M.S. Kumari, E.A. Secco, III. Order-disorder transitions and electrical conductivity studies in  $\text{Na}_2\text{SO}_4 - \text{Ag}_2\text{SO}_4$  system, *Can. J. Chem.* 61 (1983) 2804–2808. <https://doi.org/10.1139/v83-483>.
- [57] N. Kamaya, K. Homma, Y. Yamakawa, M. Hirayama, R. Kanno, M. Yonemura, T. Kamiyama, Y. Kato, S. Hama, K. Kawamoto, A. Mitsui, A lithium superionic conductor, *Nat. Mater.* 10 (2011) 682–686. <https://doi.org/10.1038/nmat3066>.
- [58] A. Unemoto, K. Yoshida, T. Ikeshoji, S. Orimo, Bulk-type all-solid-state lithium batteries using complex hydrides containing cluster-anions, *Mater. Trans.* 57 (2016) 1639–1644. <https://doi.org/10.2320/matertrans.MAW201601>.
- [59] W.S. Tang, M. Dimitrievska, V. Stavila, W. Zhou, H. Wu, A.A. Talin, T.J. Udovic, Order-disorder transitions and superionic conductivity in the sodium *nido*-undeca(carba)borates, *Chem. Mater.* 29 (2017) 10496–10509. <https://doi.org/10.1021/acs.chemmater.7b04332>.
- [60] S.H. Payandeh, D. Rentsch, Z. Łodziana, R. Asakura, L. Bigler, R. Černý, C. Battaglia, A.

- Remhof, *Nido*-Hydroborate-Based Electrolytes for All-Solid-State Lithium Batteries, *Adv. Funct. Mater.* 31 (2021) 2010046. <https://doi.org/10.1002/adfm.202010046>.
- [61] W.S. Tang, K. Yoshida, A. V. Soloninin, R. V. Skoryunov, O.A. Babanova, A. V. Skripov, M. Dimitrievska, V. Stavila, S.I. Orimo, T.J. Udovic, Stabilizing Superionic-Conducting Structures via Mixed-Anion Solid Solutions of Monocarba-*closo*-borate Salts, *ACS Energy Lett.* 1 (2016) 659–664. <https://doi.org/10.1021/acscenergylett.6b00310>.
- [62] M. Matsuo, S. Kuromoto, T. Sato, H. Oguchi, H. Takamura, S.I. Orimo, Sodium ionic conduction in complex hydrides with  $[\text{BH}_4]^-$  and  $[\text{NH}_2]^-$  anions, *Appl. Phys. Lett.* 100 (2012) 2–6. <https://doi.org/10.1063/1.4716021>.
- [63] B.R.S. Hansen, M. Paskevicius, M. Jørgensen, T.R. Jensen, Halogenated Sodium-*closo*-Dodecaboranes as Solid-State Ion Conductors, *Chem. Mater.* 29 (2017) 3423–3430. <https://doi.org/10.1021/acs.chemmater.6b04797>.
- [64] T.J. Udovic, M. Matsuo, W.S. Tang, H. Wu, V. Stavila, A. V Soloninin, R. V Skoryunov, O.A. Babanova, A. V Skripov, Exceptional Superionic Conductivity in Disordered Sodium Decahydro-*closo*-decaborate, (2014) 1–5. <https://doi.org/10.1002/adma.201403157>.
- [65] M. Jansen, Volume Effect or Paddle-Wheel Mechanism—Fast Alkali-Metal Ionic Conduction in Solids with Rotationally Disordered Complex Anions, *Angew. Chemie Int. Ed. English.* 30 (1991) 1547–1558. <https://doi.org/10.1002/anie.199115471>.
- [66] I. Crystal, J. Soulie, Lithium boro-hydride  $\text{LiBH}_4$  I. Crystal structure, 346 (2002) 200–205. [https://doi.org/10.1016/S0925-8388\(02\)00521-2](https://doi.org/10.1016/S0925-8388(02)00521-2).
- [67] P. Fischer, A. Züttel, Order-Disorder Phase Transition in  $\text{NaBD}_4$ , *Mater. Sci. Forum.* 443–444 (2004) 287–290. <https://doi.org/10.4028/www.scientific.net/MSF.443-444.287>.
- [68] K. Jimura, S. Hayashi, Reorientational motion of  $\text{BH}_4$  ions in alkali borohydrides  $\text{MBH}_4$  ( $\text{M} = \text{Li}, \text{Na}, \text{K}$ ) as studied by solid-state NMR, *J. Phys. Chem. C.* 116 (2012) 4883–4891. <https://doi.org/10.1021/jp300092q>.
- [69] M. Paskevicius, M.P. Pitt, D.H. Brown, D.A. Sheppard, First-order phase transition in the  $\text{Li}_2\text{B}_{12}\text{H}_{12}$  system, *Phys. Chem. Chem. Phys.* 15 (2013) 15825–15828. <https://doi.org/10.1039/c3cp53090f>.
- [70] N. Verdal, J. Her, V. Stavila, A. V Soloninin, O.A. Babanova, A. V Skripov, T.J. Udovic, J.J. Rush, Journal of Solid State Chemistry Complex high-temperature phase transitions in  $\text{Li}_2\text{B}_{12}\text{H}_{12}$  and, *J. Solid State Chem.* 212 (2014) 81–91. <https://doi.org/10.1016/j.jssc.2014.01.006>.

- [71] M. Dimitrievska, P. Shea, K.E. Kweon, M. Bercx, B.C. Wood, Carbon Incorporation and Anion Dynamics as Synergistic Drivers for Ultrafast Diffusion in Superionic  $\text{LiCB}_{11}\text{H}_{12}$  and  $\text{NaCB}_{11}\text{H}_{12}$ , *Adv. Energy Mater.* 8 (2018) 1703422. <https://doi.org/10.1002/aenm.201703422>.
- [72] W.S. Tang, A. Unemoto, W. Zhou, V. Stavila, M. Matsuo, H. Wu, S. Orimo, T.J. Udovic, Unparalleled lithium and sodium superionic conduction in solid electrolytes with large monovalent cage-like anions, *Energy Environ. Sci.* 8 (2015) 3637–3645. <https://doi.org/10.1039/C5EE02941D>.
- [73] H. Wu, W.S. Tang, V. Stavila, W. Zhou, J.J. Rush, T.J. Udovic, Structural behavior of  $\text{Li}_2\text{B}_{10}\text{H}_{10}$ , *J. Phys. Chem. C.* 119 (2015) 6481–6487. <https://doi.org/10.1021/acs.jpcc.5b00533>.
- [74] W.S. Tang, M. Matsuo, H. Wu, V. Stavila, W. Zhou, A.A. Talin, A. V. Soloninin, R. V. Skoryunov, O.A. Babanova, A. V. Skripov, A. Unemoto, S.I. Orimo, T.J. Udovic, Liquid-Like Ionic Conduction in Solid Lithium and Sodium Monocarpa-*closo*-Decaborates Near or at Room Temperature, *Adv. Energy Mater.* 6 (2016) 1–6. <https://doi.org/10.1002/aenm.201502237>.
- [75] H. Wu, W.S. Tang, W. Zhou, J.D. Tarver, V. Stavila, C.M. Brown, T.J. Udovic, The low-temperature structural behavior of sodium 1-carba-*closo*-decaborate:  $\text{NaCB}_9\text{H}_{10}$ , *J. Solid State Chem.* 243 (2016) 162–167. <https://doi.org/10.1016/j.jssc.2016.08.024>.
- [76] G. Renaudin, S. Gomes, H. Hagemann, L. Keller, K. Yvon, Structural and spectroscopic studies on the alkali borohydrides  $\text{MBH}_4$  ( $M = \text{Na}, \text{K}, \text{Rb}, \text{Cs}$ ), *J. Alloys Compd.* 375 (2004) 98–106. <https://doi.org/10.1016/j.jallcom.2003.11.018>.
- [77] S. Kim, N. Toyama, H. Oguchi, T. Sato, S. Takagi, T. Ikeshoji, S. Orimo, Fast Lithium-Ion Conduction in Atom-Deficient *closo*-Type Complex Hydride Solid Electrolytes, *Chem. Mater.* 30 (2018) 386–391. <https://doi.org/10.1021/acs.chemmater.7b03986>.
- [78] F. Murgia, M. Brighi, L. Piveteau, C.E. Avalos, V. Gulino, M.C. Nierstenh, P. Ngene, P. De Jongh, C. Radovan, Enhanced Room-Temperature Ionic Conductivity of  $\text{NaCB}_{11}\text{H}_{12}$  via High-Energy Mechanical Milling, *ACS Appl. Mater. Interfaces.* 13 (2021) 61346–61356. <https://doi.org/10.1021/acsami.1c21113>.
- [79] Y. Sadikin, M. Brighi, P. Schouwink, R. Černý, Superionic Conduction of Sodium and Lithium in Anion-Mixed Hydroborates  $\text{Na}_3\text{BH}_4\text{B}_{12}\text{H}_{12}$  and  $(\text{Li}_{0.7}\text{Na}_{0.3})_3\text{BH}_4\text{B}_{12}\text{H}_{12}$ , *Adv. Energy Mater.* 5 (2015) 1501016. <https://doi.org/10.1002/aenm.201501016>.



- [80] Y.S. Choi, Y.S. Lee, D.J. Choi, K.H. Chae, K.H. Oh, Y.W. Cho, Enhanced Li ion conductivity in  $\text{LiBH}_4\text{-Al}_2\text{O}_3$  mixture via interface engineering, *J. Phys. Chem. C.* 121 (2017) 26209–26215. <https://doi.org/10.1021/acs.jpcc.7b08862>.
- [81] A. Takano, I. Oikawa, A. Kamegawa, H. Takamura, Enhancement of the lithium-ion conductivity of  $\text{LiBH}_4$  by hydration, *Solid State Ionics.* 285 (2016) 47–50. <https://doi.org/10.1016/j.ssi.2015.06.004>.
- [82] Y. Yan, J.B. Grinderslev, Y.-S. Lee, M. Jørgensen, Y.W. Cho, R. Černý, T.R. Jensen, Ammonia-assisted fast Li-ion conductivity in a new hemiammine lithium borohydride,  $\text{LiBH}_4 \cdot 1/2\text{NH}_3$ , *Chem. Commun.* 56 (2020) 3971–3974. <https://doi.org/10.1039/c9cc09990e>.
- [83] S. Kim, H. Oguchi, N. Toyama, T. Sato, S. Takagi, T. Otomo, D. Arunkumar, N. Kuwata, J. Kawamura, S. Orimo, A complex hydride lithium superionic conductor for high-energy-density all-solid-state lithium metal batteries, *Nat. Commun.* 10 (2019) 1–9. <https://doi.org/10.1038/s41467-019-09061-9>.
- [84] M. Matsuo, A. Remhof, P. Martelli, R. Caputo, M. Ernst, Y. Miura, T. Sato, H. Oguchi, H. Maekawa, H. Takamura, A. Borgschulte, A. Züttel, S. Orimo, Complex hydrides with  $(\text{BH}_4)^-$  and  $(\text{NH}_2)^-$  anions as new lithium fast-ion conductors, *J. Am. Chem. Soc.* 131 (2009) 16389–16391. <https://doi.org/10.1021/ja907249p>.
- [85] T. Zhang, Y. Wang, T. Song, H. Miyaoka, K. Shinzato, H. Miyaoka, T. Ichikawa, S. Shi, X. Zhang, S. Isobe, N. Hashimoto, Y. Kojima, Ammonia, a Switch for Controlling High Ionic Conductivity in Lithium Borohydride Ammoniates, *Joule.* 2 (2018) 1522–1533. <https://doi.org/10.1016/j.joule.2018.04.015>.
- [86] L. Duchêne, R.S. Kühnel, D. Rentsch, A. Remhof, H. Hagemann, C. Battaglia, A highly stable sodium solid-state electrolyte based on a dodeca/deca-borate equimolar mixture, *Chem. Commun.* 53 (2017) 4195–4198. <https://doi.org/10.1039/c7cc00794a>.
- [87] S. Payandeh, R. Asakura, P. Avramidou, D. Rentsch, Ł. Zbigniew, C. Radovan, A. Remhof, C. Battaglia, *Nido-Borate/Closo-Borate Mixed-Anion Electrolytes for All-Solid-State Batteries*, *Chem. Mater.* 32 (2020) 1101–1110. <https://doi.org/10.1021/acs.chemmater.9b03933>.
- [88] R. Asakura, D. Reber, L. Duchêne, S. Payandeh, A. Remhof, H. Hagemann, C. Battaglia, 4 V Room-Temperature All-Solid-State Sodium Battery Enabled By a Passivating Cathode/Hydroborate Solid Electrolyte Interface, *Energy Environ. Sci.* 13 (2020) 5048–

5058. <https://doi.org/10.1039/d0ee01569e>.
- [89] F. Han, Y. Zhu, X. He, Y. Mo, C. Wang, Electrochemical stability of  $\text{Li}_{10}\text{GeP}_2\text{S}_{12}$  and  $\text{Li}_7\text{La}_3\text{Zr}_2\text{O}_{12}$  solid electrolytes, *Adv. Energy Mater.* 6 (2016) 1501590. <https://doi.org/10.1002/aenm.201501590>.
- [90] R. Asakura, L. Duchêne, R.S. Kühnel, A. Remhof, H. Hagemann, C. Battaglia, Electrochemical Oxidative Stability of Hydroborate-Based Solid-State Electrolytes, *ACS Appl. Energy Mater.* 2 (2019) 6924–6930. <https://doi.org/10.1021/acsaem.9b01487>.
- [91] Z. Lu, F. Ciucci, Metal Borohydrides as Electrolytes for Solid-State Li, Na, Mg, and Ca Batteries: A First-Principles Study, *Chem. Mater.* 29 (2017) 9308–9319. <https://doi.org/10.1021/acs.chemmater.7b03284>.
- [92] V. Lacivita, Y. Wang, S.H. Bo, G. Ceder, Ab initio investigation of the stability of electrolyte/electrode interfaces in all-solid-state Na batteries, *J. Mater. Chem. A* 7 (2019) 8144–8155. <https://doi.org/10.1039/c8ta10498k>.
- [93] M. Brighi, F. Murgia, Z. Łodziana, P. Schouwink, A. Wołczyk, R. Černý, A mixed anion hydroborate/carba-hydroborate as a room temperature Na-ion solid electrolyte, *J. Power Sources* 404 (2018) 7–12. <https://doi.org/10.1016/j.jpowsour.2018.09.085>.
- [94] L. Duchêne, R.S. Kühnel, E. Stilp, E. Cuervo Reyes, A. Remhof, H. Hagemann, C. Battaglia, A stable 3 V all-solid-state sodium-ion battery based on a *closo*-borate electrolyte, *Energy Environ. Sci.* 10 (2017) 2609–2615. <https://doi.org/10.1039/c7ee02420g>.
- [95] A. Berger, C.E. Buckley, M. Paskevicius, Synthesis of *closo*- $\text{CB}_{11}\text{H}_{12}^-$  Salts Using Common Laboratory Reagents, *Inorg. Chem.* 60 (2021) 14744–14751. <https://doi.org/10.1021/acs.inorgchem.1c01896>.
- [96] Z. Jiang, Q. Han, S. Wang, H. Wang, Reducing the interfacial resistance in all-solid-state lithium batteries based on oxide ceramic electrolytes, *ChemElectroChem* 6 (2019) 2970–2983. <https://doi.org/10.1002/celec.201801898>.
- [97] V. Gulino, M. Brighi, F. Murgia, P. Ngene, P. De Jongh, R. Černý, M. Baricco, Room-Temperature Solid-State Lithium-Ion Battery Using a  $\text{LiBH}_4$ -MgO Composite Electrolyte, *ACS Appl. Energy Mater.* 4 (2021) 1228–1236. <https://doi.org/10.1021/acsaem.0c02525>.

# CHAPTER 2

## Experimental

---

## 2.1 INTRODUCTION

Several boron-hydrogen materials were synthesised throughout the course of this research, and they were characterised via different techniques. This chapter describes the methodology used for the samples' preparation, characterisation and assessment of their properties as solid-state electrolytes, as well as the theory and basic principles of the employed techniques. Some studies were performed in collaboration with other researchers, and their contributions are stated in this chapter.

## 2.2 CHEMICALS

The following table describes the list of chemicals used to conduct the experiments.

**Table 2.1** List of chemicals used and their specifications.

<b>Chemical</b>	<b>Chemical formula</b>	<b>State</b>	<b>Purity</b>	<b>Supplier</b>
<b>Sodium borohydride</b>	NaBH <sub>4</sub>	Anhydrous powder	98%	Sigma-Aldrich
<b>Diglyme</b>	C <sub>6</sub> H <sub>14</sub> O <sub>3</sub>	Anhydrous liquid	99.5%	Sigma-Aldrich
<b>1-Bromopentane</b>	C <sub>5</sub> H <sub>11</sub> Br	Liquid	98%	Sigma-Aldrich
<b>Diethyl ether</b>	C <sub>4</sub> H <sub>10</sub> O	Anhydrous liquid	99.7%	Sigma-Aldrich
<b>Trimethylamine hydrochloride</b>	(CH <sub>3</sub> ) <sub>3</sub> N·HCl	Solid	98%	Sigma-Aldrich
<b>Lithium hydroxide</b>	LiOH	Anhydrous solid	98%	Alfa Aesar
<b>Sodium hydroxide</b>	NaOH	Solid	98% 98.9%	Sigma-Aldrich VWR Chemicals
<b>Potassium hydroxide</b>	KOH	Powder	85%	Sigma-Aldrich
<b>Sulphuric acid</b>	H <sub>2</sub> SO <sub>4</sub>	Liquid	95-98%	Sigma-Aldrich
<b>Hydrochloric acid</b>	HCl	Liquid	37%	Scharlau

<b>Sodium hydride</b>	NaH	Anhydrous powder	95%	Sigma-Aldrich
<b>Tetrahydrofuran (THF) with 250 ppm BHT inhibitor</b>	C <sub>4</sub> H <sub>8</sub> O	Anhydrous liquid	99%	Sigma-Aldrich
<b>Acetone</b>	C <sub>3</sub> H <sub>6</sub> O	Liquid	99.5%	Unilab
<b>Acetonitrile</b>	CH <sub>3</sub> CN	Anhydrous liquid	99.8%	Sigma-Aldrich
<b>Boric acid</b>	H <sub>3</sub> BO <sub>3</sub>	Powder	99.5%	Sigma-Aldrich
<b>Deuterated water</b>	D <sub>2</sub> O	Liquid	99.9 atom % D	Sigma-Aldrich
<b>Deuterated acetonitrile</b>	CD <sub>3</sub> CN	Liquid	99.8 atom % D	Sigma-Aldrich
<b>Deuterated dimethyl sulfoxide (DMSO-<i>d</i><sub>6</sub>)</b>	C <sub>2</sub> D <sub>6</sub> OS	Anhydrous liquid	99.9 atom % D	Sigma-Aldrich
<b>Lithium</b>	Li	Li ribbon	99.9%	Sigma-Aldrich
<b>Sodium</b>	Na	Na lump	99%	Sigma-Aldrich
<b>Gold</b>	Au	Au foil	99.95%	Alfa Aesar
<b>Graphite</b>	C	Powder	99.9%	Sigma-Aldrich
<b>Platinum</b>	Pt	Pt foil	99.95%	Sigma-Aldrich
<b>Lithium hexafluorophosphate solution in ethylene carbonate and dimethyl carbonate</b>	LiPF <sub>6</sub> C <sub>3</sub> H <sub>4</sub> O <sub>3</sub> C <sub>3</sub> H <sub>6</sub> O <sub>3</sub>	Liquid	1.0 M LiPF <sub>6</sub> EC/DMC (v/v = 50/50)	Sigma-Aldrich
<b>Titanium(IV) sulphide</b>	TiS <sub>2</sub>	Powder	99.9%	Sigma-Aldrich
<b>Argon</b>	Ar	Gas	99.997%	Coregas

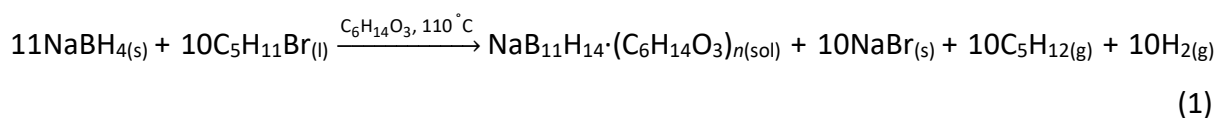
### 2.3 SYNTHESIS

Due to the air sensitivity of some boron-hydrogen materials (usually hygroscopic), all samples were synthesised using a Schlenk line, which is a dual manifold glass apparatus that allows to

alternate use of an inert gas (argon) and vacuum. All chemicals and samples were manipulated using Schlenk techniques or inside an argon filled glovebox (Mbraun) in order to minimise oxygen and water exposure. The glovebox was equipped with an argon purifier and a catalyst, which constantly recycles the inert atmosphere to keep the levels of water (H<sub>2</sub>O) and oxygen (O<sub>2</sub>) below 1 ppm. Chemicals, samples and apparatus were inserted or removed from the glovebox through antechambers that were evacuated and flushed with argon. The following methodology describes the optimised synthetic procedures, however several other synthesis methods were performed in order to achieve such optimisation.

### 2.3.1 Synthesis of trimethylammonium *nido*-tetradecahydroundecaborane, (CH<sub>3</sub>)<sub>3</sub>NHB<sub>11</sub>H<sub>14</sub>

The synthesis of (CH<sub>3</sub>)<sub>3</sub>NHB<sub>11</sub>H<sub>14</sub>, the starting material for the preparation of the *nido*-boranes reported in this thesis, was achieved through a modified method previously reported by Dunks *et al.* [1] and Muetterties *et al.* [2]. NaB<sub>11</sub>H<sub>14</sub>·(C<sub>6</sub>H<sub>14</sub>O<sub>3</sub>)<sub>n</sub> is initially synthesised through the reaction of NaBH<sub>4</sub> with 1-bromopentane in diglyme at ≈ 110 °C (reaction 1).



This reaction can be broken down into four steps in order to better represent the synthetic route for NaB<sub>11</sub>H<sub>14</sub>·(C<sub>6</sub>H<sub>14</sub>O<sub>3</sub>)<sub>n</sub> [1,3,4], but does occur in solution as a polycondensation reaction.



Sodium borohydride, a strong reducing agent, reduces the alkyl halide 1-bromopentane into diborane (reaction 2), a reactive gas that reacts with excess borohydride to form B<sub>2</sub>H<sub>7</sub><sup>-</sup> (reaction 3), which thermally decomposes into B<sub>3</sub>H<sub>8</sub><sup>-</sup> (reaction 4). Excess diborane then reacts with B<sub>3</sub>H<sub>8</sub><sup>-</sup> to yield NaB<sub>11</sub>H<sub>14</sub> (reaction 5), where its formation is favoured when the reaction temperature is 105 – 120 °C, and diglyme is used as the solvent [1,3,4].

In order to synthesise  $\text{NaB}_{11}\text{H}_{14}\cdot(\text{C}_6\text{H}_{14}\text{O}_3)_n$ , 50 g of  $\text{NaBH}_4$  (1.32 mol) was transferred to a three-neck round-bottom flask inside an argon-filled glovebox and equipped with a thermometer, a mechanical stirrer, and a pressure-equalising dropping funnel under argon using a Schlenk line. 400 mL of diglyme was added under constant stirring and an argon atmosphere, and the suspension was heated to 105 °C. 150 mL of 1-bromopentane (1.20 mol) was then added slowly through the dropping funnel to ensure a controlled temperature between 105 and 120 °C (exothermic reaction). After complete addition, the reaction mixture was stirred for six additional hours at 110 °C, which results in a suspension of yellow liquid and white powder (precipitated NaBr) (Fig. 2.1).

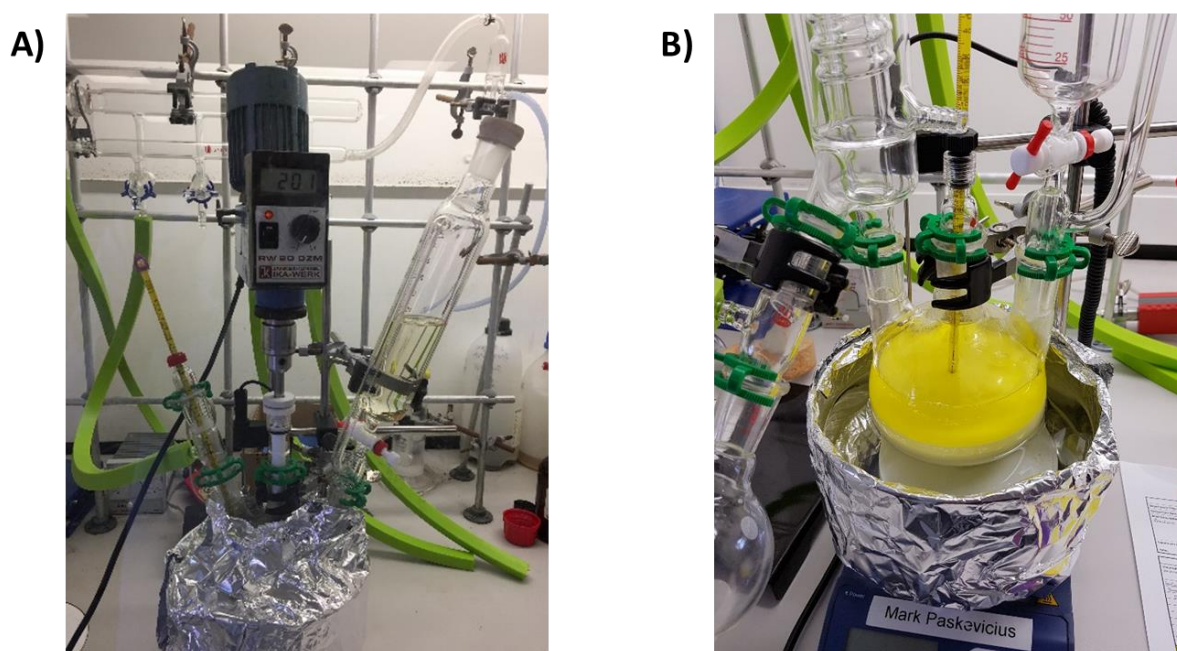
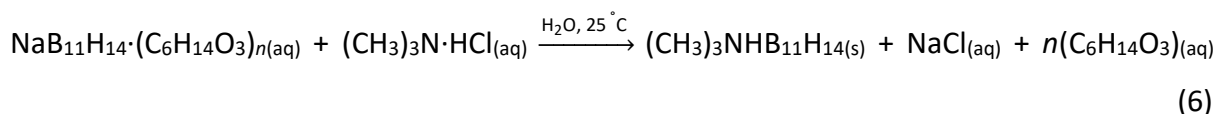


**Figure 2.1** A) Reaction set-up used to synthesise  $\text{NaB}_{11}\text{H}_{14}\cdot(\text{C}_6\text{H}_{14}\text{O}_3)_n$  in a three-neck round-bottom flask equipped with a thermometer, a mechanical stirrer and a dropping funnel under a constant stream of argon from a Schlenk line. B) Resulting suspension of yellow liquid ( $\text{NaB}_{11}\text{H}_{14}\cdot(\text{C}_6\text{H}_{14}\text{O}_3)_n$ ) and white powder (NaBr) after completion of reaction.

The yellow suspension of  $\text{NaB}_{11}\text{H}_{14}\cdot(\text{C}_6\text{H}_{14}\text{O}_3)_n$  was then filtered at room temperature and washed with  $\approx 50$  mL of diethyl ether. The filtrate was dried *in vacuo* at 110 °C until a gelatinous yellow product (40.5 g) was obtained (Fig. 2.2A). In order to remove the coordinated diglyme from the *nido*-borane,  $\text{NaB}_{11}\text{H}_{14}\cdot(\text{C}_6\text{H}_{14}\text{O}_3)_n$  was dissolved in hot water, and an aqueous solution of trimethylamine hydrochloride (31.5 g, 0.33 mol) was added in

excess ( $\approx 20\%$ ), resulting in the rapid formation of a yellow-white precipitate (reaction 6). The large trimethylammonium cation replaces the sodium and yields a product that is free of the ethereal solvent, due to its water insolubility and it is thus easily isolated [2].



The suspension was transferred to an ice bath and left resting for 30 minutes, filtered, and washed with cold water. The light yellow powder was then dried *in vacuo* at  $90^\circ\text{C}$ , yielding 9.0 g (0.047 mol, 39% yield) of trimethylammonium *nido*-tetradecahydroundecaborane  $((\text{CH}_3)_3\text{NHB}_{11}\text{H}_{14})$  (Fig. 2.2B).

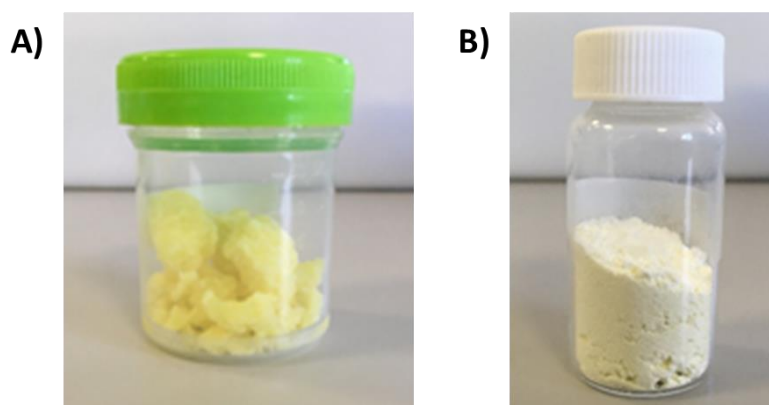


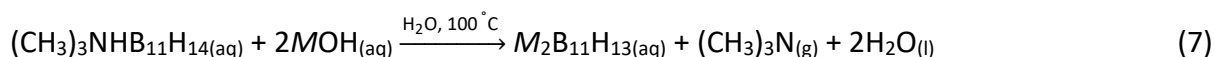
**Figure 2.2** A) Solid powder of  $\text{NaB}_{11}\text{H}_{14}\cdot(\text{C}_6\text{H}_{14}\text{O}_3)_n$ . B) Solid powder of  $(\text{CH}_3)_3\text{NHB}_{11}\text{H}_{14}$ .

### 2.3.2 Synthesis of alkali metal *nido*-tetradecahydroundecaborane, $\text{LiB}_{11}\text{H}_{14}\cdot(\text{H}_2\text{O})_n$ , $\text{NaB}_{11}\text{H}_{14}\cdot(\text{H}_2\text{O})_n$ and $\text{KB}_{11}\text{H}_{14}$

The synthesis of  $\text{MB}_{11}\text{H}_{14}\cdot(\text{H}_2\text{O})_n$  ( $M = \text{Li}$  or  $\text{Na}$ ) and  $\text{KB}_{11}\text{H}_{14}$  was achieved based on an adapted procedure presented by Klanberg and Muetterties [5] that was originally used to prepare  $\text{CsB}_{11}\text{H}_{14}$ .  $(\text{CH}_3)_3\text{NHB}_{11}\text{H}_{14}$  (1.5 g, 7.77 mmol for  $\text{LiB}_{11}\text{H}_{14}$  and  $\text{NaB}_{11}\text{H}_{14}$  and 0.5 g, 2.59 mmol for  $\text{KB}_{11}\text{H}_{14}$ ) was dissolved in a  $0.5 \text{ mol L}^{-1}$  aqueous solution of metal hydroxide ( $\text{LiOH}$ : 75 mL,  $\text{NaOH}$ : 75 mL,  $\text{KOH}$ : 30 mL) and heated at  $100^\circ\text{C}$  for  $\approx 20$  minutes (reaction 7) in an open vessel to ensure elimination of the trimethylammonium cation,  $(\text{CH}_3)_3\text{NH}^+$ , as trimethylamine gas ( $(\text{CH}_3)_3\text{N}$ , boiling point  $2.9^\circ\text{C}$  at 1 atm). The solution was filtered at room temperature (RT), and the filtrate was reheated to  $80^\circ\text{C}$  to adjust its pH to 4 – 5 by slow addition of 1.0



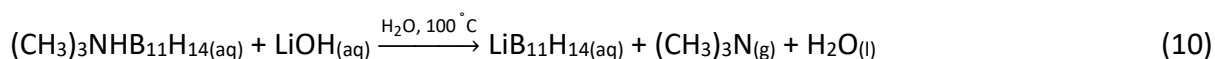
mol L<sup>-1</sup> aqueous solution of inorganic acid (LiB<sub>11</sub>H<sub>14</sub>·(H<sub>2</sub>O)<sub>n</sub> and NaB<sub>11</sub>H<sub>14</sub>·(H<sub>2</sub>O)<sub>n</sub> were prepared with HCl, reaction 8, and KB<sub>11</sub>H<sub>14</sub> with H<sub>2</sub>SO<sub>4</sub>, reaction 9).



The solution was then cooled to RT, and a liquid-liquid extraction using diethyl ether was performed to isolate the *nido*-borane from boric acid that was formed as a by-product. The organic layer, a yellowish liquid, was isolated from the aqueous solution, flushed with argon, and dried *in vacuo* at 80 °C, which resulted in the formation of a deliquescent white powder of alkali metal *nido*-tetradecahydroundecaborane (LiB<sub>11</sub>H<sub>14</sub>·(H<sub>2</sub>O)<sub>n</sub>: 0.89 g, 6.36 mmol, 82% yield, NaB<sub>11</sub>H<sub>14</sub>·(H<sub>2</sub>O)<sub>n</sub>: 0.68 g, 4.36 mmol, 56% yield, KB<sub>11</sub>H<sub>14</sub>: 0.30g, 1.74 mmol, 67% yield).

### 2.3.3 Synthesis of lithium *nido*-tetradecahydroundecaborane, LiB<sub>11</sub>H<sub>14</sub>·2H<sub>2</sub>O, *α*-LiB<sub>11</sub>H<sub>14</sub>·(H<sub>2</sub>O)<sub>n</sub> (n < 2), and LiB<sub>11</sub>H<sub>14</sub>

In order to investigate the influence of coordinated water on the properties of *nido*-boranes as solid-state electrolytes, the synthesis of compounds of LiB<sub>11</sub>H<sub>14</sub> with different water content was optimised based on reaction 10.



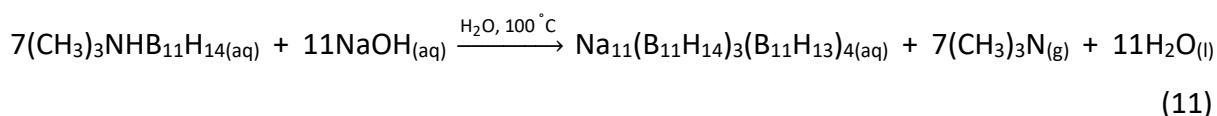
(CH<sub>3</sub>)<sub>3</sub>NHB<sub>11</sub>H<sub>14</sub> was recrystallised prior to use by dissolution in a hot aqueous solution of acetone (10% acetone) [6]. The colourless precipitate was collected by filtration, washed with cold Milli-Q water and dried *in vacuo* at 90 °C. 800 mg of recrystallised (CH<sub>3</sub>)<sub>3</sub>NHB<sub>11</sub>H<sub>14</sub> (4.14 mmol) was added to 40 mL of lithium hydroxide aqueous solution (140 mg LiOH, 40% excess, 5.85 mmol), which was sonicated several times and stirred at room temperature to ensure dissolution of the powder. The aqueous solution was stirred at 100 °C for ≈ 15 minutes in an open vessel to eliminate the volatile (CH<sub>3</sub>)<sub>3</sub>N gas, and upon cooling back to RT, the suspension was filtered. The filtrate was dried at 80 °C *in vacuo* for 2 hours to obtain a deliquescent colourless powder of LiB<sub>11</sub>H<sub>14</sub>·2H<sub>2</sub>O (0.60 g, 3.41 mmol, 82% yield). No additional step for removal of excess LiOH or possible side products was taken in order to simplify the synthetic

process and to observe the possible influence of the by-products over the properties of the material, as mentioned in chapter 4.

The same methodology used to prepare  $\text{LiB}_{11}\text{H}_{14}\cdot 2\text{H}_2\text{O}$  was applied to the synthesis of  $\text{LiB}_{11}\text{H}_{14}\cdot (\text{H}_2\text{O})_n$  with  $n < 2$ , however with different heating times *in vacuo* on the Schlenk line to dry the sample. For  $\alpha\text{-LiB}_{11}\text{H}_{14}\cdot (\text{H}_2\text{O})_n$ , the filtrate was dried for 4 hours in *vacuo* at 80 °C, yielding 0.52 g of the material. For anhydrous  $\text{LiB}_{11}\text{H}_{14}$ , the filtrate was dried for 20 hours *in vacuo* at 110 °C, yielding 0.46 g of sample (3.29 mmol, 79% yield).

### 2.3.4 Synthesis of mixed anion *nido*-borane, $\text{Na}_{11}(\text{B}_{11}\text{H}_{14})_3(\text{B}_{11}\text{H}_{13})_4$

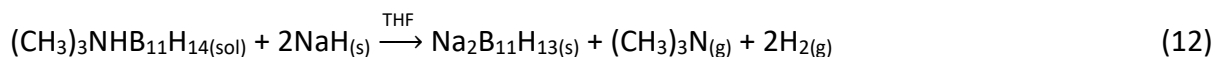
The mixed-anion borane  $\text{Na}_{11}(\text{B}_{11}\text{H}_{14})_3(\text{B}_{11}\text{H}_{13})_4$  was synthesised based on reaction 11 in an attempt to stabilise the high temperature polymorph at RT and thus enhance its ionic conductivity properties.



400 mg of recrystallised  $(\text{CH}_3)_3\text{NHB}_{11}\text{H}_{14}$  (2.1 mmol) was added to 20 mL of an aqueous solution of NaOH (177 mg, 4.4 mmol,  $\approx 33\%$  excess), which was then heated at 100 °C for 15 minutes under constant stirring in an open vessel. The resulting suspension was filtered at RT, and a liquid-liquid extraction was performed with 15 mL of diethyl ether, as an attempt to remove impurities and isolate both anions,  $\text{B}_{11}\text{H}_{14}^-$  and  $\text{B}_{11}\text{H}_{13}^{2-}$ , from the medium. The aqueous layer was dried *in vacuo* overnight at 110 °C, and a deliquescent powder composed by a mixture of both anions was obtained (0.28 g, 0.24 mmol, 80% yield). No additional step for removal of excess NaOH or possible side products was taken. The isolation of  $\text{B}_{11}\text{H}_{13}^{2-}$  from borate species can be a challenge since both share similar polarity properties, as discussed in chapter 5.

### 2.3.5 Synthesis of disodium *nido*-tridecahydroundecaborane, $\text{Na}_2\text{B}_{11}\text{H}_{13}$

Another type of sodium *nido*-borane,  $\text{Na}_2\text{B}_{11}\text{H}_{13}$ , was synthesised in order to investigate its properties as a solid-state electrolyte. The synthesis of this salt was achieved based on reaction 12, an adapted procedure proposed by Pecyna *et al.* [7] that was originally used to prepare  $(\text{C}_2\text{H}_5)_4\text{NCB}_{11}\text{H}_{12}$ .



0.11 g of NaH (4.6 mmol) was weighed in an argon-filled glovebox and transferred to a custom-made Schlenk flask equipped with an inner filter to maintain an inert atmosphere (Fig. 2.3).

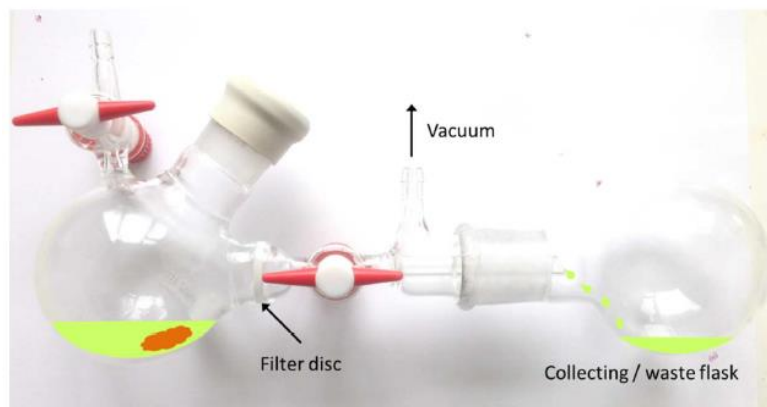


**Figure 2.3** Custom-made Schlenk flask to allow filtration of mixtures in an inert atmosphere. The solid is represented in orange and the liquid in yellow. Reproduced with permission [8]. Copyright 2018, American Chemical Society.

The flask was connected to the Schlenk line, and 5 mL of THF was added to the solid under a constant stream of argon in an ice bath. 0.25 g of recrystallised  $(\text{CH}_3)_3\text{NHB}_{11}\text{H}_{14}$  (1.3 mmol) was dissolved in 5 mL of THF, and the resulting solution was slowly added to the flask containing the suspension of NaH at 0 °C. The mixture was left stirring for 15 minutes at 0 °C, 30 minutes at RT, and then filtered to remove the excess NaH. The filtrate was dried *in vacuo* at 40 °C for 2 hours, resulting in a deliquescent white powder of  $\text{Na}_2\text{B}_{11}\text{H}_{13}$  (0.17 g, 0.9 mmol, 73% yield).

## 2.4 CHARACTERISATION

### 2.4.1 Nuclear Magnetic Resonance (NMR) spectroscopy

This analytical technique is used to determine the purity and content of a material. Its working principle is based on the application of an external magnetic field to split the energy levels of nuclear spin states. Upon a radiofrequency wave pulse, the spin flips to a high energy level, and when the spin returns to the base state, energy at the same frequency is emitted, which is detected and processed to generate an NMR spectrum [9].

$^1\text{H}$  and  $^{11}\text{B}$  NMR spectroscopy are widely used for the characterisation of boranes since structural and molecular dynamics information can be obtained from this technique [10,11].  $^{10}\text{B}$  and  $^{11}\text{B}$  are the two naturally occurring isotopes of boron, and both are NMR active with spin quantum numbers 3 and 3/2, respectively. However,  $^{11}\text{B}$  is more suitable for NMR experiments due to its higher natural abundance (81.4 %), which yields more intense peaks with better resolution [12]. The  $^{11}\text{B}$  NMR spectrum can be produced considering the effects of the coupling between boron and proton atoms ( $^{11}\text{B}$  NMR coupling), or with the elimination of these effects, which is called  $^{11}\text{B}$  NMR decoupling ( $^{11}\text{B}\{^1\text{H}\}$ ).

Solution-state  $^1\text{H}$  and  $^{11}\text{B}$  NMR spectroscopy ( $^1\text{H}$ : 400 MHz,  $^{11}\text{B}$ : 128 MHz,  $^{11}\text{B}\{^1\text{H}\}$ : 128 MHz) were performed by dissolution of the samples in 600  $\mu\text{L}$  of a deuterated solvent ( $\text{D}_2\text{O}$ ,  $\text{DMSO-}d_6$  or  $\text{CD}_3\text{CN}$ ) and analysed on a Bruker Avance III 400 MHz NanoBay spectrometer at room temperature. Tetramethylsilane ( $\text{Si}(\text{CH}_3)_4$ ) and boron trifluoride etherate ( $\text{BF}_3\text{O}(\text{C}_2\text{H}_5)_2$ ) were used as external standards of the  $^1\text{H}$  and  $^{11}\text{B}$  NMR spectra, respectively.

The  $\text{LiB}_{11}\text{H}_{14}\cdot(\text{H}_2\text{O})_n$ ,  $\alpha\text{-LiB}_{11}\text{H}_{14}\cdot(\text{H}_2\text{O})_n$ ,  $\text{NaB}_{11}\text{H}_{14}\cdot(\text{H}_2\text{O})_n$ ,  $\text{Na}_2\text{B}_{11}\text{H}_{13}$ , and  $\text{Na}_{11}(\text{B}_{11}\text{H}_{14})_3(\text{B}_{11}\text{H}_{13})_4$  samples were also analysed through solid-state  $^{11}\text{B}$  NMR spectroscopy (128 MHz) on a Varian VNMRS spectrometer. They were packed in an argon filled glovebox inside a 4 mm zirconia rotor and sealed with gas-tight inserts. They were spun at 5 kHz with proton decoupling and a relaxation delay of 10 seconds, for a total of 50 transients, and acquisition was performed with a one-pulse sequence. Data were collected at the University of Western Australia by Dr Gareth Nealon.

Solid-state  $^{11}\text{B}$  NMR spectroscopy was also performed to evaluate  $^{11}\text{B}$  spin-lattice NMR relaxation rates ( $T_1^{-1}$ ) of  $\alpha\text{-LiB}_{11}\text{H}_{14}\cdot(\text{H}_2\text{O})_n$  from -190 to 110  $^\circ\text{C}$  using a 4.7 T superconducting magnet. Spin-lattice relaxation rates were measured using a saturation-recovery sequence with spin echoes to detect the signal. Rectilinear quartz NMR tubes (5 mm diameter) had their shape adjusted with an oxy-acetylene torch to form an 'L' shape tube with  $\approx 1.5$  cm length in the bottom. The sample ( $\approx 40$  mg) was transferred to this tube inside an argon filled glovebox, sealed with grease, removed from the glovebox and flame sealed with an oxy-acetylene torch (Fig. 2.4). Data acquisition and analysis were performed by Dr Anton Gradišek from the Jožef Stefan Institute in Slovenia.



**Figure 2.4** 'L-shaped' quartz NMR tube containing  $\approx 40$  mg of sample used to investigate the  $^{11}\text{B}$  spin-lattice NMR relaxation rates.

### 2.4.2 Raman spectroscopy

This vibrational spectroscopy technique is based on the scattering of light in the near infrared or visible region by a molecule due to molecular bond vibrations at specific energy levels. The interaction of photons from the light source with the molecule promotes it to a higher energy state, and upon relaxation, the photons are scattered elastically (Rayleigh scattering) or inelastically (Stokes or anti-Stokes scattering) [9,13]. The Rayleigh scattering is filtered out, and only the inelastic scattering is considered for Raman spectroscopy [13]. This energy emitted by the photons is detected as a change in wavenumber ( $\text{cm}^{-1}$ ) from the incident laser, which generates a Raman spectrum that provides information about chemical structure and composition [14].

An Alpa300SAR+ confocal Raman microscope (WITEC GmbH, Ulm, Germany) equipped with a 2w-NdYAG laser (532 nm wavelength) and a 20x/0.4 NA objective (Zeiss, Germany) was employed to obtain the Raman spectra. The spectrometer utilises a  $600 \text{ g mm}^{-1}$  (grooves per millimetre) grating. Powder samples of  $\text{LiB}_{11}\text{H}_{14}\cdot 2\text{H}_2\text{O}$ ,  $\alpha\text{-LiB}_{11}\text{H}_{14}\cdot (\text{H}_2\text{O})_n$ , and  $\text{LiB}_{11}\text{H}_{14}$  were packed in capillaries (1 mm diameter) inside an argon filled glovebox, sealed with grease and then flame-sealed outside the glovebox. Spectra were recorded with 100 accumulations at an integration time of 400 ms. Data were processed in terms of background subtraction, cosmic ray removal and exported with the ProjectFOUR software package (WITec, Ulm, Germany). Data were acquired by Dr Thomas Becker at Curtin University.

### 2.4.3 Fourier Transformed Infrared (FTIR) Spectroscopy

FTIR is a vibrational spectroscopy technique, which is based on the absorption of infrared radiation by a molecule, and it is usually used to identify functional groups [14]. Molecular vibrations are usually classified as stretching, which is the result of a change in the bond length between two atoms, or bending, which occurs due to a change in the angle between bonds. Each type of vibration absorbs in a specific frequency of the infrared radiation spectrum, which generates a spectrum of absorbed or transmitted frequency against wavenumber ( $\text{cm}^{-1}$ ) [15]. The spectrum can then be used to identify the sample's composition and chemical structure.

A ThermoScientific Summit ATR (attenuated total reflectance) spectrometer was used to conduct FTIR spectroscopy characterisation. The samples,  $\text{LiB}_{11}\text{H}_{14}\cdot(\text{H}_2\text{O})_n$ ,  $\text{NaB}_{11}\text{H}_{14}\cdot(\text{H}_2\text{O})_n$  and  $\text{KB}_{11}\text{H}_{14}$ , were individually transferred to a vial inside the glovebox and placed on the ATR diamond stage, with brief exposition of the sample to air ( $< 10$  s) upon mounting. A total of 16 scans were collected and averaged per sample, and data was measured between  $500 - 4000 \text{ cm}^{-1}$  with a spectral resolution of  $4 \text{ cm}^{-1}$ .

### 2.4.4 X-Ray Diffraction (XRD)

XRD was used in order to identify the crystal structure and crystalline composition of the synthesised materials. In the laboratory, X-rays are usually produced in an evacuated X-ray tube that contains a tungsten (W) filament (cathode), which releases electrons when electrically heated. These electrons are then accelerated towards an anode (a metal target) by a high potential difference (30 - 60 kV). The electrons strike the target, usually a piece of copper (Cu) fixed to the anode, and a beam of X-rays is emitted to the sample (Fig. 2.5A) [16]. X-rays can also be produced in a synchrotron, a large facility that exists to accelerate electrons and make them change direction to emit powerful X-rays, which results in more informative diffractograms with high temporal and spatial resolution [16]. The beam of high-speed electrons in the storage ring emits synchrotron light, which is captured by individual beamlines (Fig. 2.5B) [17].

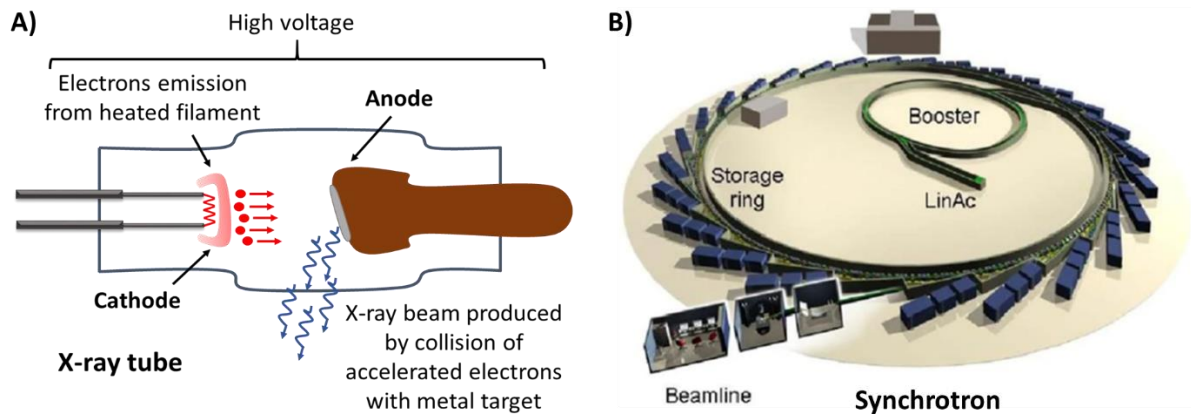


**Figure 2.5** Two different methods of production of X-rays. A) X-ray tube [18]. B) Synchrotron. The electrons are initially accelerated in the linear accelerator (LinAc), which are then transferred to the booster ring to increase energy before moving to the storage ring. Reproduced and adapted with permission [19]. Copyright 2021, Springer Nature.

Upon X-ray irradiation of a solid sample, the X-rays are scattered by the electrons of the atoms. A crystalline sample is formed by layers of atoms that are separated by an interplanar  $d$ -spacing ( $d$ ), and each atomic layer acts as a reflecting plane. The constructive interference of the scattered rays by the layers of atoms occurs at certain possible angles ( $\vartheta$ ), called the Bragg angles, and forms the X-ray diffraction pattern [14]. This constructive interference between waves of wavelength  $\lambda$  occurs when the Bragg's law is satisfied, with  $n$  as an integer (eq. 13) [20]. At angles of incidence other than the Bragg angle, reflected beams are out of phase, destructive interference occurs, and diffraction beam cannot be observed [14]. Fig. 2.6 shows the illustration for Bragg's law condition to obtain diffraction.

$$2d\sin\vartheta = n\lambda \tag{13}$$

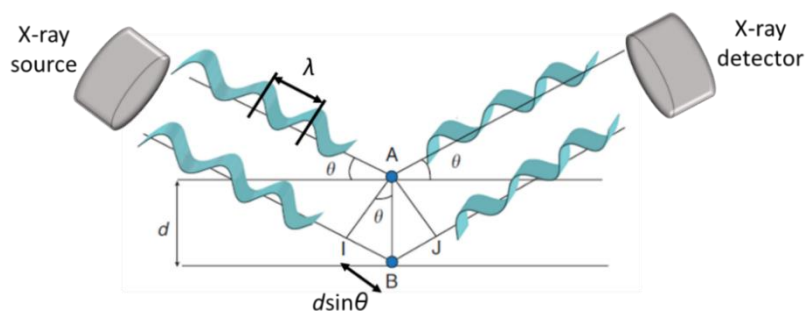


**Figure 2.6** Bragg's law illustration. Reproduced and adapted with permission [20]. Copyright 2010, Elsevier.

Powder and single-crystal XRD are the two most common X-ray techniques used to characterise a material. A polycrystalline powdered sample is formed by randomly oriented small crystals, and when this material is irradiated with X-rays in a wide angle range, for example from  $0 - 90^\circ 2\theta$ , the diffraction angles are identified, which correspond to the  $d$ -spacing of the atomic planes [14]. The diffractogram is a fingerprint of the material, in which the crystal system and the lattice parameters can be obtained based on the position and number of reflections and the wavelength used to conduct the experiment [14]. The single-crystal method is used to more easily obtain a complete structural determination of an inorganic solid, including the position of light atoms, such as H, which contain only one electron, through a method known as Hirshfeld atom refinement, for example [14,21].

X-Ray Powder Diffraction (XRPD) was conducted to characterise the synthesised borane samples at room temperature. The powdered samples were hand ground using a mortar and pestle in an argon glovebox, mounted on a single-crystal Si low background sample holder and sealed with an airtight poly(methyl-methacrylate) (PMMA) dome to avoid exposure to air during measurement. A Bruker D8 Advance Powder Diffractometer with a Cu  $K_\alpha$  radiation source ( $\lambda = 1.54056 \text{ \AA}$ ) operated at 40 kV/40mA with a LynxEye detector in the  $2\theta$  range of  $5 - 60^\circ$  was used in flat-plate Bragg-Brentano geometry.

The sample  $\text{NaB}_{11}\text{H}_{14} \cdot (\text{H}_2\text{O})_n$  was also characterised via an *in-situ* cooling experiment. The powdered material was packed inside a borosilicate capillary (0.7 mm diameter, 0.01 mm wall) in an argon glovebox, sealed with grease and flame-sealed outside the glovebox. The measurement was conducted on a ThermoFisher ARL Equinox 5000 diffractometer using a Mo source (Mo  $K_\alpha$  radiation,  $\lambda = 0.7093 \text{ \AA}$ ) from RT to  $-100^\circ\text{C}$ , with the data being collected using a curved position sensitive X-ray detector (CPS 120) with acquisition in real time over  $120^\circ 2\theta$ . The sample was cooled with a cold stream of nitrogen (from boiling liquid nitrogen), and the temperature was monitored by a K-type thermocouple  $\approx 10 \text{ mm}$  from the capillary.

Synchrotron Radiation X-ray Powder Diffraction (SR-XRPD) was also used to characterise several boron-hydrogen materials synthesised and to conduct *in-situ* experiments. The samples were ground with a mortar and pestle in an argon glovebox, packed in a borosilicate capillary (0.01 mm wall thickness) and flame-sealed to be analysed at the Powder Diffraction beamline at the Australian Synchrotron. Data collection was performed by Dr Anita D'Angelo. Information about the *in-situ* experiments for each sample is detailed in Table 2.2.



**Table 2.2** Parameters used to conduct *in-situ* SR-XRPD experiments. Wavelength was refined using a NIST LaB<sub>6</sub> 660b line position standard. Temperature was controlled using an Oxford Cryosystems Cryostream Plus.

Sample	Capillary OD (mm)	Temperature range (°C)	Rate (°C min <sup>-1</sup> )	Wavelength (Å)
<b>KB<sub>11</sub>H<sub>14</sub></b>	0.7	20 → 177 → 25	5 (heating) - 6 (cooling)	0.563476(5)
<b>α-LiB<sub>11</sub>H<sub>14</sub>·(H<sub>2</sub>O)<sub>n</sub></b>	1.0	25 → 100 → 25	5 (heating) - 6 (cooling)	0.590827(4)
<b>b-LiB<sub>11</sub>H<sub>14</sub>·(H<sub>2</sub>O)<sub>n</sub></b>	0.7	25 → -175	- 1	0.563476(5)
<b>Na<sub>2</sub>B<sub>11</sub>H<sub>13</sub></b>	1.0	30 → 230 → 30	5 (heating) - 6 (cooling)	0.590827(4)

Data were collected on a Mythen II microstrip detector at two positions, and later combined into gap-free data sets, from 1° – 76° 2θ.

Rietveld refinement is a technique widely used to perform quantitative phase analyses. This technique is based on the fitting of a comprehensive model (involving information about the sample, radiation, and diffractometer) to the diffraction patterns using a nonlinear least squares method [16]. Rietveld refinement of XRPD profiles was conducted using the Bruker *TOPAS* software (version 5) [22].

The RT KB<sub>11</sub>H<sub>14</sub> structure was solved using simulated annealing, treating the B<sub>11</sub>H<sub>14</sub><sup>-</sup> units as rigid bodies. A minor impurity of K<sub>2</sub>SO<sub>4</sub> was also modelled during structure solution. The background was defined using an 11<sup>th</sup> order Chebyshev polynomial. Unit cell parameters, scale factors, zero-point, peak shape mixing parameters and occupancies of K and B atoms were refined together with the Rietveld method. Isotropic displacement parameters, *B*<sub>iso</sub>, were refined as a single parameter for the K and B atoms, while those for H were not refined. The crystallographic data was deposited into the Inorganic Crystal Structure Database (ICSD 2090015). The Rietveld refinement, the crystallographic indexing and structure solution of KB<sub>11</sub>H<sub>14</sub>, as well as, the quantitative analysis of α-LiB<sub>11</sub>H<sub>14</sub>·(H<sub>2</sub>O)<sub>n</sub> at RT were performed by Dr Terry Humphries and Associate Professor Mark Paskevicius.

A single-crystal of  $\text{LiB}_{11}\text{H}_{14}\cdot 2\text{H}_2\text{O}$  was grown by allowing an aliquot of the diethyl ether layer (obtained during synthesis after performing the liquid-liquid extraction step – see section 2.3.2) to dry naturally at room temperature inside an argon filled glovebox. The single crystal was selected inside an argon-filled glovebox from the solid material using an optical microscope, transferred to a borosilicate capillary (0.7 mm diameter, 0.01 mm wall) using a needle (Fig. 2.7) and flame-sealed.

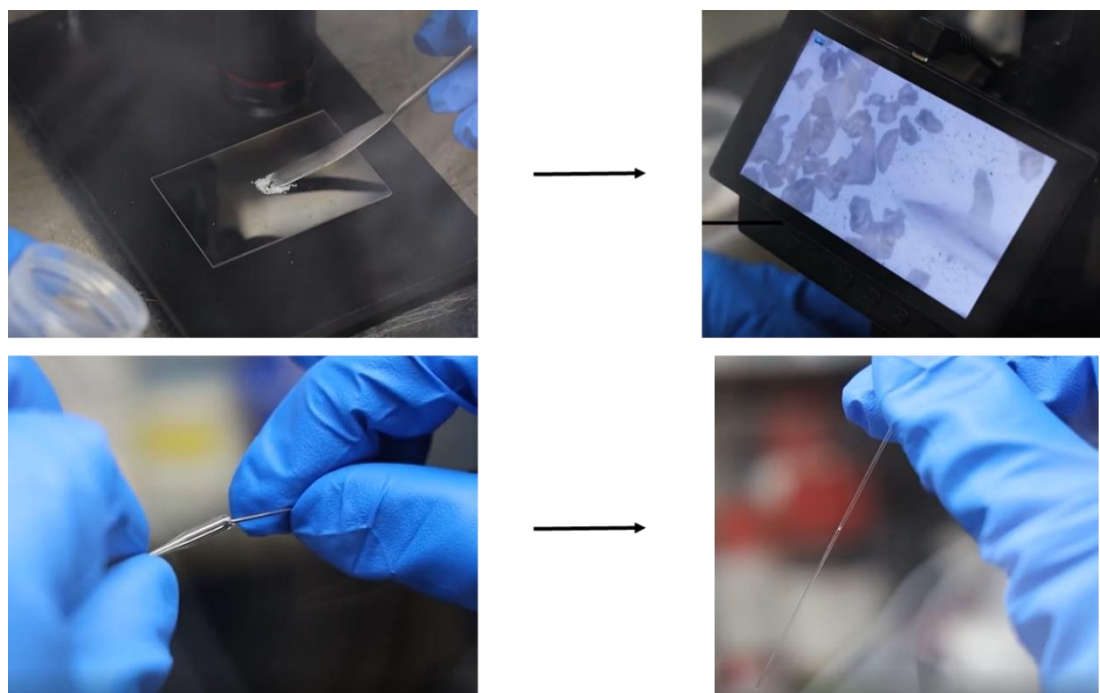


**Figure 2.7** Illustration of the method used to select and transfer a single-crystal to a capillary inside an argon glovebox for further single-crystal XRD analysis.

The sealed capillary containing the hygroscopic single-crystal was mounted onto an XtaLAB Synergy-S diffractometer, equipped with a  $\text{Cu K}\alpha$  ( $\lambda = 1.54184 \text{ \AA}$ ) source, and data were collected at  $22 \text{ }^\circ\text{C}$ . The diffraction pattern was indexed and the total number of runs and images was based on the strategy calculation from the program CrysAlisPro (Rigaku, V1.171.40.53, 2019) [23]. The maximum resolution that was achieved was  $0.83 \text{ \AA}$  at  $\theta = 67.894^\circ$ . The unit cell was refined using CrysAlisPro (Rigaku, V1.171.40.53, 2019) [23] on 3182 reflections.

Data reduction, scaling, and absorption corrections were performed using CrysAlisPro (Rigaku, V1.171.40.53, 2019) [23]. The final completeness was 66.30%, which was low, as the sample became dislodged inside the capillary during data collection and could not be

recovered. Numerous ( $\approx 22$ ) other 'single-crystal' samples were screened, however all were polycrystalline, making structure solution impossible. A multi-scan absorption correction was performed using CrysAlisPro 1.171.40.53 (Rigaku Oxford Diffraction, 2019) [23].

The structure was solved and the space group determined by the ShelXT [24,25] structure solution program using dual methods and refined by full matrix least squares minimisation on  $F^2$  using version 2018/3 of ShelXL [23–25]. All non-hydrogen atoms were refined anisotropically. Hydrogen atom positions on the water ligands, and on the  $B_{11}H_{14}^-$  cage were found in a difference map, then refined freely with 1,2 and 1,3-restraints used to optimise their geometry. The crystallographic data was deposited into the Inorganic Crystal Structure Database (ICSD 2031335). Single-crystal XRD analysis and structural solution were performed by Dr Stephen Moggach from the University of Western Australia.

#### 2.4.5 Simultaneous Differential Scanning Calorimetry and Thermogravimetry Analysis (DSC/TGA)

In order to analyse the thermal properties of the synthesised metal-boranes under heating, a DSC/TGA analyser was employed. Thermogravimetric analysis (TGA) measures the mass change of the sample on heating, and differential scanning calorimetry (DSC) determines the difference in heat flow between the sample and a reference during heating. An aluminium, Al, or alumina,  $Al_2O_3$ , crucible was used as sample holder and as a reference. A flowing atmosphere of argon gas is used during analysis in order to maintain an inert environment and to remove any volatile products (Fig. 2.8) [14]. The data retrieved from coupled DSC/TGA can give information about polymorphic changes, melting and decomposition of the sample during thermal treatment.

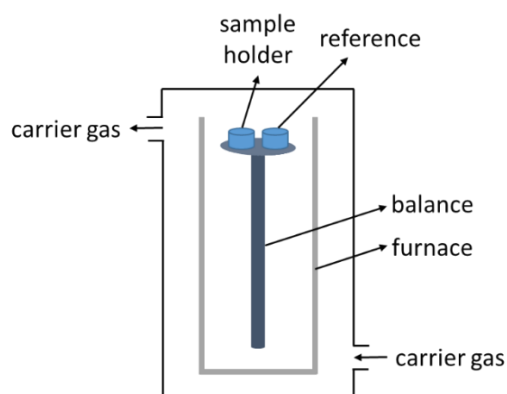


**Figure 2.8** Schematic representation of a DSC/TGA.

Thermal behaviour of the synthesised metal-boranes was analysed using a Netzsch STA 449 F3 Jupiter DSC/TGA. The solid powders were ground with a mortar and pestle inside an argon filled glovebox and a small portion (5 – 7 mg) transferred to the sample holder (Al or Al<sub>2</sub>O<sub>3</sub>). Detailed information for the analysis of each sample is provided in Table 2.3.

**Table 2.3** Parameters used to conduct DSC/TGA experiments. All samples were analysed at  $\Delta T/\Delta t = 10 \text{ }^\circ\text{C min}^{-1}$  with a constant Ar flow ( $40 \text{ mL min}^{-1}$ ).

Sample	Sample mass (mg)	Crucible	Temperature range ( $^\circ\text{C}$ )
$\text{LiB}_{11}\text{H}_{14}\cdot(\text{H}_2\text{O})_n$	7	Al	40 → 300
$\text{NaB}_{11}\text{H}_{14}\cdot(\text{H}_2\text{O})_n$	7	Al	40 → 300
$\text{KB}_{11}\text{H}_{14}$	7	Al	40 → 300 40 → 170 → 40
$\alpha\text{-LiB}_{11}\text{H}_{14}\cdot(\text{H}_2\text{O})_n$	7	Al <sub>2</sub> O <sub>3</sub>	25 → 300
$\text{LiB}_{11}\text{H}_{14}\cdot 2\text{H}_2\text{O}$	7	Al <sub>2</sub> O <sub>3</sub>	25 → 300
$\text{LiB}_{11}\text{H}_{14}$	7	Al <sub>2</sub> O <sub>3</sub>	25 → 300
$\text{Na}_2\text{B}_{11}\text{H}_{13}$	5	Al	40 → 350 40 → 220 → 40
$\text{Na}_{11}(\text{B}_{11}\text{H}_{14})_3(\text{B}_{11}\text{H}_{13})_4$	5	Al	40 → 350

Samples that were prepared in an Al crucible were crimp-sealed with a lid, and the lid was pierced  $\approx 10$  seconds prior to being transferred to the Pt furnace for the analysis. The lid of the Al<sub>2</sub>O<sub>3</sub> crucibles already has a small hole. Once the sample is loaded, the furnace is evacuated and filled with argon, which is kept under a flow of  $40 \text{ mL min}^{-1}$  during analysis. All samples were analysed over a temperature rate of  $10 \text{ }^\circ\text{C min}^{-1}$ . The temperature and sensitivity of the DSC/TGA was calibrated using In, Zn, Sn, Bi and CsCl reference materials, resulting in a temperature accuracy of  $\pm 0.2 \text{ }^\circ\text{C}$ , while the balance has an accuracy of  $\pm 20 \text{ }\mu\text{g}$ .

#### 2.4.6 Thermal Decomposition Analysis by Mass Spectrometry (TDA-MS)

The evolved gases from  $\text{LiB}_{11}\text{H}_{14}\cdot(\text{H}_2\text{O})_n$ ,  $\text{NaB}_{11}\text{H}_{14}\cdot(\text{H}_2\text{O})_n$  and  $\text{KB}_{11}\text{H}_{14}$  during thermal treatment were analysed through mass spectrometry (MS) using a Stanford Research Systems

(SRS) residual gas analyser (RGA-300) equipped with a quadrupole mass spectrometer. A heated filament produces electrons that collide against gas molecules to produce positive ions in the ionizer. Those positive ions are separated in the quadrupole filter based on their mass-to-charge ( $m/Z$ ) ratio, which are then identified by an ion detector.  $\approx 5$  mg of each sample, previously hand-ground, was placed inside a stainless steel reactor inside an argon-filled glovebox and sealed. The reactor was subjected to high vacuum ( $< 8 \times 10^{-4}$  mbar) and heated from 25 to 300 °C ( $2 \text{ }^\circ\text{C min}^{-1}$ ) while emitted gases were sampled by the MS. Temperature was controlled with a tube furnace and monitored by a K-type thermocouple  $\approx 5$  mm from the sample.

#### **2.4.7 Temperature Programmed Photographic Analysis (TPPA)**

The thermal behaviour of some solid-state metal-boranes was also investigated by analysing a pellet of the sample using photographs that were taken each five seconds during heating ( $\Delta T/\Delta t = 10 \text{ }^\circ\text{C min}^{-1}$ ).  $\approx 50$  mg of each sample ( $\text{KB}_{11}\text{H}_{14}$ ,  $\text{LiB}_{11}\text{H}_{14} \cdot 2\text{H}_2\text{O}$  and  $\alpha\text{-LiB}_{11}\text{H}_{14} \cdot (\text{H}_2\text{O})_n$ ) was pressed at 700 MPa inside an argon-filled glovebox using an electric oil-less press and a pellet press die set of 6 mm diameter. This pellet was then transferred to a glass tube, sealed with a rubber septa containing a balloon full of argon gas and placed in a custom-made brass heating block, as described by Paskevicius *et al.* [26].  $\text{KB}_{11}\text{H}_{14}$  was heated from RT to  $\approx 170 \text{ }^\circ\text{C}$ , whereas  $\text{LiB}_{11}\text{H}_{14} \cdot 2\text{H}_2\text{O}$  and  $\alpha\text{-LiB}_{11}\text{H}_{14} \cdot (\text{H}_2\text{O})_n$  were heated from RT to  $\approx 230 \text{ }^\circ\text{C}$ .

#### **2.4.8 Theoretical Calculations**

Theoretical studies using the quantum-mechanical method Density Functional Theory (DFT) were also performed to calculate the geometry and spectroscopic properties of  $\text{B}_{11}\text{H}_{14}^-$  and  $\text{B}_{11}\text{H}_{13}\text{OH}^-$  and then compared to experimental results. All geometry optimisations and vibrational frequency calculations were carried out using Gaussian 09 [27]. The geometry optimisation and vibrational frequency calculations were fully optimised on a B31LYP/aug-cc-pvdz level of theory [28]. Molecules were drawn and evaluated using Diamond v3.2 and rendered using POV-RAY. Charges were calculated via the Natural Bond Orbital (NBO) analyses [29]. NMR single-point calculations were carried out using the gauge-including atomic orbital (GIAO)-based approach [30] in acetonitrile using the conductor like polarisable continuum model (CPCM) as the solvation model [31]. It has been shown that the inclusion

of the implicit solvent model in the NMR calculation step is crucial to improve the prediction accuracy of calculated chemical shifts [32]. All  $^{11}\text{B}$  chemical shifts are relative to the computed shielding of  $\text{BF}_3\text{O}(\text{C}_2\text{H}_5)_2$  as the reference compound with an additional correction of +1.83 [33]. All theoretical studies were conducted by Dr Terry Humphries at Curtin University.

#### 2.4.9 Electrochemical Impedance Spectroscopy (EIS)

EIS is an important technique that is widely used to evaluate the properties of solid materials as ionic conductors. It assesses the electrical properties of bulk materials, which are correlated to their ionic conductivity properties, and their interfaces at different AC electrical frequencies and temperatures [34,35]. EIS measurements are conducted by applying an alternating voltage to an electrochemical cell over different frequencies and then detecting the current [34].

Electrical resistance, the capacity of a circuit to resist the flow of electrical current, is usually defined by Ohm's law:

$$R = \frac{V}{I} \quad (14)$$

where  $R$  is the resistance ( $\Omega$ ),  $V$  is the voltage (V) and  $I$  is the current (A). However, only an ideal resistor satisfies this equation, in which resistance does not change as a function of frequency, and AC (alternating current) voltage and generated current are always in phase [36] (Fig. 2.9).

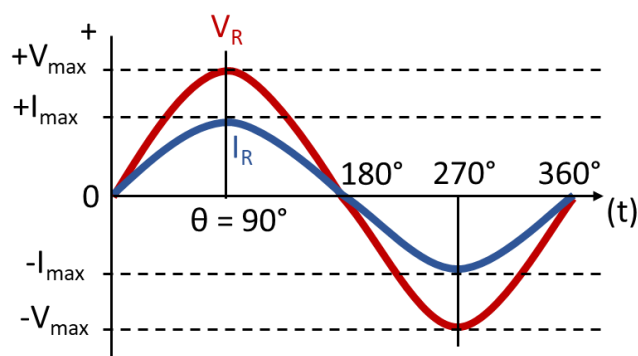


**Figure 2.9** Relationship between voltage and current as a function of time of an ideal resistor in AC circuit. It is said that voltage and current are in phase as both reach their maximum and minimum at the same time [37].

Due to the fact that resistance is idealised, impedance is used as a measurement of the circuit's ability to impede or resist the flow of electrical current, which takes in consideration the complex properties of a circuit system [36].

Typically, an AC potential presents a sinusoidal waveform that changes polarity over time, and the resulting electrical current sine wave appears shifted in phase at the same frequency, owing to the slow response of the system (Fig. 2.10) [34,36,38].

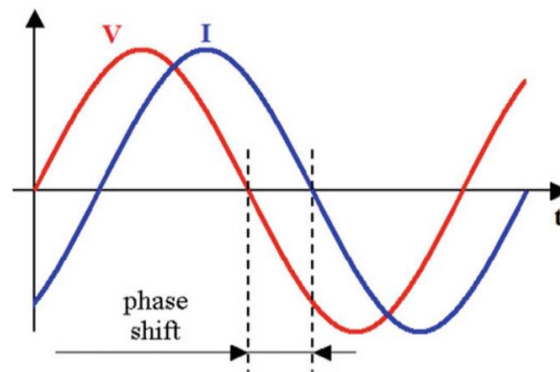


**Figure 2.10** Current response to applied AC potential as a function of time demonstrating the resulting phase shift. Reproduced with permission [38]. Copyright 2019, Springer Nature.

The applied voltage ( $V$ ) and the resulting electrical current ( $I$ ) with the corresponding phase shift ( $\varphi$ ) are defined by equations 15 and 16, respectively [34,38]:

$$V(t) = V_o \sin(\omega t) \quad (15)$$

$$I(t) = I_o \sin(\omega t + \varphi) \quad (16)$$

where  $V_o$  and  $I_o$  are the maximum potential and current intensities, respectively,  $\omega$  is the angular frequency ( $\omega = 2\pi f$ , where  $f$  is the ordinary frequency), and  $t$  is the time. Impedance ( $Z$ ) can then be defined as an equation (eq. 17) similar to Ohm's law [34,38]:

$$Z(\omega) = \frac{V(t)}{I(t)} = \frac{V_o \sin(\omega t)}{I_o \sin(\omega t + \varphi)} = Z_o \frac{\sin(\omega t)}{\sin(\omega t + \varphi)} \quad (17)$$

Impedance is usually expressed as a complex function in order to simplify mathematical operations [34]:

$$Z(\omega) = Z_{Re} + iZ_{Im} \quad (18)$$

where  $i$  is the imaginary unit defined as  $i = \sqrt{-1}$ . The real and imaginary components of the impedance equation can be determined as follows [34]:

$$Z_{Re} = |Z_o| \cos \varphi \quad (19)$$

$$Z_{Im} = |Z_o| \sin \varphi \quad (20)$$

where  $|Z_o|$  is the magnitude of the impedance [39]:

$$|Z_o| = \sqrt{Z_{Re}^2 + Z_{Im}^2} \quad (21)$$

The impedance is determined over a wide range of frequency (mHz to MHz) and the data is usually plotted in a graph of  $-Z_{Im}$  ( $y$ -axis), called reactance, vs.  $Z_{Re}$  ( $x$ -axis), called resistance, which is known as the Nyquist plot [34,38]. This graph can be modelled, and information about an equivalent electrical circuit can be extracted [34]. Fig. 2.11 shows some examples of Nyquist plots and their equivalent circuit model.

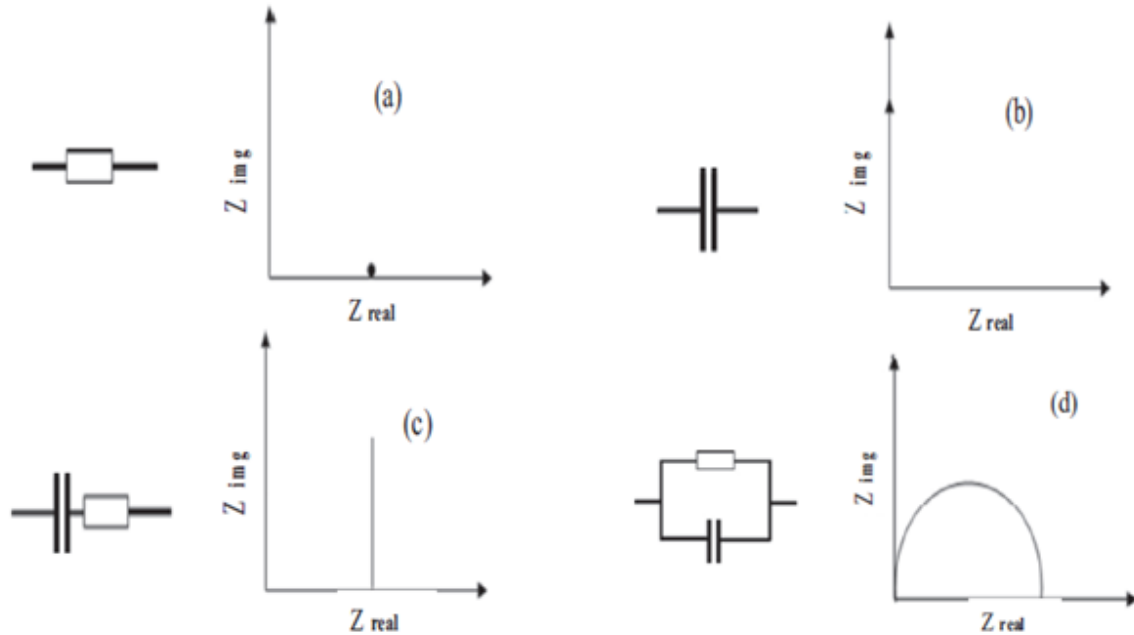


**Figure 2.11** Nyquist plots and their schematic equivalent circuit model for (a) a resistor, (b) a capacitor, (c) a capacitor and a resistor in series, (d) a resistor and a capacitor in parallel. Reproduced and adapted with permission [34]. Copyright 2018, Elsevier.



A typical equivalent circuit model that is used to represent the impedance for solid electrolytes is known as the Randles circuit, as shown in Fig. 2.12.

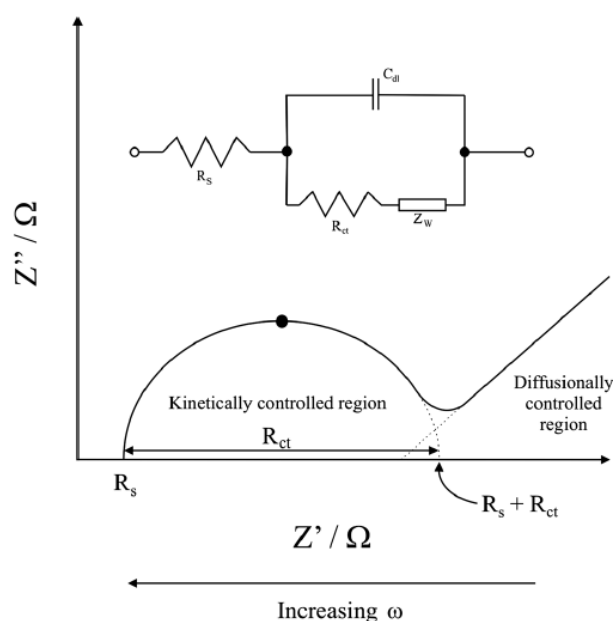


**Figure 2.12** Representation of a typical Nyquist plot observed for solid electrolytes in a symmetric cell with ion-blocking electrodes [40], and its correspondent Randles circuit model. Reproduced and adapted with permission from [41]. Copyright 2013, Royal Society of Chemistry.

The Nyquist plot of solid electrolytes assembled in a symmetric cell with two ion-blocking electrodes, such as gold, platinum or stainless steel [40], usually present a semi-circle at the high and intermediate frequency regions and a 45° line at the low frequency (Fig. 2.12). The circuit model is formed by an ohmic resistor ( $R_s$ ), which accounts for the resistance of charge carriers (contacts and wires), and a capacitor ( $C_{dl}$ ) in parallel with a resistor ( $R_{ct}$ ) representing the double layer capacitance and the charge transfer resistance through the electrolyte, respectively [40–42]. The capacitor is usually replaced by a constant phase element (CPE), as proposed by Cole and Cole [43], which takes into account electrode surface inhomogeneities, for example, in order to better represent a real system [41,42]. The Warburg element ( $Z_w$ ) represents the diffusion of ions and is usually seen in the low frequency ( $\omega$ ) region. Electrolytes with high ionic conductivity properties exhibit the Warburg impedance contribution at high frequencies as migration of ions occurs at similar periods as the operational frequency [41,42]. In that case, usually at high temperatures, the semi-circle is not evident, and only the spike line from the Warburg element can be observed. The ionic

conductivity of the solid-state electrolyte is extracted from the intercept of the Nyquist blocking tail with the x-axis, and is derived from the following equation [40,44]:

$$\sigma = \frac{d}{l \times A} \quad (22)$$

where  $\sigma$  is the ionic conductivity in  $S\text{ cm}^{-1}$ ,  $d$  is the pellet thickness in cm,  $l$  is the x-intercept of the Nyquist blocking tail, and  $A$  is the area of the pellet face in  $\text{cm}^2$ .

Pellets of each powdered sample were pressed at 700 MPa (6 mm in diameter) inside an argon glovebox, sandwiched between gold foil (0.1 mm in thickness), and sealed within an airtight ‘Swagelok-type’ Teflon cell (BOLA™) with custom 316 stainless steel electrodes and spring as shown in Fig. 2.13.

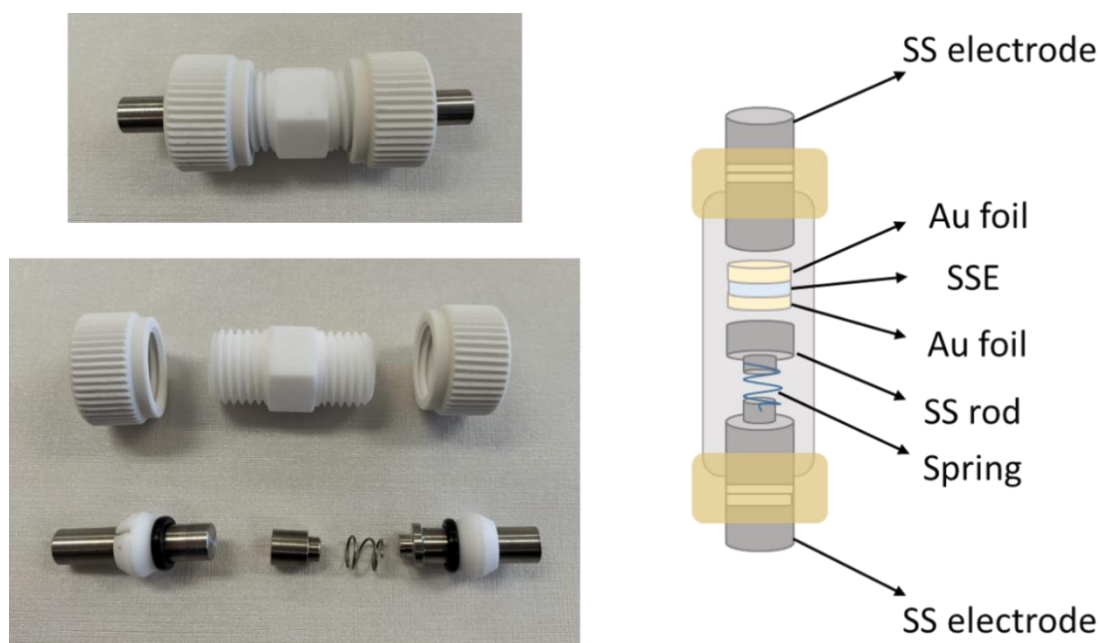


**Figure 2.13** BOLA™ PTFE (polytetrafluoroethylene) ‘Swagelok-type’ Teflon cell assembly and cross-sectional view. The electrochemical cell is formed with a pellet of the solid-state electrolyte (SSE) sandwiched between two gold foils and pressed between stainless steel (SS) electrodes. A spring is placed between SS rods to allow for a uniform pressure and possible expansion of the cell during heating [45]. PTFE is used for its high temperature resistance ( $\approx 260\text{ }^\circ\text{C}$ ) and its electrical resistance.

The measurements were performed using a ZIVE SP1 electrochemical workstation at 100 mV AC from 10 Hz to 1 MHz at different temperatures (Table 2.4).

**Table 2.4** Parameters used for EIS measurements of each sample upon heating. Temperature was monitored by a K-type thermocouple  $\approx 5$  mm from the pellet and controlled with a tube furnace. B.M. stands for ball-milled samples.

Sample	Approximate sample mass (mg)	Temperature range ( $^{\circ}\text{C}$ )	Heating step size ( $^{\circ}\text{C}$ )	Isothermal equilibrium (min)
$\text{LiB}_{11}\text{H}_{14}\cdot(\text{H}_2\text{O})_n$	40	25 $\rightarrow$ 100	25	30
$\text{NaB}_{11}\text{H}_{14}\cdot(\text{H}_2\text{O})_n$	40	25 $\rightarrow$ 100	25	30
$\text{KB}_{11}\text{H}_{14}$	40	25 $\rightarrow$ 160	10	30
$\text{NaB}_{11}\text{H}_{14}\cdot(\text{C}_6\text{H}_{14}\text{O}_3)_n$	40	25 $\rightarrow$ 100	25	30
$\text{LiB}_{11}\text{H}_{14}\cdot(\text{H}_2\text{O})_n$ (B.M.)	40	25 $\rightarrow$ 100	10	30
$\text{NaB}_{11}\text{H}_{14}\cdot(\text{H}_2\text{O})_n$ (B.M.)	40	25 $\rightarrow$ 100	10	30
$\text{KB}_{11}\text{H}_{14}$ (B.M.)	40	25 $\rightarrow$ 160	10	30
$\alpha\text{-LiB}_{11}\text{H}_{14}\cdot(\text{H}_2\text{O})_n$	50	30 $\rightarrow$ 90 90 $\rightarrow$ 30	10	50
$\text{LiB}_{11}\text{H}_{14}\cdot 2\text{H}_2\text{O}$	50	30 $\rightarrow$ 90 90 $\rightarrow$ 30	10	50
$\text{LiB}_{11}\text{H}_{14}$	50	30 $\rightarrow$ 110	10	50
$\text{Na}_2\text{B}_{11}\text{H}_{13}$	30	30 $\rightarrow$ 200	10	50
$\text{Na}_{11}(\text{B}_{11}\text{H}_{14})_3(\text{B}_{11}\text{H}_{13})_4$	30	30 $\rightarrow$ 170	10	50

Ionic conductivity measurements of samples  $\text{LiB}_{11}\text{H}_{14}\cdot(\text{H}_2\text{O})_n$ ,  $\text{NaB}_{11}\text{H}_{14}\cdot(\text{H}_2\text{O})_n$  and  $\text{KB}_{11}\text{H}_{14}$  were also performed after ball-milling (B.M.) them individually. Each powder was ball-milled inside an Across International Planetary Ball Mill (PQ-N04) with a ball-to-powder mass ratio of 10:1 employing stainless steel vials and balls (6 mm in diameter) under an argon atmosphere for 12 hours at a speed of 400 rpm.

EIS measurements were performed on Swagelok-type cells of  $\text{LiB}_{11}\text{H}_{14}\cdot(\text{H}_2\text{O})_n$  and  $\text{NaB}_{11}\text{H}_{14}\cdot(\text{H}_2\text{O})_n$  at sub-ambient temperatures. They were wrapped with a Parafilm<sup>®</sup> tape, and a K-type thermocouple was placed in close contact to the Swagelok-type cell ( $\approx 5$  mm from the pellet's sample). The wrapped cell was placed inside a plastic bag and transferred to an ice bath at  $0^{\circ}\text{C}$ , then to a bath of ice and sodium chloride at  $-20^{\circ}\text{C}$ , and to a bath of dry ice

and acetonitrile at  $-30\text{ }^{\circ}\text{C}$  and  $-40\text{ }^{\circ}\text{C}$ . The EIS measurements at each temperature were performed after 30 minutes isothermal equilibrium.

EIS measurements were performed 4 times on a Swagelok-type cell of the sample  $\alpha\text{-LiB}_{11}\text{H}_{14}\cdot(\text{H}_2\text{O})_n$  during heating and cooling, and after each cycle the cell was opened inside an argon glovebox, and the pellet thickness was measured. Each cycle was repeated after an interval of 24 hours rest at RT.

The measurement uncertainty on each ionic conductivity data point ( $\pm 10\%$ ) is based on the x-intercept of the Nyquist plot and has little impact on the logarithmic-scale of ionic conductivity, which spans many orders of magnitude.

The activation energy of ionic conductivity at a specific temperature range (Table 2.5) was calculated based on the solid-state ionic conductivity for each compound by:

$$\ln \sigma_{ion} = \ln \sigma_o - \left(\frac{E_{\sigma}}{K_B}\right)\frac{1}{T} \quad (23)$$

where  $\sigma_o$  is a pre-exponential factor ( $\text{S cm}^{-1}$ ),  $E_{\sigma}$  the activation energy (J),  $K_B$  the Boltzmann constant ( $1.3806 \times 10^{-23} \text{ J K}^{-1}$ ), and  $T$  the temperature (K) [46].

**Table 2.5** Temperature range used for determination of the activation energy of ionic conductivity for each compound.

Sample	Temperature range ( $^{\circ}\text{C}$ )
$\text{LiB}_{11}\text{H}_{14}\cdot(\text{H}_2\text{O})_n$	25 – 75
$\text{NaB}_{11}\text{H}_{14}\cdot(\text{H}_2\text{O})_n$	25 – 75
$\text{KB}_{11}\text{H}_{14}$	70 – 100
$\text{NaB}_{11}\text{H}_{14}\cdot(\text{C}_6\text{H}_{14}\text{O}_3)_n$	25 – 75
$\text{LiB}_{11}\text{H}_{14}\cdot(\text{H}_2\text{O})_n$ (B.M.)	25 – 75
$\text{NaB}_{11}\text{H}_{14}\cdot(\text{H}_2\text{O})_n$ (B.M.)	25 – 75
$\text{KB}_{11}\text{H}_{14}$ (B.M.)	70 – 100
$\alpha\text{-LiB}_{11}\text{H}_{14}\cdot(\text{H}_2\text{O})_n$	55 – 85
$\text{Na}_2\text{B}_{11}\text{H}_{13}$	30 – 50
	170 – 190
$\text{Na}_{11}(\text{B}_{11}\text{H}_{14})_3(\text{B}_{11}\text{H}_{13})_4$	30 – 80

#### 2.4.10 Linear Sweep Voltammetry (LSV)

The LSV technique was employed to assess the oxidative stability of lithium and sodium boranes against Li and Na metals, respectively. The method assesses whether the electrolyte is chemically stable against the metals and at which voltage oxidation of the electrolyte occurs. A variable potential, which increases linearly with time, is applied to the working electrode of an electrochemical cell, and the resulting current is recorded to generate a plot of current vs. voltage [47]. It is important to use a slow scanning rate for potential ( $V s^{-1}$ ) to minimise the influence of kinetics on the thermodynamic data being collected. The oxidative stability limit of a solid-state electrolyte (SSE) is then determined from the beginning of the oxidation reaction, which is represented by an anodic current peak. Two regression lines ( $R^2 > 0.99$ ) are extrapolated, one from the background current and the other from the anodic signal. The intersection point of those two lines determines the electrochemical oxidative stability limit of the material [48].

The LSV measurements were performed using a ZIVE SP1 electrochemical workstation. Initially, graphite was heated to 550 °C *in vacuo* for 12 h to remove moisture and volatiles, and it was mixed with the SSE in a weight ratio of 25:75 by grinding with a mortar and pestle. The electrochemical cell was prepared by pressing a pellet of the material to be tested (30 - 40 mg) with a top layer of the mixture of sample and graphite ( $\approx 3$  mg) at 700 MPa under argon. Graphite was added in order to improve the contact area between electrolyte and current collector, to increase the electronic conductivity of the solid electrolyte and hence the oxidation kinetics, and to simulate a bulk-type all-solid-state-battery, where the electrode is formed by a mixture of carbon, solid electrolyte and active material [48,49]. This two layered pellet was then sandwiched to form an Al/Pt/sample+C/sample/(Li or Na) configuration, which was sealed within an air tight 'Swagelok-type' Teflon cell (Fig. 2.13). All LSV measurements were performed at a very slow scan rate ( $50 \mu V s^{-1}$ ) to avoid an overestimation of the oxidative stability limit [48]. Details about the parameters used to conduct the experiment for each sample are listed in Table 2.6.

**Table 2.6** Parameters used to conduct LSV measurements for each sample.

Sample	Temperature range (°C)	Voltage range (V)
$\text{LiB}_{11}\text{H}_{14}\cdot(\text{H}_2\text{O})_n$	60	1.5 – 8.0 (1 <sup>st</sup> cycle) 1.5 – 4.5 (2 <sup>nd</sup> cycle)
$\text{NaB}_{11}\text{H}_{14}\cdot(\text{H}_2\text{O})_n$	60	1.5 – 8.0 (1 <sup>st</sup> cycle) 1.5 – 4.5 (2 <sup>nd</sup> cycle)
$\text{LiBH}_4$ (control sample)	60	1.5 – 4.5
$\alpha\text{-LiB}_{11}\text{H}_{14}\cdot(\text{H}_2\text{O})_n$	30	1.4 – 6.4 (1 <sup>st</sup> cycle) 1.5 – 5.1 (2 <sup>nd</sup> cycle)
$\text{Na}_2\text{B}_{11}\text{H}_{13}$	30	1.4 – 6.0
$\text{Na}_{11}(\text{B}_{11}\text{H}_{14})_3(\text{B}_{11}\text{H}_{13})_4$	30	1.4 – 6.0

#### 2.4.11 Galvanostatic Cycling (GC)

Galvanostatic stripping/plating cycling is a common electrochemical method used to analyse the stability of the SSE against the anode metal and the interfacial contact between SSE/electrode over time in a symmetric-type cell assembly. The electrochemical cell is evaluated under a constant current by reversing the polarity (charging and discharging), and the resulting voltage is recorded, which generates a plot of voltage vs. time. This measures the ability and stability of the SSE to undergo stripping (dissolution) and plating (deposition) of the metal over cycling. Fig. 2.14 shows an example of voltage profile during stripping/plating experiment for LLZO ( $\text{Li}_{6.25}\text{Al}_{0.25}\text{La}_3\text{Zr}_2\text{O}_{12}$ ) as SSE against Li metal at  $100 \mu\text{A cm}^{-2}$  [50]. The result shows that the interfacial resistance increases during stripping, which is attributed to the formation of pores on the surface of Li metal, resulting in a decrease in interfacial contact between SSE and electrode. These pores are reversibly filled during plating, which causes the interfacial resistance to almost reach its initial value [50].

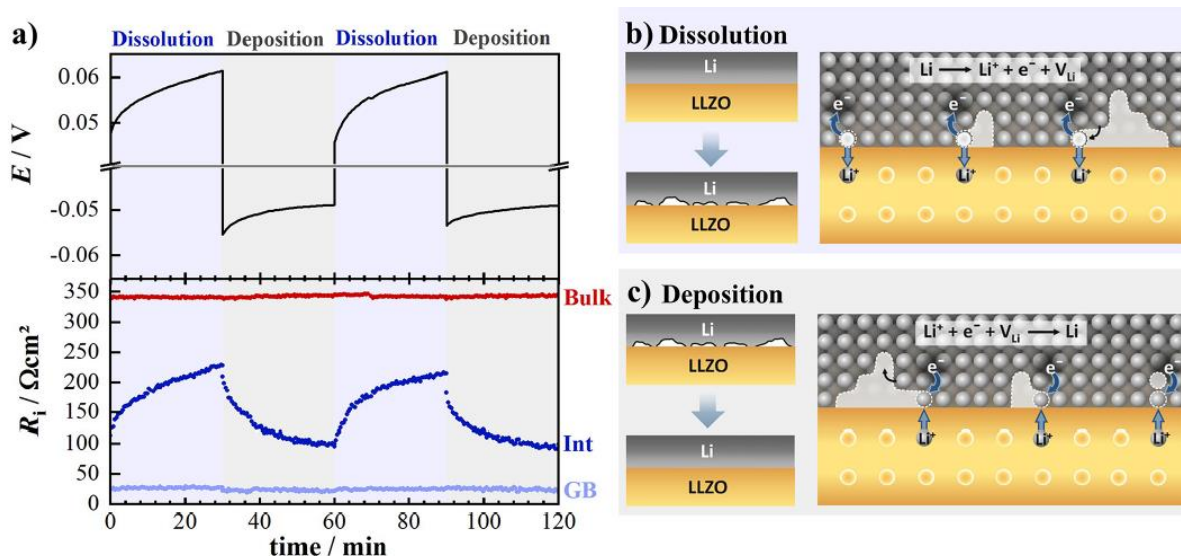


**Figure 2.14** a) Voltage profile and the corresponding interfacial (Int), bulk and grain boundary (GB) resistances during stripping/plating experiment on a Li/LLZO/Li symmetric cell at low stack pressure. b) Schematic representation of dissolution (stripping) process with resulting pore formation and reduction of contact area between Li and SSE, and c) schematic representation of deposition (plating) process. Reproduced with permission from [50]. Copyright 2019, American Chemical Society.

Contact loss between SSE and electrode due to pore formation with subsequent increase of interfacial resistance is a common issue that is observed in Li/SSE cells, which can also result in overpotential (continuous growth of interfacial resistance) due to poor reversibility of Li stripping/plating [51]. To investigate the Li stripping/plating behaviour of  $\alpha$ -LiB<sub>11</sub>H<sub>14</sub>·(H<sub>2</sub>O)<sub>n</sub> at 60 °C over time and to evaluate different strategies to reduce overpotential, three different symmetric cells of this hydrated *nido*-borane as SSE were prepared (Fig. 2.15).

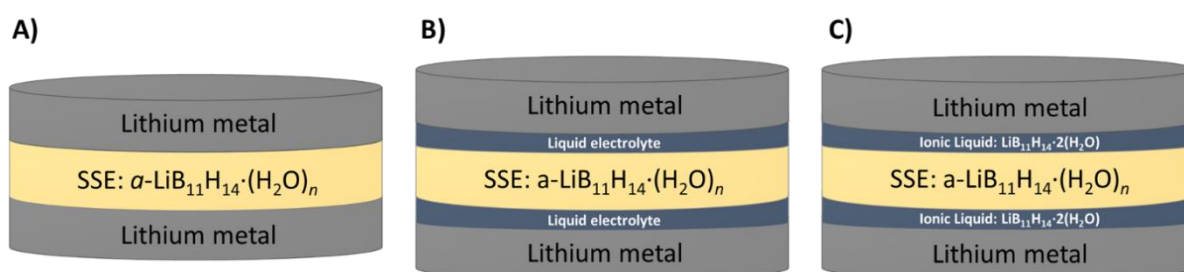


**Figure 2.15** Schematic representation of the three different cells prepared with  $\alpha$ -LiB<sub>11</sub>H<sub>14</sub>·(H<sub>2</sub>O)<sub>n</sub> as SSE to conduct galvanostatic stripping/plating cycling experiment. A) Li/ $\alpha$ -LiB<sub>11</sub>H<sub>14</sub>·(H<sub>2</sub>O)<sub>n</sub>/Li in a coin cell, B) Li/LE/ $\alpha$ -LiB<sub>11</sub>H<sub>14</sub>·(H<sub>2</sub>O)<sub>n</sub>/LE/Li in a Swagelok-type cell (LE = liquid electrolyte, 1.0 M LiPF<sub>6</sub> EC/DMC (v/v = 50/50)), C) Li/IL/ $\alpha$ -LiB<sub>11</sub>H<sub>14</sub>·(H<sub>2</sub>O)<sub>n</sub>/IL/Li in a Swagelok-type cell (IL = ionic liquid, LiB<sub>11</sub>H<sub>14</sub>·2H<sub>2</sub>O).

All cells were formed by pressing a pellet of the SSE,  $\alpha\text{-LiB}_{11}\text{H}_{14}\cdot(\text{H}_2\text{O})_n$ , at 700 MPa (6 mm in diameter,  $\approx 1.0$  mm in thickness,  $0.28\text{ cm}^2$  in surface area) inside an argon glovebox. The first cell was assembled by sandwiching the SSE (30 mg) between pure lithium disks ( $\text{Li}/\alpha\text{-LiB}_{11}\text{H}_{14}\cdot(\text{H}_2\text{O})_n/\text{Li}$ ) and placing it inside a coin cell containing a nickel foam and a separator (Fig. 2.16), which was sealed using a coin cell press under argon.

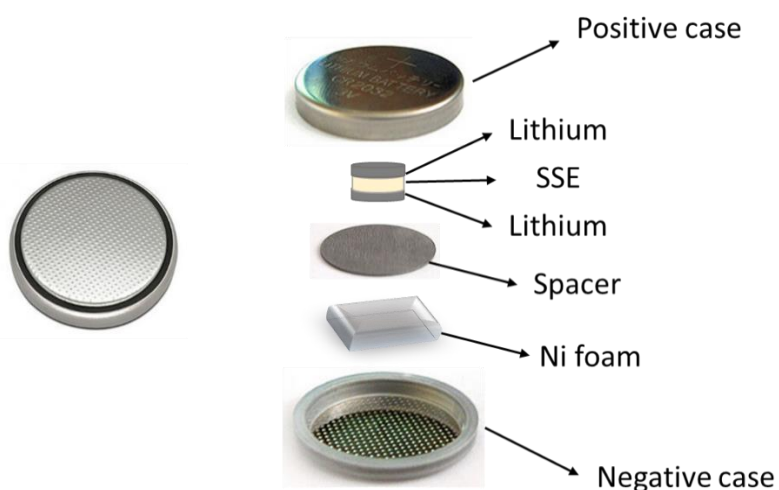


**Figure 2.16** Coin cell assembly and cross-sectional view. The electrochemical cell is formed with a nickel foam (a soft separator), a spacer, and a pellet of the solid-state electrolyte (SSE) sandwiched between two lithium foils that are all pressed between coin cases.

The second cell of  $\alpha\text{-LiB}_{11}\text{H}_{14}\cdot(\text{H}_2\text{O})_n$  was prepared in a Swagelok-type assembly with the addition of 1 drop of liquid electrolyte (LE) lithium hexafluorophosphate solution in ethylene carbonate and dimethyl carbonate (1.0 M  $\text{LiPF}_6$  EC/DMC ( $v/v = 50/50$ )) on top of each side of the SSE (30 mg) and sandwiched between lithium disks to form a  $\text{Li}/\text{LE}/\alpha\text{-LiB}_{11}\text{H}_{14}\cdot(\text{H}_2\text{O})_n/\text{LE}/\text{Li}$  cell. The third cell was prepared with the addition of 1 mg of ionic liquid (IL)  $\text{LiB}_{11}\text{H}_{14}\cdot 2\text{H}_2\text{O}$  on each side of the SSE  $\alpha\text{-LiB}_{11}\text{H}_{14}\cdot(\text{H}_2\text{O})_n$  (28 mg), which was pressed together at 700 MPa (6 mm in diameter,  $\approx 1.0$  mm in thickness,  $0.28\text{ cm}^2$  in surface area). This pellet was sandwiched between lithium disks to form a  $\text{Li}/\text{IL}/\alpha\text{-LiB}_{11}\text{H}_{14}\cdot(\text{H}_2\text{O})_n/\text{IL}/\text{Li}$  cell. Numerous other cells were prepared to optimise this experiment and arrive at the conditions described here.

All galvanostatic measurements were performed on a Landt Instruments Battery Testing System. The cells were left for 12 h at  $60\text{ }^\circ\text{C}$  at open circuit voltage prior to the commencement of the measurements. A constant current density of  $25\text{ }\mu\text{A cm}^{-2}$  was applied for 1 hour in each



direction alternating for 48 hours. Then, the current was increased to  $50 \mu\text{A cm}^{-2}$  and left running for 168 hours with 1 hour sweeps.

#### 2.4.12 Battery Assembly and Electrochemical Measurements

The SSE  $\alpha\text{-LiB}_{11}\text{H}_{14}\cdot(\text{H}_2\text{O})_n$  was also tested in a proof-of-concept battery using Li as the anode and  $\text{TiS}_2$  as the cathode. Among all types of anode materials, lithium is the one with the highest theoretical specific capacity ( $3,860 \text{ mAh g}^{-1}$ ) and the lowest redox potential ( $-3.04 \text{ V vs. standard hydrogen electrode}$ ), which can lead to batteries with more power/weight ratio and longer lifespan [52].  $\text{TiS}_2$  is a known cathode material that works through an intercalation process with Li metal as the anode, which results in a lithium titanium disulphide intercalation compound with a small lattice expansion (reaction 24) [53].



$\text{TiS}_2$  presents relatively low cost, high electrical conductivity, high theoretical capacity ( $239 \text{ mAh g}^{-1}$ ) and a working voltage  $\leq 2.5 \text{ V vs. Li}^+/\text{Li}$ , which is close to the oxidative stability limit determined for  $\alpha\text{-LiB}_{11}\text{H}_{14}\cdot(\text{H}_2\text{O})_n$  [53,54]. The theoretical gravimetric capacity of an active material is determined through the following equation [55]:

$$\text{Capacity} = \frac{nF}{M} \quad (25)$$

where  $n$  is the number of transferred electrons in the electrochemical process,  $F$  is the Faraday's constant ( $26.801 \text{ Ah mol}^{-1}$ ), and  $M$  is the molecular weight of the material ( $\text{g mol}^{-1}$ ). A common method used to perform battery tests is the galvanostatic cycling with potential limitation, in which a constant current is applied to the cell in a defined voltage range. The current is expressed in terms of  $C$ -rate, here defined as  $nC$ , in which the current fully discharges the battery in  $1/n$  hours, whereas  $C$  is the real capacity [56]. In the case of a battery with  $\text{TiS}_2$  as the cathode,  $1 C = 239 \text{ mA g}^{-1}$  (eq. 25). The result is usually plotted in a graph of voltage vs. specific capacity over several cycles. The measured voltage indicates the electrochemical intercalation reaction that happens between Li (anode) and  $\text{TiS}_2$  (cathode) mediated by the SSE, and the specific capacity that is measured during discharge demonstrates the capacity retention of the cell at different cycles. The Coulombic efficiency (CE), an estimate of the cycling life of the battery as it accounts for the loss of  $\text{Li}^+$  to side

reactions during charge/discharge process, is determined by the percentage ratio between discharge and charge capacity at each cycle [56,57].

Two different types of solid-liquid hybrid batteries were prepared with the use of  $\alpha$ -LiB<sub>11</sub>H<sub>14</sub>·(H<sub>2</sub>O)<sub>n</sub> as SSE, Li as the anode, and a mixture of SSE and TiS<sub>2</sub> as the cathode (Fig. 2.17). The latter was prepared by hand mixing  $\alpha$ -LiB<sub>11</sub>H<sub>14</sub>·(H<sub>2</sub>O)<sub>n</sub> with TiS<sub>2</sub> in a 1:1 proportion by mass in a mortar and pestle. Numerous other cells were prepared to optimise this experiment and arrive at the conditions described here.

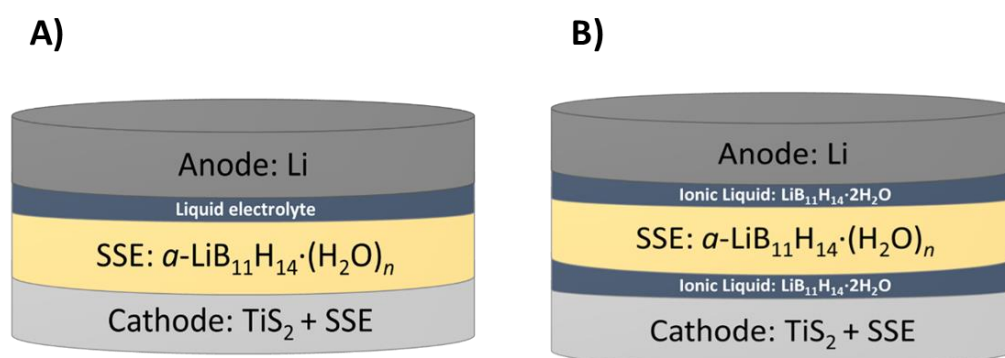


**Figure 2.17** Schematic representation of the solid-liquid hybrid batteries prepared for the conduction of the battery tests at 60 °C. A) Li/LE/ $\alpha$ -LiB<sub>11</sub>H<sub>14</sub>·(H<sub>2</sub>O)<sub>n</sub>/ $\alpha$ -LiB<sub>11</sub>H<sub>14</sub>·(H<sub>2</sub>O)<sub>n</sub>+TiS<sub>2</sub> cell prepared with addition of one drop of 1.0 M LiPF<sub>6</sub> EC/DMC (v/v = 50/50) on the interface Li/SSE. B) Li/IL/ $\alpha$ -LiB<sub>11</sub>H<sub>14</sub>·(H<sub>2</sub>O)<sub>n</sub>/IL/ $\alpha$ -LiB<sub>11</sub>H<sub>14</sub>·(H<sub>2</sub>O)<sub>n</sub>+TiS<sub>2</sub> cell prepared with addition of 1 mg of LiB<sub>11</sub>H<sub>14</sub>·2H<sub>2</sub>O on each interface.

To prepare the Li/LE/ $\alpha$ -LiB<sub>11</sub>H<sub>14</sub>·(H<sub>2</sub>O)<sub>n</sub>/ $\alpha$ -LiB<sub>11</sub>H<sub>14</sub>·(H<sub>2</sub>O)<sub>n</sub>+TiS<sub>2</sub> cell, 25 mg of  $\alpha$ -LiB<sub>11</sub>H<sub>14</sub>·(H<sub>2</sub>O)<sub>n</sub> was pressed at 350 MPa, 2 mg of the cathode mixture was then added on top of the SSE pellet, and both were pressed together at 700 MPa (6 mm diameter). One drop of LE 1.0 M LiPF<sub>6</sub> EC/DMC (v/v = 50/50) was added on top of a Li metal disk (6 mm diameter) and hand-pressed together with the pellet of SSE and cathode in a Swagelok-type cell. The second cell (Li/IL/ $\alpha$ -LiB<sub>11</sub>H<sub>14</sub>·(H<sub>2</sub>O)<sub>n</sub>/IL/ $\alpha$ -LiB<sub>11</sub>H<sub>14</sub>·(H<sub>2</sub>O)<sub>n</sub>+TiS<sub>2</sub>) was prepared by pressing a pellet (6 mm diameter) of 1 mg of LiB<sub>11</sub>H<sub>14</sub>·2H<sub>2</sub>O on each side of the SSE  $\alpha$ -LiB<sub>11</sub>H<sub>14</sub>·(H<sub>2</sub>O)<sub>n</sub> (23 mg) at 350 MPa. 2 mg of the cathode mixture was added on top of that pellet and pressed together at 700 MPa. A Li foil (6 mm diameter) was hand-pressed with the pellet in the opposite side of the cathode, which was assembled in a Swagelok-type cell.

All measurements were performed on a Landt Instruments Battery Testing System at 60 °C in the voltage range 1.7 – 2.5 V vs. Li<sup>+</sup>/Li. Only the mass of TiS<sub>2</sub> was considered for the calculation of the specific capacity. Details about the experiments performed for each cell are demonstrated in Table 2.7.

**Table 2.7** Details of the charge/discharge cycling experiments performed for each cell, with the number of cycles (discharge and charge from 1.7 – 2.5 V vs. Li<sup>+</sup>/Li) performed at each C-rate (1 C = 239 mA g<sup>-1</sup>). All batteries were assembled in a Swagelok-type cell, and all measurements were performed at 60 °C.

Cell	Experiment number	C-rate	Number of cycles
Li/LE/SSE/SSE+TiS <sub>2</sub>	1	0.05 C	1
		0.1 C	1
		0.2 C	1
		0.3 C	1
		0.4 C	50
Li/LE/SSE/SSE+TiS <sub>2</sub>	2	0.1 C	6
		0.2 C	60
Li/IL/SSE/IL/SSE+TiS <sub>2</sub>	3	0.05 C	1
		0.1 C	1
		0.2 C	1
		0.3 C	1
		0.4 C	1
Li/IL/SSE/IL/SSE+TiS <sub>2</sub>	4	0.4 C	50

#### 2.4.13 Critical Current Density (CCD) Test

A critical current density test is usually performed to determine the maximum current density that a battery can endure without cell failure. A method that can be used to estimate the CCD is called endurable time control measurement, in which the cell is analysed at each current density for several cycles. This demonstrates the effects of cycling and current density at the same time in a plot of voltage vs. time [51].

In order to determine the CCD of the symmetric Li/*a*-LiB<sub>11</sub>H<sub>14</sub>·(H<sub>2</sub>O)<sub>*n*</sub>/Li cell in a Swagelok-type assembly, an enduring time control measurement was performed. Initially, the cell was left resting for 12 h at 60 °C at open circuit voltage, and then a constant current density of 25 μA cm<sup>-2</sup> was applied for 30 minutes sweeps during 5 hours. The current density was then raised up to 750 μA cm<sup>-2</sup> with increases of 25 μA cm<sup>-2</sup> steps and left at each current density for 5 hours with 30 minutes at each direction [58]. The measurement was performed on a Landt Instruments Battery Testing System.

## 2.5 REFERENCES

- [1] G.B. Dunks, K. Barker, E. Hedaya, C. Hefner, K. Palmer-Ordóñez, P. Remec, Synthesis of B<sub>10</sub>H<sub>14</sub> from NaBH<sub>4</sub> via B<sub>11</sub>H<sub>14</sub><sup>-</sup> Ion, *Inorg. Chem.* 20 (1981) 1692–1697. <https://doi.org/10.1017/CBO9781107415324.004>.
- [2] E.L. Muetterties, J.H. Balthis, Y.T. Chia, W.H. Knoth, H.C. Miller, Chemistry of boranes. VIII. Salts and Acids of B<sub>10</sub>H<sub>10</sub><sup>2-</sup> and B<sub>12</sub>H<sub>12</sub><sup>2-</sup>, *Inorg. Chem.* 3 (1964) 444–451. <https://doi.org/10.1021/ic50013a030>.
- [3] L.V. Titov, L. V. Zhemchugova, L.A. Gavrilova, P. V. Petrovskii, Dehydrocondensation of a mixture of anions B<sub>3</sub>H<sub>8</sub><sup>-</sup> and B<sub>9</sub>H<sub>14</sub><sup>-</sup> by Diborane: Synthesis of Salts NaB<sub>11</sub>H<sub>14</sub>·3Dn and Bu<sub>4</sub>NB<sub>11</sub>H<sub>14</sub> (Dn = 1,4-Dioxane), *Russ. J. Inorg. Chem.* 50 (2005) 1215–1217.
- [4] H.C. Miller, N.E. Miller, E.L. Muetterties, Chemistry of Boranes. XX. Syntheses of Polyhedral Boranes, *Inorg. Chem.* 3 (1964) 1456–1463. <https://doi.org/10.1021/ic50020a026>.
- [5] F. Klanberg, E.L. Muetterties, Boron-Hydrogen Compounds, in: W.L. Jolly (Ed.), *Inorg. Synth.*, Volume XI, McGraw-Hill Book Company, New York, 1968: pp. 24–32.
- [6] A. Hepp, R. Labbow, F. Reiß, A. Schulz, A. Villinger, Carba-*closo*-dodecaborates – synthesis, structure, and energetics, *Eur. J. Inorg. Chem.* 2018 (2018) 2905–2914. <https://doi.org/10.1002/ejic.201800219>.
- [7] J. Pecyna, I. Rončević, J. Michl, Insertion of Carbenes into Deprotonated *nido*-Undecaborane, B<sub>11</sub>H<sub>13</sub>(2-), *Molecules.* 24 (2019) 3779. <https://doi.org/10.3390/molecules24203779>.
- [8] B. Richter, J.B. Grinderslev, K.T. Møller, M. Paskevicius, T.R. Jensen, From Metal Hydrides to Metal Borohydrides, *Inorg. Chem.* 57 (2018) 10768–10780. <https://doi.org/10.1021/acs.inorgchem.8b01398>.

- [9] J. García Solé, L. Bausá, D. Jaque, *An Introduction to the Optical Spectroscopy*, John Wiley & Sons, Madrid, 2005. <https://doi.org/10.1002/0470016043>.
- [10] S. Heřmánek, <sup>11</sup>B NMR Spectra of Boranes, Main-Group Heteroboranes, and Substituted Derivatives. Factors Influencing Chemical Shifts of Skeletal Atoms, *Chem. Rev.* 92 (1992) 325–362. <https://doi.org/10.1021/cr00010a007>.
- [11] G.R. Eaton, NMR of boron compounds, *J. Chem. Educ.* 46 (1969) 547–556. <https://doi.org/10.1021/ed046p547>.
- [12] W.L. Smith, Boron-11 NMR, *J. Chem. Educ.* 54 (1977) 469–473. <https://doi.org/10.1021/ed054p469>.
- [13] S. Assawajaruwan, B. Hitzmann, Process analysis | bioprocess analysis, *Encycl. Anal. Sci.* 8 (2019) 377–383. <https://doi.org/10.1016/B978-0-12-409547-2.11324-1>.
- [14] P.W. Atkins, T.L. Overton, J.P. Rourke, M.T. Weller, F.A. Armstrong, Shriver and Atkins' *Inorganic Chemistry*, 5th ed., Oxford University Press, Oxford, 2010.
- [15] R.C. Gore, Infrared Spectroscopy, *Anal. Chem.* 30 (1958) 570–579. <https://doi.org/10.1021/ac50163a004>.
- [16] V.K. Pecharsky, P.Y. Zavalij, *Fundamentals of Powder Diffraction and Structural Characterization of Materials Second Edition*, 2nd ed., Springer, New York, 2009.
- [17] How does the Australian Synchrotron work?, Australian Synchrotron, (2022). <http://archive.synchrotron.org.au/about-us/our-facilities/accelerator-physics/how-does-the-australian-synchrotron-work> (accessed June 2, 2022).
- [18] X-rays, Commonwealth of Australia as represented by the Australian Radiation Protection and Nuclear Safety Agency (ARPANSA), (2022). <https://www.arpansa.gov.au/understanding-radiation/what-is-radiation/ionising-radiation/x-ray> (accessed June 2, 2022).
- [19] S. Shin, New era of synchrotron radiation: fourth-generation storage ring, *AAPPS Bull.* 31 (2021). <https://doi.org/10.1007/s43673-021-00021-4>.
- [20] D.D. Le Pevelen, Small Molecule X-Ray Crystallography, Theory and Workflow, in: J.C. Lindon (Ed.), *Encycl. Spectrosc. Spectrom.*, 2nd ed., Academic Press, 2010: pp. 2559–2576. <https://doi.org/10.1016/B978-0-12-374413-5.00359-6>.
- [21] S.C. Capelli, H.B. Bürgi, B. Dittrich, S. Grabowsky, D. Jayatilaka, Hirshfeld atom refinement, *IUCrJ.* 1 (2014) 361–379. <https://doi.org/10.1107/S2052252514014845>.
- [22] A.A. Coelho, *TOPAS and TOPAS-Academic: An optimization program integrating*

- computer algebra and crystallographic objects written in C++: An, *J. Appl. Crystallogr.* 51 (2018) 210–218. <https://doi.org/10.1107/S1600576718000183>.
- [23] G.M. Sheldrick, *SHELXT* - Integrated space-group and crystal-structure determination, *Acta Crystallogr. Sect. A Found. Adv.* A71 (2015) 3–8. <https://doi.org/10.1107/S2053273314026370>.
- [24] G.M. Sheldrick, Crystal structure refinement with *SHELXL*, *Acta Crystallogr. Sect. C Struct. Chem.* C71 (2015) 3–8. <https://doi.org/10.1107/S2053229614024218>.
- [25] O. V. Dolomanov, L.J. Bourhis, R.J. Gildea, J.A.K. Howard, H. Puschmann, *OLEX2*: A complete structure solution, refinement and analysis program, *J. Appl. Crystallogr.* 42 (2009) 339–341. <https://doi.org/10.1107/S0021889808042726>.
- [26] M. Paskevicius, M.B. Ley, D.A. Sheppard, T.R. Jensen, C.E. Buckley, Eutectic melting in metal borohydrides, *Phys. Chem. Chem. Phys.* 15 (2013) 19774–19789. <https://doi.org/10.1039/c3cp53920b>.
- [27] M.J. Frisch, G.W. Trucks, H.B. Schlegel, G.E. Scuseria, M.A. Robb, J.R. Cheeseman, G. Scalmani, V. Barone, G. a. Petersson, H. Nakatsuji, X. Li, M. Caricato, a. V. Marenich, J. Bloino, B.G. Janesko, R. Gomperts, B. Mennucci, H.P. Hratchian, J. V. Ortiz, a. F. Izmaylov, J.L. Sonnenberg, Williams, F. Ding, F. Lipparini, F. Egidi, J. Goings, B. Peng, A. Petrone, T. Henderson, D. Ranasinghe, V.G. Zakrzewski, J. Gao, N. Rega, G. Zheng, W. Liang, M. Hada, M. Ehara, K. Toyota, R. Fukuda, J. Hasegawa, M. Ishida, T. Nakajima, Y. Honda, O. Kitao, H. Nakai, T. Vreven, K. Throssell, J. a. Montgomery Jr., J.E. Peralta, F. Ogliaro, M.J. Bearpark, J.J. Heyd, E.N. Brothers, K.N. Kudin, V.N. Staroverov, T. a. Keith, R. Kobayashi, J. Normand, K. Raghavachari, a. P. Rendell, J.C. Burant, S.S. Iyengar, J. Tomasi, M. Cossi, J.M. Millam, M. Klene, C. Adamo, R. Cammi, J.W. Ochterski, R.L. Martin, K. Morokuma, O. Farkas, J.B. Foresman, D.J. Fox, *Gaussian 09, Revision A. 02, Gaussian 09, Revis. A. 02.* (2009).
- [28] R.A. Kendall, T.H. Dunning, R.J. Harrison, Electron affinities of the first-row atoms revisited. Systematic basis sets and wave functions, *J. Chem. Phys.* 96 (1992) 6796–6806. <https://doi.org/10.1063/1.462569>.
- [29] A.E. Reed, R.B. Weinstock, F. Weinhold, Natural population analysis, *J. Chem. Phys.* 83 (1985) 735–746. <https://doi.org/10.1063/1.449486>.
- [30] R. Ditchfield, Self-consistent perturbation theory of diamagnetism I. A gauge-invariant LCAO method for N.M.R. Chemical shifts, *Mol. Phys.* 27 (1974) 789–807.

- <https://doi.org/10.1080/00268977400100711>.
- [31] V. Barone, M. Cossi, Quantum Calculation of Molecular Energies and Energy Gradients in Solution by a Conductor Solvent Model, *J. Phys. Chem. A.* 102 (1998) 1995–2001. <https://doi.org/10.1021/jp9716997>.
- [32] P. Gao, X. Wang, Z. Huang, H. Yu, <sup>11</sup>B NMR chemical shift predictions via density functional theory and gauge-including atomic orbital approach: Applications to structural elucidations of boron-containing molecules, *ACS Omega.* 4 (2019) 12385–12392. <https://doi.org/10.1021/acsomega.9b01566>.
- [33] H.S. Rzepa, S. Arkhipenko, E. Wan, M.T. Sabatini, V. Karaluka, A. Whiting, T.D. Sheppard, An Accessible Method for DFT Calculation of <sup>11</sup>B NMR Shifts of Organoboron Compounds, *J. Org. Chem.* 83 (2018) 8020–8025. <https://doi.org/10.1021/acs.joc.8b00859>.
- [34] S.B. Aziz, T.J. Woo, M.F.Z. Kadir, H.M. Ahmed, A conceptual review on polymer electrolytes and ion transport models, *J. Sci. Adv. Mater. Devices.* 3 (2018) 1–17. <https://doi.org/10.1016/j.jsamd.2018.01.002>.
- [35] M. Matsuo, Y. Nakamori, S. Orimo, H. Maekawa, H. Takamura, Lithium superionic conduction in lithium borohydride accompanied by structural transition, *Appl. Phys. Lett.* 91 (2007) 224103. <https://doi.org/10.1063/1.2817934>.
- [36] D. Loveday, P. Peterson, B. Rodgers, Evaluation of Organic Coatings with Electrochemical Impedance Spectroscopy Part 1 : Fundamentals of Electrochemical Impedance Spectroscopy, *JCT CoatingsTech.* (2004) 46–52.
- [37] Resistors in AC Circuits, Electronics Tutorials, (2021). [https://www.electronicstutorials.ws/resistor/res\\_8.html](https://www.electronicstutorials.ws/resistor/res_8.html) (accessed June 8, 2022).
- [38] N. Afsarimanesh, S.C. Mukhopadhyay, M. Kruger, Planar Interdigital Sensors and Electrochemical Impedance Spectroscopy, in: *Electrochem. Biosens. Point-of-Care Early Detect. Bone Loss. Smart Sensors, Meas. Instrumentation*, Vol 30, Springer, Cham, 2019. [https://doi.org/10.1007/978-3-030-03706-2\\_3](https://doi.org/10.1007/978-3-030-03706-2_3).
- [39] D.D. MacDonald, Reflections on the history of electrochemical impedance spectroscopy, *Electrochim. Acta.* 51 (2006) 1376–1388. <https://doi.org/10.1016/j.electacta.2005.02.107>.
- [40] P. Vadhva, J. Hu, M.J. Johnson, R. Stocker, M. Braglia, D.J.L. Brett, A.J.E. Rettie, *Electrochemical Impedance Spectroscopy for All-Solid-State Batteries: Theory,*

- Methods and Future Outlook, *ChemElectroChem*. 8 (2021) 1930–1947. <https://doi.org/10.1002/celec.202100108>.
- [41] E.P. Randviir, C.E. Banks, Electrochemical impedance spectroscopy: An overview of bioanalytical applications, *Anal. Methods*. 5 (2013) 1098–1115. <https://doi.org/10.1039/c3ay26476a>.
- [42] S.M.M. Alavi, C.R. Birkl, D.A. Howey, Time-domain fitting of battery electrochemical impedance models, *J. Power Sources*. 288 (2015) 345–352. <https://doi.org/10.1016/j.jpowsour.2015.04.099>.
- [43] K.S. Cole, R.H. Cole, Dispersion and absorption in dielectrics I. Alternating current characteristics, *J. Chem. Phys.* 9 (1941) 341–351. <https://doi.org/10.1063/1.1750906>.
- [44] B.R.S. Hansen, M. Paskevicius, M. Jørgensen, T.R. Jensen, Halogenated Sodium-*clos*-Dodecaboranes as Solid-State Ion Conductors, *Chem. Mater.* 29 (2017) 3423–3430. <https://doi.org/10.1021/acs.chemmater.6b04797>.
- [45] M.N. Safa, Poly (Ionic Liquid) Based Electrolyte for Lithium Battery Application, FIU Electronic Theses and Dissertations, 2018. <https://doi.org/10.25148/etd.FIDC006891>.
- [46] A. Gradišek, M. Krnel, M. Paskevicius, B.R.S. Hansen, T.R. Jensen, J. Dolinšek, Reorientational Motions and Ionic Conductivity in  $(\text{NH}_4)_2\text{B}_{10}\text{H}_{10}$  and  $(\text{NH}_4)_2\text{B}_{12}\text{H}_{12}$ , *J. Phys. Chem. C*. 122 (2018) 17073–17079. <https://doi.org/10.1021/acs.jpcc.8b04605>.
- [47] D.A. Skoog, F.J. Holler, S.R. Crouch, Principles of Instrumental Analysis, 6th ed., Thomson Brooks/Cole, Belmont, 2007. [https://doi.org/10.1016/s0003-2670\(00\)84936-3](https://doi.org/10.1016/s0003-2670(00)84936-3).
- [48] R. Asakura, L. Duchêne, R.S. Kühnel, A. Remhof, H. Hagemann, C. Battaglia, Electrochemical Oxidative Stability of Hydroborate-Based Solid-State Electrolytes, *ACS Appl. Energy Mater.* 2 (2019) 6924–6930. <https://doi.org/10.1021/acsaem.9b01487>.
- [49] F. Han, Y. Zhu, X. He, Y. Mo, C. Wang, Electrochemical stability of  $\text{Li}_{10}\text{GeP}_2\text{S}_{12}$  and  $\text{Li}_7\text{La}_3\text{Zr}_2\text{O}_{12}$  solid electrolytes, *Adv. Energy Mater.* 6 (2016) 1501590. <https://doi.org/10.1002/aenm.201501590>.
- [50] T. Krauskopf, H. Hartmann, W.G. Zeier, J. Janek, Toward a Fundamental Understanding of the Lithium Metal Anode in Solid-State Batteries - An Electrochemo-Mechanical Study on the Garnet-Type Solid Electrolyte  $\text{Li}_{6.25}\text{Al}_{0.25}\text{La}_3\text{Zr}_2\text{O}_{12}$ , *ACS Appl. Mater. Interfaces*. 11 (2019) 14463–14477. <https://doi.org/10.1021/acsaem.9b02537>.
- [51] Y. Lu, C.-Z. Zhao, H. Yuan, X.-B. Cheng, J.-Q. Huang, Q. Zhang, Critical current density in



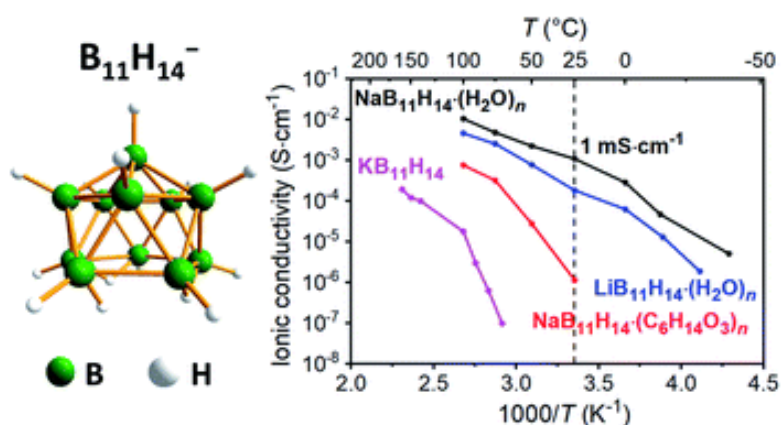
- solid-state lithium metal batteries: mechanism, influences, and strategies, *Adv. Funct. Mater.* 31 (2021) 2009925. <https://doi.org/10.1002/adfm.202009925>.
- [52] Z. Ding, J. Li, J. Li, C. An, Review—Interfaces: key issue to be solved for all solid-state lithium battery technologies, *J. Electrochem. Soc.* 167 (2020) 070541. <https://doi.org/10.1149/1945-7111/ab7f84>.
- [53] M.S. Whittingham, Electrical Energy Storage and Intercalation Chemistry, *Science*. 192 (1976) 1126–1127. <https://doi.org/10.1126/science.192.4244.1126>.
- [54] S.H. Payandeh, D. Rentsch, Z. Łodziana, R. Asakura, L. Bigler, R. Černý, C. Battaglia, A. Remhof, *Nido*-Hydroborate-Based Electrolytes for All-Solid-State Lithium Batteries, *Adv. Funct. Mater.* 31 (2021) 2010046. <https://doi.org/10.1002/adfm.202010046>.
- [55] S. Banerjee, G. Periyasamy, S.K. Pati, Possible application of 2D-boron sheets as anode material in lithium ion battery: A DFT and AIMD study, *J. Mater. Chem. A*. 2 (2014) 3856–3864. <https://doi.org/10.1039/c3ta14041e>.
- [56] V. Gulino, LiBH<sub>4</sub> as solid-state electrolyte for Li-ion batteries: modelling, synthesis, characterization and application, Thesis, University of Torino, 2020.
- [57] J. Xiao, Q. Li, Y. Bi, M. Cai, B. Dunn, T. Glossmann, J. Liu, T. Osaka, R. Sugiura, B. Wu, J. Yang, J.G. Zhang, M.S. Whittingham, Understanding and applying coulombic efficiency in lithium metal batteries, *Nat. Energy*. 5 (2020) 561–568. <https://doi.org/10.1038/s41560-020-0648-z>.
- [58] J. Su, X. Huang, Z. Song, T. Xiu, M.E. Badding, J. Jin, Z. Wen, Overcoming the abnormal grain growth in Ga-doped Li<sub>7</sub>La<sub>3</sub>Zr<sub>2</sub>O<sub>12</sub> to enhance the electrochemical stability against Li metal, *Ceram. Int.* 45 (2019) 14991–14996. <https://doi.org/10.1016/j.ceramint.2019.04.236>.

# CHAPTER 3

## Hydrated Alkali-B<sub>11</sub>H<sub>14</sub> Salts as Potential Solid-State Electrolytes

---

D. H. P. Souza, K.T. Møller, S.A. Moggach, T.D. Humphries, A.M. D'Angelo, C.E. Buckley, M. Paskevicius, Hydrated Alkali-B<sub>11</sub>H<sub>14</sub> Salts as Potential Solid-State Electrolytes, *J. Mater. Chem. A*. 9 (2021) 15027–15037. <https://doi.org/10.1039/d1ta01551f>.



## ABSTRACT

Metal boron-hydrogen compounds are considered as promising solid electrolyte candidates for the development of all-solid-state batteries (ASSB), owing to the high ionic conductivity exhibited by *closo*- and *nido*-boranes. In this study, an optimised low cost preparation method of  $MB_{11}H_{14} \cdot (H_2O)_n$ , ( $M = Li$  and  $Na$ ) and  $KB_{11}H_{14}$  is proposed and analysed. The formation of the  $B_{11}H_{14}^-$  salt is pH-dependent, and  $H_3O^+$  competes with small ionic radii cations, such as  $Li^+$  and  $Na^+$ , to produce a hydronium salt of  $B_{11}H_{14}^-$ , which forms  $B_{11}H_{13}OH^-$  upon heating. The use of diethyl ether to extract  $B_{11}H_{14}^-$  salt from the aqueous medium during synthesis is an important step to avoid hydrolysis of the compound upon drying. The proposed method of synthesis results in  $LiB_{11}H_{14}$  and  $NaB_{11}H_{14}$  coordinated with water, whereas  $KB_{11}H_{14}$  is anhydrous. Hydrated  $LiB_{11}H_{14} \cdot (H_2O)_n$  and  $NaB_{11}H_{14} \cdot (H_2O)_n$  exhibit exceptional ionic conductivities at 25 °C,  $1.8 \times 10^{-4} \text{ S cm}^{-1}$  and  $1.1 \times 10^{-3} \text{ S cm}^{-1}$ , respectively, which represent some of the highest solid-state  $Li^+$  and  $Na^+$  conductivities at room temperature. The salts also exhibit oxidative stability of 2.1 V vs.  $Li^+/Li$  and 2.6 V vs.  $Na^+/Na$ , respectively.  $KB_{11}H_{14}$  undergoes a reversible polymorphic structural transition to a metastable phase before decomposing. All synthesised *nido*-boranes decompose at temperatures greater than 200 °C.

## 3.1 INTRODUCTION

The use of natural resources, such as the sun, wind, or waves, is a clean and sustainable strategy to replace fossil fuels and to produce renewable energy. However, these sources of power are intermittent, which make them incapable of fulfilling the demands of base-load energy usage. One way to address this problem is to develop more efficient and low cost energy storage devices, such as batteries, to be coupled with renewable sources and allow continuous electricity supply [1–3].

The drawbacks of state-of-the-art lithium-ion batteries, such as the use of toxic and flammable liquid organic electrolytes, along with the risks of leakage, freezing, and vapourisation of the organic component, have led to extensive research on the development of all-solid-state-batteries (ASSBs), which are considered the next-generation electrochemical storage device [4–7]. Furthermore, the energy density of a battery cell can be increased with the use of solid electrolytes, as they are compatible with alternative electrode materials, e.g. lithium metal, which is considered the ultimate anode for ASSBs. Lithium has a low standard half-cell potential ( $-3.04 \text{ V}$  vs. standard hydrogen electrode) and a high theoretical capacity

(3860 mA g<sup>-1</sup>), thus the energy density of the battery can be increased significantly [8,9]. Another advantage that ASSBs bring is that they are easier to miniaturize, as the electrolyte is no longer a liquid [7].

The first challenge in building an ASSB is to develop a solid-state electrolyte with high ionic conductivity at room temperature ( $\geq 1 \times 10^{-3}$  S cm<sup>-1</sup>). The electrolyte must be an electrical insulator, inert, be compatible with the anode and cathode materials, and possess a wide electrochemical stability window capable of covering the working potential of the cell [7,10]. Many different classes of materials have been studied, including, but not limited to, polymers [11,12], metal oxides [13,14], sulfides [15–17], and metal boron-hydrogen compounds [18–21]. The latter have recently drawn attention from several research groups due to their ability to adopt a disordered crystallographic structure at elevated temperature that leads to superionic conductivity [22]. Additionally, complex metal hydrides are strong reducing agents and generally electrochemically stable against a metallic lithium or sodium anode. Sodium and potassium batteries are under strong consideration to replace lithium batteries due to the high abundance and lower cost of both metals [23,24]. To ensure a viable and affordable large-scale production of the battery, it is important to find an electrolyte with a low materials and synthesis cost.

*Nido*-boranes, boron-hydrogen anions with a nest like structure, can form impressive ionic conducting salts with Na<sup>+</sup> cations [21,25]. Pathways for producing the metal *nido*-boranes MB<sub>11</sub>H<sub>14</sub>, M = Li, Na, or K, free of ethereal solvent, have not been clearly elucidated. In previous research, NaB<sub>11</sub>H<sub>14</sub> was commercially obtained [21], and its ionic conductivity was considerably high at room temperature ( $\approx 1 \times 10^{-3}$  S cm<sup>-1</sup>). However, the NaB<sub>11</sub>H<sub>14</sub> was drastically different in terms of its structure and properties when supplied from two different batches from the same company [21]. Another study on the synthesis of NaB<sub>11</sub>H<sub>14</sub> lacks certain synthetic details on concentration of reactants and pH that are vital in preparing this material [25]. In addition, the ionic conductivity measurements for commercially supplied NaB<sub>11</sub>H<sub>14</sub> and for NaB<sub>11</sub>H<sub>14</sub> synthesised using decaborane are published, but not for the compound synthesised from diglyme, leading to concerns over its purity and yield [25]. This highlights how difficult it can be to achieve a reproducible and reliable synthesis of MB<sub>11</sub>H<sub>14</sub> (M = Li, Na, K). In previous research, there is also no clear evidence of the analysed borane salt being solvated by, e.g. water [21,25]. Herein, the synthesis of LiB<sub>11</sub>H<sub>14</sub>·(H<sub>2</sub>O)<sub>n</sub>, NaB<sub>11</sub>H<sub>14</sub>·(H<sub>2</sub>O)<sub>n</sub> and KB<sub>11</sub>H<sub>14</sub>, free of diglyme, through a facile, cheap, and safe synthetic route

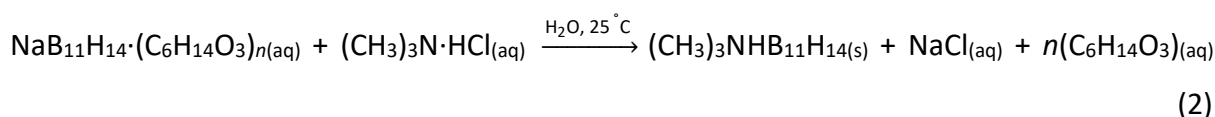
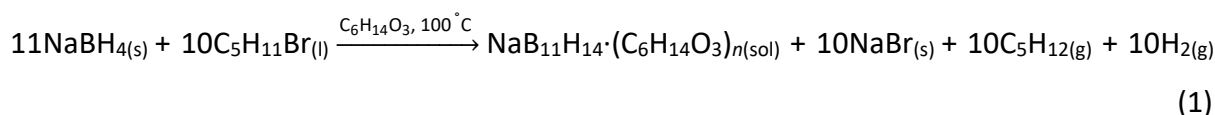
to be mass-produced is presented, alongside the electrochemical properties, the structural features, and the trends in thermal behaviour.

## 3.2 EXPERIMENTAL

### 3.2.1 Chemicals

Sodium borohydride (NaBH<sub>4</sub>, anhydrous, 98%), diglyme (C<sub>6</sub>H<sub>14</sub>O<sub>3</sub>, anhydrous, 99.5%), 1-bromopentane (C<sub>5</sub>H<sub>11</sub>Br, 98%), diethyl ether ((C<sub>2</sub>H<sub>5</sub>)<sub>2</sub>O, anhydrous, 99.7%), trimethylamine hydrochloride ((CH<sub>3</sub>)<sub>3</sub>N·HCl, 98%), potassium hydroxide (KOH, 90%), sulphuric acid (H<sub>2</sub>SO<sub>4</sub>, 95–98%), deuterated water (D<sub>2</sub>O, 99.9 atom % D), deuterated dimethyl sulfoxide (DMSO-*d*<sub>6</sub>, anhydrous, 99.9 atom % D), deuterated acetonitrile (CD<sub>3</sub>CN, 99.8 atom % D), lithium (Li ribbon, thickness 0.38 mm, 99.9%), sodium (Na lump in kerosene, 99%), and graphite powder were all purchased from Sigma-Aldrich. Lithium hydroxide (LiOH, anhydrous, 98%) and gold foil (Au, 99.95%, thickness 0.1 mm) were obtained from Alfa Aesar, sodium hydroxide (NaOH, 98.9%) from VWR Chemicals, and hydrochloric acid (HCl, 37%) from Scharlau. In order to maintain an inert atmosphere, all chemicals and samples were manipulated in an argon filled glovebox (Mbraun, O<sub>2</sub> & H<sub>2</sub>O < 1 ppm) or using Schlenk techniques.

### 3.2.2 Synthesis of trimethylammonium *nido*-tetradecahydroundecaborane, (CH<sub>3</sub>)<sub>3</sub>NHB<sub>11</sub>H<sub>14</sub>



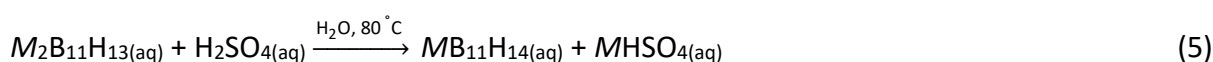
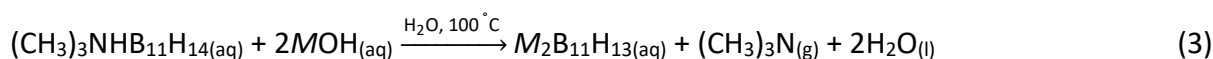
The syntheses of NaB<sub>11</sub>H<sub>14</sub>·(C<sub>6</sub>H<sub>14</sub>O<sub>3</sub>)<sub>n</sub> and (CH<sub>3</sub>)<sub>3</sub>NHB<sub>11</sub>H<sub>14</sub> (eq. 1 and 2) were performed based on methods previously reported by Dunks *et al.* [26] and Muetterties *et al.* [27] with adaptations. NaBH<sub>4</sub> (50 g, 1.32 mol) was weighed into a three-neck round-bottom flask equipped with a thermometer, a mechanical stirrer, and a pressure-equalising dropping funnel. Under stirring, and a constant stream of argon, the powder was suspended in diglyme (400 mL) and heated to 105 °C. 1-bromopentane (150 mL, 1.20 mol) was added drop-wise to ensure that the temperature was kept between 105 and 120 °C (exothermic reaction). After complete addition, the reaction mixture was stirred for six additional hours at 110 °C. The resulting suspension of yellow liquid and white powder (undissolved NaBr) was cooled to

room temperature, filtered, and washed with about 50 mL of diethyl ether. The filtrate was dried *in vacuo* at 110 °C until a gelatinous yellow substance (40.5 g) was obtained. This yellow substance was then completely dissolved in a minimum amount of hot water, and an aqueous solution of trimethylamine hydrochloride (31.5 g, 0.33 mol) was added in excess, resulting in the formation of a yellow-white precipitate. The suspension was transferred to an ice bath and left resting for 30 minutes, filtered, and washed with cold water. The light yellow powder was then dried *in vacuo* at 90 °C, yielding 9.0 g (0.047 mol, 39% yield) of trimethylammonium *nido*-tetradecahydrundecaborane ((CH<sub>3</sub>)<sub>3</sub>NHB<sub>11</sub>H<sub>14</sub>).

NaB<sub>11</sub>H<sub>14</sub>·(C<sub>6</sub>H<sub>14</sub>O<sub>3</sub>)<sub>n</sub>: <sup>1</sup>H NMR (D<sub>2</sub>O, 400 MHz): δ (ppm) 0.30 – 2.60 (m, 11H, B<sup>1-11</sup>H), 3.31 (s, 6H, OCH<sub>3</sub>), 3.55 (m, 4H, CH<sub>2</sub>) and 3.61 (m, 4H, CH<sub>2</sub>). <sup>11</sup>B{<sup>1</sup>H} NMR (D<sub>2</sub>O, 128 MHz): δ (ppm) –17.3 (B<sup>7-11</sup>H), –16.2 (B<sup>2-6</sup>H) and –15.2 (B<sup>1</sup>H). <sup>11</sup>B NMR (D<sub>2</sub>O, 128 MHz): δ (ppm) –17.3 (d, B<sup>7-11</sup>H, J = 145 Hz), –16.2 (d, B<sup>2-6</sup>H, J = 145 Hz) and –15.1 (d, B<sup>1</sup>H, J = 130 Hz).

(CH<sub>3</sub>)<sub>3</sub>NHB<sub>11</sub>H<sub>14</sub>: <sup>1</sup>H NMR (CD<sub>3</sub>CN, 400 MHz): δ (ppm) 0.50 – 2.40 (m, 11H, B<sup>1-11</sup>H), 2.73 (s, 9H, NCH<sub>3</sub>). <sup>11</sup>B{<sup>1</sup>H} NMR (CD<sub>3</sub>CN, 128 MHz): δ (ppm) –16.8 (B<sup>7-11</sup>H), –16.0 (B<sup>2-6</sup>H) and –14.2 (B<sup>1</sup>H). <sup>11</sup>B NMR (CD<sub>3</sub>CN, 128 MHz): δ (ppm) –16.9 (d, B<sup>7-11</sup>H, J = 120 Hz), –15.9 (d, B<sup>2-6</sup>H, J = 120 Hz) and –14.2 (d, B<sup>1</sup>H, J = 145 Hz).

### 3.2.3 Synthesis of alkali metal *nido*-tetradecahydrundecaborane, MB<sub>11</sub>H<sub>14</sub> (M = Li, Na, K)



The synthesis of MB<sub>11</sub>H<sub>14</sub> (M = Li, Na, K) was adapted from a methodology presented by Klanberg and Muettterties [28]. In this report, they demonstrate a procedure to obtain CsB<sub>11</sub>H<sub>14</sub> by initially synthesising Na<sub>2</sub>B<sub>11</sub>H<sub>13</sub> (eq. 3) and show that the reduction of the pH of the reaction medium to 4 – 5 with addition of H<sub>2</sub>SO<sub>4</sub> yields NaB<sub>11</sub>H<sub>14</sub> (eq. 5). However, they do not demonstrate how to isolate NaB<sub>11</sub>H<sub>14</sub>, neither how to prepare LiB<sub>11</sub>H<sub>14</sub> or KB<sub>11</sub>H<sub>14</sub>, which is presented here for the first time based on the following method.

Trimethylammonium *nido*-tetradecahydrundecaborane (1.5 g, 7.77 mmol for LiB<sub>11</sub>H<sub>14</sub> and NaB<sub>11</sub>H<sub>14</sub> and 0.5 g, 2.59 mmol for KB<sub>11</sub>H<sub>14</sub>) was dissolved in a 0.5 mol L<sup>-1</sup> aqueous solution of metal hydroxide (LiOH: 75 mL, NaOH: 75 mL, KOH: 30 mL) and heated to boiling (100 °C) for

≈ 20 minutes (eq. 3). The solution was cooled to room temperature, filtered, and the filtrate was heated to 80 °C. The pH of the solution was adjusted to 4 – 5 by slow addition of 1.0 mol L<sup>-1</sup> aqueous solution of inorganic acid (LiB<sub>11</sub>H<sub>14</sub> and NaB<sub>11</sub>H<sub>14</sub> were prepared with HCl, eq. 4, and KB<sub>11</sub>H<sub>14</sub> with H<sub>2</sub>SO<sub>4</sub>, eq. 5), and then washed with diethyl ether at room temperature. The organic layer, a yellowish liquid, was isolated from the aqueous solution, flushed with argon, and dried *in vacuo* at 80 °C, which resulted in the formation of a deliquescent white powder of alkali metal *nido*-tetradecahydroundecaborane (LiB<sub>11</sub>H<sub>14</sub>: 0.89 g, 6.36 mmol, 82% yield, NaB<sub>11</sub>H<sub>14</sub>: 0.68 g, 4.36 mmol, 56% yield, KB<sub>11</sub>H<sub>14</sub>: 0.30g, 1.74 mmol, 67% yield).

MB<sub>11</sub>H<sub>14</sub> (*M* = Li, Na and K): <sup>1</sup>H NMR (DMSO-*d*<sub>6</sub>, 400 MHz): δ (ppm) -0.30 – 2.50 (m, 11H, B<sup>1-11</sup>H). <sup>11</sup>B{<sup>1</sup>H} NMR (DMSO-*d*<sub>6</sub>, 128 MHz): δ (ppm) -16.8 (B<sup>7-11</sup>H), -16.0 (B<sup>2-6</sup>H) and -14.2 (B<sup>1</sup>H). <sup>11</sup>B NMR (DMSO-*d*<sub>6</sub>, 128 MHz): δ (ppm) -16.9 (d, B<sup>7-11</sup>H, *J* = 125 Hz), -15.9 (d, B<sup>2-6</sup>H, *J* = 125 Hz) and -14.2 (d, B<sup>1</sup>H, *J* = 135 Hz).

### 3.2.4 Characterisation

#### 3.2.4.1 Nuclear Magnetic Resonance

Nuclear Magnetic Resonance (NMR) spectra were collected on a Bruker Avance III 400 MHz NanoBay spectrometer (<sup>1</sup>H: 400 MHz, <sup>11</sup>B: 128 MHz, <sup>11</sup>B{<sup>1</sup>H}: 128 MHz) at room temperature. The powdered samples were dissolved in 600 μL of deuterated solvent (D<sub>2</sub>O, DMSO-*d*<sub>6</sub> or CD<sub>3</sub>CN) prior to analysis. The <sup>11</sup>B spectra were referenced to a boron trifluoride etherate (BF<sub>3</sub>O(C<sub>2</sub>H<sub>5</sub>)<sub>2</sub>) external standard, and the <sup>1</sup>H spectra were referenced to a tetramethylsilane (Si(CH<sub>3</sub>)<sub>4</sub>) external standard.

#### 3.2.4.2 Fourier Transformed Infrared Spectroscopy

Fourier Transformed Infrared Spectroscopy (FTIR) was conducted on a Thermoscientific Summit ATR spectrometer. Data was measured between 500 – 4000 cm<sup>-1</sup> with a spectral resolution of 4 cm<sup>-1</sup>. A total of 16 scans were collected and averaged per sample. The samples had to be briefly exposed to air (< 10 s) upon mounting.

#### 3.2.4.3 Thermogravimetry and Differential Scanning Calorimetry

Simultaneous Thermogravimetry (TGA) and Differential Scanning Calorimetry (DSC) measurements were performed with a Netzsch (STA 449 F3 Jupiter) under an argon flow of 40 mL min<sup>-1</sup> using Al crucibles containing approximately 7 mg of sample in a Pt furnace. The

crucible lids were pierced  $\approx 10$  seconds before being placed in the instrument. The analysis was conducted by heating from 40 – 300 °C at 10 °C min<sup>-1</sup>. KB<sub>11</sub>H<sub>14</sub> was also analysed under heating and cooling (40 – 170 – 40 °C) at 10 °C min<sup>-1</sup>. The furnace containing the sample was evacuated prior to being placed under an argon flow.

#### **3.2.4.4 Thermal Decomposition Analysis by Mass Spectrometry (TDA-MS)**

Thermal decomposition data was obtained by Mass Spectrometry (MS) analysis of the evolved gas using a Stanford Research Systems (SRS) residual gas analyser (RGA-300) equipped with a quadrupole mass spectrometer. The samples ( $\approx 5$  mg) were placed inside a stainless steel reactor under an argon atmosphere, sealed, and heated from 25 to 300 °C (2 °C min<sup>-1</sup>) under high vacuum ( $< 8 \times 10^{-4}$  mbar). Temperature was controlled with a tube furnace and monitored by a K-type thermocouple  $\approx 5$  mm from the sample.

#### **3.2.4.5 X-Ray Powder Diffraction**

Crystallographic phase analysis was performed at room temperature with X-Ray Powder Diffraction (XRPD) measurements by employing a Bruker D8 Advance Powder Diffractometer with a Cu K $\alpha$  radiation source ( $\lambda = 1.54056$  Å) run at 40 kV/40mA with a LynxEye detector in the  $2\theta$  range of 5 – 60°. The powder was mounted inside an argon glovebox on a single-crystal Si low background sample holder and sealed with an airtight poly(methyl-methacrylate) (PMMA) dome.

Additionally, XRPD data of the NaB<sub>11</sub>H<sub>14</sub>·(H<sub>2</sub>O)<sub>n</sub> sample were collected on a ThermoFisher ARL Equinox 5000 diffractometer using a Mo source (Mo K $\alpha$  radiation,  $\lambda = 0.7093$  Å) at room temperature and at -100 °C. The powdered sample was mounted inside an argon glovebox and sealed within a borosilicate capillary (OD 0.7 mm). The sample was cooled under a constant stream of liquid nitrogen, and the temperature was monitored by a K-type thermocouple  $\approx 10$  mm from the capillary. Data were acquired using a curved position sensitive X-ray detector (CPS 120) with acquisition in real time over 120°  $2\theta$ .

#### **3.2.4.6 Synchrotron X-Ray Powder Diffraction**

Synchrotron XRPD data were collected at the powder diffraction beamline at the Australian Synchrotron using a wavelength of  $\lambda = 0.563476(5)$  Å, which was refined using a NIST LaB<sub>6</sub>



660b line position standard.  $\text{KB}_{11}\text{H}_{14}$  powder was loaded into 0.7 mm borosilicate capillary and sealed with a flame. Data were collected on a Mythen II microstrip detector at two positions, and later combined into gap-free data sets, from  $1^\circ - 76^\circ 2\theta$ . A data set was collected at both  $20^\circ\text{C}$  and  $177^\circ\text{C}$  after collecting data for 240 s and 460 s, respectively. Additionally, *in-situ* XRPD data were collected during heating and cooling, where the sample was heated from  $20^\circ\text{C}$  to  $177^\circ\text{C}$  at  $5^\circ\text{C}/\text{min}$  and then cooled at  $6^\circ\text{C}/\text{min}$  to room temperature. Temperature was controlled using an Oxford Cryosystems Cryostream Plus. Crystallographic indexing and structure solution were performed using Bruker *TOPAS*. The room temperature  $\text{KB}_{11}\text{H}_{14}$  structure was solved using simulated annealing, treating the  $\text{B}_{11}\text{H}_{14}^-$  units as rigid bodies. The structure was then refined with the Rietveld method. A minor impurity of  $\text{K}_2\text{SO}_4$  was also modelled during structure solution. The background was defined using an 11<sup>th</sup> order Chebyshev polynomial. Unit cell parameters, scale factors, zero-point, peak shape mixing parameters and occupancies of K and B atoms were refined together. Isotropic displacement parameters,  $B_{\text{iso}}$ , were refined as a single parameter for the K and B atoms, while those for H were not refined. The supplementary crystallographic data has been deposited into the Inorganic Crystal Structure Database (CSD 2090015).

### **3.2.4.7 Single-Crystal X-Ray Crystallography**

A single crystal of  $\text{LiB}_{11}\text{H}_{14}\cdot 2\text{H}_2\text{O}$  was grown by allowing an aliquot of the diethyl ether layer (obtained during synthesis after performing the liquid-liquid extraction step) to dry naturally at room temperature inside an argon filled glovebox. The crystal was mounted inside a glovebox, where it was transferred to a borosilicate capillary and sealed. The capillary containing the clear light colourless block-shaped crystal with dimensions  $0.24 \times 0.18 \times 0.14 \text{ mm}^3$  was then mounted onto a XtaLAB Synergy-S diffractometer, with data collected at  $294.9(3) \text{ K}$ . Data were measured using  $\omega$ -scans using  $\text{Cu K}\alpha$  radiation. The diffraction pattern was indexed and the total number of runs and images was based on the strategy calculation from the program CrysAlisPro (Rigaku, V1.171.40.53, 2019). The maximum resolution that was achieved was  $\theta = 67.894^\circ$  ( $0.83 \text{ \AA}$ ). The unit cell was refined using CrysAlisPro (Rigaku, V1.171.40.53, 2019) on 3182 reflections.

Data reduction, scaling, and absorption corrections were performed using CrysAlisPro (Rigaku, V1.171.40.53, 2019). The final completeness was 66.30 %, which was low, as the sample became dislodged inside the capillary during data collection and could not be

recovered. Numerous ( $\approx 22$ ) other ‘single-crystal’ samples were screened, however all were highly polycrystalline, making structure solution impossible. A multi-scan absorption correction was performed using CrysAlisPro 1.171.40.53 (Rigaku Oxford Diffraction, 2019). The absorption coefficient  $\mu$  of this material is  $0.388 \text{ mm}^{-1}$  at this wavelength ( $\lambda = 1.54184 \text{ \AA}$ ) and the minimum and maximum transmissions are 0.154 and 1.000.

The structure was solved and the space group  $C2/c$  (# 15) determined by the ShelXT [29,30] structure solution program using dual methods and refined by full matrix least squares minimisation on  $F^2$  using version 2018/3 of ShelXL [29–31]. All non-hydrogen atoms were refined anisotropically. Hydrogen atom positions on the water ligands, and on the  $B_{11}H_{14}^-$  cage were found in a difference map, then refined freely with 1,2 and 1,3-restraints used to optimize their geometry. The supplementary crystallographic data has been deposited into the Inorganic Crystal Structure Database (CSD 2031335).

#### **3.2.4.8 Electrochemical Evaluation**

Electrochemical Impedance Spectroscopy (EIS) was performed on pellets using a ZIVE SP1 electrochemical workstation. The powdered samples were pressed into pellets (6 mm diameter,  $\approx 1$  mm thickness) under an argon atmosphere at 200 MPa, sandwiched between gold foil (0.1 mm thickness), and sealed within an air tight ‘Swagelok-type’ Teflon cell with 316 stainless steel electrodes. Temperature was monitored by a K-type thermocouple  $\approx 5$  mm from the pellet and controlled with a tube furnace from room temperature to  $100 \text{ }^\circ\text{C}$ , for  $\text{LiB}_{11}\text{H}_{14}\cdot(\text{H}_2\text{O})_n$  and  $\text{NaB}_{11}\text{H}_{14}\cdot(\text{H}_2\text{O})_n$ , and to  $160 \text{ }^\circ\text{C}$  for  $\text{KB}_{11}\text{H}_{14}$  samples. The cells of  $\text{LiB}_{11}\text{H}_{14}\cdot(\text{H}_2\text{O})_n$  and  $\text{NaB}_{11}\text{H}_{14}\cdot(\text{H}_2\text{O})_n$  were also cooled down to  $0 \text{ }^\circ\text{C}$  using an ice bath,  $-20 \text{ }^\circ\text{C}$  using a bath of ice and sodium chloride, as well as both  $-30 \text{ }^\circ\text{C}$  and  $-40 \text{ }^\circ\text{C}$  using a bath of dry ice and acetonitrile. EIS was conducted at 100 mV AC from 100 Hz to 1 MHz after 30 minutes of thermal equilibrium at each temperature. Ion conductivity data ( $\sigma$ ) were derived from Nyquist impedance plots as:

$$\sigma = \frac{d}{l \times A} \quad (1)$$

where  $\sigma$  is the conductivity value in  $\text{S cm}^{-1}$ ,  $d$  is the pellet thickness in cm,  $A$  is the area of the pellet face in  $\text{cm}^2$  and  $l$  is the x-intercept of the Nyquist blocking tail. This tail accounts for the diffusion of ions in the electrolyte [1]. The uncertainty on each ion conductivity data point ( $\pm 10 \%$ ) is based on the x-intercept of the Nyquist plot and has little impact on the logarithmic-

scale, where ion conductivities span many orders of magnitude. Ionic conductivity measurements of all samples were also performed after ball-milling them individually. Each powder was ball-milled inside an Across International Planetary Ball Mill (PQ-N04) with a ball-to-powder mass ratio of 10:1 employing stainless steel vials and balls (6 mm in diameter) under an argon atmosphere for 12 hour at a speed of 400 rpm.

Linear sweep voltammetry (LSV) was performed to investigate the oxidative stability of  $\text{LiB}_{11}\text{H}_{14}\cdot(\text{H}_2\text{O})_n$ ,  $\text{NaB}_{11}\text{H}_{14}\cdot(\text{H}_2\text{O})_n$  and  $\text{LiBH}_4$  based on a method proposed by Han *et al.* [17] and Asakura *et al.* [32]  $\text{LiBH}_4$  was used as a control sample to compare the results with previously published papers [10,32]. The material to be tested was mixed with graphite, previously heated to 550 °C under vacuum for 12 h, in a weight ratio of 75:25 by grinding 5 times with a mortar and pestle. Graphite is added in order to improve the contact area between electrolyte and current collector, to enhance the decomposition kinetics by increasing the electronic conductivity of the solid electrolyte, and to simulate a bulk-type all-solid-state-battery, where the electrode is formed by a mixture of carbon, solid electrolyte and active material [17,32]. 3 mg of the mixture was layered on top of 40 mg of the pristine material, which were pressed together at 200 MPa under argon to form a two layered pellet. This pellet was sandwiched to form a Al/Pt/sample+C/sample/(Li or Na) configuration, which was sealed within an air tight 'Swagelok-type' Teflon cell. LSV was conducted at 60 °C with a scan rate of 50  $\mu\text{V s}^{-1}$  from 1.5 V to 8.0 V for the *nido*-boranes, and from 1.5 to 4.5 V for  $\text{LiBH}_4$ . A second LSV cycle was also applied for the *nido*-boranes from 1.5 to 4.5 V at the same scan rate and temperature. The oxidative stability of the material was determined from the intersection point of two linear lines with  $R^2 > 0.99$  (the background and the oxidative current) [32].

#### **3.2.4.9 Temperature Programmed Photographic Analysis (TPPA)**

A pellet of  $\text{KB}_{11}\text{H}_{14}$  ( $\approx 50$  mg) on top of a gold foil was pressed at 200 MPa, transferred to a glass tube under an argon atmosphere and placed in a custom-made brass heating block. The sample was heated from RT to 170 °C ( $\Delta T/\Delta t = 10$  °C/min) while photos of the sample were collected every five seconds [33].

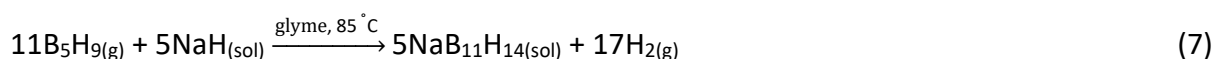
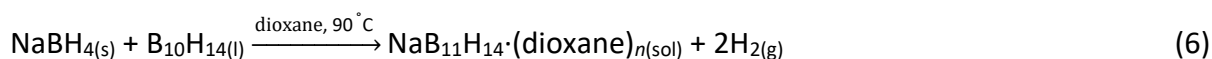
### 3.2.4.10 Theoretical Calculations

All geometry optimisations and vibrational frequency calculations were carried out using Gaussian 09 [34]. All methods were used as implemented. The geometry optimisation and vibrational frequency calculations were fully optimised on a B31LYP/aug-cc-pvdz level of theory (Tables A.1-A.4) [35]. Molecules were drawn and evaluated using Diamond v3.2 and rendered using POV-Ray (Fig. A.1). Charges were calculated via the Natural Bond Orbital (NBO) analyses (Table A.5) [36]. NMR single-point calculations were carried out using the gauge-including atomic orbital (GIAO)-based approach [37] in acetonitrile using the conductor like polarisable continuum model (CPCM) as the solvation model (Tables A.6-A.7) [38]. It has been shown that the inclusion of the implicit solvent model in the NMR calculation step is crucial to improve the prediction accuracy of calculated chemical shifts [39]. All  $^{11}\text{B}$  chemical shifts are relative to the computed shielding of  $\text{BF}_3\text{O}(\text{C}_2\text{H}_5)_2$  as the reference compound with an additional correction of +1.83 [40].

## 3.3 RESULTS AND DISCUSSION

### 3.3.1 Sample preparation and characterisation

The synthesis of  $\text{NaB}_{11}\text{H}_{14}$  can be accomplished by different synthetic routes, as demonstrated by known reactions 6 and 7 [41,42]:



The use of decaborane ( $\text{B}_{10}\text{H}_{14}$ ) and pentaborane ( $\text{B}_5\text{H}_9$ ) in chemical reactions is preferably avoided since they are highly toxic and potentially explosive. Moreover, they are expensive reactants, which make their use for the synthesis of  $\text{NaB}_{11}\text{H}_{14}$  impractical in scale-up production. Hence, the reaction of 1-bromopentane with sodium borohydride in diglyme (eq. 1), first demonstrated by Dunks *et al.* [26], becomes the safest and cheapest synthetic pathway for  $\text{B}_{11}\text{H}_{14}^-$  salts. Here, a reaction mechanism is hypothesised in equations 8 – 11 and explained as follows [26,43,44]. The reduction of the alkyl halide by  $\text{BH}_4^-$  in diglyme produces diborane ( $\text{B}_2\text{H}_6$ ), a highly reactive gas (eq. 8). Further reaction of this compound with the  $\text{BH}_4^-$  induces the formation of  $\text{B}_3\text{H}_8^-$ , a product of the thermal decomposition of  $\text{B}_2\text{H}_7^-$  (eqs. 9 and 10). High yields of  $\text{B}_3\text{H}_8^-$  are achieved when the reaction occurs at  $\approx 100^\circ\text{C}$  in an ethereal

solvent, such as diglyme.  $B_3H_8^-$  reacts with excess diborane and produces  $NaB_{11}H_{14}$  in a dehydrocondensation step (eq. 11) [26,43,44]. The overall reaction of this synthetic route is shown in equation 1.



The main drawback of the dehydrocondensation reaction (eq. 1) is the formation of  $NaB_{11}H_{14}$  strongly coordinated with diglyme, and the presence of this coordinated solvent changes its properties as an ionic conductor (see section on ‘Solid-State Ionic Conductivity’). One step that can be undertaken to remove diglyme from the salt is to substitute the sodium for a large monovalent cation, such as trimethylammonium, which yields a product that is water-insoluble, non-coordinating towards diglyme, and easily isolated (eq. 2) [27].  $^{11}B$  NMR, FTIR, and XRPD data for  $(CH_3)_3NHB_{11}H_{14}$  are summarised in Figs. 3.1 and 3.2.

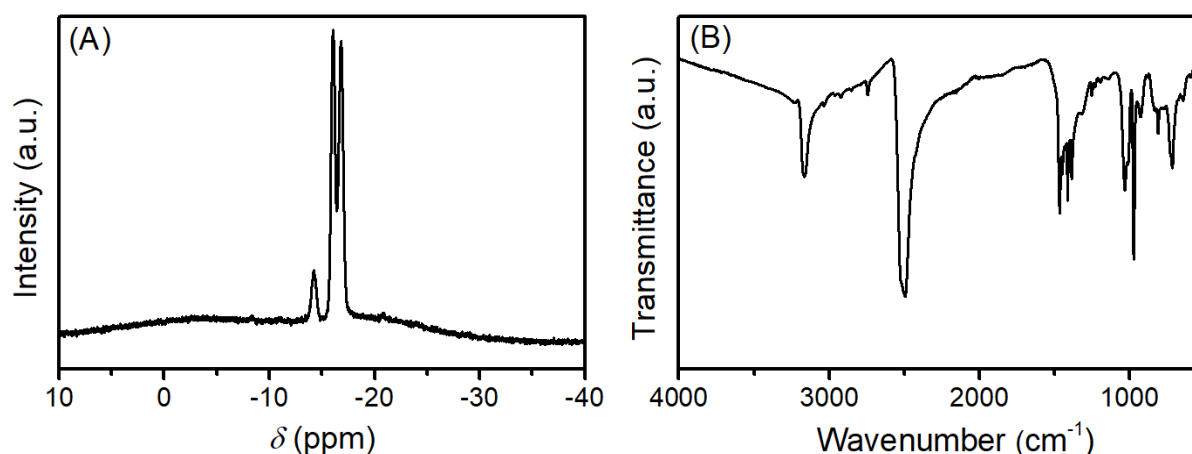


**Figure 3.1** Spectroscopic characterisation of  $(CH_3)_3NHB_{11}H_{14}$ . (A)  $^{11}B\{^1H\}$  NMR spectrum (128 MHz) in  $CD_3CN$ .  $\delta$  ( $B_{11}H_{14}^-$ ) = -14.2, -16.0 and -16.8 ppm (B) FTIR spectrum with stretching modes at 3165 ( $^+N-H$ ), 2495 (B-H), and 970  $cm^{-1}$  (C- $N^+$ ), and bending modes at 1466 ( $CH_3$ ), 1448 ( $CH_3$ ), 1385 ( $CH_3$ ), 1413 ( $^+N-H$ ) and 1032  $cm^{-1}$  (B-H) [45].

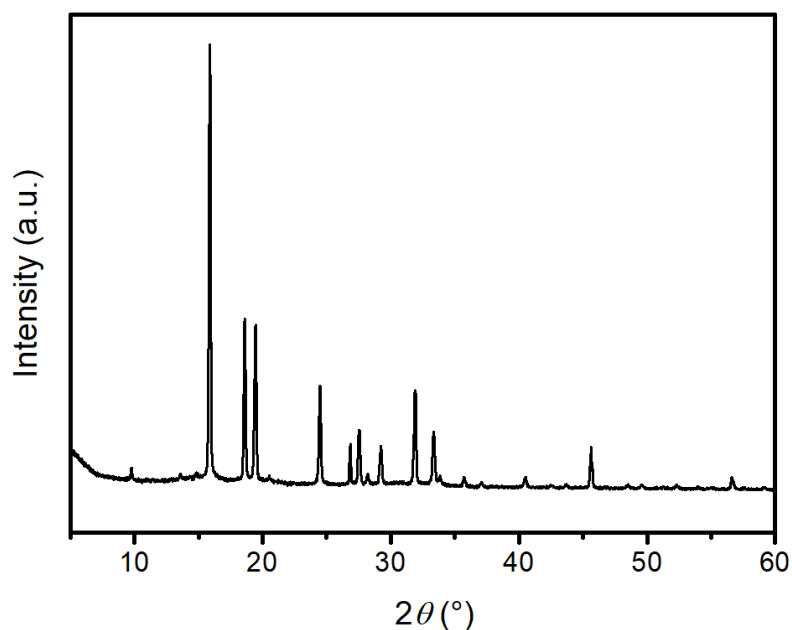


**Figure 3.2** XRPD pattern ( $\lambda_{\text{CuK}\alpha} = 1.54056 \text{ \AA}$ ) for  $(\text{CH}_3)_3\text{NHB}_{11}\text{H}_{14}$  at room temperature.

The reaction of  $(\text{CH}_3)_3\text{NHB}_{11}\text{H}_{14}$  with a strong alkaline solution (pH 10 and above) of lithium hydroxide, sodium hydroxide, or potassium hydroxide, results in the deprotonation of  $\text{B}_{11}\text{H}_{14}^-$  with consequent formation of  $\text{B}_{11}\text{H}_{13}^{2-}$  (Fig. 3.3).

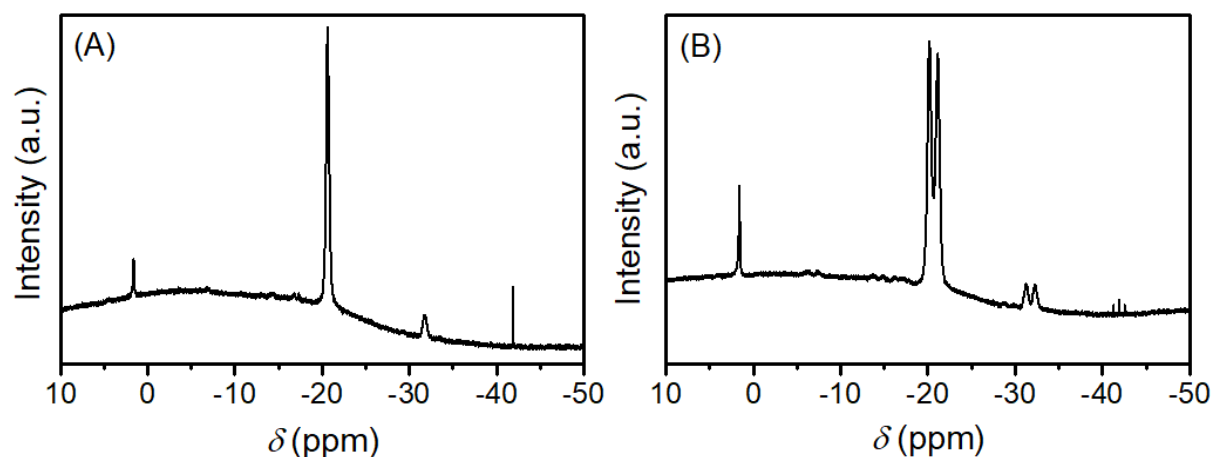


**Figure 3.3** (A)  $^{11}\text{B}\{^1\text{H}\}$  and (B)  $^{11}\text{B}$  NMR spectra ( $\text{D}_2\text{O}$ , 128 MHz) of aqueous solution resulting from the reaction of  $(\text{CH}_3)_3\text{NHB}_{11}\text{H}_{14}$  with  $\text{LiOH}$  after heating.  $\text{B}_{11}\text{H}_{13}^{2-}$  is represented by the signals at  $-20.6$  and  $-31.7$  ppm [46]. Additional resonances are also observed from  $\text{B}(\text{OH})_4^-$  at  $1.62$  ppm [47] and  $\text{BH}_4^-$  at  $-41.9$  ppm [48], which are expected to be formed in boron based aqueous solutions with high pH.

The reaction is conducted at  $100 \text{ }^\circ\text{C}$  in an open vessel to ensure that  $(\text{CH}_3)_3\text{NH}^+$  is eliminated from the reaction mixture as trimethylamine,  $(\text{CH}_3)_3\text{N}$  (boiling point  $2.9 \text{ }^\circ\text{C}$  at 1 atm) [28].

When the alkaline solution of  $B_{11}H_{13}^{2-}$  is treated with an aqueous solution of an inorganic acid, such as  $H_2SO_4$  or  $HCl$ ,  $B_{11}H_{13}^{2-}$  is progressively converted back to  $B_{11}H_{14}^-$  and a side-product of boric acid ( $B(OH)_3$ ). The resonances of  $B_{11}H_{13}^{2-}$  in the  $^{11}B$  NMR spectrum of the aqueous medium are no longer observed after reducing the pH of the reaction below 5.0 (Fig. 3.4).

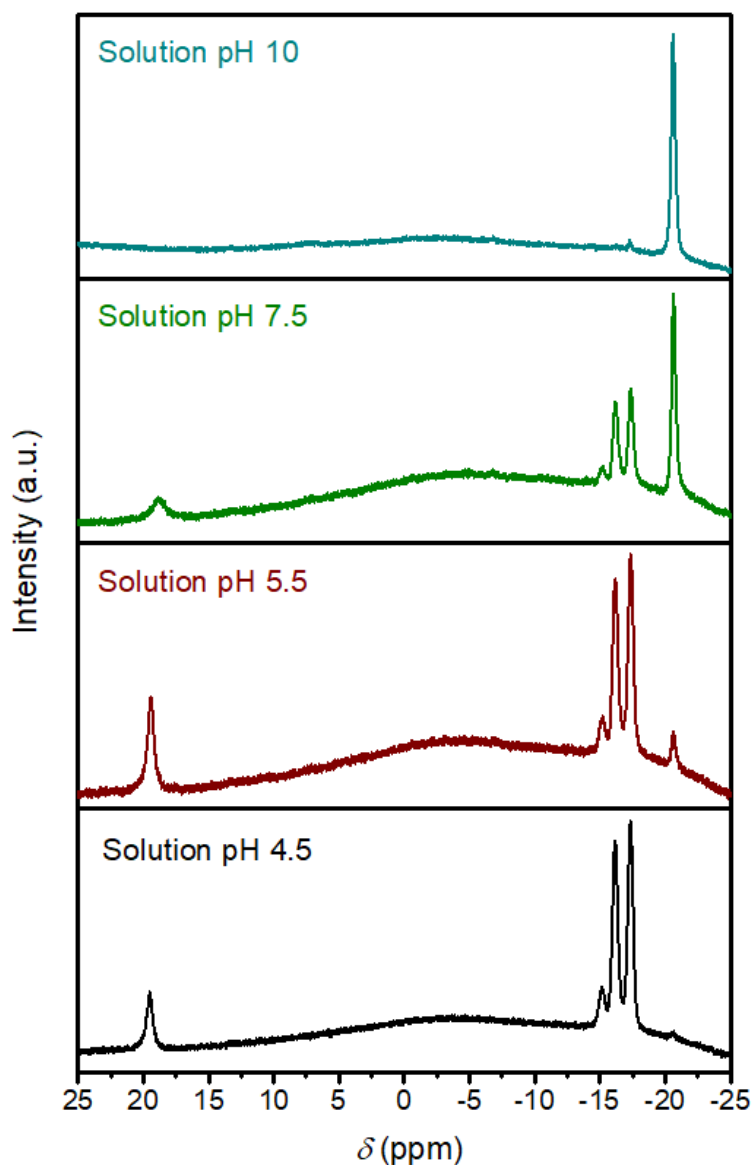


**Figure 3.4**  $^{11}B$   $\{^1H\}$  NMR spectrum (128 MHz) in  $D_2O$  of aqueous solution of  $Li_2B_{11}H_{13}$  after reducing its pH with addition of  $1 \text{ mol L}^{-1}$   $HCl$  solution to 10 (blue spectrum), 7.5 (green spectrum), 5.5 (red spectrum) and 4.5 (black spectrum).

In order to isolate  $B_{11}H_{14}^-$  from the reaction mixture that contains  $B(OH)_3$ , a liquid-liquid extraction of the aqueous solution at pH 4.5 was conducted with diethyl ether. The strong affinity of boric acid with water results in the majority of this compound remaining within the

water layer, whereas diethyl ether extracts the majority of the *nido*-tetradecahydroundecaborane salt. An aliquot of the organic layer extracted from the aqueous solution containing  $\text{LiB}_{11}\text{H}_{14}$  and  $\text{B}(\text{OH})_3$  was dissolved in  $\text{DMSO-}d_6$  and analysed using  $^{11}\text{B}$  NMR spectroscopy (Fig. 3.5).

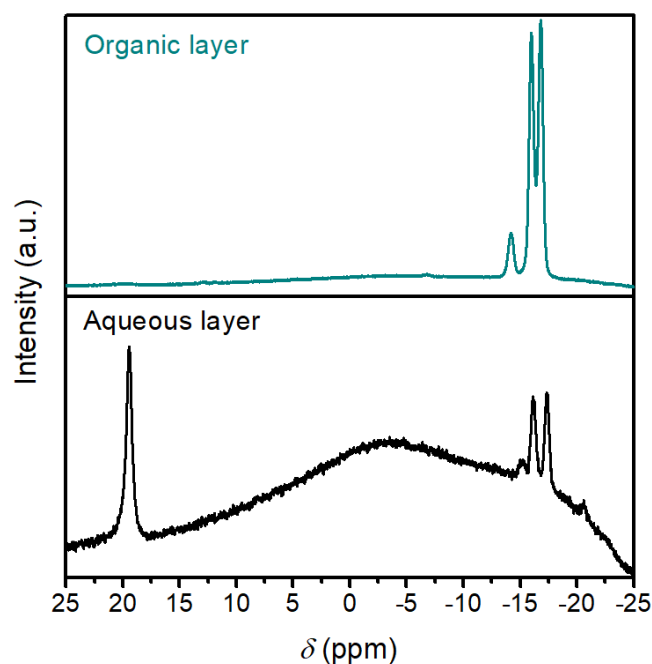


**Figure 3.5**  $^{11}\text{B}\{^1\text{H}\}$  NMR spectrum (128 MHz) of diethyl ether layer (top) in  $\text{DMSO-}d_6$  after conducting a liquid-liquid extraction of the aqueous solution at pH 4.5, and  $^{11}\text{B}\{^1\text{H}\}$  NMR spectrum (128 MHz) of the aqueous layer in  $\text{D}_2\text{O}$  after performing the extraction (bottom). The resonances at  $\delta = -14.2$ ,  $-16.0$  and  $-16.8$  ppm in the top  $^{11}\text{B}\{^1\text{H}\}$  NMR spectrum represent  $\text{B}_{11}\text{H}_{14}^-$ . Boric acid is observed at  $\delta = 19.4$  ppm in the aqueous layer (bottom spectrum), and the small triplet represent remaining  $\text{B}_{11}\text{H}_{14}^-$  that was not extracted by diethyl ether.

No resonance at 19.4 ppm from  $\text{B}(\text{OH})_3$  can be observed from the ethereal layer, which indicates that diethyl ether can be used as an extraction solvent for *nido*-undecaborane salt. Besides that,  $\text{B}_{11}\text{H}_{14}^-$  cage undergoes hydrolysis when dried in aqueous solution, therefore the extraction of the salt with diethyl ether is fundamental to avoid such event. The organic layer was then isolated from the aqueous solution and purged with argon in order to eliminate any oxygen and avoid the formation of any oxidation product of  $\text{B}_{11}\text{H}_{14}^-$ . The solution was dried *in vacuo* at 80 °C, and for all the cations used, a white deliquescent powder was obtained, which was stored under argon. An analysis on the  $^{11}\text{B}$  NMR spectrum of each compound after



drying (Fig. 3.6) shows the presence of  $B_{11}H_{14}^-$  represented by the resonances at  $\delta = -14.2$ ,  $-16.0$  and  $-16.8$  ppm.

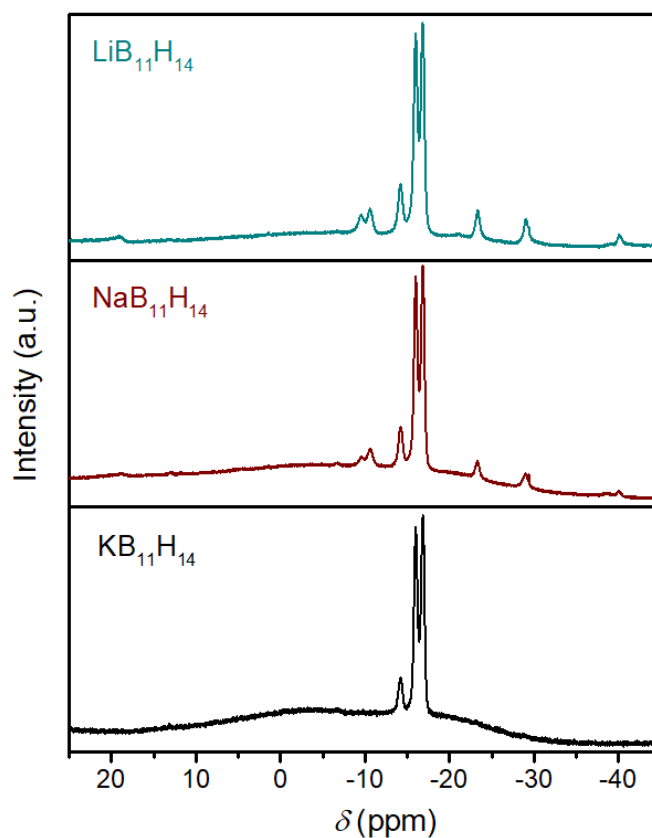


**Figure 3.6**  $^{11}B\{^1H\}$  NMR spectra (128 MHz) of  $LiB_{11}H_{14}$ ,  $NaB_{11}H_{14}$ , and  $KB_{11}H_{14}$  in  $DMSO-d_6$  (top to bottom), which show the presence of  $B_{11}H_{14}^-$  anion in all spectra, observed at  $\delta = -14.2$ ,  $-16.0$  and  $-16.8$  ppm. The resonances at  $\delta = 18.8$ ,  $-9.6$ ,  $-10.7$ ,  $-23.3$ ,  $-29.1$ , and  $-40.0$  ppm observed in the spectra of  $LiB_{11}H_{14}$  and  $NaB_{11}H_{14}$  represent  $B_{11}H_{13}OH^-$ , which is formed as a by-product in the reaction.

Additional resonances are also observed in the spectra of  $LiB_{11}H_{14}$  and  $NaB_{11}H_{14}$  ( $\delta = 18.8$ ,  $-9.6$ ,  $-10.7$ ,  $-23.3$ ,  $-29.1$ , and  $-40.0$  ppm) that represent the chemical shifts (observed and calculated, Table S10) of the hydroxo-*nido*-undecaborate  $B_{11}H_{13}OH^-$  [49], which is formed as a side product. During synthesis, in which the aqueous solution is acidified in order to convert  $B_{11}H_{13}^{2-}$  into  $B_{11}H_{14}^-$ , hydronium salts of  $B_{11}H_{14}^-$  may also be formed, which decompose into  $B_{11}H_{13}OH^-$  during evaporation of the organic layer and drying of the powder. Similar reactions have previously been observed for hydronium salts of  $B_{12}H_{12}^{2-}$  with hydrogen evolution and consequent formation of  $B_{12}H_{11}OH^{2-}$ , upon decreasing the water content or heating [27]. As  $Li^+$  and  $Na^+$  are small cations, they may compete with  $H_3O^+$  for the formation of salts of  $B_{11}H_{14}^-$ ,

whereas large monovalent cations, such as  $K^+$ ,  $(CH_3)_3NH^+$ , and  $Cs^+$  [28], yield stable salts of  $B_{11}H_{14}^-$ , not allowing formation of the hydronium salt nor  $B_{11}H_{13}OH^-$ . Furthermore, the estimated ionic radius of  $1.00 \text{ \AA}$  for  $H_3O^+$  is similar to six-coordinate  $Na^+$  ( $1.07 \text{ \AA}$ ) and even greater than the six-coordinate  $Li^+$  radius ( $0.79 \text{ \AA}$ ) [50,51], which explains the formation of acids of  $B_{11}H_{14}^-$  when small cations are used for the synthesis. The additional resonances are also observed in the  $^{11}B$  NMR data of commercial  $NaB_{11}H_{14}$  [25], however, they have previously been unidentified.

A more pure  $B_{11}H_{14}^-$  compound of  $Li^+$  or  $Na^+$  can also be obtained if the liquid-liquid extraction step is applied for the aqueous solution at pH 7.5 (rather than 4.5), and dried under the same conditions ( $80 \text{ }^\circ\text{C}$ ), as less hydronium ions are available in the medium. However, at neutral pH,  $B_{11}H_{13}^{2-}$  remains present, which reduces the yield of the synthesis. This can only be accomplished since diethyl ether does not extract  $B_{11}H_{13}^{2-}$  from the medium. Fig. 3.7 shows the  $^{11}B\{^1H\}$  NMR spectra of  $LiB_{11}H_{14}$  obtained after organic layer extractions at pH 4.5 and 7.5.

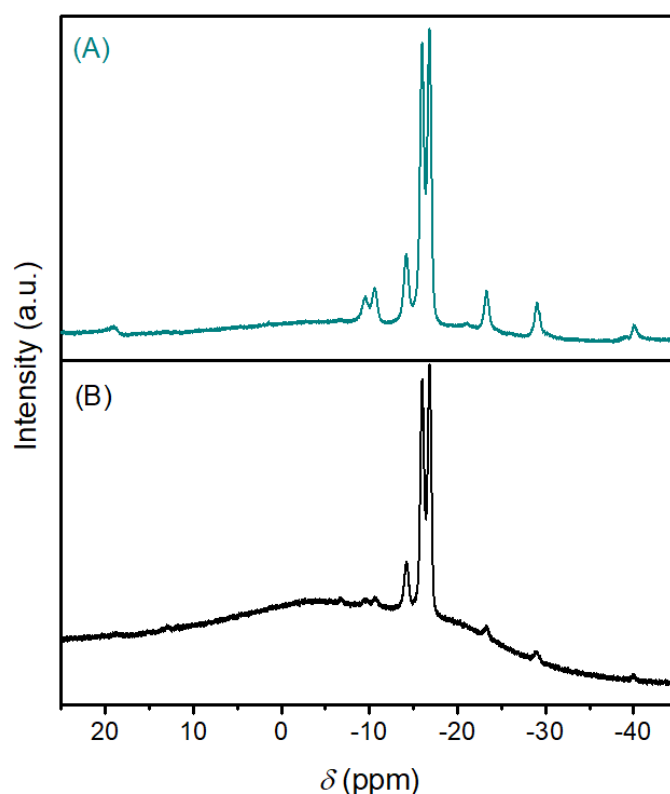


**Figure 3.7**  $^{11}B\{^1H\}$  NMR spectra (128 MHz) in  $DMSO-d_6$  of  $LiB_{11}H_{14}$  obtained after drying the organic layer that was extracted from aqueous solution at (A) pH 4.5 and (B) pH 7.5 at  $80 \text{ }^\circ\text{C}$ . The amount of  $B_{11}H_{13}OH^-$  is approximately 12 mol% in (A) and 4 mol% in (B) based on integration of the NMR peaks.

Integration of the NMR resonances shows that the sample obtained from low pH has approximately 12 mol% of  $B_{11}H_{13}OH^-$ , whereas the sample that was obtained from neutral pH contains approximately 4 mol% of  $B_{11}H_{13}OH^-$ . FTIR spectroscopy (Fig. 3.8) in conjunction with DFT calculated vibrational spectroscopy data (Fig. 3.9) confirms the presence of B–H bonds through the stretching mode at  $2500\text{ cm}^{-1}$  [52,53].

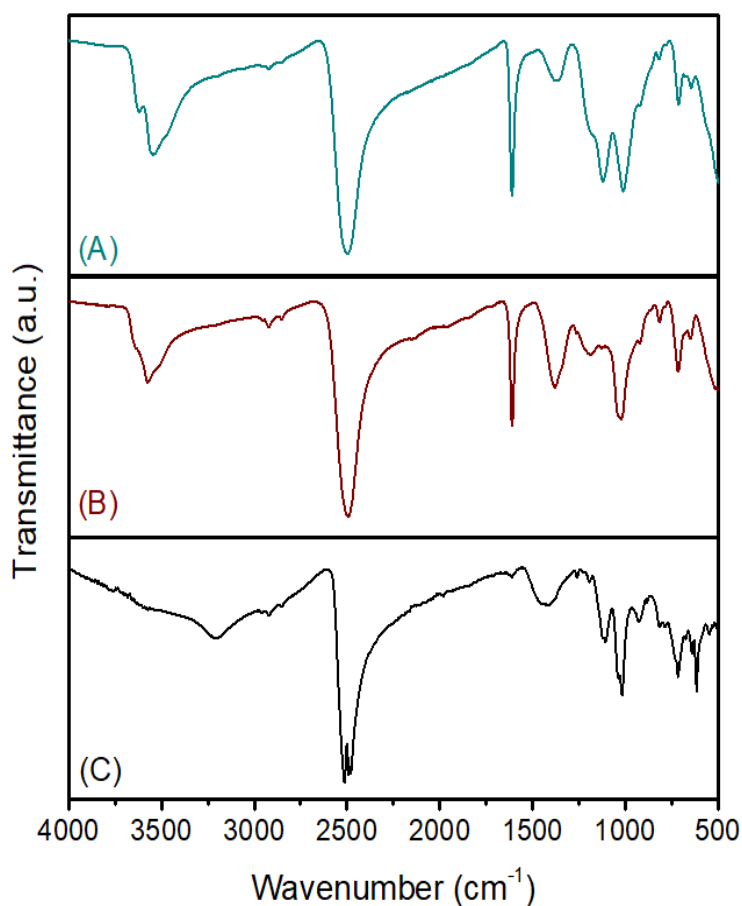


**Figure 3.8** FTIR transmittance spectra of solid-state (A)  $LiB_{11}H_{14} \cdot (H_2O)_n$ , (B)  $NaB_{11}H_{14} \cdot (H_2O)_n$ , and (C)  $KB_{11}H_{14}$ . The wide band observed at  $3200 - 3800\text{ cm}^{-1}$  (O–H stretching) and the sharp band at  $1610\text{ cm}^{-1}$  (H–O–H bending) in (A) and (B) confirm the presence of water in the compounds [54]. The B–H stretching frequency is identified as a sharp peak at  $\approx 2500\text{ cm}^{-1}$  and the B–H bending mode is observed at  $\approx 1020\text{ cm}^{-1}$  for all the samples [53].

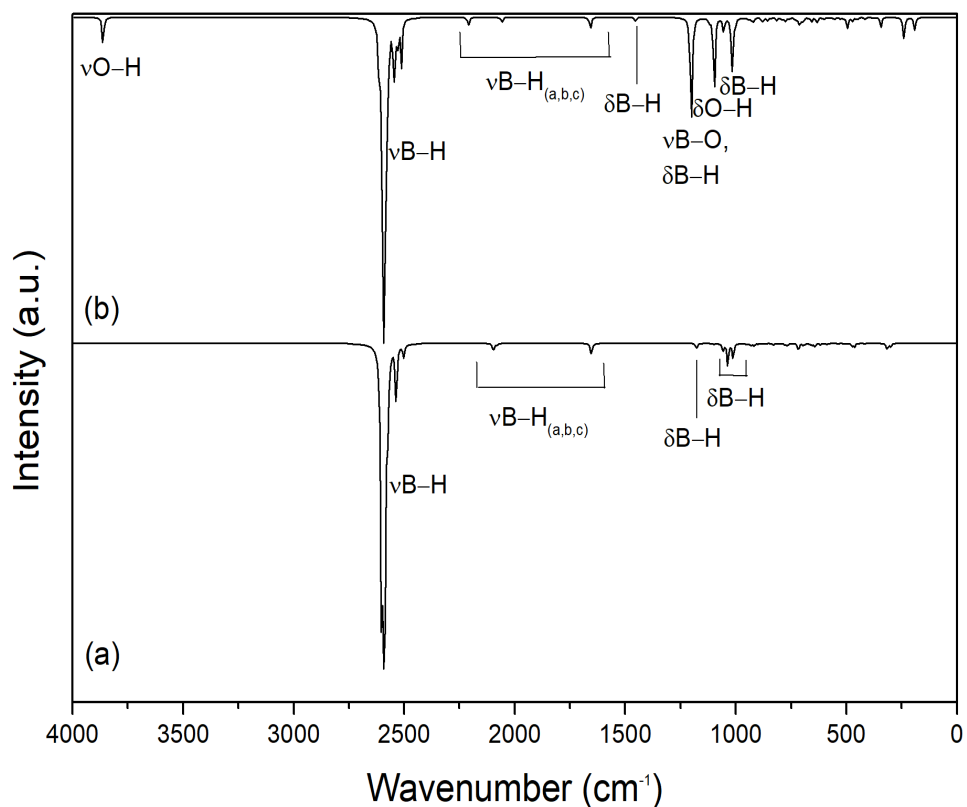


**Figure 3.9** FTIR spectra of (a)  $B_{11}H_{14}^-$  and (b)  $B_{11}H_{13}OH^-$  calculated at the B31LYP/aug-cc-pvdz level of theory.

There is also an absence of  $(CH_3)_3NH^+$  represented by the lack of the bands at  $3165\text{ cm}^{-1}$  and  $970\text{ cm}^{-1}$ , which are assigned to the stretching modes of the  $^+N-H$  and  $C-N^+$  bonds, respectively (Fig. 3.1(B)) [45]. The data reveal that water molecules are present in the cluster of the samples of Li and Na, represented by the bands at  $3800 - 3200\text{ cm}^{-1}$  (O-H stretching) and  $1610\text{ cm}^{-1}$  (H-O-H bending) [54]. The absence of a H-O-H bending mode in the FTIR spectrum of  $KB_{11}H_{14}$  proves that the cation is not solvated by water. As  $Li^+$  and  $Na^+$  have higher charge density than  $K^+$ , they coordinate more strongly to water and become strongly hydrated cations [55].

The presence of water was also confirmed by MS analysis of the gases released from the as-synthesised boranes upon heating at high vacuum (Fig. 3.10).

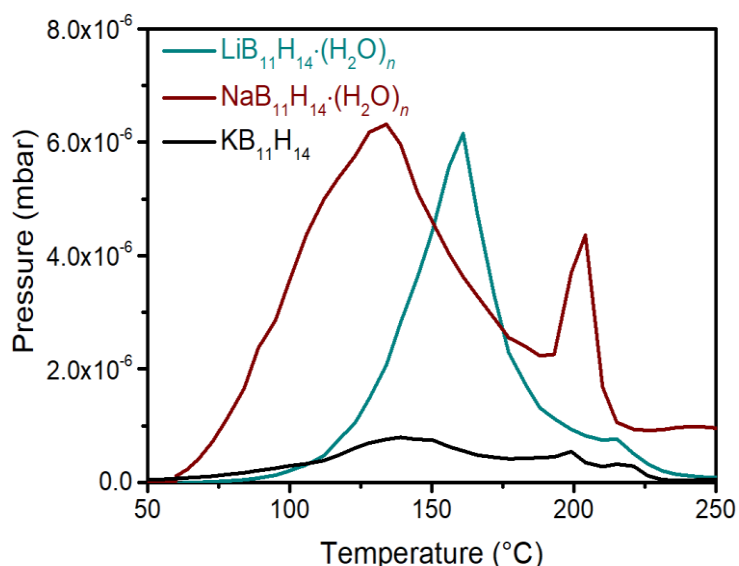


**Figure 3.10** TDA-MS data at  $m/z$  18 (water) of solid-state  $\text{LiB}_{11}\text{H}_{14}\cdot(\text{H}_2\text{O})_n$ ,  $\text{NaB}_{11}\text{H}_{14}\cdot(\text{H}_2\text{O})_n$ , and  $\text{KB}_{11}\text{H}_{14}$  samples. Approximately 5 mg of each compound was used for analysis and heated from 25 to 300 °C ( $\Delta T/\Delta t = 2 \text{ }^\circ\text{C min}^{-1}$ ) under high vacuum ( $< 8 \times 10^{-4}$  mbar).

Samples of  $\text{LiB}_{11}\text{H}_{14}$  and  $\text{NaB}_{11}\text{H}_{14}$  lead to higher intensity peaks at  $m/z = 18$  compared to the potassium version, which is in agreement with the FTIR data. MS data on all samples also show significant hydrogen evolution at temperatures above 200 °C, indicating their thermal decomposition (Fig. 3.11).

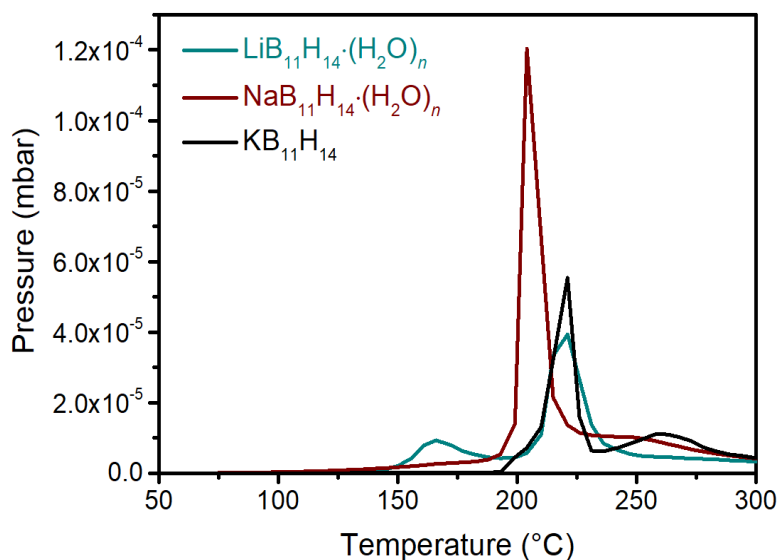


**Figure 3.11** TDA-MS data at  $m/z$  2 (hydrogen) of solid-state  $\text{LiB}_{11}\text{H}_{14}\cdot(\text{H}_2\text{O})_n$ ,  $\text{NaB}_{11}\text{H}_{14}\cdot(\text{H}_2\text{O})_n$ , and  $\text{KB}_{11}\text{H}_{14}$  samples. Approximately 5 mg of each compound was used for analysis and heated from 25 to 300 °C ( $\Delta T/\Delta t = 2 \text{ }^\circ\text{C min}^{-1}$ ) under high vacuum ( $< 8 \times 10^{-4}$  mbar).

This correlates well with TGA-DSC data (Figs. 3.12-3.14), where a significant mass loss and a clear exothermic feature at  $\approx 210$  °C are observed in all cases.

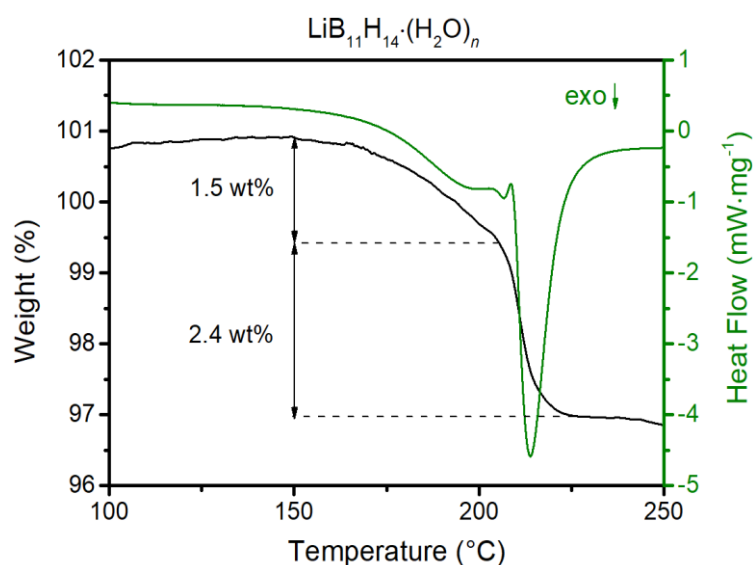


**Figure 3.12** TGA-DSC measurement of  $\text{LiB}_{11}\text{H}_{14}\cdot(\text{H}_2\text{O})_n$  in the temperature range 100 – 250 °C ( $\Delta T/\Delta t = 10$  °C  $\text{min}^{-1}$ , Ar flow = 40 mL  $\text{min}^{-1}$ ). Approximately 7 mg of compound was used for analysis. A mass loss of 1.5% is observed between 150 and 205 °C, which may be attributed to water and hydrogen release, and 2.4% between 205 and 225 °C from hydrogen release, as a result of decomposition of the material.

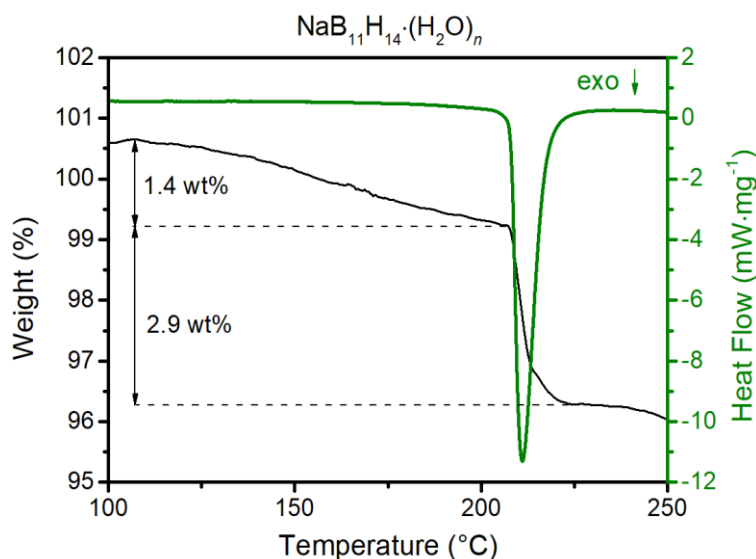


**Figure 3.13** TGA-DSC measurement of  $\text{NaB}_{11}\text{H}_{14}\cdot(\text{H}_2\text{O})_n$  in the temperature range 100 – 250 °C ( $\Delta T/\Delta t = 10$  °C  $\text{min}^{-1}$ , Ar flow = 40 mL  $\text{min}^{-1}$ ). Approximately 7 mg of compound was used for analysis. A mass loss of 1.4% is observed between 100 and 205 °C, which may be attributed to water release, and 2.9% between 205 and 225 °C from hydrogen and water release, as a result of decomposition of the material.

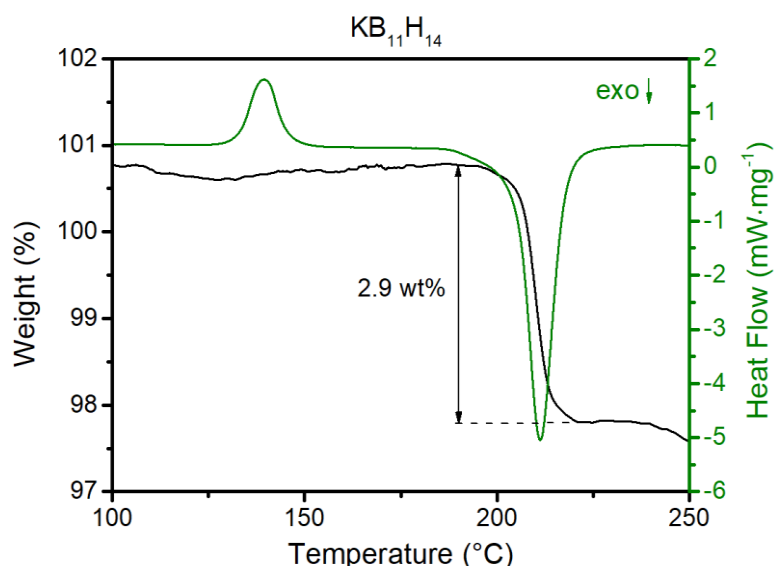


**Figure 3.14** TGA-DSC measurement of  $\text{KB}_{11}\text{H}_{14}$  in the temperature range 100 – 250 °C ( $\Delta T/\Delta t = 10\text{ °C min}^{-1}$ , Ar flow = 40 mL  $\text{min}^{-1}$ ). Approximately 7 mg of compound was used for analysis. The sample undergoes a phase transition at 140 °C represented by the endothermic peak on DSC plot and loses 2.9% of mass between 200 and 220 °C from hydrogen release, as a result of decomposition of the material.

Two steps of hydrogen evolution can be observed in the MS data for  $\text{LiB}_{11}\text{H}_{14}$  (Fig. 3.11), one at  $\approx 165\text{ °C}$ , corresponding to the water release temperature (Fig. 3.10), and another one at  $\approx 220\text{ °C}$ , which is also observed in its DSC scan (Fig. 3.12). The MS data for  $\text{NaB}_{11}\text{H}_{14}$  (Fig. 3.10) demonstrates that water is released upon heating before and at the decomposition temperature of 205 °C. The total mass loss upon decomposition of 3.9% and 4.3% for  $\text{LiB}_{11}\text{H}_{14}$  and  $\text{NaB}_{11}\text{H}_{14}$ , respectively, is attributed to the release of water and hydrogen, whereas  $\text{KB}_{11}\text{H}_{14}$  shows a total mass loss of 2.9 wt%, which accounts for hydrogen evolution. Only  $\text{KB}_{11}\text{H}_{14}$  undergoes a polymorphic phase transition, which is evident by an endothermic event at 140 °C, before it decomposes. DSC scans upon heating and cooling of pristine and ball-milled (B.M.)  $\text{KB}_{11}\text{H}_{14}$  (Fig. 3.15) show endo- and exothermic features during thermal cycling, at  $\approx 140$  and 75 °C respectively, which indicates a reversible phase transition. The reversibility obtained in pristine and ball-milled material indicates that the mechanical-induced modification does not stabilize the high temperature polymorph at room temperature, as can be seen in other ion conducting materials [56,57].

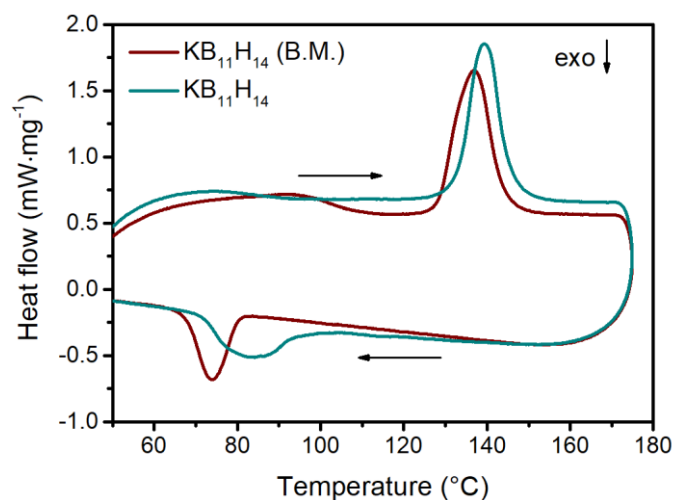


**Figure 3.15** DSC plots for pristine and ball-milled (B.M.)  $\text{KB}_{11}\text{H}_{14}$  upon heating and cooling between 40 and 170 °C ( $\Delta T/\Delta t = 10 \text{ °C min}^{-1}$ ) under 40 mL  $\text{min}^{-1}$  of argon flow.

### 3.3.2 Structural characterisation

XRPD patterns of  $\text{LiB}_{11}\text{H}_{14} \cdot (\text{H}_2\text{O})_n$ ,  $\text{NaB}_{11}\text{H}_{14} \cdot (\text{H}_2\text{O})_n$ , and  $\text{KB}_{11}\text{H}_{14}$  are illustrated in Fig. 3.16. As mentioned previously, the materials were dried at 80 °C *in vacuo* prior to analysis.

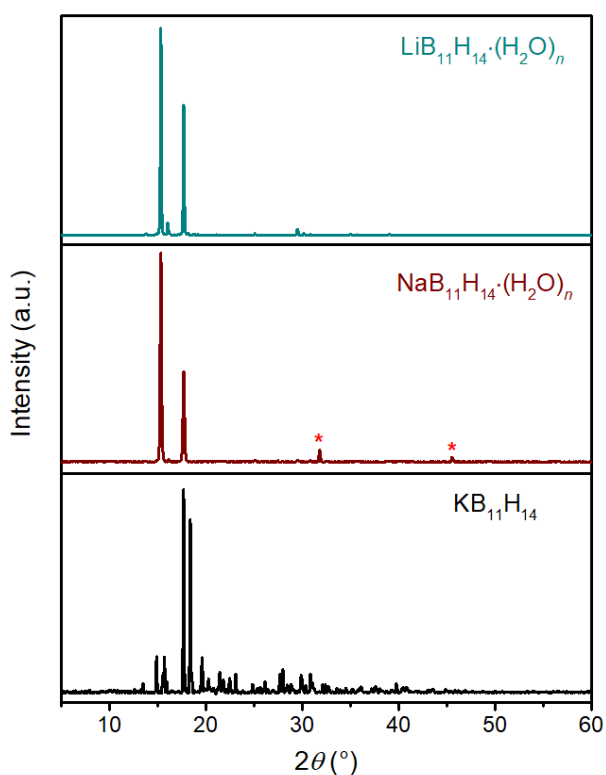


**Figure 3.16** XRPD pattern for  $\text{LiB}_{11}\text{H}_{14} \cdot (\text{H}_2\text{O})_n$ ,  $\text{NaB}_{11}\text{H}_{14} \cdot (\text{H}_2\text{O})_n$ , and  $\text{KB}_{11}\text{H}_{14}$  at room temperature.  $\lambda = 1.54056 \text{ \AA}$ . Asterisks at  $2\theta = 31.8^\circ$  and  $45.5^\circ$  in the  $\text{NaB}_{11}\text{H}_{14} \cdot (\text{H}_2\text{O})_n$  pattern represent inadvertent NaCl contamination.



XRPD data has not previously been reported for  $\text{LiB}_{11}\text{H}_{14}\cdot(\text{H}_2\text{O})_n$  nor  $\text{KB}_{11}\text{H}_{14}$ . However, it appears as though the Li and Na analogues share a structural configuration due to similarities in the XRPD pattern. The XRPD pattern of  $\text{NaB}_{11}\text{H}_{14}\cdot(\text{H}_2\text{O})_n$  appears similar to that presented by Tang *et al.* [21] for the sample ' $\alpha$ - $\text{NaB}_{11}\text{H}_{14}$ ' that exhibits a face centred cubic polymorph ( $Fm\bar{3}m$ ,  $a = 10.1520(19)$  Å) at room temperature. This also correlates well with our indexing, which suggests  $Fm\bar{3}m$ ,  $a = 10.101(1)$  Å for  $\text{NaB}_{11}\text{H}_{14}\cdot(\text{H}_2\text{O})_n$  and  $Fm\bar{3}m$ ,  $a = 10.0736(5)$  Å for  $\text{LiB}_{11}\text{H}_{14}\cdot(\text{H}_2\text{O})_n$ . In contrast, the room temperature polymorph of  $\text{KB}_{11}\text{H}_{14}$  (denoted  $\alpha$ ) was indexed in  $P\bar{1}$  (Tables 3.1-3.2 and Figures 3.17-3.18). However, a high temperature polymorphic structural transition is observed at 135 °C, in agreement with DSC data and *in-situ* XRPD data (Figure 3.19).

**Table 3.1** The refined  $\text{KB}_{11}\text{H}_{14}$  structural parameters at 25 °C in space group  $P\bar{1}$  derived from XRPD data.

Atom	Wyck.	x/a	y/b	z/c	B <sub>iso</sub> (Å <sup>2</sup> )
K1	2i	0.8851(5)	0.2735(5)	0.6002(2)	5.00(8)
K2	2i	0.2382(5)	0.8775(5)	0.9081(2)	5.00(8)
B1a	2i	0.201(7)	0.893(5)	0.081(2)	2.91(9)
B2a	2i	0.224(6)	0.653(5)	0.056(2)	2.91(9)
B3a	2i	0.045(6)	0.725(5)	0.106(2)	2.91(9)
B4a	2i	0.420(7)	0.793(6)	0.076(2)	2.91(9)
B5a	2i	0.137(8)	0.898(6)	0.167(2)	2.91(9)
B6a	2i	0.367(8)	0.939(6)	0.149(2)	2.91(9)
B7a	2i	0.158(6)	0.510(5)	0.121(2)	2.91(9)
B8a	2i	0.411(6)	0.556(6)	0.102(2)	2.91(9)
B9a	2i	0.105(7)	0.669(6)	0.194(2)	2.91(9)
B10a	2i	0.501(7)	0.741(7)	0.162(2)	2.91(9)
B11a	2i	0.316(8)	0.822(7)	0.226(2)	2.91(9)
B1b	2i	0.777(5)	0.400(8)	0.419(2)	2.91(9)
B2b	2i	0.892(5)	0.320(7)	0.347(2)	2.91(9)
B3b	2i	0.692(4)	0.461(8)	0.336(2)	2.91(9)
B4b	2i	0.876(7)	0.176(7)	0.418(2)	2.91(9)

B5b	2i	0.534(5)	0.39(1)	0.397(2)	2.91(9)
B6b	2i	0.646(7)	0.211(9)	0.447(2)	2.91(9)
B7b	2i	0.729(5)	0.276(7)	0.279(2)	2.91(9)
B8b	2i	0.852(7)	0.083(7)	0.334(2)	2.91(9)
B9b	2i	0.497(5)	0.32(1)	0.312(2)	2.91(9)
B10b	2i	0.691(8)	0.015(9)	0.398(2)	2.91(9)
B11b	2i	0.454(7)	0.15(1)	0.388(2)	2.91(9)
H1a	2i	0.150(6)	0.007(5)	0.040(2)	3
H2a	2i	0.192(5)	-0.405(4)	-0.002(2)	3
H3a	2i	-0.107(6)	-0.267(4)	0.083(2)	3
H4a	2i	0.516(6)	-0.154(6)	0.034(2)	3
H5a	2i	0.048(7)	0.024(6)	0.188(2)	3
H6a	2i	0.426(7)	0.093(7)	0.158(3)	3
H7a	2i	0.090(4)	-0.640(4)	0.110(2)	3
H8a	2i	0.501(4)	-0.566(6)	0.079(2)	3
H9a	2i	0.001(6)	-0.370(6)	0.235(2)	3
H10a	2i	0.654(6)	-0.256(7)	0.183(3)	3
H11a	2i	0.332(8)	-0.073(7)	0.274(2)	3
H12a	2i	0.356(6)	-0.332(7)	0.246(2)	3
H13a	2i	0.206(5)	-0.487(6)	0.187(2)	3
H14a	2i	0.454(5)	-0.441(6)	0.167(2)	3
H1b	2i	0.844(5)	0.517(8)	0.456(2)	3
H2b	2i	1.041(5)	0.378(5)	0.332(1)	3
H3b	2i	0.702(4)	0.618(8)	0.321(2)	3
H4b	2i	1.004(7)	0.144(7)	0.456(2)	3
H5b	2i	0.430(5)	0.490(1)	0.422(2)	3
H6b	2i	0.613(7)	0.2(1)	0.505(2)	3
H7b	2i	0.764(4)	0.296(7)	0.221(2)	3
H8b	2i	0.960(7)	-0.018(6)	0.310(2)	3
H9b	2i	0.365(5)	0.36(1)	0.277(2)	3
H10b	2i	0.685(9)	-0.139(9)	0.418(2)	3

H11b	2i	0.317(7)	0.13(1)	0.417(3)	3
H12b	2i	0.443(7)	0.05(1)	0.339(2)	3
H13b	2i	0.576(6)	0.180(9)	0.276(2)	3
H14b	2i	0.697(7)	-0.009(8)	0.330(2)	3

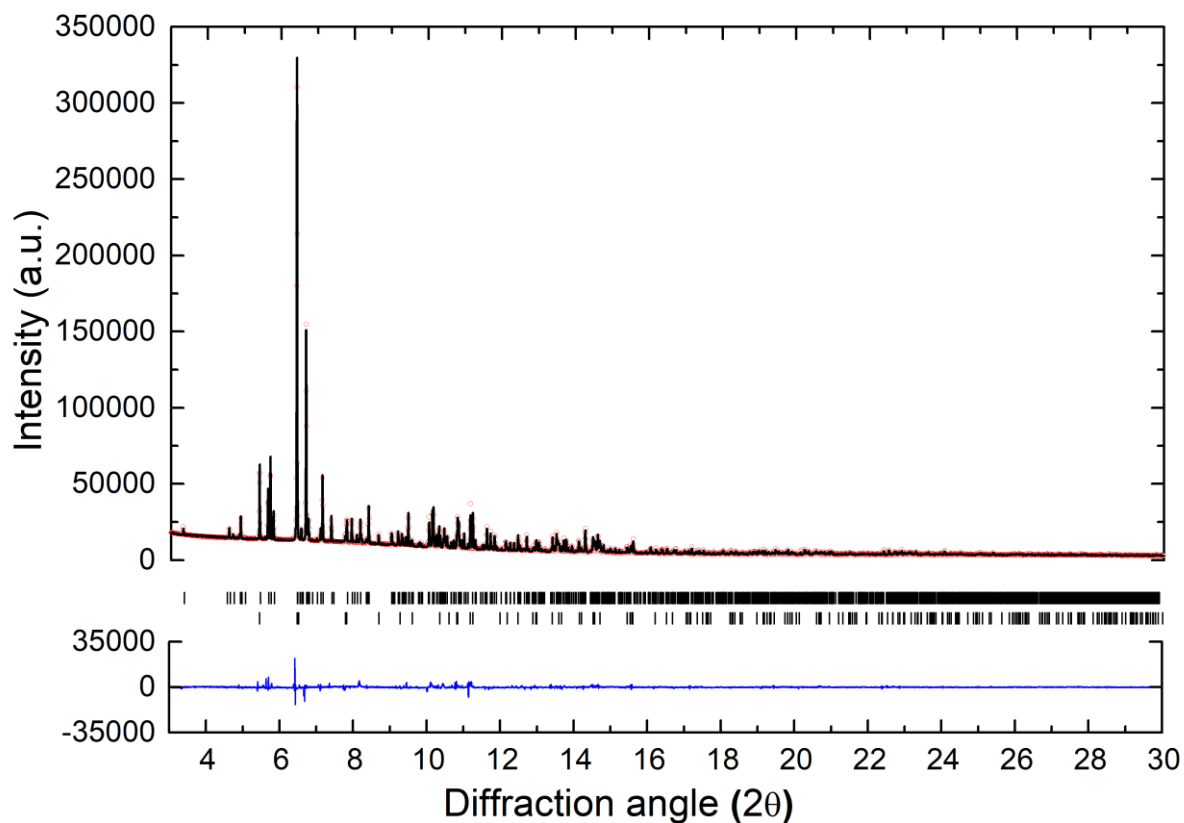


**Figure 3.17** XRPD data and Rietveld refinement plot for  $\text{KB}_{11}\text{H}_{14}$ . Experimental data as red circles, calculated diffraction pattern as black line and the difference plot in blue. Tick marks show positions (listed top to bottom) for (a)  $\alpha\text{-KB}_{11}\text{H}_{14}$  ( $P\bar{1}$ , 86.9(2) wt%); (b)  $\text{K}_2\text{SO}_4$  ( $Pnam$ , 13.1(2) wt%).  $R_{\text{wp}} = 4.85$ .  $\lambda = 0.563476(5)$  Å.

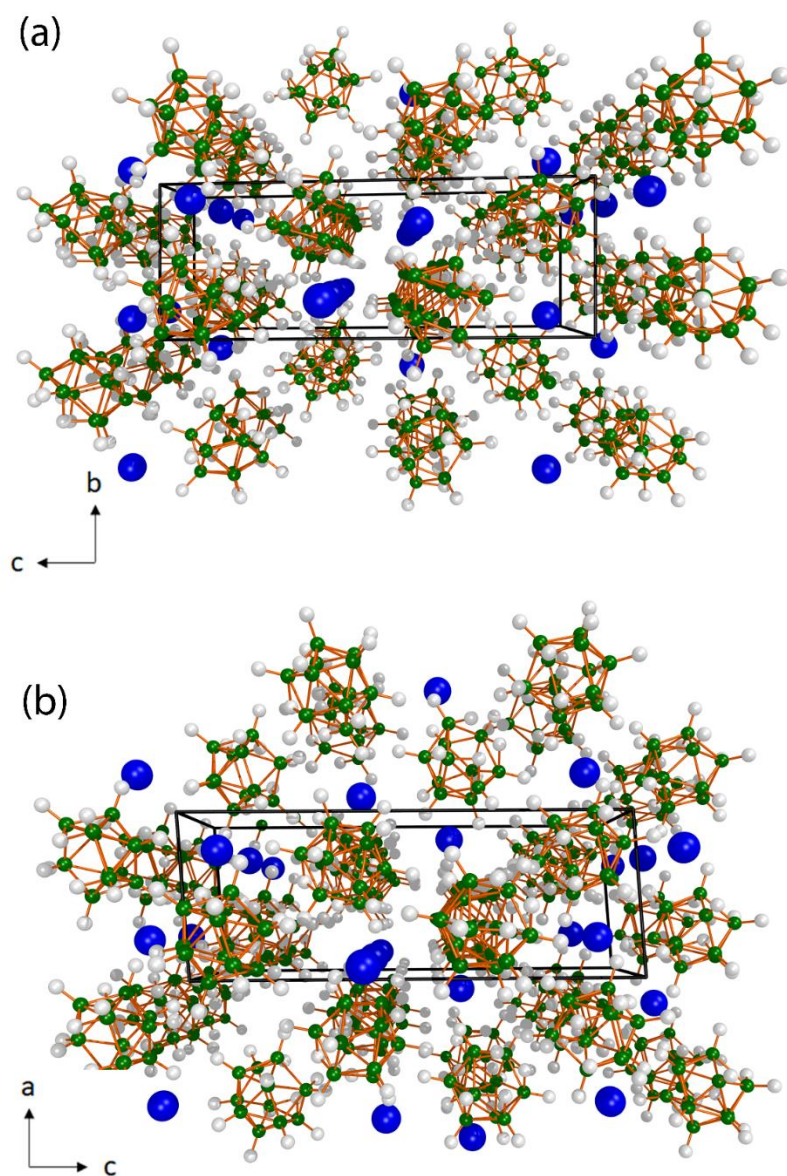


**Figure 3.18** Crystal structure of  $\alpha$ -KB<sub>11</sub>H<sub>14</sub> ( $P\bar{1}$ ). K (blue), B (green), H (white). Structure viewed (a) along the  $a$ -axis and (b) along the  $b$ -axis.

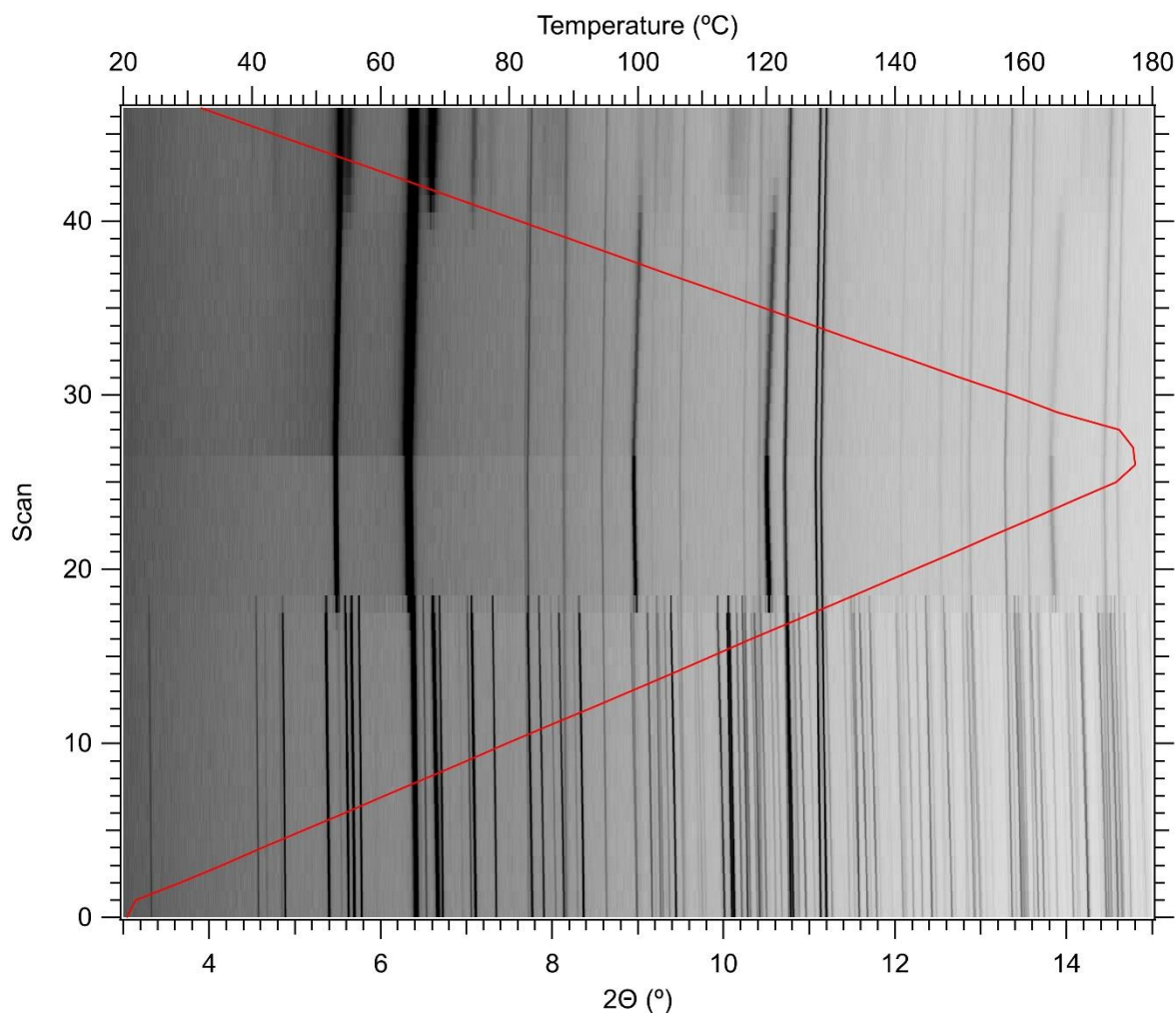


**Figure 3.19** *In-situ* synchrotron XRPD data of  $\text{KB}_{11}\text{H}_{14}$  during heating and cooling,  $\lambda = 0.563516(6)$  Å. A reversible polymorphic phase transition is seen near 135 °C on heating and 85 °C on subsequent cooling. A minor impurity of  $\text{K}_2\text{SO}_4$  is present with persistent peaks across all temperatures (red line).

The high temperature  $\text{KB}_{11}\text{H}_{14}$  polymorph (denoted  $\beta$ ) was indexed in  $Fm\bar{3}m$ ,  $a = 10.19473(4)$  Å, matching the structure type seen at room temperature for the lighter alkali metal- $\text{B}_{11}\text{H}_{14}$  compounds. The cubic space groups are reminiscent of the highly dynamic structures observed in the class of metal boron-hydrogen salts, where the anion undergoes significant reorientational motion and cannot be easily defined in the crystal structure [58]. The unit cell and structure of  $\alpha\text{-KB}_{11}\text{H}_{14}$  differs greatly to that of the hydrated  $\text{NaB}_{11}\text{H}_{14}$  and  $\text{LiB}_{11}\text{H}_{14}$  moieties. As can be seen from Fig. 3.18, the  $\text{KB}_{11}\text{H}_{14}$  packing structure, when viewed along the  $a$  and  $b$  axis consists of separate columns of K atoms and  $\text{B}_{11}\text{H}_{14}^-$  anions. The distances between K atoms through the columns along the  $a$  and  $b$  axis are  $\approx 7.1$  Å, whereas the shortest K-K distances are 5.278(5) Å. To determine the accurate hydrogen positions, neutron

diffraction would be required, especially due to the dynamic nature of these anions and the bridging hydrogens at the apex of the  $B_{11}H_{14}^-$  moieties.

Due to the high ionic conductivity of  $NaB_{11}H_{14} \cdot (H_2O)_n$  at room temperature, electrochemical impedance spectroscopy data of this sample was also collected at low temperatures, and the lowest conductance activity was achieved at  $-40$  °C ( $5.0 \times 10^{-6}$  S  $cm^{-1}$ ). AC impedance measurements were also performed at  $-70$  °C, but no activity was observed at this temperature. Below  $-40$  °C, it is hypothesised that a sudden decrease in conductivity could arise from a polymorphic phase transition upon cooling to a less symmetric crystal structure. In order to investigate this, the diffraction pattern for  $NaB_{11}H_{14} \cdot (H_2O)_n$  was acquired at  $-100$  °C, with the data showing that the material undergoes a reversible polymorphic transition at low temperature by the emergence of additional Bragg reflections in the diffraction pattern. The  $NaB_{11}H_{14} \cdot (H_2O)_n$  spontaneously returns to its original polymorph upon natural heating to room temperature (Fig. 3.20).

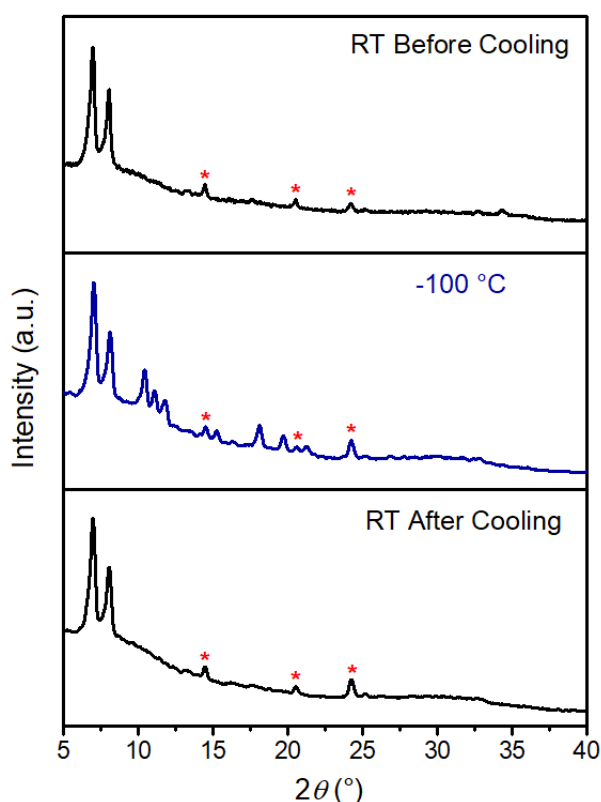


**Figure 3.20** XRPD pattern for  $NaB_{11}H_{14} \cdot (H_2O)_n$  at room temperature (top), at  $-100$  °C (centre) and at room temperature after natural heating (bottom). The sample was mounted in a capillary under argon atmosphere and measured with a Mo  $K_{\alpha}$  source ( $\lambda = 0.7093$  Å). Asterisks at  $14.5^\circ$ ,  $20.5^\circ$  and  $24.2^\circ$  represent inadvertent NaCl contamination.

This discovery raises the question as to whether the room temperature  $\text{NaB}_{11}\text{H}_{14}\cdot(\text{H}_2\text{O})_n$  crystal structure (and the Li analogue) is actually a ‘high-temperature’ polymorph that displays reorientational dynamics, akin to other metal boron-hydrogen compounds [20,22]. This may be indicated by the symmetric cubic structure-type, but further investigations into its crystal structure are required, perhaps utilising neutron diffraction.

Crystals of *nido*-tetradecahydrundecaboranes are often difficult to grow due to their extreme deliquescence. As the crystal of  $\text{LiB}_{11}\text{H}_{14}\cdot 2\text{H}_2\text{O}$  was grown without any application of heating / drying, its diffraction pattern, and thus structure and water content, differ from the sample that was used to investigate ionic conductivity. The presence of water in its crystal structure demonstrates that  $\text{Li}^+$  favourably coordinates with water, even after the compound being extracted with an organic solution. The crystal structure of  $\text{LiB}_{11}\text{H}_{14}\cdot 2\text{H}_2\text{O}$  was solved in space group  $C2/c$  with lattice parameters  $a = 10.4298(4) \text{ \AA}$ ,  $b = 10.1040(2) \text{ \AA}$ ,  $c = 42.3413(16) \text{ \AA}$ ,  $\beta = 91.236(4)^\circ$ , and  $V/Z = 278.81(2) \text{ \AA}^3$  (Fig. 3.21, Table 3.2 & 3.3).

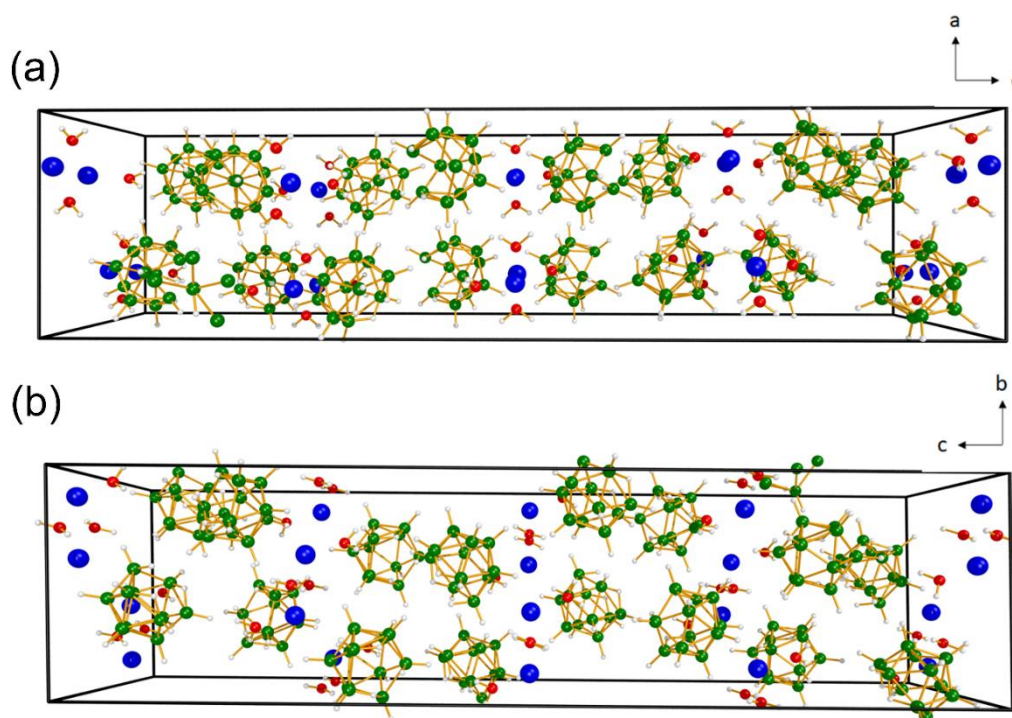


**Figure 3.21** Crystal structure of  $\text{LiB}_{11}\text{H}_{14}\cdot 2\text{H}_2\text{O}$  ( $C2/c$ ). Li (blue), B (green), O (red) and H (white). The structure is viewed along the  $b$ -axis (top) and  $a$ -axis (bottom) demonstrating the lithium coordination that alternate along the  $b$ -axis.

**Table 3.2** Structural Data Extracted from Refinements of the XRPD Data for  $\text{KB}_{11}\text{H}_{14}$  and  $\text{LiB}_{11}\text{H}_{14}\cdot 2\text{H}_2\text{O}$ .

Compound	$\alpha\text{-KB}_{11}\text{H}_{14}$	$\text{LiB}_{11}\text{H}_{14}\cdot 2\text{H}_2\text{O}$
Mr	172.13	175.99
Space group	$P\bar{1}$	$C2/c$
$T$ (°C)	25	21.9
Crystal System	Triclinic	Monoclinic
Colour/habit	-	colourless block
$a$ (Å)	7.19499(8)	10.4298(4)
$b$ (Å)	7.04622(8)	10.1040(2)
$c$ (Å)	19.4087(2)	42.341(2)
$\alpha$ (°)	90.7188(7)	90
$\beta$ (°)	94.0453(7)	91.236(4)
$\gamma$ (°)	89.9709(7)	90
$V$ (Å <sup>3</sup> )	981.44(1)	4461.0(3)
$Z$	2	16
$\rho$ (g cm <sup>-3</sup> )	1.16949(2)	1.048

**Table 3.3** The refined  $\text{LiB}_{11}\text{H}_{14}\cdot 2\text{H}_2\text{O}$  structural parameters at 21.9 °C in space group ( $C2/c$ ) derived from single crystal data.

Atom	Wyck.	$x/a$	$y/b$	$z/c$
O2	8f	0.4545(2)	0.7271(2)	0.54241(5)
H2B	8f	0.42117	0.68679	0.55859
H2C	8f	0.52588	0.76068	0.55007
O2A	8f	0.8125(2)	0.3153(2)	0.20068(6)
H2AA	8f	0.75406	0.26666	0.1911
H2AB	8f	0.84133	0.36618	0.18565
B5	8f	0.5663(4)	0.8048(4)	0.46150(7)
H5	8f	0.54815	0.84754	0.48487
B3A	8f	0.6705(4)	0.3418(4)	0.28396(7)
H3A	8f	0.67751	0.37254	0.25913



B3	8f	0.7491(4)	0.7261(4)	0.41607(7)
H3	8f	0.85034	0.71658	0.40968
B7	8f	0.4337(4)	0.7521(4)	0.43810(7)
B2A	8f	0.5407(4)	0.2437(4)	0.29710(7)
H2A	8f	0.46363	0.21069	0.28082
B1A	8f	0.6969(4)	0.1759(4)	0.29605(7)
H1A	8f	0.72186	0.09892	0.27887
B11A	8f	0.6500(4)	0.2352(4)	0.36123(7)
B6	8f	0.5425(4)	0.6338(4)	0.45308(7)
H6	8f	0.50835	0.56432	0.47104
B9	8f	0.6314(4)	0.6701(4)	0.38879(7)
B4	8f	0.6956(4)	0.8616(4)	0.43887(7)
H4	8f	0.76101	0.93936	0.44764
B1	8f	0.6990(4)	0.6992(4)	0.45494(7)
H1	8f	0.76684	0.67215	0.47412
B10	8f	0.6571(4)	0.8533(4)	0.39819(7)
B8	8f	0.4947(4)	0.6094(4)	0.41308(7)
B7A	8f	0.5025(4)	0.2813(4)	0.33670(8)
B4A	8f	0.8082(4)	0.2989(4)	0.30761(7)
H4A	8f	0.90541	0.30158	0.29804
B10A	8f	0.7877(4)	0.3402(4)	0.34743(7)
B5A	8f	0.7624(4)	0.1752(4)	0.33497(7)
H5A	8f	0.82941	0.09788	0.34321
B6A	8f	0.5983(4)	0.1415(4)	0.32833(8)
H6A	8f	0.55843	0.04208	0.33213
B9A	8f	0.7284(4)	0.4493(4)	0.31402(8)
B8A	8f	0.5511(4)	0.4134(4)	0.30712(7)
B11	8f	0.5352(4)	0.9019(4)	0.42742(8)
B2	8f	0.6569(4)	0.5848(4)	0.42515(8)
H2	8f	0.69741	0.4843	0.42499
Li1	8f	0.3882(5)	0.7388(5)	0.50118(13)

Li1A	8f	0.8648(7)	0.3113(5)	0.24386(16)
O1	8f	0.24039(17)	0.60442(16)	0.49970(4)
H1B	8f	0.20839	0.54534	0.51594
H1C	8f	0.25809	0.5614	0.48295
O1A	4e	1	0.1678(2)	0.25
O3A	4e	1	0.4543(2)	0.25
H8A	8f	0.482(2)	0.489(2)	0.2981(7)
H10A	8f	0.861(2)	0.369(3)	0.3649(7)
H9A	8f	0.772(3)	0.541(2)	0.3064(7)
H7AA	8f	0.404(2)	0.267(3)	0.3449(7)
H11A	8f	0.642(3)	0.199(3)	0.3854(5)
H10C	8f	0.703(3)	0.916(3)	0.3809(7)
H7A	8f	0.339(2)	0.766(3)	0.4476(7)
H8	8f	0.443(3)	0.518(2)	0.4087(7)
H9B	8f	0.658(3)	0.624(3)	0.3665(4)
H11	8f	0.503(3)	1.003(2)	0.4288(7)
H10D	8f	0.554(2)	0.878(3)	0.4026(5)
H10B	8f	0.737(3)	0.437(2)	0.3411(4)
H11B	8f	0.619(3)	0.3397(16)	0.3612(7)
H7AB	8f	0.525(3)	0.3877(14)	0.3317(4)
H9C	8f	0.5195(17)	0.671(3)	0.3905(5)
H7B	8f	0.421(3)	0.795(3)	0.4138(4)
H1AA	8f	1.013(4)	0.118(3)	0.2342(4)
H3AA	8f	1.017(3)	0.504(3)	0.2346(4)

Here, the Li-ions are in a pseudo-tetrahedral environment, with each Li-bound to three water molecules, with the fourth contact formed between a H-atom bound to the  $B_{11}H_{14}^-$  anion. The Li–Li distances are between 2.86(1) and 2.891(7) Å. Two of the bound water molecules bridge between two separate Li-ions, forming a dimer (Fig. 3.21), giving  $Li^+(B_{11}H_{14}) \cdot 2H_2O$  stoichiometrically, but forming  $Li_2(B_{11}H_{14})_2 \cdot 4H_2O$  units in the solid-state. In the crystal structure, two half-molecules are in the asymmetric unit, resulting in two symmetry

independent  $\text{Li}_2(\text{B}_{11}\text{H}_{14})_2 \cdot 4\text{H}_2\text{O}$  units, though no difference in the connectivity or structure could be seen here. After drying, the material exhibits a face centred cubic structure (Fig. 3.16) with less than 2 water molecules in the unit  $\text{LiB}_{11}\text{H}_{14} \cdot (\text{H}_2\text{O})_n$  ( $n < 2$ ).

### 3.3.3 Solid-state ionic conductivity

The solid-state ionic conductivity of  $M\text{B}_{11}\text{H}_{14} \cdot (\text{H}_2\text{O})_n$  ( $M = \text{Li}$  or  $\text{Na}$ ) and  $\text{KB}_{11}\text{H}_{14}$  before and after ball-milling (B.M.), along with  $\text{NaB}_{11}\text{H}_{14} \cdot (\text{C}_6\text{H}_{14}\text{O}_3)_n$ , was assessed as a function of temperature as illustrated in Fig. 3.22.

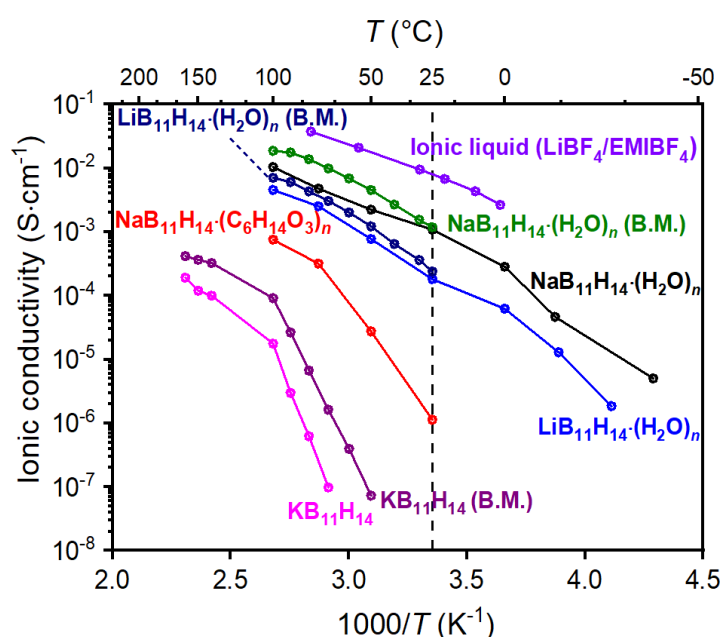


**Figure 3.22** Solid-state ionic conductivity of  $\text{NaB}_{11}\text{H}_{14} \cdot (\text{C}_6\text{H}_{14}\text{O}_3)_n$ ,  $\text{LiB}_{11}\text{H}_{14} \cdot (\text{H}_2\text{O})_n$  (before and after B.M.),  $\text{NaB}_{11}\text{H}_{14} \cdot (\text{H}_2\text{O})_n$  (before and after B.M.),  $\text{KB}_{11}\text{H}_{14}$  (before and after B.M.), and  $\text{LiBF}_4/\text{EMIBF}_4$  [59].

The liquid-state ionic conductivity of the widely-used ionic liquid electrolyte, 1 mol  $\text{L}^{-1}$  solution of 1-ethyl-3-methylimidazolium tetrafluoroborate ( $\text{EMIBF}_4$ ) with lithium tetrafluoroborate ( $\text{LiBF}_4$ ) [59], is displayed for comparison. The activation energy of ionic conductivity was calculated based on the Arrhenius plot (Fig. 3.22) for each compound by:

$$\ln \sigma_{ion} = \ln \sigma_o - \left( \frac{E_\sigma}{K_B} \right) \frac{1}{T} \quad (12)$$

where  $\sigma_o$  is a pre-exponential factor ( $\text{S cm}^{-1}$ ),  $E_\sigma$  the activation energy (J),  $K_B$  the Boltzmann constant ( $1.3806 \times 10^{-23} \text{ J K}^{-1}$ ), and  $T$  the temperature (K) [60]. The activation energy was

calculated based on the slope of the plot of each material from 25 to 75 °C, except  $\text{KB}_{11}\text{H}_{14}$  (before and after B.M.), which was measured from 70 to 100 °C. Nyquist plots of  $\text{LiB}_{11}\text{H}_{14}\cdot(\text{H}_2\text{O})_n$ ,  $\text{NaB}_{11}\text{H}_{14}\cdot(\text{H}_2\text{O})_n$ , and  $\text{KB}_{11}\text{H}_{14}$  at different temperatures are shown in Figs. 3.23 and 3.24.

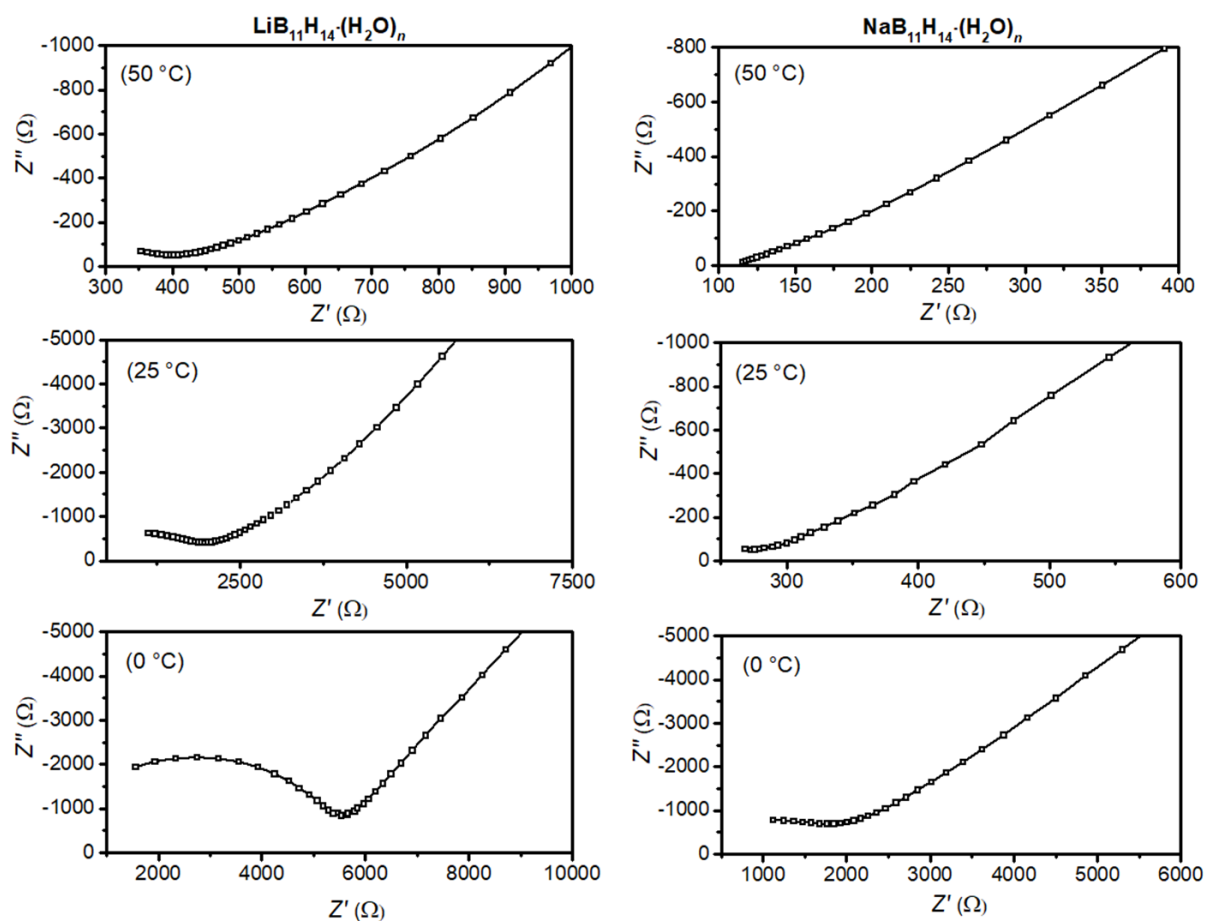


**Figure 3.23** Magnified Nyquist plot of pristine  $\text{LiB}_{11}\text{H}_{14}\cdot(\text{H}_2\text{O})_n$  (left) and  $\text{NaB}_{11}\text{H}_{14}\cdot(\text{H}_2\text{O})_n$  (right) in the high-frequency region at 0, 25, and 50 °C.

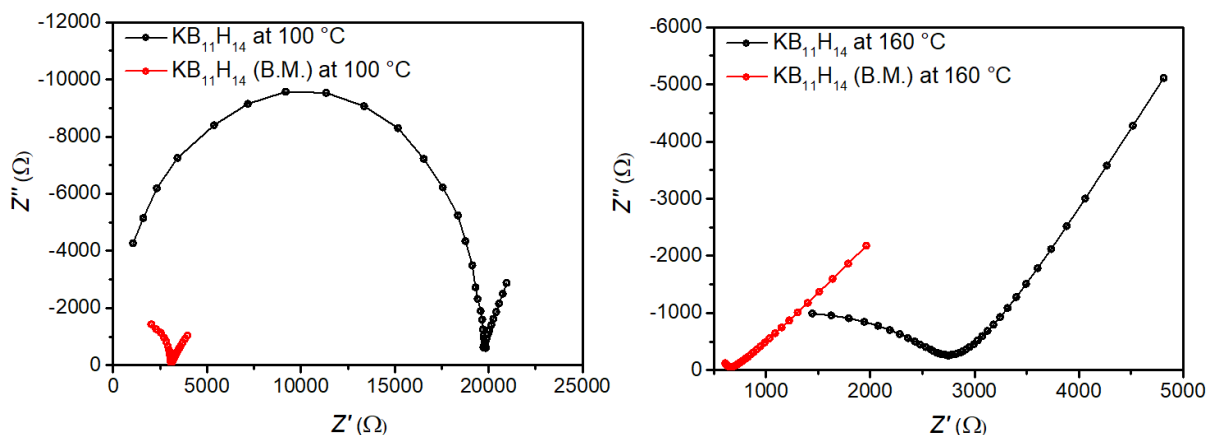


**Figure 3.24** Nyquist plot of pristine and ball-milled (B.M.)  $\text{KB}_{11}\text{H}_{14}$  at 100 °C (left) and 160 °C (right) from 100 Hz to 1 MHz.

The size of the cation plays an important role in the ionic conductivity of the material. Due to the large radius of  $\text{K}^+$  (six-coordinate  $\text{K}^+$ , 1.38 Å) [51], the sample of  $\text{KB}_{11}\text{H}_{14}$  shows a large activation energy (1.9 eV) that can only be significantly overcome at elevated temperature. Ball-milling the  $\text{KB}_{11}\text{H}_{14}$  sample reduces its activation energy to 1.5 eV, and therefore, increases its ionic conductivity by approximately one order of magnitude. Despite the unusually high activation energy compared to other potassium boron-hydrogen materials, such as  $\text{KB}_3\text{H}_8$  ( $E_\sigma = 0.44$  eV) [61],  $\text{K}_3(\text{BH}_4)(\text{B}_{12}\text{H}_{12})$  ( $E_\sigma = 0.37$  eV) [61,62] and  $\text{KCB}_{11}\text{H}_{12}$  ( $E_\sigma = 0.82$  eV) [63], the  $\text{K}^+$  conductivity in the pristine  $\text{KB}_{11}\text{H}_{14}$  reaches an ionic conductivity of  $1.2 \times 10^{-4}$   $\text{S cm}^{-1}$  at 150 °C, whereas  $\text{KB}_3\text{H}_8$  and  $\text{K}_3(\text{BH}_4)(\text{B}_{12}\text{H}_{12})$  exhibit a  $\text{K}^+$  conductivity in the order of  $10^{-7}$  and  $10^{-6}$ , respectively, at the same temperature [61,62]. The metal carborane,  $\text{KCB}_{11}\text{H}_{12}$ , in its ordered structure exhibits similar results of ionic conductivity when compared to the ball-milled sample of  $\text{KB}_{11}\text{H}_{14}$ , especially at 80 °C ( $\approx 9.5 \times 10^{-6}$   $\text{S cm}^{-1}$  and  $6.7 \times 10^{-6}$   $\text{S cm}^{-1}$ , respectively). Nevertheless, the high temperature polymorph that the metal carborane assumes presents an ionic conductivity about one order of magnitude higher than ball-milled  $\text{KB}_{11}\text{H}_{14}$ . The hysteretic conductivity behaviour observed for  $\text{KB}_{11}\text{H}_{14}$  above 100 °C is a consequence of the polymorphic phase transition that the material undergoes, indicated by the DSC plot (Fig. 3.15) and *in-situ* XRPD data (Fig. 3.19), as discussed in the ‘Structural Characterisation’ section. The potassium *nido*-borane sample assumes a disordered crystallographic structure at high temperature, which enhances its ionic conductivity, as observed for other metal boron-hydrogen materials [20,22,63].

Temperature Programmed Photographic Analysis (Fig. 3.25) of  $\text{KB}_{11}\text{H}_{14}$  was performed in order to check the condition of the pellet upon heating.

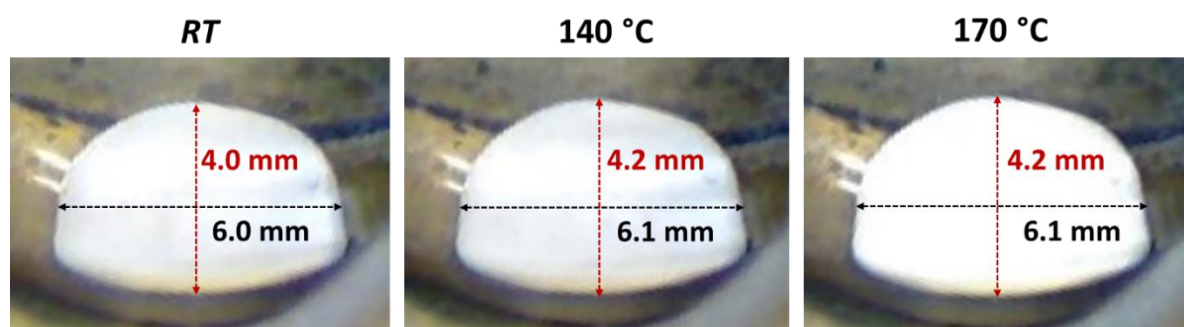


**Figure 3.25** TPPA of  $\text{KB}_{11}\text{H}_{14}$  heated from room temperature to 170 °C ( $\Delta T/\Delta t = 10 \text{ }^\circ\text{C min}^{-1}$ ). A volume increase of the pellet can be observed at  $\approx 120\text{-}140 \text{ }^\circ\text{C}$ .

The result reveals a slight volume expansion at  $\approx 120\text{-}140 \text{ }^\circ\text{C}$ , which is related to the reversible polymorphic structural transition (Fig. 3.15 & 3.19). The pellet was heated up to 170 °C with no melting or release of solvent observed. Due to the volume change that the pellet undergoes upon heating, the data points between 110 and 130 °C were omitted from the ionic conductivity plot (Fig. 3.22) of pristine and ball-milled  $\text{KB}_{11}\text{H}_{14}$ , as they represent artefacts of the measurement (full data set is presented in Fig. 3.26).

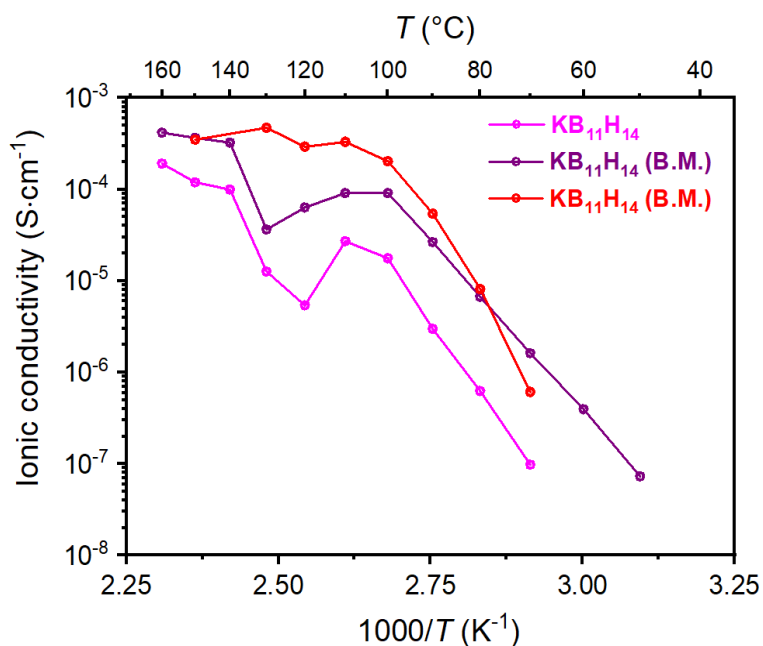


**Figure 3.26** Ionic conductivity of pristine and ball-milled (two measurements)  $\text{KB}_{11}\text{H}_{14}$  with data points between 110 and 130 °C. All measurements show a drop in ionic conductivity in this range of temperature, which is associated to the order-disorder phase transition.

Mechanical-induced modification is known to improve the cationic conductivity of other metal boron-hydrogen compounds, such as  $\text{LiBH}_4$  [56],  $\text{Li}_2\text{B}_{12}\text{H}_{12}$  [57], and  $\text{Na}_2\text{B}_{12}\text{H}_{12}$  [64] that had their ionic conductivity enhanced by at least two orders of magnitude when measured at the same temperature. Ball-milling may induce defects (cation or even hydrogen vacancies) [57,65], reduction of the crystallite size, and/or stabilisation of a potential disordered high-temperature superionic polymorph, which are all factors that boost the ionic conductivity of a material [64]. However, ball-milling did not show significant improvement in the ionic conductivity of  $\text{NaB}_{11}\text{H}_{14}\cdot(\text{H}_2\text{O})_n$  and  $\text{LiB}_{11}\text{H}_{14}\cdot(\text{H}_2\text{O})_n$ . Besides that, the activation energy of pristine  $\text{LiB}_{11}\text{H}_{14}\cdot(\text{H}_2\text{O})_n$  (0.5 eV) has not considerably changed upon ball-milling (0.5 eV), whereas  $\text{NaB}_{11}\text{H}_{14}\cdot(\text{H}_2\text{O})_n$  presented a small increase in its activation energy from 0.3 to 0.4 eV after ball-milling, but this is within the experimental uncertainty ( $\pm 0.1$  eV). Even though  $\text{Li}^+$  (six-coordinate  $\text{Li}^+$ , 0.79 Å) [51] has an ionic radius smaller than  $\text{Na}^+$  (six-coordinate  $\text{Na}^+$ , 1.07 Å) [51],  $\text{LiB}_{11}\text{H}_{14}\cdot(\text{H}_2\text{O})_n$  requires more energy to promote  $\text{Li}^+$  migration and has lower ionic conductivity than  $\text{NaB}_{11}\text{H}_{14}\cdot(\text{H}_2\text{O})_n$ . The differences in activation energy could be explained by the coordinated water, which is more strongly bound to the more charge-dense  $\text{Li}^+$ .

The presence of a coordinated solvent to the cation also shows an important contribution to the conductivity properties of the material, as reported by Møller *et al.* [66]. As shown in (Fig. 3.22),  $\text{NaB}_{11}\text{H}_{14}$  experiences a dramatic increase in cationic conductivity when replacing diglyme with water.  $\text{NaB}_{11}\text{H}_{14}\cdot(\text{C}_6\text{H}_{14}\text{O}_3)_n$  has a high activation energy of 1.0 eV and an ion conductivity of  $1.1 \times 10^{-6} \text{ S cm}^{-1}$  at 25 °C, whereas  $\text{NaB}_{11}\text{H}_{14}\cdot(\text{H}_2\text{O})_n$  at the same temperature shows an outstanding result of  $1.1 \times 10^{-3} \text{ S cm}^{-1}$  and activation energy of 0.3 eV.

Diglyme molecules easily chelate with small cations, such as  $\text{Na}^+$ , due to the presence of ether-type oxygen atoms. These molecules solvate the metal and usually behave like crown glymes [67], which may inhibit the cation displacement in the crystal structure. Small solvent molecules, like tetrahydrofuran (THF) and acetonitrile, have already been reported to assist the cationic diffusion through the crystal structure of  $\text{Li}_2\text{B}_{12}\text{H}_{12}$  [66]. The coordination of  $\text{LiBH}_4$  with ammonia also increases its ionic conductivity, and it is proposed that  $\text{NH}_3$  facilitates the migration of  $\text{Li}^+$  through the lattice of  $\text{LiBH}_4\cdot 1/2\text{NH}_3$  [68]. In a similar way, water molecules coordinated to  $\text{Na}^+$  may assist the diffusion of the cation through the crystal structure of  $\text{NaB}_{11}\text{H}_{14}\cdot(\text{H}_2\text{O})_n$  and contribute to its higher ionic conductivity and lower activation energy when compared to  $\text{NaB}_{11}\text{H}_{14}\cdot(\text{C}_6\text{H}_{14}\text{O}_3)$ .

Even though the presence of diglyme interferes with the ion conductivity,  $\text{NaB}_{11}\text{H}_{14}\cdot(\text{C}_6\text{H}_{14}\text{O}_3)_n$  still exhibits higher ionic conductivities from 25 to 100 °C than other metal boron-hydrogen compounds, such as  $\text{Na}_2\text{B}_{10}\text{H}_{10}$  [69] and  $\text{Na}_2\text{B}_{12}\text{H}_{12}$  [22], as shown in Fig. 3.27.



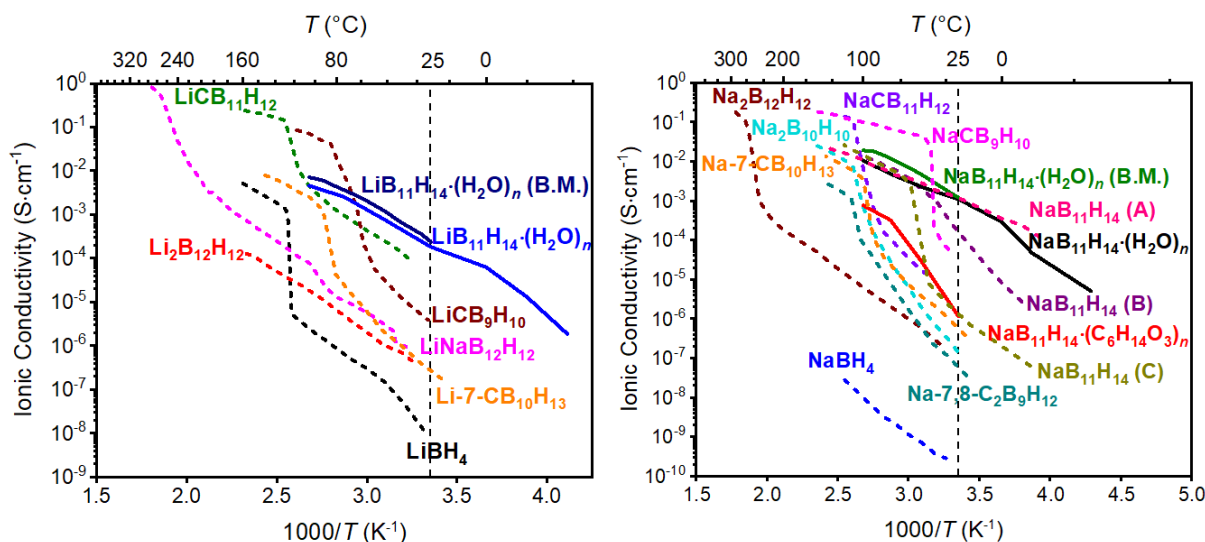


**Figure 3.27** Arrhenius plots of ionic conductivities of  $\text{LiB}_{11}\text{H}_{14}\cdot(\text{H}_2\text{O})_n$ ,  $\text{NaB}_{11}\text{H}_{14}\cdot(\text{H}_2\text{O})_n$ , and  $\text{NaB}_{11}\text{H}_{14}\cdot(\text{C}_6\text{H}_{14}\text{O}_3)_n$  compared with other Li (left) and Na (right) single anion boron-hydrogen materials:  $\text{LiCB}_{11}\text{H}_{12}$  [70],  $\text{LiCB}_9\text{H}_{10}$  [9],  $\text{LiBH}_4$  [22],  $\text{Li}_2\text{B}_{12}\text{H}_{12}$  [71],  $\text{LiNaB}_{12}\text{H}_{12}$  [72],  $\text{Li-7-CB}_{10}\text{H}_{13}$  [21],  $\text{NaCB}_{11}\text{H}_{12}$  [70],  $\text{Na}_2\text{B}_{12}\text{H}_{12}$  [22],  $\text{Na}_2\text{B}_{10}\text{H}_{10}$  [69],  $\text{NaBH}_4$  [69],  $\text{Na-7-CB}_{10}\text{H}_{13}$  [21],  $\text{Na-7,8-C}_2\text{B}_9\text{H}_{12}$  [21],  $\text{NaCB}_9\text{H}_{10}$  [20].  $\text{NaB}_{11}\text{H}_{14}$  (A) and (C) are the commercial version of  $\text{NaB}_{11}\text{H}_{14}$  that were obtained from two different batches [21], and (B) is a sample of  $\text{NaB}_{11}\text{H}_{14}$  that was synthesised using decaborane [25]. The solid lines represent the ionic conductivity of the materials synthesised in this work.

Additionally,  $\text{NaB}_{11}\text{H}_{14}\cdot(\text{H}_2\text{O})_n$  exhibits considerably good cationic conductivity even at low temperatures, such as  $-40\text{ }^\circ\text{C}$  ( $5.0 \times 10^{-6}\text{ S cm}^{-1}$ ), as well as  $\text{LiB}_{11}\text{H}_{14}\cdot(\text{H}_2\text{O})_n$ , which shows an ionic conductivity of  $1.8 \times 10^{-6}\text{ S cm}^{-1}$  at  $-30\text{ }^\circ\text{C}$ . The feature of reasonable solid-state ionic conductivities at sub-zero temperatures is vital for battery operation in cold climates.

Ball-milled  $\text{LiB}_{11}\text{H}_{14}\cdot(\text{H}_2\text{O})_n$  and  $\text{NaB}_{11}\text{H}_{14}\cdot(\text{H}_2\text{O})_n$  exhibit a lithium and sodium conductivity of  $2.4 \times 10^{-4}\text{ S cm}^{-1}$  and  $1.2 \times 10^{-3}\text{ S cm}^{-1}$ , respectively, at  $25\text{ }^\circ\text{C}$ . To the author's knowledge, these results represent some of the highest  $\text{Li}^+$  and  $\text{Na}^+$  conductivities reported at room temperature for a metal boron-hydrogen compound (Fig. 3.27 and 3.28). Additionally, they exhibit superionic conductivity upon heating, with  $\text{Li}^+$ , and  $\text{Na}^+$  conductivities of  $7.1 \times 10^{-3}\text{ S cm}^{-1}$  and  $1.9 \times 10^{-2}\text{ S cm}^{-1}$  at  $100\text{ }^\circ\text{C}$  for ball-milled  $\text{LiB}_{11}\text{H}_{14}\cdot(\text{H}_2\text{O})_n$  and  $\text{NaB}_{11}\text{H}_{14}\cdot(\text{H}_2\text{O})_n$ , respectively.

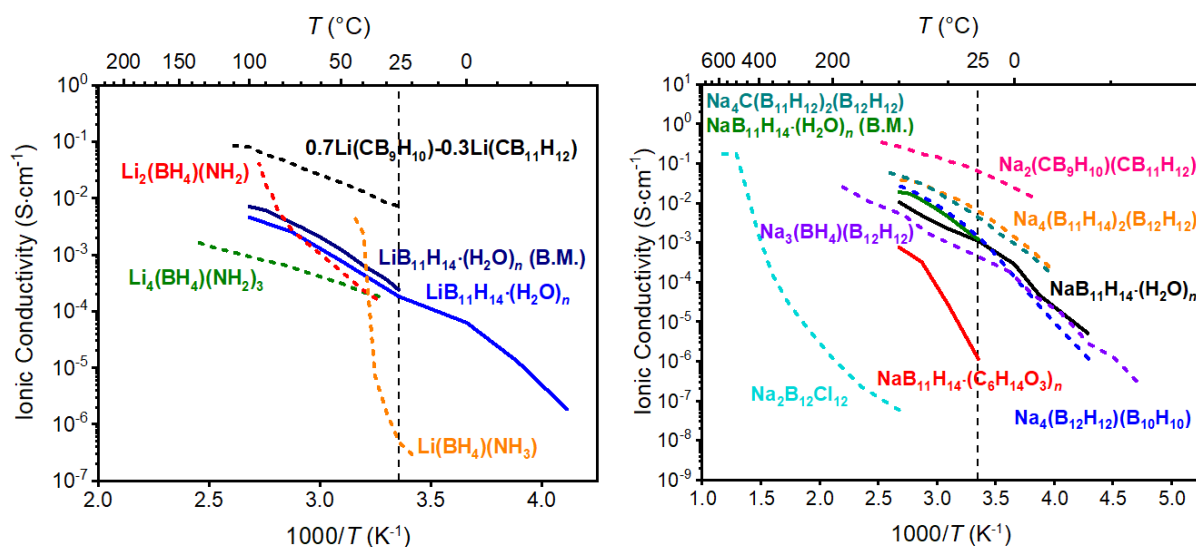


**Figure 3.28** Arrhenius plots of ionic conductivities of  $\text{LiB}_{11}\text{H}_{14}\cdot(\text{H}_2\text{O})_n$ ,  $\text{NaB}_{11}\text{H}_{14}\cdot(\text{H}_2\text{O})_n$ , and  $\text{NaB}_{11}\text{H}_{14}\cdot(\text{C}_6\text{H}_{14}\text{O}_3)_n$  compared with other Li (left) [9,73,74] and Na (right) [1,25,75–78] mixed anion boron-hydrogen solid-state electrolytes. The solid lines represent the ionic conductivity of the materials synthesised in this work.

$\text{LiB}_{11}\text{H}_{14}\cdot(\text{H}_2\text{O})_n$  and  $\text{NaB}_{11}\text{H}_{14}\cdot(\text{H}_2\text{O})_n$  also exhibit higher ionic conductivity than other *nido*-anions, such as  $7\text{-CB}_{10}\text{H}_{13}^-$  and  $7,8\text{-C}_2\text{B}_9\text{H}_{12}^-$  [21], in the temperature range used in this study (Fig. 6). The incorporation of carbon to the *nido*-anion structure increases the charge polarisation, and thus reduces its ionic conductivity [21].

The  $\text{NaB}_{11}\text{H}_{14}\cdot(\text{H}_2\text{O})_n$  sample prepared in the present study exhibits the same crystal structure as a commercial sample in a previous study reported as ‘ $\alpha\text{-NaB}_{11}\text{H}_{14}$ ’ [21], here denoted as  $\text{NaB}_{11}\text{H}_{14}$  (A). The DSC (Fig. 3.13) and ionic conductivity results we obtain for  $\text{NaB}_{11}\text{H}_{14}\cdot(\text{H}_2\text{O})_n$  also match those for  $\text{NaB}_{11}\text{H}_{14}$  (A) (Fig. 3.27). It is also clear that the ionic conductivity for  $\text{NaB}_{11}\text{H}_{14}\cdot(\text{H}_2\text{O})_n$  and  $\text{NaB}_{11}\text{H}_{14}$  (A) is far superior to samples prepared in an alternative manner,  $\text{NaB}_{11}\text{H}_{14}$  (B) and  $\text{NaB}_{11}\text{H}_{14}$  (C).  $\text{NaB}_{11}\text{H}_{14}$  (B) is a sample of  $\text{NaB}_{11}\text{H}_{14}$  that was synthesised using decaborane in a previous work [25], and  $\text{NaB}_{11}\text{H}_{14}$  (C) is another commercial version of  $\text{NaB}_{11}\text{H}_{14}$  [21]. Both present an orthorhombic crystal structure, which differs completely from the *fcc* polymorph that  $\text{NaB}_{11}\text{H}_{14}\cdot(\text{H}_2\text{O})_n$  and  $\text{NaB}_{11}\text{H}_{14}$  (A) exhibit. It may be that the previously reported “minor unknown impurities” [21] in  $\text{NaB}_{11}\text{H}_{14}$  (A) are associated with coordinated water. Perhaps the presence of water molecules in the crystal structure stabilize its *fcc* disordered polymorph, and are responsible for the high ionic conductivity at room temperature ( $1.1 \times 10^{-3} \text{ S cm}^{-1}$ ).

Many solid-state electrolytes, including metal boron-hydrogen materials, may not present a wide electrochemical stability against Li or Na metal anodes [79]. For instance,  $\text{NaBH}_4$  and  $\text{LiBH}_4$  are stable up to  $\approx 2.0$  V [10,79], whereas  $\text{Na}_2\text{B}_{12}\text{H}_{12}$  and  $\text{Li}_2\text{B}_{12}\text{H}_{12}$  decompose at  $\approx 3.4$  V [10,79]. It was also reported that  $\text{NaB}_{11}\text{H}_{14}$  oxidizes at 2.6 V, and it exhibits a thermodynamic electrochemical window from 0.15 to 2.6 V vs.  $\text{Na}/\text{Na}^+$  [25]. Therefore, in order to investigate the oxidative stability of  $\text{LiB}_{11}\text{H}_{14}\cdot(\text{H}_2\text{O})_n$  and  $\text{NaB}_{11}\text{H}_{14}\cdot(\text{H}_2\text{O})_n$ , a linear sweep voltammetry experiment as proposed by Asakura *et al.* [32] was performed.

Fig. 3.29 shows the linear sweep voltammograms of the electrolytes tested.  $\text{NaB}_{11}\text{H}_{14}\cdot(\text{H}_2\text{O})_n$  exhibits an oxidative stability limit at 2.6 V, which is the same as previously reported for  $\text{NaB}_{11}\text{H}_{14}$  [25].  $\text{LiB}_{11}\text{H}_{14}\cdot(\text{H}_2\text{O})_n$  demonstrated the first oxidation step at 2.1 V vs.  $\text{Li}/\text{Li}^+$ , which might be associated to residual water [75], and a second step with high oxidative current at 2.9 V. The second linear sweep voltammogram cycle data for both materials do not demonstrate any oxidative current peaks, which indicates the irreversibility of the oxidation reaction [17].

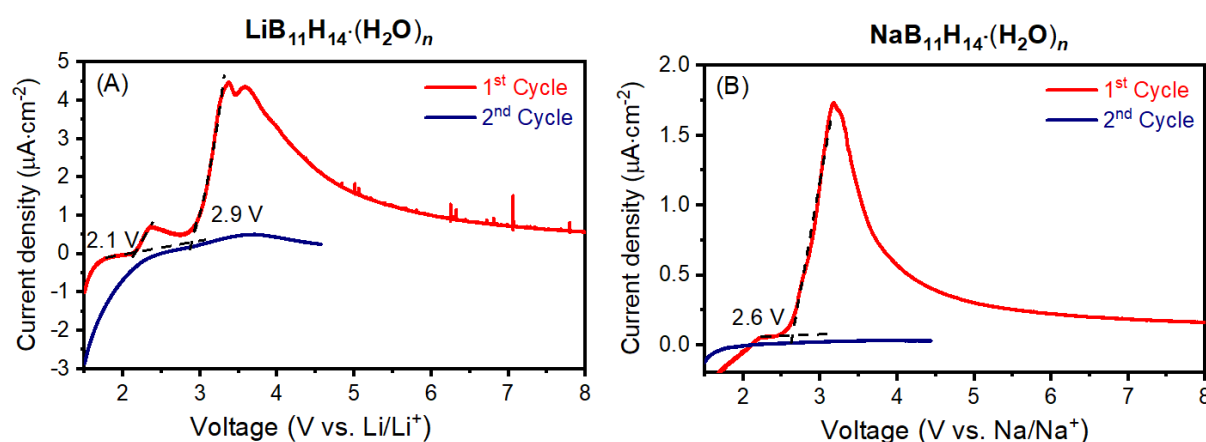


**Figure 3.29** Linear Sweep Voltammograms of (A)  $\text{Li}/\text{LiB}_{11}\text{H}_{14}\cdot(\text{H}_2\text{O})_n/\text{LiB}_{11}\text{H}_{14}\cdot(\text{H}_2\text{O})_n+\text{C}/\text{Pt}/\text{Al}$  and (B)  $\text{Na}/\text{NaB}_{11}\text{H}_{14}\cdot(\text{H}_2\text{O})_n/\text{NaB}_{11}\text{H}_{14}\cdot(\text{H}_2\text{O})_n+\text{C}/\text{Pt}/\text{Al}$  cells at a scan rate of  $50 \mu\text{V s}^{-1}$  at  $60^\circ\text{C}$  between 1.5 and 8.0 V (1<sup>st</sup> run) and 1.5 and 4.5 V (2<sup>nd</sup> run). The black dashed lines represent the linear regression lines fitted to the background and to the anodic current to obtain the oxidation potential.

The same experiment was conducted with  $\text{LiBH}_4$  as a control sample. The result that was obtained for  $\text{LiBH}_4$  (2.2 V) (Fig. 3.30) is close to the one previously detected using the same experimental method (2.04 V) [32] and from the one calculated by first principles

computational methods (2.0 V) [10]. This demonstrates the efficacy of the experiment to determine the oxidative stability limit of the *nido*-boranes investigated.

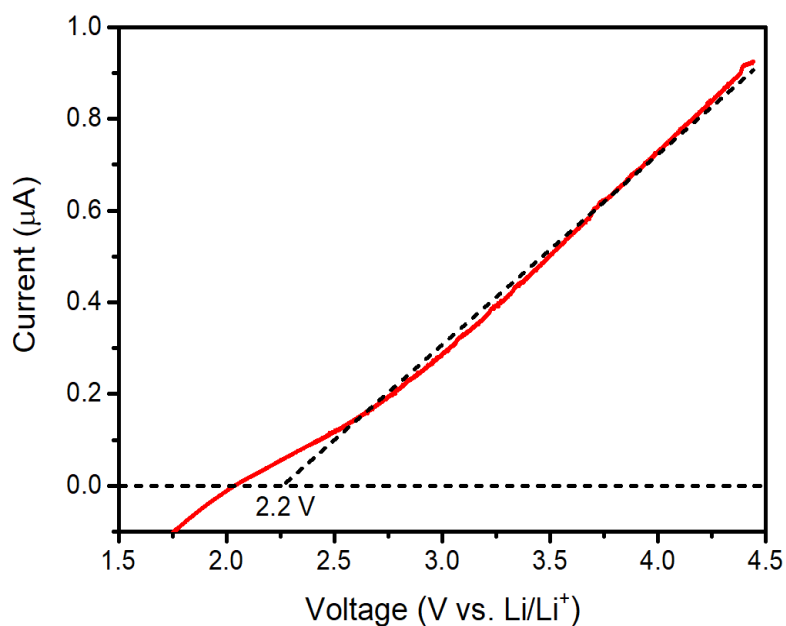


**Figure 3.30** Linear Sweep Voltammogram of Li/LiBH<sub>4</sub>/LiBH<sub>4</sub>+C/Pt/Al cell at a scan rate of 50 μV s<sup>-1</sup> at 60 °C between 1.5 and 4.5 V. The black dashed lines represent the linear regression lines fitted to the background and to the anodic current to obtain the oxidation potential.

Interestingly, no observed changes are noted in the XRPD patterns of LiB<sub>11</sub>H<sub>14</sub>·(H<sub>2</sub>O)<sub>n</sub> and NaB<sub>11</sub>H<sub>14</sub>·(H<sub>2</sub>O)<sub>n</sub> (Fig. 3.31) after the second cycle of LSV. This implies a bulk stability of both *nido*-boranes against Li and Na metal, respectively [80]. Nevertheless, oxidation of the sample can form an oxidised interphase between the electrolyte and the electrode, and depending on its properties, the performance of an ASSB can be greatly affected [17]. Discovering the properties of the created interphase, which also depends on the chosen cathode, is important for the development of an effective ASSB and requires future study.

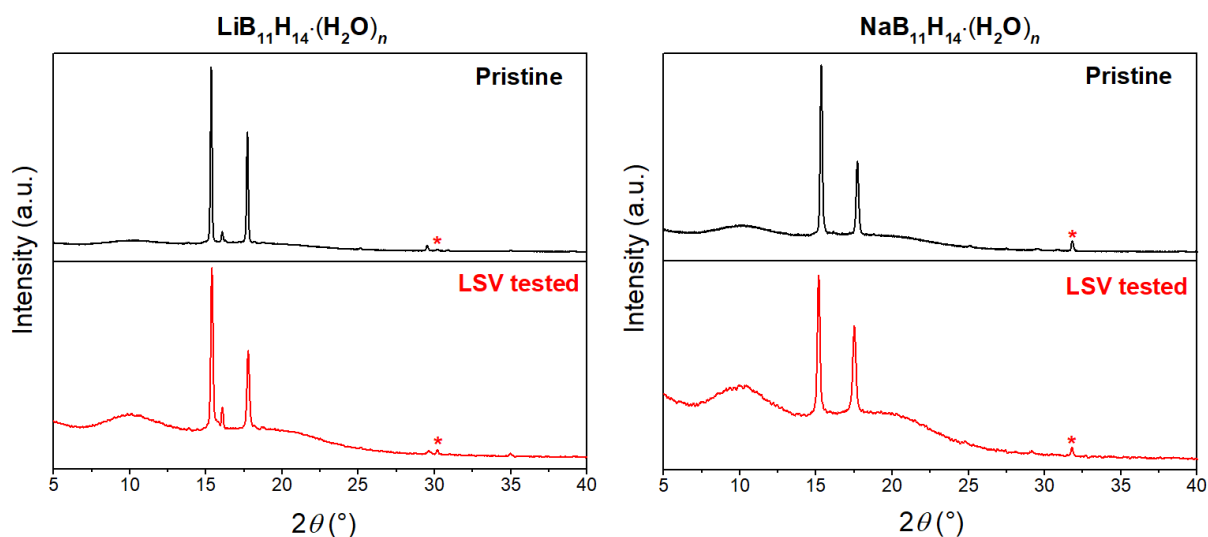


**Figure 3.31** XRPD profiles of  $\text{LiB}_{11}\text{H}_{14}\cdot(\text{H}_2\text{O})_n$  (left) and  $\text{NaB}_{11}\text{H}_{14}\cdot(\text{H}_2\text{O})_n$  (right) at room temperature before (black) and after (red) second run of LSV experiment. Asterisks at  $2\theta = 30.2^\circ$  in the  $\text{LiB}_{11}\text{H}_{14}\cdot(\text{H}_2\text{O})_n$  and at  $31.8^\circ$  in the  $\text{NaB}_{11}\text{H}_{14}\cdot(\text{H}_2\text{O})_n$  patterns represent inadvertent LiCl and NaCl contamination, respectively.

The high ionic conductivity exhibited by  $\text{LiB}_{11}\text{H}_{14}\cdot(\text{H}_2\text{O})_n$  and  $\text{NaB}_{11}\text{H}_{14}\cdot(\text{H}_2\text{O})_n$  and their stability against Li and Na metal anodes, respectively, means that both materials become promising candidates to be used to form new mixed-anion boranes as solid-state electrolytes. Fig. 3.28 shows the Arrhenius plots of the ionic conductivities of some mixed-anion metal boron-hydrogen materials compared to  $\text{LiB}_{11}\text{H}_{14}\cdot(\text{H}_2\text{O})_n$  and  $\text{NaB}_{11}\text{H}_{14}\cdot(\text{H}_2\text{O})_n$ . As previously reported [9], the  $0.7\text{Li}(\text{CB}_9\text{H}_{10})\text{-}0.3\text{Li}(\text{CB}_{11}\text{H}_{12})$  mixed-anion system exhibits superionic conductivity at room temperature,  $6.7 \times 10^{-3} \text{ S cm}^{-1}$  (Fig. 3.28), however, this material is formed by a mixture of two metal carboranes that present lower  $\text{Li}^+$  conductivity than  $\text{LiB}_{11}\text{H}_{14}\cdot(\text{H}_2\text{O})_n$  at room temperature (Fig. 3.27) and higher cost.  $\text{Na}_2(\text{CB}_9\text{H}_{10})(\text{CB}_{11}\text{H}_{12})$  [76] and  $\text{Na}_4\text{C}(\text{B}_{11}\text{H}_{12})_2(\text{B}_{12}\text{H}_{12})$  [75] are also formed by a mixture of metal boranes that individually exhibit lower ionic conductivity at  $25^\circ\text{C}$  (Fig. 3.27) and higher cost than  $\text{NaB}_{11}\text{H}_{14}\cdot(\text{H}_2\text{O})_n$ . The hydrated sodium *nido*-borane even presents higher ionic conductivity than other mixed-anion compounds, such as  $\text{Na}_4(\text{B}_{12}\text{H}_{12})(\text{B}_{10}\text{H}_{10})$  [78] and  $\text{Na}_3(\text{BH}_4)(\text{B}_{12}\text{H}_{12})$  [77] (Fig. 3.28).

It should be noted that the presence of solvated water in the as-synthesised  $\text{NaB}_{11}\text{H}_{14}\cdot(\text{H}_2\text{O})_n$  confirmed by FTIR, TDA-MS, and TGA-DSC data has not previously been identified by researchers in their  $\text{NaB}_{11}\text{H}_{14}$  samples [21,25]. Second, inconsistencies are reported between different batches of commercial  $\text{NaB}_{11}\text{H}_{14}$  [21], which raises doubts on their exact stoichiometry or purity. In previous research [25], heating  $\text{NaB}_{11}\text{H}_{14}$  above  $100^\circ\text{C}$ , results in a

significant formation ( $\approx 50\%$  from NMR) of, what is identified here as,  $B_{11}H_{13}OH^-$ . Based on our investigation of the synthesis, this by-product is only formed if the powder contains acidic hydronium ( $H_3O^+$ ) cations, akin to previous research on  $B_{10}H_{10}^{2-}$  and  $B_{12}H_{12}^-$  [27]. Possibly, the reported  $NaB_{11}H_{14}$  ionic conductivity studies had solid-solutions, solvates, or multi-phase compounds, which would explain the differences observed between the many different crystallographic polymorphs or phases present [21,25]. Despite this, the measured ionic conductivities of  $NaB_{11}H_{14}$  are, in most cases, similar.

### 3.4 CONCLUSIONS

An optimised low cost procedure for the preparation of  $MB_{11}H_{14}\cdot(H_2O)_n$  ( $M = Li$  and  $Na$ ), and  $KB_{11}H_{14}$  and a proposed reaction mechanism are presented. This comprehensive study fills a gap in the literature, which has unexplained differences between  $NaB_{11}H_{14}$  samples depending on their origin or synthetic method. The use of diethyl ether to extract *nido*-borane salts from the aqueous medium is an important finding in order to avoid hydrolysis of the cage and to isolate it from boric acid. Of great importance is also the discovery that acidification of the  $B_{11}H_{13}^{2-}$ , precursor during synthesis, can also form the hydronium salt of  $B_{11}H_{14}^-$ , i.e.  $(H_3O)B_{11}H_{14}$ . The hydronium salt reacts upon heating / drying and releases hydrogen to form  $B_{11}H_{13}OH^-$  as a side product. This important finding may explain some of the differing literature results on  $NaB_{11}H_{14}$ . The hydronium salt formation is more prevalent with smaller cations as  $KB_{11}H_{14}$  is formed without this impurity. The presence of solvated water in powders of  $LiB_{11}H_{14}$  and  $NaB_{11}H_{14}$  is confirmed by FTIR, TDA-MS, and TGA-DSC, whereas  $KB_{11}H_{14}$  is anhydrous, likely due to its larger radius and thus lower charge density, making it less coordinating towards this molecule. All  $MB_{11}H_{14}$  compounds decompose at  $\approx 210$  °C with release of hydrogen. Additionally,  $KB_{11}H_{14}$  undergoes a reversible polymorphic phase transition upon heating / cooling between 40 and 170 °C. The room temperature crystal structure of  $KB_{11}H_{14}$  was solved in space group  $P\bar{1}$  and assume a high temperature face centred cubic polymorph ( $Fm\bar{3}m$ ) exhibiting increased ionic conductivity results. The crystal structure of  $LiB_{11}H_{14}\cdot 2H_2O$  was indexed in  $C2/c$ , and upon dehydration,  $LiB_{11}H_{14}\cdot(H_2O)_n$  ( $n < 2$ ) exhibits a face centred cubic polymorph, which matches with the structure type seen for  $NaB_{11}H_{14}\cdot(H_2O)_n$  at room temperature and  $\beta$ - $KB_{11}H_{14}$  polymorph. This suggests that the high ionic conductivity observed for those samples may be related to the dynamics in the cubic crystal structure they exhibit.

$\text{LiB}_{11}\text{H}_{14}\cdot(\text{H}_2\text{O})_n$  and  $\text{NaB}_{11}\text{H}_{14}\cdot(\text{H}_2\text{O})_n$  feature promising ionic conductivity at room temperature,  $1.8 \times 10^{-4} \text{ S cm}^{-1}$  and  $1.1 \times 10^{-3} \text{ S cm}^{-1}$ , respectively, and even show conductivity at sub-zero temperatures, such as  $-30 \text{ }^\circ\text{C}$ . These outstanding results may be related to as-yet-unknown reorientational dynamics within the crystal structure or due to the fact that the cation is solvated with water, which may facilitate the migration of the cation through the crystal structure. Moreover, the oxidative stability limit of  $\text{LiB}_{11}\text{H}_{14}\cdot(\text{H}_2\text{O})_n$  and  $\text{NaB}_{11}\text{H}_{14}\cdot(\text{H}_2\text{O})_n$  were identified as 2.1 V vs.  $\text{Li}^+/\text{Li}$  and 2.6 V vs.  $\text{Na}^+/\text{Na}$ , respectively.

$\text{LiB}_{11}\text{H}_{14}\cdot(\text{H}_2\text{O})_n$  and  $\text{NaB}_{11}\text{H}_{14}\cdot(\text{H}_2\text{O})_n$  are considered some of the best metal boron-hydrogen ion conductors within the respective cation compound class. Besides that, the safe and low-cost synthesis method enables these materials to be produced on a scale for practical applications. Finally, the synthesised compounds may act as precursors in future work to prepare mixed-anion compounds with even higher ionic conductivities. The results show great promise towards the development of a solid-state electrolyte, and eventually ASSBs, however further battery studies involving these electrolytes need to be undertaken.

### 3.6 REFERENCES

- [1] B.R.S. Hansen, M. Paskevicius, M. Jørgensen, T.R. Jensen, Halogenated Sodium-*closo*-Dodecaboranes as Solid-State Ion Conductors, *Chem. Mater.* 29 (2017) 3423–3430. <https://doi.org/10.1021/acs.chemmater.6b04797>.
- [2] B.C. Liu, F. Li, L. Ma, H. Cheng, Advanced Materials for Energy Storage, *Adv. Mater.* 22 (2010) E28–E62. <https://doi.org/10.1002/adma.200903328>.
- [3] H. Chen, T. Ngoc Cong, W. Yang, C. Tan, Y. Li, Y. Ding, Progress in electrical energy storage system: A critical review, *Prog. Nat. Sci.* 19 (2009) 291–312. <https://doi.org/10.1016/j.pnsc.2008.07.014>.
- [4] A. Mauger, C.M. Julien, A. Paoletta, M. Armand, K. Zaghib, Building Better Batteries in the Solid State: A Review, *Materials.* 12 (2019) 3892. <https://doi.org/10.3390/ma12233892>.
- [5] J.C. Bachman, S. Muy, A. Grimaud, H. Chang, N. Pour, S.F. Lux, O. Paschos, F. Maglia, S. Lupart, P. Lamp, L. Giordano, Y. Shao-Horn, Inorganic Solid-State Electrolytes for Lithium Batteries: Mechanisms and Properties Governing Ion Conduction, *Chem. Rev.* 116 (2016) 140–162. <https://doi.org/10.1021/acs.chemrev.5b00563>.
- [6] A. Gigante, L. Duchene, R. Moury, M. Pupier, A. Remhof, H. Hagemann, Direct Solution-

- Based Synthesis of  $\text{Na}_4(\text{B}_{12}\text{H}_{12})(\text{B}_{10}\text{H}_{10})$  Solid Electrolyte, *ChemSusChem*. 12 (2019) 4832–4837. <https://doi.org/10.1002/cssc.201902152>.
- [7] F. Zheng, M. Kotobuki, S. Song, M.O. Lai, L. Lu, Review on solid electrolytes for all-solid-state lithium-ion batteries, *J. Power Sources*. 389 (2018) 198–213. <https://doi.org/10.1016/j.jpowsour.2018.04.022>.
- [8] M. Ue, K. Uosaki, Recent progress in liquid electrolytes for lithium metal batteries, *Curr. Opin. Electrochem*. 17 (2019) 106–113. <https://doi.org/10.1016/j.coelec.2019.05.001>.
- [9] S. Kim, H. Oguchi, N. Toyama, T. Sato, S. Takagi, T. Otomo, D. Arunkumar, N. Kuwata, J. Kawamura, S. Orimo, A complex hydride lithium superionic conductor for high-energy-density all-solid-state lithium metal batteries, *Nat. Commun*. 10 (2019) 1–9. <https://doi.org/10.1038/s41467-019-09061-9>.
- [10] Z. Lu, F. Ciucci, Metal Borohydrides as Electrolytes for Solid-State Li, Na, Mg, and Ca Batteries: A First-Principles Study, *Chem. Mater*. 29 (2017) 9308–9319. <https://doi.org/10.1021/acs.chemmater.7b03284>.
- [11] S.B. Aziz, T.J. Woo, M.F.Z. Kadir, H.M. Ahmed, A conceptual review on polymer electrolytes and ion transport models, *J. Sci. Adv. Mater. Devices*. 3 (2018) 1–17. <https://doi.org/10.1016/j.jsamd.2018.01.002>.
- [12] T. Yang, J. Zheng, Q. Cheng, Y. Hu, C.K. Chan, Composite Polymer Electrolytes with  $\text{Li}_7\text{La}_3\text{Zr}_2\text{O}_{12}$  Garnet-Type Nanowires as Ceramic Fillers: Mechanism of Conductivity Enhancement and Role of Doping and Morphology, *ACS Appl. Mater. Interfaces*. 9 (2017) 21773–21780. <https://doi.org/10.1021/acsami.7b03806>.
- [13] Y. Ren, K. Chen, R. Chen, T. Liu, Y. Zhang, C. Nan, Oxide Electrolytes for Lithium Batteries, *J. Am. Ceram. Soc*. 98 (2015) 3603–3623. <https://doi.org/10.1111/jace.13844>.
- [14] V. Thangadurai, S. Narayanan, D. Pinzaru, Garnet-type solid-state fast Li ion conductors for Li batteries: critical review, *Chem. Soc. Rev*. 43 (2014) 4714–4727. <https://doi.org/10.1039/c4cs00020j>.
- [15] Z. Jiang, T. Liang, Y. Liu, S. Zhang, Z. Li, D. Wang, X. Wang, X. Xia, C. Gu, J. Tu, Improved Ionic Conductivity and Li Dendrite Suppression Capability toward  $\text{Li}_7\text{P}_3\text{S}_{11}$ -Based Solid Electrolytes Triggered by Nb and O Cosubstitution, *ACS Appl. Mater. Interfaces*. 12 (2020) 54662–54670. <https://doi.org/10.1021/acsami.0c15903>.
- [16] H. Pan, Z. Cheng, P. He, H. Zhou, A Review of Solid-State Lithium-Sulfur Battery: Ion



- Transport and Polysulfide Chemistry, *Energy and Fuels*. 34 (2020) 11942–11961. <https://doi.org/10.1021/acs.energyfuels.0c02647>.
- [17] F. Han, Y. Zhu, X. He, Y. Mo, C. Wang, Electrochemical stability of  $\text{Li}_{10}\text{GeP}_2\text{S}_{12}$  and  $\text{Li}_7\text{La}_3\text{Zr}_2\text{O}_{12}$  solid electrolytes, *Adv. Energy Mater.* 6 (2016) 1501590. <https://doi.org/10.1002/aenm.201501590>.
- [18] B.R.S. Hansen, M. Paskevicius, H. Li, E. Akiba, T.R. Jensen, Metal boranes: Progress and applications, *Coord. Chem. Rev.* 323 (2016) 60–70. <https://doi.org/10.1016/j.ccr.2015.12.003>.
- [19] M. Paskevicius, L.H. Jepsen, P. Schouwink, R. Černý, D.B. Ravnsbæk, Y. Filinchuk, M. Dornheim, F. Besenbacher, T.R. Jensen, Metal borohydrides and derivatives - synthesis, structure and properties, *Chem. Soc. Rev.* 46 (2017) 1565–1634. <https://doi.org/10.1039/c6cs00705h>.
- [20] W.S. Tang, M. Matsuo, H. Wu, V. Stavila, W. Zhou, A.A. Talin, A. V Soloninin, R. V Skoryunov, O.A. Babanova, A. V Skripov, A. Unemoto, S.I. Orimo, T.J. Udovic, Liquid-like ionic conduction in solid lithium and sodium monocarba-*closo*-decaborates near or at room temperature, *Adv. Energy Mater.* 6 (2016) 1502237. <https://doi.org/10.1002/aenm.201502237>.
- [21] W.S. Tang, M. Dimitrievska, V. Stavila, W. Zhou, H. Wu, A.A. Talin, T.J. Udovic, Order-disorder transitions and superionic conductivity in the sodium *nido*-undeca(carba)borates, *Chem. Mater.* 29 (2017) 10496–10509. <https://doi.org/10.1021/acs.chemmater.7b04332>.
- [22] T.J. Udovic, M. Matsuo, A. Unemoto, N. Verdál, V. Stavila, A. V. Skripov, J.J. Rush, H. Takamura, S.I. Orimo, Sodium superionic conduction in  $\text{Na}_2\text{B}_{12}\text{H}_{12}$ , *Chem. Commun.* 50 (2014) 3750–3752. <https://doi.org/10.1039/c3cc49805k>.
- [23] Z. Jian, W. Luo, X. Ji, Carbon Electrodes for K-Ion Batteries, *J. Am. Chem. Soc.* 137 (2015) 11566–11569. <https://doi.org/10.1021/jacs.5b06809>.
- [24] B.L. Ellis, L.F. Nazar, Sodium and sodium-ion energy storage batteries, *Curr. Opin. Solid State Mater. Sci.* 16 (2012) 168–177. <https://doi.org/10.1016/j.cossms.2012.04.002>.
- [25] S. Payandeh, R. Asakura, P. Avramidou, D. Rentsch, Ł. Zbigniew, C. Radovan, A. Remhof, C. Battaglia, *Nido-Borate/Closo-Borate Mixed-Anion Electrolytes for All-Solid-State Batteries*, *Chem. Mater.* 32 (2020) 1101–1110. <https://doi.org/10.1021/acs.chemmater.9b03933>.

- [26] G.B. Dunks, K. Barker, E. Hedaya, C. Hefner, K. Palmer-Ordonez, P. Remec, Synthesis of  $B_{10}H_{14}$  from  $NaBH_4$  via  $B_{11}H_{14}^-$  Ion, *Inorg. Chem.* 20 (1981) 1692–1697. <https://doi.org/10.1017/CBO9781107415324.004>.
- [27] E.L. Muetterties, J.H. Balthis, Y.T. Chia, W.H. Knoth, H.C. Miller, Chemistry of boranes. VIII. Salts and Acids of  $B_{10}H_{10}^{2-}$  and  $B_{12}H_{12}^{2-}$ , *Inorg. Chem.* 3 (1964) 444–451. <https://doi.org/10.1021/ic50013a030>.
- [28] F. Klanberg, E.L. Muetterties, Boron-Hydrogen Compounds, in: W.L. Jolly (Ed.), *Inorg. Synth.*, Volume XI, McGraw-Hill Book Company, New York, 1968: pp. 24–32.
- [29] G.M. Sheldrick, *SHELXT* - Integrated space-group and crystal-structure determination, *Acta Crystallogr. Sect. A Found. Adv.* A71 (2015) 3–8. <https://doi.org/10.1107/S2053273314026370>.
- [30] G.M. Sheldrick, Crystal structure refinement with *SHELXL*, *Acta Crystallogr. Sect. C Struct. Chem.* C71 (2015) 3–8. <https://doi.org/10.1107/S2053229614024218>.
- [31] O. V. Dolomanov, L.J. Bourhis, R.J. Gildea, J.A.K. Howard, H. Puschmann, *OLEX2*: A complete structure solution, refinement and analysis program, *J. Appl. Crystallogr.* 42 (2009) 339–341. <https://doi.org/10.1107/S0021889808042726>.
- [32] R. Asakura, L. Duchêne, R.S. Kühnel, A. Remhof, H. Hagemann, C. Battaglia, Electrochemical Oxidative Stability of Hydroborate-Based Solid-State Electrolytes, *ACS Appl. Energy Mater.* 2 (2019) 6924–6930. <https://doi.org/10.1021/acsaem.9b01487>.
- [33] M. Paskevicius, M.B. Ley, D.A. Sheppard, T.R. Jensen, C.E. Buckley, Eutectic melting in metal borohydrides, *Phys. Chem. Chem. Phys.* 15 (2013) 19774–19789. <https://doi.org/10.1039/c3cp53920b>.
- [34] M.J. Frisch, G.W. Trucks, H.B. Schlegel, G.E. Scuseria, M.A. Robb, J.R. Cheeseman, G. Scalmani, V. Barone, G. a. Petersson, H. Nakatsuji, X. Li, M. Caricato, a. V. Marenich, J. Bloino, B.G. Janesko, R. Gomperts, B. Mennucci, H.P. Hratchian, J. V. Ortiz, a. F. Izmaylov, J.L. Sonnenberg, Williams, F. Ding, F. Lipparini, F. Egidi, J. Goings, B. Peng, A. Petrone, T. Henderson, D. Ranasinghe, V.G. Zakrzewski, J. Gao, N. Rega, G. Zheng, W. Liang, M. Hada, M. Ehara, K. Toyota, R. Fukuda, J. Hasegawa, M. Ishida, T. Nakajima, Y. Honda, O. Kitao, H. Nakai, T. Vreven, K. Throssell, J. a. Montgomery Jr., J.E. Peralta, F. Ogliaro, M.J. Bearpark, J.J. Heyd, E.N. Brothers, K.N. Kudin, V.N. Staroverov, T. a. Keith, R. Kobayashi, J. Normand, K. Raghavachari, a. P. Rendell, J.C. Burant, S.S. Iyengar, J. Tomasi, M. Cossi, J.M. Millam, M. Klene, C. Adamo, R. Cammi, J.W. Ochterski, R.L.

- Martin, K. Morokuma, O. Farkas, J.B. Foresman, D.J. Fox, Gaussian 09, Revision A. 02, Gaussian 09, Revis. A. 02. (2009).
- [35] R.A. Kendall, T.H. Dunning, R.J. Harrison, Electron affinities of the first-row atoms revisited. Systematic basis sets and wave functions, *J. Chem. Phys.* 96 (1992) 6796–6806. <https://doi.org/10.1063/1.462569>.
- [36] A.E. Reed, R.B. Weinstock, F. Weinhold, Natural population analysis, *J. Chem. Phys.* 83 (1985) 735–746. <https://doi.org/10.1063/1.449486>.
- [37] R. Ditchfield, Self-consistent perturbation theory of diamagnetism I. A gauge-invariant LCAO method for N.M.R. Chemical shifts, *Mol. Phys.* 27 (1974) 789–807. <https://doi.org/10.1080/00268977400100711>.
- [38] V. Barone, M. Cossi, Quantum Calculation of Molecular Energies and Energy Gradients in Solution by a Conductor Solvent Model, *J. Phys. Chem. A.* 102 (1998) 1995–2001. <https://doi.org/10.1021/jp9716997>.
- [39] P. Gao, X. Wang, Z. Huang, H. Yu, <sup>11</sup>B NMR chemical shift predictions via density functional theory and gauge-including atomic orbital approach: Applications to structural elucidations of boron-containing molecules, *ACS Omega.* 4 (2019) 12385–12392. <https://doi.org/10.1021/acsomega.9b01566>.
- [40] H.S. Rzepa, S. Arkhipenko, E. Wan, M.T. Sabatini, V. Karaluka, A. Whiting, T.D. Sheppard, An Accessible Method for DFT Calculation of <sup>11</sup>B NMR Shifts of Organoboron Compounds, *J. Org. Chem.* 83 (2018) 8020–8025. <https://doi.org/10.1021/acs.joc.8b00859>.
- [41] V.D. Aftandilian, H.C. Miller, G.W. Parshall, E.L. Muetterties, Chemistry of Boranes. V. First Example of a B<sub>11</sub> Hydride, the B<sub>11</sub>H<sub>14</sub><sup>-</sup> Anion, *Inorg. Chem.* 1 (1962) 734–737. <https://doi.org/10.1021/ic50004a003>.
- [42] N.S. Hosmane, J.R. Wermer, Z. Hong, T.D. Getman, S.G. Shore, High-Yield Preparation of the Tetradecahydroundecaborate(1-) Anion, [B<sub>11</sub>H<sub>14</sub>]<sup>-</sup> from Pentaborane(9), *Inorg. Chem.* 26 (1987) 3638–3639. <https://doi.org/10.1021/ic00268a045>.
- [43] H.C. Miller, N.E. Miller, E.L. Muetterties, Chemistry of Boranes. XX. Syntheses of Polyhedral Boranes, *Inorg. Chem.* 3 (1964) 1456–1463. <https://doi.org/10.1021/ic50020a026>.
- [44] L.V. Titov, L. V. Zhemchugova, L.A. Gavrilova, P. V. Petrovskii, Dehydrocondensation of a mixture of anions B<sub>3</sub>H<sub>8</sub><sup>-</sup> and B<sub>9</sub>H<sub>14</sub><sup>-</sup> by Diborane: Synthesis of Salts NaB<sub>11</sub>H<sub>14</sub>.3Dn and

- Bu<sub>4</sub>NB<sub>11</sub>H<sub>14</sub> (Dn = 1,4-Dioxane), Russ. J. Inorg. Chem. 50 (2005) 1215–1217.
- [45] E.A.V. Ebsworth, N. Sheppard, The infra-red spectra of some methylammonium iodides: angle deformation frequencies of <sup>+</sup>NH and <sup>+</sup>NH<sub>2</sub> groups, Spectrochim. Acta. 13 (1959) 261–270. [https://doi.org/10.1016/0371-1951\(59\)80026-6](https://doi.org/10.1016/0371-1951(59)80026-6).
- [46] J. Pecyna, I. Rončević, J. Michl, Insertion of Carbenes into Deprotonated *nido*-Undecaborane, B<sub>11</sub>H<sub>13</sub>(2-), Molecules. 24 (2019) 3779. <https://doi.org/10.3390/molecules24203779>.
- [47] M. Bishop, N. Shahid, J. Yang, A.R. Barron, Determination of the mode and efficacy of the cross-linking of guar by borate using MAS <sup>11</sup>B NMR of borate cross-linked guar in combination with solution <sup>11</sup>B NMR of model systems, Dalt. Trans. (2004) 2621–2634. <https://doi.org/10.1039/b406952h>.
- [48] Z. Łodziana, P. Błoński, Y. Yan, D. Rentsch, A. Remhof, NMR Chemical Shifts of <sup>11</sup>B in Metal Borohydrides from First Principle Calculations, He J. Phys. Chem. C. 118 (2014) 6594–6603. <https://doi.org/10.1021/jp4120833>.
- [49] O. Volkov, K. Radacki, P. Paetzold, X. Zheng, Dodecahydro-*closo*-undecaborate [B<sub>11</sub>H<sub>12</sub>]<sup>-</sup>, Zeitschrift Für Anorg. Und Allg. Chemie. 627 (2001) 1185–1191. [https://doi.org/10.1002/1521-3749\(200106\)627:6<1185::AID-ZAAC1185>3.0.CO;2-F](https://doi.org/10.1002/1521-3749(200106)627:6<1185::AID-ZAAC1185>3.0.CO;2-F).
- [50] Y. Marcus, Volumes of aqueous hydrogen and hydroxide ions at 0 to 200 °C, J. Chem. Phys. 137 (2012) 154501. <https://doi.org/10.1063/1.4758071>.
- [51] J. Mähler, I. Persson, A study of the hydration of the alkali metal ions in aqueous solution, Inorg. Chem. 51 (2012) 425–438. <https://doi.org/10.1021/ic2018693>.
- [52] L.A. Leites, Vibrational Spectroscopy of Carboranes and Parent Boranes and Its Capabilities in Carborane Chemistry, Chem. Rev. 92 (1992) 279–323. <https://doi.org/10.1021/cr00010a006>.
- [53] D. Sethio, L.M. Lawson Daku, H. Hagemann, Computational study of the vibrational spectroscopy properties of boron-hydrogen compounds: Mg(B<sub>3</sub>H<sub>8</sub>)<sub>2</sub>, CB<sub>9</sub>H<sub>10</sub><sup>-</sup> and CB<sub>11</sub>H<sub>12</sub><sup>-</sup>, Int. J. Hydrogen Energy. 42 (2017) 22496–22501. <https://doi.org/10.1016/j.ijhydene.2017.03.044>.
- [54] P. Broadhead, G.A. Newman, OH groups and hydrogen bonding in some boron-oxygen compounds, Spectrochim. Acta Part A Mol. Spectrosc. 28 (1972) 1915–1923. [https://doi.org/10.1016/0584-8539\(72\)80163-6](https://doi.org/10.1016/0584-8539(72)80163-6).
- [55] B. Hribar, N.T. Southall, V. Vlachy, K.A. Dill, How ions affect the structure of water, J.

- Am. Chem. Soc. 124 (2002) 12302–12311. <https://doi.org/10.1021/ja026014h>.
- [56] D. Sveinbjörnsson, J.S.G. Myrdal, D. Blanchard, J.J. Bentzen, T. Hirata, M.B. Mogensen, P. Norby, S.I. Orimo, T. Vegge, Effect of heat treatment on the lithium ion conduction of the  $\text{LiBH}_4\text{-LiI}$  solid solution, *J. Phys. Chem. C.* 117 (2013) 3249–3257. <https://doi.org/10.1021/jp310050g>.
- [57] S. Kim, N. Toyama, H. Oguchi, T. Sato, S. Takagi, T. Ikeshoji, S. Orimo, Fast Lithium-Ion Conduction in Atom-Deficient *closo*-Type Complex Hydride Solid Electrolytes, *Chem. Mater.* 30 (2018) 386–391. <https://doi.org/10.1021/acs.chemmater.7b03986>.
- [58] R. Černý, M. Brighi, F. Murgia, The Crystal Chemistry of Inorganic Hydroborates, *Chemistry.* 2 (2020) 805–826. <https://doi.org/10.3390/chemistry2040053>.
- [59] N. Kamaya, K. Homma, Y. Yamakawa, M. Hirayama, R. Kanno, M. Yonemura, T. Kamiyama, Y. Kato, S. Hama, K. Kawamoto, A. Mitsui, A lithium superionic conductor, *Nat. Mater.* 10 (2011) 682–686. <https://doi.org/10.1038/nmat3066>.
- [60] A. Gradišek, M. Krnel, M. Paskevicius, B.R.S. Hansen, T.R. Jensen, J. Dolinšek, Reorientational Motions and Ionic Conductivity in  $(\text{NH}_4)_2\text{B}_{10}\text{H}_{10}$  and  $(\text{NH}_4)_2\text{B}_{12}\text{H}_{12}$ , *J. Phys. Chem. C.* 122 (2018) 17073–17079. <https://doi.org/10.1021/acs.jpcc.8b04605>.
- [61] J.B. Grinderslev, K.T. Møller, Y. Yan, X.M. Chen, Y. Li, H.W. Li, W. Zhou, J. Skibsted, X. Chen, T.R. Jensen, Potassium octahydridotriborate: Diverse polymorphism in a potential hydrogen storage material and potassium ion conductor, *Dalt. Trans.* 48 (2019) 8872–8881. <https://doi.org/10.1039/c9dt00742c>.
- [62] Y. Sadikin, R. V. Skoryunov, O.A. Babanova, A. V. Soloninin, Z. Lodziana, M. Brighi, A. V. Skripov, R. Černý, Anion Disorder in  $\text{K}_3\text{BH}_4\text{B}_{12}\text{H}_{12}$  and Its Effect on Cation Mobility, *J. Phys. Chem. C.* 121 (2017) 5503–5514. <https://doi.org/10.1021/acs.jpcc.7b00364>.
- [63] M. Dimitrievska, H. Wu, V. Stavila, O.A. Babanova, R. V. Skoryunov, A. V. Soloninin, W. Zhou, B.A. Trump, M.S. Andersson, A. V. Skripov, T.J. Udovic, Structural and dynamical properties of potassium dodecahydro-monocarpa-*closo*-dodecaborate:  $\text{KCB}_{11}\text{H}_{12}$ , *J. Phys. Chem. C.* 124 (2020) 17992–18002. <https://doi.org/10.1021/acs.jpcc.0c05038>.
- [64] W.S. Tang, M. Matsuo, H. Wu, V. Stavila, A. Unemoto, S.I. Orimo, T.J. Udovic, Stabilizing lithium and sodium fast-ion conduction in solid polyhedral-borate salts at device-relevant temperatures, *Energy Storage Mater.* 4 (2016) 79–83. <https://doi.org/10.1016/j.ensm.2016.03.004>.
- [65] M.N. Guzik, R. Mohtadi, S. Sartori, Lightweight complex metal hydrides for Li-, Na-, and

- Mg-based batteries, *J. Mater. Res.* 34 (2019) 877–904. <https://doi.org/10.1557/jmr.2019.82>.
- [66] K.T. Møller, M. Paskevicius, J.G. Andreasen, J. Lee, N. Chen-Tan, J. Overgaard, S. Payandeh, D.S. Silvester, C.E. Buckley, T.R. Jensen, Molten metal *closo*-borate solvates, *Chem. Commun.* 55 (2019) 3410–3413. <https://doi.org/10.1039/c9cc00187e>.
- [67] S. Tang, H. Zhao, Glymes as versatile solvents for chemical reactions and processes: From the laboratory to industry, *RSC Adv.* 4 (2014) 11251–11287. <https://doi.org/10.1039/c3ra47191h>.
- [68] Y. Yan, J.B. Grinderslev, Y.-S. Lee, M. Jørgensen, Y.W. Cho, R. Černý, T.R. Jensen, Ammonia-assisted fast Li-ion conductivity in a new hemiammine lithium borohydride,  $\text{LiBH}_4 \cdot 1/2\text{NH}_3$ , *Chem. Commun.* 56 (2020) 3971–3974. <https://doi.org/10.1039/c9cc09990e>.
- [69] T.J. Udovic, M. Matsuo, W.S. Tang, H. Wu, V. Stavila, A. V Soloninin, R. V Skoryunov, O.A. Babanova, A. V Skripov, J.J. Rush, A. Unemoto, H. Takamura, S. Orimo, Exceptional Superionic Conductivity in Disordered Sodium Decahydro-*closo*-decaborate, *Adv. Mater.* 26 (2014) 7622–7626. <https://doi.org/10.1002/adma.201403157>.
- [70] W.S. Tang, A. Unemoto, W. Zhou, V. Stavila, M. Matsuo, H. Wu, S. Orimo, T.J. Udovic, Unparalleled lithium and sodium superionic conduction in solid electrolytes with large monovalent cage-like anions, *Energy Environ. Sci.* 8 (2015) 3637–3645. <https://doi.org/10.1039/c5ee02941d>.
- [71] A. Unemoto, K. Yoshida, T. Ikeshoji, S. Orimo, Bulk-type all-solid-state lithium batteries using complex hydrides containing cluster-anions, *Mater. Trans.* 57 (2016) 1639–1644. <https://doi.org/10.2320/matertrans.MAW201601>.
- [72] L. He, H. Li, H. Nakajima, N. Tumanov, Y. Filinchuk, S. Hwang, M. Sharma, H. Hagemann, E. Akiba, Synthesis of a Bimetallic Dodecaborate  $\text{LiNaB}_{12}\text{H}_{12}$  with Outstanding Superionic Conductivity, *Chem. Mater.* 27 (2015) 5483–5486. <https://doi.org/10.1021/acs.chemmater.5b01568>.
- [73] M. Matsuo, A. Remhof, P. Martelli, R. Caputo, M. Ernst, Y. Miura, T. Sato, H. Oguchi, H. Maekawa, H. Takamura, A. Borgschulte, A. Züttel, S.I. Orimo, Complex hydrides with  $(\text{BH}_4)^-$  and  $(\text{NH}_2)^-$  anions as new lithium fast-ion conductors, *J. Am. Chem. Soc.* 131 (2009) 16389–16391. <https://doi.org/10.1021/ja907249p>.
- [74] T. Zhang, Y. Wang, T. Song, H. Miyaoka, K. Shinzato, H. Miyaoka, T. Ichikawa, S. Shi, X.

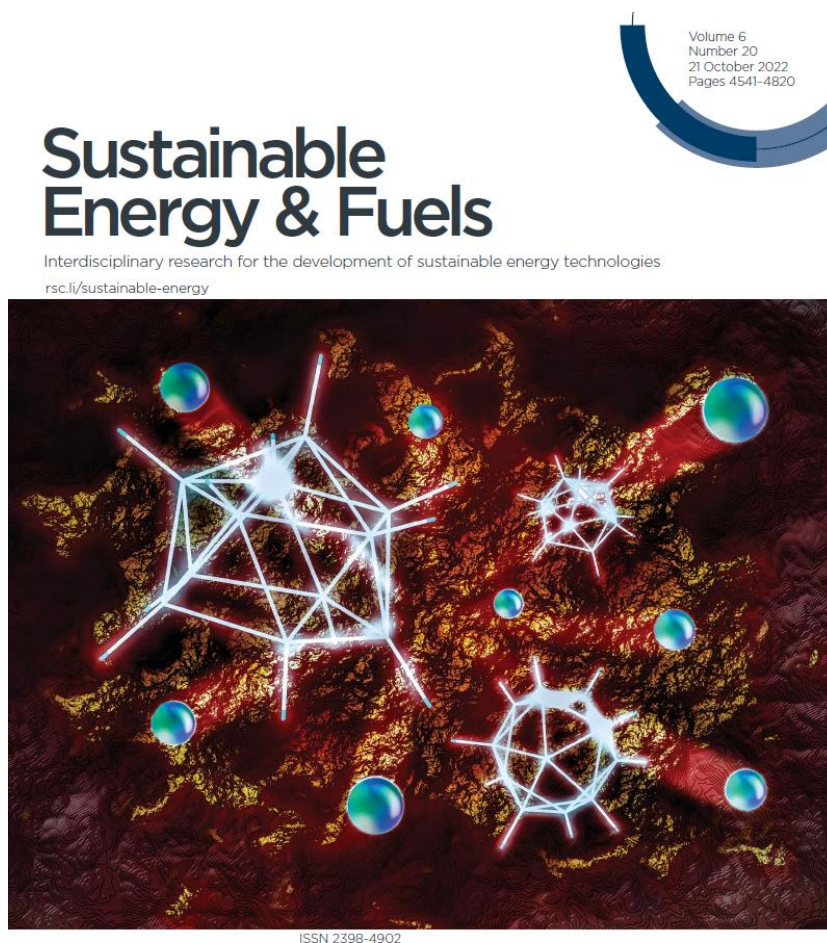
- Zhang, S. Isobe, N. Hashimoto, Y. Kojima, Ammonia, a Switch for Controlling High Ionic Conductivity in Lithium Borohydride Ammoniates, *Joule*. 2 (2018) 1522–1533. <https://doi.org/10.1016/j.joule.2018.04.015>.
- [75] R. Asakura, D. Reber, L. Duchêne, S. Payandeh, A. Remhof, H. Hagemann, C. Battaglia, 4 V Room-Temperature All-Solid-State Sodium Battery Enabled By a Passivating Cathode/Hydroborate Solid Electrolyte Interface, *Energy Environ. Sci.* 13 (2020) 5048–5058. <https://doi.org/10.1039/d0ee01569e>.
- [76] W.S. Tang, K. Yoshida, A. V. Soloninin, R. V. Skoryunov, O.A. Babanova, A. V. Skripov, M. Dimitrievska, V. Stavila, S.I. Orimo, T.J. Udovic, Stabilizing Superionic-Conducting Structures via Mixed-Anion Solid Solutions of Monocarba-*closo*-borate Salts, *ACS Energy Lett.* 1 (2016) 659–664. <https://doi.org/10.1021/acsenergylett.6b00310>.
- [77] Y. Sadikin, M. Brighi, P. Schouwink, R. Černý, Superionic Conduction of Sodium and Lithium in Anion-Mixed Hydroborates  $\text{Na}_3\text{BH}_4\text{B}_{12}\text{H}_{12}$  and  $(\text{Li}_{0.7}\text{Na}_{0.3})_3\text{BH}_4\text{B}_{12}\text{H}_{12}$ , *Adv. Energy Mater.* 5 (2015) 1501016. <https://doi.org/10.1002/aenm.201501016>.
- [78] L. Duchêne, R.S. Kühnel, D. Rentsch, A. Remhof, H. Hagemann, C. Battaglia, A highly stable sodium solid-state electrolyte based on a dodeca/deca-borate equimolar mixture, *Chem. Commun.* 53 (2017) 4195–4198. <https://doi.org/10.1039/c7cc00794a>.
- [79] V. Lacivita, Y. Wang, S.H. Bo, G. Ceder, Ab initio investigation of the stability of electrolyte/electrode interfaces in all-solid-state Na batteries, *J. Mater. Chem. A*. 7 (2019) 8144–8155. <https://doi.org/10.1039/c8ta10498k>.
- [80] L. Zhang, D. Zhang, K. Yang, X. Yan, L. Wang, J. Mi, B. Xu, Y. Li, Vacancy-Contained Tetragonal  $\text{Na}_3\text{SbS}_4$  Superionic Conductor, *Adv. Sci.* 3 (2016) 1–6. <https://doi.org/10.1002/advs.201600089>.

# CHAPTER 4

## Hydrated Lithium *nido*-Boranes for Solid-Liquid Hybrid Batteries

D. H. P. Souza, T.D. Humphries, Y. Liu, A. Gradišek, A.M. D'Angelo, C.E. Buckley, M. Paskevicius, Hydrated Lithium *nido*-Boranes for Solid-Liquid Hybrid Batteries, *Sustain. Energy Fuels*. 6 (2022) 4614–4625. <https://doi.org/10.1039/D2SE00843B>.

Front cover, *Sustain. Energy Fuels*. 6 (2022) 4541–4542. <https://doi.org/10.1039/D2SE90067J>.



 ROYAL SOCIETY  
OF CHEMISTRY

PAPER  
Mark Paskevicius *et al.*  
Hydrated lithium *nido*-boranes for solid-liquid  
hybrid batteries



## ABSTRACT

Hydridoborate salts are considered as promising solid-state electrolyte candidates for the development of solid-state batteries (SSBs). The presence of coordinated water in the crystal structure may facilitate the migration of the cation, yielding compounds with high ionic conductivity. In the present study, two samples of hydrated  $\text{LiB}_{11}\text{H}_{14}$ , here called  $\text{LiB}_{11}\text{H}_{14}\cdot 2\text{H}_2\text{O}$  and  $\alpha\text{-LiB}_{11}\text{H}_{14}\cdot(\text{H}_2\text{O})_n$  ( $n < 2$ ), demonstrate remarkably different properties as solid-state electrolytes.  $\text{LiB}_{11}\text{H}_{14}\cdot 2\text{H}_2\text{O}$  is identified as a new class of ionic liquid, as it melts at  $\approx 70^\circ\text{C}$ , whereas the sample  $\alpha\text{-LiB}_{11}\text{H}_{14}\cdot(\text{H}_2\text{O})_n$  undergoes a polymorphic phase transition close to this temperature, reaching the liquid-like ionic conductivity of  $3.2 \times 10^{-2} \text{ S cm}^{-1}$  at  $70^\circ\text{C}$  and an oxidative stability limit of 2.8 V against  $\text{Li}^+/\text{Li}$ . Galvanostatic cycling and battery tests were conducted with  $\alpha\text{-LiB}_{11}\text{H}_{14}\cdot(\text{H}_2\text{O})_n$  as the solid-state electrolyte (SSE) at  $60^\circ\text{C}$  with the addition of traces of either the ionic liquid (IL)  $\text{LiB}_{11}\text{H}_{14}\cdot 2\text{H}_2\text{O}$  or the liquid electrolyte (LE) 1.0 M  $\text{LiPF}_6$  EC/DMC ( $v/v = 50/50$ ) at their interfaces. Galvanostatic experiments for the cell  $\text{Li}/\text{IL}/\text{SSE}/\text{IL}/\text{Li}$  showed an overpotential of only 21 mV after 9 days cycling (48 h at  $25 \mu\text{A cm}^{-2}$  and 168 h at  $50 \mu\text{A cm}^{-2}$ ), and the battery  $\text{Li}/\text{LE}/\text{SSE}/\text{SSE}+\text{TiS}_2$  retained 83% of its capacity shown in the first cycle at 0.4 C after 50 cycles.  $\text{LiB}_{11}\text{H}_{14}\cdot 2\text{H}_2\text{O}$  and 1.0 M  $\text{LiPF}_6$  EC/DMC work effectively as wetting agents to improve SSE/Li contact.

## 4.1 INTRODUCTION

Liquid-based lithium-ion batteries (LIBs) have been used to power the majority of electronic devices for the last three decades due to their long cycle life and ability to quickly charge [1,2]. However, the development of high-power technologies, such as electric vehicles and large-scale energy storage, require batteries with higher energy density, durability, lower costs and lighter components [3]. Those limitations have brought extensive research on the development of solid-state electrolytes to replace the liquid component of the current generation LIBs as an attempt to resolve their drawbacks [4,5]. Solid-state electrolytes can provide higher thermal stability, improved safety and higher energy storage capacity, as they can be compatible with alternative electrode materials, e.g. lithium metal, which is the target anode material due to its low redox potential ( $-3.04 \text{ V}$  vs. standard hydrogen electrode) and high theoretical capacity ( $3,860 \text{ mAh g}^{-1}$ ) [6–9].

In order to develop the next generation of batteries, the solid-state electrolyte must meet several requirements, including, but not limited to, high ionic conductivity ( $\geq 1 \times 10^{-3} \text{ S cm}^{-1}$ ),

wide electrochemical stability, compatibility with anode and cathode materials, affordable cost, be an electrical insulator and environmentally friendly [1,10,11]. The interfacial resistance between a solid-state electrolyte and the electrode (SSE/electrode) is also a crucial factor for practical solid-state battery applications [12,13]. The formation of a solid-liquid hybrid electrolyte is now seen as a strategy to overcome this issue [14,15]. It has been proven that wetting the interface with the addition of a small amount of an ionic liquid [16–18] or an organic liquid electrolyte [19–21] can improve interfacial contact and performance of the battery [13].

Oxides [22,23] and sulphides [24,25] are commonly studied materials as solid-state electrolytes due to their high ionic conductivities, however some aspects, such as, low electrochemical stability, high interfacial resistance and/or high costs for large-scale production hinder their use in solid-state batteries (SSBs) [26,27]. Lithium boron-hydrogen salts have been recently investigated as solid-state electrolytes due to the disordered polymorphic crystal structures with high ionic conductivity that some of them can assume at higher than ambient temperatures [28–34]. Moreover, some of them present stability against the lithium metal anode [11,35] and a reproducible manufacturing processes [11]. Several attempts to stabilise the superionically conductive high temperature polymorphs to room temperature or to increase the room temperature  $\text{Li}^+$  conductivity of the boron-hydrogen salts have already been conducted with some successful strategies, such as chemical and/or mechanical modification [32,35–40]. The coordination of the borane salts with small neutral molecules, such as water and ammonia, also seem to increase their ionic conductivity as those molecules may facilitate the migration of the cation through the crystal structure [41–43].

Recently, the hydrated *nido*-borane lithium tetradecahydroundecaborane ( $\text{LiB}_{11}\text{H}_{14}\cdot(\text{H}_2\text{O})_n$ ), with cubic space-group  $Fm\bar{3}m$  at room temperature (RT), had its synthesis elucidated and ionic conductivity properties investigated [42]. This material exhibits a  $\text{Li}^+$  conductivity of  $1.8 \times 10^{-4} \text{ S cm}^{-1}$  at  $25^\circ\text{C}$ , which is some of the highest  $\text{Li}^+$  conductivities at RT among the boron-hydrogen salts [42]. Another recent study detailed the synthesis of dehydrated  $\text{LiB}_{11}\text{H}_{14}$ , which presents an orthorhombic unit cell with space group  $Pbca$  and ionic conductivity of  $1.5 \times 10^{-6} \text{ S cm}^{-1}$  at RT. This sample undergoes a polymorphic phase transition at  $\approx 112^\circ\text{C}$  assuming a disordered cubic  $Fm\bar{3}$  space group and has a liquid-like ionic conductivity [32].

Some of the most promising lithium-boranes as solid-state electrolytes have carboranes in their structure, such as  $0.7\text{Li}(\text{CB}_9\text{H}_{10})\cdot 0.3\text{Li}(\text{CB}_{11}\text{H}_{12})$  and  $\text{Li}_3(\text{B}_{11}\text{H}_{14})(\text{CB}_9\text{H}_{10})_2$ , which present

ionic conductivities higher than  $1 \times 10^{-3} \text{ S cm}^{-1}$  at  $25 \text{ }^\circ\text{C}$  [32,35]. However, carboranes usually present high-costs due to the need for expensive and dangerous reagents, as well as, long synthetic processes [44,45]. The optimisation of synthetic processes of metal-boranes with reduced costs is important for further research and application as solid-state electrolyte.

Here, the synthesis of  $\text{LiB}_{11}\text{H}_{14}$  with different levels of water content and structures are demonstrated through a facile method using common laboratory reagents, as well as, their thermal and solid-state electrochemical properties. Battery tests with the salt, here denoted as  $\alpha\text{-LiB}_{11}\text{H}_{14}\cdot(\text{H}_2\text{O})_n$ , were also performed using Li as the anode and  $\text{TiS}_2$  as the cathode. A liquid electrolyte and an ionic liquid are used to investigate the effect of the interfacial contact over the performance of the battery. The difficulties that surround the application of  $\alpha\text{-LiB}_{11}\text{H}_{14}\cdot(\text{H}_2\text{O})_n$  as solid-state electrolyte are also discussed in this paper for further consideration in solid-state electrolyte research.

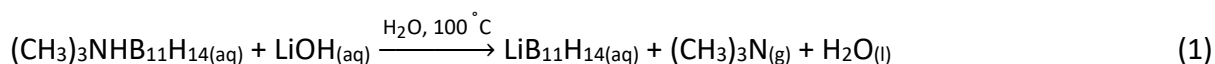
## 4.2 EXPERIMENTAL SECTION

### 4.2.1 Chemicals

Sodium borohydride ( $\text{NaBH}_4$ , anhydrous, 98%), diglyme ( $\text{C}_6\text{H}_{14}\text{O}_3$ , anhydrous, 99.5%), 1-bromopentane ( $\text{C}_5\text{H}_{11}\text{Br}$ , 98%), diethyl ether ( $(\text{C}_2\text{H}_5)_2\text{O}$ , anhydrous, 99.7%), trimethylamine hydrochloride ( $(\text{CH}_3)_3\text{N}\cdot\text{HCl}$ , 98%), deuterated water ( $\text{D}_2\text{O}$ , 99.9 atom % D), deuterated acetonitrile ( $\text{CD}_3\text{CN}$ , 99.8 atom % D), lithium (Li ribbon, thickness 0.38 mm, 99.9%), graphite powder ( $< 20 \mu\text{m}$ ), lithium hexafluorophosphate solution in ethylene carbonate and dimethyl carbonate (1.0 M  $\text{LiPF}_6$  EC/DMC ( $v/v = 50/50$ )), titanium(IV) sulphide ( $\text{TiS}_2$ , 99.9%), acetonitrile ( $\text{CH}_3\text{CN}$ , anhydrous, 99.8%), boric acid ( $\text{H}_3\text{BO}_3$ , 99.5%) and platinum foil (Pt, 99.95%, thickness 0.1 mm) were all purchased from Sigma-Aldrich. Lithium hydroxide ( $\text{LiOH}$ , anhydrous, 98%) and gold foil (Au, 99.95%, thickness 0.1 mm) were obtained from Alfa Aesar, acetone ( $\text{C}_3\text{H}_6\text{O}$ , 99.5%) from Unilab, and hydrochloric acid ( $\text{HCl}$ , 37%) from Scharlau. In order to maintain an inert atmosphere, all chemicals and samples were manipulated in an argon filled glovebox (Mbraun,  $\text{O}_2$  &  $\text{H}_2\text{O} < 1 \text{ ppm}$ ) or using Schlenk techniques under argon.

### 4.2.2 Synthesis of lithium *nido*-tetradecahydrundecaborane, $\text{LiB}_{11}\text{H}_{14}\cdot 2\text{H}_2\text{O}$ , $\alpha\text{-LiB}_{11}\text{H}_{14}\cdot(\text{H}_2\text{O})_n$ ( $n < 2$ ), and $\text{LiB}_{11}\text{H}_{14}$

$\text{LiB}_{11}\text{H}_{14}\cdot 2\text{H}_2\text{O}$  was prepared based on the reaction of  $(\text{CH}_3)_3\text{NHB}_{11}\text{H}_{14}$  and  $\text{LiOH}$  in aqueous solution according to reaction 1, containing 40% excess  $\text{LiOH}$ :



$(\text{CH}_3)_3\text{NHB}_{11}\text{H}_{14}$  was synthesised according to a previously reported method [42]. This material was further recrystallised by dissolution in a hot aqueous solution of acetone (10% acetone) [46]. The colourless precipitate was collected by filtration, washed with cold Milli-Q water and dried *in vacuo* at 90 °C. 140 mg of lithium hydroxide (5.85 mmol) was dissolved in 40 mL of Milli-Q water (0.15 mol L<sup>-1</sup>), and 800 mg of recrystallised  $(\text{CH}_3)_3\text{NHB}_{11}\text{H}_{14}$  (4.14 mmol) was added to this solution. To ensure dissolution of the powder, the mixture was sonicated several times and stirred at room temperature. The aqueous solution was stirred at 100 °C for ≈ 15 minutes in an open vessel to ensure elimination of trimethylammonium cation,  $(\text{CH}_3)_3\text{NH}^+$ , as trimethylamine gas,  $(\text{CH}_3)_3\text{N}$ . After cooling to room temperature, the suspension formed was filtered, and the filtrate dried at 80 °C under vacuum for 2 hours. No additional step for removal of excess LiOH or possible byproducts was taken. This yielded 0.60 g (3.41 mmol, 82% yield) of a deliquescent colourless powder of  $\text{LiB}_{11}\text{H}_{14}\cdot 2\text{H}_2\text{O}$ .

In order to synthesise  $\text{LiB}_{11}\text{H}_{14}\cdot(\text{H}_2\text{O})_n$  with  $n < 2$ , the same methodology to prepare  $\text{LiB}_{11}\text{H}_{14}\cdot 2\text{H}_2\text{O}$  was used, however different heating times to dry the sample were applied. For  $\alpha\text{-LiB}_{11}\text{H}_{14}\cdot(\text{H}_2\text{O})_n$ , the filtrate was dried for 4 hours *in vacuo* at 80 °C, yielding 0.52 g of the material. For anhydrous  $\text{LiB}_{11}\text{H}_{14}$ , the filtrate was dried for 20 hours *in vacuo* at 110 °C, yielding 0.46 g of sample (3.29 mmol, 79% yield).

#### 4.2.3 Synthesis of hydrated lithium *nido*-tetradecahydroundecaborane ( $Fm\bar{3}m$ polymorph), $b\text{-LiB}_{11}\text{H}_{14}\cdot(\text{H}_2\text{O})_n$

The synthesis of  $b\text{-LiB}_{11}\text{H}_{14}\cdot(\text{H}_2\text{O})_n$  was performed by following the same methodology previously reported [42]. 600 mg of  $(\text{CH}_3)_3\text{NHB}_{11}\text{H}_{14}$  was dissolved into 40 mL of an aqueous solution of LiOH (0.47 mol L<sup>-1</sup>), which was heated at 100 °C for 15 minutes in an open vessel. At room temperature, the solution was filtered, the filtrate was reheated to 90 °C and had its pH adjusted to ≈ 4.5 using an aqueous solution of HCl 2%. The solution was then washed with diethyl ether at room temperature, and the organic layer was flushed with argon and dried *in vacuo* at 80 °C to crystallise the known cubic  $Fm\bar{3}m$  polymorph.

## 4.2.4 Characterisation

### 4.2.4.1 Raman Spectroscopy

Raman spectra were obtained with an Alpa300SAR+ confocal Raman microscope (WITEC GmbH, Ulm, Germany) equipped with a 2w-NdYAG laser (532 nm wavelength) and a 20x/0.4 NA objective (Zeiss, Germany). The spectrometer utilises a  $600 \text{ g mm}^{-1}$  grating. Powder samples were packed in capillaries inside an argon filled glovebox (Mbraun,  $\text{O}_2$  &  $\text{H}_2\text{O} < 1$  ppm), sealed with grease and then flame-sealed. Spectra were recorded with 100 accumulations at an integration time of 400 ms. Data were processed in terms of background subtraction, cosmic ray removal and exported with the ProjectFOUR software package (WITec, Ulm, Germany).

### 4.2.4.2 Nuclear Magnetic Resonance (NMR) Spectroscopy

A Bruker Avance III 400 MHz NanoBay spectrometer was used to collect  $^{11}\text{B}\{^1\text{H}\}$  (128 MHz) NMR data at room temperature (RT). The powdered samples were dissolved in 600  $\mu\text{L}$  of deuterated solvent ( $\text{D}_2\text{O}$  or  $\text{CD}_3\text{CN}$ ) prior to analysis. In case of a solution-state sample, an aliquot of 100  $\mu\text{L}$  was dissolved in 600  $\mu\text{L}$  of its deuterated solvent and analysed. The  $^{11}\text{B}$  NMR spectra were referenced to a boron trifluoride etherate ( $\text{BF}_3\text{O}(\text{C}_2\text{H}_5)_2$ ) external standard.

$^{11}\text{B}$  (128.29 MHz) solid-state NMR spectroscopy was performed on a Varian VNMRs spectrometer at RT. The samples were packed inside a 4 mm zirconia rotor in an argon filled glovebox and sealed with gas-tight inserts. The samples were spun at 5 kHz, and acquisition was performed with a one-pulse sequence, with proton decoupling and a relaxation delay of 10 seconds, for a total of 50 transients.

$^{11}\text{B}$  spin-lattice NMR relaxation rates ( $T_1^{-1}$ ) of  $b\text{-LiB}_{11}\text{H}_{14}\cdot(\text{H}_2\text{O})_n$  were measured as a function of temperature in a heating run from -190 to 110  $^\circ\text{C}$  (setup limit) using a 4.7 T superconducting magnet, corresponding to the  $^{11}\text{B}$  Larmor frequency of 64.168 MHz. This approach has been previously successfully attempted on similar systems, such as  $(\text{NH}_4)_2\text{B}_{12}\text{H}_{12}$  [47,48],  $(\text{NH}_4)_2\text{B}_{10}\text{H}_{10}$  [48], and  $\text{Ag}_2\text{B}_{12}\text{H}_{12}$  [49]. Spin-lattice relaxation rates were measured using a saturation-recovery sequence with spin echoes to detect the signal. The relaxation recovery data is well-described using a stretch-exponent function.

#### **4.2.4.3 Structural Characterisation**

X-Ray Powder Diffraction (XRPD) measurements were performed at room temperature (RT) on a Bruker D8 Advance Powder Diffractometer with a Cu K $\alpha$  radiation source ( $\lambda = 1.54056 \text{ \AA}$ ) operated at 40 kV/40mA with a LynxEye detector in the  $2\theta$  range of 5 – 60°. The powder was mounted inside an argon glovebox on a single-crystal Si low background sample holder and sealed with an airtight poly(methyl-methacrylate) (PMMA) dome. Broad diffraction halos from the sample holder are seen at  $\sim 10^\circ$  and  $\sim 20^\circ 2\theta$  in the diffraction data.

The samples  $\alpha\text{-LiB}_{11}\text{H}_{14}\cdot(\text{H}_2\text{O})_n$  and  $b\text{-LiB}_{11}\text{H}_{14}\cdot(\text{H}_2\text{O})_n$  were also characterised using Synchrotron Radiation X-ray Powder Diffraction (SR-XRPD) that was collected at the powder diffraction beamline at the Australian Synchrotron using a wavelength of  $\lambda = 0.590827(4) \text{ \AA}$ , which was refined using a NIST LaB $_6$  660b line position standard. The samples were ground in a mortar and pestle and mounted into a 1.0 mm borosilicate capillary inside an argon glovebox, sealed with grease and flame-sealed outside the glovebox. Data was collected on a Mythen II microstrip detector at two positions, and later combined into gap-free data sets, from  $1^\circ - 81^\circ 2\theta$ . *In-situ* SR-XRPD data for  $\alpha\text{-LiB}_{11}\text{H}_{14}\cdot(\text{H}_2\text{O})_n$  were collected during heating and cooling, where the sample was heated from 25 °C to 100 °C at 5 °C min $^{-1}$  and then cooled at 6 °C min $^{-1}$  to RT. *In-situ* SR-XRPD data for  $b\text{-LiB}_{11}\text{H}_{14}\cdot(\text{H}_2\text{O})_n$  was collected during cooling to -175 °C at 1 °C min $^{-1}$ . Temperature was controlled using an Oxford Cryosystems Cryostream Plus.

Diffraction patterns were indexed and quantitative analysis performed with the Rietveld method using Bruker *TOPAS* software. The refinement of the samples was conducted without the use of an internal/external standard. The percentage of each phase is based on the crystalline components only and does not take into account unidentified phases or amorphous material [50]. Reported uncertainties are based on mathematical fitting uncertainty in *TOPAS* software.

#### **4.2.4.4 Simultaneous Differential Scanning Calorimetry (DSC) and Thermogravimetry Analysis (TGA)**

Measurements were performed with a Netzsch (STA 449 F3 Jupiter) under an argon flow of 40 mL min $^{-1}$  using Al $_2$ O $_3$  crucibles containing approximately 7 mg of sample in a Pt furnace. The analysis was conducted from 25 – 300 °C at 10 °C min $^{-1}$ . The temperature and sensitivity

of the DSC was calibrated using In, Zn, Sn, Bi and CsCl reference materials, resulting in a temperature accuracy of  $\pm 0.2$  °C, while the balance has an accuracy of  $\pm 20$   $\mu\text{g}$ .

#### **4.2.4.5 Temperature Programmed Photographic Analysis (TPPA)**

A pellet of  $\text{LiB}_{11}\text{H}_{14}\cdot 2\text{H}_2\text{O}$  and  $\alpha\text{-LiB}_{11}\text{H}_{14}\cdot(\text{H}_2\text{O})_n$  (50 mg, 6 mm diameter) were pressed at 700 MPa inside an argon glovebox, transferred to a glass tube under an argon atmosphere and placed in a custom-made brass heating block. The sample was heated from RT to  $\approx 230$  °C ( $\Delta T/\Delta t = 10$  °C  $\text{min}^{-1}$ ) while photos of the sample were collected every five seconds.

#### **4.2.4.6 Electrochemical Impedance Spectroscopy (EIS)**

Pellets of each sample (50 mg) were pressed at 700 MPa (6 mm in diameter,  $\approx 1.4$  mm in thickness) inside an argon glovebox, sandwiched between gold foil (0.1 mm in thickness), and sealed within an airtight 'Swagelok-type' Teflon cell with 316 stainless steel electrodes. The measurements were performed using a ZIVE SP1 electrochemical workstation at 100 mV AC from 10 Hz to 1 MHz at RT and at isothermal temperatures after heating and cooling by maintaining 50 minutes of thermal equilibrium at each temperature. Temperature was monitored by a K-type thermocouple  $\approx 5$  mm from the pellet and controlled with a tube furnace from 30 – 90 °C and 90 – 30 °C for samples  $\text{LiB}_{11}\text{H}_{14}\cdot 2\text{H}_2\text{O}$  and  $\alpha\text{-LiB}_{11}\text{H}_{14}\cdot(\text{H}_2\text{O})_n$  with 10 °C steps. This measurement was performed four times for sample  $\alpha\text{-LiB}_{11}\text{H}_{14}\cdot(\text{H}_2\text{O})_n$ , and after each cycle the Swagelok cell was opened inside an argon glovebox, and the pellet thickness was measured. Each cycle was performed after an interval of 24 hours at RT. Sample  $\text{LiB}_{11}\text{H}_{14}$  was heated from 30 – 110 °C in intervals of 10 °C. Ionic conductivity data ( $\sigma$ ) was derived from the equation:  $\sigma = d/lA$ , where  $\sigma$  is the ionic conductivity in  $\text{S cm}^{-1}$ ,  $d$  is the pellet thickness in cm,  $l$  is the  $x$ -intercept of the Nyquist blocking tail, and  $A$  is the area of the pellet face in  $\text{cm}^2$ . This tail accounts for the diffusion of ions in the solid-state electrolyte [51]. The measurement uncertainty on each ionic conductivity data point ( $\pm 10$  %) is based on the  $x$ -intercept of the Nyquist plot and has little impact on the logarithmic-scale of ionic conductivity, which spans many orders of magnitude [42]. The activation energy of  $\alpha\text{-LiB}_{11}\text{H}_{14}\cdot(\text{H}_2\text{O})_n$  was determined from the slope of the solid-state ionic conductivity plot between 55 and 85 °C (Fig. 4.16B) for cycles 1 and 4 and averaged using the Arrhenius equation:  $\ln \sigma_{ion} = \ln \sigma_o - (E_a/K_B T)$ , where  $\sigma_o$  is a pre-exponential factor ( $\text{S cm}^{-1}$ ),  $E_a$  the

activation energy (J),  $K_B$  the Boltzmann constant ( $1.3806 \times 10^{-23} \text{ J K}^{-1}$ ), and  $T$  the temperature (K) [42,48].

#### **4.2.4.7 Linear Sweep Voltammetry (LSV)**

This experiment was performed to determine the oxidative stability limit of  $\alpha\text{-LiB}_{11}\text{H}_{14}\cdot(\text{H}_2\text{O})_n$  against Li metal, and it was based on a method proposed by Han *et al.* [52] and Asakura *et al.* [53]  $\alpha\text{-LiB}_{11}\text{H}_{14}\cdot(\text{H}_2\text{O})_n$  was mixed with graphite, previously heated to 550 °C under vacuum for 12 h, in a weight ratio of 75:25 by grinding 5 times with a mortar and pestle. 3 mg of the mixture was layered on top of 40 mg of the sample, which was pressed together at 700 MPa under argon to form a two layered pellet. This pellet was sandwiched to form an Al/Pt/sample+C/sample/Li configuration, which was sealed within an airtight ‘Swagelok-type’ Teflon cell. LSV was conducted at 30 °C with a scan rate of  $50 \mu\text{V s}^{-1}$  from 1.4 V to 6.4 V. A second LSV cycle was also conducted from 1.5 to 5.1 V at the same scan rate and temperature. The oxidative stability of the material was determined from the intersection point of two linear lines with  $R^2 > 0.99$  (the background and the oxidative current) [53].

#### **4.2.4.8 Galvanostatic Cycling (GC)**

All galvanostatic measurements were performed on a Landt Instruments Battery Testing System using a coin cell or a Swagelok-type cell at 60 °C. All cells were prepared by pressing a pellet of the solid-state electrolyte (SSE),  $\alpha\text{-LiB}_{11}\text{H}_{14}\cdot(\text{H}_2\text{O})_n$  (30 mg) at 700 MPa (6 mm in diameter,  $\approx 1.0$  mm in thickness,  $0.28 \text{ cm}^2$  in surface area) inside an argon glovebox. The coin cell of Li/ $\alpha\text{-LiB}_{11}\text{H}_{14}\cdot(\text{H}_2\text{O})_n$ /Li was assembled by sandwiching the SSE between pure lithium disks and placing it inside a coin cell containing a nickel foil and a separator, which was sealed using a coin press machine. Another symmetric cell of  $\alpha\text{-LiB}_{11}\text{H}_{14}\cdot(\text{H}_2\text{O})_n$  was prepared in a Swagelok-type assembly with the addition of 1 drop of liquid electrolyte lithium hexafluorophosphate solution in ethylene carbonate and dimethyl carbonate (1.0 M  $\text{LiPF}_6$  EC/DMC ( $v/v = 50/50$ )) on top of each side of the SSE and sandwiched between lithium disks to form a Li/LE/ $\alpha\text{-LiB}_{11}\text{H}_{14}\cdot(\text{H}_2\text{O})_n$ /LE/Li cell. Another cell was prepared with the addition of 1 mg of ionic liquid (IL)  $\text{LiB}_{11}\text{H}_{14}\cdot 2\text{H}_2\text{O}$  on each side of the SSE  $\alpha\text{-LiB}_{11}\text{H}_{14}\cdot(\text{H}_2\text{O})_n$  (28 mg), which was pressed together at 700 MPa (6 mm in diameter,  $\approx 1.0$  mm in thickness,  $0.28 \text{ cm}^2$  in surface area). This pellet was sandwiched between lithium disks to form a Li/IL/ $\alpha\text{-LiB}_{11}\text{H}_{14}\cdot(\text{H}_2\text{O})_n$ /IL/Li cell. All batteries were left for 12 h at 60 °C at open circuit voltage prior



to the commencement of the measurements. A constant current density of  $25 \mu\text{A cm}^{-2}$  was applied for 1 hour in each direction during 48 hours. Then, the current was increased to  $50 \mu\text{A cm}^{-2}$  and left running for 96 hours with 1 hour sweeps. These current densities were chosen to compare with recent literature on other boron-hydrogen systems [4,32,54].

#### **4.2.4.9 Critical Current Density (CCD) Test**

The symmetric  $\text{Li}/\alpha\text{-LiB}_{11}\text{H}_{14}\cdot(\text{H}_2\text{O})_n/\text{Li}$  cell was left for 12 h at  $60^\circ\text{C}$  at open circuit voltage. A constant current of  $25 \mu\text{A cm}^{-2}$  was applied for 30 minutes at each direction during 5 hours. Then the current was raised up to  $750 \mu\text{A cm}^{-2}$  with increases of  $25 \mu\text{A cm}^{-2}$  steps and left at each current density for 5 hours with 30 minutes sweeps, following a similar methodology proposed by Su *et al.* [55].

#### **4.2.4.10 Battery Assembly and Electrochemical Measurements**

All measurements were performed on a Landt Instruments Battery Testing System using a Swagelok-type cell at  $60^\circ\text{C}$ . The solid-state cell was prepared based on a similar methodology described by Gulino *et al.* [4] The cathode was prepared by mixing  $\alpha\text{-LiB}_{11}\text{H}_{14}\cdot(\text{H}_2\text{O})_n$  and  $\text{TiS}_2$  in a 1:1 proportion by mass. The mixture was ground 5 times with a mortar and pestle, and 2 mg of the mixture was layered on top of a pellet (6 mm diameter) of 25 mg of  $\alpha\text{-LiB}_{11}\text{H}_{14}\cdot(\text{H}_2\text{O})_n$ , previously pressed at 350 MPa. The cathode loading was chosen to be similar to other recent publications on similar materials [4,32,35]. Both, cathode and solid-electrolyte, were pressed together at 700 MPa. A drop of liquid electrolyte 1.0 M  $\text{LiPF}_6$  EC/DMC ( $v/v = 50/50$ ) was added on top of a Li metal disk (6 mm diameter) that was used as the anode and hand-pressed together with the pellet of SSE and cathode in a Swagelok-type cell against the stainless steel electrodes, resulting in the  $\text{Li}/\text{LE}/\alpha\text{-LiB}_{11}\text{H}_{14}\cdot(\text{H}_2\text{O})_n/\alpha\text{-LiB}_{11}\text{H}_{14}\cdot(\text{H}_2\text{O})_n+\text{TiS}_2$  assembly. The cell containing ionic liquid at the interface was prepared by pressing a pellet (6 mm diameter) of 1 mg of  $\text{LiB}_{11}\text{H}_{14}\cdot 2\text{H}_2\text{O}$  on each side of the SSE  $\alpha\text{-LiB}_{11}\text{H}_{14}\cdot(\text{H}_2\text{O})_n$  (23 mg) at 350 MPa. Both, cathode (2 mg) and electrolyte, were pressed together at 700 MPa and hand-pressed with lithium resulting in a  $\text{Li}/\text{IL}/\alpha\text{-LiB}_{11}\text{H}_{14}\cdot(\text{H}_2\text{O})_n/\text{IL}/\alpha\text{-LiB}_{11}\text{H}_{14}\cdot(\text{H}_2\text{O})_n+\text{TiS}_2$  cell. Galvanostatic charge/discharge experiments ( $1\text{ C} = 239\text{ mA g}^{-1}$ ) were conducted with the cell at  $60^\circ\text{C}$  in the voltage range 1.7 – 2.5 V vs.  $\text{Li}^+/\text{Li}$ . Only the mass of  $\text{TiS}_2$  was considered for the calculation of the specific capacity.

## 4.3 RESULTS AND DISCUSSION

### 4.3.1 Sample characterisation

The samples were characterised through Raman spectroscopy (Fig. 4.1), and the presence of B–H bonds was confirmed by Raman modes at around  $2500\text{ cm}^{-1}$  [56–58].

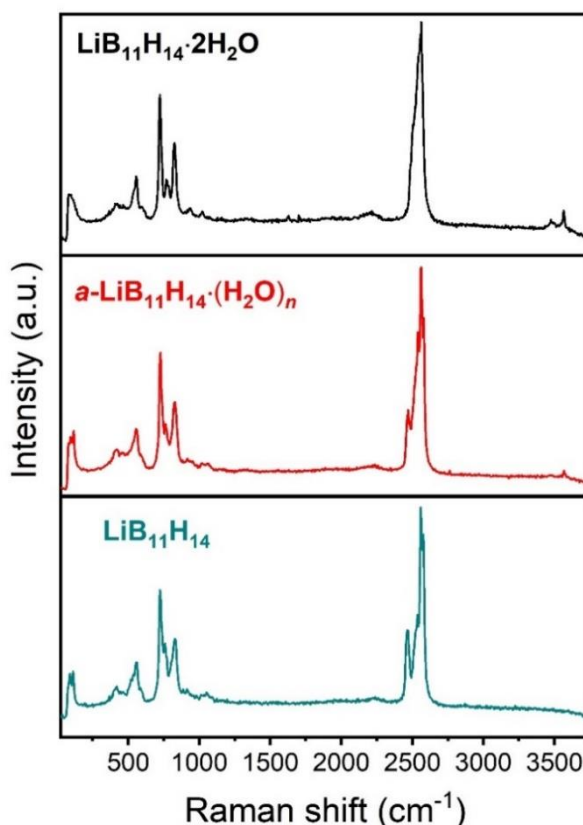


**Figure 4.1** Raman spectra of solid-state  $\text{LiB}_{11}\text{H}_{14}\cdot 2\text{H}_2\text{O}$  (black),  $\alpha\text{-LiB}_{11}\text{H}_{14}\cdot (\text{H}_2\text{O})_n$  (red), and  $\text{LiB}_{11}\text{H}_{14}$  (green).

The lack of a N–H Raman shift between  $3400 - 3200\text{ cm}^{-1}$  that would be observed from unreacted  $(\text{CH}_3)_3\text{NHB}_{11}\text{H}_{14}$  was not detected, confirming that there is no remnant trimethylammonium-borane in the solid [42,59]. Moreover, the presence of water was confirmed for samples  $\text{LiB}_{11}\text{H}_{14}\cdot 2\text{H}_2\text{O}$  and  $\alpha\text{-LiB}_{11}\text{H}_{14}\cdot (\text{H}_2\text{O})_n$  through the observation of an O–H stretching band at  $3600 - 3450\text{ cm}^{-1}$  [60]. The intensity of this band is higher in the doubly hydrated salt than in  $\alpha\text{-LiB}_{11}\text{H}_{14}\cdot (\text{H}_2\text{O})_n$ , as the latter contains less water molecules. The same O–H mode was not observed for  $\text{LiB}_{11}\text{H}_{14}$ , which suggests that the heating treatment that was applied to dry this sample was enough to obtain an anhydrous salt. The Raman mode observed at  $\approx 770\text{ cm}^{-1}$  in all samples may be related to the presence of B–O bonds from an

amorphous borate byproduct, e. g.  $\text{LiB}(\text{OH})_4$ , that is formed and remains in the composition of the solid [61–63].

$^{11}\text{B}$  NMR spectroscopy (Fig. 4.2) was conducted in deuterated acetonitrile ( $\text{CD}_3\text{CN}$ ), and  $\text{B}_{11}\text{H}_{14}^-$  resonances ( $\delta = -14.2, -16.0$  and  $-16.8$  ppm) were identified in the spectra of all samples [32,42]. The presence of additional resonances representing  $\text{B}_{11}\text{H}_{13}\text{OH}^-$  at  $\delta = 18.8, -9.6, -10.7, -23.3, -29.1,$  and  $-40.0$  ppm can only be observed in the spectrum of anhydrous  $\text{LiB}_{11}\text{H}_{14}$  [42]. The formation of this species is expected for samples of  $\text{B}_{11}\text{H}_{14}^-$  and other boron-hydrogen salts, such as  $\text{B}_{12}\text{H}_{12}^{2-}$  and  $\text{B}_{10}\text{H}_{10}^{2-}$ , when exposed to long periods of heating and/or dehydration [42,64].

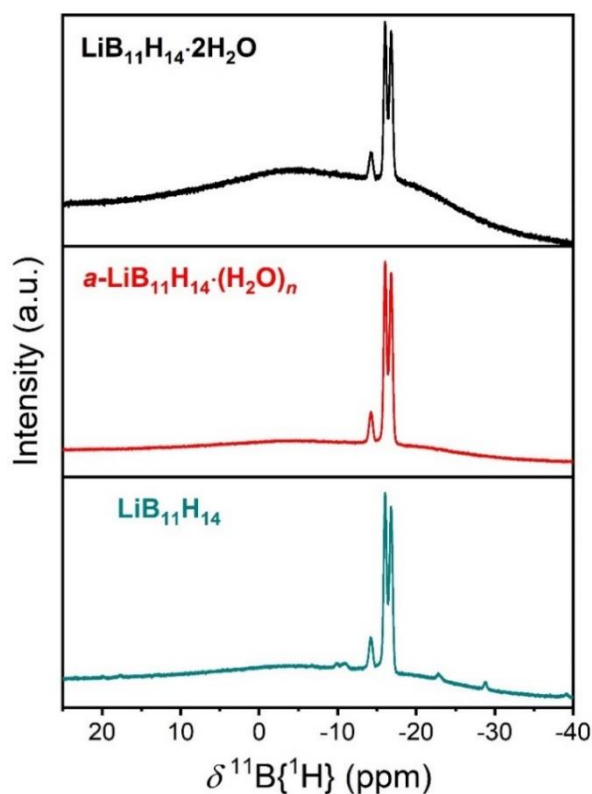


**Figure 4.2**  $^{11}\text{B}\{^1\text{H}\}$  NMR spectra (128 MHz) of  $\text{LiB}_{11}\text{H}_{14}\cdot 2\text{H}_2\text{O}$  (black),  $\alpha\text{-LiB}_{11}\text{H}_{14}\cdot(\text{H}_2\text{O})_n$  (red), and  $\text{LiB}_{11}\text{H}_{14}$  (green) in  $\text{CD}_3\text{CN}$ . The resonances at  $\delta = -14.2, -16.0$  and  $-16.8$  ppm that are observed in all spectra are due to  $\text{B}_{11}\text{H}_{14}^-$ .  $\text{B}_{11}\text{H}_{13}\text{OH}^-$  ( $\delta = 18.8, -9.6, -10.7, -23.3, -29.1,$  and  $-40.0$  ppm) can be identified in the spectra of  $\text{LiB}_{11}\text{H}_{14}$  by small intensity peaks.

It is important to highlight that a white precipitate was formed in the NMR tube for all samples after dissolution of the salts in acetonitrile. In order to further investigate the composition of that precipitate, 40 mg of  $\alpha\text{-LiB}_{11}\text{H}_{14}\cdot(\text{H}_2\text{O})_n$  was mixed with 6 mL of acetonitrile and sonicated

several times at room temperature, which formed a white precipitate. After filtration, an aliquot of the filtrate was dissolved into CD<sub>3</sub>CN, and an aliquot of the residue was dissolved into D<sub>2</sub>O for further NMR analysis. Fig. 4.3 shows that the filtrate contained B<sub>11</sub>H<sub>14</sub><sup>-</sup>, whereas the NMR spectrum of the residue shows the presence of a borate species.

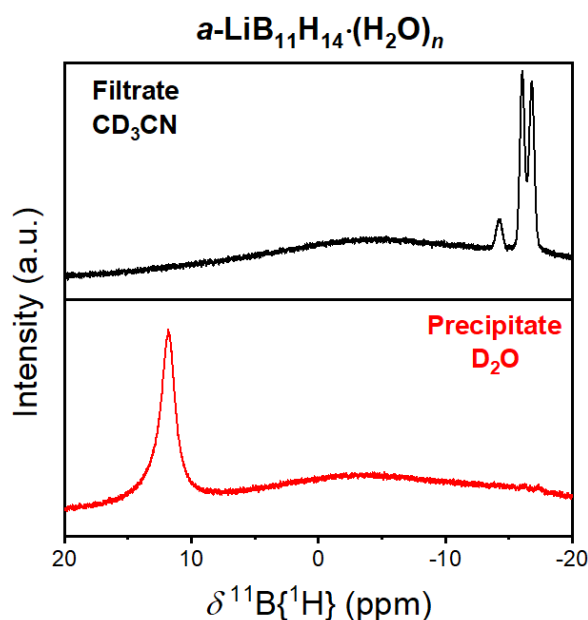


**Figure 4.3** <sup>11</sup>B{<sup>1</sup>H} NMR spectra (128 MHz) of filtrate in CD<sub>3</sub>CN (top) and precipitate in D<sub>2</sub>O (bottom) after mixing  $\alpha\text{-LiB}_{11}\text{H}_{14}\cdot(\text{H}_2\text{O})_n$  in acetonitrile. The <sup>11</sup>B{<sup>1</sup>H} NMR spectrum of the filtrate shows the presence of B<sub>11</sub>H<sub>14</sub><sup>-</sup> anion ( $\delta = -14.2, -16.0$  and  $-16.8$  ppm), whereas the precipitate shows the presence of a borate species at 11.8 ppm.

Solid-state <sup>11</sup>B NMR spectroscopy of  $\alpha\text{-LiB}_{11}\text{H}_{14}\cdot(\text{H}_2\text{O})_n$  (Fig. 4.4) also reveals the presence of B<sub>11</sub>H<sub>14</sub><sup>-</sup>, which was compared with the spectrum of the previously reported LiB<sub>11</sub>H<sub>14</sub>·(H<sub>2</sub>O)<sub>n</sub> in the *Fm* $\bar{3}$ *m* space-group (denoted here as *b*-LiB<sub>11</sub>H<sub>14</sub>·(H<sub>2</sub>O)<sub>n</sub>) [42], and a borate species at a chemical shift of  $\approx 1$  ppm. Boric acid is formed as a byproduct of the reaction of (CH<sub>3</sub>)<sub>3</sub>NHB<sub>11</sub>H<sub>14</sub> with an alkaline metal hydroxide in aqueous solution [42]. The reaction of unreacted lithium hydroxide with boric acid forms a lithium borate species, e.g. LiB(OH)<sub>4</sub>, that is observed through solid-state <sup>11</sup>B NMR spectroscopy at  $\approx 1$  ppm (Fig. 4.4) [65,66].

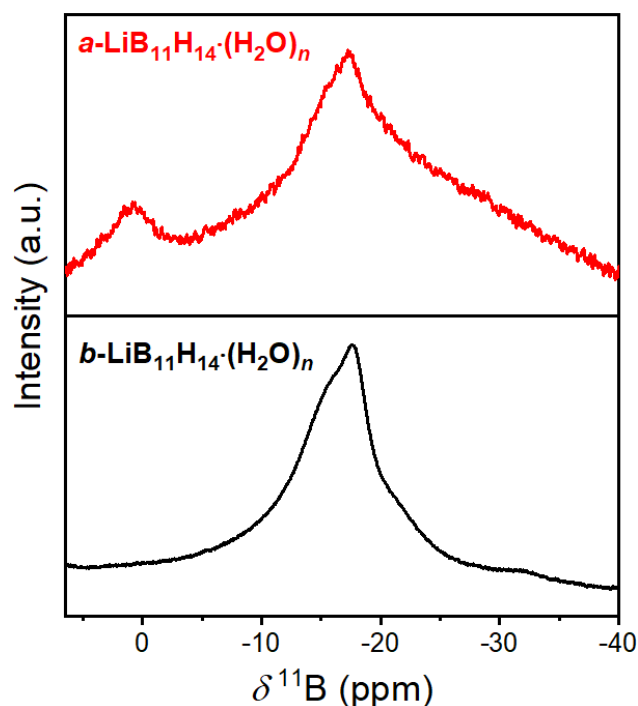


**Figure 4.4** Solid-state  $^{11}\text{B}$  MAS NMR spectra of  $\alpha\text{-LiB}_{11}\text{H}_{14}\cdot(\text{H}_2\text{O})_n$  (red) and  $b\text{-LiB}_{11}\text{H}_{14}\cdot(\text{H}_2\text{O})_n$  (black), which was added for comparison to show the position of  $\text{B}_{11}\text{H}_{14}^-$  ( $\delta = -15.4$  and  $-17.7$  ppm), at RT [42,54]. The presence of a borate species can be seen in the spectrum of  $\alpha\text{-LiB}_{11}\text{H}_{14}\cdot(\text{H}_2\text{O})_n$  at  $\approx 1$  ppm.

In aqueous solution, an equilibrium exists between  $\text{B}(\text{OH})_4^-$  and  $\text{H}_3\text{BO}_3$ , according to reaction 2, which shifts the  $^{11}\text{B}$  NMR chemical signal of the borate species as a function of pH in the range of 1 - 20 ppm (Fig. 4.3) [67].



XRPD patterns of  $\text{LiB}_{11}\text{H}_{14}\cdot 2\text{H}_2\text{O}$ ,  $\alpha\text{-LiB}_{11}\text{H}_{14}\cdot(\text{H}_2\text{O})_n$ , and  $\text{LiB}_{11}\text{H}_{14}$  are illustrated in Fig. 4.5. The presence of unreacted  $\text{LiOH}$  or any crystalline borate species were not observed in any diffraction pattern, which suggests the presence of an amorphous borate compound, in conjunction with  $^{11}\text{B}$  NMR and Raman spectroscopy results. The formation of lithium borate species from the reaction of lithium hydroxide and boric acid in aqueous solution has been previously reported [68].

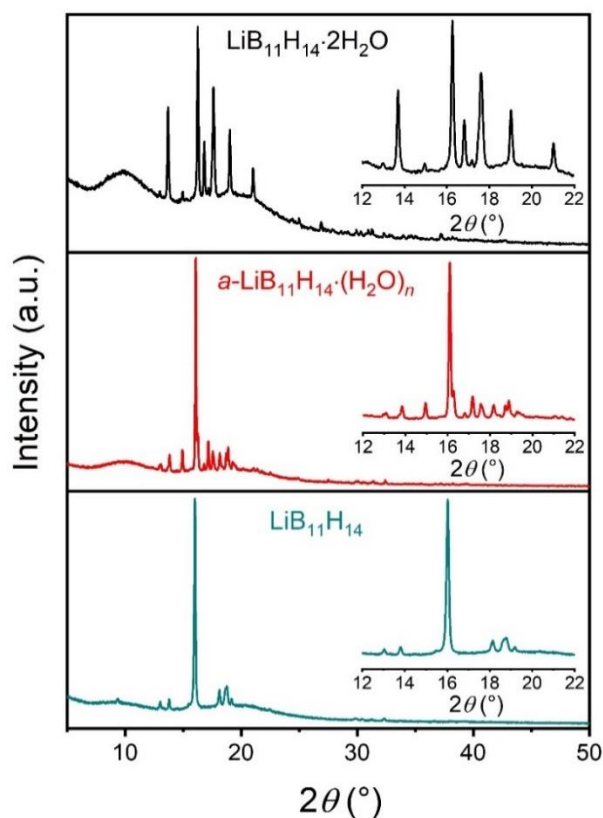


**Figure 4.5** XRPD pattern for  $\text{LiB}_{11}\text{H}_{14}\cdot 2\text{H}_2\text{O}$ ,  $\alpha\text{-LiB}_{11}\text{H}_{14}\cdot (\text{H}_2\text{O})_n$ , and  $\text{LiB}_{11}\text{H}_{14}$  at room temperature with magnified insets in the range of  $2\theta = 12 - 22^\circ$ .  $\lambda = 1.54056 \text{ \AA}$ .

Furthermore, as a test, 0.1 g of  $\text{H}_3\text{BO}_3$  was dissolved into 30 mL of an aqueous solution containing 0.1 g of LiOH, and that solution was submitted to the same process that is conducted to synthesise any  $\text{LiB}_{11}\text{H}_{14}$  reported here. Therefore, the solution was heated at  $100^\circ\text{C}$  for 15 minutes in an open vessel, filtered at room temperature and left drying in *vacuo* at  $80^\circ\text{C}$ . The resulting white solid was characterised through XRPD and  $^{11}\text{B}$  NMR in  $\text{D}_2\text{O}$  at room temperature (Fig. 4.6).

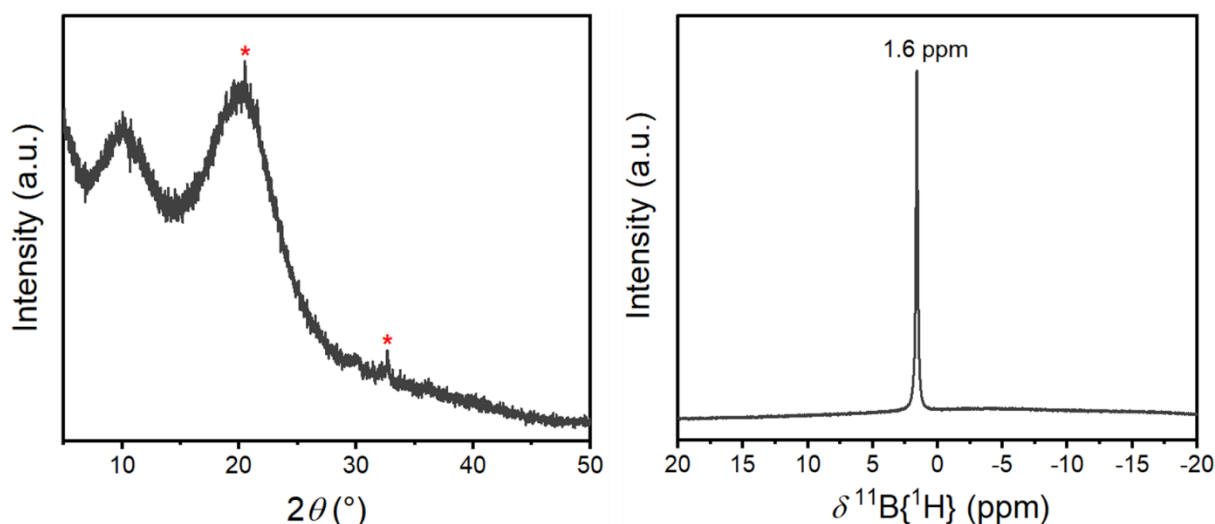


**Figure 4.6** XRPD ( $\lambda = 1.54056 \text{ \AA}$ ) pattern (left) and  $^{11}\text{B}\{^1\text{H}\}$  NMR spectrum (128 MHz) in  $\text{D}_2\text{O}$  (right) for the product of the reaction of  $\text{LiOH}$  and  $\text{H}_3\text{BO}_3$  at RT. Red stars in the XRPD pattern at  $2\theta = 20.5^\circ$  and  $32.6^\circ$  represent unreacted  $\text{LiOH}$  and the broad diffraction halos at  $\approx 10^\circ$  and  $\approx 20^\circ$   $2\theta$  are due to the sample holder, but may mask other amorphous halos.

The XRPD pattern infers the formation of an amorphous  $\text{LiB}(\text{OH})_4$  structure, and solution-state  $^{11}\text{B}$  NMR shows a peak at 1.6 ppm, which is in agreement with the chemical shift of  $\text{B}(\text{OH})_4^-$  in a high pH aqueous solution [67]. These results suggest that all samples of  $\text{LiB}_{11}\text{H}_{14}$  presented here do not contain any unreacted  $\text{LiOH}$ , but instead contain some quantity of an amorphous lithium borate species.

Rietveld refinement analysis of  $\text{LiB}_{11}\text{H}_{14} \cdot 2\text{H}_2\text{O}$  XRPD data (Fig. 4.7) reveals that the material is predominantly formed by the dihydrate in the monoclinic space group  $C2/c$  (97.0(3) wt%), which is the same as that previously reported from single-crystal XRD data [42]. The presence of a minor amount (3.0(3) wt%) of a compound in the orthorhombic space-group  $Pbcn$  ( $a = 41.431(30) \text{ \AA}$ ,  $b = 10.114(8) \text{ \AA}$ ,  $c = 10.454(11) \text{ \AA}$ ,  $V/Z = 273.8 \text{ \AA}^3$ ) can also be observed in the diffractogram of this sample (indexing details below, also see Table 4.1).

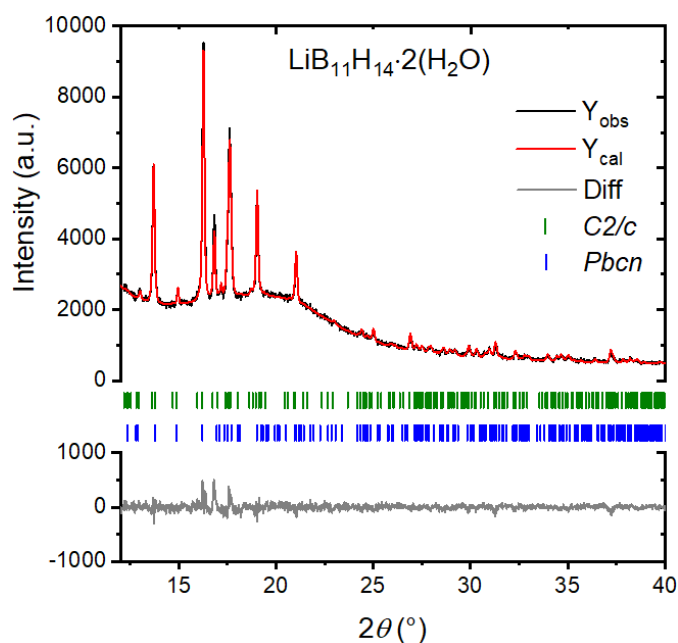


**Figure 4.7** XRPD ( $\lambda = 1.54056 \text{ \AA}$ ) and Rietveld refinement of  $\text{LiB}_{11}\text{H}_{14}\cdot 2\text{H}_2\text{O}$ .  $R_{\text{wp}} = 3.71 \%$ . Green and blue lines represent Bragg position from space group  $C2/c$  ( $\text{LiB}_{11}\text{H}_{14}\cdot 2\text{H}_2\text{O}$ ) [42], 97.0(3) wt%, and the indexed space group  $Pbcn$  ( $\text{LiB}_{11}\text{H}_{14}\cdot (\text{H}_2\text{O})_n$ ), 3.0(3) wt%, respectively.

DSC-TGA was conducted on  $\text{LiB}_{11}\text{H}_{14}\cdot 2\text{H}_2\text{O}$  in order to investigate its thermal behaviour (Fig. 4.8). A strong endothermic event was observed at 73 °C, which was first assumed to be related to a polymorphic phase transition.

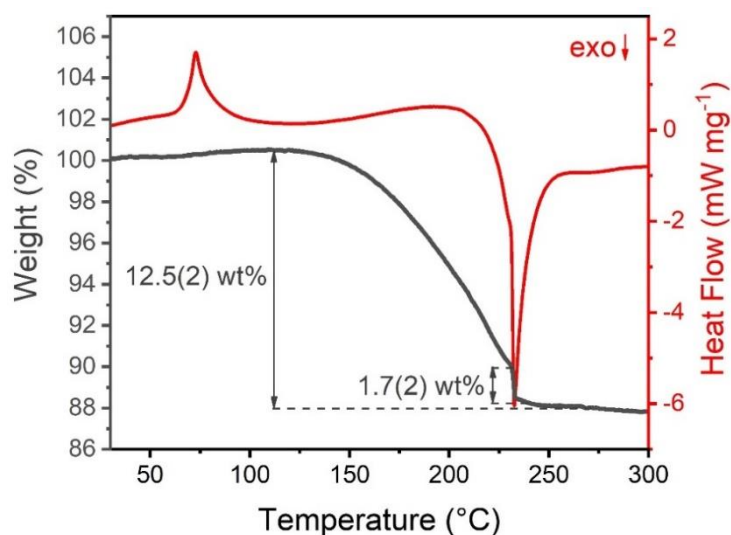


**Figure 4.8** DSC/TGA measurement of  $\text{LiB}_{11}\text{H}_{14}\cdot 2\text{H}_2\text{O}$  in the temperature range 30 – 300 °C ( $\Delta T/\Delta t = 10 \text{ }^\circ\text{C min}^{-1}$ , Ar flow = 40 mL  $\text{min}^{-1}$ ). Approximately 7 mg of sample was used for analysis. The melting event is characterised by the endothermic feature at 73 °C, and the exothermic peak at 233 °C represents its decomposition accompanied by a mass loss of 12.5(2)%.



However, TPPA (Fig. 4.9) shows that the pellet of  $\text{LiB}_{11}\text{H}_{14}\cdot 2\text{H}_2\text{O}$  becomes a liquid at  $\approx 70\text{ }^\circ\text{C}$ , therefore, the endothermic peak corresponds to the melting point of the material. The DSC-TGA plot also showed an exothermic peak at  $230\text{ }^\circ\text{C}$  with a corresponding weight loss of  $12.5(2)\%$ , indicative of its decomposition (Fig. 4.8). TPPA also showed that the sample becomes a solid again above  $200\text{ }^\circ\text{C}$ , along with water loss and the subsequent change to a yellow colour.

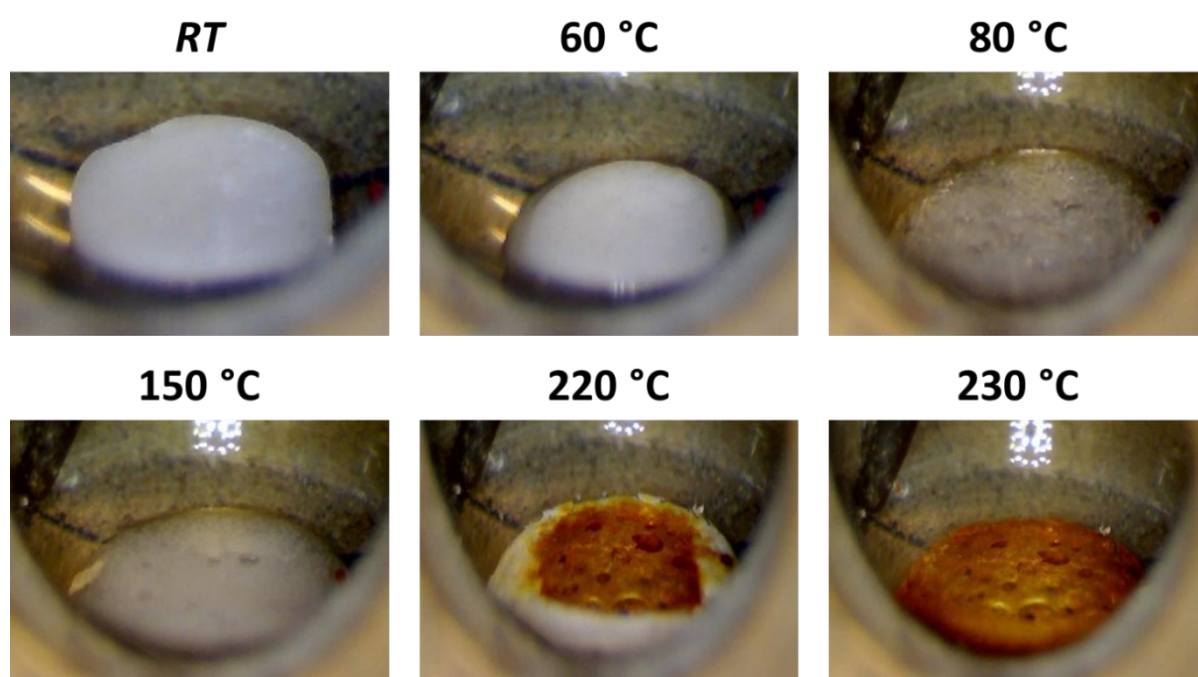


**Figure 4.9** TPPA of  $\text{LiB}_{11}\text{H}_{14}\cdot 2\text{H}_2\text{O}$  heated from RT to  $230\text{ }^\circ\text{C}$  ( $\Delta T/\Delta t = 10\text{ }^\circ\text{C min}^{-1}$ ). The sample starts melting at  $\approx 60\text{ }^\circ\text{C}$ , solidifies again upon heating, and starts decomposing at  $\approx 220\text{ }^\circ\text{C}$ , when it becomes a yellow solid.

It should be noted that salts with low melting points below  $100\text{ }^\circ\text{C}$ , are classified as ionic liquids, of which most are composed of an organic cation and an inorganic anion [69,70]. Furthermore, ionic liquids present several different applications, including chemical reactions as solvents or catalysts and in energy storage applications as electrolyte materials [69–72].  $\text{LiB}_{11}\text{H}_{14}\cdot 2\text{H}_2\text{O}$  is reported here as a new class of ionic liquid, which is simple to prepare, free of an organic component and should therefore be further studied for future battery applications. It is important to clarify that the water in this system is not ‘free water’, instead it is strongly bound to the  $\text{Li}^+$  cation in the salt as a solvated molecule [42]. Thus the ionic liquid, or molten  $\text{LiB}_{11}\text{H}_{14}\cdot 2\text{H}_2\text{O}$ , is simply a molten salt, not a wet salt. This means that the

H<sub>2</sub>O molecules are bound to the Li<sup>+</sup> cation and are less prone to reacting with other parts of a battery due to enhanced electrochemical stability [73,74].

To understand its thermal behaviour,  $\alpha$ -LiB<sub>11</sub>H<sub>14</sub>·(H<sub>2</sub>O)<sub>n</sub> was analysed through SR-XRPD, and the RT and HT (high temperature, 100 °C) data were treated by Rietveld refinement (Fig. 4.10).

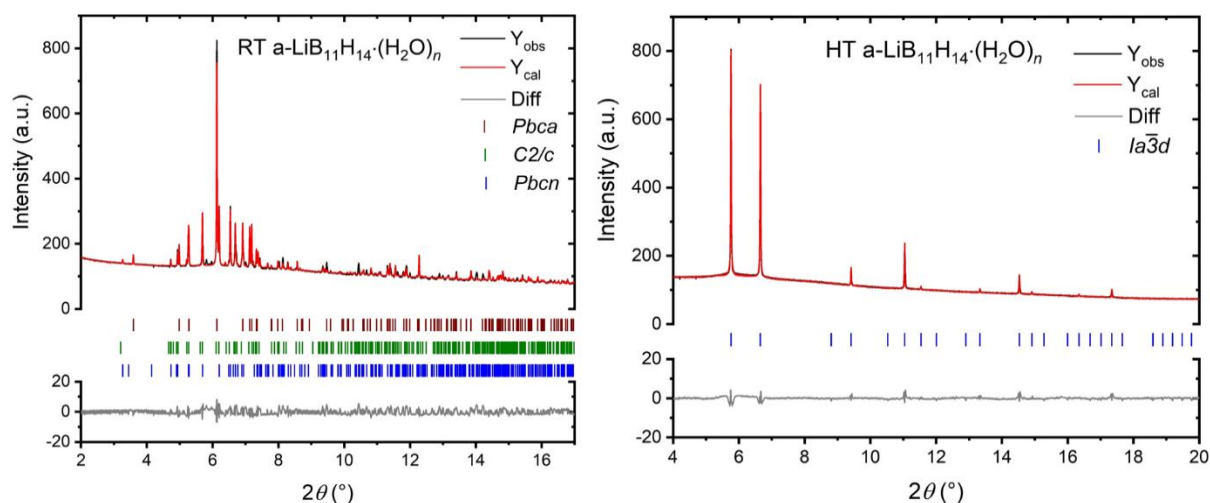


**Figure 4.10** Left: SR-XRPD ( $\lambda = 0.590827(4)$  Å) and Rietveld refinement of sample  $\alpha$ -LiB<sub>11</sub>H<sub>14</sub>·(H<sub>2</sub>O)<sub>n</sub> at RT,  $R_{wp} = 5.37\%$ . Brown, green and blue lines indicate Bragg positions from space groups *PbcA* (LiB<sub>11</sub>H<sub>14</sub>) [32], 70.0(1) wt%, *C2/c* (LiB<sub>11</sub>H<sub>14</sub>·2H<sub>2</sub>O) [42], 4.10(11) wt%, and the indexed space group *Pbcn* (LiB<sub>11</sub>H<sub>14</sub>·(H<sub>2</sub>O)<sub>n</sub>), 25.9(1) wt%, respectively. Right: SR-XRPD ( $\lambda = 0.590827(4)$  Å) and Rietveld refinement of  $\alpha$ -LiB<sub>11</sub>H<sub>14</sub>·(H<sub>2</sub>O)<sub>n</sub> at 100 °C,  $R_{wp} = 3.08\%$ . Blue lines indicate Bragg position from space group *Ia* $\bar{3}d$ .

The sample measured at RT is a mixture of three LiB<sub>11</sub>H<sub>14</sub> containing compounds. Two of the major phases were LiB<sub>11</sub>H<sub>14</sub> (space group *PbcA*, 70.0(1) wt%) [32] and LiB<sub>11</sub>H<sub>14</sub>·2H<sub>2</sub>O (space group *C2/c*, 4.10(11) wt%) [42] (see Table 4.1 below). The second most abundant phase was indexed in the orthorhombic space group *Pbcn* with lattice parameters  $a = 41.446(1)$  Å,  $b = 10.127(1)$  Å,  $c = 10.440(1)$  Å, and  $V/Z = 273.9$  Å<sup>3</sup>. As this phase was only present as 25.9(1) wt% of the sample, it was not possible to solve the structure, although it is deemed that it is a hydrated LiB<sub>11</sub>H<sub>14</sub> complex. As such, the sample itself is denoted as  $\alpha$ -LiB<sub>11</sub>H<sub>14</sub>·(H<sub>2</sub>O)<sub>n</sub> with an unknown water content. Upon heating past 70 °C, this mixture of LiB<sub>11</sub>H<sub>14</sub> and its hydrates undergoes a polymorphic phase transition to a cubic HT polymorph (Fig. 4.10 and 4.11).

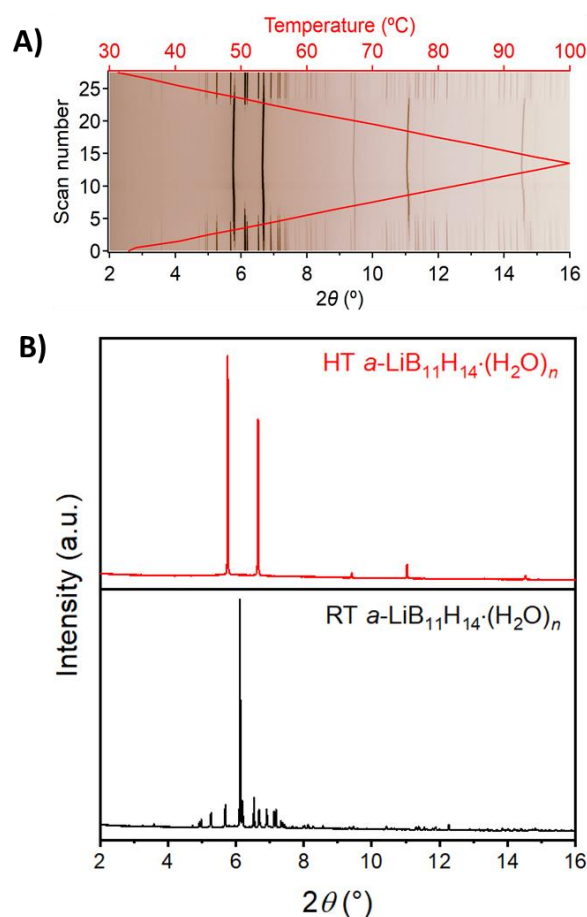


**Figure 4.11** (A) *In-situ* SR-XRPD data of  $\alpha$ -LiB<sub>11</sub>H<sub>14</sub>·(H<sub>2</sub>O)<sub>n</sub> during heating (5 °C min<sup>-1</sup>) and cooling (6 °C min<sup>-1</sup>). A reversible polymorphic phase transition occurs at  $\approx$  70 °C on heating and at  $\approx$  55 °C on subsequent cooling. Red line represents temperature. (B) SR-XRPD patterns of HT (high temperature)  $\alpha$ -LiB<sub>11</sub>H<sub>14</sub>·(H<sub>2</sub>O)<sub>n</sub> at 100 °C (red) and RT (room temperature)  $\alpha$ -LiB<sub>11</sub>H<sub>14</sub>·(H<sub>2</sub>O)<sub>n</sub> (black).  $\lambda$  = 0.590827(4) Å.

It has been reported that dehydrated LiB<sub>11</sub>H<sub>14</sub> undergoes an orthorhombic to cubic polymorphic phase change at  $\approx$  110 °C [32]. Therefore, it is proposed that the presence of hydrates reduces the cubic polymorphic phase transition temperature closer to RT. The structure observed for the HT  $\alpha$ -LiB<sub>11</sub>H<sub>14</sub>·(H<sub>2</sub>O)<sub>n</sub> at 100 °C was indexed in cubic space group  $Ia\bar{3}d$  with  $a$  = 14.399(1) Å and  $V$  = 2985.6(1) Å<sup>3</sup> (see Fig. 4.10 and Table 4.1 below). Anhydrous LiB<sub>11</sub>H<sub>14</sub> was previously indexed in space group  $Fm\bar{3}$  ( $a$  = 9.9465(6) Å) at high temperature (140 °C) [32]. Unfortunately, due to the inherently disordered structure and possible dynamics of the B<sub>11</sub>H<sub>14</sub><sup>-</sup> anions along with the fractional coordinated water, it was not possible to solve the crystal structure for HT  $\alpha$ -LiB<sub>11</sub>H<sub>14</sub>·(H<sub>2</sub>O)<sub>n</sub>.

DSC/TGA data for  $\alpha$ -LiB<sub>11</sub>H<sub>14</sub>·(H<sub>2</sub>O)<sub>n</sub> (Fig. 4.12) demonstrated an endothermic event at  $\approx 70$  °C, which corresponds to the polymorphic phase change to  $I\alpha\bar{3}d$  (Fig. 4.11) along with a simultaneous partial melting event.

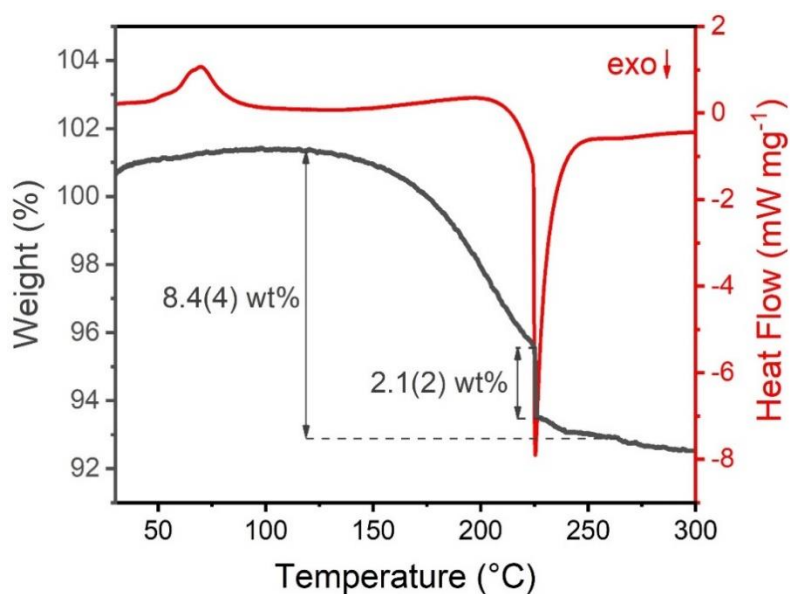


**Figure 4.12** DSC/TGA measurement of  $\alpha$ -LiB<sub>11</sub>H<sub>14</sub>·(H<sub>2</sub>O)<sub>n</sub> in the temperature range 30 – 300 °C ( $\Delta T/\Delta t = 10$  °C min<sup>-1</sup>, Ar flow = 40 mL min<sup>-1</sup>). Approximately 7 mg of sample was used for analysis. The phase change event is characterised by the endothermic feature at 70 °C, and the exothermic peak at 225 °C represents its decomposition accompanied by a mass loss of 8.4(4)%.

TPPA (Fig. 4.13), exhibits slight liquification on the surface of the  $\alpha$ -LiB<sub>11</sub>H<sub>14</sub>·(H<sub>2</sub>O)<sub>n</sub> pellet upon reaching the polymorphic phase change temperature ( $\approx 70$  °C). This is the same melting temperature observed for the salt of LiB<sub>11</sub>H<sub>14</sub>·2H<sub>2</sub>O (Fig. 4.8 and 4.9), which may be related to the presence of 2 water molecules in its crystal structure.

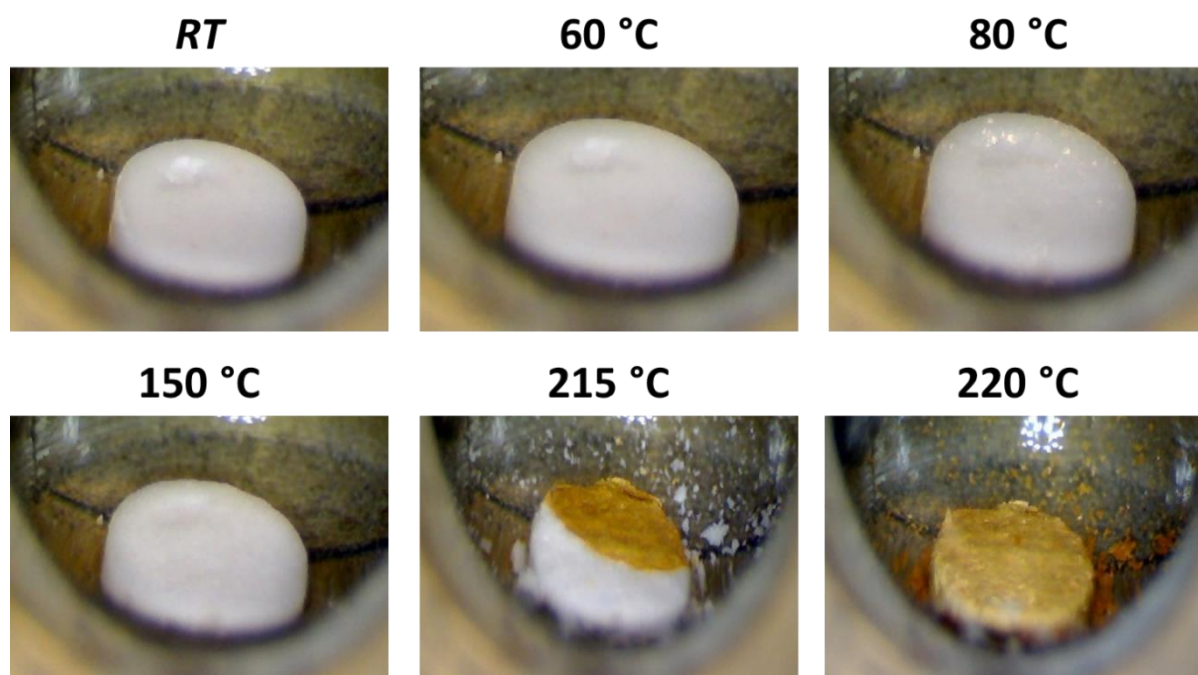


**Figure 4.13** TPPA of  $\alpha\text{-LiB}_{11}\text{H}_{14}\cdot(\text{H}_2\text{O})_n$  heated from RT to 220 °C ( $\Delta T/\Delta t = 10 \text{ }^\circ\text{C min}^{-1}$ ). The sample changes phase near 70 °C, and it does not melt. The pellet expands and keeps its solid shape upon heating. It starts decomposing at  $\approx 215 \text{ }^\circ\text{C}$ , when it becomes a yellow solid.

$\alpha\text{-LiB}_{11}\text{H}_{14}\cdot(\text{H}_2\text{O})_n$  is a mixture of  $\text{LiB}_{11}\text{H}_{14}$  (70 wt.%) with 2 of its hydrates, including only 4.1 wt.% of the monoclinic ( $C2/c$ ) dihydrate, which melts at  $\approx 70 \text{ }^\circ\text{C}$ , but may induce a lower polymorphic phase transition temperature than that seen for dehydrated  $\text{LiB}_{11}\text{H}_{14}$  at 110 °C [32]. Upon heating,  $\alpha\text{-LiB}_{11}\text{H}_{14}\cdot(\text{H}_2\text{O})_n$  does not lose its solid shape and finally decomposes at 225 °C, which is represented by a sharp exothermic peak, mass loss of 8.4(4)% (Fig. 4.12) and change in colour (Fig. 4.13).

XRPD of the fully dehydrated  $\text{LiB}_{11}\text{H}_{14}$  sample shows that this salt exists in an orthorhombic space group  $Pbca$  identical to the published structure [32] (see Fig. 4.14 and Table 4.1 below), while its DSC/TGA plot (Fig. S4.15) shows an endothermic polymorphic phase change event at 112 °C, also identical to data published previously [32]. The  $\text{LiB}_{11}\text{H}_{14}$  sample also share similar  $\text{Li}^+$  conductivity as a function of temperature to published anhydrous  $\text{LiB}_{11}\text{H}_{14}$  [32], as shown below in the ‘solid-state ionic conductivity’ section (section 4.3.2). It is important to highlight that the previously published anhydrous  $\text{LiB}_{11}\text{H}_{14}$  was reported to be free of any  $\text{LiOH}$  or borate impurity meaning that these impurities may not greatly impact the material properties [32].

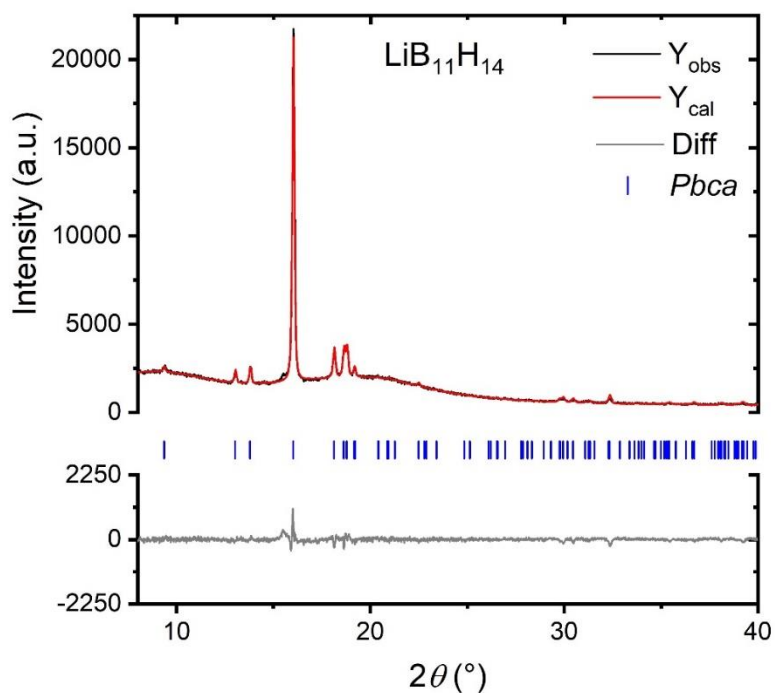


**Figure 4.14** XRPD ( $\lambda = 1.54056 \text{ \AA}$ ) and Rietveld refinement of  $\text{LiB}_{11}\text{H}_{14}$ .  $R_{\text{wp}} = 4.05\%$ . Blue lines represent Bragg position from space group  $Pbca$  [32].

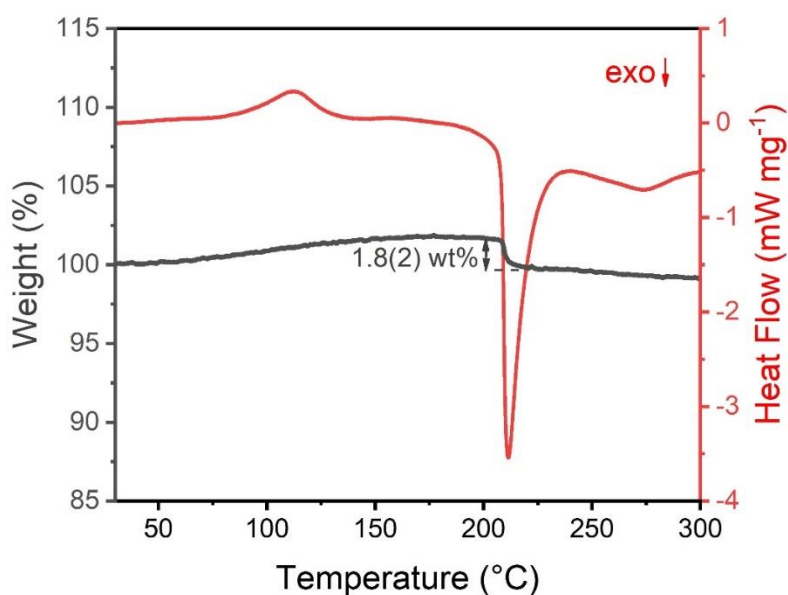


**Figure 4.15** DSC/TGA measurement of  $\text{LiB}_{11}\text{H}_{14}$  in the temperature range 30 – 300 °C ( $\Delta T/\Delta t = 10 \text{ }^\circ\text{C min}^{-1}$ , Ar flow = 40  $\text{mL min}^{-1}$ ). Approximately 7 mg of sample was used for analysis. The phase change event is characterised by the endothermic feature at 112 °C, and the exothermic peak at 211 °C represents its decomposition accompanied by a mass loss of 1.8(2)%.

**Table 4.1** Structural parameters determined from Rietveld refinement of the XRPD data from this work and other related compounds.

Sample	T (°C)	Space Group and Lattice Parameters
<b>LiB<sub>11</sub>H<sub>14</sub>·2H<sub>2</sub>O</b>	25	<p><i>C2/c</i> (LiB<sub>11</sub>H<sub>14</sub>·2H<sub>2</sub>O) [42], 97.0(3) wt%            Monoclinic  <math>a = 10.431(3) \text{ \AA}</math>  <math>b = 10.110(3) \text{ \AA}</math>  <math>c = 42.329(10) \text{ \AA}</math>  <math>\beta = 91.212(3)^\circ</math>  <math>V = 4463.1(19) \text{ \AA}^3</math>  <math>Z = 16</math></p>
		<p><i>Pbcn</i> (LiB<sub>11</sub>H<sub>14</sub>·(H<sub>2</sub>O)<sub>n</sub>), 3.0(3) wt%            Orthorhombic  <math>a = 41.431(30) \text{ \AA}</math>  <math>b = 10.114(8) \text{ \AA}</math>  <math>c = 10.454(11) \text{ \AA}</math>  <math>V = 4380.8(64) \text{ \AA}^3</math>  <math>Z = 16</math></p>
<b><math>\alpha</math>-LiB<sub>11</sub>H<sub>14</sub>·(H<sub>2</sub>O)<sub>n</sub></b>	25	<p><i>Pbca</i> (LiB<sub>11</sub>H<sub>14</sub>) [32], 70.0(1) wt%            Orthorhombic  <math>a = 9.7999(1) \text{ \AA}</math>  <math>b = 9.5073(1) \text{ \AA}</math>  <math>c = 18.856(1) \text{ \AA}</math>  <math>V = 1756.8(1) \text{ \AA}^3</math>  <math>Z = 8</math></p>
		<p><i>Pbcn</i> (LiB<sub>11</sub>H<sub>14</sub>·(H<sub>2</sub>O)<sub>n</sub>), 25.9(1) wt%            Orthorhombic  <math>a = 41.446(1) \text{ \AA}</math>  <math>b = 10.127(1) \text{ \AA}</math>  <math>c = 10.440(1) \text{ \AA}</math>  <math>V = 4382.0(2) \text{ \AA}^3</math>  <math>Z = 16</math></p>
		<p><i>C2/c</i> (LiB<sub>11</sub>H<sub>14</sub>·2H<sub>2</sub>O) [42], 4.10(11) wt%            Monoclinic  <math>a = 10.421(1) \text{ \AA}</math>  <math>b = 10.142(1) \text{ \AA}</math>  <math>c = 42.295(3) \text{ \AA}</math>  <math>\beta = 91.097(6)^\circ</math>  <math>V = 4469.1(7) \text{ \AA}^3</math></p>

		Z = 16
$\alpha\text{-LiB}_{11}\text{H}_{14}\cdot(\text{H}_2\text{O})_n$	100	$Ia\bar{3}d$ Cubic $a = 14.399(1) \text{ \AA}$ $V = 2985.6(1) \text{ \AA}^3$ Z = 12
$\text{LiB}_{11}\text{H}_{14}$	25	$Pbca$ ( $\text{LiB}_{11}\text{H}_{14}$ ) [32] Orthorhombic $a = 9.786(2) \text{ \AA}$ $b = 9.5241(19) \text{ \AA}$ $c = 18.892(4) \text{ \AA}$ $V = 1760.8(6) \text{ \AA}^3$ Z = 8

#### 4.3.2. Solid-State Ionic Conductivity

The lithium ion conductivity for each synthesised material was assessed as a function of temperature as illustrated in Fig. 4.16A. The reported ionic conductivities of dehydrated  $\text{LiB}_{11}\text{H}_{14}$  [32],  $b\text{-LiB}_{11}\text{H}_{14}\cdot(\text{H}_2\text{O})_n$  [42], and of the ionic liquid electrolyte 1 mol L<sup>-1</sup> solution of 1-ethyl-3-methylimidazolium tetrafluoroborate (EMIBF<sub>4</sub>) with lithium tetrafluoroborate (LiBF<sub>4</sub>) [24], are also displayed for comparison. The EIS measurements for the  $\alpha\text{-LiB}_{11}\text{H}_{14}\cdot(\text{H}_2\text{O})_n$  sample were performed at discrete isothermal temperatures during four heating and cooling cycles, in order to check the reproducibility of the results and the conditions of the pellet after each experiment, with the results illustrated in Fig. 4.16B. The Nyquist plots for this sample at 30 and 90 °C, as well as the battery circuit model used to fit this data, are depicted in Fig. 4.17. Ionic conductivity measurements above 60 °C for sample  $\text{LiB}_{11}\text{H}_{14}\cdot 2\text{H}_2\text{O}$  could not be measured due to melting of the material (Fig. 4.9), which causes a short circuit in the measurement cell.



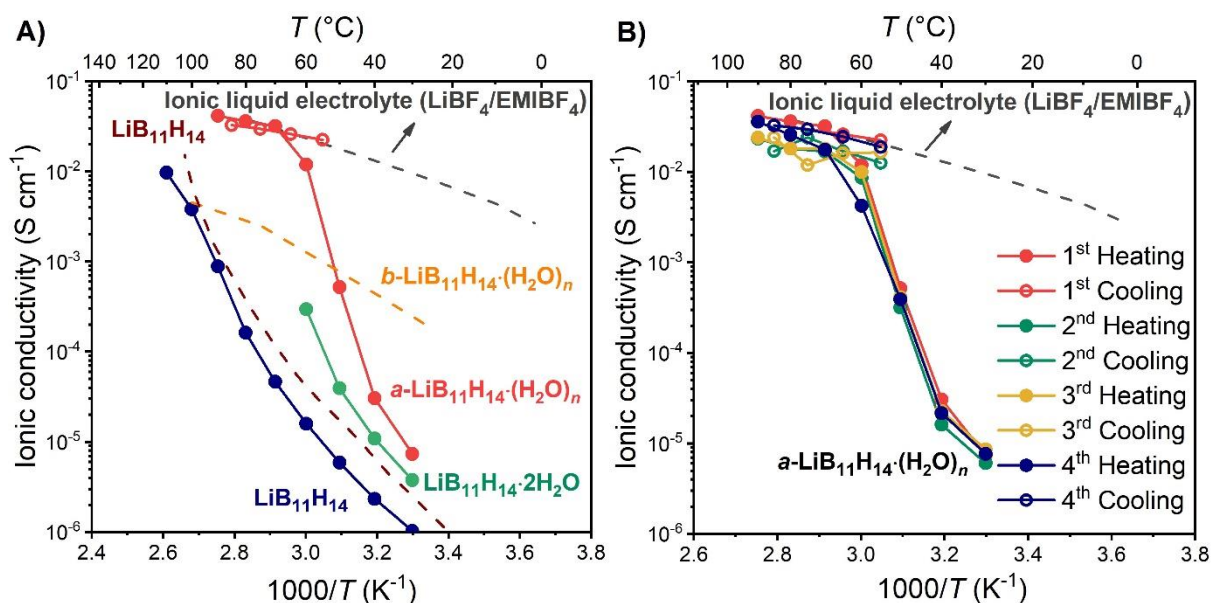


**Figure 4.16** A) Solid-state ionic conductivity of  $\text{LiB}_{11}\text{H}_{14}\cdot 2\text{H}_2\text{O}$  (green),  $a\text{-LiB}_{11}\text{H}_{14}\cdot(\text{H}_2\text{O})_n$  (red), and  $\text{LiB}_{11}\text{H}_{14}$  (blue), as a function of temperature. Dehydrated  $\text{LiB}_{11}\text{H}_{14}$  (brown) [32],  $b\text{-LiB}_{11}\text{H}_{14}\cdot(\text{H}_2\text{O})_n$  (orange) [42], and ionic liquid electrolyte  $\text{LiBF}_4/\text{EMIBF}_4$  (grey) [24] are plotted for comparison. The solid lines denote the ionic conductivity of the materials synthesised in this work. Closed and open symbols represent heating and cooling regimes, respectively. B) Solid-state ionic conductivity of  $a\text{-LiB}_{11}\text{H}_{14}\cdot(\text{H}_2\text{O})_n$  over four cycles of heating and cooling measurements.

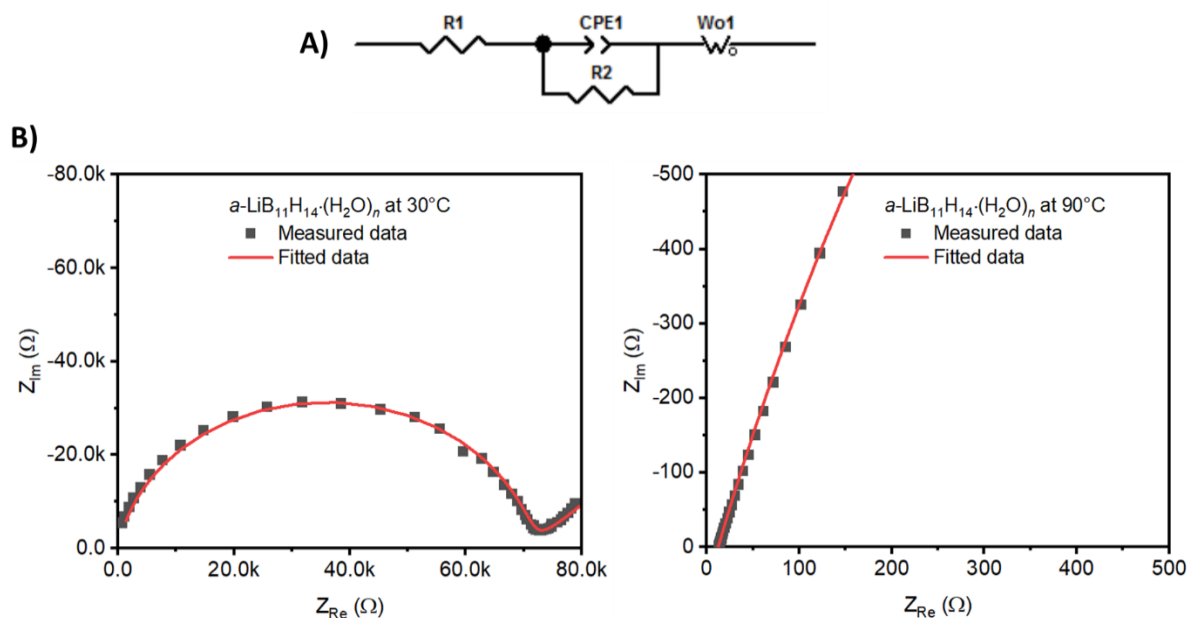


**Figure 4.17** A) Equivalent circuit model used to fit impedance data ( $R1+Q1/R2+Wo$ ), where  $R1$  is the internal resistance,  $R2$  is the surface-layer resistance,  $CPE1$  ( $Q1$ ) is the constant phase element and  $Wo1$  is the open Warburg element [75,76]. B) Nyquist plots of the Au-symmetric cell for  $a\text{-LiB}_{11}\text{H}_{14}\cdot(\text{H}_2\text{O})_n$  at 30 and 90 °C.

Anhydrous  $\text{LiB}_{11}\text{H}_{14}$  exhibits similar  $\text{Li}^+$  conductivity to that previously reported for dehydrated  $\text{LiB}_{11}\text{H}_{14}$  [32], which shows that the synthesis of the anhydrous salt was also achieved by a different method. All samples present an ionic conductivity in the order of  $10^{-6} \text{ S cm}^{-1}$  at 30 °C, but only  $\alpha\text{-LiB}_{11}\text{H}_{14}\cdot(\text{H}_2\text{O})_n$  reaches an impressive conductivity in the order of  $10^{-2} \text{ S cm}^{-1}$  at 60 °C due to its polymorphic phase transition. Upon cooling,  $\alpha\text{-LiB}_{11}\text{H}_{14}\cdot(\text{H}_2\text{O})_n$  maintains its superionic conductivity until  $\approx 55$  °C, when it reverses back to its RT crystal structure (Fig. 4.11). Within the temperature range of 60 - 90 °C,  $\alpha\text{-LiB}_{11}\text{H}_{14}\cdot(\text{H}_2\text{O})_n$  exhibits an ionic conductivity identical to the liquid electrolyte  $\text{LiBF}_4/\text{EMIBF}_4$ , making it an ideal candidate for the development of next generation solid-state-batteries. The Nyquist plot at 30 °C (Fig. 4.17) shows a semi-circle at the high and intermediate frequencies, which is assigned as the sample's charge-transfer resistance, and a spike line (Warburg element) at the low frequency, indicative of  $\text{Li}^+$  diffusion [51]. At 90 °C, only the Warburg element can be observed, which indicates a low charge-transfer resistance and a high ionic diffusion [51,75,76]. Fig. 4.16B demonstrates that the results of lithium ionic conductivity for  $\alpha\text{-LiB}_{11}\text{H}_{14}\cdot(\text{H}_2\text{O})_n$  is reproducible after thermally treating the pellet multiple times. The pellet maintained its solid consistency throughout the four cycles, and only small variations on its thickness were measurable, but all within experimental uncertainty (Table 4.2).

**Table 4.2** Pellet thickness at RT and ionic conductivity results at 30 and 90 °C for sample  $\alpha\text{-LiB}_{11}\text{H}_{14}\cdot(\text{H}_2\text{O})_n$  at different cycles.

Cycle	Pellet thickness at RT before cycle (mm)	Ionic conductivity at 30 °C ( $\text{S cm}^{-1}$ )	Ionic conductivity at 90 °C ( $\text{S cm}^{-1}$ )	Pellet thickness at RT after cycle (mm)
1	1.4 ( $\pm 0.1$ )	$7.4 \times 10^{-6}$	$4.2 \times 10^{-2}$	1.2 ( $\pm 0.1$ )
2	1.2 ( $\pm 0.1$ )	$6.0 \times 10^{-6}$	$2.3 \times 10^{-2}$	1.2 ( $\pm 0.1$ )
3	1.2 ( $\pm 0.1$ )	$8.6 \times 10^{-6}$	$2.4 \times 10^{-2}$	1.2 ( $\pm 0.1$ )
4	1.2 ( $\pm 0.1$ )	$7.7 \times 10^{-6}$	$3.6 \times 10^{-2}$	1.1 ( $\pm 0.1$ )

The activation energy required for  $\text{Li}^+$  migration for the HT  $\alpha\text{-LiB}_{11}\text{H}_{14}\cdot(\text{H}_2\text{O})_n$  structure was measured from the slope of the solid-state ionic conductivity plot as  $0.16 \pm 0.01$  eV between

55 and 85 °C (Fig. 4.16A), which is low compared to other lithium boron-hydrogen materials (Table 4.3), but the same as that previously reported for HT anhydrous LiB<sub>11</sub>H<sub>14</sub> (0.16 eV) [32].

**Table 4.3** Activation energy of some lithium boron-hydrogen salts.

Lithium boron-hydrogen salt	Activation energy (eV)	Reference
HT <sup>a</sup> $\alpha$ -LiB <sub>11</sub> H <sub>14</sub> ·(H <sub>2</sub> O) <sub>n</sub>	0.16 ( $\pm$ 0.01)	This work
LiCB <sub>9</sub> H <sub>10</sub>	0.29	[30]
LiCB <sub>11</sub> H <sub>12</sub>	0.22	[31]
0.7Li(CB <sub>9</sub> H <sub>10</sub> )-0.3Li(CB <sub>11</sub> H <sub>12</sub> )	0.29	[35]
Li-7-CB <sub>10</sub> H <sub>13</sub>	0.39	[29]
<i>b</i> -LiB <sub>11</sub> H <sub>14</sub> ·(H <sub>2</sub> O) <sub>n</sub>	0.5	[42]
Li <sub>2</sub> B <sub>11</sub> H <sub>12</sub>	0.49	[77]
LT <sup>b</sup> LiB <sub>11</sub> H <sub>14</sub>	0.81	[32]
HT LiB <sub>11</sub> H <sub>14</sub>	0.16	[32]
LT LiBH <sub>4</sub>	0.69	[28]
HT LiBH <sub>4</sub>	0.53	[28]

<sup>a</sup>HT = High Temperature polymorph. <sup>b</sup>LT = Low Temperature polymorph

Comparing the results of ionic conductivity of  $\alpha$ -LiB<sub>11</sub>H<sub>14</sub>·(H<sub>2</sub>O)<sub>n</sub> with other boron-hydrogen salts and mixtures (Fig. 4.18),  $\alpha$ -LiB<sub>11</sub>H<sub>14</sub>·(H<sub>2</sub>O)<sub>n</sub> shows similar conductivity trends with temperature as seen for carboranes, such as LiCB<sub>9</sub>H<sub>10</sub> [35]. Both compounds present an ionic conductivity in the order of 10<sup>-6</sup> S cm<sup>-1</sup> at 30 °C, although conductivity increases significantly to  $\approx$  10<sup>-1</sup> S cm<sup>-1</sup> (superionic conductivity) when the temperature is increased to 90 and 70 °C for LiCB<sub>9</sub>H<sub>10</sub> and  $\alpha$ -LiB<sub>11</sub>H<sub>14</sub>·(H<sub>2</sub>O)<sub>n</sub>, respectively, which also incurs a polymorphic phase change. These superionic results observed for  $\alpha$ -LiB<sub>11</sub>H<sub>14</sub>·(H<sub>2</sub>O)<sub>n</sub> between 60 and 90 °C also correlate to the results observed for the 0.7Li(CB<sub>9</sub>H<sub>10</sub>)-0.3Li(CB<sub>11</sub>H<sub>12</sub>) mixture [35], of which, to date, is the lithium boron-hydrogen sample with the highest ionic conductivity at room temperature (6.7 x 10<sup>-3</sup> S cm<sup>-1</sup>). It is important to highlight that carboranes are more expensive and more difficult to synthesise than carbon free boron-hydrogen salts [44], such as  $\alpha$ -LiB<sub>11</sub>H<sub>14</sub>·(H<sub>2</sub>O)<sub>n</sub> reported here.

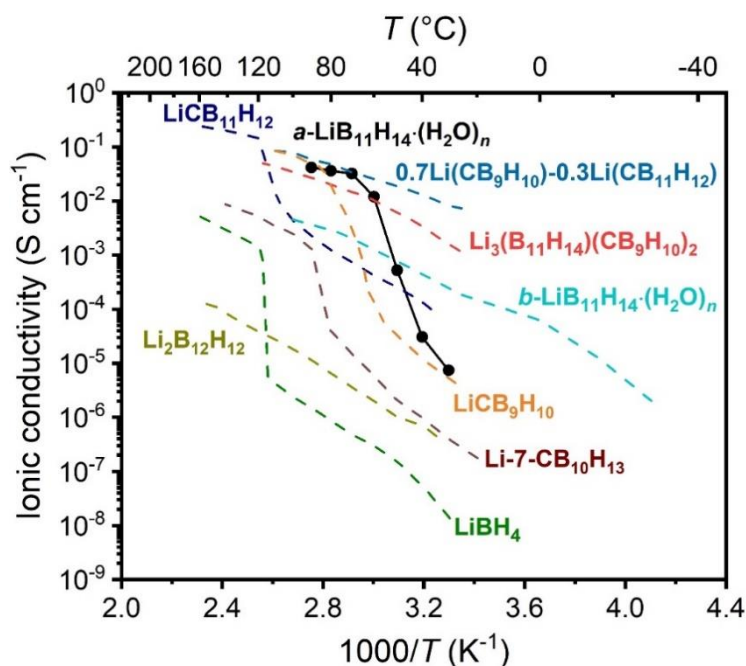


**Figure 4.18** Solid-state ionic conductivity of  $\alpha$ - $\text{LiB}_{11}\text{H}_{14}\cdot(\text{H}_2\text{O})_n$  compared with other lithium boron-hydrogen salts [28–32,35,42,78].

The step-function jump in ionic conductivity due to a polymorphic phase change is also observed in other lithium boron-hydrogen salts, such as  $\text{LiBH}_4$  [28],  $\text{Li-7-CB}_{10}\text{H}_{13}$  [29], and  $\text{LiCB}_{11}\text{H}_{12}$  [31]. Similarly to  $\text{LiCB}_{11}\text{H}_{12}$ ,  $\alpha$ - $\text{LiB}_{11}\text{H}_{14}\cdot(\text{H}_2\text{O})_n$  likely assumes a disordered cubic phase at high temperature, which, coupled with the large size and high orientation mobility of the anion, yields a salt with liquid-like ionic conductivity [31]. Besides that, the presence of water in its crystal structure may also assist the  $\text{Li}^+$  transport through the high-symmetry cubic polymorph [41,79]. It has already been reported that hydrated  $\text{LiBH}_4$  can exhibit higher ionic conductivity than anhydrous  $\text{LiBH}_4$ , and that enhancement of  $\text{Li}^+$  conduction might be associated to the motion of structural water [41]. In a similar manner, the presence of ammonia molecules in hemi-ammine lithium borohydride ( $\text{LiBH}_4\cdot 1/2\text{NH}_3$ ) assists the migration of  $\text{Li}^+$  through the crystal structure, increasing its ionic conductivity [43].

The sample of  $b$ - $\text{LiB}_{11}\text{H}_{14}\cdot(\text{H}_2\text{O})_n$  presents a cubic  $Fm\bar{3}m$  space group at room temperature [42], however it does not reach such high  $\text{Li}^+$  conductivity (close to  $10^{-1} \text{ S cm}^{-1}$ ) as  $\alpha$ - $\text{LiB}_{11}\text{H}_{14}\cdot(\text{H}_2\text{O})_n$  even at high temperatures. This might be related to the fact that sample  $\alpha$ - $\text{LiB}_{11}\text{H}_{14}\cdot(\text{H}_2\text{O})_n$  exhibits a small quantity of the molten  $\text{LiB}_{11}\text{H}_{14}\cdot 2\text{H}_2\text{O}$  phase and a disordered HT polymorph above  $60^\circ\text{C}$ , which significantly enhances its ionic conductivity. It is also hypothesised that the salt  $b$ - $\text{LiB}_{11}\text{H}_{14}\cdot(\text{H}_2\text{O})_n$  may exhibit disordered structural behaviour in its

cubic polymorph at room temperature and might undergo a polymorphic phase transition to a more ordered crystal structure at sub-zero temperatures [42]. In order to further investigate any possible order-disorder phase transition and to assess the information concerning structural dynamics (including rotations/reorientations of boron cages) *in-situ* SR-XRPD and  $^{11}\text{B}$  spin-lattice NMR relaxation rates ( $T_1^{-1}$ ) of  $b\text{-LiB}_{11}\text{H}_{14}\cdot(\text{H}_2\text{O})_n$  were measured as a function of temperature (Fig. 4.19).

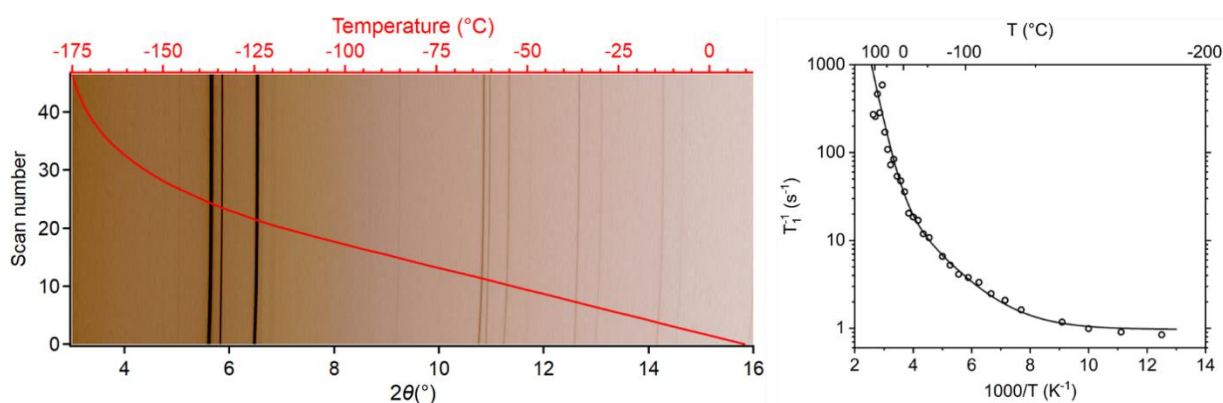


**Figure 4.19** Left: *In-situ* SR-XRPD ( $\lambda = 0.563516(6)$  Å) data of  $b\text{-LiB}_{11}\text{H}_{14}\cdot(\text{H}_2\text{O})_n$  during cooling at  $1$  °C  $\text{min}^{-1}$ . No significant change can be observed in the temperature range used to conduct the experiment (RT to  $-175$  °C). Red line represents temperature. Right:  $^{11}\text{B}$  spin-lattice relaxation rates of  $b\text{-LiB}_{11}\text{H}_{14}\cdot(\text{H}_2\text{O})_n$  as a function of inverse temperature. The solid line represents the best model fit to a relaxation model considering two types of dynamic processes with different activation energies and a temperature-independent contribution to relaxation due to interactions with paramagnetic impurities in the sample.

The *in-situ* SR-XRPD results are displayed in Fig. 4.19 when cooling from RT to  $-175$  °C, and there is no clear evidence of a polymorphic transition, nor in the NMR data when the sample is cooled. Boron spin-lattice relaxation in NMR data is influenced by fluctuations in dipolar interactions of boron nuclei with other boron atoms, protons, and Li nuclei, as well as by fluctuations of the interaction between the nuclear quadrupole moment of boron nuclei and the electric field gradient tensor (EFG) at the site of the nuclei. These fluctuations are caused by the motions of the units. As the relaxation rate increases with temperature, the same approach is followed as previously reported [49] to understand the dynamic processes in  $b\text{-LiB}_{11}\text{H}_{14}\cdot(\text{H}_2\text{O})_n$ . It is found that there are two contributions from two types of dynamic processes, assuming the asymptotic form of the simple relaxation model and an additional

temperature-independent contribution to relaxation due to paramagnetic impurities that are present in the sample. The dynamic process with the higher activation energy,  $E_{a1} = 0.32(1)$  eV, is associated with thermally-activated rotations/reorientations of the boron cages, and is in line with the activation energies for similar systems [29,47–49]. This activation energy is lower than the one obtained from ionic conductivity for this sample (0.5 eV) [42], however this is expected, as a jump of  $\text{Li}^+$  also includes some breaking of the lattice, which requires additional energy [30]. The process with the lower activation energy,  $E_{a2} = 0.074(5)$  eV, is likely associated with tumbling or twitching of a small fraction of loosely-bound  $\text{B}_{11}\text{H}_{14}^-$  units in the system, and the activation energy is similar to what has been previously observed for that type of dynamic process in  $\text{Ag}_2\text{B}_{12}\text{H}_{12}$  [49].

### 4.3.3 Electrochemical stability

The oxidative stability limit of  $\alpha\text{-LiB}_{11}\text{H}_{14}\cdot(\text{H}_2\text{O})_n$  against Li metal was determined through a linear sweep voltammetry experiment at 30 °C following the method proposed by Asakura *et al.* [53]. The voltammogram shows two oxidation onsets (Fig. 4.20), a minor event at 2.1 V and another more significant oxidation event at 2.8 V, which is in agreement with results previously published for  $b\text{-LiB}_{11}\text{H}_{14}\cdot(\text{H}_2\text{O})_n$  [42].

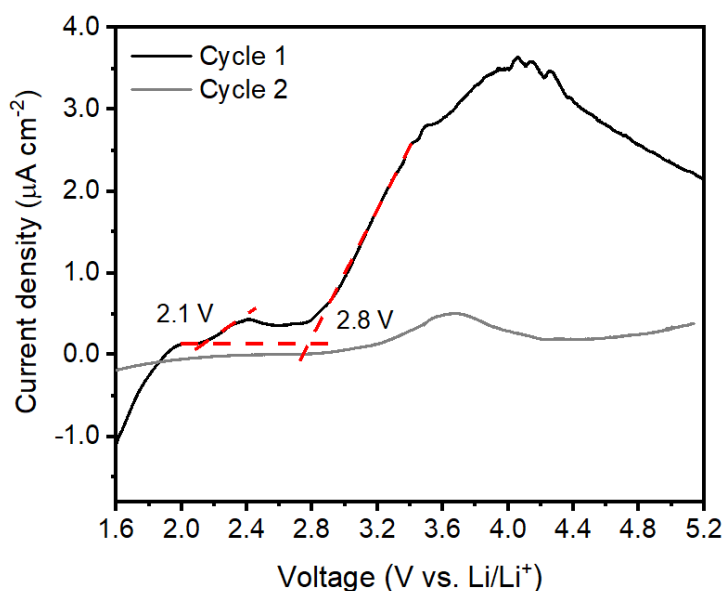


**Figure 4.20** Linear Sweep Voltammogram of  $\text{Li}/\alpha\text{-LiB}_{11}\text{H}_{14}\cdot(\text{H}_2\text{O})_n/\alpha\text{-LiB}_{11}\text{H}_{14}\cdot(\text{H}_2\text{O})_n+\text{C}/\text{Pt}/\text{Al}$  cells at a scan rate of  $50 \mu\text{V s}^{-1}$  at 30 °C between 1.6 and 5.2 V (1<sup>st</sup> cycle) and 1.6 and 5.1 V (2<sup>nd</sup> cycle). The oxidative limit was estimated by the interception of the red dashed lines, which represent the linear regression lines of the background and the anodic current.

The first oxidation onset is low in intensity and may be due to the background current, which is a non-faradaic current attributed to the double-layer capacitance [53], rather than an onset of decomposition of the material. A similar voltammogram is observed for a previously reported solid-mixture of  $\text{LiB}_{11}\text{H}_{14}:\text{LiB}_{11}\text{H}_{13}\text{R}'$  ( $\text{R}' = \text{OH}$  and  $\text{OB}_{11}\text{H}_{13}\text{Li}$ ) [32], which presents a steep background current prior to its Faradaic oxidative current at 2.52 V. Besides that, the solid-solution  $\text{Li}_2(\text{B}_{11}\text{H}_{14})(\text{CB}_{11}\text{H}_{12})$  also exhibits an onset of decomposition at  $\approx 2.6$  V [32], similar to other *nido*-boranes, such as  $\text{NaB}_{11}\text{H}_{14}$  [54] and  $\text{NaB}_{11}\text{H}_{14}\cdot(\text{H}_2\text{O})_n$  [42] that exhibit an oxidative current of 2.6 V vs.  $\text{Na}^+/\text{Na}$ . Therefore,  $\alpha\text{-LiB}_{11}\text{H}_{14}\cdot(\text{H}_2\text{O})_n$  exhibits a similar oxidative stability limit of 2.8 V against  $\text{Li}^+/\text{Li}$ . The small peak current ( $\approx 4.0 \mu\text{A cm}^{-2}$ ) during oxidation indicates that only a small amount of  $\alpha\text{-LiB}_{11}\text{H}_{14}\cdot(\text{H}_2\text{O})_n$  was oxidised, and the presence of a small onset in the same region near 2.8 V during the second LSV cycle (Fig. 4.20), might indicate a further oxidation of its surface layer [52]. It is important to highlight that this reaction is an event that occurs on the interface electrode/electrolyte, thus the bulk stability of  $\alpha\text{-LiB}_{11}\text{H}_{14}\cdot(\text{H}_2\text{O})_n$  might be preserved, as it has already been observed for other *nido*-boranes [42].

The electrochemical stability of  $\alpha\text{-LiB}_{11}\text{H}_{14}\cdot(\text{H}_2\text{O})_n$  against lithium metal was also evaluated through galvanostatic cycling of three different types of symmetric cells at 60 °C. Initially, a pellet of  $\alpha\text{-LiB}_{11}\text{H}_{14}\cdot(\text{H}_2\text{O})_n$  was prepared and assembled between Li disks in a coin cell to form a  $\text{Li}/\alpha\text{-LiB}_{11}\text{H}_{14}\cdot(\text{H}_2\text{O})_n/\text{Li}$  configuration. However, the insufficient contact between Li and solid electrolyte can form voids at the interface, which increases interfacial resistance and overpotential that is required to generate and maintain a constant current [4,80]. One way to increase surface contact and reduce the magnitude of the overpotential upon cycling is by applying a continuous stack pressure to the cell [80,81]. An alternative strategy is to utilise a wetting agent, such as an ionic liquid, between the solid electrolyte and the Li metal interface [17]. Even the type of battery (e.g. coin cell or a Swagelok cell) that is used to conduct the experiments can influence the results of interfacial resistance [82]. In this work, a second symmetric cell of  $\text{Li}/\alpha\text{-LiB}_{11}\text{H}_{14}\cdot(\text{H}_2\text{O})_n/\text{Li}$  was prepared with the addition of a drop of liquid electrolyte (LE, 1.0 M  $\text{LiPF}_6$  EC/DMC) between the interfaces of the lithium metal and the SSE to form a  $\text{Li}/\text{LE}/\alpha\text{-LiB}_{11}\text{H}_{14}\cdot(\text{H}_2\text{O})_n/\text{LE}/\text{Li}$  configuration. A third symmetric cell was also prepared with the addition of a small amount (1 mg) of  $\text{LiB}_{11}\text{H}_{14}\cdot 2\text{H}_2\text{O}$  on the interface between Li/SSE in order to evaluate the properties of  $\text{LiB}_{11}\text{H}_{14}\cdot 2\text{H}_2\text{O}$  as an ionic liquid as it melts at  $\approx 60$  °C. This cell configuration is here referred to as  $\text{Li}/\text{IL}/\alpha\text{-LiB}_{11}\text{H}_{14}\cdot(\text{H}_2\text{O})_n/\text{IL}/\text{Li}$ . Both hybrid

solid/liquid cells were prepared in a Swagelok-type assembly, as this set-up provides a slightly higher stack pressure, even though small, than for a coin cell.

The results for galvanostatic cycling of the symmetric cells at 60 °C are displayed in Fig. 4.21, where it is possible to observe the reversibility of Li plating/stripping for 108 cycles with a flat polarisation (no side reactions can be observed) in all different cells used for this study.

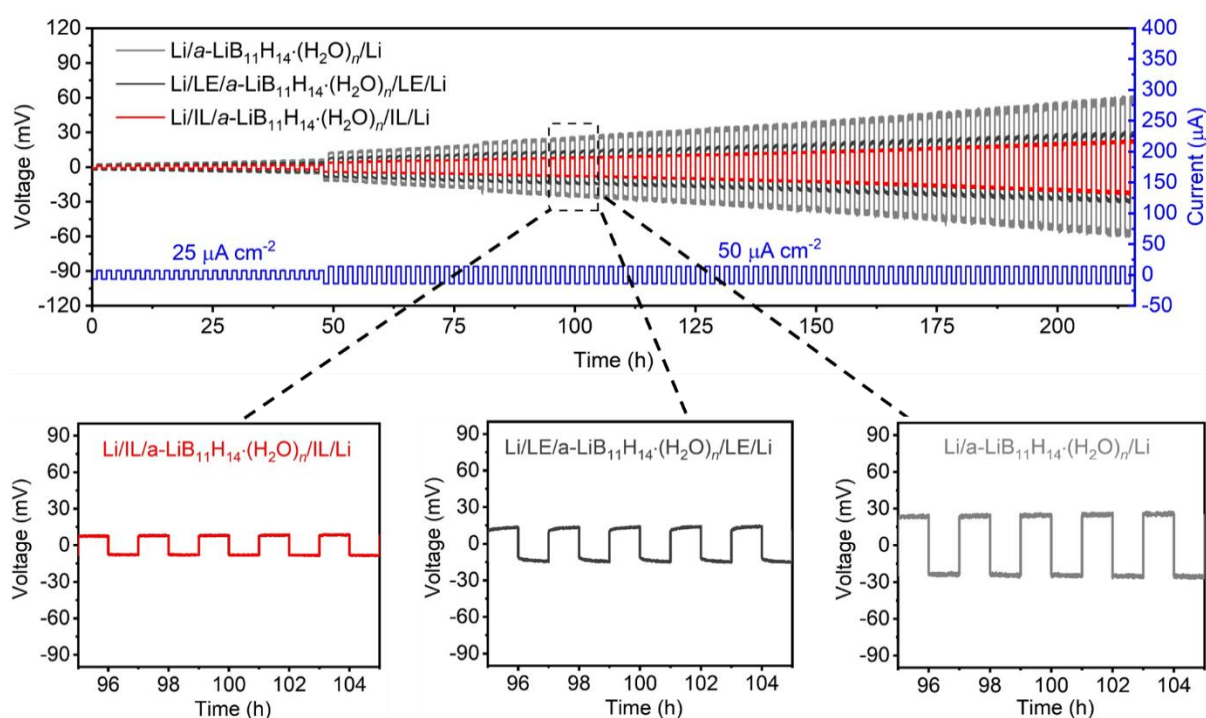


**Figure 4.21** Galvanostatic cycling profiles at 60 °C with a current density of 25 and 50  $\mu\text{A cm}^{-2}$  for 1 h in each direction of a Li/a-LiB<sub>11</sub>H<sub>14</sub>·(H<sub>2</sub>O)<sub>n</sub>/Li coin cell (grey), Li/LE/a-LiB<sub>11</sub>H<sub>14</sub>·(H<sub>2</sub>O)<sub>n</sub>/LE/Li Swagelok-type cell (black), and Li/IL/a-LiB<sub>11</sub>H<sub>14</sub>·(H<sub>2</sub>O)<sub>n</sub>/IL/Li Swagelok-type cell (red), where LE stands for liquid electrolyte (1.0 M LiPF<sub>6</sub> EC/DMC) and IL is ionic liquid (LiB<sub>11</sub>H<sub>14</sub>·2H<sub>2</sub>O).

The results in Fig. 4.21 demonstrate that the overpotential for all cells increases upon cycling, however the magnitude of the overpotential for the cell with ionic liquid (LiB<sub>11</sub>H<sub>14</sub>·2H<sub>2</sub>O) is the smallest, being 21 mV after 216 h cycling (48 h at 25  $\mu\text{A cm}^{-2}$  and 168 h at 50  $\mu\text{A cm}^{-2}$ ) compared to the cells with a LE ( $\approx$  27 mV after 48 h at 25  $\mu\text{A cm}^{-2}$  and 168 h at 50  $\mu\text{A cm}^{-2}$ ) and without an additive in a coin cell ( $\approx$  55 mV after 48 h at 25  $\mu\text{A cm}^{-2}$  and 168 h at 50  $\mu\text{A cm}^{-2}$ ). This indicates that in the absence of an effective stack pressure set-up, the use of a Swagelok-type cell instead of a coin cell and addition of an ionic liquid or liquid electrolyte



can improve the stability of Li/SSE [17], and that  $\text{LiB}_{11}\text{H}_{14}\cdot 2\text{H}_2\text{O}$  works effectively as a wetting agent for this purpose.

An enduring time control measurement was performed with a Li symmetric cell of  $\alpha\text{-LiB}_{11}\text{H}_{14}\cdot(\text{H}_2\text{O})_n$  ( $\text{Li}/\alpha\text{-LiB}_{11}\text{H}_{14}\cdot(\text{H}_2\text{O})_n/\text{Li}$ ) to evaluate its chemical stability against Li metal and to identify its critical current density (CCD). The cell was analysed from 25 to  $775 \mu\text{A cm}^{-2}$  for 30 min sweeps during 5 hours at each current with the step gap of  $25 \mu\text{A cm}^{-2}$  (Fig. 4.22).

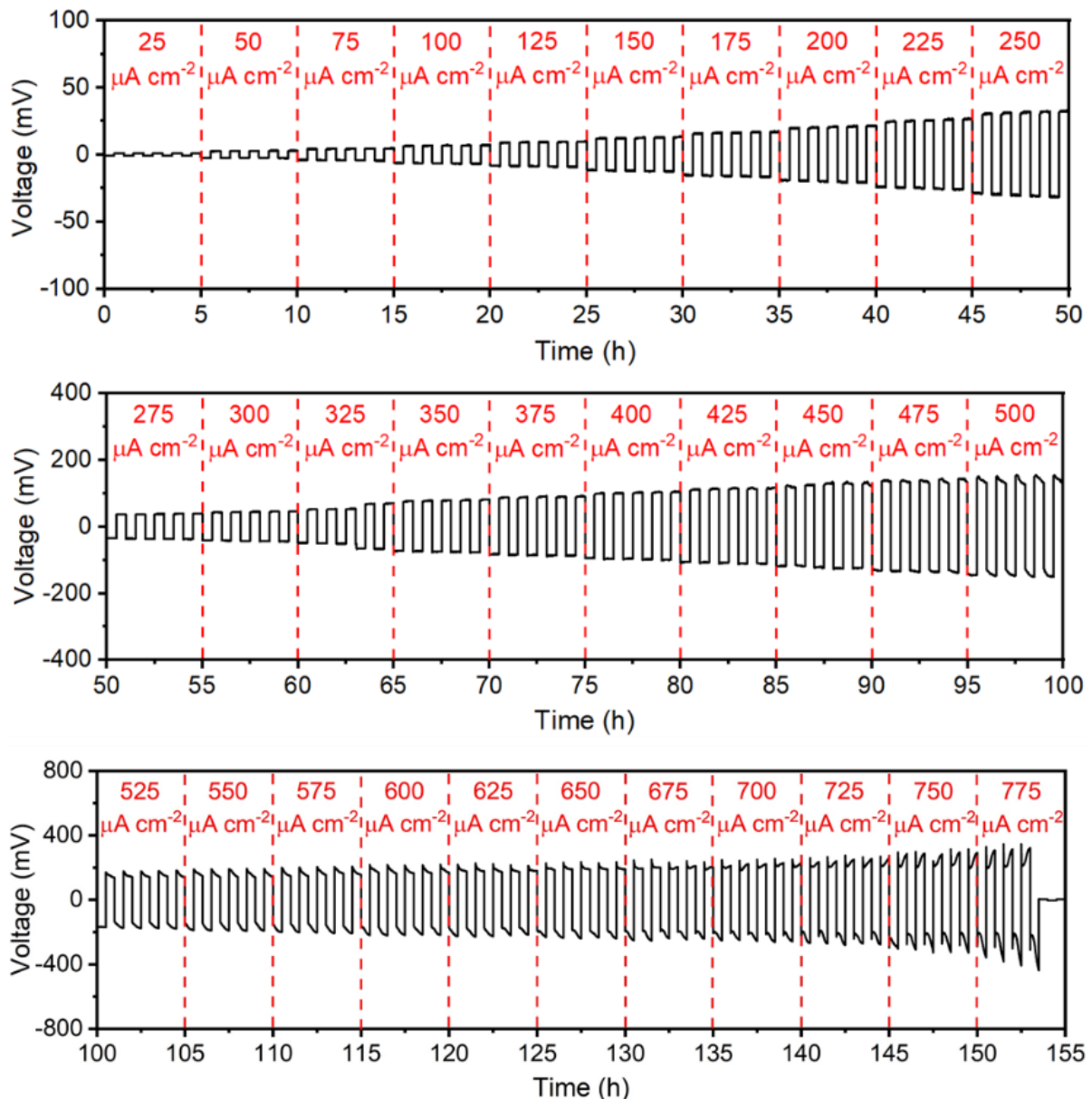


**Figure 4.22** Endurable time control measurement used to identify the critical current density of the  $\text{Li}/\alpha\text{-LiB}_{11}\text{H}_{14}\cdot(\text{H}_2\text{O})_n/\text{Li}$  symmetric cell at  $60 \text{ }^\circ\text{C}$  from 25 to  $775 \mu\text{A cm}^{-2}$ . Short circuit failure happens at  $775 \mu\text{A cm}^{-2}$ , therefore the CCD is determined to be  $750 \mu\text{A cm}^{-2}$ .

The voltage increases with increase of current density, however no major changes can be detected during cycling at each current. Polarisation can be observed as the current density reaches  $500 \mu\text{A cm}^{-2}$ , which might be attributed to an increased contact loss between Li/SSE that occurs during lithium stripping/plating leading to enhanced interfacial resistance [83]. A short circuit can be identified at the current density of  $775 \mu\text{A cm}^{-2}$ , which determines the CCD to be  $750 \mu\text{A cm}^{-2}$  at  $60^\circ\text{C}$ . This is a similar result to what is observed for Ga-doped  $\text{Li}_7\text{La}_3\text{Zr}_2\text{O}_{12}$  ( $700 \mu\text{A cm}^{-2}$  at  $27^\circ\text{C}$ ) [55] and higher than what was estimated for  $\text{Li}_2(\text{B}_{11}\text{H}_{14})(\text{CB}_{11}\text{H}_{12})$  ( $160 \mu\text{A cm}^{-2}$  at  $60^\circ\text{C}$ ) [32].

The electrode/electrolyte interfacial resistances ( $R_{\text{SEI}}$ ) for the systems  $\text{Li}/\text{IL}/\alpha\text{-LiB}_{11}\text{H}_{14}\cdot(\text{H}_2\text{O})_n/\text{IL}/\text{Li}$  and  $\text{Li}/\alpha\text{-LiB}_{11}\text{H}_{14}\cdot(\text{H}_2\text{O})_n/\text{Li}$  were calculated after a 1 hour isothermal equilibrium at  $60^\circ\text{C}$  based on the fitting of the Nyquist plots (Fig. 4.23) with the equivalent circuit model (Fig. 4.17A).

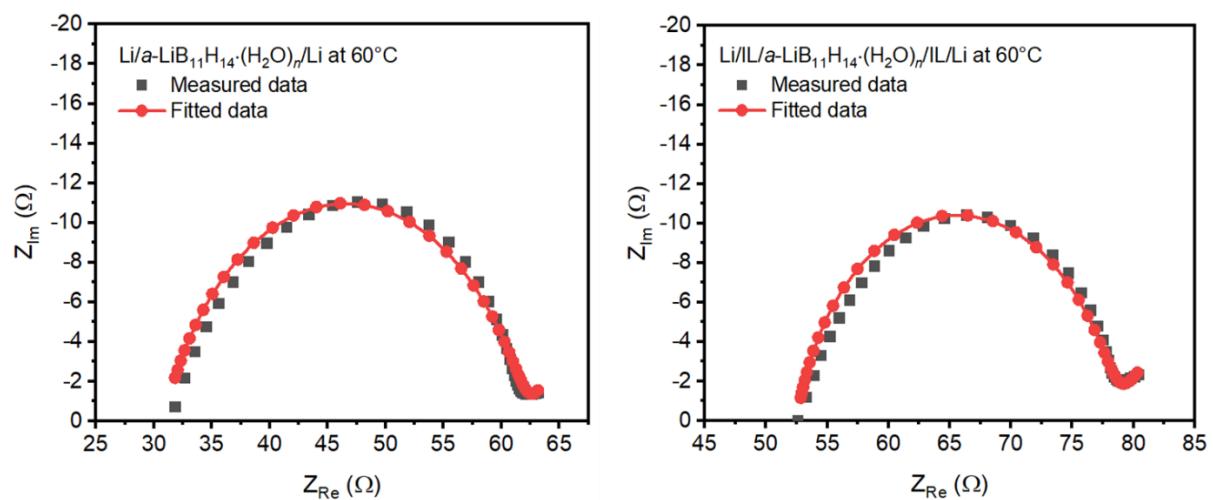


**Figure 4.23** Nyquist plots of the Li-symmetric cell (Swagelok-type) for  $\alpha\text{-LiB}_{11}\text{H}_{14}\cdot(\text{H}_2\text{O})_n$  after 1 hour stabilisation at  $60^\circ\text{C}$  with (right) and without (left) addition of the ionic liquid ( $\text{LiB}_{11}\text{H}_{14}\cdot 2\text{H}_2\text{O}$ ) at the interface Li/SSE. Data was fitted using the equivalent circuit model ( $R_1+Q_1/R_2+Wo$ ) presented in Fig. 4.17A.

As the capacitance components for both systems are in the order of  $10^{-6}$  F, the value of the parallel resistance component is attributed to the contact surface resistance [84]. In order to obtain the final result of interfacial resistance, the resistance is divided in half, as both interfaces are equivalent, and normalised by the surface area [4,35,84,85]. The results are presented in Table 4.4.

**Table 4.4** Interfacial resistance for the systems Li/IL/ $\alpha$ -LiB<sub>11</sub>H<sub>14</sub>·(H<sub>2</sub>O)<sub>n</sub>/IL/Li (IL = LiB<sub>11</sub>H<sub>14</sub>·2H<sub>2</sub>O) and Li/ $\alpha$ -LiB<sub>11</sub>H<sub>14</sub>·(H<sub>2</sub>O)<sub>n</sub>/Li and circuit component values  $R_1$  and  $R_2$  from Nyquist plots shown in Fig. 4.23.

System	$R_1$ ( $\Omega$ )	$R_2$ ( $\Omega$ )	$R_{SEI}$ ( $\Omega$ cm <sup>2</sup> )
Li/SSE/Li	30.8 $\pm$ 0.7	31.1 $\pm$ 2.1	4.4 $\pm$ 0.3
Li/IL/SSE/IL/Li	52.5 $\pm$ 0.5	25.7 $\pm$ 1.5	3.6 $\pm$ 0.2

The interfacial resistance was calculated to be 3.6  $\Omega$  cm<sup>2</sup> ( $\pm$  0.2) for the system containing ionic liquid and 4.4  $\Omega$  cm<sup>2</sup> ( $\pm$  0.3) for the system with bare SSE/Li. Even though the initial difference in interfacial resistance is small, over time and with the application of a current, the overpotential (and thus interfacial resistance) increases at a higher rate for the system that does not contain a wetting agent and is assembled in a coin cell (Fig. 4.21). Despite the growth in interfacial resistance seen in Fig. 4.21 the magnitude of interfacial resistance is still small [12], which makes  $\alpha$ -LiB<sub>11</sub>H<sub>14</sub>·(H<sub>2</sub>O)<sub>n</sub> coupled with LiB<sub>11</sub>H<sub>14</sub>·2H<sub>2</sub>O promising materials for lithium ion technology applications.

#### 4.3.4 Battery Test

The electrochemical properties of  $\alpha$ -LiB<sub>11</sub>H<sub>14</sub>·(H<sub>2</sub>O)<sub>n</sub> as a solid-state electrolyte (SSE) were also evaluated in a solid-liquid hybrid battery with a mixture of TiS<sub>2</sub> (active cathode material with a high electronic conductivity) with the SSE as a cathode, Li metal as the anode, and a coating of a drop of LE (1.0 M LiPF<sub>6</sub> EC/DMC) on the side of Li/SSE to reduce interfacial resistance (Fig. 4.24A). Titanium disulphide is a known solid cathode material with a layered structure that has the ability to favourably intercalate and store Li ions with minor lattice expansion [86–88]. Moreover, it presents high electronic conductivity, low weight and relatively low cost, which makes it suitable for battery studies [86–88]. With the superionic conductivity exhibited by  $\alpha$ -LiB<sub>11</sub>H<sub>14</sub>·(H<sub>2</sub>O)<sub>n</sub> at 60 °C ( $1.2 \times 10^{-2}$  S cm<sup>-1</sup>), this temperature was selected to perform all battery tests. The cell Li/LE/ $\alpha$ -LiB<sub>11</sub>H<sub>14</sub>·(H<sub>2</sub>O)<sub>n</sub>/ $\alpha$ -LiB<sub>11</sub>H<sub>14</sub>·(H<sub>2</sub>O)<sub>n</sub>+TiS<sub>2</sub> was cycled at different C-rates, from 0.05 to 0.4 C (1 C = 239 mA g<sup>-1</sup>) in the voltage range 1.7 – 2.5 V, and reversible charge-discharge profiles can be observed (Fig. 4.24B). The C-rate is here defined as  $nC$ , in which the current fully discharges and charges the battery in  $1/n$  hours. The discharge capacity in the first cycle was 190 mAh g<sup>-1</sup>, which corresponds to 79% of the theoretical gravimetric energy storage capacity of TiS<sub>2</sub> (239 mAh g<sup>-1</sup>), the same observed when using

$\text{Li}_2(\text{B}_{11}\text{H}_{14})(\text{CB}_{11}\text{H}_{12})$  as an SSE [32]. With the increase of  $C$ -rate from 0.05  $C$  by 2, 4, 6 and 8 times, the capacity retention of the battery dropped to 72, 69, 67 and 65%, respectively (Fig. 4.24C), which is expected, as there is an increase in current density. The battery was then cycled 50 more times at the highest  $C$ -rate (0.4  $C = 95.6 \text{ mA g}^{-1}$ ) (Fig. 4.24D), and the cell retained 83% of its capacity shown in the first cycle at 0.4  $C$  ( $156 \text{ mAh g}^{-1}$ ), which corresponds to a retention of 68% of the first discharge capacity obtained at 0.05  $C$  ( $190 \text{ mAh g}^{-1}$ ). Fig. 4.24E shows that similar discharge capacity of  $200 \text{ mAh g}^{-1}$  was obtained at 0.1  $C$  in the first cycle, and the cell retained 84% of this initial capacity after 5 more cycles at 0.1  $C$ . At the 7<sup>th</sup> cycle,  $C$ -rate was doubled, and a slight drop of specific capacity occurred, which is expected with  $C$ -rate increase. After 60 cycles at 0.2  $C$ , the cell retained 82% of its capacity from its first cycle at this  $C$ -rate ( $162 \text{ mAh g}^{-1}$ ). A similar result is observed for the battery containing the SSE composite  $\text{LiBH}_4\text{-MgO}$ , which holds more than 80% capacity after 65 cycles at 60 °C, however at the lower  $C$ -rate of 0.05  $C$  [4]. The retained capacity obtained here is slightly lower than the one observed for a  $\text{Li}_2(\text{B}_{11}\text{H}_{14})(\text{CB}_{11}\text{H}_{12})$  SSE, which exhibits a retention capacity of  $\approx 84\%$  (from the 6<sup>th</sup> cycle) after 100 cycles [32]. Nevertheless, it is important to highlight that the experiment with  $\text{Li}_2(\text{B}_{11}\text{H}_{14})(\text{CB}_{11}\text{H}_{12})$  was conducted with a continuous stack pressure to the cell [32]. Cycling causes morphological changes at the interface of the electrode/electrolyte, which leads to loss of contact and reduces the performance and stability of a solid-state battery [4,80]. The addition of the liquid electrolyte between Li and SSE reduces its interfacial resistance but it still does increase upon cycling. When high external pressures are applied to the cell, more contact can be maintained between electrode/electrolyte that may be more effective than just adding a wetting agent to the interface [89]. Fig. 4.24E also shows that the cell of  $\text{Li}/\text{LE}/\alpha\text{-LiB}_{11}\text{H}_{14}\cdot(\text{H}_2\text{O})_n/\alpha\text{-LiB}_{11}\text{H}_{14}\cdot(\text{H}_2\text{O})_n+\text{TiS}_2$  exhibited a Coulombic efficiency of  $\approx 98\%$  during the first 6 cycles, and it slightly increased to 99% after shifting to a higher  $C$ -rate, keeping this Coulombic efficiency for the rest of the experiment.

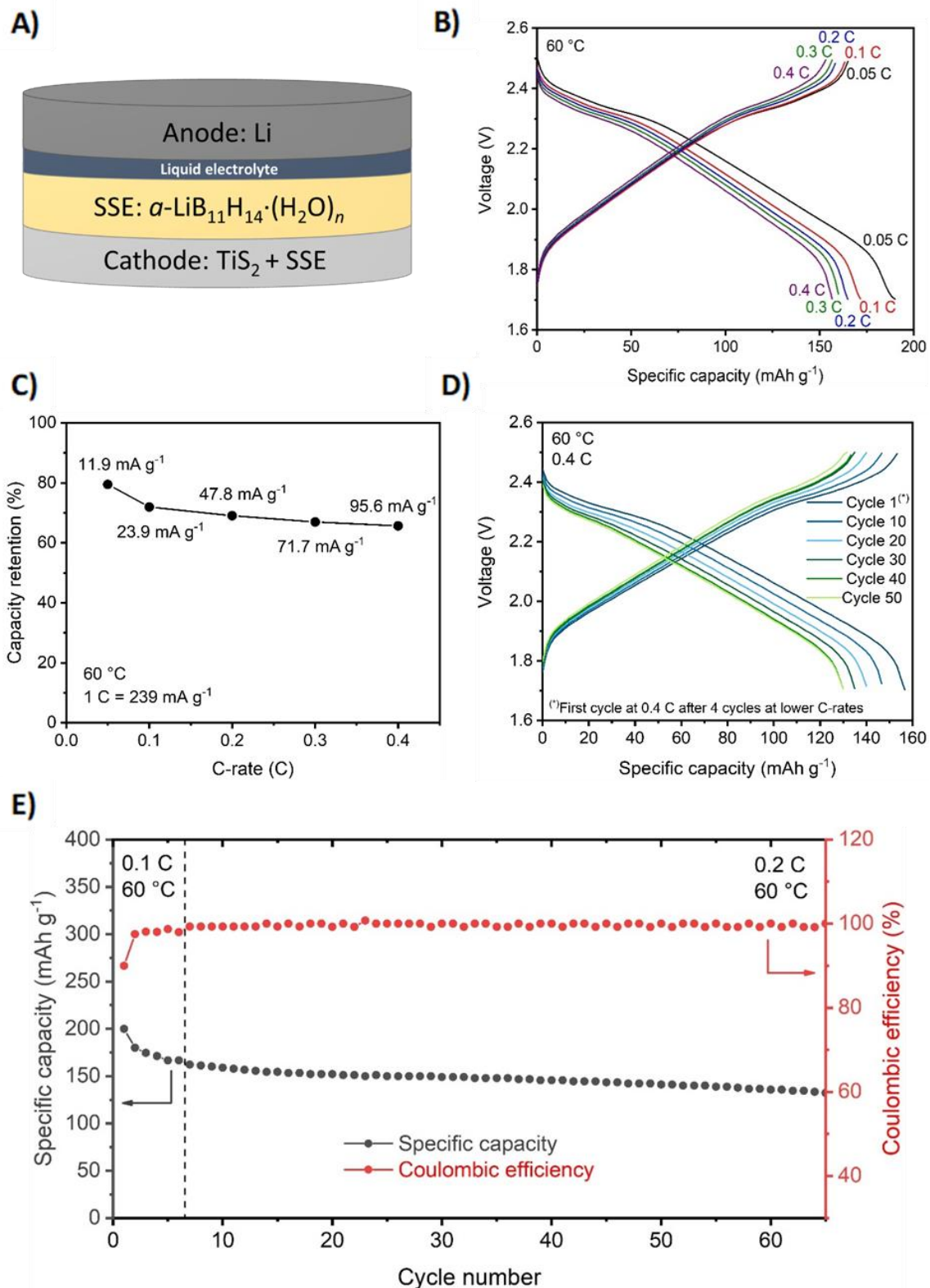


**Figure 4.24** A) Schematic representation of the solid-state battery  $\text{Li}/\text{LE}/\alpha\text{-LiB}_{11}\text{H}_{14}\cdot(\text{H}_2\text{O})_n/\alpha\text{-LiB}_{11}\text{H}_{14}\cdot(\text{H}_2\text{O})_n+\text{TiS}_2$  in a Swagelok-type cell. B) Discharge/charge profiles at 0.05, 0.1, 0.2, 0.3 and 0.4 C (1.7 – 2.5 V) at 60 °C. C) Capacity retention at different C-rates. D) Discharge/charge profiles at 0.4 C for 50 cycles at 60 °C after being initially cycled at 0.05, 0.1, 0.2 and 0.3 C. E) Coulombic efficiency and discharge specific capacity at 0.1 C for the first 6 cycles and at 0.2 C from the 7<sup>th</sup> to the 65<sup>th</sup> cycle.

A battery of Li/IL/ $\alpha$ -LiB<sub>11</sub>H<sub>14</sub>·(H<sub>2</sub>O)<sub>n</sub>/IL/ $\alpha$ -LiB<sub>11</sub>H<sub>14</sub>·(H<sub>2</sub>O)<sub>n</sub>+TiS<sub>2</sub> was also prepared (IL instead of LE wetting agent) and had its electrochemical properties evaluated in the same way as the cell containing LE. Based on the results presented in Fig. 4.25, it is possible to observe reversible charge-discharge cycling and that the discharge capacity in the first cycle at 0.05 C (194 mAh g<sup>-1</sup>) was similar to the one observed for the cell with LE. This corresponds to 81% of theoretical capacity of TiS<sub>2</sub> (239 mAh g<sup>-1</sup>). However, the increase of C-rate from 0.05 C by 2, 4, 6 and 8 times causes the capacity retention of the battery to drop to 59, 46, 39 and 34%, respectively (Fig. 4.25B), which indicates a much lower performance than when the battery is prepared with the addition of LE (Fig. 4.25C). When the cell is cycled only at 0.4 C (Fig. 4.25D), its discharge capacity in the first cycle was 186 mAh g<sup>-1</sup>, which corresponds to 78% of the theoretical capacity of TiS<sub>2</sub> (239 mAh g<sup>-1</sup>), and it drops to 63 mAh g<sup>-1</sup> in the 50<sup>th</sup> cycle, which means that the capacity retention was only 34% from its first cycle.

The addition of LiB<sub>11</sub>H<sub>14</sub>·2H<sub>2</sub>O at the interface of SSE/Li is a good strategy to reduce interfacial resistance and overpotential during cycling (Fig. 4.21), however it does not improve the performance of the battery as much as a traditional LE wetting agent when TiS<sub>2</sub> is used as the cathode (Fig. 4.25). This may be related to some instability or reactivity between LiB<sub>11</sub>H<sub>14</sub>·2H<sub>2</sub>O and TiS<sub>2</sub>, but other types of cathode materials, such as sulphur [35] or oxide cathodes [27,84,90], should be investigated to analyse their suitability. The preparation of a cell with the application of LiB<sub>11</sub>H<sub>14</sub>·2H<sub>2</sub>O only at the SSE/Li interface should also be assessed. Surface chemistry analyses should also be conducted to assess the interface Li/SSE after lithium stripping/plating. Experiments to improve the battery performance of  $\alpha$ -LiB<sub>11</sub>H<sub>14</sub>·(H<sub>2</sub>O)<sub>n</sub> should be considered for further studies with the application of a stack pressure combined with the use of an ionic liquid or liquid electrolyte in the interface SSE/Li and SSE/cathode. This would increase the interfacial contact and hence aid capacity retention. Further research on the application of  $\alpha$ -LiB<sub>11</sub>H<sub>14</sub>·(H<sub>2</sub>O)<sub>n</sub> with the use of sulphur as the cathode, for example, should also be considered due to the increased energy density (1672 mAh g<sup>-1</sup>) and applicable working voltage (2.1 V vs. Li<sup>+</sup>/Li) [35] of this electrode with  $\alpha$ -LiB<sub>11</sub>H<sub>14</sub>·(H<sub>2</sub>O)<sub>n</sub> as SSE.

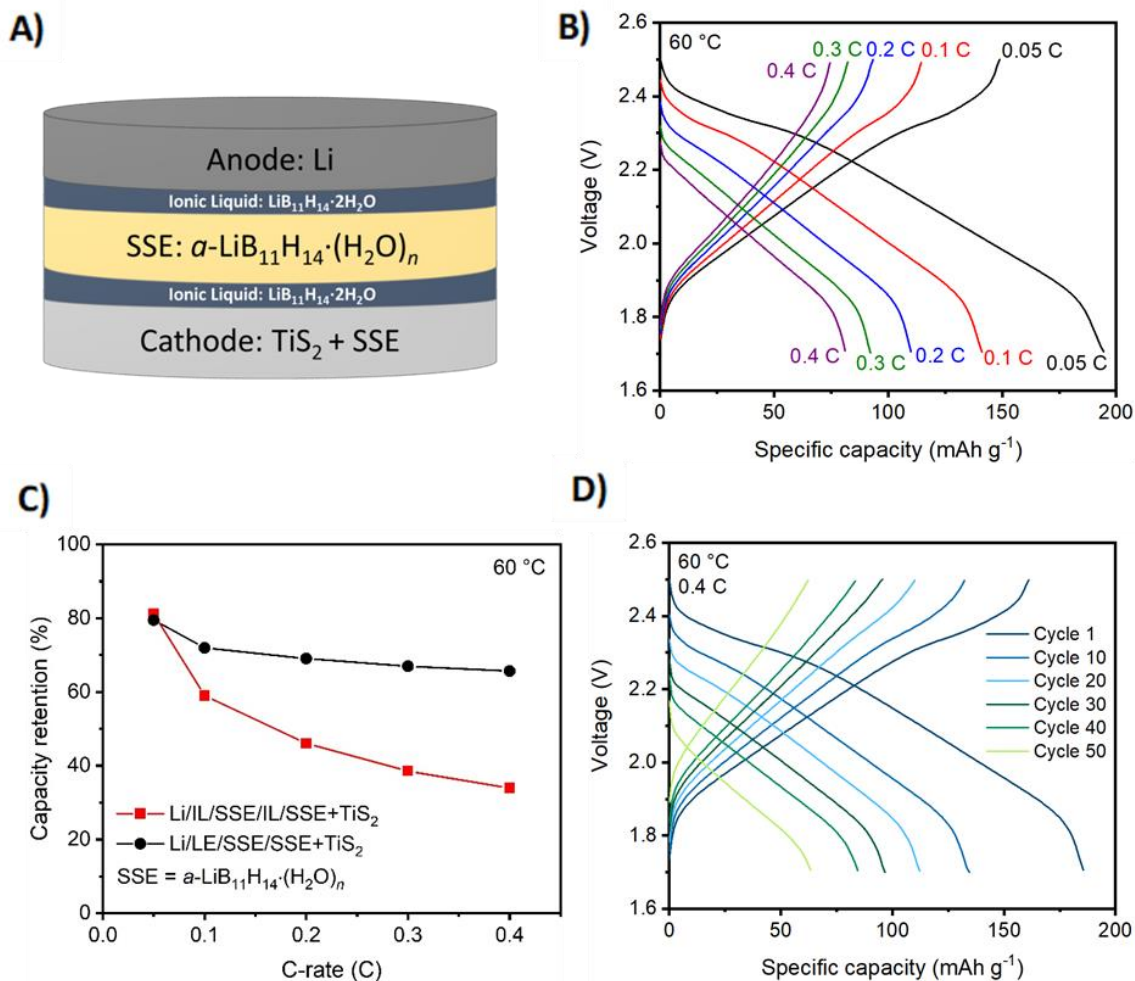


**Figure 4.25** A) Schematic representation of the solid-state battery  $\text{Li}/\text{IL}/\alpha\text{-LiB}_{11}\text{H}_{14}\cdot (\text{H}_2\text{O})_n/\text{IL}/\alpha\text{-LiB}_{11}\text{H}_{14}\cdot (\text{H}_2\text{O})_n + \text{TiS}_2$  in a Swagelok-type cell. B) Discharge/charge profiles at 0.05, 0.1, 0.2, 0.3 and 0.4 C (1.7 – 2.5 V) at 60 °C. C) Capacity retention at different C-rates compared to the cell of  $\text{Li}/\text{LE}/\alpha\text{-LiB}_{11}\text{H}_{14}\cdot (\text{H}_2\text{O})_n/\alpha\text{-LiB}_{11}\text{H}_{14}\cdot (\text{H}_2\text{O})_n + \text{TiS}_2$ . D) Discharge/charge profiles at 0.4 C for 50 cycles at 60 °C.

#### 4.4 CONCLUSION

A low cost synthesis of hydrated and anhydrous  $\text{LiB}_{11}\text{H}_{14}$  salts is presented. It was observed that the salt  $\text{LiB}_{11}\text{H}_{14}\cdot 2\text{H}_2\text{O}$  consists of a new class of ionic liquid, as it melts at  $\approx 70$  °C. The sample  $\alpha\text{-LiB}_{11}\text{H}_{14}\cdot (\text{H}_2\text{O})_n$  undergoes a polymorphic phase transition at the same temperature and assumes a HT polymorph with a cubic  $Ia\bar{3}d$  space group and superionic conductivity ( $3.2 \times 10^{-2} \text{ S cm}^{-1}$  at 70 °C). Hence, the water content in the  $\text{LiB}_{11}\text{H}_{14}$  salt seems to be a good strategy to tune the thermal and ionic conductivity properties.  $\alpha\text{-LiB}_{11}\text{H}_{14}\cdot (\text{H}_2\text{O})_n$  also shows an oxidative stability limit of 2.8 V against  $\text{Li}^+/\text{Li}$  and reversible Li plating/stripping for at least 216 hours cycling.

The material  $\text{LiB}_{11}\text{H}_{14}\cdot 2\text{H}_2\text{O}$  worked effectively as an ionic liquid additive to the interface between lithium and solid state electrolyte at 60 °C in a Swagelok-type cell as it significantly reduced the magnitude of the overpotential (and thus interfacial resistance) upon cycling. However, it was not enough to completely resolve the overpotential issue during lithium stripping/plating. Further optimisation is required, such as the application of an external pressure to increase interfacial contact, for future SSE research. The use of  $\text{LiB}_{11}\text{H}_{14}\cdot 2\text{H}_2\text{O}$  as an ionic liquid in the interface SSE/electrode did not demonstrate good performance with  $\text{TiS}_2$  as a battery cathode. However, its application should be investigated against other types of cathode materials and electrolytes. The use of the liquid electrolyte 1.0 M  $\text{LiPF}_6$  EC/DMC (v/v = 50/50) as a wetting agent in the solid-liquid hybrid cell was more efficient and exhibited good performance.

Despite the high temperature required (60 °C) for the use of  $\alpha\text{-LiB}_{11}\text{H}_{14}\cdot(\text{H}_2\text{O})_n$  as SSE, the promising features this salt exhibits, such as, liquid-like ionic conductivity, relatively high oxidative stability limit vs. Li metal, cyclability against Li metal anode and  $\text{TiS}_2$  cathode, and a facile low cost synthesis, make it an important contribution for future hydridoborate SSE research. The variation of water content in the crystal structure can also be considered a novel strategy to tune ionic conductivity properties and to perhaps obtain a SSE with enhanced properties at RT in the future. The application of a liquid electrolyte or an ionic liquid at the interface SSE/electrode with the use of an apparatus that provides an external pressure seems to be a good strategy to increase performance of the battery with  $\alpha\text{-LiB}_{11}\text{H}_{14}\cdot(\text{H}_2\text{O})_n$  as SSE.

#### 4.5 REFERENCES

- [1] F. Zheng, M. Kotobuki, S. Song, M.O. Lai, L. Lu, Review on solid electrolytes for all-solid-state lithium-ion batteries, *J. Power Sources*. 389 (2018) 198–213. <https://doi.org/10.1016/j.jpowsour.2018.04.022>.
- [2] Y. Nishi, Lithium ion secondary batteries; past 10 years and the future, *J. Power Sources*. 100 (2001) 101–106. [https://doi.org/10.1016/S0378-7753\(01\)00887-4](https://doi.org/10.1016/S0378-7753(01)00887-4).
- [3] H.W. Kim, P. Manikandan, Y.J. Lim, J.H. Kim, S. Nam, Y. Kim, Hybrid solid electrolyte with the combination of  $\text{Li}_7\text{La}_3\text{Zr}_2\text{O}_{12}$  ceramic and ionic liquid for high voltage pseudo-solid-state Li-ion batteries, *J. Mater. Chem. A*. 4 (2016) 17025–17032. <https://doi.org/10.1039/c6ta07268b>.



- [4] V. Gulino, M. Brighi, F. Murgia, P. Ngene, P. De Jongh, R. Černý, M. Baricco, Room-Temperature Solid-State Lithium-Ion Battery Using a  $\text{LiBH}_4\text{-MgO}$  Composite Electrolyte, *ACS Appl. Energy Mater.* 4 (2021) 1228–1236. <https://doi.org/10.1021/acsaem.0c02525>.
- [5] S. Kim, K. Kisu, S. Takagi, H. Oguchi, S. Orimo, Complex hydride solid electrolytes of the  $\text{Li}(\text{CB}_9\text{H}_{10})\text{-Li}(\text{CB}_{11}\text{H}_{12})$  quasi-binary system: relationship between the solid solution and phase transition, and the electrochemical properties, *ACS Appl. Energy Mater.* 3 (2020) 4831–4839. <https://doi.org/10.1021/acsaem.0c00433>.
- [6] L. Han, M.L. Lehmann, J. Zhu, T. Liu, Z. Zhou, X. Tang, C. Te Heish, A.P. Sokolov, P. Cao, X.C. Chen, T. Saito, Recent Developments and Challenges in Hybrid Solid Electrolytes for Lithium-Ion Batteries, *Front. Energy Res.* 8 (2020) 1–19. <https://doi.org/10.3389/fenrg.2020.00202>.
- [7] H. Zhang, C. Li, M. Piszcz, E. Coya, T. Rojo, L.M. Rodriguez-Martinez, M. Armand, Z. Zhou, Single lithium-ion conducting solid polymer electrolytes: advances and perspectives, *Chem. Soc. Rev.* 46 (2017) 797–815. <https://doi.org/10.1039/c6cs00491a>.
- [8] Z. Ding, J. Li, J. Li, C. An, Review—Interfaces: key issue to be solved for all solid-state lithium battery technologies, *J. Electrochem. Soc.* 167 (2020) 070541. <https://doi.org/10.1149/1945-7111/ab7f84>.
- [9] H. Kim, G. Jeong, Y.-U. Kim, J.-H. Kim, C.-M. Park, H.-J. Sohn, Metallic anodes for next generation secondary batteries, *Chem. Soc. Rev.* 42 (2013) 9011–9034. <https://doi.org/10.1039/c3cs60177c>.
- [10] Z. Lu, F. Ciucci, Metal Borohydrides as Electrolytes for Solid-State Li, Na, Mg, and Ca Batteries: A First-Principles Study, *Chem. Mater.* 29 (2017) 9308–9319. <https://doi.org/10.1021/acs.chemmater.7b03284>.
- [11] A. Manthiram, X. Yu, S. Wang, Lithium battery chemistries enabled by solid-state electrolytes, *Nat. Rev. Mater.* 2 (2017) 1–16. <https://doi.org/10.1038/natrevmats.2016.103>.
- [12] Z. Jiang, Q. Han, S. Wang, H. Wang, Reducing the interfacial resistance in all-solid-state lithium batteries based on oxide ceramic electrolytes, *ChemElectroChem.* 6 (2019) 2970–2983. <https://doi.org/10.1002/celec.201801898>.
- [13] X. Pan, L. Liu, P. Yang, J. Zhang, M. An, Effect of interface wetting on the performance

- of gel polymer electrolytes-based solid-state lithium metal batteries, *Solid State Ionics*. 357 (2020) 115466. <https://doi.org/10.1016/j.ssi.2020.115466>.
- [14] T. Kim, D.-Y. Son, L.K. Ono, Y. Jiang, Y. Qi, A solid-liquid hybrid electrolyte for lithium ion batteries enabled by a single-body polymer/indium tin oxide architecture, *J. Phys. D: Appl. Phys.* 54 (2021) 475501. <https://doi.org/10.1088/1361-6463/ac196e>.
- [15] J. Tang, L. Wang, L. You, X. Chen, T. Huang, L. Zhou, Z. Geng, A. Yu, Effect of organic electrolyte on the performance of solid electrolyte for solid-liquid hybrid lithium batteries, *ACS Appl. Mater. Interfaces*. 13 (2021) 2685–2693. <https://doi.org/10.1021/acscami.0c19671>.
- [16] J. Zheng, M. Gu, H. Chen, P. Meduri, M.H. Engelhard, J.-G. Zhang, J. Liu, J. Xiao, Ionic liquid-enhanced solid state electrolyte interface (SEI) for lithium-sulfur batteries, *J. Mater. Chem. A*. 1 (2013) 8464–8470. <https://doi.org/10.1039/c3ta11553d>.
- [17] B. Zheng, J. Zhu, H. Wang, M. Feng, E. Umeshbabu, Y. Li, Q.-H. Wu, Y. Yang, Stabilizing  $\text{Li}_{10}\text{SnP}_2\text{S}_{12}/\text{Li}$  Interface via an in Situ Formed Solid Electrolyte Interphase Layer, *ACS Appl. Mater. Interfaces*. 10 (2018) 25473–25482. <https://doi.org/10.1021/acscami.8b08860>.
- [18] H. Huo, N. Zhao, J. Sun, F. Du, Y. Li, X. Guo, Composite electrolytes of polyethylene oxides/garnets interfacially wetted by ionic liquid for room-temperature solid-state lithium battery, *J. Power Sources*. 372 (2017) 1–7. <https://doi.org/10.1016/j.jpowsour.2017.10.059>.
- [19] K.-W. Kim, H.W. Kim, Y. Kim, J.-K. Kim, Composite gel polymer electrolyte with ceramic particles for  $\text{LiNi}_{1/3}\text{Mn}_{1/3}\text{Co}_{1/3}\text{O}_2\text{-Li}_4\text{Ti}_5\text{O}_{12}$  lithium ion batteries, *Electrochim. Acta*. 236 (2017) 394–398. <https://doi.org/10.1016/j.electacta.2017.03.176>.
- [20] N.M. Asl, J. Keith, C. Lim, L. Zhu, Y. Kim, Inorganic solid/organic liquid hybrid electrolyte for use in Li-ion battery, *Electrochim. Acta*. 79 (2012) 8–16. <https://doi.org/10.1016/j.electacta.2012.06.038>.
- [21] C. Wang, Q. Sun, Y. Liu, Y. Zhao, X. Li, X. Lin, M.N. Banis, M. Li, W. Li, K.R. Adair, D. Wang, J. Liang, R. Li, L. Zhang, R. Yang, S. Lu, X. Sun, Boosting the performance of lithium batteries with solid-liquid hybrid electrolytes: Interfacial properties and effects of liquid electrolytes, *Nano Energy*. 48 (2018) 35–43. <https://doi.org/10.1016/j.nanoen.2018.03.020>.
- [22] X. Han, Y. Gong, K. Fu, X. He, G.T. Hitz, J. Dai, A. Pearse, B. Liu, H. Wang, G. Rubloff, Y.

- Mo, V. Thangadurai, E.D. Wachsman, L. Hu, Negating interfacial impedance in garnet-based solid-state Li metal batteries, *Nat. Mater.* 16 (2017) 572–579. <https://doi.org/10.1038/nmat4821>.
- [23] V. Thangadurai, S. Narayanan, D. Pinzarú, Garnet-type solid-state fast Li ion conductors for Li batteries: critical review, *Chem. Soc. Rev.* 43 (2014) 4714–4727. <https://doi.org/10.1039/c4cs00020j>.
- [24] N. Kamaya, K. Homma, Y. Yamakawa, M. Hirayama, R. Kanno, M. Yonemura, T. Kamiyama, Y. Kato, S. Hama, K. Kawamoto, A. Mitsui, A lithium superionic conductor, *Nat. Mater.* 10 (2011) 682–686. <https://doi.org/10.1038/nmat3066>.
- [25] J. Lau, R.H. DeBlock, D.M. Butts, D.S. Ashby, C.S. Choi, B.S. Dunn, Sulfide solid electrolytes for lithium battery applications, *Adv. Energy Mater.* 8 (2018) 1800933. <https://doi.org/10.1002/aenm.201800933>.
- [26] Q. Zhang, D. Cao, Y. Ma, A. Natan, P. Aurora, H. Zhu, Sulfide-based solid-state electrolytes: synthesis, stability, and potential for all-solid-state batteries, *Adv. Mater.* 31 (2019) 1901131. <https://doi.org/10.1002/adma.201901131>.
- [27] F. Lu, Y. Pang, M. Zhu, F. Han, J. Yang, F. Fang, D. Sun, S. Zheng, C. Wang, A high-performance Li–B–H electrolyte for all-solid-state Li batteries, *Adv. Funct. Mater.* 29 (2019) 1809219. <https://doi.org/10.1002/adfm.201809219>.
- [28] M. Matsuo, Y. Nakamori, S. Orimo, H. Maekawa, H. Takamura, Lithium superionic conduction in lithium borohydride accompanied by structural transition, *Appl. Phys. Lett.* 91 (2007) 224103. <https://doi.org/10.1063/1.2817934>.
- [29] W.S. Tang, M. Dimitrievska, V. Stávila, W. Zhou, H. Wu, A.A. Talin, T.J. Udovic, Order-disorder transitions and superionic conductivity in the sodium *nido*-undeca(carba)borates, *Chem. Mater.* 29 (2017) 10496–10509. <https://doi.org/10.1021/acs.chemmater.7b04332>.
- [30] W.S. Tang, M. Matsuo, H. Wu, V. Stávila, W. Zhou, A.A. Talin, A. V Soloninin, R. V Skoryunov, O.A. Babanova, A. V Skripov, A. Unemoto, S.I. Orimo, T.J. Udovic, Liquid-like ionic conduction in solid lithium and sodium monocarba-*c/oso*-decaborates near or at room temperature, *Adv. Energy Mater.* 6 (2016) 1502237. <https://doi.org/10.1002/aenm.201502237>.
- [31] W.S. Tang, A. Unemoto, W. Zhou, V. Stávila, M. Matsuo, H. Wu, S. Orimo, T.J. Udovic, Unparalleled lithium and sodium superionic conduction in solid electrolytes with large

- monovalent cage-like anions, *Energy Environ. Sci.* 8 (2015) 3637–3645. <https://doi.org/10.1039/c5ee02941d>.
- [32] S.H. Payandeh, D. Rentsch, Z. Łodziana, R. Asakura, L. Bigler, R. Černý, C. Battaglia, A. Remhof, *Nido-Hydroborate-Based Electrolytes for All-Solid-State Lithium Batteries*, *Adv. Funct. Mater.* 31 (2021) 2010046. <https://doi.org/10.1002/adfm.202010046>.
- [33] P.E. de Jongh, D. Blanchard, M. Matsuo, T.J. Udovic, S. Orimo, Complex hydrides as room-temperature solid electrolytes for rechargeable batteries, *Appl. Phys. A Mater. Sci. Process.* 122 (2016) 251. <https://doi.org/10.1007/s00339-016-9807-2>.
- [34] R. Mohtadi, S.I. Orimo, The renaissance of hydrides as energy materials, *Nat. Rev. Mater.* 2 (2016) 1–16. <https://doi.org/10.1038/natrevmats.2016.91>.
- [35] S. Kim, H. Oguchi, N. Toyama, T. Sato, S. Takagi, T. Otomo, D. Arunkumar, N. Kuwata, J. Kawamura, S. Orimo, A complex hydride lithium superionic conductor for high-energy-density all-solid-state lithium metal batteries, *Nat. Commun.* 10 (2019) 1–9. <https://doi.org/10.1038/s41467-019-09061-9>.
- [36] Y.S. Choi, Y.-S. Lee, K.H. Oh, Y.W. Cho, Interface-enhanced Li ion conduction in a  $\text{LiBH}_4\text{-SiO}_2$  solid electrolyte, *Phys. Chem. Chem. Phys.* 18 (2016) 22540–22547. <https://doi.org/10.1039/c6cp03563a>.
- [37] V. Gulino, L. Barberis, P. Ngene, M. Baricco, P.E. De Jongh, Enhancing Li-ion conductivity in  $\text{LiBH}_4$ -based solid electrolytes by adding various nanosized oxides, *ACS Appl. Energy Mater.* 3 (2020) 4941–4948. <https://doi.org/10.1021/acsaem.9b02268>.
- [38] Y.S. Choi, Y.S. Lee, D.J. Choi, K.H. Chae, K.H. Oh, Y.W. Cho, Enhanced Li ion conductivity in  $\text{LiBH}_4\text{-Al}_2\text{O}_3$  mixture via interface engineering, *J. Phys. Chem. C.* 121 (2017) 26209–26215. <https://doi.org/10.1021/acs.jpcc.7b08862>.
- [39] M. Matsuo, A. Remhof, P. Martelli, R. Caputo, M. Ernst, Y. Miura, T. Sato, H. Oguchi, H. Maekawa, H. Takamura, A. Borgschulte, A. Züttel, S. Orimo, Complex hydrides with  $(\text{BH}_4)^-$  and  $(\text{NH}_2)^-$  anions as new lithium fast-ion conductors, *J. Am. Chem. Soc.* 131 (2009) 16389–16391. <https://doi.org/10.1021/ja907249p>.
- [40] D. Sveinbjörnsson, J.S.G. Myrdal, D. Blanchard, J.J. Bentzen, T. Hirata, M.B. Mogensen, P. Norby, S.-I. Orimo, T. Vegge, Effect of heat treatment on the lithium ion conduction of the  $\text{LiBH}_4\text{-LiI}$  solid solution, *J. Phys. Chem. C.* 117 (2013) 3249–3257. <https://doi.org/10.1021/jp310050g>.
- [41] A. Takano, I. Oikawa, A. Kamegawa, H. Takamura, Enhancement of the lithium-ion

- conductivity of  $\text{LiBH}_4$  by hydration, *Solid State Ionics*. 285 (2016) 47–50. <https://doi.org/10.1016/j.ssi.2015.06.004>.
- [42] D. H. P. Souza, K.T. Møller, S.A. Moggach, T.D. Humphries, A.M. D’Angelo, C.E. Buckley, M. Paskevicius, Hydrated alkali- $\text{B}_{11}\text{H}_{14}$  salts as potential solid-state electrolytes, *J. Mater. Chem. A*. 9 (2021) 15027–15037. <https://doi.org/10.1039/d1ta01551f>.
- [43] Y. Yan, J.B. Grinderslev, Y.-S. Lee, M. Jørgensen, Y.W. Cho, R. Černý, T.R. Jensen, Ammonia-assisted fast Li-ion conductivity in a new hemiammine lithium borohydride,  $\text{LiBH}_4 \cdot 1/2\text{NH}_3$ , *Chem. Commun.* 56 (2020) 3971–3974. <https://doi.org/10.1039/c9cc09990e>.
- [44] A. Berger, C.E. Buckley, M. Paskevicius, Synthesis of *closo*- $\text{CB}_{11}\text{H}_{12}$ -Salts Using Common Laboratory Reagents, *Inorg. Chem.* 60 (2021) 14744–14751. <https://doi.org/10.1021/acs.inorgchem.1c01896>.
- [45] B. Ringstrand, D. Bateman, R.K. Shoemaker, Z. Jano-user, Improved synthesis of [*closo*-1- $\text{CB}_9\text{H}_{10}$ ]<sup>-</sup> anion and new C-substituted derivatives, *Collect. Czechoslov. Chem. Commun.* 74 (2009) 419–431. <https://doi.org/10.1135/cccc2008151>.
- [46] A. Hepp, R. Labbow, F. Reiß, A. Schulz, A. Villinger, Carba-*closo*-dodecaborates – synthesis, structure, and energetics, *Eur. J. Inorg. Chem.* 2018 (2018) 2905–2914. <https://doi.org/10.1002/ejic.201800219>.
- [47] A. V. Skripov, R. V. Skoryunov, A. V. Soloninin, O.A. Babanova, V. Stavila, T.J. Udovic, Nuclear Magnetic Resonance Study of Anion and Cation Reorientational Dynamics in  $(\text{NH}_4)_2\text{B}_{12}\text{H}_{12}$ , *J. Phys. Chem. C*. 122 (2018) 3256–3262. <https://doi.org/10.1021/acs.jpcc.7b12046>.
- [48] A. Gradišek, M. Krnel, M. Paskevicius, B.R.S. Hansen, T.R. Jensen, J. Dolinšek, Reorientational Motions and Ionic Conductivity in  $(\text{NH}_4)_2\text{B}_{10}\text{H}_{10}$  and  $(\text{NH}_4)_2\text{B}_{12}\text{H}_{12}$ , *J. Phys. Chem. C*. 122 (2018) 17073–17079. <https://doi.org/10.1021/acs.jpcc.8b04605>.
- [49] A. Gradišek, M. Jørgensen, M. Paskevicius, B.R.S. Hansen, T.R. Jensen, Molecular dynamics in  $\text{Ag}_2\text{B}_{12}\text{H}_{12}$  studied by nuclear magnetic resonance, *J. Phys. Chem. C*. 125 (2021) 5534–5541. <https://doi.org/10.1021/acs.jpcc.1c00528>.
- [50] I.C. Madsen, N.V.Y. Scarlett, R. Kleeberg, K. Knorr, Quantitative phase analysis, *Int. Tables Crystallogr. H* (2019) 344–373. <https://doi.org/10.1107/97809553602060000954>.
- [51] B.R.S. Hansen, M. Paskevicius, M. Jørgensen, T.R. Jensen, Halogenated Sodium-*closo*-

- Dodecaboranes as Solid-State Ion Conductors, *Chem. Mater.* 29 (2017) 3423–3430. <https://doi.org/10.1021/acs.chemmater.6b04797>.
- [52] F. Han, Y. Zhu, X. He, Y. Mo, C. Wang, Electrochemical stability of  $\text{Li}_{10}\text{GeP}_2\text{S}_{12}$  and  $\text{Li}_7\text{La}_3\text{Zr}_2\text{O}_{12}$  solid electrolytes, *Adv. Energy Mater.* 6 (2016) 1501590. <https://doi.org/10.1002/aenm.201501590>.
- [53] R. Asakura, L. Duchêne, R.S. Kühnel, A. Remhof, H. Hagemann, C. Battaglia, Electrochemical Oxidative Stability of Hydroborate-Based Solid-State Electrolytes, *ACS Appl. Energy Mater.* 2 (2019) 6924–6930. <https://doi.org/10.1021/acsaem.9b01487>.
- [54] S. Payandeh, R. Asakura, P. Avramidou, D. Rentsch, Ł. Zbigniew, C. Radovan, A. Remhof, C. Battaglia, *Nido-Borate/Closo-Borate Mixed-Anion Electrolytes for All-Solid-State Batteries*, *Chem. Mater.* 32 (2020) 1101–1110. <https://doi.org/10.1021/acs.chemmater.9b03933>.
- [55] J. Su, X. Huang, Z. Song, T. Xiu, M.E. Badding, J. Jin, Z. Wen, Overcoming the abnormal grain growth in Ga-doped  $\text{Li}_7\text{La}_3\text{Zr}_2\text{O}_{12}$  to enhance the electrochemical stability against Li metal, *Ceram. Int.* 45 (2019) 14991–14996. <https://doi.org/10.1016/j.ceramint.2019.04.236>.
- [56] D. Reed, D. Book, Recent applications of raman spectroscopy to the study of complex hydrides for hydrogen storage, *Curr. Opin. Solid State Mater. Sci.* 15 (2011) 62–72. <https://doi.org/10.1016/j.cossms.2010.12.001>.
- [57] L.A. Leites, Vibrational Spectroscopy of Carboranes and Parent Boranes and Its Capabilities in Carborane Chemistry, *Chem. Rev.* 92 (1992) 279–323. <https://doi.org/10.1021/cr00010a006>.
- [58] D. Sethio, L.M. Lawson Daku, H. Hagemann, Computational study of the vibrational spectroscopy properties of boron-hydrogen compounds:  $\text{Mg}(\text{B}_3\text{H}_8)_2$ ,  $\text{CB}_9\text{H}_{10}^-$  and  $\text{CB}_{11}\text{H}_{12}^-$ , *Int. J. Hydrogen Energy.* 42 (2017) 22496–22501. <https://doi.org/10.1016/j.ijhydene.2017.03.044>.
- [59] S. Najiba, J. Chen, High-pressure study of lithium amidoborane using Raman spectroscopy and insight into dihydrogen bonding absence, *Proc. Natl. Acad. Sci. U. S. A.* 109 (2012) 19140–19144. <https://doi.org/10.1073/pnas.1211369109>.
- [60] M. Silva, E.F. O'Bannon, Q. Williams, A vibrational spectroscopic study of kernite to 25 GPa: implications for the high-pressure stability of borate polyhedra, *Am. Mineral.* 103 (2018) 1306–1318. <https://doi.org/10.2138/am-2018-6253>.

- [61] Z. Yongquan, F. Chunhui, F. Yan, Z.H.U. Fayan, Volumetric and Transport Properties of Aqueous  $\text{NaB}(\text{OH})_4$  Solutions, *Chinese J. Chem. Eng.* 21 (2013) 1048–1056. [https://doi.org/10.1016/S1004-9541\(13\)60561-3](https://doi.org/10.1016/S1004-9541(13)60561-3).
- [62] D. Maniua, T. Iliescu, I. Ardelean, S. Cinta-Pinzaru, N. Tarcea, W. Kiefer, Raman study on  $\text{B}_2\text{O}_3$ -CaO glasses, *J. Mol. Struct.* 651–653 (2003) 485–488. [https://doi.org/10.1016/S0022-2860\(03\)00129-7](https://doi.org/10.1016/S0022-2860(03)00129-7).
- [63] B.N. Meera, J. Ramakrishna, Raman spectral studies of borate glasses, *J. Non. Cryst. Solids.* 159 (1993) 1–21. [https://doi.org/10.1016/0022-3093\(93\)91277-A](https://doi.org/10.1016/0022-3093(93)91277-A).
- [64] E.L. Muetterties, J.H. Balthis, Y.T. Chia, W.H. Knoth, H.C. Miller, Chemistry of boranes. VIII. Salts and Acids of  $\text{B}_{10}\text{H}_{10}^{2-}$  and  $\text{B}_{12}\text{H}_{12}^{2-}$ , *Inorg. Chem.* 3 (1964) 444–451. <https://doi.org/10.1021/ic50013a030>.
- [65] Z. Huang, M. Eagles, S. Porter, E.G. Sorte, B. Billet, R.L. Corey, M.S. Conradi, J.C. Zhao, Thermolysis and solid state NMR studies of  $\text{NaB}_3\text{H}_8$ ,  $\text{NH}_3\text{B}_3\text{H}_7$ , and  $\text{NH}_4\text{B}_3\text{H}_8$ , *Dalt. Trans.* 42 (2013) 701–708. <https://doi.org/10.1039/c2dt31365k>.
- [66] B. Liu, A. Rose, N. Zhang, Y.Y. Hu, M. Ma, Efficient Co-Nanocrystal-Based Catalyst for Hydrogen Generation from Borohydride, *J. Phys. Chem. C.* 121 (2017) 12610–12616. <https://doi.org/10.1021/acs.jpcc.7b03094>.
- [67] M. Bishop, N. Shahid, J. Yang, A.R. Barron, Determination of the mode and efficacy of the cross-linking of guar by borate using MAS  $^{11}\text{B}$  NMR of borate cross-linked guar in combination with solution  $^{11}\text{B}$  NMR of model systems, *Dalt. Trans.* (2004) 2621–2634. <https://doi.org/10.1039/b406952h>.
- [68] M. Touboul, E. Bétourné, Dehydration process of lithium borates, *Solid State Ionics.* 84 (1996) 189–197. [https://doi.org/10.1016/0167-2738\(96\)00027-6](https://doi.org/10.1016/0167-2738(96)00027-6).
- [69] K. Karuppasamy, J. Theerthagiri, D. Vikraman, C.-J. Yim, S. Hussain, R. Sharma, T. Maiyalagan, J. Qin, H.-S. Kim, Ionic liquid-based electrolytes for energy storage devices: A brief review on their limits and applications, *Polymers.* 12 (2020) 918. <https://doi.org/10.3390/POLYM12040918>.
- [70] R. Ratti, Ionic liquids: synthesis and applications in catalysis, *Adv. Chem.* 2014 (2014) 1–16. <https://doi.org/10.1155/2014/729842>.
- [71] Z. Lei, B. Chen, Y.M. Koo, D.R. MacFarlane, Introduction: ionic liquids, *Chem. Rev.* 117 (2017) 6633–6635. <https://doi.org/10.1021/acs.chemrev.7b00246>.
- [72] M. Kar, O. Tutusaus, D.R. MacFarlane, R. Mohtadi, Novel and versatile room

- temperature ionic liquids for energy storage, *Energy Environ. Sci.* 12 (2019) 566–571. <https://doi.org/10.1039/c8ee02437e>.
- [73] I. Popov, R.L. Sacci, N.C. Sanders, R.A. Matsumoto, M.W. Thompson, N.C. Osti, T. Kobayashi, M. Tyagi, E. Mamontov, M. Pruski, P.T. Cummings, A.P. Sokolov, Critical Role of Anion-Solvent Interactions for Dynamics of Solvent-in-Salt Solutions, *J. Phys. Chem. C.* 124 (2020) 8457–8466. <https://doi.org/10.1021/acs.jpcc.9b10807>.
- [74] V.A. Azov, K.S. Egorova, M.M. Seitkhalieva, A.S. Kashin, V.P. Ananikov, “Solvent-in-Salt” Systems for Design of New Materials in Chemistry, Biology and Energy Research, *Chem. Soc. Rev.* 47 (2018) 1250–1284. <https://doi.org/10.1039/c7cs00547d>.
- [75] Y. Bai, X. Wang, X. Zhang, H. Shu, X. Yang, B. Hu, Q. Wei, H. Wu, Y. Song, The kinetics of Li-ion deintercalation in the Li-rich layered  $\text{Li}_{1.12}[\text{Ni}_{0.5}\text{Co}_{0.2}\text{Mn}_{0.3}]_{0.89}\text{O}_2$  studied by electrochemical impedance spectroscopy and galvanostatic intermittent titration technique, *Electrochim. Acta.* 109 (2013) 355–364. <https://doi.org/10.1016/j.electacta.2013.06.134>.
- [76] C. Song, W. Wang, H. Peng, Y. Wang, C. Zhao, H. Zhang, Q. Tang, J. Lv, X. Du, Y. Dou, Improving the electrochemical performance of  $\text{LiNi}_{0.80}\text{Co}_{0.15}\text{Al}_{0.05}\text{O}_2$  in lithium ion batteries by  $\text{LiAlO}_2$  surface modification, *Appl. Sci.* 8 (2018) 378. <https://doi.org/10.3390/app8030378>.
- [77] S. Kim, N. Toyama, H. Oguchi, T. Sato, S. Takagi, T. Ikeshoji, S. Orimo, Fast Lithium-Ion Conduction in Atom-Deficient *closo*-Type Complex Hydride Solid Electrolytes, *Chem. Mater.* 30 (2018) 386–391. <https://doi.org/10.1021/acs.chemmater.7b03986>.
- [78] A. Unemoto, K. Yoshida, T. Ikeshoji, S. Orimo, Bulk-type all-solid-state lithium batteries using complex hydrides containing cluster-anions, *Mater. Trans.* 57 (2016) 1639–1644. <https://doi.org/10.2320/matertrans.MAW201601>.
- [79] M. Joos, C. Schneider, A. Münchinger, I. Moudrakovski, R. Usiskin, J. Maier, B. V. Lotsch, Impact of hydration on ion transport in  $\text{Li}_2\text{Sn}_2\text{S}_5 \cdot x\text{H}_2\text{O}$ , *J. Mater. Chem. A.* 9 (2021) 16532–16544. <https://doi.org/10.1039/d1ta04736a>.
- [80] M.J. Wang, R. Choudhury, J. Sakamoto, Characterizing the Li-solid-electrolyte interface dynamics as a function of stack pressure and current density, *Joule.* 3 (2019) 2165–2178. <https://doi.org/10.1016/j.joule.2019.06.017>.
- [81] J. Sakamoto, More pressure needed, *Nat. Energy.* 4 (2019) 827–828. <https://doi.org/10.1038/s41560-019-0478-z>.



- [82] Y. Lu, C.-Z. Zhao, H. Yuan, X.-B. Cheng, J.-Q. Huang, Q. Zhang, Critical current density in solid-state lithium metal batteries: mechanism, influences, and strategies, *Adv. Funct. Mater.* 31 (2021) 2009925. <https://doi.org/10.1002/adfm.202009925>.
- [83] E. Kazyak, R. Garcia-Mendez, W.S. LePage, A. Sharafi, A.L. Davis, A.J. Sanchez, K.H. Chen, C. Haslam, J. Sakamoto, N.P. Dasgupta, Li Penetration in Ceramic Solid Electrolytes: Operando Microscopy Analysis of Morphology, Propagation, and Reversibility, *Matter.* 2 (2020) 1025–1048. <https://doi.org/10.1016/j.matt.2020.02.008>.
- [84] S. Kim, K. Harada, N. Toyama, H. Oguchi, K. Kisu, S. Orimo, Room temperature operation of all-solid-state battery using a *closo*-type complex hydride solid electrolyte and a LiCoO<sub>2</sub> cathode by interfacial modification, *J. Energy Chem.* 43 (2020) 47–51. <https://doi.org/10.1016/j.jechem.2019.08.007>.
- [85] L. Cheng, E.J. Crumlin, W. Chen, R. Qiao, H. Hou, S. Franz Lux, V. Zorba, R. Russo, R. Kostecki, Z. Liu, K. Persson, W. Yang, J. Cabana, T. Richardson, G. Chen, M. Doeff, The origin of high electrolyte-electrode interfacial resistances in lithium cells containing garnet type solid electrolytes, *Phys. Chem. Chem. Phys.* 16 (2014) 18294–18300. <https://doi.org/10.1039/c4cp02921f>.
- [86] M.S. Whittingham, Electrical Energy Storage and Intercalation Chemistry, *Science.* 192 (1976) 1126–1127. <https://doi.org/10.1126/science.192.4244.1126>.
- [87] J. Xie, Y.-C. Lu, A retrospective on lithium-ion batteries, *Nat. Commun.* 11 (2020) 2499. <https://doi.org/10.1038/s41467-020-16259-9>.
- [88] J.Y. Kim, J. Park, S.H. Kang, S. Jung, D.O. Shin, M.J. Lee, J. Oh, K.M. Kim, J. Zausch, Y.-G. Lee, Y.M. Lee, Revisiting TiS<sub>2</sub> as a diffusion-dependent cathode with promising energy density for all-solid-state lithium secondary batteries, *Energy Storage Mater.* 41 (2021) 289–296. <https://doi.org/10.1016/j.ensm.2021.06.005>.
- [89] T. Krauskopf, H. Hartmann, W.G. Zeier, J. Janek, Toward a Fundamental Understanding of the Lithium Metal Anode in Solid-State Batteries - An Electrochemo-Mechanical Study on the Garnet-Type Solid Electrolyte Li<sub>6.25</sub>Al<sub>0.25</sub>La<sub>3</sub>Zr<sub>2</sub>O<sub>12</sub>, *ACS Appl. Mater. Interfaces.* 11 (2019) 14463–14477. <https://doi.org/10.1021/acsami.9b02537>.
- [90] C. Lu, C. Dong, H. Wu, D. Ni, W. Sun, Z. Wang, K. Sun, Achieving high capacity hybrid-cathode FeF<sub>3</sub>@Li<sub>2</sub>C<sub>6</sub>O<sub>6</sub>/rGO based on morphology control synthesis and interface engineering, *Chem. Commun.* 54 (2018) 3235–3238.

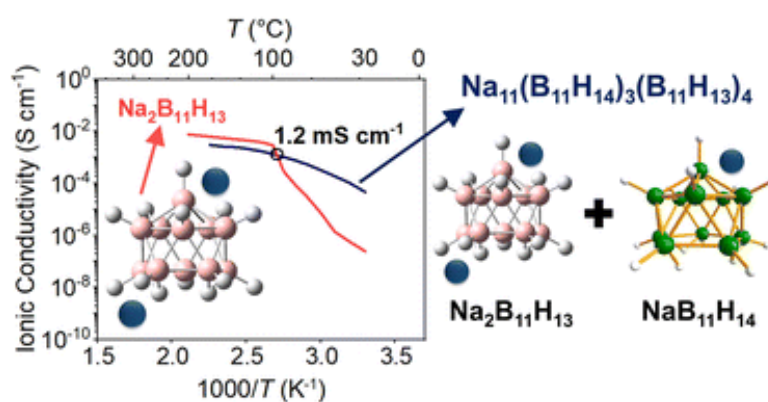
<https://doi.org/10.1039/c8cc00350e>.

# CHAPTER 5

## $\text{Na}_2\text{B}_{11}\text{H}_{13}$ and $\text{Na}_{11}(\text{B}_{11}\text{H}_{14})_3(\text{B}_{11}\text{H}_{13})_4$ as Potential Solid-State Electrolytes for Na-Ion Batteries

---

D. H. P. Souza, A.M. D'Angelo, T.D. Humphries, C.E. Buckley, M. Paskevicius,  $\text{Na}_2\text{B}_{11}\text{H}_{13}$  and  $\text{Na}_{11}(\text{B}_{11}\text{H}_{14})_3(\text{B}_{11}\text{H}_{13})_4$  as Potential Solid-State Electrolytes for Na-Ion Batteries, *Dalton Trans.* 51 (2022) 13848–13857. <https://doi.org/10.1039/D2DT01943D>.



## ABSTRACT

Solid-state sodium batteries have attracted great attention owing to their improved safety, high energy density, large abundance and low cost of sodium compared to current Li-ion batteries. Sodium-boranes have been studied as potential solid-state electrolytes and the search for new materials is necessary for future battery applications. Here, a facile and cost-effective solution-based synthesis of  $\text{Na}_2\text{B}_{11}\text{H}_{13}$  and  $\text{Na}_{11}(\text{B}_{11}\text{H}_{14})_3(\text{B}_{11}\text{H}_{13})_4$  is demonstrated.  $\text{Na}_2\text{B}_{11}\text{H}_{13}$  presents an ionic conductivity in the order of  $10^{-7} \text{ S cm}^{-1}$  at  $30^\circ\text{C}$ , but undergoes an order-disorder phase transition and reaches  $10^{-3} \text{ S cm}^{-1}$  at  $100^\circ\text{C}$ , close to that of liquids and the solid-state electrolyte  $\text{Na-}\beta\text{-Al}_2\text{O}_3$ . The formation of the mixed-anion solid-solution,  $\text{Na}_{11}(\text{B}_{11}\text{H}_{14})_3(\text{B}_{11}\text{H}_{13})_4$ , partially stabilises the high temperature structural polymorph observed for  $\text{Na}_2\text{B}_{11}\text{H}_{13}$  to room temperature and it exhibits  $\text{Na}^+$  conductivity higher than its constituents ( $4.7 \times 10^{-5} \text{ S cm}^{-1}$  at  $30^\circ\text{C}$ ).  $\text{Na}_2\text{B}_{11}\text{H}_{13}$  and  $\text{Na}_{11}(\text{B}_{11}\text{H}_{14})_3(\text{B}_{11}\text{H}_{13})_4$  exhibit an oxidative stability limit of 2.1 V vs.  $\text{Na}^+/\text{Na}$ .

## 5.1 INTRODUCTION

Hydridoborate compounds have attracted the interest of researchers in the past decades due to their rich chemistry and variety of compositions and structures [1,2]. These compounds have shown applicability in a number of different fields, such as medicinal chemistry [3], military [4], organic synthesis [5,6], hydrogen storage [7–9] and as ionic conductors [10,11]. *Closo*-boranes, negatively charged hydridoborate clusters with a cage-like structure, form metal salts with high chemical and thermal stability as well as superionic conductivity of their respective metal cations at high temperatures [12–15]. Generally, these compounds undergo an order-disorder polymorphic phase transition at a specific temperature, which results in fast anion reorientational dynamics and high cation mobility [16,17]. Several attempts to improve the performance of hydridoborate salts as solid-state electrolytes at room temperature have been reported, such as chemical modification of the anion [12,15,18], mechanical-induced modification [19–21], and anion mixtures with other borane compounds [22–24] or metal oxides [25,26]. These strategies seem to create defects into the structure and/or stabilise the disordered high temperature polymorph to room temperature, which increases the ionic conductivity of the material [21,22]. Recently, *nido*-boranes, boron anions with a nest-like open-cage structure, have also been investigated as potential solid-state electrolytes due to their high ionic conductivity properties at room temperature [11,27–29].

The use of inorganic salts, such as metal boranes, as solid electrolytes seems to be an attractive choice for the development of solid-state batteries, which promise high energy storage capacity, durability and safety, with the elimination of the flammable organic liquid electrolyte used in current generation Li-ion batteries [16,30]. The energy density of a battery cell can be increased with the use of solid electrolytes, as they can be more compatible with alternative electrode materials, e.g. pure lithium or sodium metal [30,31]. Lithium-ion batteries are one of the most common types of energy storage technology, and they are used in a variety of electronic devices. However, the increasing use of lithium will limit its availability and raise its cost, which makes it necessary to search for alternative metal-ion battery technologies [32]. This is exemplified by the recent  $\approx 500\%$  increase in Li metal prices in a single year, due to rapidly rising electric vehicle demand [33]. Moreover, a conservative lithium consumption forecast, based only on the increasing demand from electric vehicles, shows that the lithium reserve on land will be totally consumed in about 60 years [34].

It has been observed that certain sodium borane salts exhibit even higher ionic conductivities than their lithium borane analogues at room temperature [11,15,27]. Na-batteries are being actively investigated as sodium metal is more abundant than lithium, has a lower cost, and presents a suitable standard half-cell potential ( $-2.71$  V vs. standard hydrogen electrode) [32,35,36]. Current sodium-sulphur (Na-S) batteries operate with molten electrodes using a solid-electrolyte, sodium  $\beta$ -alumina ( $\text{NaAl}_{11}\text{O}_{17}$ ) [37]. However, operation is required to occur at high temperatures ( $300 - 350$  °C), which incurs safety issues, limits scalability, and presents higher operating costs. Some of the difficulties surrounding the implementation of room temperature Na-S batteries can be avoided by searching for a solid-state alternative to problematic liquid electrolytes [37,38]. Due to the promising properties observed for some sodium *nido*-boranes as solid-state electrolytes [11,27,29], the synthesis and characterisation of  $\text{Na}_2\text{B}_{11}\text{H}_{13}$  is investigated, as well as the mixed-anion solid solution  $\text{Na}_{11}(\text{B}_{11}\text{H}_{14})_3(\text{B}_{11}\text{H}_{13})_4$ .

## 5.2 EXPERIMENTAL SECTION

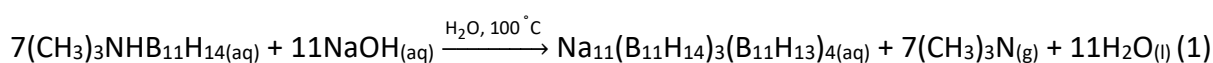
### 5.2.1 Chemicals

Sodium borohydride ( $\text{NaBH}_4$ , anhydrous, 98%), diglyme ( $\text{C}_6\text{H}_{14}\text{O}_3$ , anhydrous, 99.5%), 1-bromopentane ( $\text{C}_5\text{H}_{11}\text{Br}$ , 98%), diethyl ether ( $(\text{C}_2\text{H}_5)_2\text{O}$ , anhydrous, 99.7%), trimethylamine hydrochloride ( $(\text{CH}_3)_3\text{N}\cdot\text{HCl}$ , 98%), deuterated water ( $\text{D}_2\text{O}$ , 99.9 atom % D), sodium (Na lump in kerosene, 99%), graphite powder (C, 99.9%), tetrahydrofuran (THF, with 250 ppm BHT,

99%), sodium hydride (NaH, 90%), sodium hydroxide (NaOH, 98%) and platinum foil (Pt, 99.95%, thickness 0.1 mm) were all purchased from Sigma-Aldrich. Gold foil (Au, 99.95%, thickness 0.1 mm) was obtained from Alfa Aesar, and acetone (C<sub>3</sub>H<sub>6</sub>O, 99.5%) from Unilab. To maintain an inert atmosphere, all chemicals and samples were manipulated in an argon filled glovebox (Mbraun, O<sub>2</sub> & H<sub>2</sub>O < 1 ppm) or using Schlenk techniques under argon.

### 5.2.2 Synthesis of mixed anion *nido*-borane, Na<sub>11</sub>(B<sub>11</sub>H<sub>14</sub>)<sub>3</sub>(B<sub>11</sub>H<sub>13</sub>)<sub>4</sub>

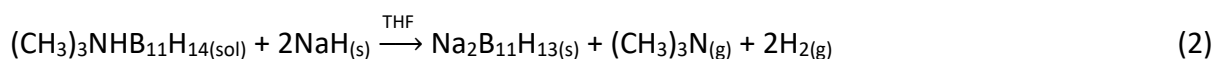
The synthesis of Na<sub>11</sub>(B<sub>11</sub>H<sub>14</sub>)<sub>3</sub>(B<sub>11</sub>H<sub>13</sub>)<sub>4</sub> was achieved through the reaction of (CH<sub>3</sub>)<sub>3</sub>NHB<sub>11</sub>H<sub>14</sub> with NaOH, according to reaction 1.



(CH<sub>3</sub>)<sub>3</sub>NHB<sub>11</sub>H<sub>14</sub> was prepared based on the same methodology described in our previous work [11]. The trimethylammonium-borane salt was recrystallised prior to use by solubilisation in a hot aqueous solution of acetone (10% acetone) [39]. The colourless powder of (CH<sub>3</sub>)<sub>3</sub>NHB<sub>11</sub>H<sub>14</sub> that was obtained was filtered and dried under vacuum at 90 °C before use. 400 mg of recrystallised (CH<sub>3</sub>)<sub>3</sub>NHB<sub>11</sub>H<sub>14</sub> (2.1 mmol) was dissolved into 20 mL of an aqueous solution of 177 mg of NaOH (4.4 mmol, ≈ 33% excess), which was then heated at 100 °C for 15 minutes under constant stirring in an open vessel. After cooling back to room temperature, the solution was filtered, and the filtrate was washed three times with 5 mL of diethyl ether. The aqueous layer was dried *in vacuo* at 110 °C overnight, and a solid containing a mixture of both anions was obtained (0.28 g, 0.24 mmol, 80% yield). No additional step for removal of excess NaOH or possible by-products was taken.

### 5.2.3 Synthesis of disodium *nido*-tridecahydroundecaborane, Na<sub>2</sub>B<sub>11</sub>H<sub>13</sub>

The synthesis of Na<sub>2</sub>B<sub>11</sub>H<sub>13</sub> was achieved based on reaction 2, an adapted procedure proposed by Pecyna *et al.* [40] that was originally used to prepare (C<sub>2</sub>H<sub>5</sub>)<sub>4</sub>NCB<sub>11</sub>H<sub>12</sub>.



0.11 g of NaH (4.6 mmol) was mixed with 5 mL of THF under argon in an ice bath. Under constant stirring, 5 mL of a THF solution containing 250 mg of recrystallised (CH<sub>3</sub>)<sub>3</sub>NHB<sub>11</sub>H<sub>14</sub> (1.3 mmol) was added slowly and left stirring for 15 minutes at 0 °C and for 30 minutes at

room temperature. The mixture was filtered, and the filtrate was dried *in vacuo* at 40 °C for 2 hours, which yielded a white powder of Na<sub>2</sub>B<sub>11</sub>H<sub>13</sub> (0.17 g, 0.9 mmol, 73% yield).

## 5.2.4 Characterisation

### 5.2.4.1 Nuclear Magnetic Resonance (NMR) Spectroscopy

Powdered samples were characterised through <sup>11</sup>B (128 MHz) solid-state NMR spectroscopy with a Varian VNMRS 400 NMR spectrometer at room temperature. The samples (≈ 30 mg) were ground using a mortar and pestle and packed inside a 4 mm zirconia rotor in an argon filled glovebox and sealed with a gas-tight insert. The samples were spun at 5 kHz, and acquisition was performed with proton decoupling and a one pulse sequence, with a relaxation delay of 10 s for a total of 50 transients.

Solution-state NMR spectroscopy was also used to characterise samples with a Bruker Avance III 400 MHz NanoBay spectrometer. <sup>1</sup>H: 400 MHz, <sup>11</sup>B: 128 MHz, <sup>11</sup>B{<sup>1</sup>H}: 128 MHz NMR data were collected after dissolution of the solids in 600 μL of deuterated water (D<sub>2</sub>O). The <sup>11</sup>B NMR spectra were referenced to a boron trifluoride etherate (BF<sub>3</sub>O(C<sub>2</sub>H<sub>5</sub>)<sub>2</sub>) external standard, and the <sup>1</sup>H NMR spectra were referenced to a tetramethylsilane (Si(CH<sub>3</sub>)<sub>4</sub>) external standard.

### 5.2.4.2 X-Ray Powder Diffraction (XRPD)

X-Ray Powder Diffraction (XRPD) data were acquired by employing a Bruker D8 Advance Powder Diffractometer with a Cu K<sub>α</sub> radiation source (λ = 1.54056 Å) operated at 40 kV/40 mA with a LynxEye detector in the 2θ range of 5 – 60°. The samples were ground using a mortar and pestle in an argon filled glovebox, mounted on a single-crystal Si low background sample holder and sealed with an airtight poly(methyl-methacrylate) (PMMA) dome under argon to prevent air exposure during data collection. The use of the dome results in two broad diffraction halos at low angle.

### 5.2.4.3 Synchrotron X-Ray Powder Diffraction (SR-XRPD)

The sample Na<sub>2</sub>B<sub>11</sub>H<sub>13</sub> was characterised using Synchrotron Radiation X-Ray Powder Diffraction (SR-XRPD) at the Australian Synchrotron Powder Diffraction beamline (λ = 0.590827(4) Å) and refined using a NIST LaB<sub>6</sub> 660b line position standard. The solid was ground using a mortar and pestle and packed inside a 1.0 mm borosilicate capillary inside an argon filled glovebox, which was then flame-sealed. A Mythen II microstrip detector was used

to collect the data at two positions from  $1^\circ - 81^\circ 2\theta$  ( $0.0038^\circ$  steps) [41], which were merged into gap-free data sets. *In-situ* SR-XRPD experiments were performed under heating ( $\Delta T/\Delta t = 5^\circ\text{C min}^{-1}$ ) and cooling ( $\Delta T/\Delta t = 6^\circ\text{C min}^{-1}$ ) from  $30 - 230 - 30^\circ\text{C}$ , which was controlled by an Oxford Cryosystems Cryostream Plus using a 60 s data collection time for each scan.

Rietveld refinement of diffraction patterns was conducted using Bruker *TOPAS* software (version 5) [42], and reported uncertainties are based on mathematical fitting uncertainty in the *TOPAS* software. Refinements were conducted by Le Bail method for the identification of phases, but no atomic information was used.

#### **5.2.4.4 Differential Scanning Calorimetry and Thermogravimetric analysis (DSC/TGA)**

Thermal behaviour was analysed using a Netzsch STA 449 F3 Jupiter DSC/TGA. The powders were ground with a mortar and pestle inside an argon filled glovebox, and approximately 5 mg of each sample was mounted inside an Al crucible and crimp-sealed with a lid. The lid was pierced ( $\approx 10$  seconds prior to analysis), and the crucible was transferred to the Pt furnace, which was evacuated and filled with argon ( $40\text{ mL min}^{-1}$ ). The data were obtained from  $40 - 350^\circ\text{C}$  at  $10^\circ\text{C min}^{-1}$ . The sample  $\text{Na}_2\text{B}_{11}\text{H}_{13}$  was also analysed under heating and cooling from  $40 - 220 - 40^\circ\text{C}$  under the same conditions already described. The temperature and sensitivity of the DSC/TGA was calibrated using In, Zn, Sn, Bi and CsCl reference materials, resulting in a temperature accuracy of  $\pm 0.2^\circ\text{C}$ , while the balance has an accuracy of  $\pm 20\ \mu\text{g}$ .

#### **5.2.4.5 Electrochemical Impedance Spectroscopy (EIS)**

Solid-state ionic conductivity measurements were collected as a function of temperature by using a ZIVE SP1 electrochemical workstation at 100 mV AC from 10 Hz to 1 MHz at RT (room temperature) and isothermally after heating with 50 minutes of thermal equilibrium at each  $10^\circ\text{C}$  temperature step.  $\text{Na}_2\text{B}_{11}\text{H}_{13}$  was analysed from  $30 - 200^\circ\text{C}$ , and  $30 - 170^\circ\text{C}$  for  $\text{Na}_{11}(\text{B}_{11}\text{H}_{14})_3(\text{B}_{11}\text{H}_{13})_4$ . The samples were ground with a mortar and pestle inside an argon filled glovebox, and approximately 30 mg of each sample was pressed into pellets (6 mm diameter) at 700 MPa between two gold foils (0.1 mm thickness). They were sealed within an air-tight 'Swagelok-type' Teflon cell with 316 stainless steel electrodes. The temperature was recorded using a K-type thermocouple, which was placed  $\approx 5$  mm from the pellet inside a sealed tube furnace. The Nyquist plots at low temperature were fitted using the equivalent circuit model  $(R_1 + Q_1)/(R_2 + W_o)$ , in which  $R_1$  is the internal resistance,  $R_2$  the charge transfer



resistance,  $Q_1$  is the constant phase element and  $W_o$  is the Warburg element to obtain the impedance of the pellet [43]. At high temperatures, due to the absence of the semi-circle at high and intermediate frequencies, the pellet impedance was determined through the intercept of the linear spike with the x-axis in the Nyquist plots [43].

Solid-state ionic conductivity data ( $\sigma$ ) were determined from:  $\sigma = d/lA$ , where  $\sigma$  is the ionic conductivity in  $S\text{ cm}^{-1}$ ,  $d$  is the pellet thickness in cm,  $l$  is the x-intercept of the Nyquist blocking tail (pellet impedance), and  $A$  is the area of the pellet face in  $\text{cm}^2$ .

The activation energy of each material was determined from the slope of the solid-state ionic conductivity plot between 30 – 50 °C for LT (low temperature)  $\text{Na}_2\text{B}_{11}\text{H}_{13}$ , 170 – 190 °C for HT (high temperature)  $\text{Na}_2\text{B}_{11}\text{H}_{13}$  and 30 – 80 °C for  $\text{Na}_{11}(\text{B}_{11}\text{H}_{14})_3(\text{B}_{11}\text{H}_{13})_4$  using the logarithm of the Arrhenius equation:  $\ln \sigma_{\text{ion}} = \ln \sigma_o - (E_a/K_B T)$ , where  $\sigma_o$  is a pre-exponential factor ( $S\text{ cm}^{-1}$ ),  $E_a$  the activation energy (J),  $K_B$  Boltzmann's constant ( $1.3806 \times 10^{-23}\text{ J K}^{-1}$ ), and  $T$  the temperature (K) [11,44].

#### **5.2.4.6 Linear Sweep Voltammetry (LSV)**

A mixture of 75(SSE):25(graphite), where SSE =  $\text{Na}_2\text{B}_{11}\text{H}_{13}$  or  $\text{Na}_{11}(\text{B}_{11}\text{H}_{14})_3(\text{B}_{11}\text{H}_{13})_4$  was prepared by grinding in a mortar and pestle repeatedly until a fine mixture was obtained. Graphite was previously dried under vacuum at 550 °C for 12 hours to remove any moisture or volatiles. 2.5 mg of that mixture was layered on top of 28 mg of SSE and pressed at 700 MPa to form a pellet that was sandwiched between aluminium, platinum and sodium foil in the following configuration (Al/Pt/SSE+C/SSE/Na), which was then sealed within an air-tight 'Swagelok-type' Teflon cell with stainless steel electrodes. LSV was conducted from 1.4 – 6.0 V at 30 °C with a scan rate of  $50\ \mu\text{V s}^{-1}$ . The oxidative stability voltage limit of each sample was determined from the intersection point of the regression lines ( $R^2 > 0.99$ ) fitted to the background and anodic currents in the voltammogram following a known method [45].

### **5.3 RESULTS AND DISCUSSION**

#### **5.3.1 Sample characterisation**

Solid-state  $^{11}\text{B}$  MAS NMR spectroscopy was used to identify the composition of each material synthesised in the powdered state (Fig. 5.1).  $\text{NaB}_{11}\text{H}_{14} \cdot (\text{H}_2\text{O})_n$ , reported in our previous work [11], was also characterised and added for comparison.

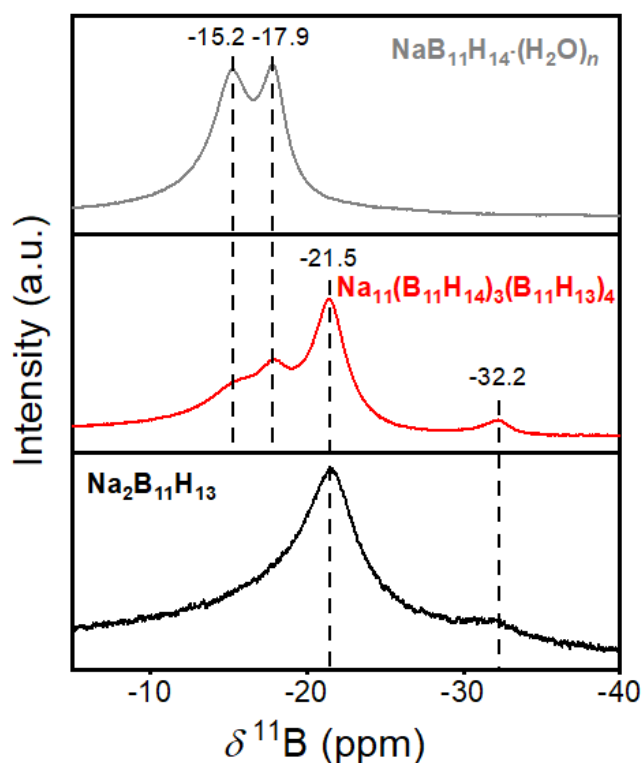


**Figure 5.1** Solid-state  $^{11}\text{B}$  MAS NMR spectra of  $\text{NaB}_{11}\text{H}_{14}\cdot(\text{H}_2\text{O})_n$ ,  $\text{Na}_{11}(\text{B}_{11}\text{H}_{14})_3(\text{B}_{11}\text{H}_{13})_4$  and  $\text{Na}_2\text{B}_{11}\text{H}_{13}$  at room temperature.  $\delta(\text{B}_{11}\text{H}_{14}^-) = -15.2$  and  $-17.9$  ppm, and  $\delta(\text{B}_{11}\text{H}_{13}^{2-}) = -21.5$  and  $-32.2$  ppm.

The resonances at  $\delta^{11}\text{B} -15.2$  and  $-17.9$  ppm are assigned to  $\text{B}_{11}\text{H}_{14}^-$  [29], whereas  $\text{B}_{11}\text{H}_{13}^{2-}$  is represented by the signals at  $\delta^{11}\text{B} -21.5$  and  $-32.2$  ppm [11].  $\text{B}_{11}\text{H}_{13}^{2-}$  resonances cannot be observed in the spectra of hydrated  $\text{NaB}_{11}\text{H}_{14}$  samples, and there is no apparent signal of  $\text{B}_{11}\text{H}_{14}^-$  in the sample of  $\text{Na}_2\text{B}_{11}\text{H}_{13}$ . The asymmetry of the main peak in the  $\text{Na}_2\text{B}_{11}\text{H}_{13}$  pattern ( $\delta^{11}\text{B} -21.5$  ppm) may indicate that some  $\text{NaB}_{11}\text{H}_{14}$  could exist in that powder, however an analysis of solution-state  $^{11}\text{B}$  NMR of  $\text{Na}_2\text{B}_{11}\text{H}_{13}$  in  $\text{D}_2\text{O}$  also does not show any presence of  $\text{B}_{11}\text{H}_{14}^-$  peaks (Fig. 5.2).

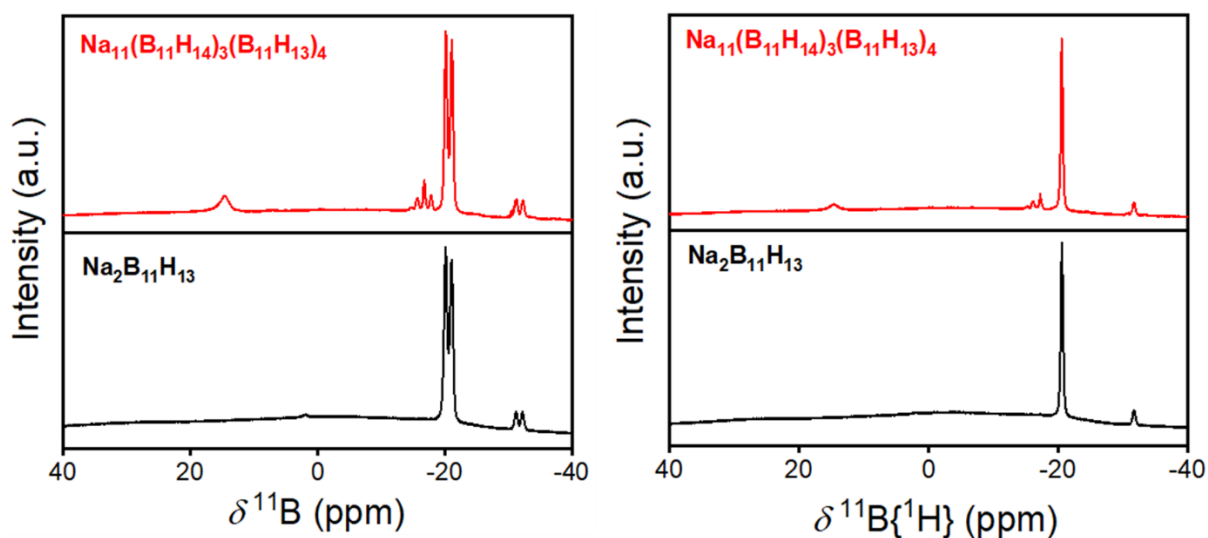


**Figure 5.2**  $^{11}\text{B}$  NMR (left) and  $^{11}\text{B}\{^1\text{H}\}$  NMR (right) spectra (128 MHz) of  $\text{Na}_{11}(\text{B}_{11}\text{H}_{14})_3(\text{B}_{11}\text{H}_{13})_4$  and  $\text{Na}_2\text{B}_{11}\text{H}_{13}$  in  $\text{D}_2\text{O}$  at room temperature.  $\delta(\text{B}_{11}\text{H}_{14}^-) = -15.1, -16.2$  and  $-17.3$  ppm, and  $\delta(\text{B}_{11}\text{H}_{13}^{2-}) = -20.6$  and  $-31.8$  ppm. The peak observed at the resonance 14.6 ppm for  $\text{Na}_{11}(\text{B}_{11}\text{H}_{14})_3(\text{B}_{11}\text{H}_{13})_4$  is assigned to a boron oxide species formed as a by-product.

The only material that shows the presence of both anions in the solid-state is  $\text{Na}_{11}(\text{B}_{11}\text{H}_{14})_3(\text{B}_{11}\text{H}_{13})_4$ , which consists of 0.75 mol of  $\text{B}_{11}\text{H}_{14}^-$  to 1 mol of  $\text{B}_{11}\text{H}_{13}^{2-}$  based on the integration of the solid-state NMR resonances. However, it is interesting that when  $\text{Na}_{11}(\text{B}_{11}\text{H}_{14})_3(\text{B}_{11}\text{H}_{13})_4$  is dissolved in  $\text{D}_2\text{O}$  and analysed through solution-state  $^{11}\text{B}$  NMR, the integration of the NMR signals provides a composition of 0.13 mol of  $\text{B}_{11}\text{H}_{14}^-$  to 1 mol of  $\text{B}_{11}\text{H}_{13}^{2-}$  (Fig. 5.2). The observation of less  $\text{B}_{11}\text{H}_{14}^-$  in the solution-state  $^{11}\text{B}$  NMR spectrum of  $\text{Na}_{11}(\text{B}_{11}\text{H}_{14})_3(\text{B}_{11}\text{H}_{13})_4$  could be due to the deprotonation of this anion into  $\text{B}_{11}\text{H}_{13}^{2-}$  in an alkaline medium as follows [11,28]:



During synthesis, excess NaOH was not specifically removed, which could remain to some degree within the solid product, however the XRPD pattern for  $\text{Na}_{11}(\text{B}_{11}\text{H}_{14})_3(\text{B}_{11}\text{H}_{13})_4$  (Fig. 5.3 & 5.4) does not show any presence of unreacted NaOH, which instead suggests the formation of an amorphous sodium borate, which could be alkaline on dissolution [46–48]. The diffractogram of  $\text{Na}_2\text{B}_{11}\text{H}_{13}$  also does not show any presence of unreacted NaH (Fig. 5.3 & 5.4), which implies that all the excess starting material used was successfully removed through filtration.

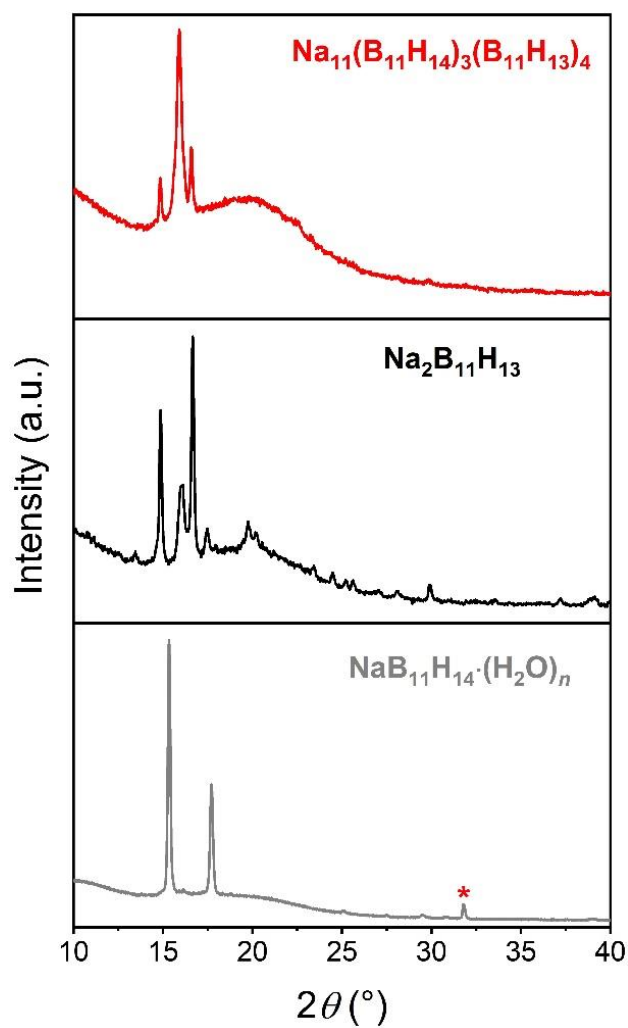


**Figure 5.3** XRPD pattern ( $\lambda = 1.54056 \text{ \AA}$ ) for  $\text{Na}_{11}(\text{B}_{11}\text{H}_{14})_3(\text{B}_{11}\text{H}_{13})_4$ ,  $\text{Na}_2\text{B}_{11}\text{H}_{13}$  and  $\text{NaB}_{11}\text{H}_{14}\cdot(\text{H}_2\text{O})_n$  [11] (added for comparison) at room temperature. Asterisk at  $2\theta = 31.8^\circ$  in the  $\text{NaB}_{11}\text{H}_{14}\cdot(\text{H}_2\text{O})_n$  pattern represent inadvertent NaCl contamination from synthesis [11].

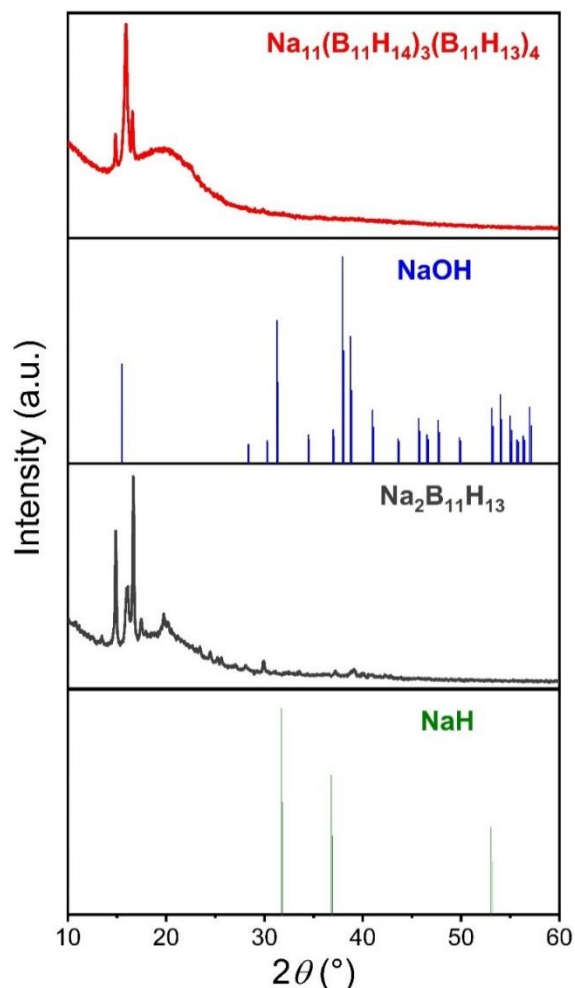


**Figure 5.4** XRPD pattern ( $\lambda = 1.54056 \text{ \AA}$ ) for  $\text{Na}_{11}(\text{B}_{11}\text{H}_{14})_3(\text{B}_{11}\text{H}_{13})_4$  and  $\text{Na}_2\text{B}_{11}\text{H}_{13}$  at room temperature and simulated diffraction lines for NaOH [49] and NaH [50] that were obtained from the Crystallography Open Database (COD) [51–56]. Data show that there is no evidence for remanent crystalline NaOH in the sample of  $\text{Na}_{11}(\text{B}_{11}\text{H}_{14})_3(\text{B}_{11}\text{H}_{13})_4$ , neither remanent crystalline NaH in the  $\text{Na}_2\text{B}_{11}\text{H}_{13}$  powder.

The possibility of alkaline aqueous solutions upon dissolution of  $\text{Na}_{11}(\text{B}_{11}\text{H}_{14})_3(\text{B}_{11}\text{H}_{13})_4$  can be elucidated by analysing the NMR data in more detail. Solid-state  $^{11}\text{B}$  MAS NMR spectroscopy of  $\text{Na}_{11}(\text{B}_{11}\text{H}_{14})_3(\text{B}_{11}\text{H}_{13})_4$  (Fig. 5.5) shows the presence of small resonances at  $\approx +1$  ppm and between  $+10$  and  $+22$  ppm, which represent  $\text{BO}_4$  and  $\text{BO}_3$  units, respectively, of an inorganic borate [57–59], e.g. hydrated sodium metaborate,  $\text{NaB}(\text{OH})_4$  [47,60,61].

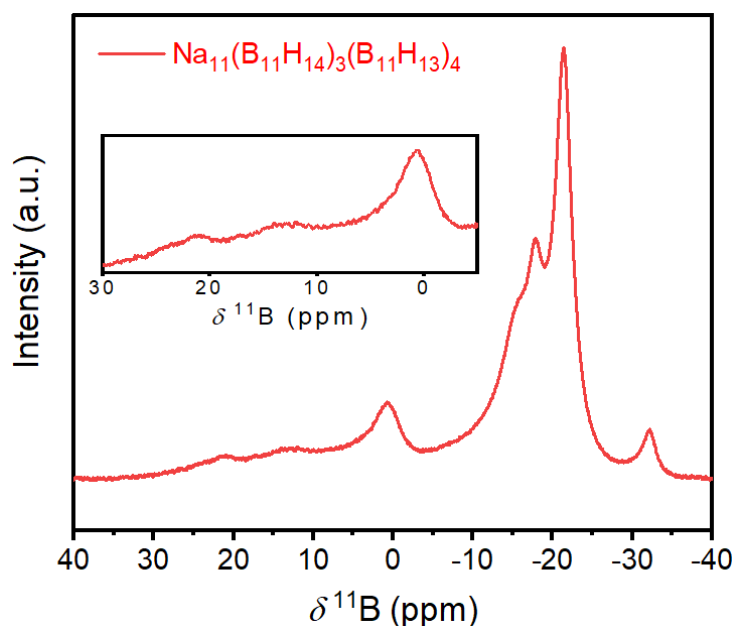


**Figure 5.5** Solid-state  $^{11}\text{B}$  MAS NMR spectra of  $\text{Na}_{11}(\text{B}_{11}\text{H}_{14})_3(\text{B}_{11}\text{H}_{13})_4$  at room temperature with magnified region from 30 to -5 ppm.  $\delta(\text{B}_{11}\text{H}_{14}^-) = -15.2$  and  $-17.9$  ppm,  $\delta(\text{B}_{11}\text{H}_{13}^{2-}) = -21.5$  and  $-32.2$  ppm. The peaks observed between 10 and 22 ppm, and the peak at  $\approx 1$  ppm are assigned to a boron oxide species (by-product) formed with  $\text{BO}_3$  and  $\text{BO}_4$  units, respectively [57–59].

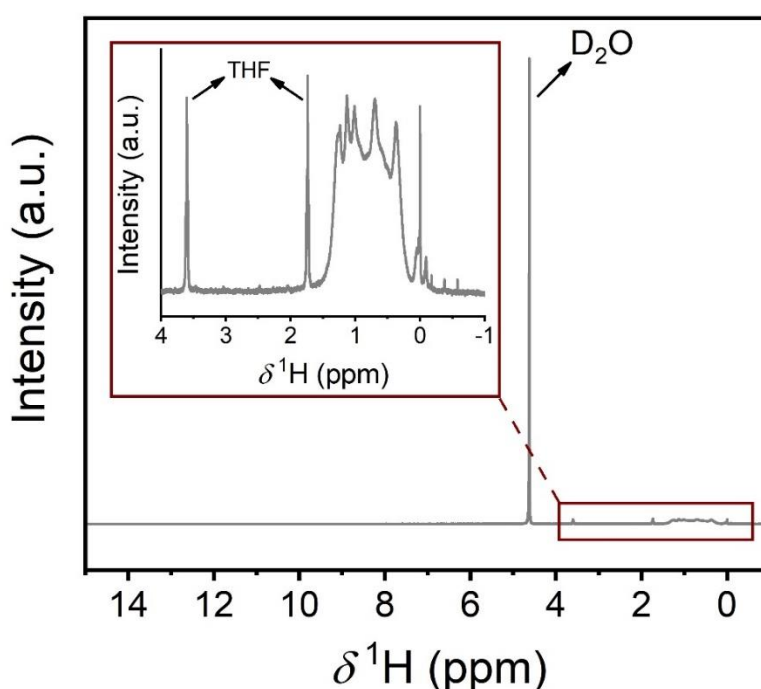
It has been reported that the reaction of  $(\text{CH}_3)_3\text{NHB}_{11}\text{H}_{14}$  with a metal hydroxide in aqueous solution under heating yields boric acid as a side product [11]. Sodium metaborate can then be formed by the reaction of boric acid with excess  $\text{NaOH}$  [62,63]. In aqueous solution,  $\text{NaB}(\text{OH})_4$  dissociates, releasing  $\text{NaOH}$  and yielding a solution with a high pH, which induces deprotonation of  $\text{B}_{11}\text{H}_{14}^-$  into  $\text{B}_{11}\text{H}_{13}^{2-}$  (reactions 3 and 4) [11,28,62,63], and formation of boric acid, which is observed in the  $^{11}\text{B}$  solution-state NMR of  $\text{Na}_{11}(\text{B}_{11}\text{H}_{14})_3(\text{B}_{11}\text{H}_{13})_4$  in  $\text{D}_2\text{O}$  at 14.6 ppm (Fig. 5.2).



As such, it is postulated that  $\text{Na}_{11}(\text{B}_{11}\text{H}_{14})_3(\text{B}_{11}\text{H}_{13})_4$  contains some quantity of  $\text{NaB}(\text{OH})_4$  ( $\approx 8$  mol% based on integration of the MAS NMR resonances), or a derivative thereof, that only affects the structure of the undecaborane upon aqueous dissolution. It should be highlighted that it is critical to characterise *nido*-borane anions through solid-state  $^{11}\text{B}$  MAS NMR, as the results of solution-state NMR can be misleading due to possible side reactions upon dissolution. This has also been a problem identified in NMR studies of higher boranes formed during metal borohydride decomposition [64]. The specific issue faced with impurities in

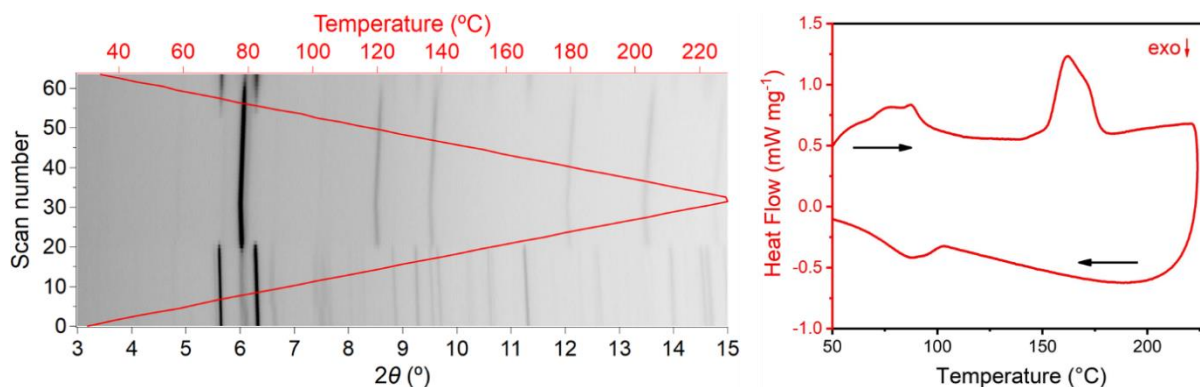
$\text{Na}_{11}(\text{B}_{11}\text{H}_{14})_3(\text{B}_{11}\text{H}_{13})_4$  may also be solved by the removal of the inorganic borate from solution, however, in the case of  $\text{Na}_{11}(\text{B}_{11}\text{H}_{14})_3(\text{B}_{11}\text{H}_{13})_4$ , the separation of a borate species from a sample that contains  $\text{Na}_2\text{B}_{11}\text{H}_{13}$  can be challenging as both have strong polar features and similar solubility properties in polar and apolar solvents. Prior to drying, the aqueous solution of  $\text{Na}_{11}(\text{B}_{11}\text{H}_{14})_3(\text{B}_{11}\text{H}_{13})_4$  was washed three times with diethyl ether, as an attempt to remove impurities and isolate both anions,  $\text{B}_{11}\text{H}_{14}^-$  and  $\text{B}_{11}\text{H}_{13}^{2-}$ , from the medium. However, upon drying the aqueous layer, a solid was obtained that was a mixture of both anions and the inorganic borate.

The  $^1\text{H}$  solution-state NMR of  $\text{Na}_2\text{B}_{11}\text{H}_{13}$  in  $\text{D}_2\text{O}$  shows the presence of THF (Fig. 5.6), which accounts for only 0.15 mol of THF to 1 mol of  $\text{Na}_2\text{B}_{11}\text{H}_{13}$  based on the integration of the NMR resonances. The multiplets at 1.7 and 3.6 ppm represent the resonances of  $\text{CH}_2$  and  $\text{CH}_2\text{O}$  from THF, respectively [65,66], and those between  $-0.6$  and  $1.5$  ppm were assigned to  $\text{B}_{11}\text{H}_{13}^{2-}$ .  $\text{Na}_2\text{B}_{11}\text{H}_{13}$  was only briefly dried at  $40^\circ\text{C}$  during synthesis to avoid unwanted decomposition, which may allow some THF to remain coordinated to the dried solid.



**Figure 5.6**  $^1\text{H}$  NMR spectrum (400 MHz) of  $\text{Na}_2\text{B}_{11}\text{H}_{13}$  in  $\text{D}_2\text{O}$ .  $\delta(\text{D}_2\text{O}) = 4.6$  ppm [66],  $\delta(\text{THF}) = 1.7$  and  $3.6$  ppm [65,66], and  $\delta(\text{B}_{11}\text{H}_{13}^{2-}) = -0.6 - 1.5$  ppm.

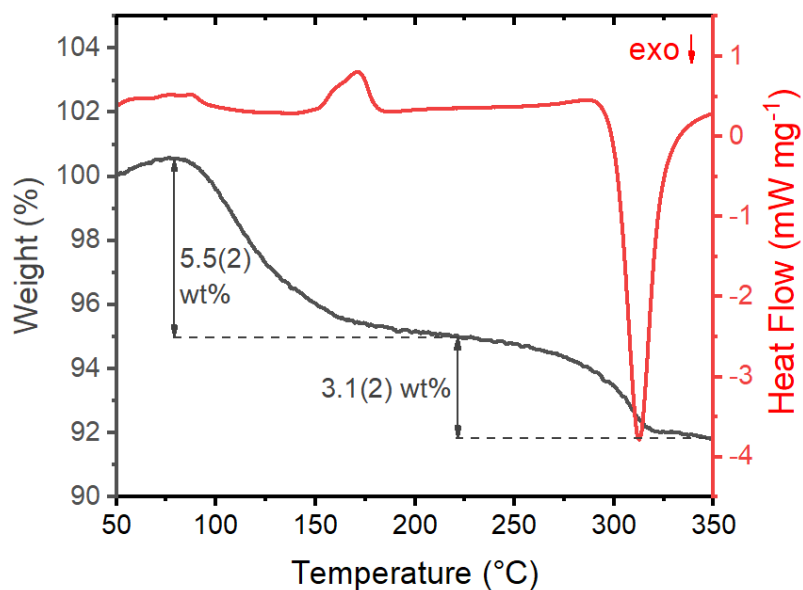
$\text{Na}_2\text{B}_{11}\text{H}_{13}$  was also analysed through *in-situ* SR-XRPD and DSC (Fig. 5.7), and it can be seen that a polymorphic phase transition occurs at  $\approx 170$  °C upon heating (endothermic) and 90 °C on cooling (exothermic).



**Figure 5.7** Left: *In-situ* SR-XRPD data ( $\lambda = 0.590827(4)$  Å) of  $\text{Na}_2\text{B}_{11}\text{H}_{13}$  during heating ( $5$  °C  $\text{min}^{-1}$ ) and cooling ( $6$  °C  $\text{min}^{-1}$ ). A reversible polymorphic phase transition is seen at  $\approx 170$  °C on heating and 90 °C on subsequent cooling. Red line represents temperature. Right: DSC plot ( $\Delta T/\Delta t = 10$  °C  $\text{min}^{-1}$ , Ar flow =  $40$  mL  $\text{min}^{-1}$ ) for  $\text{Na}_2\text{B}_{11}\text{H}_{13}$  upon heating and cooling between 40 and 220 °C.

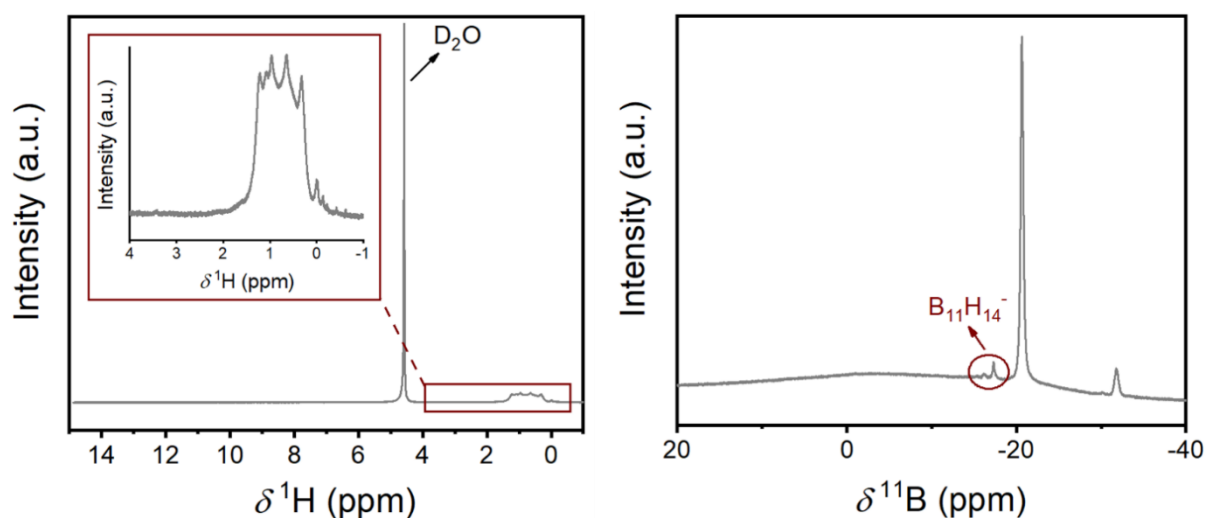
Another endothermic event, between 60 – 90 °C, can be identified during heating in the DSC (Fig. 5.7) and DSC/TGA (Fig. 5.8) plots with a subsequent mass loss of 5.5(2) wt%, which accounts for the release of residual coordinated THF. This mass loss is in close agreement with the amount of THF that was calculated through integration of the  $^1\text{H}$  NMR peaks (Fig. 5.6), which corresponds to 0.15 mol of THF to 1 mol of  $\text{Na}_2\text{B}_{11}\text{H}_{13}$ . A mass loss of 3.1(2) wt% observed between 320 and 340 °C (Fig. 5.8) is assigned to the decomposition of the sample, commensurate with a large exothermic feature. The decomposition temperatures of other *nido*-boranes, such as  $\text{LiB}_{11}\text{H}_{14}\cdot(\text{H}_2\text{O})_n$ ,  $\text{NaB}_{11}\text{H}_{14}\cdot(\text{H}_2\text{O})_n$  and  $\text{KB}_{11}\text{H}_{14}$  have already been identified to be  $\approx 210$  °C with a sharp exothermic peak in their DSC/TGA plot coupled with hydrogen release [11].





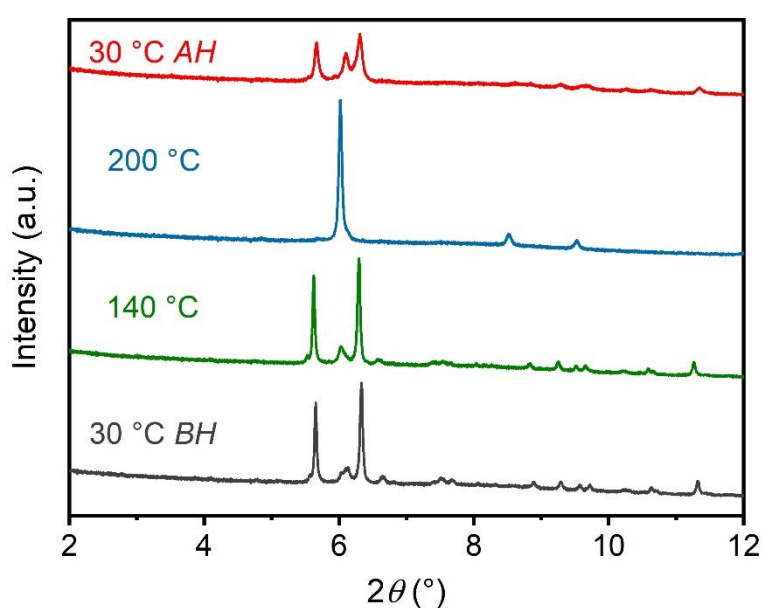
**Figure 5.8** DSC/TGA measurement for  $\text{Na}_2\text{B}_{11}\text{H}_{13}$  in the temperature range 50 – 350 °C. Approximately 5 mg of sample was used for the analysis ( $\Delta T/\Delta t = 10 \text{ }^\circ\text{C min}^{-1}$ , Ar flow = 40 mL  $\text{min}^{-1}$ ). A mass loss of 5.5(2) wt% is observed between 80 and 220 °C and 3.1(2) wt% between 220 and 340 °C.

Solution-state  $^1\text{H}$  NMR spectroscopy of  $\text{Na}_2\text{B}_{11}\text{H}_{13}$  after DSC/TGA, in which the sample was heated to 220 °C and cooled back to room temperature, reveals that THF resonances are no longer detected (Fig. 5.9). However, the  $^{11}\text{B}$  NMR spectrum does reveal a 5 mol% impurity of  $\text{B}_{11}\text{H}_{14}^-$  that is present after heating.



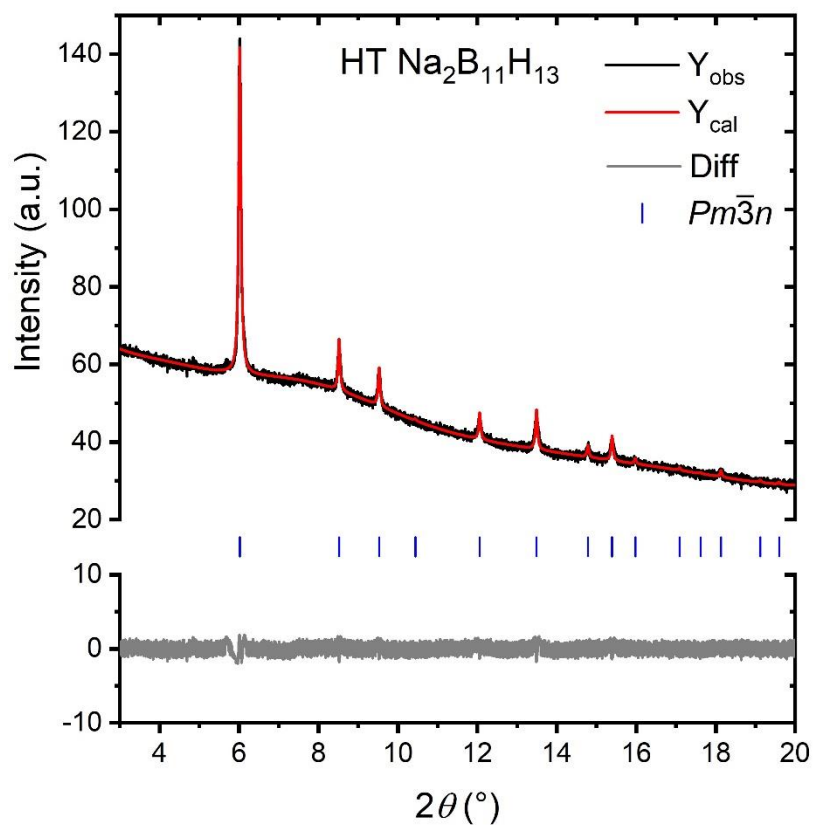
**Figure 5.9** Left:  $^1\text{H}$  NMR spectrum (400 MHz) of  $\text{Na}_2\text{B}_{11}\text{H}_{13}$  in  $\text{D}_2\text{O}$  after a DSC/TGA experiment heated to 220 °C.  $\delta(\text{D}_2\text{O}) = 4.6 \text{ ppm}$  [66], and  $\delta(\text{B}_{11}\text{H}_{13}^{2-}) = -0.6 - 1.5 \text{ ppm}$ . Right:  $^{11}\text{B}$   $\{^1\text{H}\}$  NMR spectrum (128 MHz) of the same sample in  $\text{D}_2\text{O}$ .  $\delta(\text{B}_{11}\text{H}_{14}^-) = -15.3, -16.2 \text{ and } -17.3 \text{ ppm}$ , and  $\delta(\text{B}_{11}\text{H}_{13}^{2-}) = -20.6 \text{ and } -31.7 \text{ ppm}$  [11].

Fig. 5.10 shows select SR-XRPD diffractograms of  $\text{Na}_2\text{B}_{11}\text{H}_{13}$  at different temperatures during and after heating. No major differences can be observed between the diffractogram at 30 °C (before heating) and after the minor THF release. This implies that the small amount of THF detected in the sample (0.15 mol of THF to 1 mol of  $\text{Na}_2\text{B}_{11}\text{H}_{13}$ ) could be solvent adsorbed to the powder, or that the material is composed of a mixture of  $\text{Na}_2\text{B}_{11}\text{H}_{13}$  and  $\text{Na}_2\text{B}_{11}\text{H}_{13}\cdot(\text{THF})_x$ . The THF is considered a small impurity, and the sample is here called  $\text{Na}_2\text{B}_{11}\text{H}_{13}$ . Samples of  $\text{Na}_2\text{B}_{11}\text{H}_{13}$  can then be prepared THF free by desolvating the powder under vacuum at slightly higher temperatures than the one here adopted (40 °C) without its decomposition.



**Figure 5.10** SR-XRPD patterns ( $\lambda = 0.590827(4)$  Å) for  $\text{Na}_2\text{B}_{11}\text{H}_{13}$  at 30 °C BH (before heating), 30 °C AH (after heating), 140 °C and 200 °C (during *in-situ* heating experiment).

At 200 °C,  $\text{Na}_2\text{B}_{11}\text{H}_{13}$  has completely undergone a polymorphic phase change, assuming a disordered body-centered cubic (bcc) structure, indexed in  $Pm\bar{3}n$  with  $a = 7.955(1)$  Å and  $V = 503.32(2)$  Å<sup>3</sup> (Fig. 5.11). This is the same symmetry observed for the high temperature  $\text{Na}_2\text{B}_{12}\text{H}_{12}$ , which undergoes the first polymorphic transition near 257 °C [67]. After cooling from 220 °C to 30 °C after heating, the SR-XRPD (Fig. 5.10) shows that the HT polymorph is only metastable and is predominantly transformed back into the original structure, with a minor portion of the  $Pm\bar{3}n$  phase remaining, as seen in Figs. 5.7 & 5.10.



**Figure 5.11** SR-XRPD ( $\lambda = 0.590827(4) \text{ \AA}$ ) and Rietveld refinement of  $\text{Na}_2\text{B}_{11}\text{H}_{13}$  at 200 °C (heating). Experimental data as black line, calculated diffraction pattern as red line, and difference plot in grey. Blue tick marks represent Bragg position from space group  $Pm\bar{3}n$ .  $R_{wp} = 2.93\%$ .

Interestingly, there are similarities in the room temperature diffraction patterns of  $\text{Na}_2\text{B}_{11}\text{H}_{13}$  after heating and  $\text{Na}_{11}(\text{B}_{11}\text{H}_{14})_3(\text{B}_{11}\text{H}_{13})_4$ , with the three main diffraction peaks located at  $Q = 1.05, 1.13$  and  $1.17 \text{ \AA}^{-1}$  in both diffractograms ( $Q = (4\pi\sin\vartheta)/\lambda$ , Fig. 5.12).

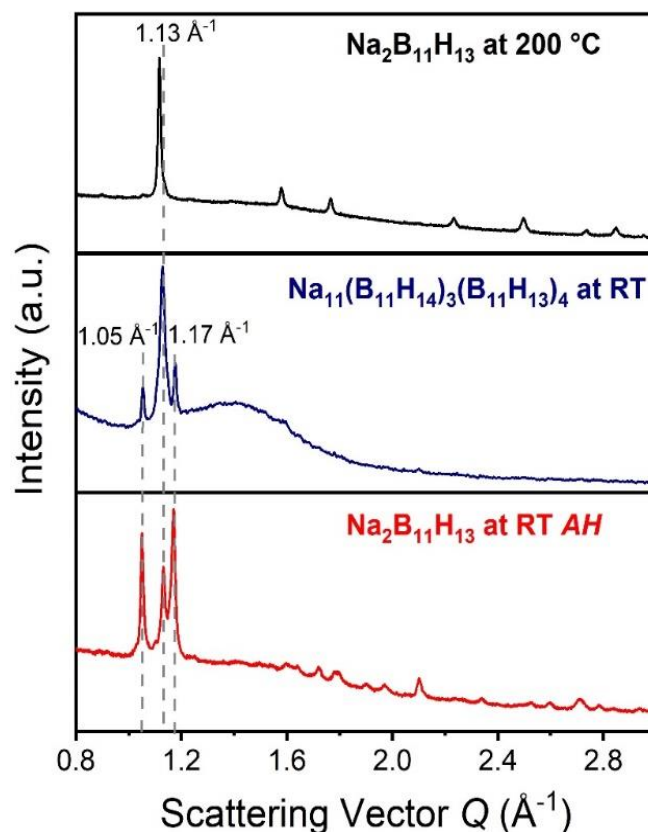


**Figure 5.12** XRPD pattern ( $\lambda = 1.54056 \text{ \AA}$ ) for  $\text{Na}_{11}(\text{B}_{11}\text{H}_{14})_3(\text{B}_{11}\text{H}_{13})_4$  at room temperature (blue), and SR-PXD data ( $\lambda = 0.590827(4) \text{ \AA}$ ) for  $\text{Na}_2\text{B}_{11}\text{H}_{13}$  at  $200 \text{ }^\circ\text{C}$  (black) and at room temperature after being heated to  $220 \text{ }^\circ\text{C}$  (red). Dashed lines at  $1.05$ ,  $1.17 \text{ \AA}^{-1}$  (RT polymorph) and at  $1.13 \text{ \AA}^{-1}$  (HT polymorph) were added to show the similarities between the diffractograms. The diffractograms were plotted with the  $x$ -axis in scattering vector to compare XRPD results obtained using different wavelengths.

In fact, the cubic  $Pm\bar{3}n$  polymorph, represented by the peak at  $Q = 1.13 \text{ \AA}^{-1}$ , seems to be present in the diffractogram of both samples,  $\text{Na}_2\text{B}_{11}\text{H}_{13}$  at RT after heating (AH) and  $\text{Na}_{11}(\text{B}_{11}\text{H}_{14})_3(\text{B}_{11}\text{H}_{13})_4$  at RT, with greater intensity, relative to the peaks at  $Q = 1.05$  and  $1.17 \text{ \AA}^{-1}$ , in  $\text{Na}_{11}(\text{B}_{11}\text{H}_{14})_3(\text{B}_{11}\text{H}_{13})_4$  than in  $\text{Na}_2\text{B}_{11}\text{H}_{13}$ . This is also shown in Fig. 5.13 where the  $Pm\bar{3}n$  polymorph in  $\text{Na}_2\text{B}_{11}\text{H}_{13}$  at  $200 \text{ }^\circ\text{C}$  is refined to  $a = 7.955(1) \text{ \AA}$  and  $V = 503.32(2) \text{ \AA}^3$  and in  $\text{Na}_{11}(\text{B}_{11}\text{H}_{14})_3(\text{B}_{11}\text{H}_{13})_4$  at room temperature it is refined to  $a = 7.983(1) \text{ \AA}$  and  $V = 487.94(9) \text{ \AA}^3$ . The peaks observed at  $Q = 1.05$  and  $1.17 \text{ \AA}^{-1}$  represent the Bragg reflections from the low temperature structures of the sodium borane. These data suggest that samples of  $\text{Na}_2\text{B}_{11}\text{H}_{13}$  and  $\text{Na}_{11}(\text{B}_{11}\text{H}_{14})_3(\text{B}_{11}\text{H}_{13})_4$  have some degree of dynamics in their structures at room temperature, which is enhanced to a greater degree in the mixed anion compound.

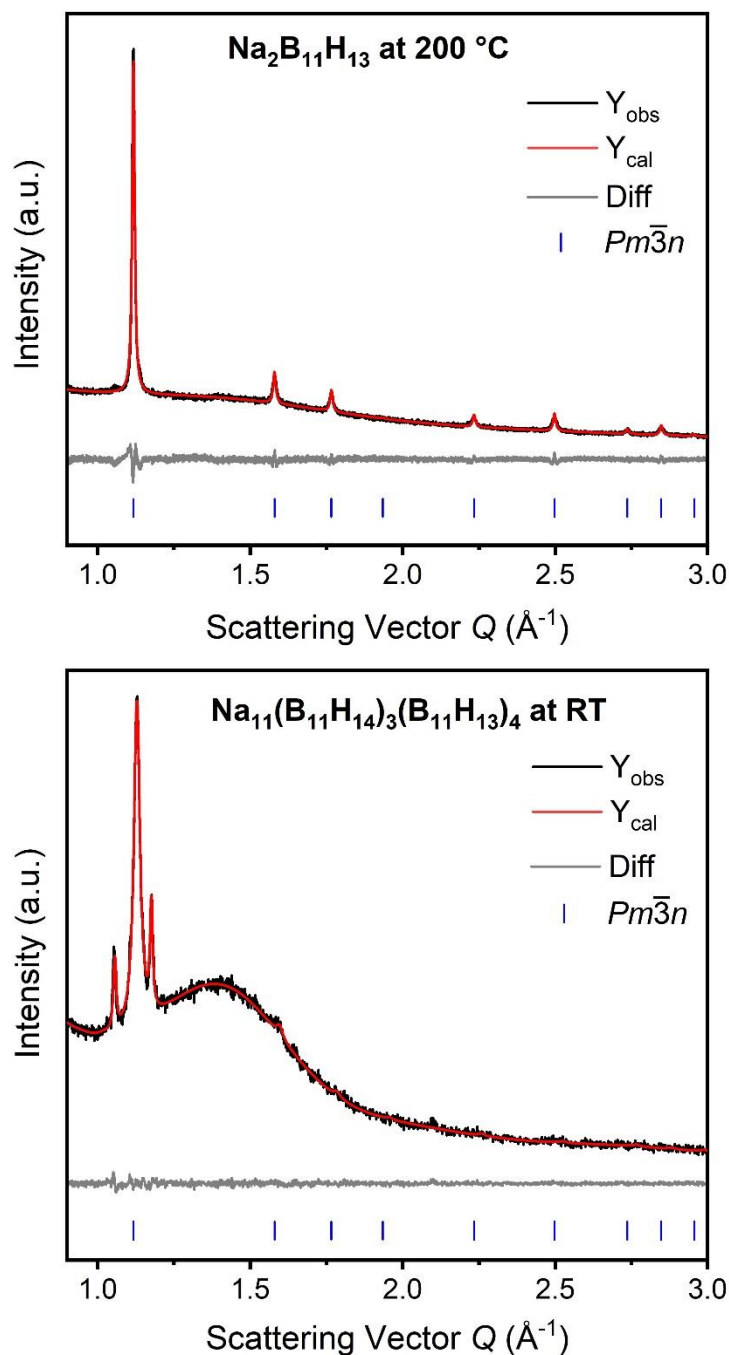


**Figure 5.13** Top: SR-XRPD ( $\lambda = 0.590827(4)$  Å) and Rietveld refinement of Na<sub>2</sub>B<sub>11</sub>H<sub>13</sub> at 200 °C (heating).  $R_{wp} = 2.93\%$ . Bottom: XRPD pattern ( $\lambda = 1.54056$  Å) and partial Rietveld refinement for Na<sub>11</sub>(B<sub>11</sub>H<sub>14</sub>)<sub>3</sub>(B<sub>11</sub>H<sub>13</sub>)<sub>4</sub> at room temperature. Peaks at  $Q = 1.05$  and  $1.17$  Å<sup>-1</sup> were fitted using simple peak functions and are not indexed or based on a crystal structure.  $R_{wp} = 3.44\%$ . Experimental data, calculated diffraction pattern and difference plot are shown in black, red and grey, respectively. Blue tick marks represent Bragg position from space group  $Pm\bar{3}n$  for both samples. The diffractograms were plotted with the x-axis in scattering vector to compare XRPD results that were obtained using different wavelengths.

The DSC/TGA plot for  $\text{Na}_{11}(\text{B}_{11}\text{H}_{14})_3(\text{B}_{11}\text{H}_{13})_4$  (Fig. 5.14) shows a subtle endothermic event ( $\approx 160\text{ }^\circ\text{C}$ ) close to the temperature observed for  $\text{Na}_2\text{B}_{11}\text{H}_{13}$  ( $170\text{ }^\circ\text{C}$ ), which may indicate the complete transformation to the same  $Pm\bar{3}n$  polymorph seen in  $\text{Na}_2\text{B}_{11}\text{H}_{13}$ . Based on the XRPD data (Fig. 5.12), most of the sample  $\text{Na}_{11}(\text{B}_{11}\text{H}_{14})_3(\text{B}_{11}\text{H}_{13})_4$  at RT is already in the  $Pm\bar{3}n$  polymorph, and it is surmised that the remaining portion of that sample would transition into this polymorph at  $160\text{ }^\circ\text{C}$ , which generates a discrete endothermic feature.  $\text{Na}_{11}(\text{B}_{11}\text{H}_{14})_3(\text{B}_{11}\text{H}_{13})_4$  also exhibits an exothermic peak at  $265\text{ }^\circ\text{C}$  with a weight loss of  $1.7(4)\text{ wt}\%$ , which indicates its decomposition.

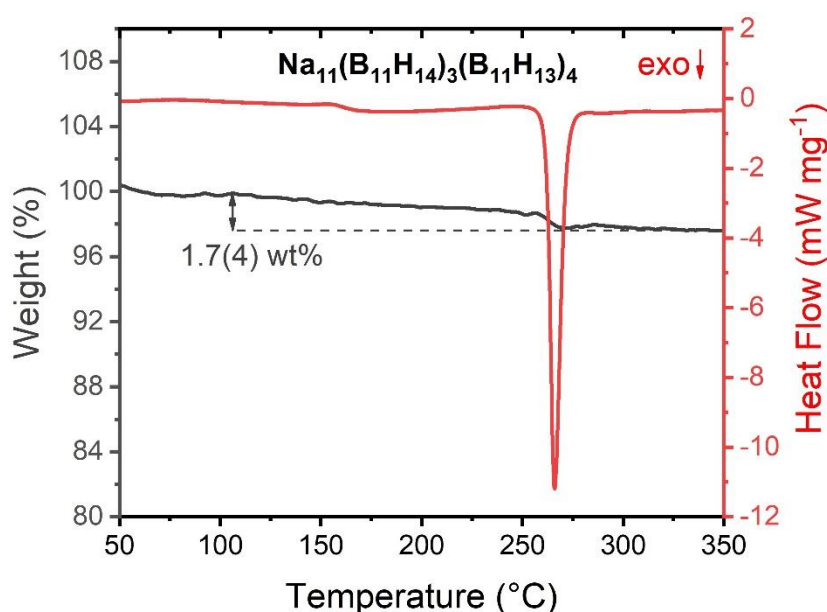


**Figure 5.14** DSC/TGA measurement for  $\text{Na}_{11}(\text{B}_{11}\text{H}_{14})_3(\text{B}_{11}\text{H}_{13})_4$  in the temperature range  $50 - 350\text{ }^\circ\text{C}$ . Approximately  $5\text{ mg}$  of the sample was used ( $\Delta T/\Delta t = 10\text{ }^\circ\text{C min}^{-1}$ , Ar flow =  $40\text{ mL min}^{-1}$ ).

Fig. 5.15 shows a comparison between the DSC results obtained for  $\text{NaB}_{11}\text{H}_{14}\cdot(\text{H}_2\text{O})_n$  [11],  $\text{Na}_{11}(\text{B}_{11}\text{H}_{14})_3(\text{B}_{11}\text{H}_{13})_4$  and  $\text{Na}_2\text{B}_{11}\text{H}_{13}$  from  $50 - 350\text{ }^\circ\text{C}$ . It is possible to observe that samples containing a larger proportion of  $\text{B}_{11}\text{H}_{13}^{2-}$ , rather than  $\text{B}_{11}\text{H}_{14}^-$ , exhibit a higher thermal stability, with elevated temperatures for their exothermic decomposition. This may be due to the fact that salts of  $\text{Na}_2\text{B}_{11}\text{H}_{13}$  present higher lattice energy than salts of  $\text{NaB}_{11}\text{H}_{14}$  [68,69].

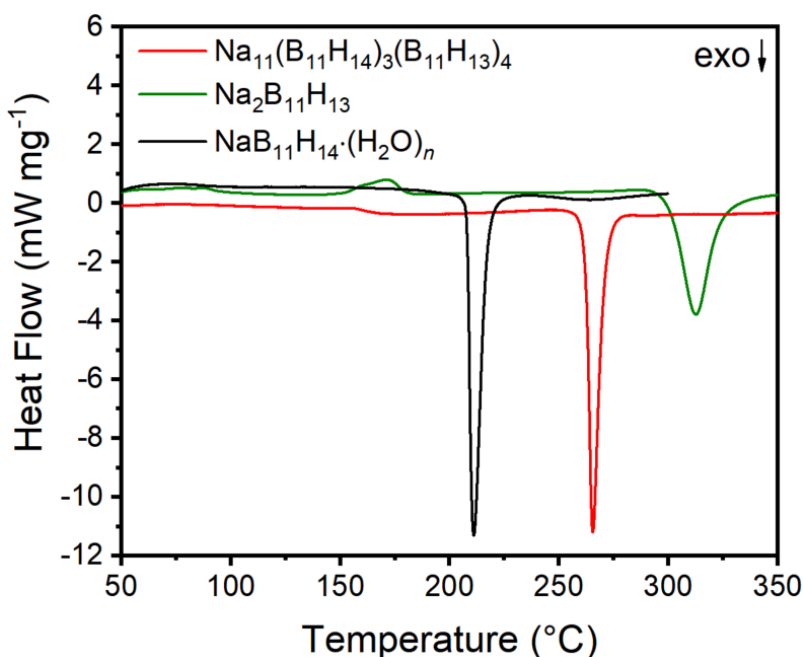


**Figure 5.15** DSC plots for  $\text{NaB}_{11}\text{H}_{14}\cdot(\text{H}_2\text{O})_n$ ,  $\text{Na}_{11}(\text{B}_{11}\text{H}_{14})_3(\text{B}_{11}\text{H}_{13})_4$  and  $\text{Na}_2\text{B}_{11}\text{H}_{13}$  from 50 – 350 °C. Approximately 5 mg of each sample was used ( $\Delta T/\Delta t = 10 \text{ }^\circ\text{C min}^{-1}$ , Ar flow = 40 mL  $\text{min}^{-1}$ ). The exothermic event occurs at a higher temperature as the  $\text{B}_{11}\text{H}_{14}^-$  content in the sample decreases.

### 5.3.2 Electrochemical Analysis

The solid-state  $\text{Na}^+$  conductivity of  $\text{Na}_{11}(\text{B}_{11}\text{H}_{14})_3(\text{B}_{11}\text{H}_{13})_4$  and  $\text{Na}_2\text{B}_{11}\text{H}_{13}$  was investigated through AC impedance measurements as a function of temperature and compared to other single-anion and mixed-anion sodium hydridoborate salts and the solid-state electrolyte  $\text{Na}\beta\text{-Al}_2\text{O}_3$  [1] (Fig. 5.16). For simplicity, an Arrhenius plot of ionic conductivity of  $\text{Na}_{11}(\text{B}_{11}\text{H}_{14})_3(\text{B}_{11}\text{H}_{13})_4$  and  $\text{Na}_2\text{B}_{11}\text{H}_{13}$  compared only to anhydrous and hydrated  $\text{NaB}_{11}\text{H}_{14}$  was also plotted (Fig. 5.17). The Nyquist plots for  $\text{Na}_2\text{B}_{11}\text{H}_{13}$  and  $\text{Na}_{11}(\text{B}_{11}\text{H}_{14})_3(\text{B}_{11}\text{H}_{13})_4$  at certain temperatures with the corresponding circuit model used to fit the impedance data are shown in Fig. 5.18.

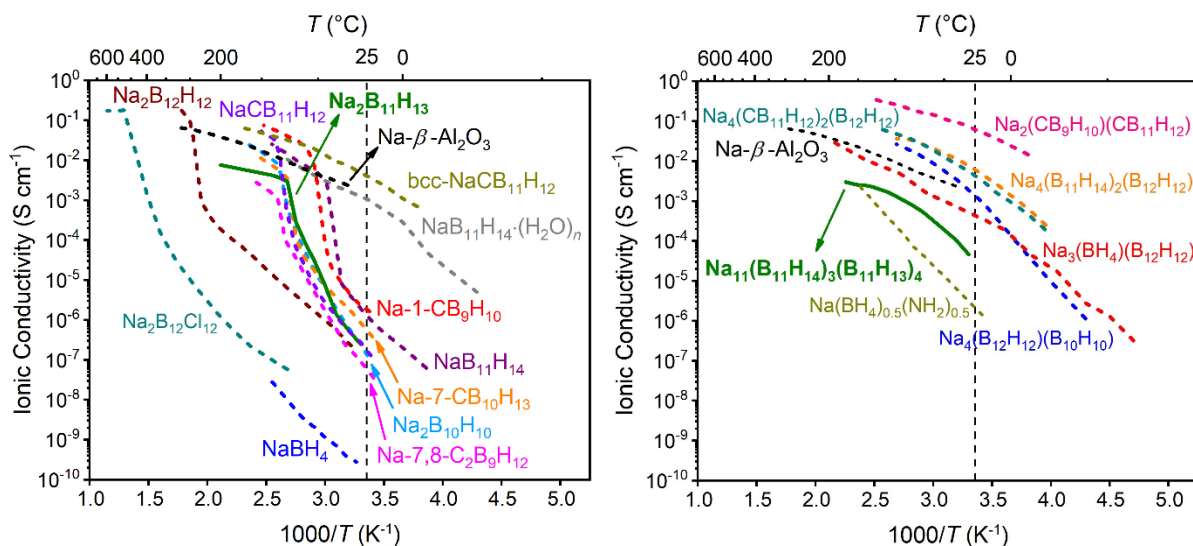


**Figure 5.16** Solid-state ionic conductivity of  $\text{Na}_2\text{B}_{11}\text{H}_{13}$  and  $\text{Na}_{11}(\text{B}_{11}\text{H}_{14})_3(\text{B}_{11}\text{H}_{13})_4$  as a function of temperature compared to other sodium single anion (left) [11,12,14,15,27,43,70,71] and mixed anion (right) [22,23,29,31,70,72] hydridoborate materials. bcc- $\text{NaCB}_{11}\text{H}_{12}$  represents the ionic conductivity of the mechanically-milled  $\text{NaCB}_{11}\text{H}_{12}$ , which presents a body-centered cubic (bcc) polymorph at RT [19]. The solid-state electrolyte  $\text{Na-}\beta\text{-Al}_2\text{O}_3$  was also added for comparison in both plots [1]. The solid green lines denote the ionic conductivity of the samples synthesised in the present work.

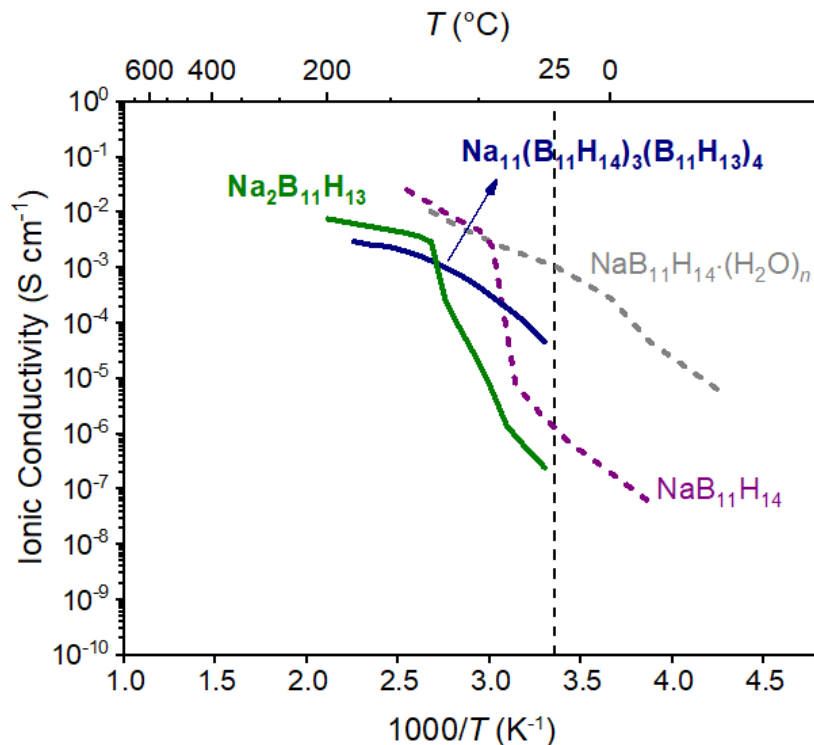


**Figure 5.17** Solid-state ionic conductivity of  $\text{Na}_2\text{B}_{11}\text{H}_{13}$  and  $\text{Na}_{11}(\text{B}_{11}\text{H}_{14})_3(\text{B}_{11}\text{H}_{13})_4$  as a function of temperature compared to  $\text{NaB}_{11}\text{H}_{14}$  [27] and  $\text{NaB}_{11}\text{H}_{14} \cdot (\text{H}_2\text{O})_n$  [11].



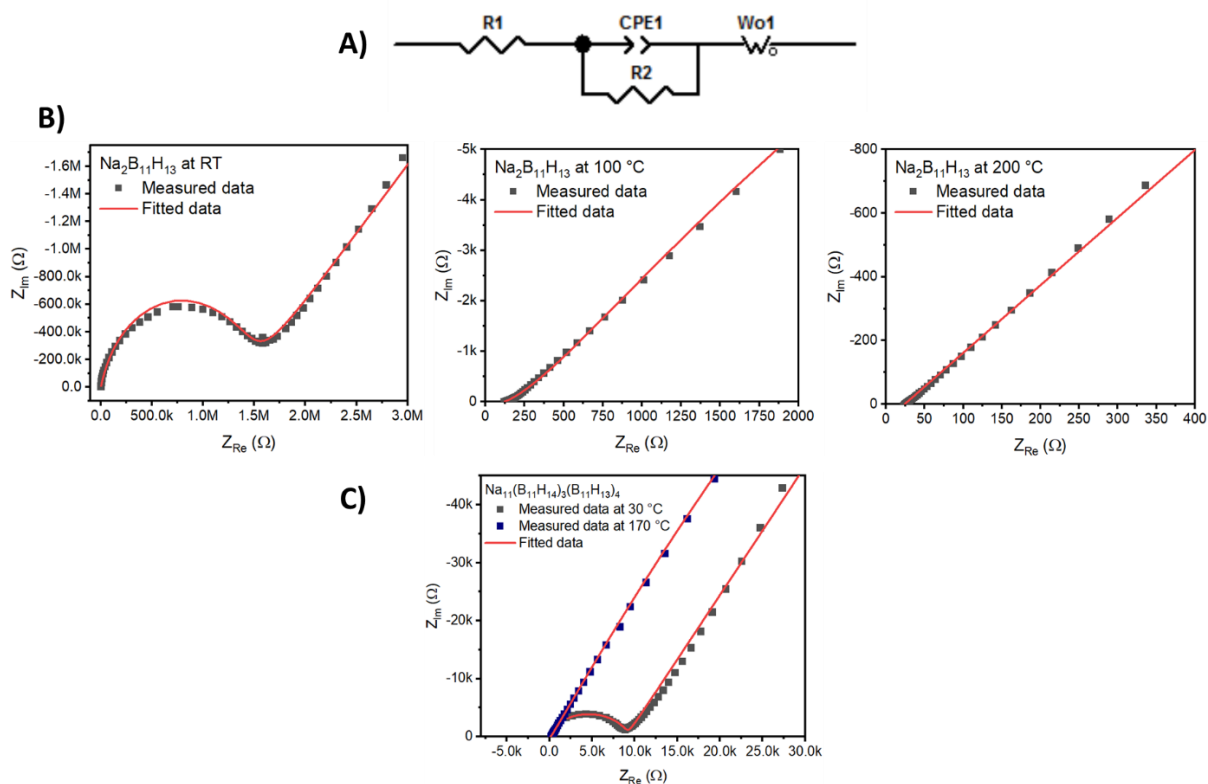


**Figure 5.18** A) Impedance circuit model used to fit Nyquist plots, where  $R_1$  is the internal resistance,  $R_2$  is the surface-layer resistance,  $CPE_1$  or  $Q_1$  is the constant phase element and  $W_{o1}$  is the open Warburg element [73,74]. B) Nyquist plots of the Au-symmetric cell for  $\text{Na}_2\text{B}_{11}\text{H}_{13}$  at room temperature, 100 and 200 °C. C) Nyquist plots of the Au-symmetric cell for  $\text{Na}_{11}(\text{B}_{11}\text{H}_{14})_3(\text{B}_{11}\text{H}_{13})_4$  at 30 and 170 °C. At low temperatures, the data is presented as a semi-circle (charge transfer resistance of the sample) with a spike line (Warburg element) at the low frequency region, which is related to the  $\text{Na}^+$  diffusion [43,73,74]. Upon increase of temperature, the semi-circle decreases, and only the linear component can be observed.

$\text{Na}_2\text{B}_{11}\text{H}_{13}$  presents an ionic conductivity of  $2.5 \times 10^{-7} \text{ S cm}^{-1}$  at 30 °C with a sudden increase upon heating, reaching  $2.9 \times 10^{-3} \text{ S cm}^{-1}$  at 100 °C, a similar result to that observed for  $\text{Na-}\beta\text{-Al}_2\text{O}_3$  and  $\text{NaB}_{11}\text{H}_{14} \cdot (\text{H}_2\text{O})_n$  at the same temperature ( $\approx 1 \times 10^{-2} \text{ S cm}^{-1}$ ). This step-function type behaviour is similar to the results observed for the *nido*-boranes  $\text{Na-7,8-C}_2\text{B}_9\text{H}_{12}$  and  $\text{Na-7-CB}_{10}\text{H}_{13}$  [27], and the *closo*-borane  $\text{Na}_2\text{B}_{10}\text{H}_{10}$  [14] as they undergo an order-disorder polymorphic transition with temperature increase. Even though  $\text{Na}_2\text{B}_{11}\text{H}_{13}$  assumes a disordered *bcc* structure as  $\text{NaB}_{11}\text{H}_{14}$  (space group  $\bar{1}43d$ ) at high temperature [27], the  $\text{Na}^+$  conductivity observed for the former is  $7.7 \times 10^{-3} \text{ S cm}^{-1}$  at 200 °C, whereas the latter exhibits results in the order of  $10^{-2} \text{ S cm}^{-1}$  at 100 °C. The lower ionic conductivity observed for

Na<sub>2</sub>B<sub>11</sub>H<sub>13</sub> compared to NaB<sub>11</sub>H<sub>14</sub> may be a result of the reduced number of vacant sites for cation hopping, since despite having a similarly sized unit cell, Na<sub>2</sub>B<sub>11</sub>H<sub>13</sub> has twice the number of Na<sup>+</sup> ions in its structure for charge-balance. There is also an increased Coulombic attraction between divalent anions, as in B<sub>11</sub>H<sub>13</sub><sup>2-</sup>, and Na<sup>+</sup>, as opposed to monovalent B<sub>11</sub>H<sub>14</sub><sup>-</sup>, which may also reduce cationic conductivity in Na<sub>2</sub>B<sub>11</sub>H<sub>13</sub> [27,75]. Despite this, the ionic conductivity observed in Na<sub>2</sub>B<sub>11</sub>H<sub>13</sub> is significantly higher than either Na<sub>2</sub>B<sub>12</sub>H<sub>12</sub> [71], NaBH<sub>4</sub> [70] and Na<sub>2</sub>B<sub>12</sub>Cl<sub>12</sub> [43], in the temperature range of 30 – 200 °C (Fig. 5.16). The B<sub>11</sub>H<sub>13</sub><sup>2-</sup> anion exhibits an asymmetric charge distribution (or polarisation), which is analogous to other *nido*-boranes as well as carboranes, such as CB<sub>9</sub>H<sub>10</sub><sup>-</sup>, which have interesting reorientational dynamics governed by their charge polarity [75]. In contrast, Na<sub>2</sub>B<sub>12</sub>H<sub>12</sub> [71] contains an isotropic *closo*-borane anion, which yields a salt with lower ionic conductivity [27].

The activation energy ( $E_a$ ) for Na<sup>+</sup> conduction for LT Na<sub>2</sub>B<sub>11</sub>H<sub>13</sub> was measured to be 0.73 eV ( $\pm$  0.02 eV). This is similar to other sodium *nido*-boranes, such as Na-7-CB<sub>10</sub>H<sub>13</sub>, Na-7,8-C<sub>2</sub>B<sub>9</sub>H<sub>12</sub> and NaB<sub>11</sub>H<sub>14</sub> [27], which demonstrate an  $E_a$  of 0.68, 0.78 and 0.61 eV, respectively, for Na<sup>+</sup> ion conduction in their low temperature ordered crystallographic phases (Table 5.1). Upon the order-disorder polymorphic transition, the  $E_a$  for Na<sup>+</sup> conductivity in Na<sub>2</sub>B<sub>11</sub>H<sub>13</sub> decreases to 0.36 ( $\pm$  0.03 eV) eV, which is within the range for other disordered high temperature sodium boranes, such as Na-7-CB<sub>10</sub>H<sub>13</sub> (0.42 eV) [27], Na-7,8-C<sub>2</sub>B<sub>9</sub>H<sub>12</sub> (0.39 eV) [27], NaB<sub>11</sub>H<sub>14</sub> (0.41 eV) [27], Na<sub>2</sub>B<sub>10</sub>H<sub>10</sub> (0.47 eV) [14], and Na<sub>2</sub>B<sub>12</sub>H<sub>12</sub> (0.21 eV) [71] (Table 5.1).

**Table 5.1** Activation energy of Na<sub>11</sub>(B<sub>11</sub>H<sub>14</sub>)<sub>3</sub>(B<sub>11</sub>H<sub>13</sub>)<sub>4</sub> and Na<sub>2</sub>B<sub>11</sub>H<sub>13</sub> compared to other sodium hydridoborate salts.

Sample	Activation energy (eV)	Reference
LT <sup>a</sup> Na <sub>2</sub> B <sub>11</sub> H <sub>13</sub>	0.73 ( $\pm$ 0.02 eV)	This work
HT <sup>b</sup> Na <sub>2</sub> B <sub>11</sub> H <sub>13</sub>	0.36 ( $\pm$ 0.03 eV)	This work
Na <sub>11</sub> (B <sub>11</sub> H <sub>14</sub> ) <sub>3</sub> (B <sub>11</sub> H <sub>13</sub> ) <sub>4</sub>	0.51 ( $\pm$ 0.02 eV)	This work
NaB <sub>11</sub> H <sub>14</sub> ·(H <sub>2</sub> O) <sub>n</sub>	0.3	[11]
LT NaB <sub>11</sub> H <sub>14</sub>	0.61	[27]
HT NaB <sub>11</sub> H <sub>14</sub>	0.41	[27]
LT Na-7-CB <sub>10</sub> H <sub>13</sub>	0.68	[27]
HT Na-7-CB <sub>10</sub> H <sub>13</sub>	0.42	[27]

LT Na-7,8-C <sub>2</sub> B <sub>9</sub> H <sub>12</sub>	0.78	[27]
HT Na-7,8-C <sub>2</sub> B <sub>9</sub> H <sub>12</sub>	0.39	[27]
HT Na <sub>2</sub> B <sub>10</sub> H <sub>10</sub>	0.47	[14]
HT Na <sub>2</sub> B <sub>12</sub> H <sub>12</sub>	0.21	[71]

<sup>a</sup>LT = Low temperature. <sup>b</sup>HT = High temperature.

Mixed-anion Na<sub>11</sub>(B<sub>11</sub>H<sub>14</sub>)<sub>3</sub>(B<sub>11</sub>H<sub>13</sub>)<sub>4</sub> presents higher Na<sup>+</sup> conductivity than the LT Na<sub>2</sub>B<sub>11</sub>H<sub>13</sub> and NaB<sub>11</sub>H<sub>14</sub> [27], which shows that the formation of the solid-solution results in a material with better ionic conductivity properties near room temperature ( $4.6 \times 10^{-5} \text{ S cm}^{-1}$  at 30 °C) than its constituents (Fig. 5.17). The results of Na<sup>+</sup> conductivity for Na<sub>11</sub>(B<sub>11</sub>H<sub>14</sub>)<sub>3</sub>(B<sub>11</sub>H<sub>13</sub>)<sub>4</sub> from 100 – 170 °C are also close to that observed for the HT Na<sub>2</sub>B<sub>11</sub>H<sub>13</sub> (Fig. 5.17), with the mixed-anion solid-solution reaching an ionic conductivity of  $3.0 \times 10^{-3} \text{ S cm}^{-1}$  at 170 °C, and Na<sub>2</sub>B<sub>11</sub>H<sub>13</sub> exhibiting a result of  $6.1 \times 10^{-3} \text{ S cm}^{-1}$  at the same temperature. Again, this is thought to be related to the presence of the *Pm* $\bar{3}$ *n* polymorph in the Na<sub>11</sub>(B<sub>11</sub>H<sub>14</sub>)<sub>3</sub>(B<sub>11</sub>H<sub>13</sub>)<sub>4</sub> structure at RT (Figs. 5.12 & 5.13). The stabilisation of the disordered superionic structure at RT via formation of mixed-borane-anion solid-solution has been previously seen as in Na<sub>2</sub>(CB<sub>9</sub>H<sub>10</sub>)(CB<sub>11</sub>H<sub>12</sub>) [22] and Na<sub>2</sub>(B<sub>12</sub>H<sub>12</sub>)<sub>0.5</sub>(B<sub>10</sub>H<sub>10</sub>)<sub>0.5</sub> [23]. The mixture of monovalent with divalent hydridoborate species, such as Na<sub>3</sub>(BH<sub>4</sub>)(B<sub>12</sub>H<sub>12</sub>) [72], Na<sub>4</sub>(B<sub>11</sub>H<sub>14</sub>)<sub>2</sub>(B<sub>12</sub>H<sub>12</sub>) [29], Na<sub>4</sub>(CB<sub>11</sub>H<sub>12</sub>)<sub>2</sub>(B<sub>12</sub>H<sub>12</sub>) [31], and Na<sub>3</sub>(NH<sub>2</sub>)(B<sub>12</sub>H<sub>12</sub>) [76] has also already been presented as an efficient strategy to enhance the ionic conductivity properties of the material. The result observed for the Na<sup>+</sup> conductivity of Na<sub>11</sub>(B<sub>11</sub>H<sub>14</sub>)<sub>3</sub>(B<sub>11</sub>H<sub>13</sub>)<sub>4</sub> near room temperature is also higher than the majority of the single-anion sodium-borane compounds reported so far at the same temperature (Fig. 5.16) and presents lower ionic conductivity when compared to NaB<sub>11</sub>H<sub>14</sub>·(H<sub>2</sub>O)<sub>*n*</sub> ( $1.1 \times 10^{-3} \text{ S cm}^{-1}$  at 25 °C) as water may facilitate the Na<sup>+</sup> migration (Fig. 5.17) [11], and to bcc-NaCB<sub>11</sub>H<sub>12</sub> ( $4 \times 10^{-3} \text{ S cm}^{-1}$  at 25 °C) as mechanical modification induces stabilisation of the bcc polymorph at RT [19].

The activation energy for Na<sup>+</sup> conductivity in Na<sub>11</sub>(B<sub>11</sub>H<sub>14</sub>)<sub>3</sub>(B<sub>11</sub>H<sub>13</sub>)<sub>4</sub> was measured to be 0.51 eV ( $\pm 0.02 \text{ eV}$ ) from 30 – 80 °C, which lies between the results observed for the HT and the LT Na<sub>2</sub>B<sub>11</sub>H<sub>13</sub> and NaB<sub>11</sub>H<sub>14</sub> (Table 5.1).

Fig. 5.16 also shows that the mixture Na<sub>11</sub>(B<sub>11</sub>H<sub>14</sub>)<sub>3</sub>(B<sub>11</sub>H<sub>13</sub>)<sub>4</sub> presents higher ionic conductivity results than Na(BH<sub>4</sub>)<sub>0.5</sub>(NH<sub>2</sub>)<sub>0.5</sub> in the temperature range of 30 – 170 °C [70], yet lower results when compared to other mixed-anion solid solutions. However, the synthesis of

$\text{Na}_{11}(\text{B}_{11}\text{H}_{14})_3(\text{B}_{11}\text{H}_{13})_4$  reported here requires only the use of wet chemistry approaches and common laboratory consumables, which may be more cost-effective than when compared to the majority of the syntheses reported for carboranes [77].

The oxidative stability limit of  $\text{Na}_2\text{B}_{11}\text{H}_{13}$  was determined to be 2.1 V against Na metal based on the anodic peak observed in its linear sweep voltammogram at 30 °C (Fig. 5.19). This result is similar to the one determined for  $\text{NaBH}_4$  (1.9 V vs.  $\text{Na}^+/\text{Na}$ ) [78,79] and higher than the oxidative stability limit estimated for  $\text{Li}_2\text{B}_{11}\text{H}_{13}$  against Li metal (< 1.0 V), which was based on DFT calculations [28]. However, the oxidative stability limit of  $\text{Na}_2\text{B}_{11}\text{H}_{13}$  is lower than the ones for  $\text{NaB}_{11}\text{H}_{14}$  [29] and  $\text{NaB}_{11}\text{H}_{14}\cdot(\text{H}_2\text{O})_n$  [11] with both exhibiting an onset of decomposition at 2.6 V vs.  $\text{Na}^+/\text{Na}$ . The mixed-anion  $\text{Na}_{11}(\text{B}_{11}\text{H}_{14})_3(\text{B}_{11}\text{H}_{13})_4$  exhibited two onsets of anodic current, one at 2.1 V and another one at  $\approx 2.7$  V (Fig. 5.19), which is in agreement with the electrochemical decomposition of  $\text{Na}_2\text{B}_{11}\text{H}_{13}$  and  $\text{NaB}_{11}\text{H}_{14}$ , respectively. A multistep oxidation process has been reported for other mixed-anion boranes, such as  $\text{Na}_4(\text{B}_{12}\text{H}_{12})(\text{B}_{10}\text{H}_{10})$ , which presents two onsets of decomposition, one at 3.02 V vs.  $\text{Na}^+/\text{Na}$  and another one at 3.22 V vs.  $\text{Na}^+/\text{Na}$  that were attributed to  $\text{Na}_2\text{B}_{10}\text{H}_{10}$  and  $\text{Na}_2\text{B}_{12}\text{H}_{12}$ , respectively [45].

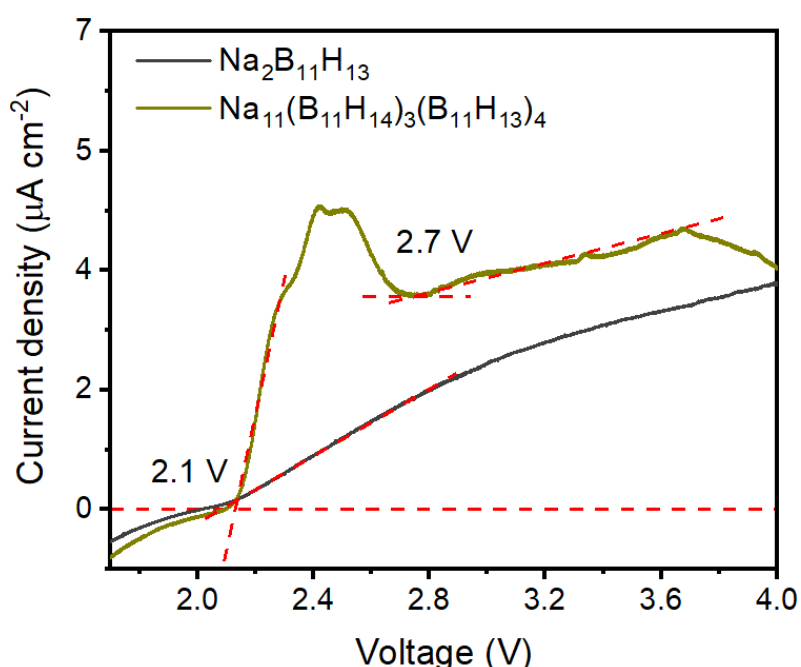


**Figure 5.19** Linear Sweep Voltammogram of Na/SSE/SSE+C/Pt/Al cell, with SSE =  $\text{Na}_2\text{B}_{11}\text{H}_{13}$  (grey) and  $\text{Na}_{11}(\text{B}_{11}\text{H}_{14})_3(\text{B}_{11}\text{H}_{13})_4$  (yellow) cell at a scan rate of  $50 \mu\text{V s}^{-1}$  at 30 °C between 1.7 and 4.0 V. The red dashed lines represent the background and the anodic current fitted to obtain the oxidation potential.

The higher electrochemical stability of *closo*-boranes, such as  $\text{Na}_2\text{B}_{10}\text{H}_{10}$  and  $\text{Na}_2\text{B}_{12}\text{H}_{12}$ , than *nido*-boranes, as in  $\text{NaB}_{11}\text{H}_{14}$  and  $\text{Na}_2\text{B}_{11}\text{H}_{13}$ , can be expected as the latter present an open borane cage with delocalised hydrogen atoms, which tend to reduce their stability, with hydrogen release or dimer formation upon oxidation [29]. Despite that, an oxidative stability limit of 2.1 V vs.  $\text{Na}^+/\text{Na}$ , as in samples of  $\text{Na}_2\text{B}_{11}\text{H}_{13}$ , may not be an issue for their application as solid-state electrolytes in Na-S batteries as such batteries present a working potential in the range of 1.78 – 2.08 V [37,80]. Besides that, the use of Na as the anode in solid-state batteries brings additional challenges that may need to be overcome prior to practical applications. For example, pure Na-metal can lead the battery to short circuit due to Na dendrite formation [81], and the use of a Na-Sn alloy as the anode can result in battery capacity fade owing to the volume expansion of Sn [82]. Therefore, the compatibility of sodium-borane electrolytes, such as  $\text{Na}_2\text{B}_{11}\text{H}_{13}$ ,  $\text{NaB}_{11}\text{H}_{14}$ ,  $\text{NaB}_{11}\text{H}_{14}\cdot(\text{H}_2\text{O})_n$ , and  $\text{Na}_{11}(\text{B}_{11}\text{H}_{14})_3(\text{B}_{11}\text{H}_{13})_4$ , should also be assessed against other types of anode materials, for instance, hard carbon and  $\text{Na}_2\text{Ti}_3\text{O}_7$  [83–85].

#### 5.4 CONCLUSION

A facile synthesis of the solid-state  $\text{Na}_2\text{B}_{11}\text{H}_{13}$  and the mixed-anion solid-solution  $\text{Na}_{11}(\text{B}_{11}\text{H}_{14})_3(\text{B}_{11}\text{H}_{13})_4$  was reported.  $\text{Na}_2\text{B}_{11}\text{H}_{13}$  undergoes a polymorphic phase change at  $\approx 170^\circ\text{C}$  assuming a body-centered cubic structure indexed in  $Pm\bar{3}n$ , isostructural to the first HT phase observed for  $\text{Na}_2\text{B}_{12}\text{H}_{12}$ . Even though both  $\text{Na}_2\text{B}_{11}\text{H}_{13}$  and  $\text{NaB}_{11}\text{H}_{14}$  assume a bcc polymorph at HT, the latter presents higher  $\text{Na}^+$  conductivity than the former, with  $\text{Na}_2\text{B}_{11}\text{H}_{13}$  reaching  $7.7 \times 10^{-3} \text{ S cm}^{-1}$  at  $200^\circ\text{C}$ . It is proposed that the increased Coulombic attraction between  $\text{Na}^+$  and divalent  $\text{B}_{11}\text{H}_{13}^{2-}$ , along with the increased cation site occupancy, decreases the mobility of the cation in the crystal structure compared to the monovalent  $\text{B}_{11}\text{H}_{14}^-$  analogue.

At  $30^\circ\text{C}$ ,  $\text{Na}_{11}(\text{B}_{11}\text{H}_{14})_3(\text{B}_{11}\text{H}_{13})_4$  exhibits an ionic conductivity ( $4.7 \times 10^{-5} \text{ S cm}^{-1}$ ) higher than its constituents  $\text{NaB}_{11}\text{H}_{14}$  ( $2 \times 10^{-6} \text{ S cm}^{-1}$ ) and  $\text{Na}_2\text{B}_{11}\text{H}_{13}$  ( $2.5 \times 10^{-7} \text{ S cm}^{-1}$ ). XRPD data for  $\text{Na}_{11}(\text{B}_{11}\text{H}_{14})_3(\text{B}_{11}\text{H}_{13})_4$  shows the disordered  $Pm\bar{3}n$  polymorph at RT, which is observed for  $\text{Na}_2\text{B}_{11}\text{H}_{13}$  at high temperatures. This shows that a mixed-anion solid-solution could partially stabilise the HT disordered-polymorph at RT, which results in a sample with increased ionic conductivity properties.

$\text{Na}_2\text{B}_{11}\text{H}_{13}$  presents higher thermal stability than  $\text{NaB}_{11}\text{H}_{14}$ , however the former is more susceptible to voltage induced oxidation against Na metal, with an oxidative stability limit of 2.1 V vs.  $\text{Na}^+/\text{Na}$  at 30 °C compared to 2.6 V vs.  $\text{Na}^+/\text{Na}$  for  $\text{NaB}_{11}\text{H}_{14}$  or  $\text{NaB}_{11}\text{H}_{14}\cdot(\text{H}_2\text{O})_n$  at same temperature.  $\text{Na}_{11}(\text{B}_{11}\text{H}_{14})_3(\text{B}_{11}\text{H}_{13})_4$  exhibits two onsets of electrochemical decomposition at 2.1 V and 2.7 V vs.  $\text{Na}^+/\text{Na}$  at 30 °C, which are in agreement with the oxidative stability limit observed for its counterparts. Sodium *nido*-boranes show great potential as solid-state ion conductors and should be implemented in all-solid-state battery cells in the near future to assess their performance against promising anode and cathode materials.

## 5.5 REFERENCES

- [1] B.R.S. Hansen, M. Paskevicius, H. Li, E. Akiba, T.R. Jensen, Metal boranes: Progress and applications, *Coord. Chem. Rev.* 323 (2016) 60–70. <https://doi.org/10.1016/j.ccr.2015.12.003>.
- [2] R. Černý, F. Murgia, M. Brighi, Metal hydroborates: From hydrogen stores to solid electrolytes, *J. Alloys Compd.* 895 (2022) 162659. <https://doi.org/10.1016/j.jallcom.2021.162659>.
- [3] F. Ali, N. S Hosmane, Y. Zhu, Boron Chemistry for Medical Applications, *Molecules*. 25 (2020) 1–24. <https://doi.org/10.3390/molecules25040828>.
- [4] J.D. Clark, *Ignition!: An Informal History of Liquid Rocket Propellants*, Rutgers University Press, New Brunswick, 1972.
- [5] C. Faverio, M.F. Boselli, F. Medici, M. Benaglia, Biomolecular Chemistry Ammonia borane as a reducing agent in organic, *Org. Biomol. Chem.* 18 (2020) 7789–7813. <https://doi.org/10.1039/d0ob01351j>.
- [6] J. Michel, B. Faure, M. Ma, Phosphane–boranes: synthesis, characterization and synthetic applications, *Coord. Chem. Rev.* 178–180 (1998) 665–698.
- [7] L.H. Rude, T.K. Nielsen, D.B. Ravnsbæk, U. Bo, M.B. Ley, B. Richter, L.M. Arnbjerg, M. Dornheim, Y. Filinchuk, F. Besenbacher, Tailoring properties of borohydrides for hydrogen storage: A review, *Phys. Status Solidi A*. 208 (2011) 1754–1773. <https://doi.org/10.1002/pssa.201001214>.
- [8] H. Hagemann, Boron Hydrogen Compounds: Hydrogen Storage and Battery Applications, *Molecules*. 26 (2021) 7425.

- [9] C. Frommen, M.H. Sørby, M. Heere, T.D. Humphries, J.E. Olsen, B.C. Hauback, Rare earth borohydrides - Crystal structures and thermal properties, *Energies*. 10 (2017) 2115. <https://doi.org/10.3390/en10122115>.
- [10] D.B. Ravnsbæk, Y. Filinchuk, M. Dornheim, Metal borohydrides and derivatives – synthesis, structure and properties, *Chem. Soc. Rev.* 46 (2017) 1565–1634. <https://doi.org/10.1039/C6CS00705H>.
- [11] D. H. P. Souza, K.T. Møller, S.A. Moggach, T.D. Humphries, A.M. D’Angelo, C.E. Buckley, M. Paskevicius, Hydrated alkali-B<sub>11</sub>H<sub>14</sub> salts as potential solid-state electrolytes, *J. Mater. Chem. A*. 9 (2021) 15027–15037. <https://doi.org/10.1039/d1ta01551f>.
- [12] W.S. Tang, A. Unemoto, W. Zhou, V. Stavila, M. Matsuo, H. Wu, S. Orimo, T.J. Udovic, Unparalleled lithium and sodium superionic conduction in solid electrolytes with large monovalent cage-like anions, *Energy Environ. Sci.* 8 (2015) 3637–3645. <https://doi.org/10.1039/c5ee02941d>.
- [13] M. Paskevicius, B.R.S. Hansen, M. Jørgensen, B. Richter, T.R. Jensen, Multifunctionality of silver *closo*-boranes, *Nat. Commun.* 8 (2017) 10–15. <https://doi.org/10.1038/ncomms15136>.
- [14] T.J. Udovic, M. Matsuo, W.S. Tang, H. Wu, V. Stavila, A. V Soloninin, R. V Skoryunov, O.A. Babanova, A. V Skripov, J.J. Rush, A. Unemoto, H. Takamura, S. Orimo, Exceptional Superionic Conductivity in Disordered Sodium Decahydro-*closo*-decaborate, *Adv. Mater.* 26 (2014) 7622–7626. <https://doi.org/10.1002/adma.201403157>.
- [15] W.S. Tang, M. Matsuo, H. Wu, V. Stavila, W. Zhou, A.A. Talin, A. V Soloninin, R. V Skoryunov, O.A. Babanova, A. V Skripov, A. Unemoto, S.I. Orimo, T.J. Udovic, Liquid-like ionic conduction in solid lithium and sodium monocarba-*closo*-decaborates near or at room temperature, *Adv. Energy Mater.* 6 (2016) 1502237. <https://doi.org/10.1002/aenm.201502237>.
- [16] T.A. Dobbins, Overview of the Structure – Dynamics – Function Relationships in Borohydrides for Use as Solid-State Electrolytes in Battery Applications, *Molecules*. 26 (2021) 3239. <https://doi.org/10.3390/molecules26113239>.
- [17] A. Gradisek, M. Jørgensen, M. Paskevicius, B.R.S. Hansen, T.R. Jensen, Molecular Dynamics in Ag<sub>2</sub>B<sub>12</sub>H<sub>12</sub> Studied by Nuclear Magnetic Resonance, *J. Phys. Chem. C*. 125 (2021) 5534–5541. <https://doi.org/10.1021/acs.jpcc.1c00528>.
- [18] Y. Sadikin, P. Schouwink, M. Brighi, Z. Łodziana, R. Černý, Modified Anion Packing of

- Na<sub>2</sub>B<sub>12</sub>H<sub>12</sub> in Close to Room Temperature Superionic Conductors, *Inorg. Chem.* 56 (2017) 5006–5016. <https://doi.org/10.1021/acs.inorgchem.7b00013>.
- [19] F. Murgia, M. Brighi, L. Piveteau, C.E. Avalos, V. Gulino, M.C. Nierstenh, P. Ngene, P. De Jongh, C. Radovan, Enhanced Room-Temperature Ionic Conductivity of NaCB<sub>11</sub>H<sub>12</sub> via High-Energy Mechanical Milling, *ACS Appl. Mater. Interfaces.* 13 (2021) 61346–61356. <https://doi.org/10.1021/acsami.1c21113>.
- [20] S. Kim, N. Toyama, H. Oguchi, T. Sato, S. Takagi, T. Ikeshoji, S. Orimo, Fast Lithium-Ion Conduction in Atom-Deficient *closo*-Type Complex Hydride Solid Electrolytes, *Chem. Mater.* 30 (2018) 386–391. <https://doi.org/10.1021/acs.chemmater.7b03986>.
- [21] W.S. Tang, M. Matsuo, H. Wu, V. Stavila, A. Unemoto, S.I. Orimo, T.J. Udovic, Stabilizing lithium and sodium fast-ion conduction in solid polyhedral-borate salts at device-relevant temperatures, *Energy Storage Mater.* 4 (2016) 79–83. <https://doi.org/10.1016/j.ensm.2016.03.004>.
- [22] W.S. Tang, K. Yoshida, A. V. Soloninin, R. V. Skoryunov, O.A. Babanova, A. V. Skripov, M. Dimitrievska, V. Stavila, S.I. Orimo, T.J. Udovic, Stabilizing Superionic-Conducting Structures via Mixed-Anion Solid Solutions of Monocarba-*closo*-borate Salts, *ACS Energy Lett.* 1 (2016) 659–664. <https://doi.org/10.1021/acsenergylett.6b00310>.
- [23] L. Duchêne, R.S. Kühnel, D. Rentsch, A. Remhof, H. Hagemann, C. Battaglia, A highly stable sodium solid-state electrolyte based on a dodeca/deca-borate equimolar mixture, *Chem. Commun.* 53 (2017) 4195–4198. <https://doi.org/10.1039/c7cc00794a>.
- [24] M. Brighi, F. Murgia, Z. Łodziana, P. Schouwink, A. Wołczyk, R. Černý, A mixed anion hydroborate/carba-hydroborate as a room temperature Na-ion solid electrolyte, *J. Power Sources.* 404 (2018) 7–12. <https://doi.org/10.1016/j.jpowsour.2018.09.085>.
- [25] Y.S. Choi, Y.S. Lee, D.J. Choi, K.H. Chae, K.H. Oh, Y.W. Cho, Enhanced Li ion conductivity in LiBH<sub>4</sub>-Al<sub>2</sub>O<sub>3</sub> mixture via interface engineering, *J. Phys. Chem. C.* 121 (2017) 26209–26215. <https://doi.org/10.1021/acs.jpcc.7b08862>.
- [26] V. Gulino, L. Barberis, P. Ngene, M. Baricco, P.E. De Jongh, Enhancing Li-ion conductivity in LiBH<sub>4</sub>-based solid electrolytes by adding various nanosized oxides, *ACS Appl. Energy Mater.* 3 (2020) 4941–4948. <https://doi.org/10.1021/acsaem.9b02268>.
- [27] W.S. Tang, M. Dimitrievska, V. Stavila, W. Zhou, H. Wu, A.A. Talin, T.J. Udovic, Order-disorder transitions and superionic conductivity in the sodium *nido*-undeca(carba)borates, *Chem. Mater.* 29 (2017) 10496–10509.



- <https://doi.org/10.1021/acs.chemmater.7b04332>.
- [28] S.H. Payandeh, D. Rentsch, Z. Łodziana, R. Asakura, L. Bigler, R. Černý, C. Battaglia, A. Remhof, *Nido*-Hydroborate-Based Electrolytes for All-Solid-State Lithium Batteries, *Adv. Funct. Mater.* 31 (2021) 2010046. <https://doi.org/10.1002/adfm.202010046>.
- [29] S. Payandeh, R. Asakura, P. Avramidou, D. Rentsch, Ł. Zbigniew, C. Radovan, A. Remhof, C. Battaglia, *Nido*-Borate/*Closo*-Borate Mixed-Anion Electrolytes for All-Solid-State Batteries, *Chem. Mater.* 32 (2020) 1101–1110. <https://doi.org/10.1021/acs.chemmater.9b03933>.
- [30] S. Kim, H. Oguchi, N. Toyama, T. Sato, S. Takagi, T. Otomo, D. Arunkumar, N. Kuwata, J. Kawamura, S. Orimo, A complex hydride lithium superionic conductor for high-energy-density all-solid-state lithium metal batteries, *Nat. Commun.* 10 (2019) 1–9. <https://doi.org/10.1038/s41467-019-09061-9>.
- [31] R. Asakura, D. Reber, L. Duchêne, S. Payandeh, A. Remhof, H. Hagemann, C. Battaglia, 4 V Room-Temperature All-Solid-State Sodium Battery Enabled By a Passivating Cathode/Hydroborate Solid Electrolyte Interface, *Energy Environ. Sci.* 13 (2020) 5048–5058. <https://doi.org/10.1039/d0ee01569e>.
- [32] F. Murgia, M. Brighi, R. Černý, Electrochemistry Communications Room-temperature-operating Na solid-state battery with complex hydride as electrolyte, *Electrochem. Commun.* 106 (2019) 106534. <https://doi.org/10.1016/j.elecom.2019.106534>.
- [33] R. Kurmelovs, ‘Gone ballistic’: lithium price rockets nearly 500% in a year amid electric vehicle rush, *Guard.* (2022). <https://www.theguardian.com/australia-news/2022/feb/09/gone-ballistic-lithium-price-rockets-nearly-500-in-a-year-amid-electric-vehicle-rush> (accessed May 5, 2022).
- [34] S. Yang, F. Zhang, H. Ding, P. He, H. Zhou, Lithium Metal Extraction from Seawater, *Joule.* 2 (2018) 1648–1651. <https://doi.org/10.1016/j.joule.2018.07.006>.
- [35] B.L. Ellis, L.F. Nazar, Sodium and sodium-ion energy storage batteries, *Curr. Opin. Solid State Mater. Sci.* 16 (2012) 168–177. <https://doi.org/10.1016/j.cossms.2012.04.002>.
- [36] Y. Zhao, K.R. Adair, X. Sun, Recent developments and insights into the understanding of Na metal anodes for Na-metal batteries Yang, *Energy Environ. Sci.* 11 (2018) 2673–2695. <https://doi.org/10.1039/C8EE01373J>.
- [37] S. Xin, Y.X. Yin, Y.G. Guo, L.J. Wan, A high-energy room-temperature sodium-sulfur battery, *Adv. Mater.* 26 (2014) 1261–1265. <https://doi.org/10.1002/adma.201304126>.

- [38] J. He, A. Bhargav, W. Shin, A. Manthiram, Stable Dendrite-Free Sodium-Sulfur Batteries Enabled by a Localized High-Concentration Electrolyte, *J. Am. Chem. Soc.* 143 (2021) 20241–20248. <https://doi.org/10.1021/jacs.1c08851>.
- [39] A. Hepp, R. Labbow, F. Reiß, A. Schulz, A. Villinger, Carba-*closo*-dodecaborates – synthesis, structure, and energetics, *Eur. J. Inorg. Chem.* 2018 (2018) 2905–2914. <https://doi.org/10.1002/ejic.201800219>.
- [40] J. Pecyna, I. Rončević, J. Michl, Insertion of Carbenes into Deprotonated *nido*-Undecaborane,  $B_{11}H_{13}(2-)$ , *Molecules*. 24 (2019) 3779. <https://doi.org/10.3390/molecules24203779>.
- [41] A. Bergamaschi, A. Cervellino, R. Dinapoli, F. Gozzo, B. Henrich, I. Johnson, P. Kraft, A. Mozzanica, B. Schmitt, X. Shi, The MYTHEN detector for X-ray powder diffraction experiments at the Swiss Light Source, *J. Synchrotron Radiat.* 17 (2010) 653–668. <https://doi.org/10.1107/S0909049510026051>.
- [42] A.A. Coelho, *TOPAS* and *TOPAS-Academic*: An optimization program integrating computer algebra and crystallographic objects written in C++: An, *J. Appl. Crystallogr.* 51 (2018) 210–218. <https://doi.org/10.1107/S1600576718000183>.
- [43] B.R.S. Hansen, M. Paskevicius, M. Jørgensen, T.R. Jensen, Halogenated Sodium-*closo*-Dodecaboranes as Solid-State Ion Conductors, *Chem. Mater.* 29 (2017) 3423–3430. <https://doi.org/10.1021/acs.chemmater.6b04797>.
- [44] A. Gradišek, M. Krnel, M. Paskevicius, B.R.S. Hansen, T.R. Jensen, J. Dolinšek, Reorientational Motions and Ionic Conductivity in  $(NH_4)_2B_{10}H_{10}$  and  $(NH_4)_2B_{12}H_{12}$ , *J. Phys. Chem. C*. 122 (2018) 17073–17079. <https://doi.org/10.1021/acs.jpcc.8b04605>.
- [45] R. Asakura, L. Duchêne, R.S. Kühnel, A. Remhof, H. Hagemann, C. Battaglia, Electrochemical Oxidative Stability of Hydroborate-Based Solid-State Electrolytes, *ACS Appl. Energy Mater.* 2 (2019) 6924–6930. <https://doi.org/10.1021/acsaem.9b01487>.
- [46] M. Wang, L. Ouyang, M. Zeng, J. Liu, C. Peng, H. Shao, M. Zhu, Magnesium borohydride hydrolysis with kinetics controlled by ammoniate formation, *Int. J. Hydrogen Energy*. 44 (2019) 7392–7401. <https://doi.org/10.1016/j.ijhydene.2019.01.209>.
- [47] X. Luo, Exploring Novel Methods for Enhancing Ionic Conductivities of Complex Borohydrides (Li, Na, K and Mg), Master Thesis, University of New South Wales, 2019.
- [48] D. Schubert, Boron Oxides, Boric Acid, and Borates, in: *Kirk-Othmer Encycl. Chem. Technol.*, 2011: pp. 1–68.

- [49] H.J. Bleif, H. Dachs, Crystalline modifications and structural phase transitions of NaOH and NaOD, *Acta Crystallogr. Sect. A.* **A38** (1982) 470–476. <https://doi.org/10.1107/S0567739482001028>.
- [50] R.W.G. Wyckoff, *Crystal Structures - Volume 1*, 2nd ed., Interscience Publishers, New York, 1963.
- [51] A. Vaitkus, A. Merkys, S. Gražulis, Validation of the Crystallography Open Database using the Crystallographic Information Framework, *J. Appl. Crystallogr.* **54** (2021) 661–672. <https://doi.org/10.1107/S1600576720016532>.
- [52] M. Quirós, S. Gražulis, S. Girdzijauskaitė, A. Merkys, A. Vaitkus, Using SMILES strings for the description of chemical connectivity in the Crystallography Open Database, *J. Cheminform.* **10** (2018) 1–17. <https://doi.org/10.1186/s13321-018-0279-6>.
- [53] A. Merkys, A. Vaitkus, J. Butkus, M. Okulič-Kazarinas, V. Kairys, S. Gražulis, *COD::CIF::Parser*: An error-correcting CIF parser for the Perl language, *J. Appl. Crystallogr.* **49** (2016) 292–301. <https://doi.org/10.1107/S1600576715022396>.
- [54] S. Gražulis, A. Merkys, A. Vaitkus, M. Okulič-Kazarinas, Computing stoichiometric molecular composition from crystal structures, *J. Appl. Crystallogr.* **48** (2015) 85–91. <https://doi.org/10.1107/S1600576714025904>.
- [55] S. Graulis, D. Chateigner, R.T. Downs, A.F.T. Yokochi, M. Quirós, L. Lutterotti, E. Manakova, J. Butkus, P. Moeck, A. Le Bail, Crystallography Open Database - An open-access collection of crystal structures, *J. Appl. Crystallogr.* **42** (2009) 726–729. <https://doi.org/10.1107/S0021889809016690>.
- [56] S. Gražulis, A. Daškevič, A. Merkys, D. Chateigner, L. Lutterotti, M. Quirós, N.R. Serebryanaya, P. Moeck, R.T. Downs, A. Le Bail, Crystallography Open Database (COD): An open-access collection of crystal structures and platform for world-wide collaboration, *Nucleic Acids Res.* **40** (2012) 420–427. <https://doi.org/10.1093/nar/gkr900>.
- [57] M.R. Hansen, G.K.H. Madsen, H.J. Jakobsen, J. Skibsted, Refinement of borate structures from  $^{11}\text{B}$  MAS NMR spectroscopy and density functional theory calculations of  $^{11}\text{B}$  electric field gradients, *J. Phys. Chem. A.* **109** (2005) 1989–1997. <https://doi.org/10.1021/jp045767i>.
- [58] M.R. Hansen, T. Vosegaard, H.J. Jakobsen, J. Skibsted,  $^{11}\text{B}$  chemical shift anisotropies in borates from  $^{11}\text{B}$  MAS, MQMAS, and single-crystal NMR spectroscopy, *J. Phys. Chem.*

- A. 108 (2004) 586–594. <https://doi.org/10.1021/jp030939h>.
- [59] S. Kroeker, J.F. Stebbins, Three-coordinated boron-11 chemical shifts in borates, *Inorg. Chem.* 40 (2001) 6239–6246. <https://doi.org/10.1021/ic010305u>.
- [60] B. Liu, A. Rose, N. Zhang, Y.Y. Hu, M. Ma, Efficient Co-Nanocrystal-Based Catalyst for Hydrogen Generation from Borohydride, *J. Phys. Chem. C.* 121 (2017) 12610–12616. <https://doi.org/10.1021/acs.jpcc.7b03094>.
- [61] C. Lang, Y. Jia, J. Liu, H. Wang, L. Ouyang, M. Zhu, X. Yao, NaBH<sub>4</sub> regeneration from NaBO<sub>2</sub> by high-energy ball milling and its plausible mechanism, *Int. J. Hydrogen Energy.* 42 (2017) 13127–13135. <https://doi.org/10.1016/j.ijhydene.2017.04.014>.
- [62] M. Bishop, N. Shahid, J. Yang, A.R. Barron, Determination of the mode and efficacy of the cross-linking of guar by borate using MAS <sup>11</sup>B NMR of borate cross-linked guar in combination with solution <sup>11</sup>B NMR of model systems, *Dalt. Trans.* (2004) 2621–2634. <https://doi.org/10.1039/b406952h>.
- [63] R.K. Momii, N.H. Nachtrieb, Nuclear Magnetic Resonance Study Of Borate-polyborate Equilibria In Aqueous Solution, *Inorg. Chem.* 6 (1967) 1189–1192. <https://doi.org/10.1021/ic50052a026>.
- [64] M. Paskevicius, M.P. Pitt, C.J. Webb, D.A. Sheppard, U. Filsø, E.M. Gray, C.E. Buckley, In-Situ X-ray Diffraction Study of  $\gamma$ -Mg(BH<sub>4</sub>)<sub>2</sub> Decomposition, *J. Phys. Chem. C.* 116 (2012) 15231–15240. <https://doi.org/10.1021/jp302898k>.
- [65] H.E. Gottlieb, G. Graczyk-Millbrandt, G.G.A. Inglis, A. Nudelman, D. Perez, Y. Qian, L.E. Shuster, H.F. Sneddon, R.J. Upton, Development of GSK's NMR guides-a tool to encourage the use of more sustainable solvents, *Green Chem.* 18 (2016) 3867–3878. <https://doi.org/10.1039/c6gc00446f>.
- [66] H.E. Gottlieb, V. Kotlyar, A. Nudelman, NMR Chemical Shifts of Common Laboratory Solvents as Trace Impurities, *J. Org. Chem.* 62 (1997) 7512–7515. <https://doi.org/10.1021/jo971176v>.
- [67] N. Verdal, J.H. Her, V. Stavila, A. V. Soloninin, O.A. Babanova, A. V. Skripov, T.J. Udovic, J.J. Rush, Complex high-temperature phase transitions in Li<sub>2</sub>B<sub>12</sub>H<sub>12</sub> and Na<sub>2</sub>B<sub>12</sub>H<sub>12</sub>, *J. Solid State Chem.* 212 (2014) 81–91. <https://doi.org/10.1016/j.jssc.2014.01.006>.
- [68] W. Dirk, P. Paetzold, Dodecahydro-*nido*-undecaborate [B<sub>11</sub>H<sub>12</sub>]<sup>3-</sup>, *Z. Anorg. Allg. Chem.* 627 (2001) 2615–2618. [https://doi.org/10.1002/1521-3749\(200112\)627:12<2615::AID-ZAAC2615>3.0.CO;2-M](https://doi.org/10.1002/1521-3749(200112)627:12<2615::AID-ZAAC2615>3.0.CO;2-M).

- [69] O. Volkov, P. Paetzold, The chemistry of the undecaborates, *J. Organomet. Chem.* 680 (2003) 301–311. [https://doi.org/10.1016/S0022-328X\(03\)00460-1](https://doi.org/10.1016/S0022-328X(03)00460-1).
- [70] M. Matsuo, S. Kuromoto, T. Sato, H. Oguchi, H. Takamura, S.I. Orimo, Sodium ionic conduction in complex hydrides with  $[\text{BH}_4]^-$  and  $[\text{NH}_2]^-$  anions, *Appl. Phys. Lett.* 100 (2012) 2–6. <https://doi.org/10.1063/1.4716021>.
- [71] T.J. Udovic, M. Matsuo, A. Unemoto, N. Verdál, V. Stavila, A. V. Skripov, J.J. Rush, H. Takamura, S.I. Orimo, Sodium superionic conduction in  $\text{Na}_2\text{B}_{12}\text{H}_{12}$ , *Chem. Commun.* 50 (2014) 3750–3752. <https://doi.org/10.1039/c3cc49805k>.
- [72] Y. Sadikin, M. Brighi, P. Schouwink, R. Černý, Superionic Conduction of Sodium and Lithium in Anion-Mixed Hydroborates  $\text{Na}_3\text{BH}_4\text{B}_{12}\text{H}_{12}$  and  $(\text{Li}_{0.7}\text{Na}_{0.3})_3\text{BH}_4\text{B}_{12}\text{H}_{12}$ , *Adv. Energy Mater.* 5 (2015) 1501016. <https://doi.org/10.1002/aenm.201501016>.
- [73] Y. Bai, X. Wang, X. Zhang, H. Shu, X. Yang, B. Hu, Q. Wei, H. Wu, Y. Song, The kinetics of Li-ion deintercalation in the Li-rich layered  $\text{Li}_{1.12}[\text{Ni}_{0.5}\text{Co}_{0.2}\text{Mn}_{0.3}]_{0.89}\text{O}_2$  studied by electrochemical impedance spectroscopy and galvanostatic intermittent titration technique, *Electrochim. Acta.* 109 (2013) 355–364. <https://doi.org/10.1016/j.electacta.2013.06.134>.
- [74] C. Song, W. Wang, H. Peng, Y. Wang, C. Zhao, H. Zhang, Q. Tang, J. Lv, X. Du, Y. Dou, Improving the electrochemical performance of  $\text{LiNi}_{0.80}\text{Co}_{0.15}\text{Al}_{0.05}\text{O}_2$  in lithium ion batteries by  $\text{LiAlO}_2$  surface modification, *Appl. Sci.* 8 (2018) 378. <https://doi.org/10.3390/app8030378>.
- [75] A. V. Soloninin, M. Dimitrievska, R. V. Skoryunov, O.A. Babanova, A. V. Skripov, W.S. Tang, V. Stavila, S.I. Orimo, T.J. Udovic, Comparison of Anion Reorientational Dynamics in  $\text{MCB}_9\text{H}_{10}$  and  $\text{M}_2\text{B}_{10}\text{H}_{10}$  ( $\text{M} = \text{Li}, \text{Na}$ ) via Nuclear Magnetic Resonance and Quasielastic Neutron Scattering Studies, *J. Phys. Chem. C.* 121 (2017) 1000–1012. <https://doi.org/10.1021/acs.jpcc.6b09113>.
- [76] L. He, H. Lin, H.F. Li, Y. Filinchuk, J. Zhang, Y. Liu, M. Yang, Y. Hou, Y. Deng, H.W. Li, H. Shao, L. Wang, Z. Lu,  $\text{Na}_3\text{NH}_2\text{B}_{12}\text{H}_{12}$  as high performance solid electrolyte for all-solid-state Na-ion batteries, *J. Power Sources.* 396 (2018) 574–579. <https://doi.org/10.1016/j.jpowsour.2018.06.054>.
- [77] A. Berger, C.E. Buckley, M. Paskevicius, Synthesis of *closo*- $\text{CB}_{11}\text{H}_{12}$ -Salts Using Common Laboratory Reagents, *Inorg. Chem.* 60 (2021) 14744–14751. <https://doi.org/10.1021/acs.inorgchem.1c01896>.

- [78] V. Lacivita, Y. Wang, S.H. Bo, G. Ceder, Ab initio investigation of the stability of electrolyte/electrode interfaces in all-solid-state Na batteries, *J. Mater. Chem. A*. 7 (2019) 8144–8155. <https://doi.org/10.1039/c8ta10498k>.
- [79] Z. Lu, F. Ciucci, Metal Borohydrides as Electrolytes for Solid-State Li, Na, Mg, and Ca Batteries: A First-Principles Study, *Chem. Mater.* 29 (2017) 9308–9319. <https://doi.org/10.1021/acs.chemmater.7b03284>.
- [80] Z. Wen, Y. Hu, X. Wu, J. Han, Z. Gu, Main challenges for high performance NAS battery: Materials and interfaces, *Adv. Funct. Mater.* 23 (2013) 1005–1018. <https://doi.org/10.1002/adfm.201200473>.
- [81] B. Lee, E. Paek, D. Mitlin, S.W. Lee, Sodium Metal Anodes: Emerging Solutions to Dendrite Growth, *Chem. Rev.* 119 (2019) 5416–5460. <https://doi.org/10.1021/acs.chemrev.8b00642>.
- [82] L. Duchêne, D.H. Kim, Y.B. Song, S. Jun, R. Moury, A. Remhof, H. Hagemann, Y.S. Jung, C. Battaglia, Crystallization of *closo*-borate electrolytes from solution enabling infiltration into slurry-casted porous electrodes for all-solid-state batteries, *Energy Storage Mater.* 26 (2020) 543–549. <https://doi.org/10.1016/j.ensm.2019.11.027>.
- [83] K. Niitani, S. Ushiroda, H. Kuwata, H.N. Ohata, Y. Shimo, M. Hozumi, T. Matsunaga, S. Nakanishi, Hard Carbon Anode with a Sodium Carborane Electrolyte for Fast-Charging All-Solid-State Sodium-Ion Batteries, *ACS Energy Lett.* 7 (2022) 145–149. <https://doi.org/10.1021/acsenergylett.1c02307>.
- [84] C. Zhou, S. Bag, V. Thangadurai, Engineering Materials for Progressive All-Solid-State Na Batteries, *ACS Energy Lett.* 3 (2018) 2181–2198. <https://doi.org/10.1021/acsenergylett.8b00948>.
- [85] R.P. Rao, H. Chen, L.L. Wong, S. Adams,  $\text{Na}_{3+x}\text{M}_x\text{P}_{1-x}\text{S}_4$  ( $\text{M} = \text{Ge}^{4+}, \text{Ti}^{4+}, \text{Sn}^{4+}$ ) enables high rate all-solid-state Na-ion batteries  $\text{Na}_{2+2\delta}\text{Fe}_{2-\delta}(\text{SO}_4)_3 | \text{Na}_{3+x}\text{M}_x\text{P}_{1-x}\text{S}_4 | \text{Na}_2\text{Ti}_3\text{O}_7$ , *J. Mater. Chem. A*. 5 (2017) 3377–3388. <https://doi.org/10.1039/c6ta09809f>.

# CHAPTER 6

## Conclusions and Directions for Future Work

---

The increasing global warming effects around the world are becoming more evident and severe. During summer 2019 - 2020, Australia faced some of the worst bushfire seasons in history, which burned more than 20% of its forests with the consequent death of millions of animals. In 2021, a severe heat wave reached Canada and the US killing over one hundred people. Recently, the summer in Europe started earlier and has caused wildfires, temperature records broken and more than 2,000 human deaths in Spain and Portugal. These are just some examples of the consequences of the greenhouse gases emission related to the excessive burning of fossil fuels. Moreover, fossil fuels have a limited supply, and they are feedstock for the production of plastic, lubricants and other consumables, which make their replacement as the main source of energy urgent.

Renewable energy is seen as the most promising alternative to fossil fuels as the main energy source to reduce global warming impacts, however its intermittency has still hindered our independency on fossil fuels. Batteries could be used as energy storage devices, however the current state-of-the-art batteries, e.g. liquid-based Li-ion batteries, present high costs, safety problems and incompatibility with electrode materials that can generate batteries with increased energy density. This brings the need for the development of new energy storage devices, such as solid-state batteries, that have the potential to overcome these issues. Research on solid-state lithium batteries is thriving due to the increased energy density that could be achieved, owing to the high theoretical capacity ( $3,860 \text{ mAh g}^{-1}$ ) and low redox potential ( $-3.04 \text{ V}$  vs. standard hydrogen electrode) of the Li metal anode. However, due to the growing demand and price of lithium, potassium (K) and, especially, sodium (Na)-ion solid-state batteries have been considered as promising alternatives, as they are more abundant and cheaper metals than Li.

In this research, it was demonstrated that metal-alkali *nido*-boranes have strong potential to be used as solid-state electrolytes for the next generation of batteries. In chapter 3, the synthesis of hydrated  $\text{LiB}_{11}\text{H}_{14}\cdot(\text{H}_2\text{O})_n$ ,  $\text{NaB}_{11}\text{H}_{14}\cdot(\text{H}_2\text{O})_n$  and anhydrous  $\text{KB}_{11}\text{H}_{14}$  was optimised and/or elucidated for the first time.  $\text{LiB}_{11}\text{H}_{14}\cdot(\text{H}_2\text{O})_n$  and  $\text{NaB}_{11}\text{H}_{14}\cdot(\text{H}_2\text{O})_n$  exhibit a disordered polymorphic cubic structure ( $Fm\bar{3}m$ ) at room temperature (RT) with high ionic conductivity properties. Metal boranes usually undergo a polymorphic structural transition at high temperatures (HT) assuming a disordered structure with superionic conductivity. It is theorised that the presence of water in the crystal structure of  $\text{LiB}_{11}\text{H}_{14}\cdot(\text{H}_2\text{O})_n$  and  $\text{NaB}_{11}\text{H}_{14}\cdot(\text{H}_2\text{O})_n$  may be responsible for the stabilisation of the disordered cubic structure,



which leads to enhanced ionic conductivity. They present the highest ionic conductivity at RT when compared to other Li and Na single-anion boron-hydrogen materials reported so far.  $\text{KB}_{11}\text{H}_{14}$  also presents similar or even higher ionic conductivity properties when compared to other potassium boron-hydrogen salts. This may be due to the fact that *nido*-boranes also possess a large size anion, as well as *closo*-boranes, and high dynamics, which coupled with the defects present in the structure, facilitate cation migration. The mechanical modification applied to all three samples,  $\text{LiB}_{11}\text{H}_{14}\cdot(\text{H}_2\text{O})_n$ ,  $\text{NaB}_{11}\text{H}_{14}\cdot(\text{H}_2\text{O})_n$  and  $\text{KB}_{11}\text{H}_{14}$ , did not significantly enhance their ionic conductivity properties, neither stabilised the HT  $\text{KB}_{11}\text{H}_{14}$  polymorph at RT. Perhaps another approach for the improvement of their ionic conductivity could be used, such as anion-mixtures, or chemical modification of the anion.  $\text{LiB}_{11}\text{H}_{14}\cdot(\text{H}_2\text{O})_n$  and  $\text{NaB}_{11}\text{H}_{14}\cdot(\text{H}_2\text{O})_n$  also exhibited relatively high electrochemical stability, 2.1 V vs.  $\text{Li}^+/\text{Li}$  and 2.6 V vs.  $\text{Na}^+/\text{Na}$ , respectively. Due to the high ionic conductivity presented by  $\text{NaB}_{11}\text{H}_{14}\cdot(\text{H}_2\text{O})_n$  at RT ( $1.1 \times 10^{-3} \text{ S cm}^{-1}$ ), battery tests should be considered for this salt as a solid-state electrolyte for future work. A detailed study with the use of different cathode materials, such as  $\text{NaCrO}_2$  or  $\text{Na}_2\text{C}_6\text{O}_6$ , and anode materials, like Na-metal, hard carbon and  $\text{Na}_2\text{Ti}_3\text{O}_7$ , could be performed. Interfacial studies between SSE/electrode are also important for future battery applications in order to reduce dendrite formation and to improve battery performance.

In chapter 4, salts of  $\text{LiB}_{11}\text{H}_{14}$  containing different water contents in their structure, as well as the anhydrous version, were prepared through a facile approach and with the use of common laboratory reactants. It was found that  $\text{LiB}_{11}\text{H}_{14}\cdot 2\text{H}_2\text{O}$  is a new class of ionic liquid, as it melts near 70 °C, and it can be used as a wetting agent to improve interfacial contact between Li/SSE in batteries.  $\alpha\text{-LiB}_{11}\text{H}_{14}\cdot(\text{H}_2\text{O})_n$  ( $n < 2$ ) assumes a disordered polymorphic structure ( $Ia\bar{3}d$ ) at  $\approx 70$  °C with superionic conductivity, whereas the anhydrous  $\text{LiB}_{11}\text{H}_{14}$  undergoes an order-disordered polymorphic transition at  $\approx 110$  °C. This stabilisation of the HT polymorph at a lower temperature observed for the sample  $\alpha\text{-LiB}_{11}\text{H}_{14}\cdot(\text{H}_2\text{O})_n$ , when compared to anhydrous  $\text{LiB}_{11}\text{H}_{14}$ , may be a result of the presence of water in the crystal structure. The amount of coordinated water in the crystal structure completely changes the properties of the *nido*-borane salts. The coordination of metal-boranes with other solvents should be considered in future work as a strategy to possibly improve the ionic conductivity of the material. Due to the liquid-like ionic conductivity properties observed for  $\alpha\text{-LiB}_{11}\text{H}_{14}\cdot(\text{H}_2\text{O})_n$  at temperatures higher than 60 °C and to an electrochemical stability of 2.8 V vs.  $\text{Li}^+/\text{Li}$ , galvanostatic cycling experiments against Li metal, battery tests using  $\text{TiS}_2$  as the cathode, and interfacial

improvements between SSE/Li were conducted. It was observed that the assembly of batteries in a Swagelok-type cell can promote a better interfacial contact between SSE/electrode than a coin cell. The application of  $\text{LiB}_{11}\text{H}_{14}\cdot 2\text{H}_2\text{O}$  or liquid electrolyte 1.0 M  $\text{LiPF}_6$  EC/DMC ( $v/v = 50/50$ ) at their interfaces Li/SSE also promoted a better interfacial contact by reducing the magnitude of the overpotential. Solid-liquid hybrid batteries with the use of a liquid electrolyte at the interface Li/SSE demonstrated good performance with the use of  $\text{TiS}_2$  as the cathode, however when the ionic liquid  $\text{LiB}_{11}\text{H}_{14}\cdot 2\text{H}_2\text{O}$  was applied to both interfaces, the performance of the battery decreased significantly. This may be due to a low stability between liquid  $\text{LiB}_{11}\text{H}_{14}\cdot 2\text{H}_2\text{O}$  and  $\text{TiS}_2$ . The use of  $\text{LiB}_{11}\text{H}_{14}\cdot 2\text{H}_2\text{O}$  or liquid electrolyte as a wetting agent should be assessed in future studies with other boron-hydrogen materials as SSE for improvement of the interfacial contact. This can be more effective than the application of an external stack pressure for practical applications. Further chemical or mechanical modification of  $\alpha\text{-LiB}_{11}\text{H}_{14}\cdot (\text{H}_2\text{O})_n$ , or anion-mixture, should be investigated as potential approaches for stabilisation of the HT polymorph with increased ionic conductivity at RT. Battery tests could also be performed with the use of other types of cathode materials, such as sulphur-carbon composite or oxide cathodes.

In chapter 5, the synthesis of  $\text{Na}_2\text{B}_{11}\text{H}_{13}$  and the mixed-anion solid-solution  $\text{Na}_{11}(\text{B}_{11}\text{H}_{14})_3(\text{B}_{11}\text{H}_{13})_4$  was demonstrated through a facile wet-chemistry approach. Similar to other metal-boranes,  $\text{Na}_2\text{B}_{11}\text{H}_{13}$  undergoes an order-disordered polymorphic transition at high temperature to a cubic structure ( $Pm\bar{3}n$ ), which enhances its ionic conductivity. The formation of the mixed-anion solid-solution could partially stabilise the HT  $\text{Na}_2\text{B}_{11}\text{H}_{13}$  polymorph at room temperature, which increases the ionic conductivity of  $\text{Na}_{11}(\text{B}_{11}\text{H}_{14})_3(\text{B}_{11}\text{H}_{13})_4$  to  $4.7 \times 10^{-5} \text{ S cm}^{-1}$ , higher than its counterparts  $\text{NaB}_{11}\text{H}_{14}$  ( $2 \times 10^{-6} \text{ S cm}^{-1}$ ) and  $\text{Na}_2\text{B}_{11}\text{H}_{13}$  ( $2.5 \times 10^{-7} \text{ S cm}^{-1}$ ) at 30 °C. This confirms that the strategy of mixing different boron-hydrogen anions can be a successful approach to enhance ionic conductivity properties of boranes as solid-state electrolytes. It was observed that compounds containing  $\text{Na}_2\text{B}_{11}\text{H}_{13}$  are more thermally stable than compounds purely formed by  $\text{NaB}_{11}\text{H}_{14}$ , which may be related to the lattice energy of the former being higher. Therefore mixing  $\text{Na}_2\text{B}_{11}\text{H}_{13}$  with other boranes with lower decomposition temperature can be a strategy to enhance thermal stability of the composite. However, the electrochemical stability of  $\text{Na}_2\text{B}_{11}\text{H}_{13}$  against Na metal (2.1 V vs.  $\text{Na}^+/\text{Na}$ ) is lower than the one observed for  $\text{NaB}_{11}\text{H}_{14}$  (2.6 V vs.  $\text{Na}^+/\text{Na}$ ). Na-S batteries exhibit a working voltage between 1.78 – 2.08 V, which makes  $\text{Na}_2\text{B}_{11}\text{H}_{13}$  or

$\text{Na}_{11}(\text{B}_{11}\text{H}_{14})_3(\text{B}_{11}\text{H}_{13})_4$  a suitable solid-state electrolyte. Other types of anode materials, such as hard carbon and  $\text{Na}_2\text{Ti}_3\text{O}_7$ , could also be assessed in order to investigate their electrochemical stability.

In conclusion, different metal-alkali-boranes had their synthetic process optimised using facile and low cost wet-chemistry techniques throughout the course of this research. Some reported modifications of the metal-boranes were used in an attempt to enhance their ionic conductivity properties. Coordination of the salt with water and formation of a mixed-anion solid-solution seem to be the most successful approaches. Despite the presence of water in the crystal structure, hydrated  $\text{LiB}_{11}\text{H}_{14}$  and  $\text{NaB}_{11}\text{H}_{14}$  exhibit electrochemical stability against Li and Na metals, respectively, and improved ionic conductivity, which make them promising candidates to be used as solid-state electrolytes for the next generation of batteries. The research of metal-boranes as solid-state electrolytes should be continued as they show promising features for practical applications.

# APPENDIX A

## DFT Calculations for $B_{11}H_{14}^-$ and $B_{11}H_{13}OH^-$

---

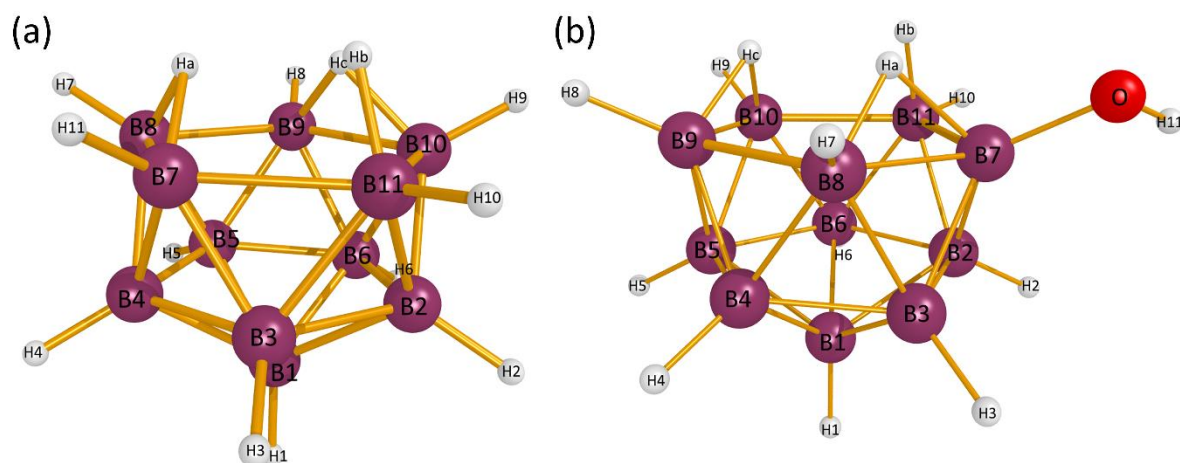


**Figure A.1** Calculated structure of (a)  $B_{11}H_{14}^-$  and (b)  $B_{11}H_{13}OH^-$ . Boron atoms are violet spheres; H atoms are white spheres; O atom is red sphere.

**Table A.1** Calculated bond distances and angles for  $B_{11}H_{14}^-$  at B31LYP/aug-cc-pvdz level of theory.

Atoms	Bond distance (Å)	Atoms	Bond Angles (°)
B1 – B3	1.779	B1 – B2 – B10	110.49
B1 – B4	1.790	B1 – B2 – B11	111.17
B1 – H1	1.197	B1 – B2 – H2	121.16
B2 – B1	1.779	B1 – B3 – B11	111.17
B2 – B10	1.746	B1 – B3 – H3	121.15
B2 – B11	1.793	B1 – B4 – H4	119.98
B2 – B3	1.817	B1 – B5 – H5	125.56
B2 – H2	1.198	B1 – B6 – B10	108.03
B3 – H3	1.198	B1 – B6 – H6	119.98
B4 – B3	1.789	B2 – B1 – B4	110.01
B4 – H4	1.198	B2 – B1 – H1	121.15
B5 – B1	1.779	B2 – B10 – H9	125.04
B5 – B4	1.785	B2 – B10 – Hc	129.32
B5 – B6	1.785	B2 – B11 – H10	112.43
B5 – B8	1.760	B2 – B11 – Hb	128.77

B5 – B9	1.760	B2 – B3 – B4	108.36
B5 – H5	1.198	B2 – B3 – H3	120.57
B6 – B1	1.790	B2 – B6 – H6	122.31
B6 – B10	1.789	B3 – B1 – H1	121.15
B6 – B2	1.789	B3 – B11 – H10	112.42
B6 – H6	1.198	B3 – B11 – Hb	128.71
B7 – B3	1.746	B3 – B2 – B10	112.03
B7 – B4	1.789	B3 – B2 – H2	120.56
B7 – B8	1.860	B3 – B4 – H4	122.30
B7 – H11	1.196	B3 – B7 – H11	125.03
B7 – Ha	1.354	B3 – B7 – Ha	129.34
B8 – B4	1.778	B4 – B1 – H1	120.20
B8 – H7	1.199	B4 – B3 – B11	116.45
B8 – Ha	1.285	B4 – B3 – H3	121.51
B9 – B10	1.860	B4 – B5 – H5	120.68
B9 – B6	1.778	B4 – B7 – H11	125.74
B9 – H8	1.199	B4 – B7 – Ha	101.41
B9 – Hc	1.285	B4 – B8 – H7	123.04
B10 – H9	1.197	B4 – B8 – Ha	104.94
B10 – Hc	1.354	B5 – B1 – B2	106.64
B11 – B3	1.793	B5 – B1 – B3	106.64
B11 – H10	1.204	B5 – B1 – H1	123.56
B11 – Hb	1.211	B5 – B4 – B3	105.95
		B5 – B4 – H4	122.54
		B5 – B6 – B10	108.60
		B5 – B6 – B2	105.95
		B5 – B6 – H6	122.54
		B5 – B8 – H7	122.84
		B5 – B8 – Ha	130.40
		B5 – B9 – B10	106.58
		B5 – B9 – H8	122.85

	B5 - B9 - Hc	130.38
	B6 - B1 - B3	110.01
	B6 - B1 - B4	110.65
	B6 - B1 - H1	120.20
	B6 - B10 - H9	125.74
	B6 - B10 - Hc	101.42
	B6 - B2 - B11	116.45
	B6 - B2 - B3	108.37
	B6 - B2 - H2	121.52
	B6 - B5 - B4	111.09
	B6 - B5 - H5	120.69
	B6 - B9 - H8	123.05
	B6 - B9 - Hc	104.94
	B7 - B3 - B1	110.48
	B7 - B3 - B11	68.15
	B7 - B3 - B2	112.03
	B7 - B3 - H3	119.17
	B7 - B4 - B1	108.03
	B7 - B4 - B5	108.60
	B7 - B4 - H4	121.95
	B7 - B8 - B5	106.58
	B7 - B8 - H7	123.09
	B8 - B4 - B1	108.46
	B8 - B4 - B3	108.06
	B8 - B4 - H4	122.22
	B8 - B5 - B1	109.79
	B8 - B5 - B6	114.66
	B8 - B5 - B9	67.33
	B8 - B5 - H5	114.93
	B8 - B7 - B3	106.35
	B8 - B7 - H11	122.52

	B9 – B10 – B2	106.35
	B9 – B10 – H9	122.51
	B9 – B5 – B1	109.79
	B9 – B5 – B4	114.66
	B9 – B5 – H5	114.94
	B9 – B6 – B1	108.46
	B9 – B6 – B2	108.05
	B9 – B6 – H6	122.23
	B10 – B2 – H2	119.17
	B10 – B6 – H6	121.95
	B10 – B9 – H8	123.09
	B11 – B2 – B10	68.16
	B11 – B2 – H2	115.02
	B11 – B3 – H3	115.03
	H8 – B9 – Hc	105.06
	H11 – B7 – Ha	104.23
	Ha – B8 – H7	105.06
	Hb – B11 – H10	107.19
	Hc – B10 – H9	104.24

**Table A.2** Calculated bond distances and angles for  $B_{11}H_{13}OH^-$  at B31LYP/aug-cc-pvdz level of theory.

Atoms	Bond distance (Å)	Atoms	Bond Angles (°)
B1 – B2	1.784	B1 – B2 – B11	110.92
B1 – B3	1.776	B1 – B2 – B7	110.76
B1 – B4	1.778	B1 – B2 – H2	120.56
B1 – B5	1.793	B1 – B3 – B7	109.03
B1 – B6	1.781	B1 – B3 – B8	109.22
B1 – H2	1.197	B1 – B3 – H3	120.79
B2 – B11	1.805	B1 – B4 – B8	109.75
B2 – B3	1.795	B1 – B4 – B9	109.74



B2 – B6	1.813	B1 – B4 – H4	125.78
B2 – B7	1.749	B1 – B5 – B10	108.51
B2 – H2	1.202	B1 – B5 – B9	108.18
B3 – B4	1.776	B1 – B5 – H5	119.51
B3 – B7	1.794	B1 – B6 – B10	110.67
B3 – B8	1.781	B1 – B6 – B11	112.23
B3 – H3	1.198	B1 – B6 – H6	120.78
B4 – B5	1.783	B2 – B1 – B4	106.48
B4 – B8	1.768	B2 – B1 – B5	109.79
B4 – B9	1.760	B2 – B11 – H10	111.86
B4 – H4	1.198	B2 – B11 – Hb	124.65
B5 – B10	1.778	B2 – B3 – B4	106.10
B5 – B6	1.791	B2 – B3 – B8	107.55
B5 – B9	1.780	B2 – B3 – H3	121.93
B5 – H5	1.198	B2 – B6 – B10	112.89
B6 – B10	1.743	B2 – B6 – B5	108.57
B6 – B11	1.781	B2 – B6 – H6	120.13
B6 – H6	1.198	B2 – B7 – B8	105.98
B7 – B8	1.863	B2 – B7 – Ha	126.22
B7 – Ha	1.404	B2 – B7 – O	127.25
B7 – Hb		B3 – B1 – B5	110.77
B7 – O	1.409	B3 – B1 – B6	110.27
B8 – H7	1.198	B3 – B2 – B11	117.34
B8 – Ha	1.266	B3 – B2 – B6	107.96
B9 – B10	1.856	B3 – B2 – H2	120.53
B9 – B11	1.294	B3 – B4 – B5	111.23
B9 – H8	1.198	B3 – B4 – B9	114.79
B10 – H2	1.197	B3 – B4 – H4	120.14
B10 – Hc	1.341	B3 – B7 – Ha	100.01
B11 – H10	1.206	B3 – B7 – O	127.87
B11 – Hb	1.207	B3 – B8 – H7	122.18

O - H11	0.962	B3 - B8 - Ha	106.65
		B4 - B1 - B6	106.42
		B4 - B3 - B7	109.43
		B4 - B3 - H3	123.80
		B4 - B5 - B10	109.20
		B4 - B5 - B6	105.74
		B4 - B5 - H5	122.13
		B4 - B8 - B7	106.71
		B4 - B8 - H7	122.11
		B4 - B8 - Ha	129.36
		B4 - B9 - B10	106.77
		B4 - B9 - H8	122.72
		B4 - B9 - Hc	130.73
		B5 - B10 - H9	125.34
		B5 - B10 - Hc	102.17
		B5 - B4 - B8	115.21
		B5 - B4 - H4	120.98
		B5 - B6 - B11	116.83
		B5 - B6 - H6	121.63
		B5 - B9 - H8	123.45
		B5 - B9 - Hc	104.12
		B6 - B10 - B9	106.17
		B6 - B10 - H9	125.38
		B6 - B10 - Hc	128.31
		B6 - B11 - H10	112.07
		B6 - B11 - Hb	132.50
		B6 - B2 - B7	113.62
		B6 - B2 - H2	121.15
		B6 - B5 - B9	107.40
		B6 - B5 - H5	122.66
		B7 - B2 - B11	70.37

	B7 – B2 – H2	117.98
	B7 – B3 – H3	119.45
	B7 – B8 – H7	122.71
	B8 – B3 – H3	121.72
	B8 – B4 – B9	67.56
	B8 – B4 – H4	114.25
	B8 – B7 – O	121.98
	B9 – B10 – H9	122.69
	B9 – B4 – H4	115.22
	B9 – B5 – H5	122.84
	B10 – B5 – H5	121.86
	B10 – B6 – H6	118.96
	B10 – B9 – H8	122.81
	B11 – B2 – H2	115.82
	B11 – B6 – B10	68.69
	B11 – B6 – H6	114.32
	H1 – B1 – B2	121.19
	H1 – B1 – B3	120.00
	H1 – B1 – B4	123.89
	H1 – B1 – B5	120.23
	H1 – B1 – B6	121.09
	H7 – B8 – Ha	106.44
	H10 – B11 – Hb	107.71
	Hc – B10 – H9	104.58
	Hc – B9 – H8	105.05
	O – B7 – Ha	104.66

**Table A.3** Optimised atomic coordinates for  $B_{11}H_{14}^-$  at B31LYP/aug-cc-pvdz level of theory.

B	-1.56331	0.50444	-0.80203
B	0.00038	-1.5354	0.54625
B	-0.97547	-1.25756	-0.89188

B	0.97591	-1.25703	-0.89199
B	1.47225	-0.53083	0.65324
B	0.90827	1.16649	0.67459
B	0.00012	-0.07742	1.56505
B	-1.47191	-0.53146	0.6534
B	-0.00038	1.72421	-0.76662
B	-0.90867	1.16616	0.67474
B	1.56312	0.50505	-0.80215
H	-2.56885	0.87492	-1.33412
H	-0.96679	-0.28229	-1.72861
H	0.00056	-2.66496	0.94604
H	-1.59608	-2.12762	-1.43427
H	1.59679	-2.12671	-1.43471
H	0.9664	-0.28149	-1.72855
H	2.45399	-0.8867	1.24023
H	1.51707	2.02123	1.2516
H	0.00015	-0.10643	2.76199
H	-2.45346	-0.88772	1.24048
H	-0.00132	1.26493	-1.8868
H	-0.00067	2.92321	-0.8737
H	-1.5178	2.02055	1.25193
H	2.56846	0.87582	-1.33442

**Table A.4** Optimised atomic coordinates for  $B_{11}H_{13}OH^-$  at B31LYP/aug-cc-pvdz level of theory.

B	0.86891	-0.09122	1.51075
H	1.2593	-0.12378	2.64195
B	-0.61776	0.79208	1.07138
B	-0.58295	-1.00238	1.0458
B	0.99884	-1.45481	0.37785
B	2.03862	-0.02353	0.15401
B	1.00678	1.3905	0.53285

B	-1.49924	-0.05975	-0.17546
B	-0.417	1.64758	-0.50521
H	-1.25005	1.37849	1.90832
B	-0.43541	-1.51269	-0.65441
H	-1.17865	-1.65912	1.85104
B	1.31452	-0.8513	-1.24517
H	1.47123	-2.52769	0.62433
B	1.35599	1.00029	-1.12934
H	3.21336	-0.04703	0.38614
H	1.46336	2.39361	1.00112
O	-2.89074	-0.04974	-0.3941
H	0.74982	0.09968	-1.91714
H	-0.81622	2.78425	-0.45327
H	-0.73708	1.19458	-1.57769
H	-0.89219	-2.54607	-1.05217
H	-0.95801	-0.59677	-1.35477
H	1.95268	-1.46586	-2.05186
H	1.98977	1.68099	-1.88238
H	-3.2978	0.65874	0.11389

**Table A.5** NPA charge and  $^{11}\text{B}$  NMR spectroscopy chemical shift (ppm) analysis for  $\text{B}_{11}\text{H}_{14}^-$  and  $\text{B}_{11}\text{H}_{13}\text{OH}^-$  calculated at the B31LYP/aug-cc-pvdz level of theory.

Atom	NPA Charge		Mulliken Charge	
	$\text{B}_{11}\text{H}_{14}^-$	$\text{B}_{11}\text{H}_{13}\text{OH}^-$	$\text{B}_{11}\text{H}_{14}^-$	$\text{B}_{11}\text{H}_{13}\text{OH}^-$
B1	-0.130	-0.123	-1.853	-1.910
B2	-0.203	-0.270	-1.078	-1.494
B3	-0.203	-0.214	-1.080	-1.908
B4	-0.189	-0.192	-1.587	-0.460
B5	-0.192	-0.201	-0.376	-1.566
B6	-0.189	-0.206	-1.587	-0.975
B7	0.000	0.613	-2.554	1.132

B8	-0.147	-0.192	-2.835	-3.290
B9	-0.147	-0.122	-2.835	-2.878
B10	0.000	-0.022	-2.555	-2.674
B11	-0.308	-0.303	-2.800	-2.961
H1	0.032	0.032	1.484	1.517
H2	0.039	0.038	1.479	1.467
H3	0.039	0.037	1.479	1.492
H4	0.032	0.046	1.453	1.488
H5	0.044	0.034	1.431	1.423
H6	0.032	0.041	1.453	1.474
H7	0.025	0.032	1.639	1.634
H8	0.025	0.023	1.639	1.678
H9	0.010	0.013	1.653	1.659
H10	0.039	0.034	1.608	1.607
H11	0.010	0.495	1.653	0.185
Ha	0.127	0.117	1.115	1.080
Hb	0.124	0.101	0.936	0.955
Hc	0.127	0.128	1.115	1.134
O	-	-0.938	-	-0.812

**Table A.6** Observed and calculated  $^{11}\text{B}$  NMR chemical shifts (ppm) for  $\text{B}_{11}\text{H}_{14}^-$  calculated at the B31LYP/aug-cc-pvdz level of theory. Solvent is  $\text{CD}_3\text{CN}$ .

Atoms	$\text{B}_{11}\text{H}_{14}^-$	
	Observed	Calculated
B1	-14.2	-10.9
B2-6	-16.8	-18.4
B7-11	-16.0	-13.2

**Table A.7** Observed and calculated  $^{11}\text{B}$  NMR chemical shifts (ppm) for  $\text{B}_{11}\text{H}_{13}\text{OH}^-$  calculated at the B31LYP/aug-cc-pvdz level of theory. Solvent is  $\text{CD}_3\text{CN}$ .

Atoms	$\text{B}_{11}\text{H}_{13}\text{OH}^-$		
	Observed <sup>a</sup>	Observed [1]	Calculated <sup>a</sup>
B1	-14.2	-14.1	-12.4
B2, B3	-23.3	-22.9	-23.6
B4, B6	-10.7	-11.0	-11.8
B5	-40.0	-39.3	-40.6
B7	18.8	18.0	20.6
B8, B11	-29.1	-28.9	-27.2
B9, B10	-9.6	-9.7	-8.1

<sup>a</sup>This work.

## REFERENCE

- [1] O. Volkov, K. Radacki, P. Paetzold, X. Zheng, Dodecahydro-*closo*-undecaborate [ $\text{B}_{11}\text{H}_{12}$ ]<sup>-</sup>, *Zeitschrift Für Anorg. Und Allg. Chemie.* 627 (2001) 1185–1191. [https://doi.org/10.1002/1521-3749\(200106\)627:6<1185::AID-ZAAC1185>3.0.CO;2-F](https://doi.org/10.1002/1521-3749(200106)627:6<1185::AID-ZAAC1185>3.0.CO;2-F).

# APPENDIX B

## Co-author Attribution Statement

---



**Chapter 3:** D. H. P. Souza, K.T. Møller, S.A. Moggach, T.D. Humphries, A.M. D'Angelo, C.E. Buckley, M. Paskevicius, Hydrated Alkali-B<sub>11</sub>H<sub>14</sub> Salts as Potential Solid-State Electrolytes, *J. Mater. Chem. A*. 9 (2021) 15027–15037. <https://doi.org/10.1039/d1ta01551f>.

Name	Conception and design	Experiments conduction and data acquisition	Data processing and analysis	Interpretation and discussion	Manuscript writing and revision
Diego H. P. Souza	X	X	X	X	X
I acknowledge that these represent my contribution to the above research output and I have approved the final version. Signature:					
Kasper T. Møller	X	X			X
I acknowledge that these represent my contribution to the above research output and I have approved the final version. Signature:					
Stephen A. Moggach		X	X		X
I acknowledge that these represent my contribution to the above research output and I have approved the final version. Signature:					
Terry D. Humphries		X	X	X	X
I acknowledge that these represent my contribution to the above research output and I have approved the final version. Signature:					
Anita M. D'Angelo		X			
I acknowledge that these represent my contribution to the above research output and I have approved the final version. Signature:					
Craig E. Buckley					X
I acknowledge that these represent my contribution to the above research output and I have approved the final version. Signature:					
Mark Paskevicius	X			X	X

I acknowledge that these represent my contribution to the above research output and I have approved the final version.

Signature:

**Chapter 4:** D. H. P. Souza, T.D. Humphries, Y. Liu, A. Gradišek, A.M. D'Angelo, C.E. Buckley, M. Paskevicius, Hydrated Lithium *nido*-Boranes for Solid-Liquid Hybrid Batteries, *Sustain. Energy Fuels*. 6 (2022) 4614–4625. <https://doi.org/10.1039/D2SE00843B>.

Name	Conception and design	Experiments conduction and data acquisition	Data processing and analysis	Interpretation and discussion	Manuscript writing and revision
Diego H. P. Souza	X	X	X	X	X
I acknowledge that these represent my contribution to the above research output and I have approved the final version. Signature:					
Terry D. Humphries				X	X
I acknowledge that these represent my contribution to the above research output and I have approved the final version. Signature:					
Yu Liu	X				
I acknowledge that these represent my contribution to the above research output and I have approved the final version. Signature:					
Anton Gradišek		X	X	X	X
I acknowledge that these represent my contribution to the above research output and I have approved the final version. Signature:					
Anita M. D'Angelo		X			
I acknowledge that these represent my contribution to the above research output and I have approved the final version. Signature:					
Craig E. Buckley					X
I acknowledge that these represent my contribution to the above research output and I have approved the final version. Signature:					
Mark Paskevicius	X			X	X

I acknowledge that these represent my contribution to the above research output and I have approved the final version.

Signature:

**Chapter 5:** D. H. P. Souza, A.M. D'Angelo, T.D. Humphries, C.E. Buckley, M. Paskevicius, Na<sub>2</sub>B<sub>11</sub>H<sub>13</sub> and Na<sub>11</sub>(B<sub>11</sub>H<sub>14</sub>)<sub>3</sub>(B<sub>11</sub>H<sub>13</sub>)<sub>4</sub> as Potential Solid-State Electrolytes for Na-Ion Batteries, *Dalton Trans.* 51 (2022) 13848–13857. <https://doi.org/10.1039/D2DT01943D>.

Name	Conception and design	Experiments conduction and data acquisition	Data processing and analysis	Interpretation and discussion	Manuscript writing and revision
Diego H. P. Souza	X	X	X	X	X
I acknowledge that these represent my contribution to the above research output and I have approved the final version. Signature:					
Anita M. D'Angelo		X			
I acknowledge that these represent my contribution to the above research output and I have approved the final version. Signature:					
Terry D. Humphries					X
I acknowledge that these represent my contribution to the above research output and I have approved the final version. Signature:					
Craig E. Buckley					X
I acknowledge that these represent my contribution to the above research output and I have approved the final version. Signature:					
Mark Paskevicius	X			X	X
I acknowledge that these represent my contribution to the above research output and I have approved the final version. Signature:					

# APPENDIX C

## Permission from the Copyright Owners

---

Permission to use articles in thesis.

### Hydrated alkali-B<sub>11</sub>H<sub>14</sub> salts as potential solid-state electrolytes

D. H. P. Souza, K. T. Møller, S. A. Moggach, T. D. Humphries, A. M. D'Angelo, C. E. Buckley and M. Paskevicius, *J. Mater. Chem. A*, 2021, **9**, 15027 DOI: 10.1039/D1TA01551F

To request permission to reproduce material from this article, please go to the [Copyright Clearance Center request page](#).

If you are **an author contributing to an RSC publication, you do not need to request permission** provided correct acknowledgement is given.

If you are **the author of this article, you do not need to request permission to reproduce figures and diagrams** provided correct acknowledgement is given. If you want to reproduce the whole article in a third-party publication (excluding your thesis/dissertation for which permission is not required) please go to the [Copyright Clearance Center request page](#).

Read more about [how to correctly acknowledge RSC content](#).

### Hydrated lithium *nido*-boranes for solid-liquid hybrid batteries

D. H. P. Souza, T. D. Humphries, Y. Liu, A. Gradišek, A. M. D'Angelo, C. E. Buckley and M. Paskevicius, *Sustainable Energy Fuels*, 2022, **6**, 4614 DOI: 10.1039/D2SE00843B

To request permission to reproduce material from this article, please go to the [Copyright Clearance Center request page](#).

If you are **an author contributing to an RSC publication, you do not need to request permission** provided correct acknowledgement is given.

If you are **the author of this article, you do not need to request permission to reproduce figures and diagrams** provided correct acknowledgement is given. If you want to reproduce the whole article in a third-party publication (excluding your thesis/dissertation for which permission is not required) please go to the [Copyright Clearance Center request page](#).

Read more about [how to correctly acknowledge RSC content](#).

## $\text{Na}_2\text{B}_{11}\text{H}_{13}$ and $\text{Na}_{11}(\text{B}_{11}\text{H}_{14})_3(\text{B}_{11}\text{H}_{13})_4$ as potential solid-state electrolytes for Na-ion batteries

D. H. P. Souza, A. M. D'Angelo, T. D. Humphries, C. E. Buckley and M. Paskevicius, *Dalton Trans.*, 2022, **51**, 13848 DOI: 10.1039/D2DT01943D

To request permission to reproduce material from this article, please go to the [Copyright Clearance Center request page](#).

If you are **an author contributing to an RSC publication, you do not need to request permission** provided correct acknowledgement is given.

If you are **the author of this article, you do not need to request permission to reproduce figures and diagrams** provided correct acknowledgement is given. If you want to reproduce the whole article in a third-party publication (excluding your thesis/dissertation for which permission is not required) please go to the [Copyright Clearance Center request page](#).

Read more about [how to correctly acknowledge RSC content](#).

Permission to use cover in thesis.

## Front cover

*Sustainable Energy Fuels*, 2022, **6**, 4541 DOI: 10.1039/D2SE90067J

To request permission to reproduce material from this article, please go to the [Copyright Clearance Center request page](#).

If you are **an author contributing to an RSC publication, you do not need to request permission** provided correct acknowledgement is given.

If you are **the author of this article, you do not need to request permission to reproduce figures and diagrams** provided correct acknowledgement is given. If you want to reproduce the whole article in a third-party publication (excluding your thesis/dissertation for which permission is not required) please go to the [Copyright Clearance Center request page](#).

Read more about [how to correctly acknowledge RSC content](#).



License agreement for Figures 1.2, 1.5, and 1.6.

ELSEVIER LICENSE  
TERMS AND CONDITIONS

Sep 15, 2022

---

This Agreement between Mr. Diego Holanda Pereira de Souza ("You") and Elsevier ("Elsevier") consists of your license details and the terms and conditions provided by Elsevier and Copyright Clearance Center.

License Number	5390070289246
License date	Sep 15, 2022
Licensed Content Publisher	Elsevier
Licensed Content Publication	Renewable and Sustainable Energy Reviews
Licensed Content Title	Energy storage for electricity generation and related processes: Technologies appraisal and grid scale applications
Licensed Content Author	Maria C. Argyrou,Paul Christodoulides,Soteris A. Kalogirou
Licensed Content Date	Oct 1, 2018
Licensed Content Volume	94
Licensed Content Issue	n/a
Licensed Content Pages	18
Start Page	804
End Page	821
Type of Use	reuse in a thesis/dissertation

## License agreement for Figure 1.4.

### SPRINGER NATURE LICENSE TERMS AND CONDITIONS

Jun 21, 2022

---

This Agreement between Mr. Diego Holanda Pereira de Souza ("You") and Springer Nature ("Springer Nature") consists of your license details and the terms and conditions provided by Springer Nature and Copyright Clearance Center.

License Number	5333580775561
License date	Jun 21, 2022
Licensed Content Publisher	Springer Nature
Licensed Content Publication	Nature
Licensed Content Title	Building better batteries
Licensed Content Author	M. Armand et al
Licensed Content Date	Feb 6, 2008
Type of Use	Thesis/Dissertation
Requestor type	academic/university or research institute
Format	print and electronic
Portion	figures/tables/illustrations
Number of figures/tables/illustrations	1
High-res required	n/a

License agreement for Figure 1.8.

**ELSEVIER LICENSE  
TERMS AND CONDITIONS**

Sep 15, 2022

---

This Agreement between Mr. Diego Holanda Pereira de Souza ("You") and Elsevier ("Elsevier") consists of your license details and the terms and conditions provided by Elsevier and Copyright Clearance Center.

License Number	5390060558787
License date	Sep 15, 2022
Licensed Content Publisher	Elsevier
Licensed Content Publication	Joule
Licensed Content Title	Electrolyte and Interface Engineering for Solid-State Sodium Batteries
Licensed Content Author	Yong Lu, Lin Li, Qiu Zhang, Zhiqiang Niu, Jun Chen
Licensed Content Date	Sep 19, 2018
Licensed Content Volume	2
Licensed Content Issue	9
Licensed Content Pages	24
Start Page	1747
End Page	1770
Type of Use	reuse in a thesis/dissertation
Portion	figures/tables/illustrations

## License agreement for Figure 1.9A.

### SPRINGER NATURE LICENSE TERMS AND CONDITIONS

Apr 28, 2022

---

This Agreement between Mr. Diego Holanda Pereira de Souza ("You") and Springer Nature ("Springer Nature") consists of your license details and the terms and conditions provided by Springer Nature and Copyright Clearance Center.

License Number	5297491142455
License date	Apr 28, 2022
Licensed Content Publisher	Springer Nature
Licensed Content Publication	Nature Reviews Materials
Licensed Content Title	Designing solid-state electrolytes for safe, energy-dense batteries
Licensed Content Author	Qing Zhao et al
Licensed Content Date	Feb 5, 2020
Type of Use	Thesis/Dissertation
Requestor type	academic/university or research institute
Format	print and electronic
Portion	figures/tables/illustrations
Number of figures/tables/illustrations	1
High-res required	no

## License agreement for Figure 1.9B.

**Structural, Chemical, and Dynamical Frustration: Origins of Superionic Conductivity in closo-Borate Solid Electrolytes**

**Author:** Kyoung E. Kweon, Joel B. Varley, Patrick Shea, et al  
**Publication:** Chemistry of Materials  
**Publisher:** American Chemical Society  
**Date:** Nov 1, 2017

Copyright © 2017, American Chemical Society

**PERMISSION/LICENSE IS GRANTED FOR YOUR ORDER AT NO CHARGE**

This type of permission/license, instead of the standard Terms and Conditions, is sent to you because no fee is being charged for your order. Please note the following:

- Permission is granted for your request in both print and electronic formats, and translations.
- If figures and/or tables were requested, they may be adapted or used in part.
- Please print this page for your records and send a copy of it to your publisher/graduate school.
- Appropriate credit for the requested material should be given as follows: "Reprinted (adapted) with permission from {COMPLETE REFERENCE CITATION}. Copyright (YEAR) American Chemical Society." Insert appropriate information in place of the capitalized words.
- One-time permission is granted only for the use specified in your RightsLink request. No additional uses are granted (such as derivative works or other editions). For any uses, please submit a new request.

If credit is given to another source for the material you requested from RightsLink, permission must be obtained from that source.

[BACK](#) [CLOSE WINDOW](#)

## License agreement for Figure 1.11.

**Li Penetration in Ceramic Solid Electrolytes: Operando Microscopy Analysis of Morphology, Propagation, and Reversibility**

**Author:** Eric Kazyak, Regina Garcia-Mendez, William S. LePage, Asma Sharafi, Andrew L. Davis, Adrian J. Sanchez, Kuan-Hung Chen, Catherine Haslam, Jeff Sakamoto, Neil P. Dasgupta  
**Publication:** Matter  
**Publisher:** Elsevier  
**Date:** 1 April 2020

© 2020 The Author(s). Published by Elsevier Inc.

**Creative Commons Attribution-NonCommercial-No Derivatives License (CC BY NC ND)**

This article is published under the terms of the Creative Commons Attribution-NonCommercial-No Derivatives License (CC BY NC ND). For non-commercial purposes you may copy and distribute the article, use portions or extracts from the article in other works, and text or data mine the article, provided you do not alter or modify the article without permission from Elsevier. You may also create adaptations of the article for your own personal use only, but not distribute these to others. You must give appropriate credit to the original work, together with a link to the formal publication through the relevant DOI, and a link to the Creative Commons user license above. If changes are permitted, you must indicate if any changes are made but not in any way that suggests the licensor endorses you or your use of the work.

Permission is not required for this non-commercial use. For commercial use please continue to request permission via RightsLink.

[BACK](#) [CLOSE WINDOW](#)

## License agreement for Figure 1.10.

### SPRINGER NATURE LICENSE TERMS AND CONDITIONS

Apr 26, 2022

---

This Agreement between Mr. Diego Holanda Pereira de Souza ("You") and Springer Nature ("Springer Nature") consists of your license details and the terms and conditions provided by Springer Nature and Copyright Clearance Center.

License Number	5296281083233
License date	Apr 26, 2022
Licensed Content Publisher	Springer Nature
Licensed Content Publication	Nature Materials
Licensed Content Title	Local electronic structure variation resulting in Li 'filament' formation within solid electrolytes
Licensed Content Author	Xiaoming Liu et al
Licensed Content Date	May 31, 2021
Type of Use	Thesis/Dissertation
Requestor type	academic/university or research institute
Format	print and electronic
Portion	figures/tables/illustrations
Number of figures/tables/illustrations	1
High-res required	no

## License agreement for Figure 1.12.

### ELSEVIER LICENSE TERMS AND CONDITIONS

Jul 21, 2022

---

This Agreement between Mr. Diego Holanda Pereira de Souza ("You") and Elsevier ("Elsevier") consists of your license details and the terms and conditions provided by Elsevier and Copyright Clearance Center.

License Number	5353670788632
License date	Jul 21, 2022
Licensed Content Publisher	Elsevier
Licensed Content Publication	Energy Storage Materials
Licensed Content Title	Status and prospects of hydroborate electrolytes for all-solid-state batteries
Licensed Content Author	Léo Duchêne, Arndt Remhof, Hans Hagemann, Corsin Battaglia
Licensed Content Date	Mar 1, 2020
Licensed Content Volume	25
Licensed Content Issue	n/a
Licensed Content Pages	13
Start Page	782
End Page	794
Type of Use	reuse in a thesis/dissertation
Portion	figures/tables/illustrations

## License agreement for Figure 1.13.

### SPRINGER NATURE LICENSE TERMS AND CONDITIONS

Apr 28, 2022


---

This Agreement between Mr. Diego Holanda Pereira de Souza ("You") and Springer Nature ("Springer Nature") consists of your license details and the terms and conditions provided by Springer Nature and Copyright Clearance Center.

License Number	5297580313242
License date	Apr 28, 2022
Licensed Content Publisher	Springer Nature
Licensed Content Publication	Nature Chemistry
Licensed Content Title	Bonding with boron
Licensed Content Author	Ken Wade
Licensed Content Date	Dec 31, 1969
Type of Use	Thesis/Dissertation
Requestor type	academic/university or research institute
Format	print and electronic
Portion	figures/tables/illustrations
Number of figures/tables/illustrations	1
Will you be translating?	no



## License agreement for Figure 2.3.



**From Metal Hydrides to Metal Borohydrides**  
**Author:** Bo Richter, Jakob B. Grinderslev, Kasper T. Møller, et al  
**Publication:** Inorganic Chemistry  
**Publisher:** American Chemical Society  
**Date:** Sep 1, 2018  
*Copyright © 2018, American Chemical Society*

**PERMISSION/LICENSE IS GRANTED FOR YOUR ORDER AT NO CHARGE**


This type of permission/license, instead of the standard Terms and Conditions, is sent to you because no fee is being charged for your order. Please note the following:

- Permission is granted for your request in both print and electronic formats, and translations.
- If figures and/or tables were requested, they may be adapted or used in part.
- Please print this page for your records and send a copy of it to your publisher/graduate school.
- Appropriate credit for the requested material should be given as follows: "Reprinted (adapted) with permission from {COMPLETE REFERENCE CITATION}. Copyright {YEAR} American Chemical Society." Insert appropriate information in place of the capitalized words.
- One-time permission is granted only for the use specified in your RightsLink request. No additional uses are granted (such as derivative works or other editions). For any uses, please submit a new request.


If credit is given to another source for the material you requested from RightsLink, permission must be obtained from that source.

[BACK](#) [CLOSE WINDOW](#)

## License agreement for Figure 2.5B.



[Help](#) [Email Support](#)



**New era of synchrotron radiation: fourth-generation storage ring**  
**Author:** Seunghwan Shin  
**Publication:** AAPPS Bulletin  
**Publisher:** Springer Nature  
**Date:** Aug 30, 2021  
*Copyright © 2021, The Author(s)*

**Creative Commons**

This is an open access article distributed under the terms of the Creative Commons CC BY license, which permits unrestricted use, distribution, and reproduction in any medium, provided the original work is properly cited.

You are not required to obtain permission to reuse this article.  
To request permission for a type of use not listed, please contact [Springer Nature](#)

## License agreement for Figure 2.6.

### ELSEVIER LICENSE TERMS AND CONDITIONS

Jun 02, 2022

---

This Agreement between Mr. Diego Holanda Pereira de Souza ("You") and Elsevier ("Elsevier") consists of your license details and the terms and conditions provided by Elsevier and Copyright Clearance Center.

License Number	5320580762718
License date	Jun 02, 2022
Licensed Content Publisher	Elsevier
Licensed Content Publication	Elsevier Books
Licensed Content Title	Encyclopedia of Spectroscopy and Spectrometry
Licensed Content Author	Delphine D. Le Pevelen
Licensed Content Date	Jan 1, 2010
Licensed Content Pages	18
Start Page	2559
End Page	2576
Type of Use	reuse in a thesis/dissertation
Portion	figures/tables/illustrations
Number of figures/tables/illustrations	1
Format	both print and electronic

## License agreement for Figure 2.10.

### SPRINGER NATURE LICENSE TERMS AND CONDITIONS


Jun 08, 2022

---

This Agreement between Mr. Diego Holanda Pereira de Souza ("You") and Springer Nature ("Springer Nature") consists of your license details and the terms and conditions provided by Springer Nature and Copyright Clearance Center.

License Number	5324111478844
License date	Jun 08, 2022
Licensed Content Publisher	Springer Nature
Licensed Content Publication	Springer eBook
Licensed Content Title	Planar Interdigital Sensors and Electrochemical Impedance Spectroscopy
Licensed Content Author	Nasrin Afsarimanesh, Subhas Chandra Mukhopadhyay, Marlena Kruger
Licensed Content Date	Jan 1, 2019
Type of Use	Thesis/Dissertation
Requestor type	academic/university or research institute
Format	print and electronic
Portion	figures/tables/illustrations
Number of figures/tables/illustrations	1
Will you be translating?	no

## License agreement for Figure 2.11.


 ? Help ✉ Email Support


**Publisher:** Elsevier  
*Copyright © 1969, Elsevier*

**Creative Commons**  
This is an open access article distributed under the terms of the Creative Commons CC-BY license, which permits unrestricted use, distribution, and reproduction in any medium, provided the original work is properly cited.  
You are not required to obtain permission to reuse this article.  
To request permission for a type of use not listed, please contact Elsevier Global Rights Department.  
Are you the author of this Elsevier journal article?

© 2022 Copyright - All Rights Reserved | Copyright Clearance Center, Inc. | Privacy statement | Terms and Conditions  
Comments? We would like to hear from you. E-mail us at [customercare@copyright.com](mailto:customercare@copyright.com)

## License agreement for Figure 2.14.

 Home ? Help ✉ Email Support 👤 Sign in 👤 Create Account

 **ACS Publications**  
Most Trusted. Most Cited. Most Read.

**Toward a Fundamental Understanding of the Lithium Metal Anode in Solid-State Batteries—An Electrochemo-Mechanical Study on the Garnet-Type Solid Electrolyte Li<sub>6</sub>.25Al<sub>0.25</sub>La<sub>3</sub>Zr<sub>2</sub>O<sub>12</sub>**  
Author: Thorben Krauskopf, Hannah Hartmann, Wolfgang G. Zeier, et al  
Publication: Applied Materials  
Publisher: American Chemical Society  
Date: Apr 1, 2019  
*Copyright © 2019, American Chemical Society*

**PERMISSION/LICENSE IS GRANTED FOR YOUR ORDER AT NO CHARGE**

This type of permission/license, instead of the standard Terms and Conditions, is sent to you because no fee is being charged for your order. Please note the following:

- Permission is granted for your request in both print and electronic formats, and translations.
- If figures and/or tables were requested, they may be adapted or used in part.
- Please print this page for your records and send a copy of it to your publisher/graduate school.
- Appropriate credit for the requested material should be given as follows: "Reprinted (adapted) with permission from {COMPLETE REFERENCE CITATION}. Copyright (YEAR) American Chemical Society." Insert appropriate information in place of the capitalized words.
- One-time permission is granted only for the use specified in your RightsLink request. No additional uses are granted (such as derivative works or other editions). For any uses, please submit a new request.

If credit is given to another source for the material you requested from RightsLink, permission must be obtained from that source.

BACK CLOSE WINDOW

License agreement for Figure 2.12.



This is a License Agreement between Diego Holanda Pereira de Souza ("User") and Copyright Clearance Center, Inc. ("CCC") on behalf of the Rightsholder identified in the order details below. The license consists of the order details, the CCC Terms and Conditions below, and any Rightsholder Terms and Conditions which are included below.

All payments must be made in full to CCC in accordance with the CCC Terms and Conditions below.

Order Date	09-Jun-2022	Type of Use	Republish in a thesis/dissertation
Order License ID	1230502-1	Publisher	RSC Publishing
ISSN	1759-9679	Portion	Image/photo/illustration

#### LICENSED CONTENT

Publication Title	Analytical methods	Rightsholder	Royal Society of Chemistry
Article Title	Electrochemical impedance spectroscopy: an overview of bioanalytical applications	Publication Type	e-journal
Author/Editor	Royal Society of Chemistry (Great Britain)	Start Page	1098
Date	01/01/2009	Issue	5
Language	English	Volume	5
Country	United Kingdom of Great Britain and Northern Ireland	URL	<a href="http://www.rsc.org/Publishing/journals/AY/index.asp">http://www.rsc.org/Publishing/journals/AY/index.asp</a>

#### REQUEST DETAILS

Portion Type	Image/photo/illustration	Distribution	Worldwide
Number of images / photos / illustrations	1	Translation	Original language of publication
Format (select all that apply)	Print, Electronic	Copies for the disabled?	Yes
Who will republish the content?	Academic institution	Minor editing privileges?	Yes
Duration of Use	Life of current edition	Incidental promotional use?	No
Lifetime Unit Quantity	More than 2,000,000	Currency	AUD
Rights Requested	Main product		

#### NEW WORK DETAILS

Title	Synthesis of Metal Boranes as Solid-State Electrolytes for Next Generation Battery Applications	Institution name	Curtin University
Instructor name	Mark Paskevidius	Expected presentation date	2022-09-02

#### ADDITIONAL DETAILS

Order reference number	N/A	The requesting person / organization to appear on the license	Diego Holanda Pereira de Souza
------------------------	-----	---	--------------------------------

Every reasonable effort has been made to acknowledge the owners of copyright material. I would be pleased to hear from any copyright owner who has been omitted or incorrectly acknowledged.